Transactions of the ASME, Journal of Heat Transfer (ISSN 0022-1481) is published monthly by The American Society of Mechanical Engineers, Three Park Avenue, New York, NY 10016. Periodicals postage paid at New York, NY and additional mailing offices. POSTMASTER: Send address changes to Transactions of the ASME, Journal of Heat Transfer, c/o THE AMERICAN SOCIETY OF MECHANICAL ENGINEERS, 22 Law Drive, Box 2300, Fairfield, NJ 07007-2300. **CHANGES OF ADDRESS** must be received at Society headquarters seven weeks before they are to be effective. Please send old label and new address. **STATEMENT from By-Laws.** The Society shall not be responsible for statements or opinions advanced in papers or ... printed in its publications (B7.1, Para. 3).

Journal of Heat Transfer

Published Monthly by ASME

VOLUME 131 • NUMBER 9 • SEPTEMBER 2009

RESEARCH PAPERS

(Contents continued on inside back cover)

This journal is printed on acid-free paper, which exceeds the ANSI Z39.48-1992 specification for permanence of paper and library materials. ♾™
♻ 85% recycled content, including 10% post-consumer fibers.

Journal of Heat Transfer **Volume 131, Number 9** **SEPTEMBER 2009**

The ASME Journal of Heat Transfer is abstracted and indexed in the following:

Applied Science and Technology Index, Chemical Abstracts, Chemical Engineering and Biotechnology Abstracts (Electronic equivalent of Process and Chemical Engineering), Civil Engineering Abstracts, Compendex (The electronic equivalent of Engineering Index), Corrosion Abstracts, Current Contents, E & P Health, Safety, and Environment, Ei EncompassLit, Engineered Materials Abstracts, Engineering Index, Enviroline (The electronic equivalent of Environment Abstracts), Environment Abstracts, Environmental Engineering Abstracts, Environmental Science and Pollution Management, Fluidex, Fuel and Energy Abstracts, Index to Scientific Reviews, INSPEC, International Building Services Abstracts, Mechanical & Transportation Engineering Abstracts, Mechanical Engineering Abstracts, METADEX (The electronic equivalent of Metals Abstracts and Alloys Index), Petroleum Abstracts, Process and Chemical Engineering, Referativnyi Zhurnal, Science Citation Index, SciSearch (The electronic equivalent of Science Citation Index), Theoretical Chemical Engineering

Macro- to Microscale Boiling Heat Transfer From Metal-Graphite Composite Surfaces[1]

Wen-Jei Yang
Department of Mechanical Engineering,
University of Michigan,
Ann Arbor, MI 48109-2125
e-mail: wjyang@umich.eduf

Nengli Zhang
Ohio Aerospace Institute at NASA Glen
Research Center,
Cleveland, OH 44184

Daniel L. Vrable
Thermal Management and Materials Technology,
Del Mar, CA 92014-4217

This paper introduces a novel heat transfer enhancement surface, referred to as metal-graphite composite surface. It is comprised of high thermal conductivity graphite microfibers interspersed within a metal matrix (copper or aluminum) to enhance the bubble formation at the nucleation sites, and significantly improve the nucleate boiling heat transfer. Experiments revealed that its boiling heat transfer enhancement is comparable or in some respect even superior to the commercially available boiling heat transfer enhancement surfaces such as porous boiling surface and integral roughness surface. In addition, it does not result in any extra pressure loss and it minimizes surface fouling. Macro- to microscale heat transfer phenomena of the composite surfaces is treated. Discussions include characteristics of the surface, enhancement mechanisms, critical heat flux, boiling thermal hysteresis, bubble generation, growth and departure, and applications in electronic cooling, and under reduced gravity conditions.
[DOI: 10.1115/1.3153556]

Keywords: micrographite fiber, metal matrix, enhancement, nucleate boiling heat transfer, bubble, reduced gravity

1 Introduction

The use of commercially available boiling enhancement surfaces such as porous boiling surface (PBS) and integral roughness surface (IRS) is well known in the heat transfer community. Bergles and Chyu [1] discussed the characteristics of nucleate boiling from the PBS whose coating typically consisting of sintered, porous, metallic matrix bounded to a basic surface. Webb [2] reported studies and development of the IRS whose enhancement is formed by cold working the metal to form re-entrant nucleate sites, while Nakayama et al. [3] evaluated machined microstuds that help sustain bubble nucleation and increase the surface area available for boiling. However, the use of all these surface enhancement techniques has the negative attribute of increasing the pressure drop and losing of enhancement efficiency by the fouling of the small pores and re-entrant cavities, which can impact performance and reliability as discussed by Yang et al. [4,5]. The literature review pertaining to enhancement of boiling heat transfer performance is available, and thus is not repeated here.

This paper introduces a novel boiling heat transfer enhancement surface, referred to as metal-graphite composite surface. It consists of multiple graphite microfibers ($8-12$ μm in diameter) embedded in the matrix base of a pure metal (copper or aluminum). The pitch-based graphite fiber has a high axial thermal conductivity of about 1200 W/m K, as compared with pure copper of 401 W/m K at 300 K. The process leading to the use of intrinsic material properties (localized high thermal conductivity and nonwetting spots) integral with the composite surface to enhance nucleate boiling heat transfer was reported by Vrable [6]. Publications listed in Refs. [7–21] except Ref. [15] by the authors and their associates are included in the present paper.

2 Characteristics of Metal-Graphite Composite Surfaces

The metal-graphite composite surface consists of graphite filaments of $8-12$ μm in diameter embedded uniaxially within a metal (copper or aluminum) matrix of certain percentage area fraction. Figure 1 depicts a scanning electron microscope (SEM) photograph of the composite surface with 50% volume fraction graphite microfibers in copper matrix. Its key properties are listed in Table 1.

There are several merits of the metal-graphite composites:

(1) Through adjusting both the directionality of fibers and the volume fraction of the fibers (ϕ), the directional conductivity, coefficient of thermal expansion, and strength and stiffness can be tailored to optimize the thermal/structural performance of graphite microfiber composite.
(2) The graphite fibers act as highly efficient pin fins that perpendicularly penetrate into the heat transfer surface. Hence, they may provide an intrinsic enhancement of heat transfer, bubble generation, and its departure frequency when employed as boiling surfaces.
(3) The fiber diameter of 8 μm is comparable to the critical size for bubble nucleation sites in boiling water. It is smaller than those of pores on PBS and re-entrant cavities on IRS. Hence, each microfiber tip may act as a site activator for bubble nucleation.
(4) The local high thermal conductivity provides a more efficient conduction to or from the nucleation site.
(5) The metal-graphite composite surfaces enhance boiling heat transfer without the drawbacks that PBS and IRS suffer from, such as the pressure drop, the loss of enhancement efficiency due to fouling, and the cost of fabrication and maintenance.

This physical insight has promoted a series of experimental studies on various aspects of pool boiling heat transfer for over a decade since 1991 [4,5].

[1]Max Jakob Memorial Award paper.

Contributed by the Heat Transfer Division of ASME for publication in the JOURNAL OF HEAT TRANSFER. Manuscript received May 4, 2009; final manuscript received May 8, 2009; published online June 19, 2009. Review conducted by Yogesh Jaluria.

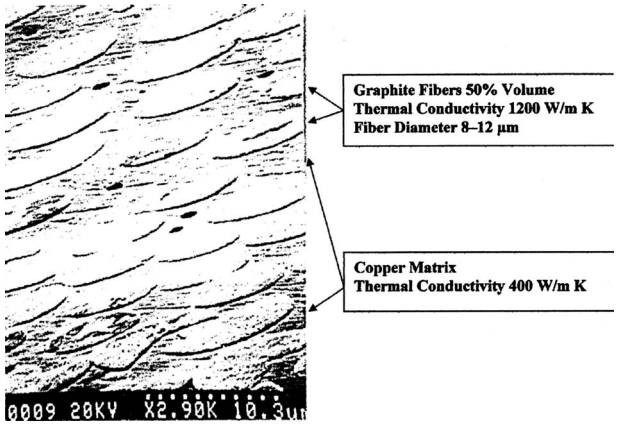

Fig. 1 Scanning electron microscope photograph of the graphite/copper boiling surface showing the 8–12 μm diameter fibers consolidated in a copper matrix

3 Pool Boiling Heat Transfer Performance and Enhancement Mechanisms

3.1 Experiments. Figure 2 illustrates the experimental apparatus used in the study. It consists of a boiling test facility, a condenser assembly, and an instrumentation system. The boiling test facility was composed of a main heater assembly, auxiliary heater, two optical windows for illumination and observation/photographing, glass sleeve, and thermocouple probes. The condenser assembly had a vapor line, a long path condenser, a Liebig condenser, a condensate collector, a condensate return line, and a cooling water tank. The test facility was monitored by an instrumentation system, which included thermocouples, a precision digital multimeter, and a computer. With the digital multimeter to control the data transfer and A/D conversion, a computer program was coded for data processing. A camera was used to record the bubble behavior during nucleate pool boiling.

Two families of composites were tested: one was a graphite-copper (Gr–Cu) composite consisting of graphite fibers in a copper matrix with graphite-fiber volume concentrations of nearly 0%, 25%, and 50%. The other was graphite aluminum (Gr–Al) composite consisting of graphite fibers in an aluminum matrix with a graphite-fiber concentration of 50%. Pure copper and aluminum surfaces were also tested for comparison. Each test piece, 2.5 cm in diameter and 1.0 cm in thickness, was placed on top of a main heater assembly to serve as a boiling surface.

Two kinds of test liquids, highly wetting fluids, such as freon 113 and *n*-pentane, and a moderately wetting fluid, water, were used. Boiling of freon 113 was up to a heat flux of 19 W/cm^2 at a maximum wall superheat of 48°C at atmospheric pressure.

Two kinds of experiments were performed: an overall boiling performance experiment and a boiling thermal hysteresis experiment (establishing the startup and restart processes). Details of experimental apparatus and procedure are available in Refs. [7,8].

Table 1 Key properties of graphite and copper at 300 K

Property	Graphite	Copper
Thermal conductivity, k (axial), W/m K	1200	401
Density, ρ, gm/cm^3	2.25	8.93
Coefficient of thermal expansion, β, K^{-1}	3×10^{-6}	17×10^{-6}
Elastic modulus, GPa (axial/transverse)	894/19	106

3.2 Pool Boiling Performance. The nucleate boiling heat transfer performance using freon 113 is shown in Fig. 3 for both the composite surface with 50% fiber volume and the pure copper surface [4,5]. It is observed that the composite surface increased the heat transfer coefficient by a factor of three to six times the pure copper surface, depending on the level of superheat. This initial experimental study validated our premise that the characteristics of the metal graphite composite could be used to enhance boiling heat transfer.

3.3 Enhancement Mechanisms. A theoretical model based on the experimental results was developed by Yang and Zhang [9] in order to better understand the mechanisms involved in the boiling heat transfer. Zhang et al. [10] and Yang et al. [11] continued to update and improve the theoretical model, as more experimental data became available for validation. A sophisticated two-tier

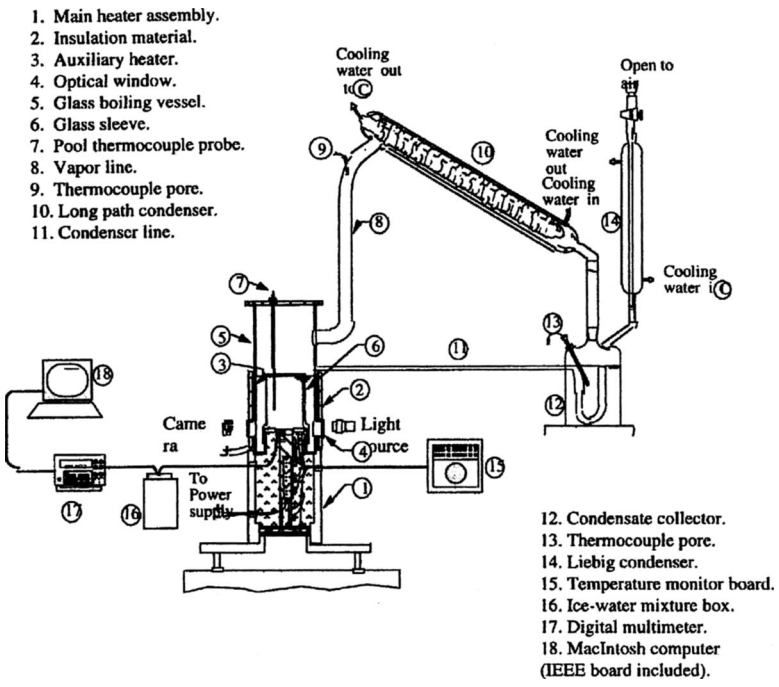

Fig. 2 Experimental test apparatus schematic

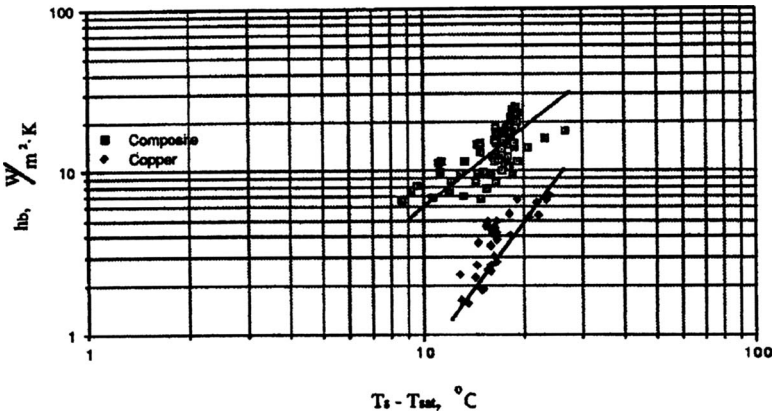

Fig. 3 Experimental data comparison between the graphite/copper (50% fiber volume) and the baseline copper boiling surfaces showing boiling heat transfer improvement of three to six times (depending on the amount of superheat) using refrigerant 113 from Yang et al. [4,5]

model divided the characteristics of the nucleate pool boiling phenomena into two distinct regions: the low or discrete bubble region and the high-heat flux or vapor mushroom region. The boiling phenomena in these two regions coupled with the composite surface provided support to the theory of explaining the mechanisms of pool boiling on the graphite-copper composite surface.

3.3.1 Effects of Varying ϕ on Boiling Performance. Figure 4 provides the boiling heat flux plotted against the wall superheat for pool boiling of refrigerant 113 on the graphite-copper composite surfaces with different graphite-fiber volume fractions [12]. Notice that $\phi=0$ corresponds to the pure copper case. The effects of ϕ continue to support the three to six times boiling heat transfer enhancement over the baseline copper surface. The experimental heat transfer data for nucleate pool boiling was correlated using Rohsenow's empirical formula as follows:

$$C_p\Delta T_{\text{sat}}/(h_{fg}\ \text{Pr}^{1.7}) = C_{\text{sf}}[(q''/\mu h_{fg})(\sigma/g\Delta\rho)^{1/2}]^{1/3} \qquad (1)$$

Here, C_p denotes the heat capacity, J/kg K; ΔT_{sat} is the coolant superheat temperature difference, °C; h_{fg} is the latent heat of vaporization, J/kg; Pr represents Prandtl number; C_{sf} is the Rohsenow surface/fluid constant; g is the gravitational acceleration, m/s^2; and $\Delta\rho$ is the saturated liquid-vapor density difference, kg/m^3. The coefficient C_{sf} depends on the heating surface-fluid combination and was found to be 0.0085, 0.0083, 0.0066, and 0.0069 for the test surfaces of pure copper, near 0%, 25%, and 50% graphite-copper composite materials, respectively.

3.4 Enhancement Mechanisms. Figure 5 presents the overall comparison of the two different composite surfaces and the baseline pure metal surfaces using pentane as the boiling liquid [13]. It is observed that the improvement of the composite surface in either a copper or aluminum matrix is significantly superior to the baseline metal surfaces with three to six times improvement.

To better understand the mechanisms for increasing the boiling performance from the composite surfaces, measurements were also made on the temperature distribution and thickness of the superheated boundary layer [14]. The superheated boundary layer thickness correlated directly with the measured boiling performance values using the approach of Marcus and Dropkin [15]. It was found (not shown) that the 25% fiber volume surface result-

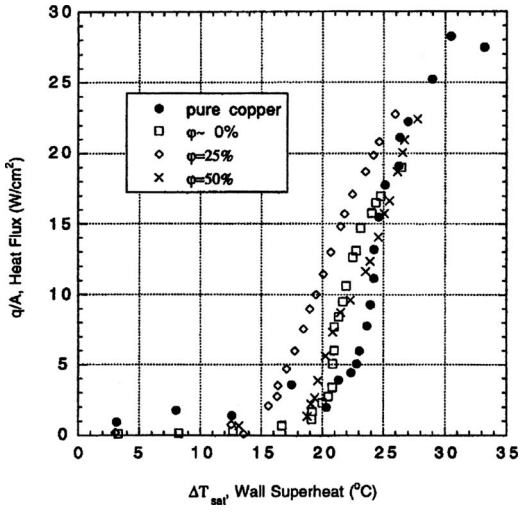

Fig. 4 Experimental Data comparison between the graphite/copper ($\phi\cong$0%, 25%, and 50% fiber volume) and the baseline copper boiling surfaces showing boiling heat transfer improvement optimum of between 25–50% using refrigerant 113 from Yang et al. [12]

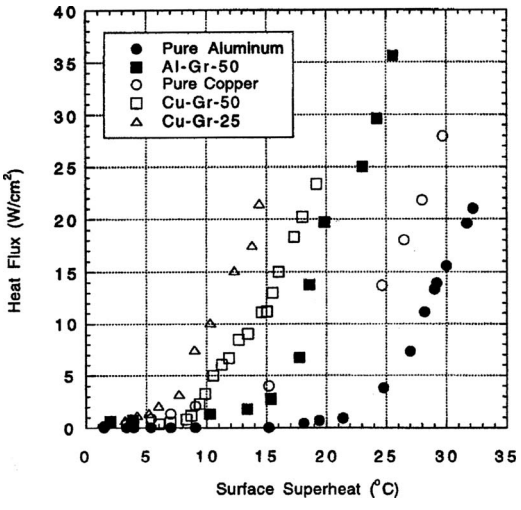

Fig. 5 Experimental data comparison between the graphite/copper (25% and 50% fiber volume), graphite/aluminum (50% fiber volume), and the baseline copper and aluminum boiling surfaces showing boiling heat transfer improvement of three to six times (depending on the amount of superheat) using *n*-pentane from Liang et al. [14]

ing in the thinnest boundary layer of 73 μm, the 50% fiber volume surface was 83 μm, and the pure copper surface was 92 μm. As bubbles are emitted from the surface at higher frequency with increasing heat flux, the increased mixing results in a thinner superheated boundary layer thickness and improving boiling performance.

4 Critical Heat Flux and Physical Model

Throughout the transition boiling regime, vapor rises into the liquid on the nodes of the Taylor waves in reference to the Rayleigh–Taylor instability (R–T I) theory. At the critical heat flux (CHF), this rising vapor forms into jets. These jets come from the graphite microfiber tips, which act as bubble nucleation sites. The basic spacing of the grid is a two-dimensional Taylor wavelength, which is the spacing of the most basic module of jets. At the peak heat flux, the Kevin–Helmholtz instability (K–H I) causes the jets to become unstable and brings about burnout. In other words, this instability predicts when the vapor velocity in the jet will reach a critical value to cause the vapor jet to cave in. The mechanisms of incipience of the CHF are considered to be due to instabilities which arise from two causes:

(i) The R–T I type is derived from the character of the equilibrium of two fluids of different densities superposed one over the other.
(ii) The K–H I type arises when two fluids of different densities are in relative motion. Both the R–T I and the K–H I demonstrate the instability of the plane interface between two fluids.

A theory [16] was developed on CHF in pool boiling by relating the R–T I to the active nucleation sites. That is, the tips of graphite fibers coincide with the nodes of the Taylor waves. Meanwhile, the K–H I is connected to the flow of bubble columns at each nucleation site. The jet velocity is directly associated with the maximum boiling heat flux. Experimental results indicated that the nucleate pool boiling curves for metal-graphite composites of different graphite microfiber concentrations congregate near the CHF of the composite for the optimum performance as the degree of superheat increases. With this particular graphite-fiber concentration known, a balance of the heat flux by the latent heat carried away in the jets when the fluid is saturated yields the maximum (i.e., critical) heat flux, as

$$\mathrm{CHF} = (\rho_v h_{fg} U_{\mathrm{vc}} \pi)/(2 \times 3^{1/2} \phi) \tag{2}$$

where U_{vc} denotes the jet (i.e., vapor flow) velocity.

5 Boiling Thermal Hysteresis

5.1 Physics of Hysteresis. Hysteresis is important and unique dynamic characteristics in two-phase systems in motion with or without rotation. In pool boiling, which produces vapor phase, the system is set in motion due to a pumping action near the heating surface induced by the departure of bubbles whose space is replaced by the surrounding liquid body. The phenomenon may be simulated using a spring-damper-mass system. However, its dynamic behavior at the same temperature overheat differs when the boiling heat flux undergoes an increasing trend, and when it undertakes a decreasing trend. Liang et al. [14] conducted a comprehensive study on boiling thermal hysteresis to determine startup/restart cycles on the heat flux versus degree of superheat in nucleate pool boiling.

To be useful as an immersion micro-electronic cooling device, it must have the good overall heat dissipation, as well as the ability to suppress thermal excursions which occur during the initiation of nucleate boiling. It is essential to eliminate or reduce boiling thermal hysteresis in order to keep surface superheat low to initiate boiling. Graphite fiber surfaces have two properties that are suitable to avoid retardation in bubble nucleation in highly wetting electronic cooling liquids. One is their poorly-wetting character for most liquids and the other is their high axial thermal conductivity.

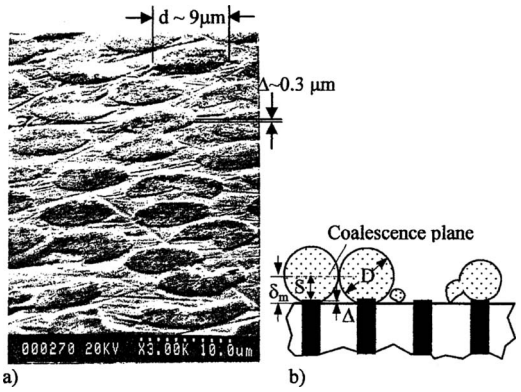

Fig. 6 Summary of boiling hysteresis on the surfaces

An experimental study was performed by Liang and Yang [13] to determine the mechanisms for the reduction in thermal hysteresis and to simulate the effects of boiling startup/restart conditions on the boiling hysteresis. Nucleation on microfiber graphite composites depends not only on the embryos of trapped vapor/gas microcavities, but also on micrographite fibers. The latter, with high thermal conductivity functioning as fins, can serve as nucleation activators and preservers during startup and restart conditions. As shown in Fig. 1, the spaces (matrix material) were filled with many low-lying grooves with the size of approximately 0.5 μm. When immersed in highly wetting liquids, these spaces might be flooded by the liquids. However, each fiber tip appears as a rugged plateau with microcavities of the correct size for boiling (0.05 to 0.1 micro according to embryo theory), which can be easily activated, forming a nuclei on each fiber tip.

(i) With a higher temperature on the fiber tips relative to the base matrix and with an easier activation mechanism, nucleation during the startup was inclined to be activated on the fiber tips at a relatively lower surface-averaged temperature. Similarly, during the cooldown processes, most cavities on the base matrix were drowned and lost their nuclei as boiling ceased. The locally high-temperature graphite-fiber tips, however, were able to sustain enough effective nuclei to act as seeds for the next process.
(ii) Another mechanism which plays a crucial role is the poorly wetting property of the graphite-fiber tips. A test on the wettability of *n*-pentane on the copper-graphite composite surfaces in a static condition indicated that (a) liquid fronts (liquid/vapor interface) with a small contact angle on the copper base flooded the cavity and expelled the vapor/gas and (b) those with large contact angle on a graphite-fiber tip preserved the vapor to seed the cavity.

5.2 Simulation Experiment on Hysteresis. The startup/restart hysteresis simulation experiment began with a stepwise heatup process from zero heat flux to a fully established nucleation state, followed by a stepwise cooldown process to a specific minimum preset power output and a subsequent restart of an increasing heat flux cycle. The minimum power output is called minimum restart heat flux (MRHF). The startup/restart hysteresis in various MRHFs is defined as the deviation between the normal boiling curve and the corresponding heatup cycle. Two different quantitative characterizations of the hysteresis are employed: hysteresis area A_{hys} and extrapolated maximum temperature overshoot $T_{\max}$. The former is defined as the area encompassed by a hysteresis cycle on a heat flux versus wall superheat plot, for example see Fig. 6 for the pure copper surface. The latter is de-

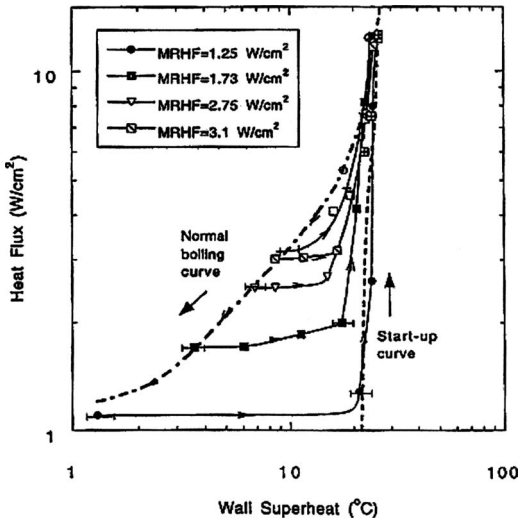

Fig. 7 (*a*) Photomicrograph (3000 times) of the copper/graphite composite surface with 50% fiber volume and (*b*) growth and coalescence of micro bubbles

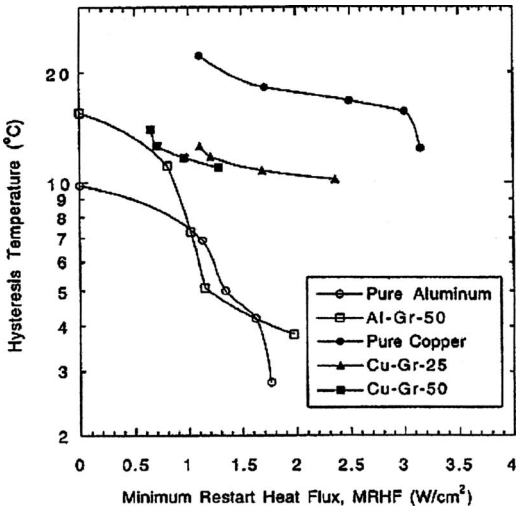

Fig. 9 Summary of boiling hysteresis on the graphite/copper composite surfaces

fined as the temperature at the intersection of the tangent to the single-phase convection curve with the nucleation boiling curve. Figure 7 presents the relationship between T_{max} and A_{hys} plotted against MRHF for the family of graphite-copper composites. It signifies that a drop of A_{hys} implies suppression in the hysteresis phenomena as the graphite-fiber concentration increase, and that a gradual decrease in T_{max} implies a gradual activation of cavities on the fiber tips. Figure 8 summarizes the boiling hysteresis temperatures on the surface. That is, the copper-based surfaces perform better in the overall heat transfer performance than the aluminum-based ones, while the reverse is true in terms of the ability to suppress thermal hysteresis.

6 Bubble Generation, Growth, and Departure

Differing from common solid surfaces, the Gr–Cu composite surfaces have a great number of poorly wetting spots formed by the graphite microfiber tips. The wettability of various liquids, even those highly wetting liquids such as freon 113, on those spots are poor. Consequently, a combination of the poorly wetting property and very high thermal conductivity of the graphite material causes embryo bubbles to be preferably formed on the microfiber tips, while some embryo bubbles occasionally generated on the copper matrix are attracted and finally swallowed up by the bubbles sitting on the graphite microfiber tips [17].

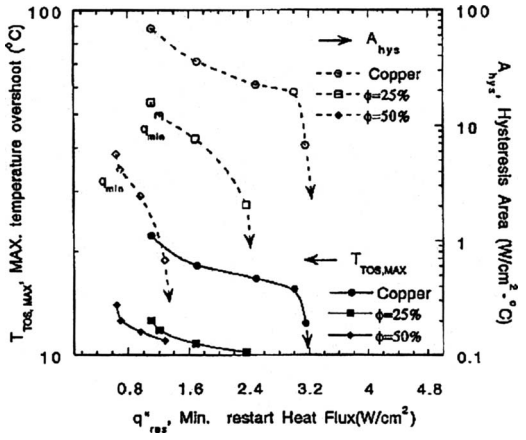

Fig. 8 Startup/restart hysteresis on the pure copper surface

6.1 Formation of Micromushrooms and a Macrobubble. Figure 9(*b*) shows the growth and coalescence of microbubbles on the fiber tip plateau Δ of about 0.3 μm, while the fiber diameter d is about 8–10 μm. Yang [7] found that the microbubbles originate from the valleys between the fiber tip plateaus instead of the fiber tips. Zhang et al. [10] found the maximum thickness of the microlayer δ_m and the average thickness of microlayer δ to be

$$\delta_m = (d/2)(\pi/4\phi - 1)^{1/2} + \Delta \tag{3}$$

and

$$\delta = (1 - \pi/6 - \phi/3)/[2(1 - \phi)][(\pi/4\phi) - 1]d + \Delta \tag{4}$$

respectively. Simple calculations yield the microlayer thicknesses at different values of ϕ listed in Table 2.

In boiling heat transfer microlayers play an essential role. Thermal energy provided by the composite surface is first conducted through the microlayers, and then delivered into micro mushrooms as latent heat by evaporation at the microlayer surface. Since the microlayers are directly connected with the bulk liquid through liquid network, the liquid evaporating off the microlayers can be immediately replenished.

6.2 Formation of Micromushrooms and Macrobubbles. The continually growing micromushrooms would eventually coalesce and merge with each other to form a larger microvapor mass, which is a macrobubble embryo. When the bubble embryo is formed from several micromushrooms, a macrolayer is created under the macrobubble embryo, connecting with the microlayers and bulk liquid through liquid network, as shown in Fig. 10. The macrobubble embryo rapidly grows and finally forms a macrobubble with a neck throat radius of r_{th} and the bottom radius of

Table 2 Microlayer thicknesses at various values of ϕ

ϕ	0.05	0.1	0.25	0.5	0.75
δ_m (μm)	17.56	12.08	6.89	3.70	1.28
δ (μm)	8.65	6.10	3.75	2.41	1.19

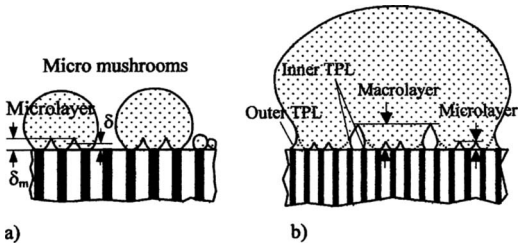

Fig. 10 Bubble formation: (*a*) formation of micromushrooms and (*b*) formation of a macro bubble

r_b whose magnitude is estimated to be 0.1–0.2 mm, as depicted in Fig. 10(*b*). The macrolayer thickness is estimated to be of the order of 0.1 mm [10].

6.3 Departure of a Macrobubble. Figure 10 depicts photographs of bubble departure during the initial stage of nucleate pool boiling in water [7]. The corresponding bubble departure diameters were determined to be about 3.6 mm on the pure copper surface in Fig. 11(*a*), and 0.3 mm on the Gr–Cu composite surface with $\phi = 25\%$ in Fig. 11(*b*). Zhang and Yang [18] developed a general model for bubble departure from a heated surface. It predicted that (i) the bubble departure radius for water on a pure copper surface is 3.2–3.7 mm, which agreed with the existing experimental data, and (ii) that for water on the Gr–Cu surfaces is 0.15–0.7 mm, which agreed with the experimental results of Zhang et al. [19]. Therefore, the model can explain the enhancement mechanism of the boiling heat transfer on the metal-graphite composite surfaces. In addition, the above analysis of the necking process has disclosed that the local heat flux at the bubble root area determines the bubble departure diameter, which diminishes with an increase in the speed of the necking process, resulting in an increased bubble departure frequency.

Recently, Chao et al. [20] developed a theory on the departure of a macrobubble. Out of three possible modes for the bubble

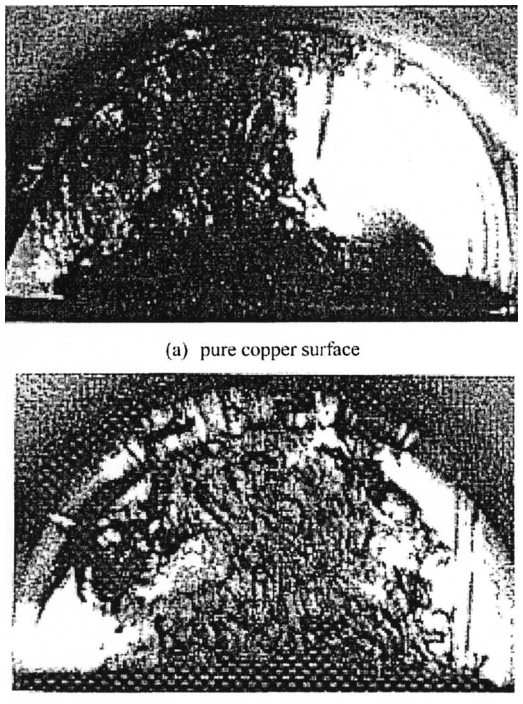

Fig. 11 Photographs of bubble departure during the incipience of nucleate pool boiling in water

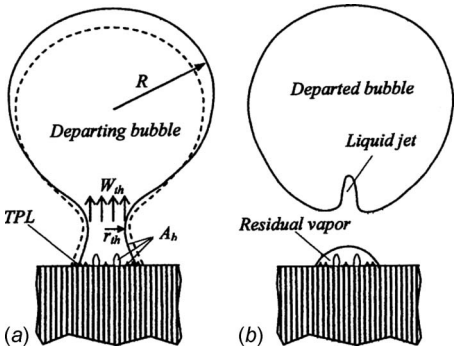

Fig. 12 Departure of a macro bubble: (*a*) contraction of throat and bottom of the departing bubble and (*b*) liquid jet in the departed bubble

necking and departure, only the timewise change in the static pressure difference applies. In such instance, the bubble neck contracts to a certain diameter and then maintains it until the bubble grows large enough to break off at the neck. Figure 12 displays the departure model of a macrobubble. Figure 12(*a*) shows the instant when the contraction rate of a three-phase line is of the same order of magnitude as that of the throat. The conservation of mass in the bubble, the pressure balance at the throat breakoff, and the force balance at the moment of bubble breakoff are combined to yield an expression for the bubble radius at departure R_d in terms of the controlling physical properties. It yields R_d to be 0.7–3.2 mm for water boiling on a pure copper surface, which agreed with the existing experimental data in Ref. [21].

Regarding the liquid jet occurring in the departed bubble, an analysis of the static pressure difference at the bubble throat yields an infinite static pressure difference because one of the two principal radii of curvature becomes infinitesimal in magnitude. This infinite pressure difference at the throat creates the liquid jet in the departed bubble, as shown in Fig. 12(*b*). After the bubble departed, it leaves a residual vapor on the composite surface after the bubble departed, which is supported by strong evaporation from the liquid network. Withstanding the action of a sudden change in the pressure difference, the residual vapor is rapidly as a new bubble.

6.4 Relevance to Enhancement Mechanisms

(i) It is the unique structure of the metal-graphite composite surfaces that creates a liquid network connected to the bulk liquid, from which an ample supply of liquid enhances evaporation at the surfaces of micro- and macrolayers, and thus fosters the development macrobubbles. An even distribution of sufficient active nucleation sites greatly reduces the thicknesses of the bubble micro- and macrolayers, resulting in increasing boiling heat transfer performance.

(ii) There exists an optimum volume fraction of the graphite fibers in the composite surfaces for the initiation of liquid supply into the microlayers.

(iii) A higher evaporation rate produces larger and larger vapor velocities and creates a negative pressure at the bubble throat, which accelerates the bubble departure with smaller departure diameters and a higher departure frequency, thus enhancing the boiling heat transfer performance.

(iv) The liquid jets created at the bubble departure also result in the enhancement of boiling heat transfer through enhancing microconvection around the new bubbles growing out of the residuals of the departed bubbles.

7 Applications

The typical range of heat transfer coefficients for various relevant fluids and cooling mechanism are illustrated in Fig. 13 [6].

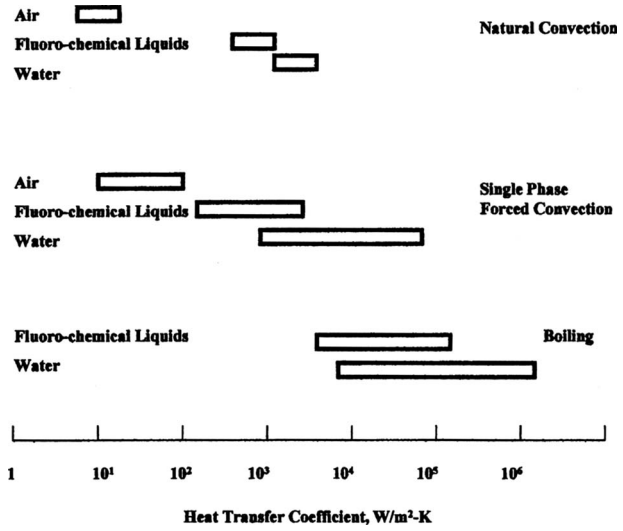

Fig. 13 Heat transfer coefficients achievable with natural convection, single-phase forced convection, and boiling for typical electronic coolants

Air is currently the most widely used coolant for electronic applications, but it will not meet the needs of the high-heat flux devices. The projected cooling requirements will transition to higher capability approaches, such as phase change (boiling) cooling. For electronic cooling applications, the boiling point of the selected coolant is typically 10–40 K below the desired chip or device operating temperature. Three potential applications of boiling heat transfer enhancement using the metal-graphite composite surfaces are anticipated

7.1 In Boiling Heat Transfer Enhancement. The metal-graphite composite surfaces can produce three to six times enhancement in pool boiling heat transfer compared with pure metal surface. In addition, these surfaces have the benefit of reduced pressure drop, less of a fouling problem, and lower costs of fabrication and maintenance compared with the commercially available enhancement surfaces such as PBS and IRS.

7.2 For Immersed Microelectronic Cooling. The study on boiling thermal hysteresis indicates that the metal-graphite composite surfaces are inherently suitable for immersed microelectronic cooling compared with other approaches. Multichip module (MCM) packaging technology, in which multiple chips are mounted and interconnected on a substrate during the wafer manufacturing process, offer tremendous advantages over traditional technology. The benefits include enhanced packaging efficiency, closer chip-to-chip spacing, improve reliability, and more miniaturization. Cooling technology for MCM packaging requires high performance two-phase systems to meet the projected heat flux levels.

7.3 Under Reduced Gravity Conditions. Three observations are generally agreed upon regarding boiling under reduced gravity environments:

(i) Bubble departure becomes more difficult and detached bubbles readily coalesce with each other.
(ii) The transition from the isolated bubble regime to the coalesced bubble regime and from the coalesced bubble regime to the vapor slug regime take place at relatively low heat fluxes.
(iii) The critical heat flux for all liquids in microgravity is considerably smaller than in normal gravity.

Zhang et al. [17] discovered two means of enhancing nucleate boiling and CHF under microgravity conditions: (i) using microconfigured metal-graphite composites as the boiling surface and (ii) using dilute aqueous solutions of long-chain alcohols as the working fluid.

Metal-graphite fiber composite surfaces are suitable as the working surface without adverse effects from the reduced gravity. The existing experimental results and a two-tier model [10] were used in deriving correlation formulas for nucleate boiling on Gr–Cu and Gr–Al composite surfaces.

Water is an ideal working fluid for boiling heat transfer in both terrestrial and microgravity environment by virtue of availability,

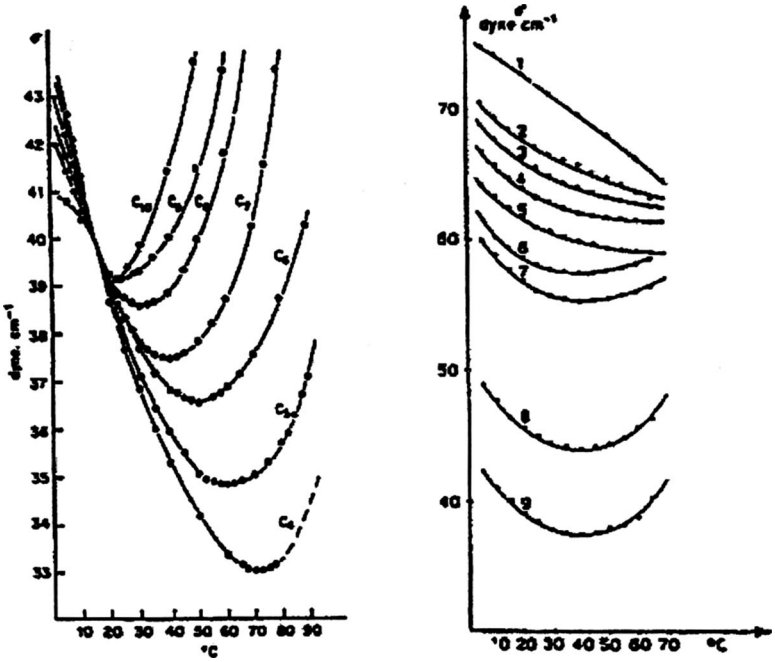

Fig. 14 Variation of the surface tension with temperature for aqueous solutions with long-chain alcohols

cost, and safety. However, due to lack of driving force for vapor detachment from the heating surface under microgravity, it suffers from significant deterioration in nucleate boiling performance and CHF with a decrease in gravity. In addition, the Marangoni flow around bubbles induced by a negative surface-tension-temperature gradient presses the bubbles onto the heating surface, resulting in an unfavorable situation for boiling performance. Using dilute aqueous solutions of long-chain alcohols as working fluids may be a good solution. Figure 14 is a plot of surface tension against temperature for a series of *n*-alcohols at concentrations with an equilibrium surface tension of 40 dyn/cm at 15°C. It shows that aqueous solution of alcohols with a chain length longer than four carbon atoms have a positive surface-tension-temperature gradient when the temperature exceeds a certain value. This surface-tension force would become the principal driving force in microgravity environments. Consequently, bubble departure from the heating surface size would be smaller in these aqueous solutions than in water, with a higher departure frequency. The character of the surface-tension-concentration gradient is useful as driving forces in microgravity environments. Correlation formulas were derived for nucleate boiling and performance equations were obtained for CHF in dilute aqueous solutions of long-chain solutions [17].

8 Perspectives

The applications of tailorable material systems to enhance and improve the thermal capability is an important new area of research that will provide the next step in high-heat flux cooling for high performance electronic applications.

References

[1] Bergles, A. E., and Chyu, M. C., 1982, "Characteristics of Nucleate Pool Boiling From Porous Metallic Coatings," ASME J. Heat Transfer, **104**, pp. 279–285.

[2] Webb, R. L., 1986, "High Performance Heat Transfer Surfaces for Boiling and Condensation," *Heat Transfer in Energy Problems*, W. J. Yang and Y. Mori, eds., Hemisphere, Washington, DC, pp. 127–132.

[3] Nakayama, W., Nakajimi, T., and Hirasawa, S. 1984, "Heat Sink Studs Having Enhanced Boiling Surfaces for Cooling of Microelectronic Components," ASME Paper No. 84-WA/HT-89.

[4] Yang, W.-J., Takizawa, H., and Vrable, D. L., 1991, "Augmented Boiling on Copper-Graphite Composite Surface," Int. J. Heat Mass Transfer, **34**(11), pp. 2751–2758.

[5] Yang, W. -J., Takizawa, H., and Vrable, D. L., 1991, "Natural Convection From Horizontal Heated Copper-Graphite Composite Surface," ASME J. Heat Transfer, **113**, pp. 1031–1033.

[6] Vrable, D. L., 2001, "Composite Material Technology to Enhance Boiling Heat Transfer Performance," Int. J. Transp. Phenom., **3**(4), pp. 395–405.

[7] Yang, G. W., 1995, "Micro- and Macro-Phenomena in Nucleate Pool Boiling on Graphite-Copper Composite Materials," Ph.D. thesis, Department of Mechanical Engineering and Applied Mechanics, University of Michigan, Ann Arbor, MI.

[8] Liang, H. S., 1997, "Nucleate Pool Boiling on Micro-Graphite-Fibers With Applications in Micro-Electronic Cooling," Ph.D. thesis, Department of Mechanical Engineering and Applied Mechanics, University of Michigan, Ann Arbor, MI.

[9] Yang, W.-J., and Zhang, N., 1992, "Boiling Performance on Non-Isothermal Surfaces," *Proceedings of the Engineering Foundation Conference on Pool and External Low Boiling*, Santa Barbara, CA, pp. 119–124.

[10] Zhang, N., Yang, W. -J., and Yang, G. W., 1992, "Two-Tier Model for Nucleate Pool Boiling on Micro Configured Composite Surfaces," Int. Commun. Heat Mass Transfer, **19**, pp. 767–779.

[11] Yang, G. W., Yang, W.-J., and Zhang, N., 1992, "Mechanisms of Nucleate Pool Boiling on Composite Surfaces," Int. Commun. Heat Mass Transfer, **19**, pp. 781–790.

[12] Yang, G. W., Liang, H. S., Yang, W.-J., and Vrable, D. L., 1996, "Nucleate Pool Boiling on Micro Graphite-Copper Composite Surfaces," ASME J. Heat Transfer, **118**, pp. 792–796.

[13] Liang, H. S., and Yang, W.-J., 1998, "Nucleate Pool Boiling Heat Transfer in a Highly Wetting Liquid on Micro-Graphite-Fiber Composite Surfaces," Int. J. Heat Mass Transfer, **41**, pp. 1993–2001.

[14] Liang, H. S., Yang, W.-J., and Vrable, D. L., 1998, "Feasibility Study of Immersion Cooling of Multi-Chip Modules on Metal-Graphite Composite Surfaces," ASME J. Heat Transfer Conference, J. S. Lee, ed., Vol. 2, pp. 547–552.

[15] Marcus, B. D., and Dropkin, D., 1965, "Measured Temperature Profiles Within the Superheated Boundary Layer Above a Horizontal Surface in Saturated Nucleate Pool Boiling of Water," ASME J. Heat Transfer, **86**, pp. 333–341.

[16] Yang, W.-J., and Zhang, N., 1999, "A Theoretical Treatment of Critical Heat Flux on Metal-Graphite Heating Surfaces," *Proceedings of the Heat Transfer Division 1999*, ASME, New York, HTD-Vol. 364-2, pp. 315–320.

[17] Zhang, N., Chao, D. F., and Yang, W.-J., 2001, "Enhancement of Nucleate Pool Boiling and Critical Heat Flux Under Microgravity Conditions," J. Thermophys. Heat Transfer, **15**, pp. 326–332.

[18] Zhang, N., and Yang, W. J., 2004, "A General Model of Bubble Departure From a Heated Solid Surface," *Heat Transfer Science and Technology 2004, Proceedings of the Sixth International Symposium on Heat Transfer (ISHT6)*, B. X. Wang, ed., Beijing, China, Jun. 15–19, Paper No. 06-01.

[19] Zhang, N., Chao, D. F., and Yang, W. -J., 2003, "Enhanced Pool Boiling on Copper-Graphite Surfaces," *Proceedings of International Conference on Energy and the Environment*, Shanghai Science and Technology Publishers, Shanghai, China, Vol. 1, pp. 678–684.

[20] Chao, D.-F., Zhang, N., and Yang, W.-J., 2008, "Growth of Micro Bubbles on Micro-Configured Metal-Graphite Composite Surfaces and Boiling Enhancement," *Proceedings of the First ASME Micro/Nanoscale Heat Transfer International Conference*, Tainan, Taiwan, Jan. 6–9, Paper No. 52010.

[21] Chao, D. F., Zhang, N., and Yang, W.-J., 2004, "Nucleate Pool Boiling on Copper-Graphite Composite Surfaces and Its Enhancement Mechanisms," J. Thermophys. Heat Transfer, **18**, pp. 236–242.

Steady-Periodic Heating of a Cylinder

Kevin D. Cole
Department of Mechanical Engineering,
University of Nebraska,
Lincoln, NE 68588-0656
e-mail: kcole1@unl.edu

Paul E. Crittenden
Department of Mathematics,
Jacksonville University,
Jacksonville, FL 32211
e-mail: pcritte@ju.edu

Steady periodic heating is an important experimental technique for measurement of thermal properties. In these methods the thermal properties are deduced from a systematic comparison between the data (such as temperature) and a detailed thermal model. This paper addresses steady-periodic heat transfer on cylindrical geometries with application to thermal-property measurements. The method of Green's functions is used to provide a comprehensive collection of exact analytical expressions for temperature in cylinders. Five kinds of boundary conditions are treated for one-, two-, and three-dimensional geometries. For some geometries an alternate form of the Green's function is given, which can be used for improvement of series convergence and for checking purposes to produce highly accurate numerical values. Numerical examples are given.
[DOI: 10.1115/1.3139107]

Keywords: frequency response, thermal transient, oscillating heat source, convective boundary, lumped boundary, surface-film boundary, extended surface

1 Introduction

Steady-periodic heat transfer in cylinders is important in several engineering applications including annular fins [1–3], rotating machinery such as electromagnetic bearings [4], and in devices experiencing periodic thermal contact such as engine exhaust valves [5].

In this paper, steady-periodic heat conduction in cylinders is presented with the method of Green's functions (GFs). This approach provides a comprehensive set of solutions and specific strategies for improving the numerical evaluation of these solutions.

There are several recent books on GF applied to heat conduction [6–8]. The book by Mandelis [9] is devoted exclusively to steady-periodic heat conduction with the method of GFs. Of the solutions given for cylindrical geometries, however, only three kinds of boundary conditions are treated, and only one form of the GF is given for each geometry.

The contributions of this paper are threefold. First, a great many steady-periodic solutions are presented systematically with the method of GFs for several cylindrical geometries. Second, five kinds of boundary conditions are treated in a unified fashion, two of which include a high-conductivity surface film. Many of these surface-film solutions have not been published before. Third, alternate forms of GFs are given for several geometries, which provide for efficient numerical computation and allow for independent verification that the numerical results are correct. Two geometries are studied in detail with numerical values computed from exact analytical solutions.

2 Steady-Periodic Relations

The steady-periodic temperature in cylindrical coordinates satisfies the following equations:

$$\frac{1}{r}\frac{\partial}{\partial r}\left(r\frac{\partial T}{\partial r}\right)+\frac{1}{r^2}\frac{\partial^2 T}{\partial \phi^2}+\frac{\partial^2 T}{\partial z^2}-\sigma^2 T=-\frac{1}{k}g(\boldsymbol{r},\omega) \quad \text{in domain } \Omega \tag{1}$$

$$k_i\frac{\partial T}{\partial n_i}+[h_i+j\omega(\rho c\epsilon)_i]T=f_i(\boldsymbol{r}_i,\omega) \quad \text{at boundary } i \tag{2}$$

where $\sigma^2=j\omega/\alpha$. Here complex-valued $T(\boldsymbol{r},\omega)$ is interpreted as the steady-periodic temperature (K) at vector location $\boldsymbol{r}$ and at a single frequency ω. The generalized boundary condition represents five types of boundary conditions depending on the choice of parameters k_i, h_i, and ϵ_i (the five kinds are (1) temperature, (2) flux, (3) convection, (4) surface film, and (5) surface film with convection). The boundary condition, Eq. (2), contains term $j\omega(\rho c\epsilon)_i T$, which represents heat storage in a surface film of thickness ϵ_i. Boundary conditions with a surface film, under steady-periodic conditions, are similar to convection boundary conditions, except that a complex quantity is added to the heat transfer coefficient. See Ref. [10] for further discussion of the steady-periodic heat equation and the five kinds of boundary conditions.

3 Green's Function Solution

The temperature will be found by the method of GF. Assume for the moment that the GF, symbol G, is known. Then the steady-periodic temperature is given by the following integral equation [6] (Chap. 3):

$$T(\boldsymbol{r},\omega)=\frac{\alpha}{k}\int g(\boldsymbol{r}',\omega)G(\boldsymbol{r},\boldsymbol{r}',\omega)dv'+\alpha\sum_i\int f_i(\boldsymbol{r}_i',\omega)\times\begin{bmatrix}-\partial G/\partial n_i' & \text{(first kind only)}\\ \frac{1}{k}G(\boldsymbol{r},\boldsymbol{r}_i',\omega) & \text{(second to fifth kinds)}\end{bmatrix}ds_i' \tag{3}$$

The first integral is the effect of internal heat generation g, and the second integral is the effect of each nonhomogeneous boundary term f_i. Note that the same GF appears in each integral but it is evaluated at locations appropriate for each integral.

The GF associated with Eqs. (1) and (2) is the response at $\boldsymbol{r}$ to a steady-periodic heat source located at $\boldsymbol{r}'$, and the GF satisfies

$$\nabla^2 G-\sigma^2 G=-\frac{1}{\alpha}\delta(\boldsymbol{r}-\boldsymbol{r}') \tag{4}$$

Contributed by the Heat Transfer Division of ASME for publication in the JOURNAL OF HEAT TRANSFER. Manuscript received May 28, 2008; final manuscript received March 26, 2009; published online June 22, 2009. Review conducted by Ofodike A. Ezekoye.

$$k_i \frac{\partial G}{\partial n_i} + \lambda_i G = 0 \quad \text{on boundary } i \tag{5}$$

Here $\lambda_i = h_i + j\omega(\rho c \epsilon)_i$ and $\delta(\mathbf{r}-\mathbf{r}')$ is the Dirac delta function. The coefficient $1/\alpha$ preceding the delta function in Eq. (4) provides for units of the steady-periodic GF that are consistent with earlier work [10]. The boundary conditions for the GF are homogeneous but of the same kind (see Ref. [6], Chap. 2) as for the temperature problem of interest. Thus, a different GF is needed for each geometry and for each combination of boundary conditions.

In Secs. 4–6, the method of GFs is applied to one-, two-, and three-dimensional cylinders. First, the GFs will be identified, and then temperature examples will be given.

4 Long Cylinder

In this section, we consider steady-periodic heating of an infinitely long cylinder. The heat conduction is along the radial direction only. The GF in this case satisfies the following equation:

$$\frac{\partial^2 G}{\partial r^2} + \frac{1}{r}\frac{\partial G}{\partial r} - \sigma^2 G = -\frac{1}{\alpha}\delta(r-r'), \quad a < r < b \tag{6}$$

Using variation of parameters, the solution may be found in the form

$$G(r|r') = \frac{1}{2\pi\alpha(1-A_1A_2)} \times \begin{Bmatrix} [A_2 I_0(\sigma r') + K_0(\sigma r')][I_0(\sigma r) + A_1 K_0(\sigma r)], & r < r' \\ [A_2 I_0(\sigma r) + K_0(\sigma r)][I_0(\sigma r') + A_1 K_0(\sigma r')], & r > r' \end{Bmatrix} \tag{7}$$

where

$$A_1 = \begin{cases} 0 & \text{if } a = 0 \text{ (solid cylinder)} \\ -\dfrac{I_0(\sigma a)}{K_0(\sigma a)} & \text{if kind 1 at } r = a \\ \dfrac{I_1(\sigma a)}{K_1(\sigma a)} & \text{if kind 2 at } r = a \\ \dfrac{k\sigma I_1(\sigma a) - \lambda_1 I_0(\sigma a)}{k\sigma K_1(\sigma a) + \lambda_1 K_0(\sigma a)} & \text{if kind 3, 4, or 5 at } r = a \end{cases} \tag{8}$$

and

$$A_2 = \begin{cases} 0 & b \to \infty \\ -\dfrac{K_0(\sigma b)}{I_0(\sigma b)} & \text{if kind 1 at } r = b \\ \dfrac{K_1(\sigma b)}{I_1(\sigma b)} & \text{if kind 2 at } r = b \\ \dfrac{k\sigma K_1(\sigma b) - \lambda_2 K_0(\sigma b)}{k\sigma I_1(\sigma b) + \lambda_2 I_0(\sigma b)} & \text{if kind 3, 4, or 5 at } r = b \end{cases} \tag{9}$$

The set of GFs given in Eq. (7) applies to 36 combinations of boundary conditions—six kinds at $r_{\min}$ and six at $r_{\max}$. This includes the zeroth kind to represent a nonphysical boundary at $r=0$ or $r \to \infty$. We use a numbering system to identify these GFs in the form *RIJ*, where *R* represents the radial coordinate, and $I, J = 0, 1, \ldots, 5$ represent the kinds of boundary condition present. For example, *R*11 denotes a hollow cylinder with type 1 boundaries. For more information on the numbering system, see Ref. [6] (Chap. 2).

5 Finite Cylinder With $T = T(r,z)$

Consider a finite-length hollow cylinder with outer radius b, inner radius a, and length L. This geometry can also describe a solid cylinder if $a=0$. Suppose the steady-periodic temperature in the finite cylinder does not depend on angle, then the temperature satisfies

$$\frac{1}{r}\frac{\partial}{\partial r}\left(r\frac{\partial T}{\partial r}\right) + \frac{\partial^2 T}{\partial z^2} - \sigma^2 T = -\frac{g(r,z,\omega)}{k} \tag{10}$$

and at the boundaries

$$k_i \frac{\partial T}{\partial n_i} + [h_i + j\omega(\rho c \epsilon)_i]T = f_i(r_i, z_i) \tag{11}$$

where $i=1$, 2, 3, and 4 represents boundaries at $r=a$, $r=b$, $z=0$, and $z=L$, respectively. Quantity ϵ_i is the thickness of a surface layer with high conductivity that may be present. The associated GF for the finite cylinder satisfies

$$\frac{1}{r}\frac{\partial}{\partial r}\left(r\frac{\partial G}{\partial r}\right) + \frac{\partial^2 G}{\partial z^2} - \sigma^2 G = -\frac{1}{\alpha}\delta(r-r')\,\delta(z-z') \tag{12}$$

and at the boundaries

$$k_i \frac{\partial G}{\partial n_i} + \lambda_i G = 0 \tag{13}$$

where $\lambda_i = h_i + j\omega(\rho c \epsilon)_i$.

The set of GFs given by Eqs. (12) and (13) represents a large number of geometries, with 36 combinations of boundary conditions along r and 36 combinations along z for a total of 1296 combinations. The number system for these GFs have the form *RIJZKL*, where *R* and *Z* represent the coordinate directions, and *I*, *J*, *K*, and *L* represent the types of boundary conditions present. For example, number *R*03*Z*33 represents a solid cylinder with convection (third kind) over the boundaries at $r=b$, $z=0$, and $z=L$.

There are two forms of the single-sum GF, one with eigenfunctions along the z-direction and the other with eigenfunction along the r-direction. Both are important, as one can be used to check the other, and where one converges slowly the other generally converges rapidly [11].

5.1 2D GF With Eigenfunctions Along *z*. The single-sum steady-periodic GF with eigenfunctions along the z-direction has the form

$$G(r,z|r',z',\omega) = \sum_{p=0}^{\infty} \frac{Z_p(z)Z_p(z')}{N_z(\nu_p)} Q_p(r,r') \tag{14}$$

where eigenfunctions Z_p satisfy

$$Z_n'' + \nu_p^2 Z_p = 0$$

along with boundary conditions at $z=0$ and $z=L$ drawn from those for G. Eigenfunctions Z_p, norm N_z, and eigenvalues ν_p are well-known values given in Table 1 (see also Refs. [11,12] (p. 35)).

Kernel function $Q_p(r,r')$ is identical with the 1D GF discussed earlier. That is,

$$Q_p(r,r') = G(r,r')|_{\sigma=\beta_p} \tag{15}$$

where $\beta_p^2 = \nu_p^2 + \sigma^2$.

5.2 2D GF With Eigenfunctions Along *r*. An alternate GF that satisfies Eq. (12) may also be constructed using eigenfunctions along the r direction. If the r-direction eigenfunctions are denoted $R_m(r)$, then the alternate single-sum GF may be written

$$G(r,z|r',z',\omega) = \sum_{m=0}^{\infty} \frac{R_m(r)R_m(r')}{N_r(\gamma_m)} P_m(z,z') \tag{16}$$

Eigenfunctions R_m satisfy

Table 1 Eigenfunctions along the *z*-direction. Note $B_1 = h_1 L/k$; $B_2 = h_2 L/k$. ((*a*) Eigenfunctions and (*b*) inverse norm and eigenvalues or conditions.)

Cases	$Z_p(z)$	
	(*a*)	
*Z*11, *Z*12, and *Z*13	$\sin(\nu_p z)$	
*Z*21, *Z*22, and *Z*23	$\cos(\nu_p z)$	
*Z*31, *Z*32, and *Z*33	$\nu_p L\cos(\nu_p z)+B_1\sin(\nu_p z)$	
Case	$N_z(p)^{-1}$	ν_p or eigencondition
	(*b*)	
*Z*11	$2/L$	$p\pi/L$
*Z*12	$2/L$	$\dfrac{(2p-1)\pi}{2L}$
*Z*13[a]	$2D_p/L$	$\nu_p L\cot(\nu_p L)=-B_2$
*Z*21	$2/L$	$\dfrac{(2p-1)\pi}{2L}$
*Z*22	$\begin{cases}2/L, & \nu_p\neq 0\\ 1/L, & \nu_p=0\end{cases}$	$p\pi/L$
*Z*23[a]	$2D_p/L$	$\nu_p L\tan(\nu_p L)=B_2$
*Z*31	$\dfrac{2}{(\nu_p L)^2+B_1^2+B_1}$	$\nu_p L\cot(\nu_p L)=-B_1$
*Z*32	$\dfrac{2}{(\nu_p L)^2+B_1^2+B_1}$	$\nu_p L\tan(\nu_p L)=B_1$
*Z*33[b]	$2d_p/L$	$\tan(\nu_p L)=\dfrac{\nu_p L(B_1+B_2)}{(\nu_p L)^2-B_1B_2}$

[a] $D_p=[(\nu_p L)^2+B_2^2]/[(\nu_p L)^2+B_2^2+B_2]$.
[b] $d_p=D_p\div[(\nu_p L)^2+B_1^2+B_1D_p]$.

$$\frac{1}{r}\frac{\partial}{\partial r}\left(r\frac{\partial R_m}{\partial r}\right)-\gamma_m^2 R_m=0$$

along with the boundary conditions at $r=a$ and $r=b$. Eigenfunctions R_m have the form of Bessel functions of order zero. Eigenfunctions R_m and norm N_r are given in Table 2 (for $n=0$) and the conditions for computing eigenvalues γ_m are given in Table 3 for solid cylinders ($0<r<b$). For hollow cylinders see Ref. [12] (pp. 108–113) or Ref. [13].

Kernel function P_m is given by Ref. [10]:

$$P_m(z,z')=\frac{S_2^-(S_1^- e^{-\beta_m(2L-|z-z'|)}+S_1^+ e^{-\beta_m(2L-z-z')})}{2\alpha\beta_m(S_1^+S_2^+-S_1^-S_2^- e^{-2\beta_m L})}+\frac{S_2^+(S_1^+ e^{-\beta_m(|z-z'|)}+S_1^- e^{-\beta_m(z+z')})}{2\alpha\beta_m(S_1^+S_2^+-S_1^-S_2^- e^{-2\beta_m L})} \quad (17)$$

where $\beta_m^2=\gamma_m^2+\sigma^2$ and where subscripts 1 and 2 indicate sides $z=0$ and $z=L$ of the cylinder, respectively. Parameters S_M^+ and S_M^- depend on the boundary conditions on side M and are given by

$$S_M^+=\begin{cases}1 & \text{if side } M \text{ is kind 1 or kind 2}\\ \beta_m L+\mathrm{B}_M & \text{if side } M \text{ is kind 3, 4, or 5}\end{cases} \quad (18)$$

$$S_M^-=\begin{cases}-1 & \text{if side } M \text{ is kind 1}\\ 1 & \text{if side } M \text{ is kind 2}\\ \beta_m L-\mathrm{B}_M & \text{if side } M \text{ is kind 3, 4, or 5}\end{cases} \quad (19)$$

Here $\mathrm{B}_M=\lambda_M L/k$ is the Biot number for side M, and k is the conductivity of the cylinder.

Table 3 Eigenconditions for solid cylinders

Case	Eigencondition
*R*01	$J_n(\gamma_{nm}b)=0$
*R*02	$J_n'(\gamma_{nm}b)=0$
*R*03	$\gamma_{nm}bJ_n'(\gamma_{nm}b)+\mathrm{B}_2J_n(\gamma_{nm}b)=0$

6 Finite Cylinder With $T=T(r,\phi,z)$

In this section, the finite-length cylinder with three-dimensional heat conduction is treated. That is, temperature depends on spatial coordinates (r,ϕ,z). The steady-periodic temperature satisfies

$$\frac{1}{r}\frac{\partial}{\partial r}\left(r\frac{\partial T}{\partial r}\right)+\frac{1}{r^2}\frac{\partial^2 T}{\partial\phi^2}+\frac{\partial^2 T}{\partial z^2}-\sigma^2 T=-\frac{g(r,z,\omega)}{k} \quad (20)$$

and at the boundaries

$$k_i\frac{\partial T}{\partial n_i}+\lambda_i T=f_i(r_i,\phi_i,z_i) \quad (21)$$

where $i=1$, 2, 3, and 4 represents boundaries at $r=a$, $r=b$, $z=0$, and $z=L$, respectively.

The associated GF for 3D steady-periodic heat conduction in the finite cylinder satisfies

$$\frac{1}{r}\frac{\partial}{\partial r}\left(r\frac{\partial G}{\partial r}\right)+\frac{1}{r^2}\frac{\partial^2 G}{\partial\phi^2}+\frac{\partial^2 G}{\partial z^2}-\sigma^2 G=-\frac{1}{\alpha}\delta(r-r')\delta(z-z')\delta(\phi-\phi') \quad (22)$$

and at the boundaries

$$k_i\frac{\partial G}{\partial n_i}+\lambda_i G=0 \quad (23)$$

The set of GFs represented by Eqs. (22) and (23) represent 1296 combinations of boundary conditions (36 along r and 36 along z), denoted by GF number *RIJZKL*Φ00. Here Φ00 denotes the angular dependence for the full cylinder, and $I,J,K,L=0,1,\ldots,5$ denote the types of boundary conditions present. Two forms of the double-sum GF are discussed in Secs. 6.1 and 6.2.

Table 2 Eigenfunctions and norm for solid cylinders. Note $B_2=\lambda_2 b/k$.

Case	Condition at $r=b$	R_{nm}	$(N_r)^{-1}$ for $n\neq 0$	$(N_r)^{-1}$ for $n=0$
*R*01	$R_{nm}=0$	$J_n(\gamma_{nm}r)$	$\dfrac{2}{b^2J_n'(\gamma_{nm}b)}$	See $n\neq 0$
*R*02	$\dfrac{dR_{nm}}{dr}=0$	$J_n(\gamma_{nm}r)$	$\dfrac{2}{b^2J_n^2(\gamma_{nm}b)}\dfrac{b^2\gamma_{nm}^2}{(b^2\gamma_{nm}^2-n^2)}$	$\dfrac{2}{b^2}$
*R*03	$k\dfrac{dR_{nm}}{dr}+hR_{nm}=0$	$J_n(\gamma_{nm}r)$	$\dfrac{2}{b^2J_n^2(\gamma_{nm}b)}\dfrac{b^2\gamma_{nm}^2}{(B_2^2+b^2\gamma_{nm}^2-n^2)}$	See $n\neq 0$

6.1 3D GF With Eigenfunctions Along *z*. The double-sum steady-periodic GF with eigenfunctions along the *z*-direction has the form

$$G(r,\phi,z|r',\phi',z',\omega)=\sum_{n=0}^{\infty}\sum_{p=0}^{\infty}\frac{Z_p(z)Z_p(z')}{N_z(\nu_p)}\frac{\cos[n(\phi-\phi')]}{N_\phi}Q_{np}(r,r') \tag{24}$$

The boundary conditions at $z=0$ and $z=L$ are satisfied by the eigenfunctions in the *z*-direction, and the conditions at $\phi=0$ and $\phi=2\pi$ are satisfied by the eigenfunctions in the ϕ-direction. Here norm N_ϕ is equal to π for $n=0$ and 2π for $n\geq 1$.

Kernel function Q_{np} can be shown to have the form

$$Q_{np}(r|r')=\frac{1}{2\pi\alpha(1-A_1A_2)}\times\begin{Bmatrix}[A_2I_n(\beta_pr')+K_n(\beta_pr')][I_n(\beta_pr)+A_1K_n(\beta_pr)], & r<r'\\ [A_2I_n(\beta_pr)+K_n(\beta_pr)][I_n(\beta_pr')+A_1K_n(\beta_pr')], & r>r'\end{Bmatrix} \tag{25}$$

where

$$A_1=\frac{[\ \beta_paI_{n+1}(\beta_pa)+nI_n(\beta_pa))]-B_1I_n(\beta_pa)}{[\beta_paK_{n+1}(\beta_pa)-nK_n(\beta_pa)]+B_1K_n(\beta_pa)} \tag{26}$$

and

$$A_2=\frac{[\beta_pbK_{n+1}(\beta_pb)-nK_n(\beta_pb)]-B_2K_n(\beta_pb)}{[\beta_pbI_{n+1}(\beta_pb)+nI_n(\beta_pb)]+B_2I_n(\beta_pb)} \tag{27}$$

The quantities $B_1=\lambda_1a/k_1$ and $B_2=\lambda_2b/k_2$ are modified Biot numbers at the inner and outer radii, respectively. The above values for A_1 and A_2 are for the most general boundary condition (fifth kind). Values for other kinds of boundaries can be found by analogy with Eqs. (27)–(29). Some care is required when combining eigenfunctions Z_p and kernel functions Q_{np}, as they depend on different Biot numbers. In the finite-length cylinder, eigenfunctions Z_p depend on Biot numbers $B_M=\lambda_ML/k$, where λ_M is associated with the boundary conditions at $z=0$ and $z=L$. As many as four distinct Biot numbers may be present in the finite cylinder.

6.2 3D GF With Eigenfunctions Along *r*. An alternate GF that satisfies Eq. (22) may be constructed using eigenfunctions along the *r*-direction. If the *r*-direction eigenfunctions are denoted $R_{nm}(r)$, then the alternate double-sum GF may be written as

$$G(r,\phi,z|r',\phi',z',\omega)=\sum_{n=0}^{\infty}\sum_{m=0}^{\infty}\frac{R_{nm}(r)R_{nm}(r')}{N_r(\gamma_{nm})}\frac{\cos[n(\phi-\phi')]}{N_\phi}\times P_m(z,z') \tag{28}$$

The $m=0$ term of the series is needed only when zero is an eigenvalue (for cases *R*02 and *R*22). The series on *n* involves the functions $\cos[n(\phi-\phi')]$, which satisfy the periodic boundary conditions at $\phi=0$ and $\phi=2\pi$. The GF given above is similar in form to the real-valued *steady* GF published previously in Ref. [13]; however, for steady-periodic conditions considered here the eigenfunctions R_{nm}, norm N_r, and eigenvalues γ_{nm} can take on complex values. Eigenfunctions R_{nm} have the form of Bessel functions of order *n* and are listed in Table 2 along with their norms. The eigenconditions for γ_{nm} are listed in Table 3. For hollow cylinders, see Ref. [12] (Chap. 3). Note that the kernel function is identical to that discussed earlier in Eq. (17); however, here β_m is defined $\beta_m^2=\gamma_{nm}^2+\sigma^2$.

7 Temperature Examples

In the next two sections, numerical examples are given of the temperature in cylindrical geometries caused by steady-periodic heating. The first example is a cylinder heated at one end and experiencing axisymmetric convective heat loss from the other surfaces. The second example is a cylinder heated over a small region on its surface with convective heat loss.

8 Pin Fin With Heat Flux at Base

Steady-periodic heat transfer in fins has been studied several times [1–3]. Generally, a fin is long and thin and the temperature varies only along the axis of the fin; however, Kraus et al. [14] (Chap. 17) described the two-dimensional temperature in a rectangular fin with an oscillating base temperature. This example is concerned with a short cylindrical fin in which two-dimensional heat transfer is present. The base of the fin is uniformly heated by a steady-periodic heat flux, and the other surfaces are cooled by convection. This is geometry *R*03*Z*23. The temperature satisfies the following equations:

$$\frac{1}{r}\frac{\partial}{\partial r}\left(r\frac{\partial T}{\partial r}\right)+\frac{\partial^2T}{\partial z^2}-\sigma^2T=0 \tag{29}$$

$$\text{at } z=0,\quad -k\frac{\partial T}{\partial r}=q_0(\omega) \tag{30}$$

$$\text{at } z=L,\quad k\frac{\partial T}{\partial z}+hT=0 \tag{31}$$

$$\text{at } r=b,\quad k\frac{\partial T}{\partial r}+hT=0 \tag{32}$$

The temperature may be expressed as an integral involving the appropriate Green's function, as follows:

$$T(r,z,\omega)=\frac{\alpha}{k}\int_{r'=0}^{b}q_0G(r,z,\omega|r',z'=0)2\pi r'dr' \tag{33}$$

Mathematically, the temperature has a unique solution. However, there are two series forms of the GF that can provide two distinct series expressions for the temperature.

8.1 Eigenfunctions Along *z*. With eigenfunctions along the *z*-direction, the GF is given by

$$G(r,z|r',z'=0,\omega)=\sum_{p=1}^{\infty}\frac{Z_p(z)Z_p(0)}{N_z(\nu_p)}Q_p(r,r') \tag{34}$$

where the eigenfunction and norm are given by (Table 1)

$$Z_p(z)=\cos(\nu_pz) \tag{35}$$

$$\frac{1}{N_z(\nu_p)}=\frac{2}{L}\frac{(\nu_pL)^2+B_2^2}{(\nu_pL)^2+B_2^2+B_2} \tag{36}$$

where $B_2=hL/k$. Eigenvalues ν_p satisfy $\nu_pL\tan(\nu_pL)=hL/k$. The kernel function is given by

$$Q_p(r|r')=\frac{1}{2\pi\alpha}\begin{Bmatrix}[A_2I_0(\beta_pr')+K_0(\beta_pr')][I_0(\beta_pr)], & r<r'\\ [A_2I_0(\beta_pr)+K_0(\beta_pr)][I_0(\beta_pr')], & r>r'\end{Bmatrix} \tag{37}$$

where A_2 is given by

$$A_2=\frac{\beta_pLK_1(\beta_pb)-B_2K_0(\beta_pb)}{\beta_pLI_1(\beta_pb)+B_2I_0(\beta_pb)} \tag{38}$$

and where $\beta_p^2=\nu_p^2+\sigma^2$. Replace this GF into the temperature integral, Eq. (33), and evaluate the integral over r' to find

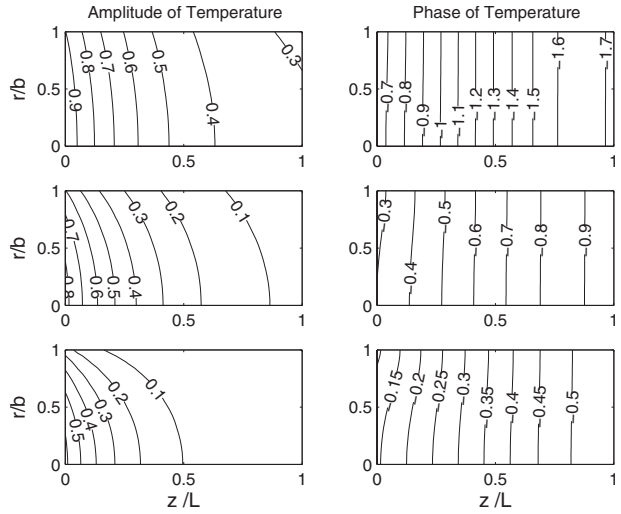

Fig. 1 Effect of varying convection on the amplitude and phase of the temperature in a cylinder of aspect ratio $b/L=0.5$. The cylinder is heated at $z=0$ and cooled by convection at $r/b=1$ and $z/L=1$. The heating frequency is fixed at $\omega b^2/\alpha=1.0$ and the boundary convection is given by $hb/k=0.2$, 1.0, and 5.0 for the top, middle, and bottom of the figure, respectively.

$$\frac{T(r,z,\omega)}{q_0 b/k}=\sum_{p=1}^{\infty}\cos(\nu_p z)\frac{2b}{L}\frac{(\nu_p L)^2+B_2^2}{(\nu_p L)^2+B_2^2+B_2}\times\left\{\frac{1}{\beta_p b}[A_2 I_1(\beta_p b)-K_1(\beta_p b)]I_0(\beta_p r)+\frac{1}{\beta_p^2 b^2}\right\} \tag{39}$$

8.2 Eigenfunctions Along *r*. An alternate form of the GF has eigenfunctions along the r-direction, and is given by

$$G(r,z|r',z'=0,\omega)=\sum_{m=1}^{\infty}\frac{R_m(r)R_m(r')}{N_r(\gamma_m)}P_m(z,z'=0) \tag{40}$$

where the eigenfunction and norm are given by (Table 2)

$$R_m(r)=J_0(\gamma_m r) \tag{41}$$

$$\frac{1}{N_r}=\frac{2}{J_0^2(\gamma_m b)}\frac{\gamma_m^2}{[(hb/k)^2+b^2\gamma_m^2)]} \tag{42}$$

where eigenvalue γ_m satisfies (Table 3)

$$\gamma_m b J_0'(\gamma_m b)+B_2 J_0(\gamma_m b)=0 \tag{43}$$

Kernel function P is given by Eq. (17) for a type 2 boundary at $z=0$ and a type 3 boundary at $z=L$ (case Z23):

$$P(z,z'=0)=\frac{S_2^- e^{-\beta_m(2L-z)}+S_2^+ e^{-\beta_m z}}{\beta_m(S_2^+-S_2^- e^{-2\beta_m L})} \tag{44}$$

where $\beta_m^2=\gamma_m^2+\sigma^2$, $S_2^+=\beta_m L+hL/k$, and $S_2^-=\beta_m L-hL/k$. This form of the GF may be substituted into the temperature integral to find an alternate series expression for the temperature

$$\frac{T(r,z,\omega)}{q_0 b/k}=\sum_{m=1}^{\infty}\frac{1}{\gamma_m b}J_0(\gamma_m r)J_1(\gamma_m b)\frac{2\gamma_m^2 b^2}{J_0^2(\gamma_m b)[(hb/k)^2+b^2\gamma_m^2]}\times\frac{(\beta_m L-hL/k)e^{-\beta_m(2L-z)}+(\beta_m L+hL/k)e^{-\beta_m z}}{\beta_m b[(\beta_m L+hL/k)-(\beta_m L-hL/k)e^{-2\beta_m L}]} \tag{45}$$

Numerical values for the temperature in the pin fin were computed using both temperature series, Eqs. (39) and (45), and the results agree to five significant figures, providing a very strong check on the correctness of the results. As both series are exact, closer agreement could have been secured by including more terms in the truncated sum. In Fig. 1, the contour plots of the amplitude and phase of the temperature are given for a fin of aspect ratio $b/L=0.5$. The frequency is fixed at $\omega b^2/\alpha=1.0$ and the results for Biot number $hb/k=0.2$, 1.0, and 5.0 are shown at the top, middle, and bottom of the figure, respectively. The amplitude of the temperature is largest where the heat is added ($z=0$) and decreases along the length of the fin. Heat leaves the fin along the $r/b=1$

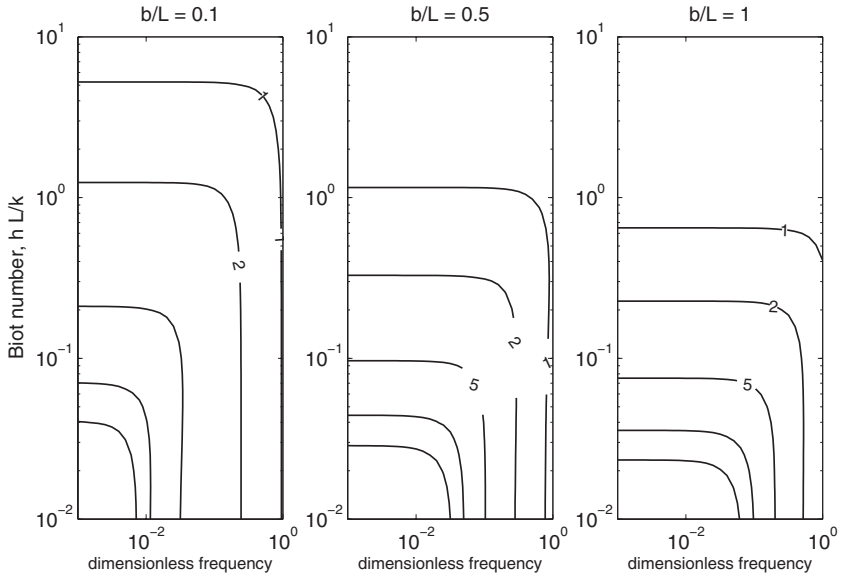

Fig. 2 Fin effectiveness in the pin fin heated at the base ($z=0$) as a function of Biot number and dimensionless frequency $\omega b^2/\alpha$ for aspect ratios $b/L=0.1$, 0.5, and 1.0

boundary, demonstrated by the slope of the temperature at the boundary, which is proportional to heat flux. Thus, as the Biot number increases, the slope at the boundary increases along with the boundary heat flux.

The phase of the temperature shown in Fig. 1 is negative and closest to zero at the heating location $z=0$. As z increases, the phase becomes more negative (moving further from zero). For the smallest Biot number (at the top of the figure), the change in phase along the fin is most pronounced, and as the Biot number increases there is less change in phase along the fin.

In Fig. 2, the effectiveness of fins with three different aspect ratios are graphed as a function of the Biot number hL/k and the dimensionless frequency $\omega b^2/\alpha$. The fin effectiveness (also called the fin-removal number) is defined as the conductive heat flow into the base of the fin divided by the convective heat flow through the fin-base area if the fin was not present [14] (p. 92). The total flow into the fin was calculated by differentiating the temperature expressions (at $z=0$) term by term and then integrating over the cross sectional area. A fin is usually considered justifiable if the effectiveness is greater than or equal to 2. At low frequencies, for a fixed aspect ratio, the fin is more effective at lower Biot numbers as expected. As frequency increases, the fin becomes less effective due to the insufficient time between the fluctuations for the heat to transfer down the fin. It is also interesting to note that thinner fins are more effective at lower frequencies but this is not necessarily true at higher frequencies. For example, a fin with a Biot number of 10^{-2}, an aspect ratio of 1, and an effectiveness of 2 would have an effectiveness somewhat less than 2 if the aspect ratio was changed to 0.1 while holding all of the other parameters constant.

9 Solid Cylinder Heated Over a Sector of Its Surface and Cooled by Convection

Consider a solid cylinder with steady-periodic heating over an angular sector of the curved surface, parallel to the cylinder axis, and cooled by convection over the entire curved surface. The flat ends of the cylinder are fixed at the fluid temperature. This geometry is an approximate thermal model of a hot-film sensor used to measure fluid flow. The temperature satisfies the following equations:

$$\frac{1}{r}\frac{\partial}{\partial r}\left(r\frac{\partial T}{\partial r}\right)+\frac{1}{r^2}\frac{\partial^2 T}{\partial \phi^2}+\frac{\partial^2 T}{\partial z^2}-\sigma^2 T+\frac{g(r,\phi,z)}{k}=0 \tag{46}$$

$$\text{at } z=0, \quad T=T_\infty \tag{47}$$

$$\text{at } z=L, \quad T=T_\infty \tag{48}$$

$$\text{at } r=b, \quad k\frac{\partial T}{\partial r}+hT=hT_\infty \tag{49}$$

The heating function is given by

$$g(r,\phi,z)=\begin{cases} q_0\delta(r-b) & 0<\phi<\phi_0 \\ 0 & \phi_0<\phi<2\pi \end{cases} \tag{50}$$

Note that the heat is introduced at surface $r=b$. This is geometry $R03Z11\Phi00$ in the heat conduction numbering system. The temperature may be stated in the form of an integral with the GF, as follows:

$$T(r,\phi,z,\omega)-T_\infty=\frac{\alpha}{k}\int_{\phi'=0}^{\phi_0}\int_{z'=0}^{L} q_0 \times G(r,\phi,z,\omega|r'=b,\phi',z')dz'd\phi' b \tag{51}$$

There are two forms of the GF that allow for two distinct series expressions for the temperature.

9.1 Eigenfunctions Along *z*. With eigenfunctions along the z-direction, the GF is given by Eq. (24). The eigenfunction and norm are given by Table 2 (case $Z11$) and the kernel function is given by Eq. (25) (for case $R03$). Replace the GF into the temperature integral, Eq. (51), and evaluate the integrals on ϕ' and z':

$$\frac{T(r,\phi,z)-T_\infty}{q_0 b/k}=\sum_{p=1}^{\infty}\sum_{n=0}^{\infty}\frac{2\sin(p\pi z/L)[1-(-1)^p]}{p\pi} \times C_n[A_2(n)I_n(\beta_p b)+K_n(\beta_p b)]\frac{I_n(\beta_p r)}{2\pi} \tag{52}$$

where

$$C_n=\begin{cases}\phi_0/\pi, & n=0 \\ \{\sin(n\phi)-\sin n(\phi-\phi_0)\}/(2\pi n), & n\neq 0\end{cases}$$

and where

$$A_2(n)=\frac{[\beta_p bK_{n_+1}(\beta_p b)-nK_n(\beta_p b)]-B_2K_n(\beta_p b)}{[\beta_p bI_{n+1}(\beta_p b)+nI_n(\beta_p b)]+B_2I_n(\beta_p b)} \tag{53}$$

with $B_2=hb/k$. Note that the integral over ϕ' must be treated separately when $n=0$.

9.2 Eigenfunctions Along *r*. An alternate form of the GF, with eigenfunctions along the r-direction, is given by Eq. (28). The eigenfunction and norm are given by case $R03$ in Table 3, and the kernel function P_m is given by Eq. (17), with $\beta^2=\gamma_{nm}^2+\sigma^2$. Replace the alternate GF into the integral expression for the GF and evaluate the integrals over ϕ' and z' to find the an alternate series expression for the temperature

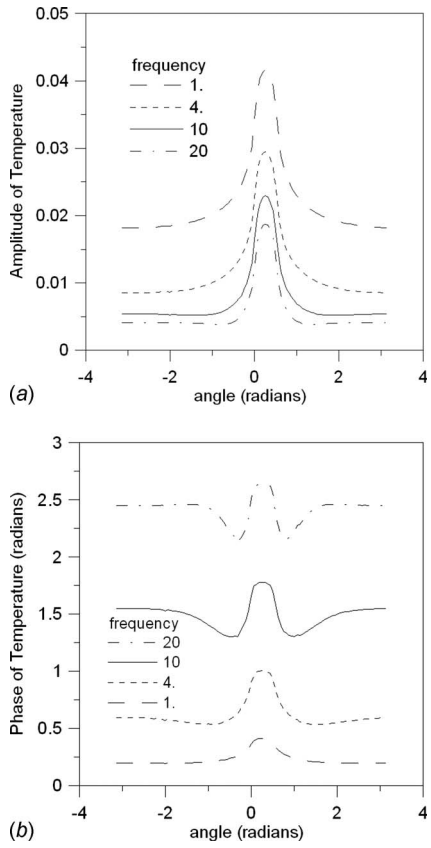

Fig. 3 Amplitude and phase of the temperature around the circumference of a cylinder ($r=b$, $z=L/2$) for several values of the (dimensionless) heating frequency. The cylinder surface is heated steady periodically over a small strip $0<\phi<0.2$ and the convection on the curved surface is characterized by $B_2=1$.

$$\frac{T(r,\phi,z)-T_\infty}{q_0 b/k}=\sum_{m=1}^{\infty}\sum_{n=0}^{\infty}J_n(\gamma_{nm}r)\frac{2\gamma_{nm}^2}{J_n(\gamma_{nm}b)(hb/k)^2+b^2\gamma_{nm}^2-n^2)}\times C_n\left[\frac{1}{\beta^2}+\frac{e^{-\beta(2L-z)}-e^{-\beta(L-z)}-e^{-2\beta L}-e^{-\beta z}}{\beta^2(1-e^{-2\beta L})}\right] \tag{54}$$

where C_n is given above. Note that additive term $1/\beta^2$, from integration on z' of the kernel function, may cause slow series convergence because this portion of the series does not contain a convergence-promoting exponential function. The series containing this additive term can be shown to correspond to a two-dimensional temperature distribution that does not depend on coordinate z and it can be replaced by a faster-converging single-sum form (see Ref. [11]).

Numerical values were computed for the amplitude and phase of the dimensionless temperature on the cylinder surface $r=b$ and at the midpoint $z=L/2$. The heated strip is located on $0<\phi<0.2$ and the aspect ratio of the cylinder is $b/L=0.2$.

Figure 3 shows the temperature amplitude and phase at the spatial location ($r=b$, $z=L/2$), with several different heating frequencies and the Biot number is fixed at $B_2=1$. The temperature amplitude decreases as the frequency increases, also the temperature becomes more localized to the heater at higher frequencies. As an explanation, there is less time for angular heat diffusion at higher frequencies. For all frequencies, the phase contains a flat region far from the heater; however, the level of this flat region increases with increasing frequency.

10 Summary

In this paper, a family of solutions to steady-periodic heating in cylinders has been presented with the method of Green's functions. Five types of boundary conditions have been treated. Solutions are given for cylinder geometries described by one, two, and three spatial coordinates, along with numerical examples. For some geometries alternate forms of the GF are given, which can be used for checking purposes and for improving the convergence behavior of the resulting temperature solutions. One application of these steady-periodic heat conduction solutions is for use with inverse methods for determining thermal properties from experimental temperature data.

Nomenclature

a = inner radius (m)
b = outer radius (m)
B_i = Biot number at boundary i
f_i = known effect at boundary i
g = internal heating at frequency ω
G = steady-periodic Green's function
h_i = heat transfer coefficient (W m^{-2} K^{-1})
i = index
I_n = modified Bessel function, order n
j = imaginary number, $\sqrt{-1}$
k = thermal conductivity (W m^{-1} K^{-1})
K_n = modified Bessel function, order n
L = length of domain in z-direction (m)
m = index
n = index
n_i = outward-facing unit normal vector on boundary i
N = norm
p = index
P = kernel function along z direction
q = steady-periodic heat flux (W m^{-2})
Q = kernel function along r direction
r = radial coordinate
R = eigenfunction along r-direction
S_M = coefficient for kernel function P
t = time (s)
T = steady-periodic temperature (K)
z = axial coordinate
Z_p = eigenfunction along z-direction

Greek Symbols

α = thermal diffusivity (m^2 s^{-1})
β = parameter for kernel function
δ = Dirac delta function
ϵ = thickness of surface layer on boundary
γ = eigenvalue associated with R
λ = boundary parameter, type 3, 4, or 5
ν_p = eigenvalue associated with Z_p
ρ = density (kg m^{-3})
σ = $[j\omega/\alpha]^{1/2}$
ϕ = angular coordinate (rad)
ω = frequency (rad s^{-1})

References

[1] Aziz, A., and Sofrata, H., 1981, "Fin Performance in an Oscillating Temperature Environment," Appl. Energy, **9**, pp. 13–21.
[2] Houghton, J. M., Ingham, D. B., and Heggs, P. J., 1992, "The One-Dimensional Analysis of Oscillatory Heat Transfer in a Fin Assembly," ASME J. Heat Transfer, **114**, pp. 548–552.
[3] Wu, S., Shiu, C. L., and Wu, W. J., 1996, "Analysis on Transient Heat Transfer in Annular Fins of Various Shapes With Their Bases Subjected to a Heat Flux Varying as a Sinusoidal Time Function," Comput. Struct., **61**(4), pp. 725–734.
[4] Jones, G. F., and Natarj, C., 1997, "Heat Transfer in an Electromagnetic Bearing," ASME J. Heat Transfer, **119**(3), pp. 611–616.
[5] Paradis, I., Wagner, J. R., and Marotta, E. E., 2002, "Thermal Periodic Contact of Exhaust Valves in Spark-Ignition Air-Cooled Engines," J. Thermophys. Heat Transfer, **16**(3), pp. 356–365.
[6] Beck, J. V., Cole, K. D., Haji-Sheikh, A., and Litkouhi, B., 1992, *Heat Conduction Using Green's Functions*, Hemisphere, New York.
[7] Duffy, D. G., 2001, *Green's Functions With Applications*, Chapman and Hall, London/CRC, Boca Raton, FL.
[8] Melnikov, Y. A., 1999, *Influence Functions and Matrices*, Dekker, New York.
[9] Mandelis, A., 2001, *Diffusion-Wave Fields, Mathematical Methods and Green's Functions*, Springer, New York.
[10] Cole, K. D., 2006, "Steady-Periodic Green's Functions and Thermal-Measurement Applications in Rectangular Coordinates," ASME J. Heat Transfer, **128**, pp. 709–716.
[11] Crittenden, P. E., and Cole, K. D., 2002, "Fast-Converging Steady-State Heat Conduction in a Rectangular Parallelepiped," Int. J. Heat Mass Transfer, **45**, pp. 3585–3596.
[12] Ozisik, M. N., 1993, *Heat Conduction*, Wiley, New York.
[13] Cole, K. D., 2004, "Fast-Converging Series for Steady Heat Conduction in the Circular Cylinder," J. Eng. Math., **49**, pp. 217–232.
[14] Kraus, A. D., Aziz, A., and Welty, J., 2001, *Extended Surface Heat Transfer*, Wiley, New York.

Flow Boiling Heat Transfer, Pressure Drop, and Flow Pattern for CO_2 in a 3.5 mm Horizontal Smooth Tube

Chang Yong Park
School of Mechanical Design and Automation Engineering,
Seoul National University of Technology,
172 Gongneung-2Dong,
Nowon-Gu, Seoul 139-743, Korea

Pega Hrnjak[1]
Department of Mechanical Science and Engineering,
University of Illinois at Urbana-Champaign,
1206 West Green Street,
Urbana, IL 61801
e-mail: pega@uiuc.edu

CO_2 flow boiling heat transfer coefficients and pressure drop in a 3.5 mm horizontal smooth tube are presented. Also, flow patterns were visualized and studied at adiabatic conditions in a 3 mm glass tube located immediately after a heat transfer section. Heat was applied by a secondary fluid through two brass half cylinders to the test section tubes. This research was performed at evaporation temperatures of −15°C and −30°C, mass fluxes of 200 kg/m² s and 400 kg/m² s, and heat flux from 5 kW/m² to 15 kW/m² for vapor qualities ranging from 0.1 to 0.8. The CO_2 heat transfer coefficients indicated the nucleate boiling dominant heat transfer characteristics such as the strong dependence on heat fluxes at a mass flux of 200 kg/m² s. However, enhanced convective boiling contribution was observed at 400 kg/m² s. Surface conditions for two different tubes were investigated with a profilometer, atomic force microscope, and scanning electron microscope images, and their possible effects on heat transfer are discussed. Pressure drop, measured at adiabatic conditions, increased with the increase of mass flux and quality, and with the decrease of evaporation temperature. The measured heat transfer coefficients and pressure drop were compared with general correlations. Some of these correlations showed relatively good agreements with measured values. Visualized flow patterns were compared with two flow pattern maps and the comparison showed that the flow pattern maps need improvement in the transition regions from intermittent to annular flow. [DOI: 10.1115/1.2909079]

Keywords: CO_2, low temperature, heat transfer, pressure drop, flow patterns, surface condition

Introduction

CO_2 was reintroduced as an alternate refrigerant because of environmental concerns, and some commercial products using CO_2 as a working fluid are already on the market. As the use of CO_2 in real systems increases, the range of operating condition for CO_2 systems becomes wider, including low temperature applications. For the better design of systems operating in low temperatures, accurate measurements of the flow boiling heat transfer and pressure drop along with a better understanding of the heat transfer mechanisms are required.

In response to this application trend, the CO_2 flow boiling heat transfer coefficients for low evaporation temperatures were measured by Bredesen et al. [1], Høgaard Knudsen and Jensen [2], and Park and Hrnjak [3,4]. Bredesen et al. [1] presented heat transfer coefficients that were nearly unchanged with quality variation at an evaporation temperature of −25°C and the decrease of heat transfer with the increase of quality was not measured at evaporation temperatures lower than −10°C. Based on their experimental data, they concluded that nucleate boiling played a more important role in flow boiling heat transfer for CO_2 than other conventional refrigerants. Høgaard Knudsen and Jensen [2] also measured the heat transfer coefficients at an evaporation temperature of −25°C and compared their results with Shah's [5] correlation. They showed that the measured heat transfer coefficients were much higher than the predicted values. However, there was a significant difference, about 40–80%, between the measured flow boiling heat transfer coefficients when comparing the two studies [1,2] under similar test conditions. Motivated by this discrepancy and the limited conditions of the previous measurements, Park and Hrnjak [3,4] presented the CO_2 heat transfer coefficients in a 6.1 mm inner diameter tube at evaporation temperatures of −30°C and −15°C. The CO_2 heat transfer coefficients, pressure drop, and flow patterns were compared with those for R410A. They confirmed the nucleate boiling dominance for flow boiling heat transfer and showed that Gungor and Winterton's [6] correlation could predict the measured values relatively well.

Two-phase flow pressure drop of CO_2 has been measured by several researchers. Yoon et al. [7] and Bredesen et al. [1] measured pressure drop in 7.53 mm and 7.0 mm tubes, respectively. Bredesen et al. [1] presented pressure drop at evaporation temperatures of −25°C and −10°C. Their results showed that pressure drop was influenced by evaporation temperatures, mass fluxes, and vapor qualities, but not by heat fluxes. Park and Hrnjak [4] reported that CO_2 pressure drop in a 6.1 mm tube at −15°C and −30°C could be predicted relatively well by the Müller-Steinhagen and Heck [8] correlation. For a 0.8 mm multiported tube, Pettersen [9] measured pressure drop, and commented that the pressure drop can be calculated by Friedel's [10] correlation without significant deviation. Many studies have been performed in studying CO_2 flow boiling heat transfer and pressure drop at evaporation temperatures higher than −5°C, and they were reviewed by Thome and Ribatski [11].

CO_2 flow visualization studies have been conducted by Pettersen [9], Yun and Kim [12], Schael and Kind [13], Park and

[1]Corresponding author.

Contributed by the Heat Transfer Division of ASME for publication in the JOURNAL OF HEAT TRANSFER. Manuscript received April 17, 2007; final manuscript received August 7, 2007; published online June 19, 2009. Review conducted by Louis C. Burmeister.

Hrnjak [4], and Jang and Hrnjak [14]. Pettersen [9] visualized the flow patterns in a tube with a diameter of 0.98 mm at an evaporation temperature of 20°C and heat flux of 13 kW/m^2. He showed the dominance of intermittent and annular flow regimes and reported that the observed flow pattern did not fit any flow pattern maps. Yun and Kim [12] visualized flow patterns at an evaporation temperature of 5.3°C in a rectangular channel, which was 2 mm high and 16 mm wide. Schael and Kind [13] observed flow patterns in a horizontal microfin tube with a base diameter of 8.62 mm, at temperatures of −10°C and 5°C. Park and Hrnjak [4] presented flow patterns in a 6.1 mm tube at temperatures of −15°C and −30°C, and mentioned that the flow patterns could be predicted by the flow pattern map of Weisman et al. [15] and Wojtan et al. [16].

A literature review indicates a limited number of reports on CO_2 flow boiling heat transfer, pressure drop, and flow patterns at low temperatures but none for tubes smaller than 6 mm. Most of the previous studies have not considered the surface conditions of their tubes, even though CO_2 flow boiling is recognized as an active heat transfer mechanism of nucleate boiling, which is influenced by surface conditions. Only a small number of studies, such as Ref. [17], were presented to show the influence of surface roughness on flow boiling heat transfer. Yu et al. [17] measured surface roughness and observed surface condition using a scanning electron microscope (SEM) for two smooth tubes with different surface conditions. From the measured flow boiling heat transfer coefficients in two different tubes, Yu et al. [17] concluded that a rougher surface could enhance not only pool boiling but also flow boiling heat transfer for conventional refrigerants.

This study was motivated by the current research trend. In order to provide experimental data for tubes less than 6 mm, CO_2 flow boiling heat transfer and pressure drop were measured in a 3.5 mm copper tube and flow patterns were visualized in a 3 mm glass tube at evaporation temperatures of −15°C and −30°C. Also, possible surface condition effects on flow boiling heat transfer are presented by comparing the heat transfer data for a 6.1 mm tube [3], and by quantifying and imaging the surface conditions of 3.5 mm and 6.1 mm copper tubes with a profilometer, SEM, and atomic force microscope (AFM). The measured heat transfer coefficients and pressure drop are compared with the predicted values from several correlations, and flow patterns were examined and compared with two flow pattern maps.

Experimental Facility and Test Conditions

The test facility consists of two independent loops: One for CO_2 and the other for the secondary fluid (methoxy-nonafluorobutane, $C_4F_9OCH_3$). A schematic of the facility is shown in Fig. 1. This facility is almost identical to the test rig presented in previous studies [3,4] with the exception of a 3.5 mm test tube for heat transfer and pressure drop measurements and a visualization section. The secondary fluid loop has two main functions. One is to subcool the CO_2 in order to avoid cavitation in the gear pump, and the other is to add heat to the test section. The secondary fluid was chilled in a heat exchanger linked with the R404A cooling unit, and it subcooled the CO_2 in the subcooler. After the subcooler, the secondary fluid was heated by the secondary fluid heater in order to maintain the secondary fluid at a temperature higher than the saturation temperature of CO_2. From the temperature difference between the secondary fluid and the saturated CO_2 in the test section, heat could be transferred from the secondary fluid to CO_2.

In the CO_2 loop, subcooled liquid CO_2 was pumped by a gear pump to a calorimeter where it was heated by electrical heaters from liquid to liquid-vapor phase with a desired quality at the inlet of a test section. The calorimeter was carefully calibrated to provide accurate measurements of inlet quality. In the 3.5 mm copper tube test section, heat was transferred to CO_2 from two half-cylinder brass pieces surrounding the copper tube. The temperature of the brass pieces was controlled by the secondary fluid circulating through the brass pieces. The cross section of the test section is illustrated schematically in Fig. 2(*a*). The brass pieces provide a uniform temperature distribution to the wall of the copper tube by dampening the influence of the secondary fluid temperature difference between the test section inlet and outlet. All

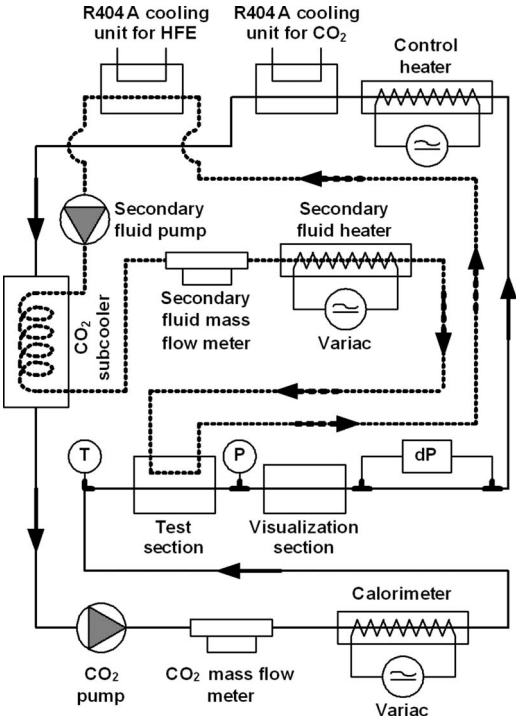

Fig. 1 Simplified schematics of test facility

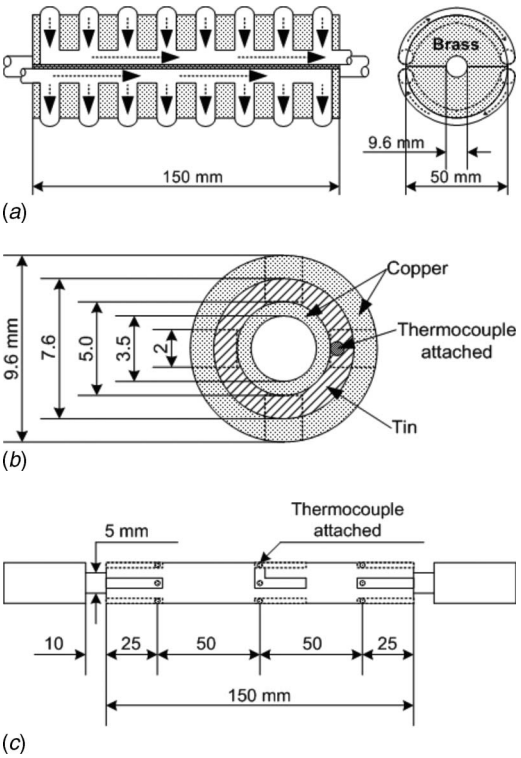

Fig. 2 Schematics for (*a*) the test section, (*b*) the cross section of the test tube, and (*c*) dimension of the test tube

gaps between the two brass pieces and the copper tube were filled with high thermal conductivity paste to reduce the thermal contact resistance, while the upper and lower parts of the brass jackets were tightened with two metal band clamps. Due to the smaller outer diameter of the tube inserted between the two brass pieces, a larger concentric tube was placed around it, with the gap between the tubes filled with tin, as illustrated in Fig. 2(*b*). A neck was machined at each of the entrance and exit of the test section, as shown in Fig. 2(*c*), in order to reduce the axial conduction heat loss from the heated region. The locations of the thermocouples placed at the top, bottom, and sides at three separate locations along the test section are illustrated in Fig. 2(*c*). As a result, temperatures at 12 points on the tube surface were measured and their average values were used as the wall temperature to calculate the heat transfer coefficient. The thermocouples were carefully calibrated by a calibration test, which was performed with the secondary fluid and CO_2 flowing through the test section at operating temperatures. The thermocouples were attached using a very thin layer of thermal epoxy in grooves carved on the outside surface of the inner tube. The remaining portion of the grooves was filled with high thermal conductivity paste.

In order to ensure a small change of vapor quality, the length of the heated region was chosen to be 150 mm, shorter than in some other studies. In order to determine possible effects, a test which effectively increased the heated length was conducted. This was accomplished by wrapping an electric heater over 1.2 m of tube upstream of the test section. In this test, the same heat flux as a test condition was applied upstream of the test section, which effectively elongated the heated length. Nearly identical results for measurement with and without electric heat supply were obtained. From these results, it could be inferred that the heated length in this study was sufficiently long to guarantee reliable measurement while providing a narrow band of qualities.

The visualization section, located immediately after the test section, consisted of a glass tube, fittings, and a polyester block. The inner and outer diameters were 3 mm and 10 mm, respectively, and the visualized length was 90 mm. A polyester block, with dimensions of $130\times70\times70$ mm^3, surrounded the glass tube in order to prevent condensation or frosting. After the visualization section, horizontal pressure drop was measured by differential pressure transducers at adiabatic conditions over 1 m long sections of the same tube. Generally, pressure drop of two-phase flow in a horizontal tube is influenced by friction and acceleration of the flow caused by flow boiling. Instead of measuring pressure drop over a heated section, it was performed at an adiabatic condition over the length of 1 m in this study; because the heated section was relatively short (150 mm). Due to the short heated section, the pressure drop generated by acceleration was small and the measurement accuracy of two-phase flow pressure drop could be influenced. The control heater added heat downstream of the last pressure drop test section to maintain a desired saturation temperature in the test section. After the control heater, CO_2 condensed in a plate heat exchanger, connected to the R404A cooling unit, and then flowed to the CO_2 subcooler.

The absolute pressure of CO_2 was determined by a pressure transducer with an uncertainty of ±3.4 kPa. Pressure drop was evaluated by differential pressure transducers with an accuracy of ±0.086 kPa. The CO_2 and the secondary fluid mass flow rates were measured by Coriolis mass flow meters with an accuracy of $\pm0.1\%$ of the reading. Electrical power inputs to the calorimeter and the secondary fluid heater were measured with watt transducers, which had 0.2% reading accuracy. *T*-type thermocouples with a calibrated accuracy of $\pm0.10°$C were used to measure the refrigerant temperature and wall temperature on the test tube. Flow boiling heat transfer coefficients were determined with a variation of saturation temperature, mass flux, heat flux, and quality. The pressure drop measurements and flow visualization were performed at adiabatic conditions with the same evaporation temperatures and mass fluxes as the measurement of heat transfer coefficients. The evaporation temperatures were set at $-15°$C and $-30°$C. The heat fluxes were 5 kW/m^2, 10 kW/m^2, and 15 kW/m^2, and the mass fluxes were 200 kg/m^2 s and 400 kg/m^2 s. The CO_2 quality at the test section inlet was controlled from 0.1 to 0.8.

Data Reduction

The same data reduction and calibration methods were used as in the previous studies [3,4]. The average flow boiling heat transfer coefficient, h, was determined from Eq. (1) where $\dot{Q}_{CO_2}$ and T_{CO_2} represent the heat transfer rate to the CO_2 and the CO_2 saturation temperature, respectively. The saturation temperature was calculated from the measured saturation pressure based on the equation of state presented by Span and Wagner [18].

$$h = \dot{Q}_{CO_2}/[A_{surf}(T_W - T_{CO_2})] \tag{1}$$

$$\dot{Q}_{CO_2} = (\dot{m}C_P)_{sf}(T_{sf,i} - T_{sf,o}) + \dot{Q}_{amb} - \dot{Q}_{cond} \tag{2}$$

The heat transfer rate to the CO_2 was calculated by Eq. (2). The first term of right hand side of Eq. (2) is the heat transfer rate from the secondary fluid to the test section. The specific heat of the secondary fluid,$C_{P,sf}$, was determined by a calibration test where the secondary fluid flowed through the test section at operating conditions, and heat was added with an electrical heater inserted between brass pieces. From the inlet and outlet temperatures, and mass flow rate of the secondary fluid, the amount of energy to the electrical heater, and ambient temperature, $C_{P,sf}$ and $\dot{Q}_{amb}$ could be determined in the calibration test. The heat transfer rate between the test section and environment was symbolized by $\dot{Q}_{amb}$. The conduction heat loss in the axial direction of the pipe, $\dot{Q}_{cond}$, was estimated by a finite element method provided by Jang and Hrnjak [19]. In this method, a temperature of a small wall element, which was adjacent to heated regions, was determined, and the $\dot{Q}_{cond}$ was calculated by the temperature gradient between the heated region and this small wall element in contact with the heated region. The method was validated by presenting an almost identical measured and calculated wall temperature for an element close to the heated region. The uncertainty propagation of heat transfer coefficient was calculated based on Ref. [20]. The uncertainty was within the range of 7.6–26.3% of the measured heat transfer coefficient and each measurement uncertainty was shown as a vertical error bar in the figures.

In order to verify the methodology applied in this study, R22 flow boiling heat transfer coefficients for a 6.1 mm tube were measured by the same facility because R22 has a large database and it is a well known refrigerant. The experimental results were compared with the predicted values calculated by the correlations of Gungor and Winterton [6], Kandlikar [21], Shah [5], and Wattelet et al. [22]. In Fig. 3, it is illustrated that R22 heat transfer coefficients determined by this experimental facility agreed well with the predicted values by the correlations at vapor qualities lower than 0.4. The measured R22 heat transfer coefficients were about 10% higher than calculated values at vapor qualities higher than 0.5, as seen in Fig. 3. Even though the measurement of heat transfer coefficients for the 3.5 mm tube with R22 was not performed in this study, the same facility, data reduction, calibration method, and other methodology as for the 6.1 mm tube were used. As a result, it could be inferred that the CO_2 flow boiling heat transfer coefficients for the 3.5 mm tube could be properly determined.

Results and Discussion

CO_2 Flow Boiling Heat Transfer Coefficient for the 3.5 mm Tube. In the previous studies [1–4] for tubes larger than 6 mm at low evaporation temperatures, CO_2 heat transfer coefficients were

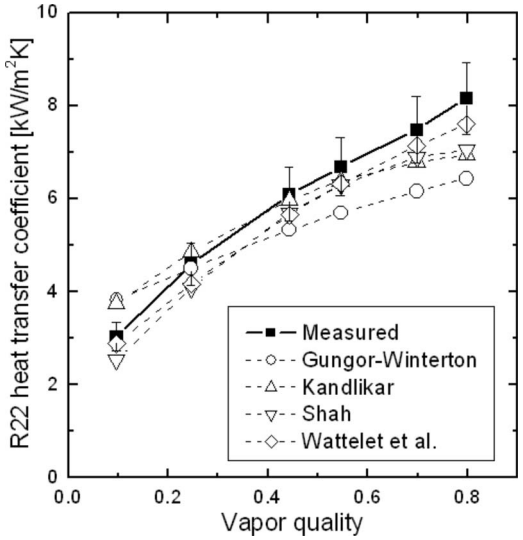

Fig. 3 Comparison of the measured and predicted R22 flow boiling heat transfer coefficients to validate the test results for a 6.1 mm tube at the evaporation temperature, heat flux, and mass flux of −15°C, 10 kW/m², and 400 kg/m² s, respectively

nearly independent of vapor quality for mass fluxes near 200 kg/m² s. Due to the large vapor density of CO_2, the change of CO_2 two-phase flow velocity with the increase of quality is not significant, which results in lower contribution of convective boiling to flow boiling heat transfer. However, the earlier studies [1,3] showed that heat transfer coefficients had a positive slope with the increase of vapor quality before dryout at mass fluxes near 400 kg/m² s because the convective boiling contribution increased.

In Fig. 4, the flow boiling heat transfer coefficients for the 3.5 mm tube and their trend are presented with the change of mass flux, heat flux, quality, and evaporation temperature. The quality shown in Fig. 4 for each heat transfer coefficient is average quality in the test section. In Fig. 4, heat transfer coefficients for the 3.5 mm tube at a mass flux of 200 kg/m² s have the characteristics of nucleate boiling dominated heat transfer at a vapor quality range below 0.5, including the strong dependence on the change of heat flux and the small influence of quality. At vapor qualities above 0.5, heat transfer coefficients increase with the increase of quality. For a mass flux of 400 kg/m² s, the heat transfer coefficients demonstrate the dominance of convective boiling heat transfer.

For the 3.5 mm tube, heat transfer coefficient change as a function of quality is very significant. These heat transfer characteristics can be explained by the relation between convective boiling heat transfer and liquid film thickness at the tube wall. Thome and El Hajal [23] gave the relation including the liquid film Reynolds number, film thickness, and liquid Prandtl number as presented by Eq. (3). In Eq. (3), vapor quality (x) can be defined thermodynamically by an enthalpy ratio as shown in Eq. (4), and void fraction (α) can be described by the ratio of vapor phase area to a total tube area at a cross section of a tube.

$$h_{cb} = 0.0133\left(\frac{4G(1-x)\delta}{(1-\alpha)\mu_l}\right)^{0.69} \mathrm{Pr}_l^{0.4}\frac{k_l}{\delta} \tag{3}$$

$$x = (i_{\text{two phase}} - i_l)/(i_v - i_l) \tag{4}$$

$$\delta = [D(1-\sqrt{\alpha})]/2 \tag{5}$$

$$\alpha = \frac{x}{\rho_v}\left\{[1+0.12(1-x)]\left(\frac{x}{\rho_v}+\frac{1-x}{\rho_l}\right) + \frac{1.18}{G}\left[\frac{g\sigma(\rho_l-\rho_v)}{\rho_l^2}\right]^{0.25}(1-x)\right\}^{-1} \tag{6}$$

From this equation, convective boiling increases with the reduction of liquid film thickness at a tube wall. If an annular flow is ideally concentric without interfacial waves and liquid entrainment in the vapor core, the liquid film thickness can be obtained by Eq. (5). As the tube diameter decreases, the liquid film thickness also decreases for an identical void fraction condition, and the convective boiling effect on heat transfer becomes stronger. With this explanation, larger convective boiling contribution for flow boiling in the 3.5 mm tube than that in the larger tubes in previous studies can be reasonably described.

In order to explain the different heat transfer trends between mass fluxes of 200 kg/m² s and 400 kg/m² s in Fig. 4, the relation between the mass flux and the liquid film thickness should be identified. As shown in the Rouhani and Axelsson [24] equation presented by Eq. (6), the void fraction increases as the mass flux increases, at a given quality. Also, the entrainment of liquid into the vapor core is enhanced with the increase of mass flux, as

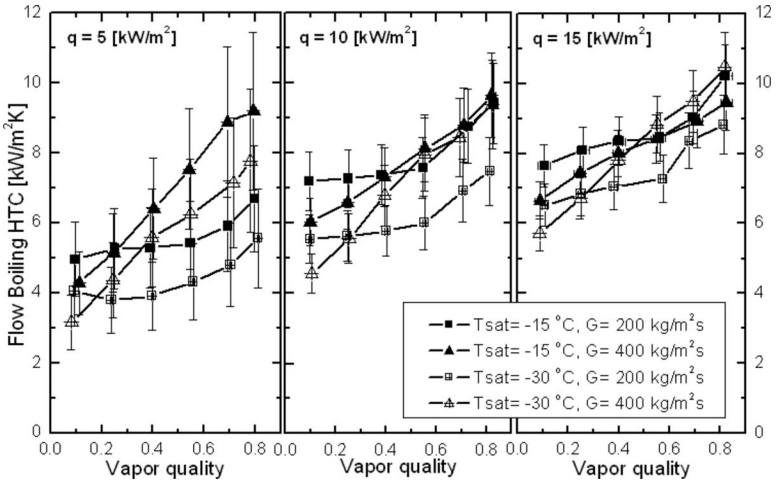

Fig. 4 CO_2 flow boiling heat transfer coefficients for the 3.5 mm tube as a function of mass flux, heat flux, vapor quality, and evaporation temperatures

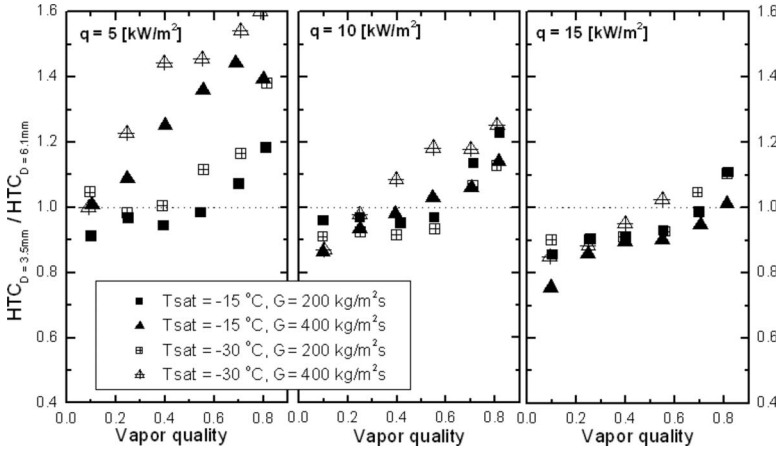

Fig. 5 The ratio of CO_2 flow boiling heat transfer coefficients for the 3.5 mm to those for the 6.1 mm tube at identical conditions

presented by Okawa et al. [25]. Consequently, the liquid film thickness becomes thinner as the mass flux increases and the tube diameter decreases, which causes the significant contribution of convective boiling on flow boiling heat transfer.

CO_2 flow boiling heat transfer coefficients become higher with the increase of evaporation temperature, because the nucleate boiling heat transfer increases. In Fig. 4, this trend can be shown for the mass flux of 200 kg/m^2 s, where nucleate boiling is the main heat transfer mechanism. For the mass flux of 400 kg/m^2 s, the effect of evaporation temperature on flow heat transfer is not as significant as at the lower mass flux.

Generally, flow boiling heat transfer coefficients are augmented with increasing mass flux due to the enlarged convective heat transfer contribution. However, Park and Hrnjak [3] reported an unexpected mass flux effect on heat transfer coefficients, which was that heat transfer coefficients for a mass flux of 400 kg/m^2 s were lower than those for a lower mass flux of 200 kg/m^2 s at low qualities in a 6.1 mm tube. The identical trend is presented for the 3.5 mm tube, as shown in Fig. 4. The unanticipated decrease in heat transfer with increasing mass flux at low quality regions could be a result of a reduction of nucleate boiling heat transfer mechanism. The decrease of nucleate boiling heat transfer may be a consequence of the liquid and vapor dynamics, which affects the thermal boundary layer needed to initiate nucleation.

Diameter Effect on CO_2 Flow Boiling Heat Transfer Coefficient. In order to investigate the tube diameter effect on heat transfer coefficients, the experimental results for the 3.5 mm tube were compared with the measured data for a 6.1 mm tube [3], and the comparison is presented in Fig. 5 with the ratio of heat transfer coefficients for the 3.5 mm to those for the 6.1 mm tube. Most previous studies with conventional refrigerants showed higher heat transfer coefficients and pressure drop for smaller tubes. However, in Fig. 5, it is illustrated that the CO_2 flow boiling heat transfer coefficients are not significantly influenced by a change of tube diameter at heat fluxes of 10 kW/m^2 and 15 kW/m^2. This trend could be explained by larger nucleate boiling contribution to flow boiling for CO_2 than for other refrigerants, which is caused by the higher reduced pressure and smaller surface tension of CO_2 than other conventional refrigerants at an identical temperature.

Even though the small effect of tube diameter on CO_2 heat transfer could be explained by nucleate boiling effects, this explanation is not sufficient to clarify the lower heat transfer coefficients for the smaller tube. In Fig. 5, the lower heat transfer for 3.5 mm tube is more obvious for higher heat fluxes at low vapor qualities. From this comparison, it can be inferred that other differences can exist between the two tubes besides the diameter of the tube. The most plausible difference is surface conditions because the nucleate boiling contribution to flow boiling heat transfer can be influenced by different surface conditions. According to pool boiling correlations presented by Gorenflo [26], the pooling boiling heat transfer coefficients increase with the increase of surface roughness. If the 6.1 mm tube was much rougher than the

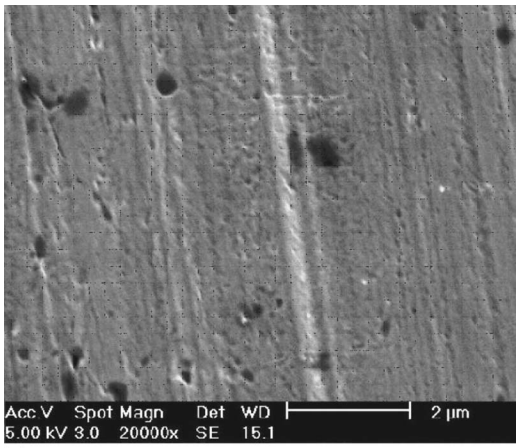

(*a*)

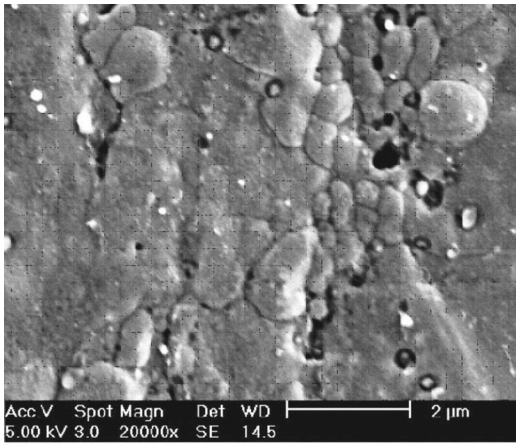

(*b*)

Fig. 6 Tube surface images with a SEM for the (*a*) 3.5 mm tube (×5000) and (*b*) 6.1 mm tube (×5000)

Table 1 Surface roughness of the 3.5 mm and 6.1 mm tubes with the profilometer and AFM

	Profilometer		
	Axial (μm)	Circumferential (μm)	AFM (μm)
3.5 mm	0.039	0.034	0.048
6.1 mm	0.059	0.054	0.072
Method	Arithmetic average of all absolute distance values from a centerline		Standard deviation of the measured values

3.5 mm tube in this study, the lower heat transfer coefficients for the smaller tube, shown in Fig. 5, can be partly explained by the roughness effect.

Surface Condition of the 3.5 mm and 6.1 mm Tubes and Its Effect on Flow Boiling Heat Transfer. In order to characterize the surface roughness of the 3.5 mm and 6.1 mm tubes, a SEM, an AFM, and a profilometer were used. The same 6.1 mm tube specimen used in the previous study [3] was investigated in this study. The SEM images for the tube surfaces are presented in Fig. 6. The linear patterns in the figures represent the axial direction of the tubes. The SEM images show that the 6.1 mm tube surface is rougher than the 3.5 mm tube, and provide more cavities to initiate the nucleation. The surface condition difference for the tubes seems to be caused by a difference in the manufacturing process. A profilometer and an AFM were used to quantify the surface roughness; measured values are summarized in Table 1. Figure 7 presents the profile of the surfaces for the 3.5 mm and 6.1 mm tubes in axial and circumferential directions. Figure 7(*b*) shows that the surface profile for the 6.1 mm tube in the axial direction has much more small protrusions than the 3.5 mm tube. The surface roughness values show that there is no significant difference of roughness for the axial and circumferential directions. An AFM was used to investigate the surface conditions because it not only provides the surface roughness, but also 3D images of a surface. Figure 8 shows the AFM images for the surface of the 3.5 mm and 6.1 mm tubes; these images illustrate the significantly rougher surface of the 6.1 mm tube. Four areas (each area of 80×80 μm^2) were scanned by an AFM to confirm the homogeneity of the two tubes. From the four surface roughness measurements of the scanned areas, the maximum and minimum values were excluded and the average of the two remaining values was taken as the surface roughness.

With the measured surface roughness, the CO_2 pool boiling heat transfer coefficients were calculated by Gorenflo's [26] correlation and the results are presented in Fig. 9. A roughness of

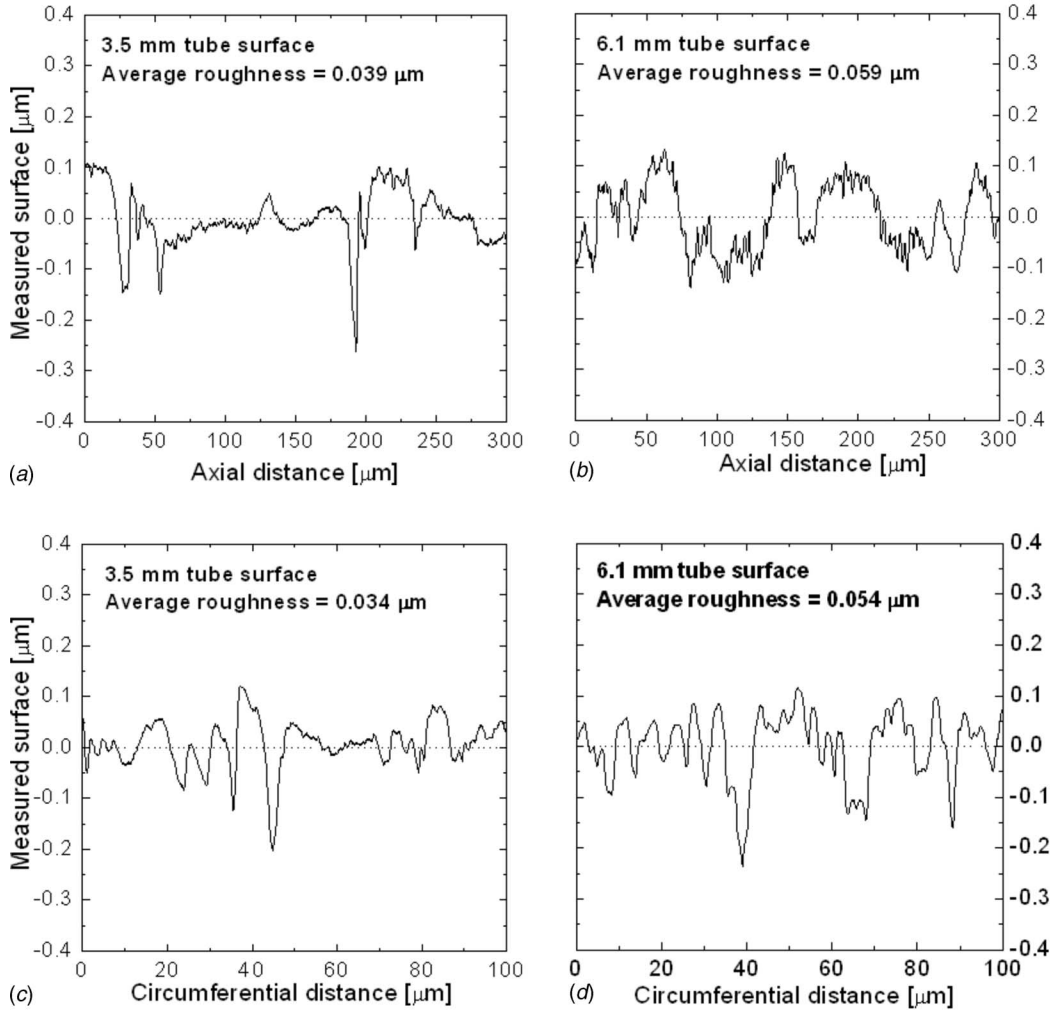

Fig. 7 Surface profile measured by a profilometer to the axial direction on the (*a*) 3.5 mm and (*b*) 6.1 mm tubes and to the circumferential direction on the (*c*) 3.5 mm and (*d*) 6.1 mm tubes

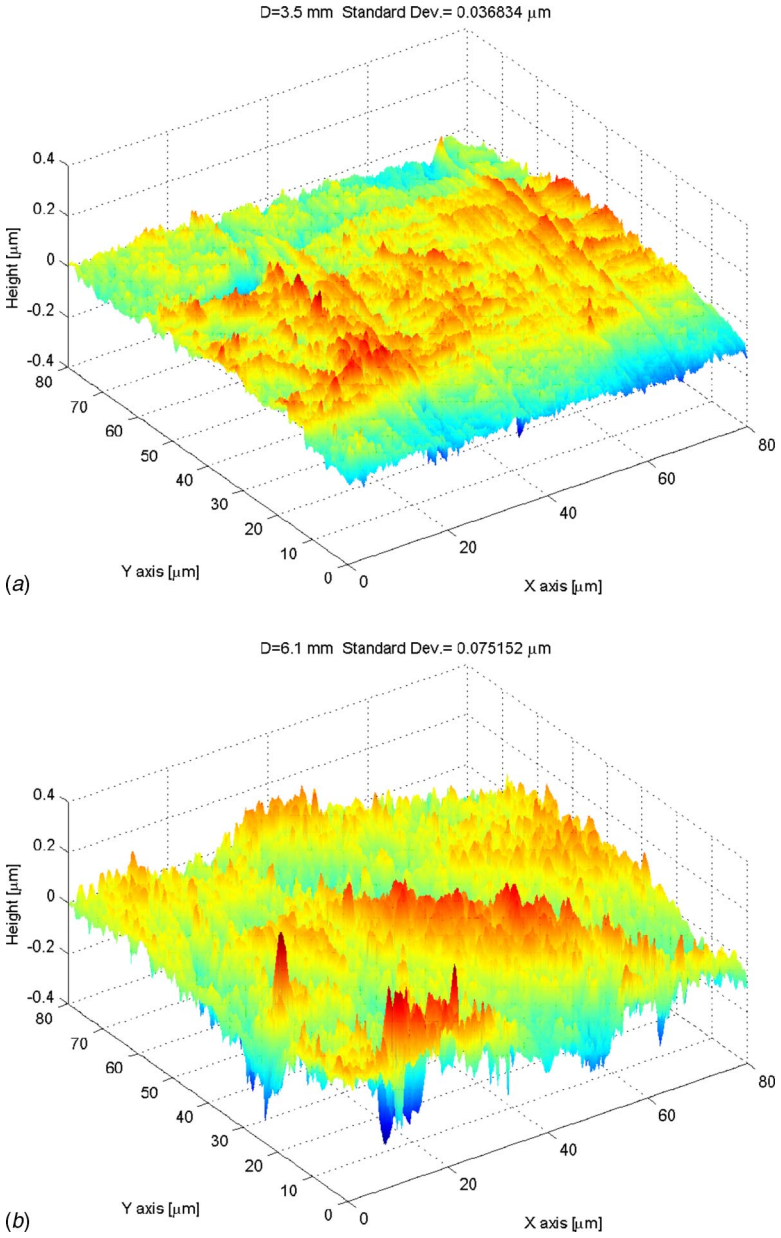

Fig. 8 Surface image measured by an AFM for the (*a*) 3.5 mm and (*b*) 6.1 mm tubes

0.5 μm is the standard roughness of the correlation, and the 0.07 μm and 0.04 μm roughnesses represent the surface roughness of the 6.1 mm and 3.5 mm tubes, respectively. The higher surface roughness results in higher pool boiling heat transfer rates for the 6.1 mm tube than for the 3.5 mm tube at an otherwise identical condition, agreeing with the finding of Yu et al. [17]. However, the effect of roughness on CO_2 nucleate boiling in Fig. 9 might be too small to explain the result of the heat transfer comparison shown in Fig. 5. Therefore, it is worth considering whether or not surface roughness can represent the essential characteristics of a surface condition. Roy Chowdhury and Winterton [27] commented that pool boiling was influenced by the number of nucleation sites, not necessarily by the roughness itself. Also, Luke [28] mentioned that a single roughness parameter could not fully explain the effect of surface condition on pool boiling heat transfer. SEM images in Fig. 6 and AFM images in Fig. 8 show that the surface conditions are significantly different between the two tubes, and the surface of the 6.1 mm tube has significantly more holes and cracks, which can be nucleation sites for boiling phenomena. Considering nucleate boiling to be a more important heat transfer contribution for CO_2 flow boiling than for other refrigerants, the different surface conditions of the two tubes partly explain why heat transfer coefficients for the 3.5 mm tube were not consistently higher than those for the 6.1 mm tube.

Comparison With General Correlations for Flow Boiling Heat Transfer Coefficients. Some general correlations for predicting flow boiling heat transfer coefficients are known to underpredict CO_2 heat transfer coefficients. Thome and El Hajal [23] presented a correlation to calculate the flow boiling heat transfer coefficient for CO_2 only, based on a heat transfer model associated with flow patterns proposed by Kattan et al. [29,30] and the correction of CO_2 nucleate boiling contribution. Recently, Cheng et al. [31] proposed a correlation for CO_2 heat transfer coefficients based on a model presented by Wojtan et al. [32]. Although most of the correlations to predict flow boiling heat transfer coefficients

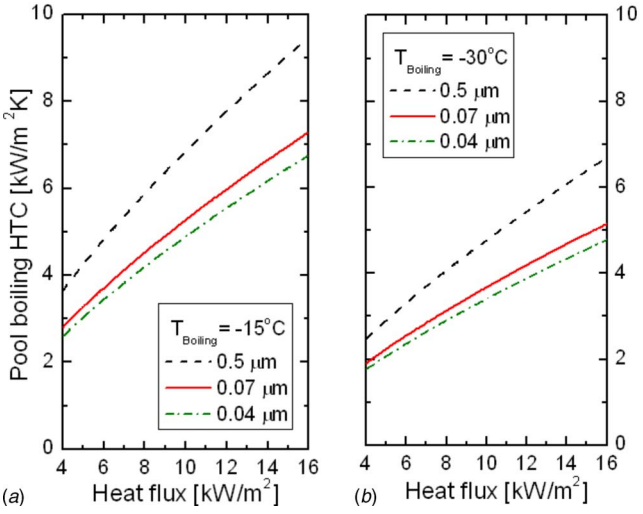

Fig. 9 Surface roughness effect on pool boiling heat transfer coefficients based on Gorenflo's [26] correlation at boiling temperatures of (*a*) −15°C and (*b*) −30°C

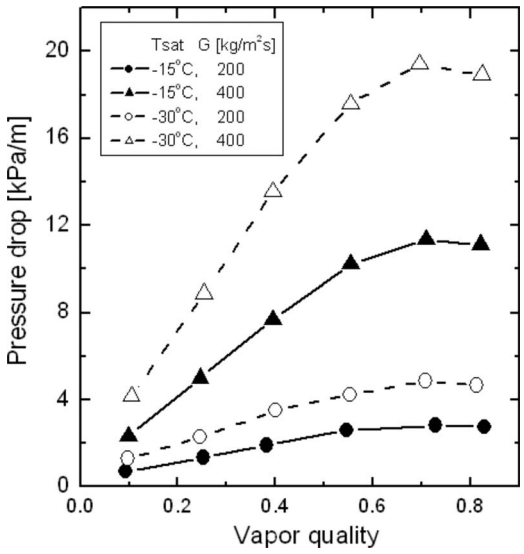

Fig. 10 Pressure drop of adiabatic two-phase flow in the 3.5 mm tube for evaporation temperatures of −15°C and −30°C, mass fluxes of 200 kg/m^2 s and 400 kg/m^2 s, and vapor qualities from 0.1 to 0.8

were generated without CO_2 data, it is valuable to compare the measured CO_2 heat transfer coefficients with the values predicted by these at low evaporation temperatures. This is because the thermophysical properties of CO_2 at this temperature range are similar to those of conventional refrigerants at their applicable temperature range, such as CO_2 at −30°C and R22 at 10 °C.

In Table 2, the bias error and absolute average deviation of the predicted values with the general correlations from the measured heat transfer coefficients are presented for the 3.5 mm tube. In Table 2, the experimental results were compared with calculated values by the correlations of Thome and El Hajal [23], Cheng et al. [31], Gungor and Winterton [6], Wattelet et al. [22], Liu and Winterton [33], and Shah [5]. For the predictions by these correlations, a measured surface roughness was not considered, because most of the correlations were developed with a fixed surface roughness. Even though a measured surface roughness can be applied to a correlation, this input cannot give a correct nucleate boiling contribution to flow boiling heat transfer. This is because the convective contribution was already determined by comparing experimental data with a guessed surface roughness. The correlation of Wattelet et al. [22] gives appropriate heat transfer coefficient predictions for the 3.5 mm tube with a bias error and absolute average deviation of −2.5% and 13.5%, respectively. Also, the correlations of Gungor and Winterton [6], and Liu and Winterton [33] can relatively well predict with a bias error and absolute average deviation within 20%.

One of the motivations to select a 3.5 mm tube for measuring heat transfer coefficients is that the tube size is close to the 3 mm hydraulic diameter, which was proposed as the criterion to categorize tubes by Kandlikar [34]. Kandlikar [34] commented that tubes with a hydraulic diameter greater than 3 mm could be classified as conventional macroscale tubes and the tubes with diameters between 3 mm and 200 μm could be grouped as minichannels. In Table 2, some general correlations, based on heat transfer coefficient data for the tubes with larger than 6 mm, can relatively well predict the coefficients for the 3.5 mm tube. As a result, it can be inferred that CO_2 flow boiling for the 3.5 mm tube has a similar characteristic heat transfer mechanism for macroscale tubes.

Table 2 Comparison of experimental data for flow boiling heat transfer coefficients for the 3.5 mm tube with some general correlations

Correlations	Bias[a] error	AAD[b]
Thome and El Hajal [23]	36.8	39.8
Cheng et al. [31]	18.9	26.0
Gungor and Winterton [6]	13.4	17.7
Wattelet et al. [22]	−2.6	13.5
Liu and Winterton [33]	−15.6	18.5
Shah [5]	−26.8	29.5

[a]Bias error,%: $1/N\Sigma[(h_{predicted}-h_{measured})/h_{measured}]\times 100$.
[b]Absolute average deviation (AAD), %: $1/N\Sigma|[(h_{predicted}-h_{measured})/h_{measured}]|\times 100$.

Pressure Drop for CO_2 Two-Phase Flow at Low Temperatures. In this study, pressure drop of two-phase flow for the 3.5 mm tube was measured at adiabatic conditions and is presented in Fig. 10. Typically, pressure drop increases with the decrease of tube diameter and increase of mass flux. It increases with the reduction of evaporation temperature as a function of thermophysical properties, such as the increase of liquid viscosity and decrease of vapor density. Pressure drop consistently increases with the increase of vapor quality up to about 0.7, as shown in Fig. 10. After this point, it maintains at a certain value for a mass flux of 200 kg/m^2 s, or drops slightly with the increase of quality for a mass flux of 400 kg/m^2 s. The decrease of pressure drop at high mass fluxes and vapor qualities can be explained by the interaction between the vapor and liquid phase, which is a major pressure drop mechanism in a two-phase flow. This interaction generates turbulent waves on the liquid surface at the interface between liquid and vapor. A stronger interaction can occur at low and medium vapor qualities, where a liquid film is thick enough to develop high turbulent waves. At high vapor qualities, the liquid film is too thin to make a wave form on the film surface or nonexistent, which results in a decrease of pressure drop with an increase of vapor quality. The relation between the turbulent wave in liquid films and pressure drop can be confirmed in Fig. 11(*b*), which presents flow patterns for a 3 mm glass tube at a saturation temperature of −15°C and a mass flux of 400 kg/m^2 s. In Fig. 11(*b*), the turbulent waves can be shown at a vapor quality of 0.7, and the intensity of the wave significantly decreases as the quality is increased to 0.8 and 0.9.

In Table 3, the bias error and absolute average deviation of the predicted values with some general correlations from the measured pressure drops are presented. For this comparison, the cor-

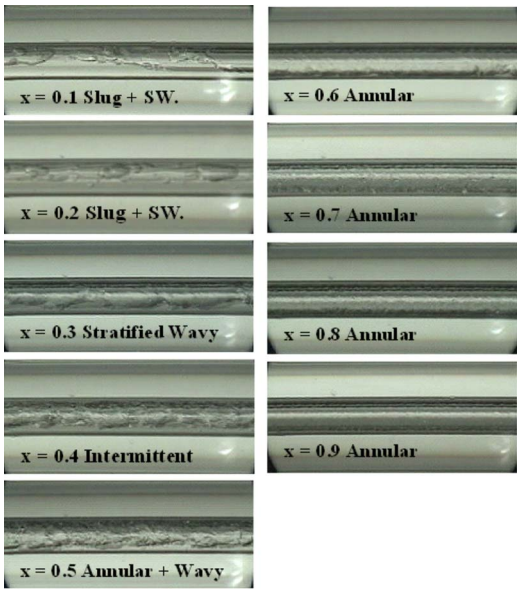

(*a*)

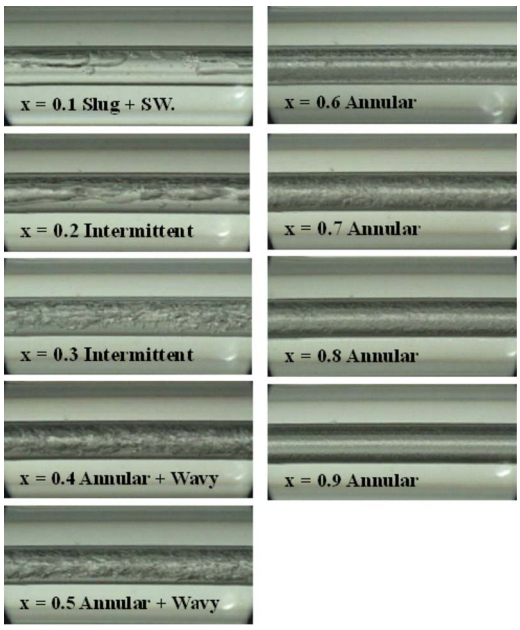

(*b*)

Fig. 11 Flow patterns in the 3 mm glass tube at a saturation temperature of −15°C for mass fluxes of (*a*) 200 kg/m² s and (*b*) 400 kg/m² s

relations presented by Friedel [10], Müller-Steinhagen and Heck [8], Lockhart and Martinelli [35], Chisholm [36], and Grönnerud [37] were used. Friedel's [10] correlation gives good agreement with the measured pressure drop for the 3.5 mm tube with a bias error and absolute average deviation of −6.0% and 13.9%, respectively. Ould Didi et al. [38] reported that the Müller-Steinhagen and Heck [8] and Friedel's [10] correlations were appropriate separated flow models to predict the pressure drop for annular flow patterns. From the flow visualization for the 3 mm glass tube in this study, annular flow pattern was observed for more than 60% of the pressure drop measurement conditions. Based on the observed flow patterns and comparison with predicted pressure drop, it can be concluded that the two-phase flow pressure drop for CO_2 at low temperatures has similar characteristics as those for conventional refrigerants. This is because Ould Didi et al. [38] studied the pressure drop for conventional refrigerants excluding CO_2.

Table 3 Comparison of experimental data for pressure drop of adiabatic two-phase flow for the 3.5 mm tube with some general correlations

Correlations	Bias error	AAD
Friedel [10]	−6.00	13.9
Müller-Steinhagen and Heck [8]	−25.3	25.7
Lockhart and Martinelli [35]	53.6	59.6
Chisholm [36]	31.7	34.1
Grönnerud [37]	49.0	58.7

Flow Patterns for CO_2 Two-Phase Flow at Low Temperatures. Flow patterns for two-phase flow can give useful information for analyzing heat transfer coefficients and pressure drop, because both heat transfer and pressure drop mechanisms are influenced by the flow pattern. Figures 11(*a*) and 11(*b*) present the change of flow patterns with the increase of vapor quality from 0.1 to 0.9 at a saturation temperature of −15°C, and mass fluxes of 200 kg/m² s and 400 kg/m² s, respectively. Before discussing two-phase flow patterns, it is necessary to define them because the classification of flow patterns is subjective for each researcher and it is difficult to categorize a certain flow pattern. In this study, the flow pattern classification presented by Wojtan et al. [16] was used for slug or plug flow, and the classification proposed by Wang et al. [39] was applied for annular flow. Slug or plug flow was subdivided into "slug+stratified smooth," "slug+stratified wavy," and "intermittent" flow. Intermittent flow was used to specify the flow containing slug, wavy, and annular flows. This combination of flow patterns made the classification of the flow pattern vague. Annular flow was classified into "annular+wavy" and "annular" flow. Annular+wavy flow was basically annular flow. However, it contained an amount of liquid, which formed the wavy flow pattern at the bottom of a tube, as presented in Fig. 11. In Fig. 11(*a*), the change in the flow patterns with the increase of a vapor quality for a mass flux of 200 kg/m² s is shown. For a higher mass flux of 400 kg/m² s, the flow patterns developed from slug to annular flow without stratified flow, as shown in Fig. 11(*b*). This is because the vapor velocity is high enough to disturb the liquid-vapor interface severely for high mass fluxes even at low quality regions.

In Fig. 12(*a*), the comparison of the flow pattern map of Weisman et al. [15] with the visualized flow patterns is shown for the 3 mm glass tube at evaporation temperatures of −15°C and −30°C, and at mass fluxes of 200 kg/m² s and 400 kg/m² s. For each connected line, vapor qualities varied from 0.1 to 0.9 in increments of 0.1. The flow pattern map of Weisman et al. [15] used a logarithmic scale of a superficial vapor and liquid velocity as *x*-axis (j_v) and *y*-axis (j_l), respectively. In Fig. 12(*a*), the flow pattern map of Weisman et al. [15] predicts the observed flow patterns accurately as slug or plug flow at superficial vapor velocities lower than 1 m/s, and as annular flow at superficial vapor velocities higher than 2 m/s. However, the flow pattern map is not accurate for the transition region from slug or plug to annular flow where superficial vapor velocities are between 1 m/s and 2 m/s.

Wojtan et al. [16] presented flow pattern maps using a coordinate containing quality and mass flux. The comparison of visualized flow patterns with their flow pattern map is presented in Figs. 12(*b*) and 12(*c*) for evaporation temperatures of −15°C and −30°C, respectively. In the flow pattern map of Wojtan et al. [16], the transitions to annular flow were presented as a line at fixed quality, which was determined by the ratio of liquid to vapor for both density and viscosity. Compared with the visualized flow patterns, a fixed quality could not predict the transition from in-

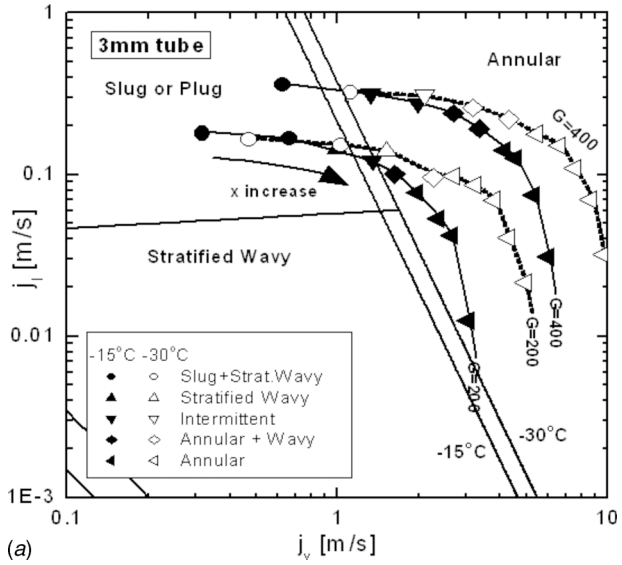

(*a*)

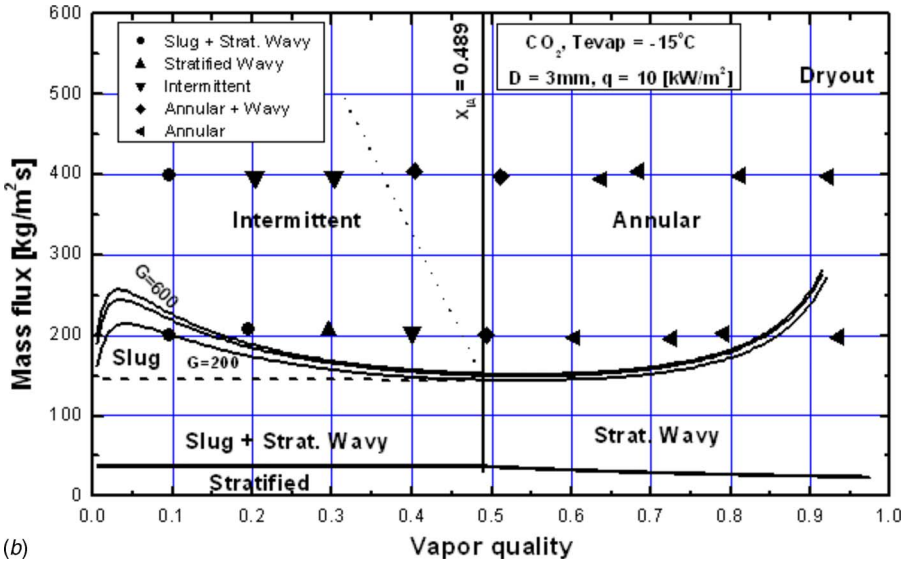

(*b*)

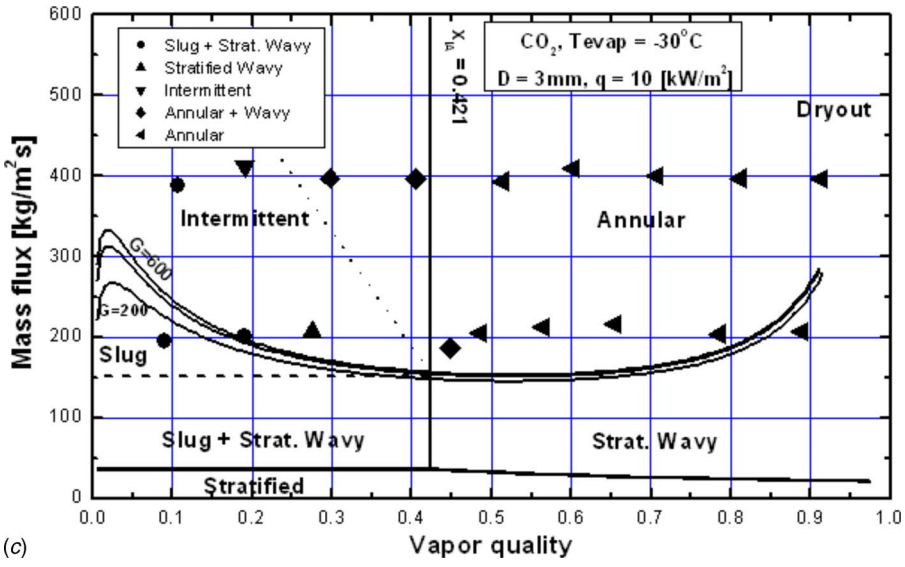

(*c*)

Fig. 12 Comparison of the visualized flow patterns in the 3 mm glass tube with the flow pattern map presented by (*a*) Weisman et al. [15] and (*b*) Wojtan et al. [16] at −15°C, and (*c*) Wojtan et al. [16] at −30°C

termittent to annular flow accurately. Instead, the vapor quality for the transition from intermittent to annular flow decreases with the increase of mass flux. This trend is shown in Figs. 12(*b*) and 12(*c*), where an approximate transition line from intermittent to annular flow is proposed as a dotted line based on the observed flow patterns. Schael and Kind [13] reported that the transition from slug to annular flow did not occur at a constant quality based on their CO_2 two-phase flow visualization at saturation temperatures of 5°C and −10°C. They also noted that the transition quality was a function of mass fluxes, as shown in this study. However, the flow pattern map of Wojtan et al. [16] showed relatively good agreement with the flow patterns in this study except for the annular flow transition.

Summary and Conclusions

For a 3.5 mm horizontal tube, CO_2 flow boiling heat transfer coefficients and pressure drop were measured at low evaporation temperatures of −15°C and −30°C. Also, flow patterns were observed at adiabatic conditions for a 3 mm glass tube. The flow boiling heat transfer coefficients for the 3.5 mm tube at a mass flux of 200 kg/m^2 s indicated a large influence of nucleate boiling, whereas those at a mass flux of 400 kg/m^2 s showed that the convective boiling contribution to heat flux was significant especially at low heat flux condition. The comparison of the heat transfer coefficients for the 3.5 mm tube with those for a 6.1 mm tube showed that the influence of tube diameter on heat transfer coefficients was relatively small due to the strong effect of CO_2 nucleate boiling on flow boiling. In order to explain why the heat transfer coefficients for the 3.5 mm tube were smaller than those for the 6.1 mm tube in several measurement conditions, surface conditions were characterized by a profilometer, AFM, and SEM images. From the measured surface roughness and the calculated pool boiling heat transfer, it was concluded that the influence of surface condition on boiling phenomena could not be characterized only by surface roughness. The correlations of Wattelet et al. [22] predicted the heat transfer coefficients for the 3.5 mm tube with relatively small deviation from measured values. It can be inferred from this comparison that the heat transfer mechanism for the 3.5 mm tube was similar to that for macroscale tubes because the correlations were generated from the heat transfer coefficient data with the conventional macroscale tubes, which were usually larger than 6 mm.

Pressure drop for the 3.5 mm tube at adiabatic conditions followed the general relation with the variation of mass flux, vapor quality, tube diameter, and evaporation temperature. The predicted pressure drop based on Friedel's [10] correlations showed a good agreement with the measured values. Flow patterns for two-phase adiabatic flow conditions were classified by using the description for "slug or plug flow" and "annular flow," respectively, of Wojtan et al. [16] and Wang et al. [39]. Flow patterns were used to explain the pressure drop trend at high vapor qualities. The flow pattern maps presented by Weisman et al. [15] and Wojtan et al. [16] were used to compare the visualized flow patterns at various flow conditions. From this, it was concluded that they need to be improved for more accurate predictions, especially in the transition regions from intermittent to annular flow.

Acknowledgment

This study was supported by the Air-Conditioning and Refrigeration Center (Project 183) at the University of Illinois at Urbana-Champaign. The authors are grateful to Wolverine Tube Co. for their support in building the facility and 3M Company for support in obtaining the secondary fluid supply.

Nomenclature

A = area (m^2)
C_P = specific heat (J/kg K)
D = tube diameter (m)
g = acceleration of gravity (m/s^2)
G = mass flux (kg/m^2 s)
h = heat transfer coefficient (W/m^2 K)
i = enthalpy (J/kg)
j_l = superficial liquid velocity (m/s) ($=G(1-x)/\rho_l$)
j_v = superficial vapor velocity (m/s) ($=Gx/\rho_v$)
k = thermal conductivity (W/m K)
$\dot{m}$ = mass flow rate (kg/s)
N = number of data points
Pr = Prandtl number ($=\mu C_P/k$)
q = heat flux (W/m^2)
$\dot{Q}$ = heat transfer rate (W)
T = temperature (°C or K)
x = vapor quality

Greek Symbols

α = void fraction
δ = liquid film thickness (m)
μ = dynamic viscosity (N s/m^2)
ρ = density (kg/m^3)
σ = surface tension (N/m)

Subscripts

amb = ambience
cb = convective boiling
cond = conduction
sf = secondary fluid
i = inlet
l = liquid
o = outlet
surf = surface
v = vapor
W = wall

References

[1] Bredesen, A. M., Hafner, A., Pettersen, J., Neksa, P., and Aflekt, P. K., 1997, "Heat Transfer and Pressure Drop for In-Tube Evaporation of CO_2," *Proceedings of the International Conference on Heat Transfer Issues in Natural Refrigerants*, University of Maryland, College Park, MD, pp. 1–15.
[2] Høgaard Knudsen, H. J., and Jensen, P. H., 1997, "Heat Transfer Coefficient for Boiling Carbon Dioxide," *Proceedings of the International R&D on Heat Pump, Air Conditioning and Refrigeration Systems*, Gatlinburg, TN, pp. 113–122.
[3] Park, C. Y., and Hrnjak, P. S., 2005, "Flow Boiling Heat Transfer of CO_2 at Low Temperatures in a Horizontal Smooth Tube," J. Heat Transfer, **127**, pp. 1305–1312.
[4] Park, C. Y., and Hrnjak, P. S., 2007, "CO_2 and R410A Flow Boiling Heat Transfer, Pressure Drop, and Flow Pattern at Low Temperatures in a Horizontal Smooth Tube," Int. J. Refrig., **30**, pp. 166–178.
[5] Shah, M. M., 1982, "Chart Correlation for Saturated Boiling Heat Transfer: Equations and Further Study," ASHRAE Trans., **88**, pp. 185–196.
[6] Gungor, K. E., and Winterton, R. H. S., 1986, "A General Correlation for Flow Boiling in Tubes and Annuli," Int. J. Heat Mass Transfer, **29**, pp. 351–358.
[7] Yoon, S. H., Cho, E. S., Hwang, Y. W., Kim, M. S., Min, K., and Kim, Y., 2004, "Characteristics of Evaporative Heat Transfer and Pressure Drop of Carbon Dioxide and Correlation Development," Int. J. Refrig., **27**, pp. 111–119.
[8] Müller-Steinhagen, H., and Heck, K., 1986, "A Simple Friction Pressure Drop Correlation for Two-Phase Flow in Pipes," Chem. Eng. Process., **20**, pp. 297–308.
[9] Pettersen, J., 2004, "Flow Boiling of CO_2 in Microchannel Tubes," Exp. Therm. Fluid Sci., **28**, pp. 111–121.
[10] Friedel, L., 1979, "Improved Friction Pressure Correlations for Horizontal and Vertical Two-Phase Pipe Flow," The European Two-Phase Flow Group Meeting, Ispra, Italy, Paper No. E2.
[11] Thome, J. R., and Ribatski, G., 2005, "State-of-Art of Two-Phase Flow and Flow Boiling Heat Transfer and Pressure Drop of CO_2 in Macro- and Micro-Channels," Int. J. Refrig., **28**, pp. 1149–1168.
[12] Yun, R., and Kim, Y., 2004, "Flow Regimes for Horizontal Two-Phase Flow of CO_2 in a Heated Narrow Rectangular Channel," Int. J. Multiphase Flow, **30**, pp. 1259–1270.
[13] Schael, A., and Kind, M., 2005, "Flow Pattern and Heat Transfer Characteristics During Flow Boiling of CO_2 in a Horizontal Micro Fin Tube and Comparison With Smooth Tube Data," Int. J. Refrig., **28**, pp. 1186–1195.
[14] Jang, J., and Hrnjak, P. S., 2003, "Flow Regimes and Heat Transfer in Condensation of Carbon Dioxide at Low Temperatures," *Proceedings of the Sec-*

ond International Conference on Heat Transfer, Fluid Mechanics and Thermodynamics, Victoria Falls, Zambia, Paper No. HP1.
[15] Weisman, J., Duncan, D., Gibson, J., and Crawford, T., 1979, "Effect of Fluid Properties and Pipe Diameter on Two-Phase Flow Patterns in Horizontal Lines," Int. J. Multiphase Flow, **5**, pp. 437–462.
[16] Wojtan, L., Ursenbacher, T., and Thome, J. R., 2005, "Investigating of Flow Boiling in Horizontal Tubes: Part I—A New Adiabatic Two-Phase Flow Pattern Map," Int. J. Heat Mass Transfer, **48**, pp. 2955–2969.
[17] Yu, J., Momoki, S., and Koyama, S., 1999, "Experimental Study of Surface Effect on Flow Boiling Heat Transfer in Horizontal Smooth Tubes," Int. J. Heat Mass Transfer, **42**, pp. 1909–1918.
[18] Span, R., and Wagner, W., 1996, "A New Equation of State for Carbon Dioxide Covering the Fluid Region From Triple-Point Temperature to 1100 K at Pressures up to 800 MPa," J. Phys. Chem. Ref. Data, **25**, pp. 1509–1596.
[19] Jang, J., and Hrnjak, P., 2004, "Condensation of R744 at Low Temperatures," ACRC Report No. CR56, University of Illinois at Urbana-Champaign, pp. 80–84.
[20] Moffat, R. J., 1988, "Describing the Uncertainties in Experimental Results," Exp. Therm. Fluid Sci., **1**, pp. 3–17.
[21] Kandlikar, S. G., 1990, "A General Correlation for Saturated Two-Phase Flow Boiling Heat Transfer Inside Horizontal and Vertical Tubes," J. Heat Transfer, **112**, pp. 219–228.
[22] Wattelet, J. P., Chato, J. C., Christoffersen, B. R., Gaibel, J. A., Ponchner, M., Kenny, P. J., Shimon, R. L., Villaneuva, T. C., Rhines, N. L., Sweeney, K. A., Allen, D. G., and Heshberger, T. T., 1994, "Heat Transfer Flow Regimes of Refrigerants in a Horizontal-Tube Evaporator," ACRC Report No. TR-55, University of Illinois at Urbana-Champaign.
[23] Thome, J. R., and El Hajal, J., 2004, "Flow Boiling Heat Transfer to Carbon Dioxide: General Prediction Method," Int. J. Refrig., **27**, pp. 294–301.
[24] Rouhani, Z., and Axelsson, E., 1970, "Calculation of Volume Void Fraction in the Subcooled and Quality Region," Int. J. Heat Mass Transfer, **13**, pp. 383–393.
[25] Okawa, T., Kitahara, T., Yoshida, K., Matsumoto, T., and Kataoka, I., 2002, "New Entrainment Correlation in Annular Two-Phase Flow Applicable to Wide Range of Flow Condition," Int. J. Heat Mass Transfer, **45**, pp. 87–98.
[26] Gorenflo, D., 1993, "Pool Boiling," *VDI Gesellschaft Verfahrenstechnic und Chemiengenieurwesen*, VDI, Dusseldorf, pp. Ha 4–Ha 18, English translation.
[27] Roy Chowdhury, S. K., and Winterton, R. H. S., 1985, "Surface Effects in Pool Boiling," Int. J. Heat Mass Transfer, **28**, pp. 1881–1889.
[28] Luke, A., 1997, "Pool Boiling Heat Transfer from Horizontal Tubes with Different Surface Roughness," Int. J. Refrig., **20**, pp. 561–574.
[29] Kattan, N., Thome, J. R., and Favrat, D., 1998, "Flow Boiling in Horizontal Tubes: Part 1—Development of an Adiabatic Two-Phase Flow Pattern Map," J. Heat Transfer, **120**, pp. 140–147.
[30] Kattan, N., Thome, J. R., and Favrat, D., 1998, "Flow Boiling in Horizontal Tubes: Part 3—Development of a New Heat Transfer Model Based on Flow Pattern," J. Heat Transfer, **120**, pp. 156–165.
[31] Cheng, L., Ribatski, G., Wojtan, L., and Thome, J. R., 2006, "New Flow Boiling Heat Transfer Model and Flow Pattern Map for Carbon Dioxide Evaporating Inside Horizontal Tubes," Int. J. Heat Mass Transfer, **49**, pp. 4082–4094.
[32] Wojtan, L., Ursebbacher, T., and Thome, J. R., 2005, "Investigation of Flow Boiling in Horizontal Tubes: Part II—Development of a New Heat Transfer Model for Stratified-Wavy, Dryout and Mist Flow Regimes," Int. J. Heat Mass Transfer, **48**, pp. 2970–2985.
[33] Liu, Z., and Winterton, R. H. S., 1991, "A General Correlation for Saturated and Subcooled Flow Boiling in Tubes and Annuli, Based on a Nucleate Pool Boiling Equation," Int. J. Heat Mass Transfer, **34**, pp. 2759–2766.
[34] Kandlikar, S. G., 2002, "Fundamental Issues Related to Flow Boiling in Minichannels and Microchannels," Exp. Therm. Fluid Sci., **26**, pp. 389–407.
[35] Lockhart, R. W., and Martinelli, R. C., 1949, "Proposed Correlation of Data for Isothermal Two-Phase Two-Component Flow in Pipes," Chem. Eng. Prog., **45**, pp. 39–45.
[36] Chisholm, D., 1973, "Pressure Gradients due to Friction During the Flow of Evaporating Two-Phase Mixtures in Smooth Tubes and Channels," Int. J. Heat Mass Transfer, **16**, pp. 347–358.
[37] Grönnerud, R., 1979, "Investigation of Liquid Hold-Up, Flow Resistance and Heat Transfer in Circulation Type Evaporators, Part IV: Two-Phase Flow Resistance in Boiling Refrigerants," Bull. De l'Inst. Du Froid, Annexe 1972-1.
[38] Ould Didi, M. B., Kattan, N., and Thome, J. R., 2002, "Prediction of Two-Phase Pressure Gradients of Refrigerants in Horizontal Tubes," Int. J. Refrig., **25**, pp. 935–947.
[39] Wang, C. C., Chiang, C., Lin, S., and Lu, D., 1997, "Two-Phase Flow Pattern for R-410a Inside of a 6.5 mm Smooth Tube," ASHRAE Trans., **103**, pp. 803–812.

Subcooled Pool Boiling in Variable Gravity Environments

Rishi Raj
e-mail: rraj@umd.edu

Jungho Kim[1]
e-mail: kimjh@umd.edu

Department of Mechanical Engineering,
University of Maryland,
College Park, MD 20742

John McQuillen
NASA Glenn Research Center,
21000 Brookpark Road,
Cleveland, OH 44135
e-mail: john.b.mcquillen@nasa.gov

Virtually all data to date regarding parametric effects of gravity on pool boiling have been inferred from experiments performed in low-g, 1g, or 1.8g conditions. The current work is based on observations of boiling heat transfer obtained over a continuous range of gravity levels (0g–1.8g) under subcooled liquid conditions (n-perfluorohexane, $\Delta T_{sub} = 26°C$, and 1 atm), two gas concentrations (220 ppm and 1216 ppm), and three heater sizes (full heater-7×7 mm^2, half heater-7×3.5 mm^2, and quarter heater-3.5×3.5 mm^2). As the gravity level changed, a sharp transition in the heat transfer mechanism was observed at a threshold gravity level. Below this threshold (low-g regime), a nondeparting primary bubble governed the heat transfer and the effect of residual gravity was small. Above this threshold (high-g regime), bubble growth and departure dominated the heat transfer and gravity effects became more important. An increase in noncondensable dissolved gas concentration shifted the threshold gravity level to lower accelerations. Heat flux was found to be heater size dependent only in the low-g regime.
[DOI: 10.1115/1.3122782]

Keywords: boiling, variable gravity, microgravity, thermocapillary convection, dissolved gas, heater size

1 Introduction

Pool boiling involves complicated nonlinear processes operating over a large range of length and time scales. The presence of more than one phase, little understanding of the nucleation process, and a strong dependence on the fluid properties have hindered researchers from developing a completely deterministic model for heat transfer in pool boiling. The mechanisms by which heat is removed from the surface and the effect of parameters such as gravity, subcooling, wall superheat, fluid properties, heater surface geometry, and structure are still unclear. Although many models and correlations include gravity as a parameter, most fail when extended beyond the range of gravity levels they were based on, namely, 1g and low-g.

Much research effort has been directed toward understanding the effect of gravity on boiling [1]. Merte and Clark [2] and Costello and Tuthill [3] used centrifuges to simulate high gravity conditions (1g–100g) in the 1950s. Increased used of satellites for communication and growing interest in space missions led to a rapid expansion of low gravity experimentation [4–6]. Most of the early low gravity experiments used ground-based facilities like drop towers [7] and magnetic fields to compensate for earth gravity [8]. Aircraft [9–11] and sounding rockets [12–14] have also been used to produce low-g environments. Lee and Merte [15] conducted pool boiling experiments on three space shuttle flights with each flight consisting of nine different test runs. NASA is currently preparing to launch two pool boiling experiments to the International Space Station. The two experiments, the microheater array boiling experiment (MABE) and the nucleate pool boiling experiment (NPBX), will use the boiling experiment facility (BXF) developed at NASA [16]. However, little data are available regarding pool boiling behavior in the partial gravity regime, such as those in the Moon (0.17g) and Mars (0.38g) environments.

Due to the absence of closed form governing equations for pool boiling, statistical approaches such as correlations and curve fits have mainly been used. The power law variation has generally been adopted to describe the effect of gravity by researchers. Fritz [17] developed a bubble departure diameter correlation based on a balance between the buoyancy and surface tension forces. Fritz [17] and Cole [18] reported that the bubble departure radius varied as $a^{-1/2}$. Siegel and Keshock [19] reported that the bubble departure radius varied approximately as $a^{-1/3}$ for $0.1g < a < 1g$ and according to $a^{-1/2}$ for lower accelerations. Son et al. [20] suggested that the bubble growth rate varies as $a^{-1.05}$. Their experimental results were also complimented by numerical predictions where the variation was found to be $a^{-0.93}$ between $0.01g < a < 1.8g$. Malenkov's correlation [21] suggests that the bubble departure frequency varies as $a^{3/4}$. There also exist a wide variety of correlations for the prediction of heat flux in the nucleate boiling regime and CHF. The Rohsenow [22] correlation suggests that the heat flux in the nucleate boiling regime varies as $a^{1/2}$. Stephan and Abdelsalam [23] developed a correlation for nucleate boiling heat transfer data using regression analysis, the role of gravity being accommodated by the departure diameter. The Kutateladze [24] and Zuber [25] correlations suggest the CHF varies as $a^{1/4}$. The correction factors for smaller heaters in the literature are dependent on the capillary length. All the above correlations are very sensitive to the range of parameters for which they were developed and do not include gas concentration, which has been found to influence the boiling process.

Noncondensable gas dissolved in the liquid influences heat transfer significantly. At lower gravity levels, thermocapillary convection, which is hypothesized to originate due to the gas dissolved in the boiling liquid, also becomes important [26]. The relationship between the dissolved gas and the physics of thermocapillary convection during subcooled boiling is not clear. It is speculated that the presence of dissolved gas inside the vapor bubble leads to the formation of a localized concentration and temperature gradient along the liquid-vapor interface and thus to the onset of thermocapillary convection [27,28]. These studies reported that the dissolved gas content determines the onset of thermocapillary convection and no thermocapillary motion was observed for subcooled boiling with pure liquid. The strength of thermocapillary convection is expected to increase with gas concentration. On the contrary, other studies performed in reduced gravity suggest that the strength of the thermocapillary convection

[1]Corresponding author.

Contributed by the Heat Transfer Division of ASME for publication in the JOURNAL OF HEAT TRANSFER. Manuscript received October 9, 2008; final manuscript received March 16, 2009; published online June 25, 2009. Review conducted by Raj M. Manglik.

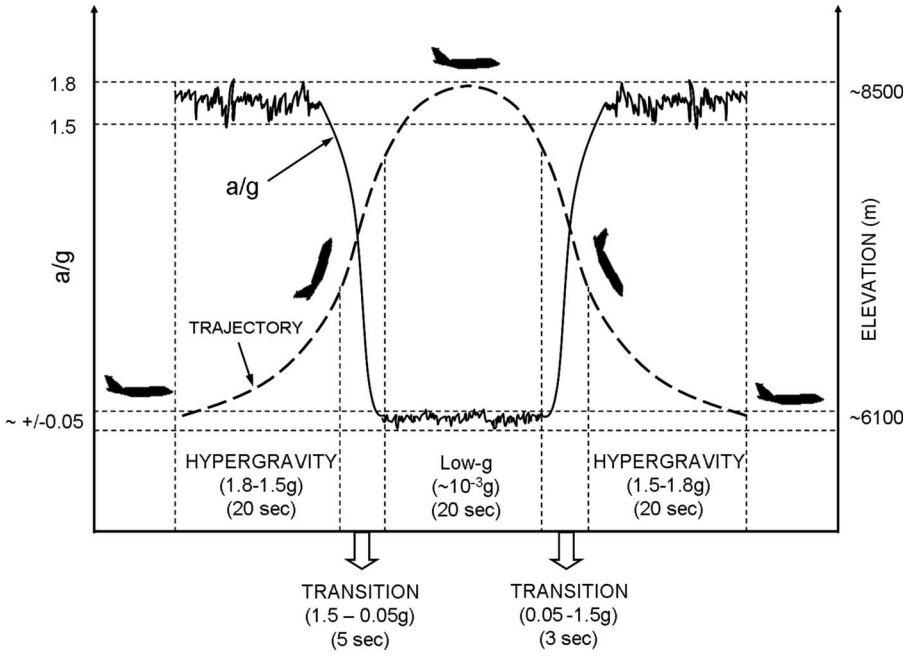

Fig. 1 Schematic of the trajectory of the parabolic flight with corresponding acceleration levels

around the primary bubble in a gas saturated fluid ($c_g \sim 3500$ ppm) was much weaker than that in a degassed fluid ($c_g < 3$ ppm) [29,30]. It was again speculated that while the increase in dissolved gas content can create temperature variations along the bubble interface, the resulting increase in bubble size, which lowers the temperature gradient, could lower of the strength of the thermocapillary convection for the gassy bubble.

The results of most of these early works are somewhat contradictory, resulting in no clear understanding of the effect of gravity and dissolved gas concentration. Other parameters such as heater frequency response, heater size, heater geometry, and fluid properties also influenced the results significantly. The primary objective of this work is to bridge the gap between the experiments conducted at low-g and high-g. Subcooled pool boiling experiments were conducted over a wide range of gravity levels for three heater sizes and two gas concentrations.

2 Experimental Apparatus

2.1 Test Rig Description. A microheater array consisting of 96 platinum resistance heaters deposited in a 10×10 configuration onto a quartz substrate was used to measure the heat transfer distribution. Each heater in the array was nominally 0.7×0.7 mm^2 in size. Power was transferred via gold power leads 1 μm in thick. Individual heaters had a nominal resistance of 250 Ω and a temperature coefficient of resistance (TCR) of $0.0022\,^{\circ}\mathrm{C}^{-1}$. The heater can provide a maximum heat flux of 220 W/cm^2 locally. The reader is referred to Ref. [31] for the details of the heater construction.

Three heated areas were used to study the heater size effect: full heater (7×7 mm^2, 96 elements), half heater (7×3.5 mm^2, 48 elements), and quarter heater (3.5×3.5 mm^2, 24 elements). The heater temperature was kept constant using a bank of feedback circuits similar to those used in constant temperature hot-wire anemometry. The power, and thus the heat flux, required to maintain these heaters at the desired temperature were obtained by sampling the voltages across the heaters. The frequency response for the heaters and feedback circuits was very high (15 kHz), since the thermal lag was negligible due to the constant temperature boundary condition. The side view and bottom view images of the boiling process were captured to visualize the phenomena occurring near the heater surface and correlated with the heat transfer data.

The test rack contained a sealed boiling chamber with about 3 liters of 98.9% n-perfluorohexane at a pressure of 1 atm, the microheater array, the electronic feedback circuits, two video cameras, a computer, an accelerometer (Entran EGCS3), a pressure sensor (PDCR 130/W), some thermocouples and RTDs for the bulk liquid and air-jet temperature measurements, and a LCD display. Everything was contained within a vertical equipment rack provided by NASA.

Backside cooling of the heater array was required to minimize the lateral conduction and to prevent individual heaters from shutting off at low heat transfer levels. Air was forced through a 1.6 mm diameter nozzle placed 10 mm from the backside of the heater. The cooling air flow was maintained by a compressed air bottle with pressure regulation nominally set at 150 kPa. The ambient pressure inside the aircraft was measured to be 83 kPa and the air-jet temperature varied between 22°C and 24°C.

2.2 Fluid Condition. n-perfluorohexane, a straight chain isomer of C_6F_{14} ($T_{sat} = 56\,^{\circ}\mathrm{C}$ at 1 atm), was used as the test fluid [32]. For all the data runs in this paper, the bulk liquid was maintained at a nominal temperature of 30°C. Two gas (air) concentrations, low gas ($c_g \sim 220$ ppm) and high gas ($c_g \sim 1216$ ppm), were used to study the effect of gas on the heat transfer. The procedure adopted by Henry et al. [29] was used to measure the gas concentration. The heater temperature was varied between 65°C ($\Delta T_w = 9\,^{\circ}\mathrm{C}$) and 100°C ($\Delta T_w = 44\,^{\circ}\mathrm{C}$), and the pressure was maintained at 1 atm throughout the experiment.

2.3 Variable Gravity Environment. Data were collected during the 48th ESA Parabolic Flight Campaign organized in March 2008 [33]. An Airbus A300 aircraft flew successive parabolic maneuvers providing ~20 s periods of low-g preceded and followed by ~20 s periods of ~1.8g. A 1g period lasting a few minutes between successive parabolas was used to set the test parameters. A typical parabola along with the acceleration levels are shown on Fig. 1. Thirty parabolas were flown per flight, and three flights were made.

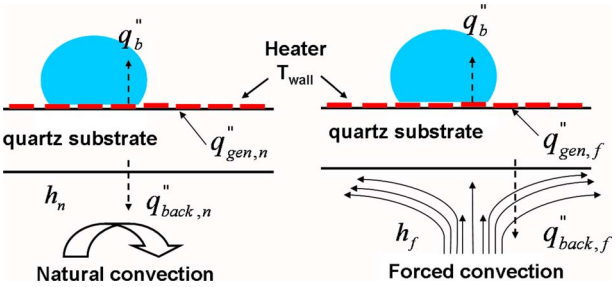

Fig. 2 The schematic of the heat transfer contributions for the natural convection (left) and forced convection (right) cases

The parabolic flight campaign has been primarily used to study phenomena under low-g and hypergravity ($>1.5g$) conditions. However, as can be seen in Fig. 1, there was a transition period of approximately 3–5 s when the acceleration varied continuously from hypergravity to low-g and vice versa. This period is generally considered too short for processes to reach equilibrium, and hence unsuitable for making measurements. However, data were acquired for this period throughout the transition from hypergravity to low-g and vice versa.

2.4 Data Acquisition and Test Procedure. The heater array was set to a desired temperature before the start of each parabola during the $1g$ period. The two cameras and the air-jet were activated during the middle of the hypergravity period, and data acquisition was started a few seconds before the transition to low-g began. The LED array illuminating the boiling chamber was then turned on—the step change in the voltage across the LED recorded by the data acquisition system and the change in illumination observed in the video were used to synchronize the video and the data. The data acquisition system was programmed to stop acquisition after 30 s. The low-g data corresponded to approximately 18 s, while 6–8 s of transition data and about 4–5 s of hypergravity data were obtained. Heat flux, acceleration, pressure, and bulk liquid temperature data were acquired at 100 Hz, while the bottom and side view images were taken at 29.97 Hz.

2.5 Data Reduction. Raw data from the accelerometer, LED voltage, and bulk liquid temperature were converted into engineering quantities. The raw voltage data obtained from the individual heaters were first converted to total heat transfer, and a spatially averaged heat flux using the heated area was computed for each time step (q_{gen}). Figure 2 illustrates the heat transfer within the chip. Only a portion of the total heat generated (q''_{gen}) was removed by the liquid (q''_b). The remaining portion was lost to the ambient either through natural convection or forced convection (q''_{back}). Figure 2 (left) represents the case without air-jet (subscript n); a small amount of heat ($q''_{back,n}$) was lost through the back of the chip by natural convection to the ambient air. Figure 2 (right) represents the situation with air-jet (subscript f), i.e., forced convection whereby considerably more heat ($q''_{gen,f}$) was lost to the ambient.

The energy balance for the natural and forced convection cases are given by

$$q''_b = q''_{gen,n} - q''_{back,n} \quad \text{(natural convection)} \tag{1}$$

$$q''_b = q''_{gen,f} - q''_{back,f} \quad \text{(forced convection)} \tag{2}$$

If the heater surface is at the same temperature for both cases, the heat supplied to the liquid q''_b for boiling remains unchanged, so

$$q''_{gen,f} - q''_{gen,n} = q''_{back,f} - q''_{back,n} \tag{3}$$

Spatially averaged heat flux data were measured with the air-jet on ($q''_{gen,f}$) and the air-jet off ($q''_{gen,n}$) at $1.8g$ for wall superheats of 39°C and 44°C. The natural convection heat transfer coefficient h_n of 10 W/m^2 K was assumed at the back of the chip for the case without the air-jet and a 3D COMSOL™ finite element model with appropriate boundary conditions and h_n was 10 W/m^2 K was used to calculate $q''_{back,n}$. With all three quantities known, Eq. (3) was solved for $q''_{back,f}$ (Table 1). With the forced convection substrate conduction loss known, the COMSOL model was used to back calculate the forced convection heat transfer coefficient (h_f). Values of 554 W/m^2 K for a wall superheat of 39°C and 547 W/m^2 K at 44°C were obtained from the COMSOL model (Table 1). A midvalue of 550 W/m^2 K was assumed for h_f for further calculations at all temperatures. Use of a uniform, area averaged h_f is justifiable since the heat transfer results presented below are also area averaged. This forced convection heat transfer coefficient with other appropriate boundary conditions was used to calculate the substrate conduction losses at other temperatures. The uncertainties associated with the selection of the natural and forced convection heat transfer coefficients are discussed next.

2.6 Uncertainty. Substrate conduction and g-jitter were the two major sources of uncertainty in the heat flux. The uncertainty in q''_{gen} is negligible since the voltage and heater resistance were accurately measured. Higher uncertainties in substrate conduction were associated with the partitioning of q''_{gen} into q''_b and q''_{back}. Natural convection heat transfer coefficients for gases can vary from 2 W/m^2 K to 25 W/m^2 K [34]. The uncertainty in $q''_{back,n}$ due to the selection of h_n of 10 W/m^2 K in Sec. 2.5 was computed to be 0.21 W/cm^2. According to Eq. (3), this uncertainty in $q''_{back,n}$ results in the same uncertainty in $q''_{back,f}$. Based on a selection of h_f=550 W/m^2 K for the forced convection heat transfer coefficient, the maximum deviation was and 4 W/m^2 K. This error resulted in an uncertainty of 0.06 W/cm^2 in $q''_{back,f}$ and hence in q''_b.

The resolution of $0.002g$ in the accelerometer data was the maximum uncertainty in the measurement of acceleration. The rapid fluctuations in the acceleration value from the mean (g-jitter) resulted in uncertainty in the estimation of q''_b. The standard deviation of the acceleration for all the test cases in the hypergravity, transition, and low-g regimes were strictly less than $0.085g$, $0.037g$, and $0.034g$, respectively. The associated uncertainty in the heat flux due to g-jitter for each of the regimes was found to be less than 1.12 W/cm^2. Hence, the uncertainty in the heat flux values at any temperature due to all these sources and acceleration was not more than 1.14 W/cm^2.

The uncertainty in gas concentration c_g due to measurement errors was estimated to be a maximum of 5.8 ppm. The uncertainties in the heater temperature and bulk liquid temperatures were

Table 1 Substrate conduction calculation

Quantity	q'' ($W/cm^2, \Delta T_w$=39°C)	q'' ($W/cm^2, \Delta T_w$=44°C)
$q''_{gen,f}$	28.1	31.5
$q''_{gen,n}$	23.2	26.4
$q''_{back,n}$	0.2	0.2
$q''_{back,f}$ (h_f, W/m^2 K)	5.1 (554)	5.3(547)

Table 2 Summary of conservative estimate of the uncertainties in the value of measured parameters

Quantity	Uncertainty
q'	1.2 W/cm^2
T_{bulk}	2°C
T_{wall}	0.5°C
T_{sat}	1.5°C
ΔT_w	1.6°C
a	0.01 g
c_g	6 ppm

calculated using the procedure adopted by Henry et al. [29]. A summary of the uncertainty estimates is given on Table 2.

2.7 Quasisteady State. As mentioned earlier, the transition from hypergravity ($>1.5g$) to low-g ($<0.05g$) and vice versa occurs over a period of 3–5 s. In order to study heat transfer during this transition, the heat flux must be in quasisteady state at any given gravity level.

A plot of q_b'' versus acceleration during the transition from hypergravity to low-g and vice versa at $\Delta T_w=9°C$ and $\Delta T_w=44°C$ is shown on Fig. 3. Ideally, if the flow field and heat transfer profiles have sufficient time to achieve steady state at each acceleration level, there should be no difference in the two curves. However, a hysteresis in the heat flux curve is present at the lower superheat ($\Delta T_w=9°C$) (Fig. 3(a)). This was observed whenever the superheat was not sufficient to initiate nucleation, and heat transfer was by natural convection. As the gravity changes, time is required for the flow field and heat transfer profiles to develop and achieve steady state. Before the transition from high-g to low-g, the natural convection flow field was fully developed. During the transition from high-g to low-g, the flow field required more time to achieve steady state than was available, resulting in higher heat transfer than the expected quasisteady value. Similarly, during the transition from low-g to high-g, the heat transfer was lower than the expected quasisteady value.

However, at $\Delta T_w=44°C$ (Fig. 3(b)), the heat transfer is independent of the direction of transition. At this temperature, the majority of heat transfer is due to bubble growth and bubble departure. Since bubble departure frequencies can be as high as 30–40 Hz at normal gravity, the heat transfer during the transitions when boiling occurs are quasisteady. The 15 kHz response of the heater and feedback circuit and the data acquisition frequency of 100 Hz rule out any chances of discrepancies due to data collection.

3 Results and Discussion

3.1 Gravity Effects. Correlations for heat flux in the nucleate boiling regime are often described using a power law of the form

$$q''_{boiling} = f(c_g, c_p, h_{lv}, p, \alpha, \mu, \rho_l, \rho_v, \sigma, \Delta T_{sub}) * \Delta T_w^n \left(\frac{a}{g}\right)^m \quad (4)$$

For constant fluid properties and subcooling, the logarithm of Eq. (4) yields

$$\log(q''_{boiling}) = [k + n \log(\Delta T_w)] + m \log\left(\frac{a}{g}\right) \quad (5)$$

If the power form assumed in Eq. (4) is valid, a linear variation in $\log(q'')$ versus $\log(a/g)$ with slope m is expected for a given superheat. Changes in wall superheat and gas concentration should affect the intercept (y at x=0) only, and not affect m.

To verify the assumed power law dependence, the boiling heat flux data were binned based on gravity level into equal intervals of $0.005g$. The average heat flux within each bin was assigned to the midpoint acceleration of each bin. Data points corresponding to negative acceleration values (g-jitter) were rejected. An example of the data is shown in Fig. 4. The squares correspond to the binned data for transition from hypergravity to low-g, while the triangles correspond to the data during transition from low-g to hypergravity. A sharp change in heat flux is observed between $0.1g-0.2g$ indicating a distinct change in the heat transfer mechanism, and rules out the possibility of the use of a unified power law for gravity dependence as per Eq. (4). The heat transfer regime that occurs below the transition acceleration will hereafter be referred to as the *low-g* regime, while the regime above this transition will be referred to as the *high-g* regime. Any acceleration higher than $1.5g$ is referred to as *hypergravity.*

Comparison of these plots with the video revealed that a primary bubble formed and remained attached to the surface in the low-g regime, while regular bubble departure occurred in the high-g regime. The three images on the right (Fig. 4, solid arrows at $0.3g$, $0.85g$, and $1.68g$, respectively) correspond to departing bubbles in the high-g regime. The dryout area and the average bubble departure diameter decreased with increasing gravity. Smaller bubble departure diameter corresponded to an increase in departure frequency, which, coupled with the decreased dryout area, resulted in an increase in heat transfer with gravity. The

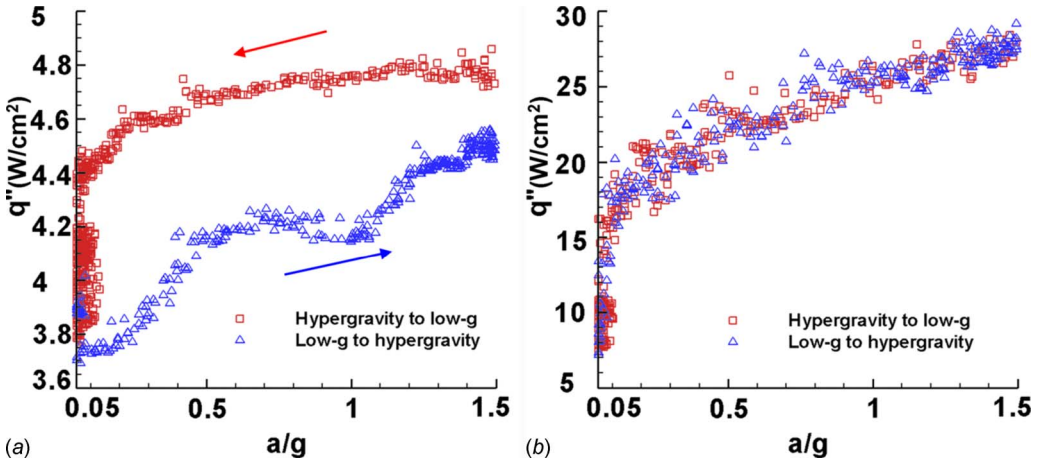

Fig. 3 Heat flux versus acceleration during transition for (a) $\Delta T_w=9°C$ and (b) $\Delta T_w=44°C$, full heater (96 elements)

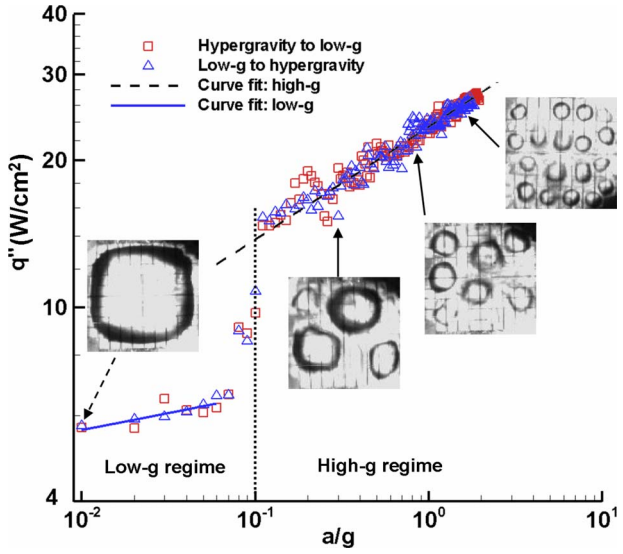

Fig. 4 Plot of heat flux versus acceleration for high gas case (c_g~1216 ppm), full heater (96 elements), at ΔT_w=44°C, with superimposed bottom view images at 0.01*g*, 0.3*g*, 0.85*g*, and 1.68*g*

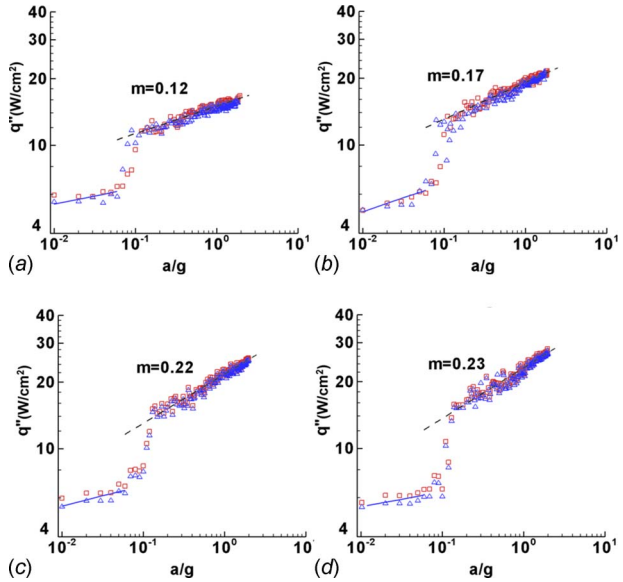

Fig. 5 Plot of heat flux versus acceleration for the high gas case (c_g~1216 ppm), full heater (96 elements) for ΔT_w (*a*) 24°C, (*b*) 29°C, (*c*) 34°C, and (*d*) 39°C

image on the left (dashed arrow) is that of a nondeparting primary bubble in the low-*g* regime with large dryout area and hence lower heat transfer. The presence of a third regime where the bubble departs due to fluid inertia cannot be ruled out for larger heaters. Lee and Merte [15] observed a third regime at very low gravity levels ($\sim 10^{-4}g$) and larger heaters (19×38 mm^2). A large bubble formed during initial nucleation hovered over the heaters acting as a vapor sink for smaller bubbles generated on surface resulting in constant rewetting of the heater surface and high heat transfer. Abarajith et al. [35] reported a decrease in departure time and departure diameter due to bubble coalescence under low gravity conditions ($\sim 10^{-2}g$). The time averaged heat flux increased with the number of coalescing bubbles. However, the current set of experiments with 7×7 mm^2 heater size did not enter any such heat transfer regime.

Similar qualitative dependence on gravity was also observed at different wall superheats (Fig. 5). The gravity dependence (m) became stronger with increasing wall superheat in the high gravity regime, as seen in Figs. 5 and 6, suggesting that the wall superheat and acceleration effects are not independent as suggested in Eq. (4). As will be stressed again in Secs. 3.2–3.4, the parametric effects of gravity, wall superheat, and gas concentration are highly interlinked, ruling out the possibility of simple power law correlations. The dependence of gravity on heat transfer is small in the low-*g* regime ($0.01<m<0.1$, Fig. 6).

Figure 5 shows that the change in heat transfer regime occurred between 0.01*g* to 0.22*g*. Since this coincides, the transition in heat flux coincides with the transition between the high-*g* regime (departing bubbles) and low-*g* regime (nondeparting primary bubble), the acceleration at which bubble departure stops during the transition to low-*g* or the acceleration at which the primary bubble departs during the transition to hypergravity will henceforth be referred to as the departure acceleration (a_{depart}).

The Fritz correlation (Eq. (6)) was used to calculate the value of a_{depart}. The Fritz correlation is simply a force balance between buoyancy and surface tension for a single bubble in quasi-equilibrium. Forces due to thermocapillary flow and interactions at the heater surface due to bubble coalescence are unaccounted for. These simplifications along with the experimental limitation like *g*-jitter add to the deviation in the predicted values, but this simplified analysis could prove useful in the study of bubble dynamics based on the force balance between the surface tension and buoyancy.

$$0.0208\theta = \sqrt{\frac{a_{\text{Fritz}}(\rho_l - \rho_v)D_{\text{depart}}^2}{\sigma}} \tag{6}$$

The apparent contact angle of the bubble was calculated from the side view images. Ten points were placed on the bubble surface close to the heater, and second, third, and fourth order polynomial fits were obtained. The camera was inclined at 20 deg from the horizontal and was accounted for in the calculation of the coordinates. The tangent was calculated at the intersection of the fit and the heater surface and used to find the apparent contact angle. The apparent contact angle varied from 69 deg to 72 deg for the high gas case (1216 ppm) and all wall superheats. The deviation between the measured apparent contact angles for all images and the three polynomial fits was smaller than 4 deg.

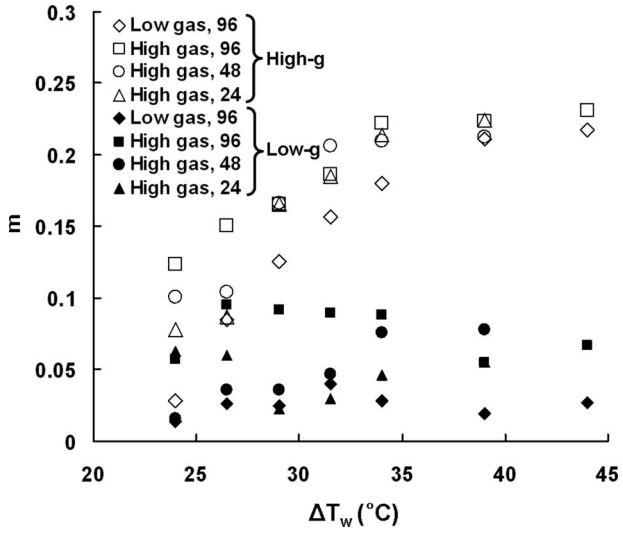

Fig. 6 A plot of the slope *m* (Eq. (4)) in low-*g* and high-*g* regime

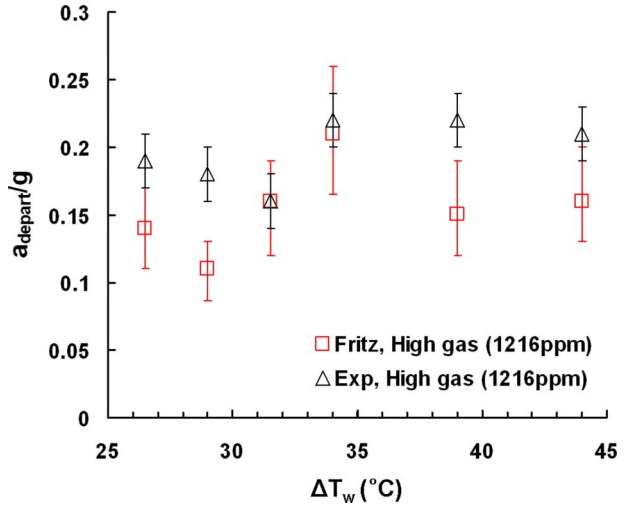

Fig. 7 Comparison between the values of a_{depart} obtained from the Fritz correlation and experiment

The departure diameter was calculated from the bottom view images. An estimate of the error in the calculation of departure diameter was found to be 0.15 mm. Based on the uncertainties of 4 deg in the apparent contact angle and 0.15 mm in the departure diameter, the error for each data point was evaluated. Based on the 29.97 Hz video frequency and the rate of change of acceleration during transition, gravity changed no more than 0.02*g* between two successive frames. The minimum resolution of the accelerometer is about 0.002*g*. Thus, the uncertainty in the experimental value of a_{depart} is about 0.02*g*.

Values of a_{depart} obtained from the Fritz correlation and experiment (Fig. 7) agree well, indicating that the surface tension and buoyancy are the principal parameters governing bubble departure. The value of a_{depart} does not show any clear dependence on wall superheat.

3.2 Wall Superheat Effects. Boiling curves for the high gas case at a number of gravity levels are shown on Fig. 8. For 0.3*g*, 0.6*g*, 1*g*, and 1.3*g*, the flow at $\Delta T_w = 9°C$ and $\Delta T_w = 14°C$ was not in quasisteady equilibrium, so these data were not included in Fig.

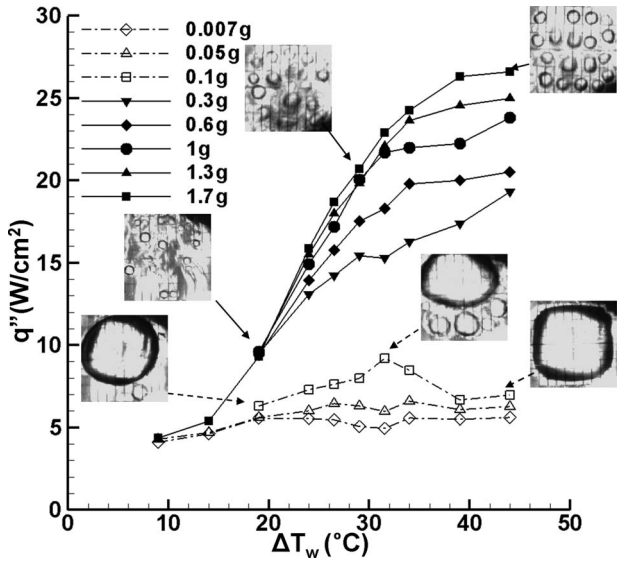

Fig. 8 Boiling curve at different gravity levels for high gas ($c_g \sim 1216$ ppm), full heater (96 elements), with superimposed bottom view images for 1.7*g* and 0.1*g* at different temperatures

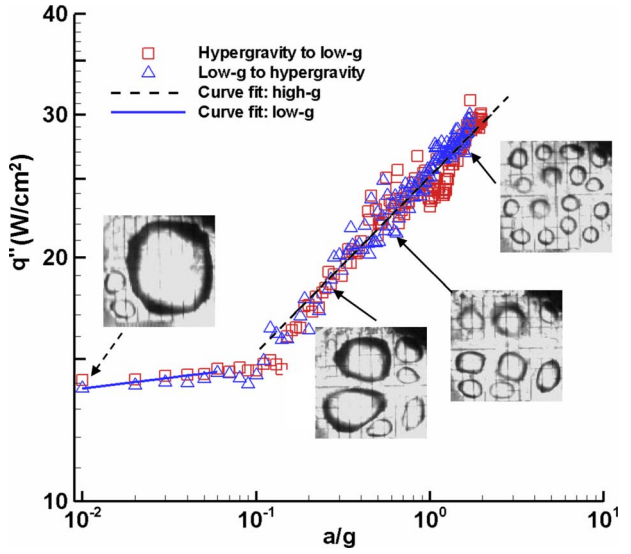

Fig. 9 Plot of heat flux versus acceleration for low gas case ($c_g \sim 220$ ppm), full heater (96 elements), at $\Delta T_w = 44°C$, and with superimposed bottom view images at 0.01*g*, 0.28*g*, 0.74*g*, and 1.71*g*

8. Heat transfer increases with wall superheat in the high-*g* regime. As seen from the superimposed bottom view images (solid arrows), most of the heated area experienced natural convection at lower superheats resulting in low heat transfer. With the onset of nucleate boiling, a significant increase in the slope of the boiling curve is observed. Wall superheat result in additional nucleation sites being activated. For a given acceleration level, the bubble departure frequency increased with superheat due to an increase in the bubble growth rate, contributing to the increase in heat transfer.

A sudden decrease in heat transfer is evident as the acceleration decreases from 0.3*g* to 0.1*g* due to the transition to low-*g* regime; this corresponds to the formation of a nondeparting primary bubble with a large dryout area on the heater. The effect of wall superheat is not very clear for the high gas case in the low-*g* regime (dashed curves, Fig. 8). At low wall superheat ($\Delta T_w = 19°C$, dashed arrow) and 0.1*g*, a large primary bubble with a few satellite bubbles formed, resulting in low heat transfer. At intermediate wall superheats ($\Delta T_w = 29°C - 31.5°C$) for the same gravity level, more nucleation sites activated and a primary bubble formed amidst numerous satellite bubbles. Lateral movement of the primary bubble along the heater array allowed coalescence and removal of the satellite bubbles, allowing new bubbles to nucleate. For 0.1*g*, the heat transfer reached a maximum at $\Delta T_w = 31.5°C$. At higher superheat ($\Delta T_w = 44°C$), a large primary bubble nearly enveloped the entire heater resulting in lower heat transfer. As the acceleration decreased to lower levels (0.007*g* and 0.05*g*), the heat transfer decreased as well, but the uncertainty in acceleration due to *g*-jitter became comparable to the acceleration values.

3.3 Noncondensable Gas Effects. A plot of the heat flux versus acceleration for the low gas case also shows the presence of two regimes (Fig. 9). Similar to the high gas case in the high-*g* regime, bubble departure diameter decreased with acceleration while the departure frequency and nucleation site density increased (Fig. 9, solid arrows), resulting in higher heat transfer. Dependence on gravity, *m*, increased with wall superheat in the high-*g* regime (Fig. 6).

Boiling curves for both low and high gas cases at three acceleration levels are shown in Fig. 10(*a*). At low wall superheats, natural convection is the prominent heat transfer mechanism re-

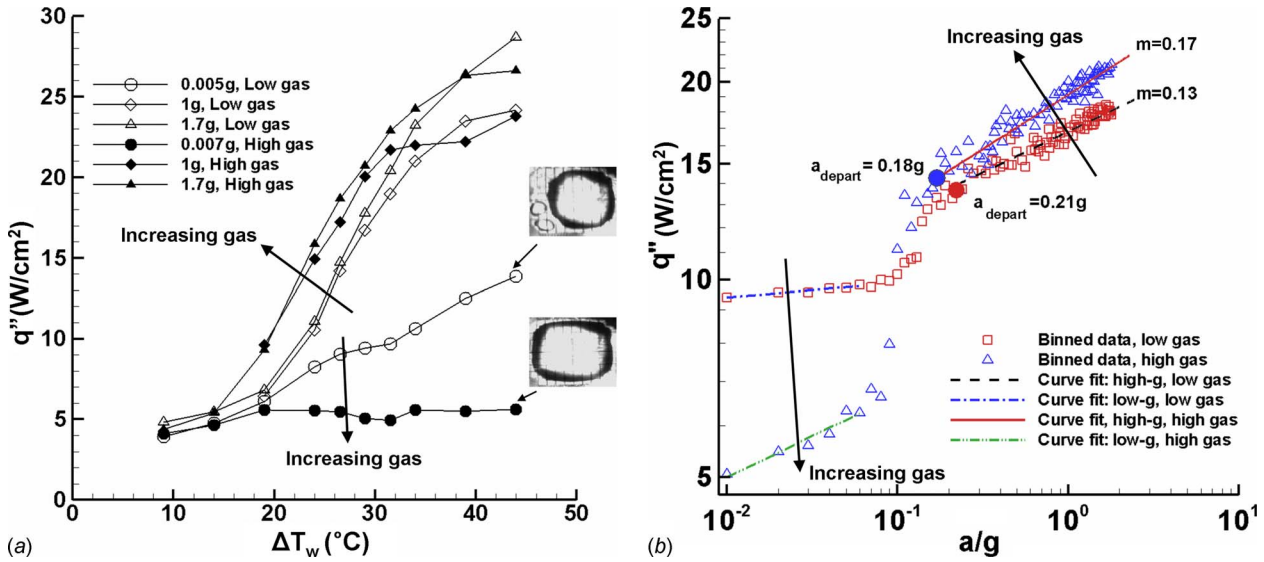

Fig. 10 (*a*) **Boiling curve at three accelerations for low and high gas,** (*b*) **heat flux versus acceleration in at $\Delta T_w = 29°C$, for two dissolved gas concentrations, full heater (96 elements)**

sulting in similar heat transfer coefficients for both gas concentrations. In the high-g regime ($1g$ and $1.7g$), the slope of the boiling curves increased significantly after the onset of nucleate boiling. However, onset of nucleate boiling for the low gas concentration (open symbols) occurred at higher superheat (as observed by other researchers [36–38]) since the presence of dissolved gas reduces the vapor pressure required to activate nucleating bubbles. For the accelerations in the high-g regime, nucleate boiling heat transfer is lower for the low gas case than for the high gas case (Figs. 10(*a*) and 10(*b*)), which is consistent with the observations of Rainey et al. [37] and Honda et al. [38]. The presence of gas results in faster bubble growth and increased bubble departure frequency, resulting in higher heat transfer.

The size of the primary bubble that forms in low-g is smaller for the low gas case than for the high gas case (Figs. 4 and 9). For boiling within the low-g regime, the presence of gas on heat transfer is opposite of that observed in the high-g regime; heat transfer for the low gas case was higher than for the high gas case (Fig. 10(*b*)). Similar observations based on the experimental work were reported by Henry et al. [29], where heat fluxes for the degassed fluid ($c_g < 3$ ppm) were higher than for gas saturated fluid ($c_g \sim 3500$ ppm). At lower gravity levels, thermocapillary convection can be a major contributor to the heat transfer. Thermocapillary convection results from surface tension gradients along the bubble interface, which can form due to temperature gradients.

$$\frac{d\sigma}{dx} = \frac{\Delta\sigma}{\Delta T}\frac{\Delta T}{\Delta x} \tag{7}$$

The first term on the right hand side of Eq. (7) is a function of the fluid property, while the second term is a function of the available temperature difference along the bubble interface and bubble size. Figure 11 illustrates the differences between the primary bubbles that form at two gas concentrations. The temperature difference between the heater and the bubble top is generally similar for both cases ($\Delta T = T_{wall} - T_{bulk}$). However, due to the smaller bubble diameter ($D_{low} < D_{high}$) and larger contact angle for the low gas case ($\theta_{low} > \theta_{high}$), the available length for the surface tension variation was significantly smaller ($\Delta x_{AB} < \Delta x_{CD}$) for the low gas case. The resulting increase in temperature and surface tension gradients along the bubble interface leads to stronger thermocapillary flows for the low gas case, which combined with the smaller dryout area results in higher heat transfer. For a high gas case, a larger bubble is formed with a smaller surface tension gradient and a large dryout area resulting in decreased heat transfer in the low-g regime (Figs. 10(*a*) and 10(*b*)). Raj and Kim [30] confirmed the behavior observed by Henry et al. [29] by comparing the strength of thermocapillary convection for varied bubble sizes and contact angles.

The acceleration at which transition occurs between the heat transfer regimes was again compared with the prediction from the Fritz correlation (Eq. (6)). The apparent contact angle was measured to vary between 79 deg and 84 deg for the low gas case (220 ppm). The Fritz correlation suggests transition to occur between $0.25g$ and $0.31g$, while the experimental value of a_{depart} varied between $0.19g$ and $0.33g$ (Fig. 12).

The experimentally measured values of a_{depart} for the two gas levels can be compared from Figs. 7 and 12. With the exception of one data point ($\Delta T_w = 24°C$), transition was observed to occur at lower accelerations for the high gas case. Figure 10(*b*) shows the value of a_{depart} obtained from the experiment for the two gas concentrations at $\Delta T_w = 29°C$. For the high gas case, the high-g regime extended to lower accelerations (triangles). An increase in bubble diameter due to the presence of dissolved gas increases the buoyancy force, while the surface tension force normal to the heater surface decreases due to the smaller contact angle. The combination of these two effects, i.e., an increase in the buoyancy force and a decrease in the surface tension force case shifts a_{depart} to lower accelerations for the high gas case.

3.4 Heater Size Effects. Data were obtained for three heater sizes: full array (96 elements), half array (48 elements), and quarter array (24 elements). The gas concentration and subcooling were maintained at ~ 1216 ppm and $\Delta T_{sub} = 26°C$, respectively. Boiling curves for the three heater sizes at four accelerations are shown in Fig. 13. In the high-g regime (Figs. 13(*a*)–13(*c*)), the

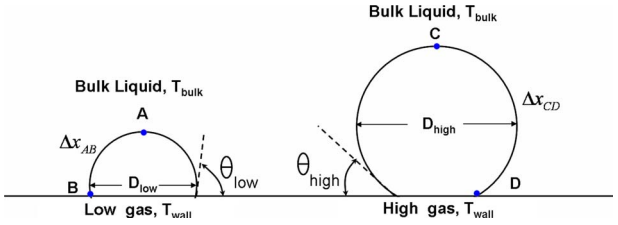

Fig. 11 A schematic of the bubble size and apparent contact angle for the two gas concentrations in the low-g regime

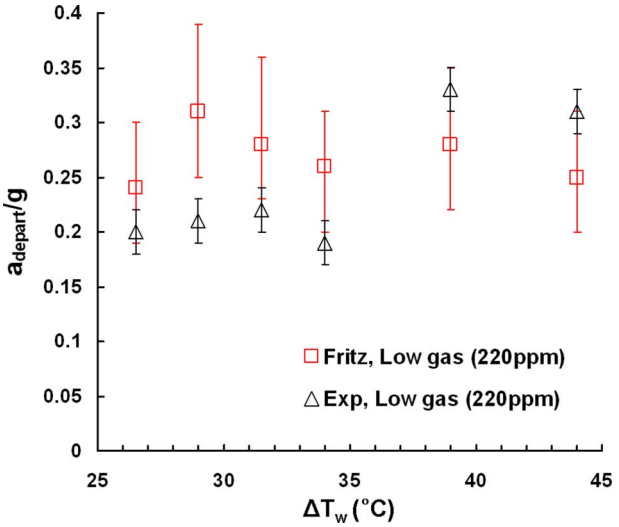

Fig. 12 Comparison between the values of a_{depart} obtained from the Fritz correlation and experiment (low gas)

boiling curves are independent of the heater size. The bottom view images in Fig. 13(*a*) show that the heater size is sufficient for the nucleation site density (and hence the heat transfer) to remain unaffected.

A heater size effect is observed in the low-*g* case, however. Heat flux increases as the heater size decreases. Similar to the observations of Henry et al. [39], a laterally oscillating primary bubble was observed at lower superheats ($\Delta T_w < 29°C$) for the quarter and half heaters (double sided arrow on Fig. 13(*d*)). Occasional rewetting due to translation of the primary bubble along the full heater was also observed. The frequency of oscillation was inversely related to the heater size—slow oscillations for the full heater and rapid oscillations for the quarter heater. More frequent oscillations result in more frequent rewetting and removal of the satellite bubbles, resulting in shorter bubble life cycle and hence higher heat transfer. The dryout area fraction (the ratio of dry area to heated area) was observed to decrease with decreasing heater size resulting in an increase in heat flux. At higher superheats $\Delta T_w \geq 39°C$, a stable primary bubble occupying the entire heater was observed for all three sizes (Fig. 13(*d*)), but the heat transfer was higher for the smaller heater. It is speculated that this is due to stronger thermocapillary convection around the smaller primary bubbles. Although the temperature difference available for thermocapillary convection remains the same for the three cases, a decreasing heater size results in a larger temperature gradient and stronger thermocapilly convection. Further experiments with particle image velocimetry (PIV) and various heater sizes are required to verify this hypothesis.

The slope of the logarithmic plots of acceleration versus heat flux for the three heater sizes in the high-*g* and the low-*g* regime was shown in Fig. 6. Gravity dependence (*m*) was observed to increase with wall temperature in the high-*g* regime. Moreover, as observed for the boiling curves, the quarter, half, and full heater configurations had similar variations in slope and hence heat transfer in the high-*g* regime. In the low-*g* regime, gravity dependence was small.

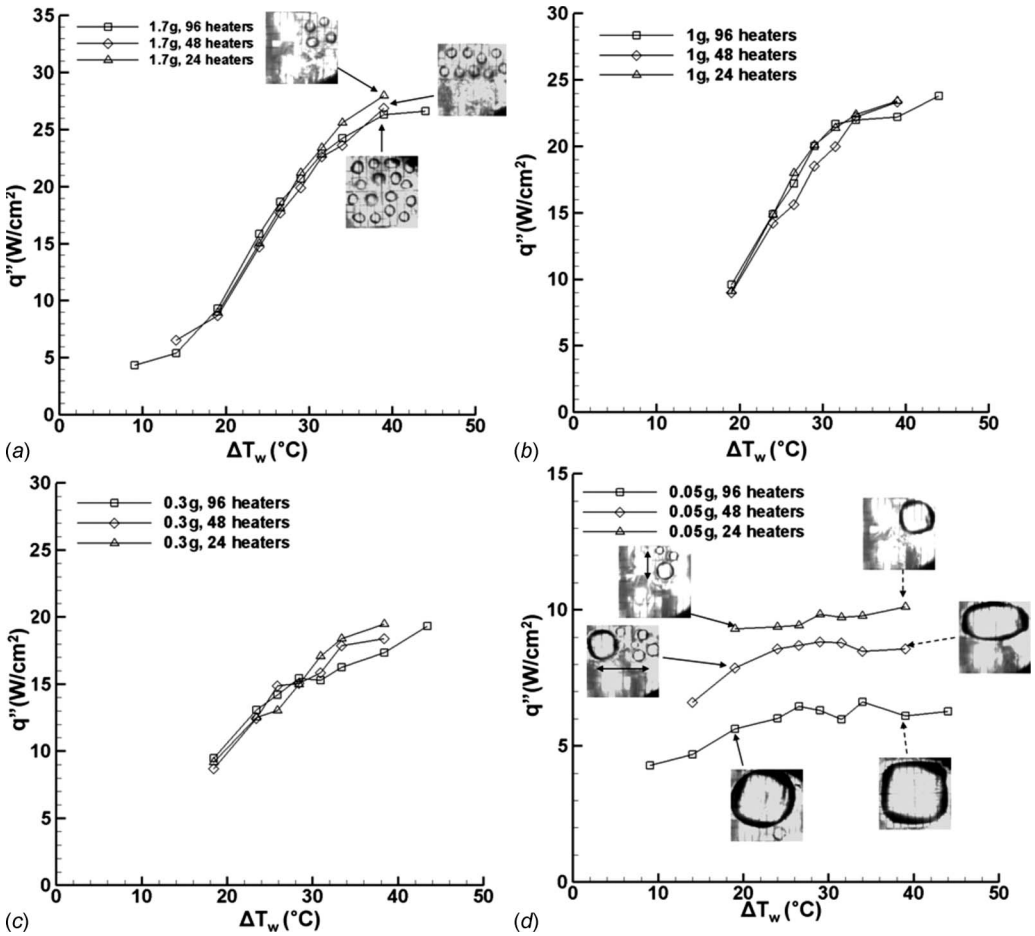

Fig. 13 Boiling curve for three different heater sizes, high gas ($c_g \sim 1216$ ppm) at (*a*) 1.7*g* and (*b*) 1*g*, (*c*) 0.3*g*, and (*d*) 0.05*g*

Insight into the effect of heater size on heat transfer can be obtained by considering the ratio of heater size to the capillary length, L_h/L_c [39]. L_h is the length of the shortest side for a given heater configuration: 7 mm for the full heater and 3.5 mm for the half and quarter heaters. The capillary length L_c is used to quantify the interplay between surface tension to body forces:

$$L_c = \left(\frac{\sigma}{g(\rho_l - \rho_v)} \right)^{1/2} \tag{8}$$

If L_h/L_c is large, then the heater size should not affect the heat flux. For small values of L_h/L_c, the size of the departing bubbles becomes of the same order as the heater size, and the heater size is expected to influence the heat transfer. At $L_h/L_c=1$, a/g is 0.012 for the full heater and 0.05 for the half and quarter heaters. At 1.7g, 1g, and 0.3g (high-g regime), L_h is much larger than L_c, so the heat flux is independent of heater size. In the low-g regime, however, L_h is comparable to or smaller than L_c, indicating that there should be a heater size effect. As discussed above, this behavior was observed in the boiling curve at 0.05g (Fig. 13(d)).

4 Conclusions

The heat flux variation with gravity at various wall superheats for two gas concentrations and three heater sizes were studied under subcooled pool boiling conditions. The effects of the test parameters are summarized below.

4.1 Gravity Effects. Two heat transfer regimes were observed: a low-g regime (primary nondeparting bubble) and a high-g regime (departing bubbles). The low-g regime was dominated by the presence of a primary bubble and surrounding satellite bubbles. The dependence of heat flux on gravity was small in the low-g regime, while a larger dependence was observed in the high-g regime. The slope of the heat flux versus acceleration curve was different in the two regimes, ruling out the possibility of a unified power law dependence across all gravity levels.

4.2 Wall Superheat Effects. In the high-g regime, the heat flux increased with wall superheat. The effect of wall superheat in the low-g regime was not clear and dependent on the dissolved gas concentration. Wall superheat did not appear to influence the acceleration at which the transition in heat transfer mechanisms occurred. The slope of the heat flux versus acceleration curve was dependent on the superheat.

4.3 Noncondensable Gas Effects. Onset of nucleate boiling occurred at lower wall superheat for the high gas case. The presence of dissolved gas increased the nucleate boiling heat transfer in the high-g regime but decreased the heat transfer in the low-g regime. In the low-g regime, the primary bubble size increased with gas concentration, resulting in larger dryout area and weaker thermocapillary convection. Transition from the low-g to high-g regimes occurred at higher acceleration for the low gas case compared with the high gas case.

4.4 Heater Size Effects. For accelerations at which the capillary length was significantly smaller than the characteristic heater size, the nucleation site density (and hence the heat flux) remained unaffected. The heat transfer only depends on the heater size when it became comparable to, or smaller than, the capillary length. In this regime, the heat flux increased with decreasing heater size. Oscillating bubbles were observed at lower wall temperatures. A stable primary bubble formed at higher temperatures for all three heater sizes. Heat flux dependence on gravity was small in the low-g regime.

Acknowledgment

This work was supported by NASA Grant No. NNX08AI60A. The authors are very grateful to the European Space Agency for accommodating the experiment on the 48th ESA Parabolic Flight Campaign in March 2008. The authors would also like to acknowledge Martin Karch and Jack Coursey for their help during the preparation and operation of test rig.

Nomenclature

a = acceleration (m/s^2)
c = concentration (ppm)
C = concentration (moles/moles)
c_p = specific heat at constant pressure (W/kg K)
D = bubble diameter (m)
g = acceleration due to gravity (m/s^2)
h = heat transfer coefficient (W/m^2 K)
h_{lv} = latent heat (J/kg)
L = length scale (mm)
H = Henry's constant (mole/mole Pa)
P = pressure (Pa)
q'' = heat flux (W/cm^2)
T = temperature (°C)
x = location along the bubble surface

Greek

α = thermal diffusivity (m^2/s)
μ = dynamic viscosity (Pa-s)
ρ = density (kg/m^3)
σ = surface tension (N/m)
θ = apparent contact angle (deg)

Subscripts

b = boiling
back = back of the chip
bulk = bulk liquid
c = capillary
depart = departure
exp = experimental value
f = forced convection, air-jet on
g = gas
gen = generated
h = shortest side
high = high gas
l = liquid
low = low gas
n = natural convection, air-jet off
sat = saturation
sub = subcooling
v = vapor
w = superheat
wall = heater wall

References

[1] Arlabosse, P., Reynard, C., and Tadrist, L., 2000, "Overview of Pool Boiling Heat Transfer Studies in Variable Gravity," *Proceedings of the American Institute of Physics Conference*, 504, pp. 744–750.
[2] Merte, H., Jr., and Clark, J. A., 1961, "Pool Boiling in Accelerating Systems," ASME J. Heat Transfer, **83**, pp. 233–242.
[3] Costello, C. P., and Tuthill, W. E., 1961, "Effect of Acceleration on Nucleate Pool Boiling," Chem. Eng. Prog., Symp. Ser., **57**, pp. 189–196.
[4] Di Marco, P., 2003, "Review of Reduced Gravity Boiling Heat Transfer: European Research," J. Jpn. Soc. Microgravity Appl., **20**(4), pp. 252–263.
[5] Kim, J., 2003, "Review of Reduced Gravity Boiling Heat Transfer: US Research," J. Jpn. Soc. Microgravity Appl., **20**(4), pp. 264–271.
[6] Ohta, H., 2003, "Review of Reduced Gravity Boiling Heat Transfer: Japanese Research," J. Jpn. Soc. Microgravity Appl., **20**(4), pp. 272–285.
[7] Siegel, R., 1968, "Effects of Reduced Gravity on Heat Transfer," Adv. Heat Transfer, **4**, pp. 143–227.
[8] Verkin, B. J., and Kirichenko, Y. A., 1976, "Heat Transfer Under Reduced Gravity Conditions," Acta Astronaut., **3**, pp. 471–480.
[9] Straub, J., Zell, M., and Vogel, B., 1990, "Pool Boiling in Reduced Gravity Field," *Proceedings of the 9th International Heat Transfer Conference*, Jerusalem, Israel, Hemisphere, pp. 91–112.
[10] Oka, T., Abe, Y., Tanak, K., Mori, Y. H., and Nagashima, A., 1992, "Observational Study of Pool Boiling in Microgravity," JSME Int. J., Ser. II, **35**(2), pp. 280.

[11] Kim, J., Benton, J. F., and Wisniewski, D., 2002, "Pool Boiling Heat Transfer on Small Heaters: Effect of Gravity and Subcooling," Int. J. Heat Mass Transfer, **45**(9), pp. 3921–3934.
[12] Straub, J., and Vogel, B., 1992, "Boiling Under Microgravity Conditions," *Proceedings of the First European Symposium in Space*, Paper No. ESA SP-353, p. 269.
[13] Ohta, H., Kawaji, M., Azuma, H., Kakehi, K., and Morita, T. S., 1998, "Heat Transfer in Nucleate Pool Boiling Under Microgravity Condition," *Proceedings of the 11th International Heat Transfer Conference*, Kyongju, Korea, Vol. 2, pp. 401–406.
[14] Kim, J., and Benton, J. F., 2002, "Highly Subcooled Pool Boiling Heat Transfer at Various Gravity Levels," Int. J. Heat Fluid Flow, **23**, pp. 497–508.
[15] Lee, H. S., and Merte, H., Jr., 1997, "Pool Boiling Curve in Microgravity," J. Thermophys. Heat Transfer, **11**(2), pp. 216–222.
[16] DeLombard, R., McQuillen, J., and Chao, D., 2008, "Boiling Experiment Facility for Heat Transfer Studies in Microgravity," 46th AIAA Aerospace Sciences Meeting and Exhibit, Reno, NV, Jan. 7–10.
[17] Fritz, W., 1935, "Berechnung des Maximalvolume von Dampfblasen," Phys. Z., **36**, pp. 379–388.
[18] Cole, R., 1967, "Bubble Frequencies and Departure Volumes at Subatmospheric Pressures," AIChE J., **13**, pp. 779–783.
[19] Siegel, R., and Keshock, F. G., 1964, "Effects of Reduced Gravity on Nucleate Boiling Bubble Dynamics in Saturated Water," AIChE J., **10**(4), pp. 509–517.
[20] Son, G., Dhir, V. K., and Ramanujapu, N., 1999, "Dynamics and Heat Transfer Associated With a Single Bubble During Nucleate Boiling on a Horizontal Surface," ASME J. Heat Transfer, **121**(3), pp. 623–631.
[21] Malenkov, I. G., 1971, "The Frequency of Vapor Bubble Separation as a Function of Bubble Size," Fluid Mech.-Sov. Res., **1**, pp. 36–42.
[22] Rohsenow, W. M., 1962, "A Method of Correlating Heat Transfer Data for Surface Boiling of Liquids," Trans. ASME, Ser. B, **84**, pp. 969–976.
[23] Stephan, K., and Abdelsalam, M., 1980, "Heat Transfer Correlations for Natural Convection Boiling," Int. J. Heat Mass Transfer, **23**, pp. 73–87.
[24] Kutateladze, S. S., 1948, "On the Transition Film Boiling Under Natural Convection," *Kotloturbostroenie*, Vol. 3, pp. 10–12.
[25] Zuber, N., 1959, "Hydrodynamic Aspects of Boiling Heat Transfer," AEC Report No. AECU-4439.
[26] Straub, J., 2002, "Origin and Effect of Thermocapillary Convection in Subcooled Boiling: Observations and Conclusions From Experiments Performed at Microgravity," Ann. N.Y. Acad. Sci., **974**, pp. 348–363.
[27] Marek, R., and Straub, J., 2001, "The Origin of Thermocapillary Convection in Subcooled Nucleate Pool Boiling," Int. J. Heat Mass Transfer, **44**, pp. 619–632.
[28] Barthes, M., Reynard, C., Santini, R., and Tadrist, L., 2007, "Non-Condensable Gas Influence on the Marangoni Convection During a Single Vapor Bubble Growth in a Subcooled Liquid," EPL, **77**, pp. 14001.
[29] Henry, C. D., Kim, J., and McQuillen, J., 2006, "Dissolved Gas Effects on Thermocapillary Convection During Subcooled Boiling in Reduced Gravity Environments," Int. J. Heat Mass Transfer, **42**, pp. 919–928.
[30] Raj, R., and Kim, J., 2009, "Thermocapillary Convection During Subcooled Boiling in Reduced Gravity Environments," Ann. N.Y. Acad. Sci., **1161**, pp. 173–181.
[31] Rule, T. D., and Kim, J., 1999, "Heat Transfer Behavior on Small Heaters During Pool Boiling of FC-72," ASME J. Heat Transfer, **121**(2), pp. 386–393.
[32] Product Manual, FLORINERT® Electronic Liquid, 3M Center, St. Paul, MN.
[33] Pletser, V., Pacros, A., and Minster, O., 2008, "International Heat and Mass Transfer Experiments on the 48th ESA Parabolic Flight Campaign of March 2008," Microgravity Sci. Technol., **20**, 177–182.
[34] Incropera, F. P., Dewitt, D. P., Bergman, T. T., and Lavine, A. S., 2007, *Fundamentals of Heat and Mass Transfer*, 6th ed., Wiley, New York, Chap. 1, p. 8.
[35] Aparajith, H. S., Dhir, V. K., Warrier, G., and Son, G., 2003, "Numerical Simulation and Experimental Validation of the Dynamics of Multiple Bubble Merger During Pool Boiling Under Microgravity Conditions," Microgravity Transport Processes Conference, Davos, Switzerland, Sep. 14–19.
[36] You, S. M., Simon, T. W., Bar-Cohen, A., and Hong, Y. S., 1995, "Effects of Dissolved Gas on Pool Boiling of a Highly Wetting Fluid," ASME J. Heat Transfer, **117**, pp. 687–692.
[37] Rainey, K. N., You, S. M., and Lee, S., 2003, "Effect of Pressure, Subcooling, and Dissolved Gas on Pool Boiling Heat Transfer From Microporous Surfaces in FC-72," ASME J. Heat Transfer, **125**, pp. 75–83.
[38] Honda, H., Takamastu, H., and Wei, J. J., 2002, "Enhanced Boiling of FC-72 on Silicon Chips With Micro-Pin-Fins and Submicron-Scale Roughness," ASME J. Heat Transfer, **124**(2), pp. 383–390.
[39] Henry, C. D., and Kim, J., 2004, "A Study of the Effects of Heater Size, Subcooling, and Gravity Level on Pool Boiling Heat Transfer," Int. J. Heat Fluid Flow, **25**, pp. 262–273.

Measurement of Fluid Temperature Across Microscale Gap Using Two-Color Ratiometric Laser-Induced Fluorescence Technique in Combination With Confocal Microscopy

Dong Woon Jeong
e-mail: d.w.jeong@kaist.ac.kr

Chi Young Lee

Sang Yong Lee

Department of Mechanical Engineering,
KAIST,
Daejeon 305-701, South Korea

In the present work, for noninvasive measurement of the liquid temperature in microchannels, the two-color ratiometric laser-induced fluorescence (LIF) technique was combined with the confocal microscopy. By using this technique, the fluorescent light from the tiny volume around a focusing spot can be selectively detected, and it enables us to measure the local liquid temperatures even at the close vicinity of the walls. To check the general performance of this method, as the preliminary stage, a test section consisting of two horizontal plates in different temperatures, separated by a narrow gap filled with a mixture of rhodamine B (a temperature-sensitive dye) and methanol was made, and the temperature distribution was examined. Based on the relationship between the fluorescence intensity and the temperature, a linear temperature distribution across the gap (by conduction heat transfer) could be confirmed. However, the measured results were subject to external disturbances such as the excitation laser intensity fluctuation and the irregular reflection of the light from the glossy walls. Therefore, in the second stage, rhodamine 110 (a temperature-insensitive dye), having a different emission spectrum peak (520 nm) from the rhodamine B (575 nm), was added to the mixture. In principle, the external disturbance effects cancel out each other when the intensity ratio between rhodamine B and rhodamine 110 is considered (instead of taking data only with rhodamine B). To compensate a substantial reduction in the fluorescence intensity from rhodamine 110 by the re-absorption phenomenon within the liquid, which is inherent in using the two-color thermometry, dependency of the intensity ratio on the depth of the measuring point was examined as well. In summary, the two-color ratiometric confocal-LIF thermometry was found to be a very useful tool in measuring the local temperatures of the liquid flow field in microfluidic devices. [DOI: 10.1115/1.2976553]

Keywords: laser-induced fluorescence (LIF), confocal microscopy, thermometry, re-absorption

1 Introduction

Recently, the laser-induced fluorescence (LIF) technique is becoming of interest because of its capability in measuring the liquid temperatures. In principle, the light intensity signals emitted from fluorescent dyes depend on the liquid temperature [1]. Figure 1 shows the absorption and emission characteristics of rhodamine B (RB) against the wavelength in the visible range. The decrease in the fluorescent light intensity with the temperature increase in the dyed water is clearly seen. The emissive light intensity per unit volume (W/m^3) of a liquid with single dye, excited by the external light source, can be expressed as follows:

$$I = I_0 c \varepsilon \varphi \tag{1}$$

Here, I denotes the emissive fluorescence light intensity, I_0 the incident-light-energy flux (W/m^2), c the dye concentration (kg/m^3), ε the absorption coefficient (m^2/kg), and φ the quantum efficiency (−). With some exceptions, the quantum efficiency of the organic dyes shows a dependency on temperature. For the case of RB, the dependency of φ on the temperature is relatively high by 2.3%/°C. However, the dependency of ε on the temperature is very low, about less than 0.05%/°C. Therefore, provided that the values of I_0 and c of the dyed solution are maintained constant, the temperature could be estimated only from the change in the fluorescence intensity.

There have been some works related to the temperature measurement using the LIF technique: Cross-section-averaged temperature measurement of fluid in channels of microscale devices has been attempted by Ross et al. [3] and Erickson et al. [4] using RB to examine the Joule heating effect in electrokinetic pumping. On the other hand, Sato et al. [5] and Jung et al. [6] monitored the wall temperature variation by coating a fluorescent dye on the wall surface of microdevices; a very thin film of photoresist mixed with RB was deposited on the wall surface.

However, in general, the fluorescence lights are emitted from all parts of the illuminated space (of a finite size) and contribute to image formation simultaneously in using the LIF method. There-

Contributed by the Heat Transfer Division of ASME for publication in the JOURNAL OF HEAT TRANSFER. Manuscript received September 13, 2007; final manuscript received May 18, 2008; published online June 22, 2009. Review conducted by Bengt Sunden. Paper presented at the Fifth International Conference on Nanochannels, Microchannels and Minichannels (ICNMM2007), Puebla, Mexico, June 18–20, 2007.

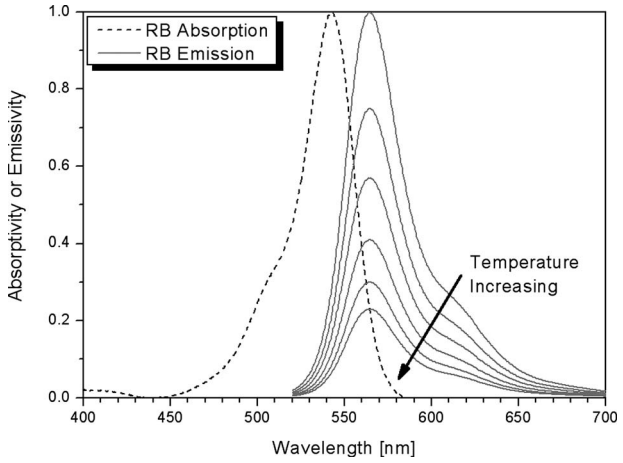

Fig. 1 Absorption and emission spectra of RB and dependency of fluorescence (emission) intensity on temperature [2]

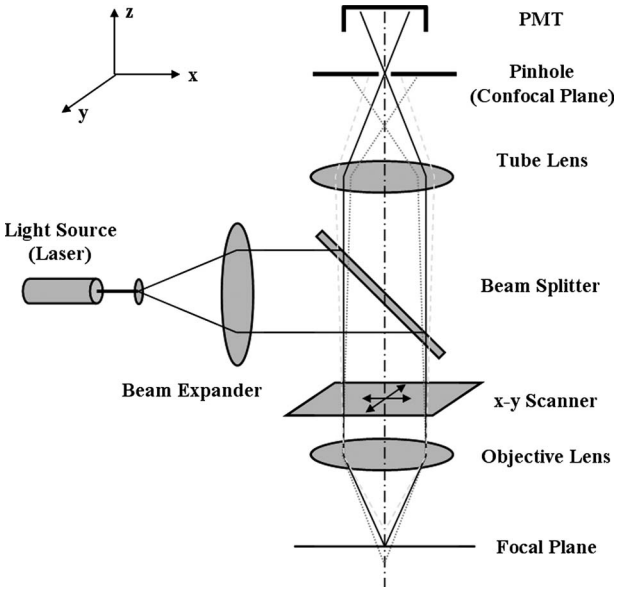

Fig. 2 Principles of CLSM

fore, it is difficult to measure the local quantities in a 3D flow field, especially in the depth direction.

As a way to overcome this difficulty, a technique of irradiation of a very thin (about 5 μm) planar laser sheet (in the normal direction to the optical axis) has been attempted by Yoon et al. [7] to measure the concentration distribution in the corresponding plane. However, the extent of the laser sheet having a constant thickness is usually very short (say, about several hundred microns), and the light source should be placed very close to the test section. Moreover, the side walls have to be transparent, which is also a limitation in applying this technique.

Another method to resolve the problem of the volumetric illumination, Park et al. [8] combined the confocal microscopy with the μ-PIV (particle image velocimetry) technique and successfully measured the internal flow velocity field in a capillary tube of about 500 μm in diameter. Through this work, a 3D measurement with a fine resolution in the light-axis direction in microfluidic devices as well as the lateral direction was confirmed to be feasible. Because of the excellent optical slicing capability (with very thin depth-of-focus (DOF)) of the confocal microscopy (originally developed for inspecting the 3D structure of biological cells), precise positioning along the light-axis was possible.

The operating principle of the confocal microscopy is shown in Fig. 2. Also, Fig. 3 illustrates a 3D numerically calculated spatial point-spread function (PSF) distribution of light intensity around a focal volume imaged by a lens, representing a brightness distribution. More specifically, Fig. 3(*a*) shows the intensity distribution along the optical axis (z) indicated in Fig. 2, while Fig. 3(*b*) shows the intensity distribution in the focal plane (x-y), known as the Airy diffraction pattern. In principle, as shown in Fig. 2, a portion of the light coming from the off-focus location is spatially blocked by a pinhole located at the confocal plane in front of the image acquisition devices. Here, the diameter of pinhole should be determined the same with that of Airy disk, and the local position along the optical axis should be around the middle part of ellipsoid volume shown in Fig. 3(*a*). In other words, only the light from the focal-point region in the flow field is accepted by the light detector. As the pinhole size gets smaller, the DOF gets thinner (i.e., the measurement resolution is enhanced), but at the same time, the amount of the light reaching the detecting device is also reduced substantially. Therefore, more sensitive light detectors, such as photomultiplier tubes (PMTs), are generally used instead of charge coupled device (CCD) cameras to detect extremely low level of fluorescence light to achieve high signal-to-noise ratio (SNR). Nevertheless, in spite of such a high sensitivity, a PMT itself has no function of scanning, and additional scanning devices should be installed in the middle of the optical paths to cover the interrogation area.

As explained in the references on elementary optics such as by Wihelm et al. [9], the optical slice thickness cannot be defined for general-purpose microscopes (without a pinhole). On the other hand, for confocal microscopes in the air medium with the number of numerical aperture (NA) 0.6, the magnification ratio of the object lens 40, the absorption and emission peaks of the exciting laser 473 nm and 550 nm, respectively, and the pinhole diameter 25 μm, only the fluorescence light emitted from the region within the thickness of 2–3 μm contributes to the formation of the final images.

Recently, based on the previous development of the LIF technique and the confocal microscopy, Jeong and Lee [10] combined those two techniques (LIF technique along with the confocal microscopy) for point measurement of temperature in microscale flow fields. In their work, a commercial confocal laser scanning microscope (CLSM) has been adopted to check the feasibility of this combined method, and it was concluded to be successful for the local temperature measurement.

Similar (but somewhat different) works have been performed by Migler and Bur [11] and Bur and Roth [12]. They constructed a single confocal optical system using an optical fiber (instead of using a pinhole) to monitor the temperature variation in polymer processing. For axial movement of the optics (to scan the cross section of the measuring space), a micrometer was installed. With this technique, temperature measurement with the axial resolution of about several hundred microns became also available.

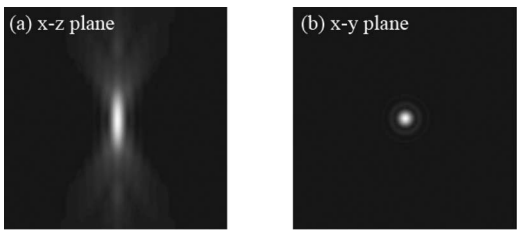

Fig. 3 Cross-sectional light intensity distributions computed from the 3D point-spread function

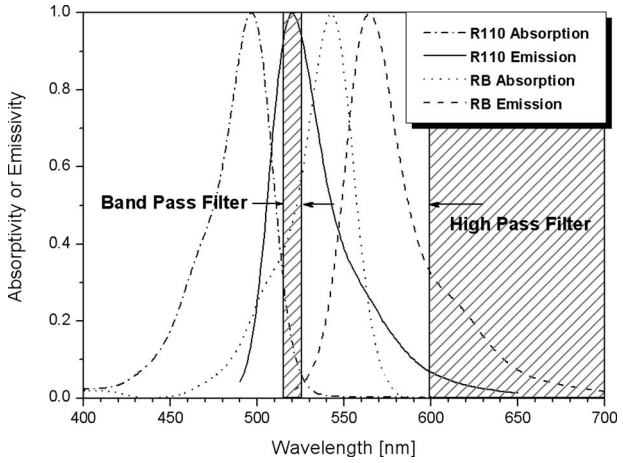

Fig. 4 Absorption and emission peaks of RB and R110

However, in practice, it is not easy to maintain the incident light for excitation (I_0) either spatially or temporally in using the single-color method, especially with large test devices. Moreover, there are irregular reflection of the light from the glossy walls, nonuniform mixing of fluorescent dyes in the liquid medium, and imperfectness of the detecting sensitivity of the cells in CCD cameras. As already noted, Sato et al. [5] and Jung et al. [6] monitored the wall temperature variation by coating a fluorescent dye on the wall surface of microdevices. In their works, every pixel of the acquired images has to be calibrated for compensation of the unevenness of the coated-layer thickness, dye content, and the light illumination. To avoid the laborious point-calibration process with the single-color method, the two-color ratiometric LIF technique has been proposed by Kim et al. [13] and Kim [14]. This technique may be used to take into account the fluctuation of the incident light as well. However, in those works, two different fluorescent images could not be recorded by a CCD camera at the same time, and these were recorded alternately by changing the light filters in front of the CCD camera.

General principles of two-color ratiometric LIF thermometry are well explained in the study of Sakakibara and Adrian [1]. Two kinds of fluorescent dyes having different emission wavelength characteristics were used simultaneously: rhodamine B (RB) and rhodamine 110 (R110) are both soluble in water. R110 was adopted because it has a very low φ dependency on temperature ($\varphi = 0.13\%/°C$) compared with RB ($\varphi = 2.3\%/°C$), but with the dependency of the absorption coefficient on the temperature remaining very low ($\varepsilon < 0.05\%/°C$). At the same time, two separate CCD cameras for each dye were used. Using the Ar-ion laser (488 nm) for excitation, the 3D temperature measurement of a wide flow field could be realized within the error range of 1.4°C. When the two dyes emit fluorescence lights excited by the same light source, the ratio between the two intensities becomes independent of the incident-light intensity. Of course, separate detection is available by using two CCDs because those dyes have different emission wavelengths. Thus, with a fixed dye concentration, the ratio depends only on the effect of quantum efficiencies as follows:

$$\frac{I_{RB}}{I_{R110}} = \frac{\varphi_{RB}}{\varphi_{R110}} \tag{2}$$

Here, subscripts RB and R110 denote rhodamine B and rhodamine 110, respectively. Since the dependence of φ_{R110} on the temperature is negligible, the intensity ratio varies with temperature only through φ_{RB}.

Thus, in the present study, based on the works of Jeong and Lee [10], Kim et al. [13], and Kim [14], a new two-color ratiometric LIF technique in combination with the confocal microscopy is proposed for noninvasive point measurement of the liquid temperature in microchannels. Also, the effects of the spherical aberration, absorption of the incident light (by passing through the transparent channel walls and the liquid layer, having different indices of refraction), and re-absorption of the fluorescence (emitted) light on the accuracy of the measurement are considered in detail.

2 Experiment

2.1 Working Fluid and Fluorescent Dyes. In the present work, liquid methanol was chosen as the working fluid. Methanol is an excellent solvent for both the RB (temperature sensitive, absorption peak=554 nm, and emission peak=575 nm) and R110 (temperature insensitive, absorption peak=496 nm, and emission peak=520 nm) dyes. Since the fluorescence of RB decreases considerably with an increase in the fluid temperature, the temperature of the test section was kept below 100°C. Figure 4 shows the wavelength characteristics of the absorption and emission for each dye. In the same figure, the transmission characteristics of the light filters used in this study were also shown: a high pass filter (HPF) (threshold=600 nm) for RB and a band pass filter (BPF) (10 nm bandwidth, centered at 520 nm) for R110.

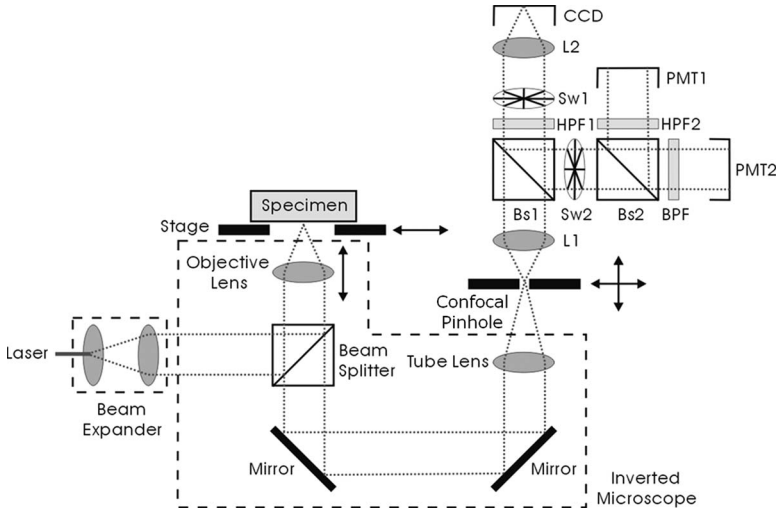

Fig. 5 Schematic of the experimental setup

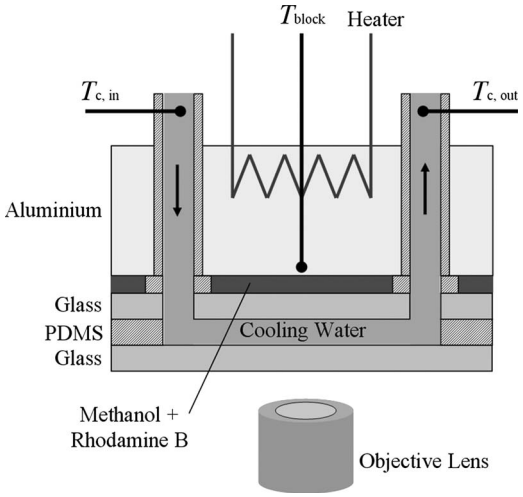

Fig. 6 Schematic of the test section for a one-color thermometry

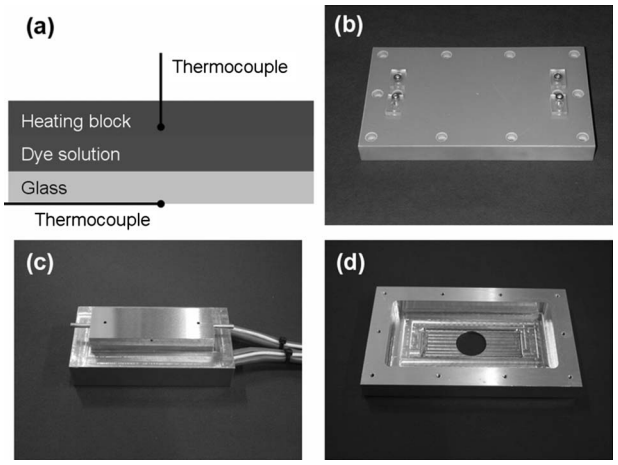

Fig. 7 Schematic and pictures of the test section for a two-color thermometry

Especially, the threshold wavelength for HPF was chosen to avoid re-absorption of the fluorescent light containing the temperature information of the fluid medium.

2.2 Optical Systems. As the preliminary stage, to check the feasibility of the single-color CLSM-LIF thermometry, a commercial inverted CLSM (Carl Zeiss, LSM 5 PASCAL) with a He–Ne laser (543 nm wavelength) was used. Then, later on, a simple confocal microscope system using the general-purpose inverted microscope (Nikon, TS100F) was constructed separately for the two-color ratiometric confocal-LIF thermometry with a blue diode laser (473 nm wavelength), as shown in Fig. 5. It consists of a confocal pinhole, two different filter-PMT assemblies (HPF2-PMT1 and BPF-PMT2), and an additional light port for occasional CCD imaging through HPF1.

The incident laser light with specific wavelength for excitation passes through the beam expander, and then partly reflected by the beam splitter to the objective lens and reaches the focal point in a specimen. The emitted fluorescence light from the specimen comes down (with the temperature information) and passes through the objective lens and the beam splitter and reflected by two mirrors consecutively, and reaches the tube lens of the microscope to be condensed, and then spatially filtered by a confocal pinhole. The fluorescent signals can be selectively detected by CCD or PMT, using optical switches (Sw1 or Sw2). The spatially filtered fluorescence light is divided into two parts with the same intensity by a beam splitter (Bs2), and they are detected by PMT1 and PMT2, respectively. Finally, the light signals are converted into electric signals for data processing.

2.3 Test Sections. Figure 6 shows the test section used in the preliminary stage for single-color CLSM-LIF thermometry to measure the temperature distribution across the microgap filled with a mixture of RB and methanol. The actual thickness of the microgap is estimated to be about 240 μm. The upper surface of the gap was electrically heated while the lower surface was cooled with a flow of cold water through the transparent channel at the bottom. Therefore, the liquid layer becomes stabilized and is subject to conduction heat transfer between the upper and the lower surfaces without any convection effect. The measurements were made in the range of 25–45°C. The heated surface temperature was maintained to be constant within the variation range of ± 0.8°C by using an ON/OFF controller with K-type thermocouples, and the cooling water was supplied from the constant temperature bath maintained within the range of ± 0.5°C. The temperature rise of the cooling water between the inlet and the outlet of the cooling channel was below 1°C.

Another test section for two-color ratiometric confocal-LIF thermometry was constructed for the simplified confocal microscope, as shown in Fig. 7. While the concept of the heating is the same with the previous one in Fig. 6, the cooling channel at the bottom part was removed and the lower plate (glass) was simply exposed to the ambient for air cooling. Figures 7(*b*)–7(*d*) show the photographs of each component of the test section. The heating block at the top of the microgap was made of copper with cartridge heaters. The glass plate at the bottom was transparent with the thickness of 1.1 mm and the refraction index was 1.523. Between these two plates, the inlet- and outlet-flow passages made of the polydimethylsiloxane (PDMS) material were connected to the microgap (thickness = 1.1 mm) for easy exchange of the test fluid. Two K-type thermocouples were installed, as shown in Fig. 7(*a*): one was on the bottom surface of the glass plate and the other was buried in the heating (copper) block. The temperature measurement range was within 24–44°C. During every experiment, the temperatures of both surfaces were kept constant within the range of ± 0.5°C.

3 Results

3.1 Single-Color CLSM-LIF Thermometry. The details of the single-color CLSM-LIF thermometry are well explained by Jeong and Lee [10], and only the results of the calibration test are briefly explained here. In this test, the temperatures of the upper and the lower surfaces of the microgap (Fig. 6) were kept the same, and measurements were made for three cases, i.e., 25°C, 35°C, and 45°C. The purity of the liquid methanol (Merck) was higher than 99.6 wt % and that of RB (Aldrich) was above 95 wt %. The concentration of the dyed methanol was 3.95 mg/l for all cases. A He–Ne laser (543 nm, 1 mW) was used as the excitation light source. For observation, a 40X objective lens (Carl Zeiss, LD Achroplan, working distance of 2.0 mm, NA = 0.6) for the air medium was used. The fluorescence light filtered by 560 nm HPF was imaged in 4096 gray-level scales. The gray-level values of each pixel in the same image planes were averaged, and the measurement was repeated for 12 times under the fixed temperature conditions for each depth. The pinhole diameter was 158 μm, and each image covered the thickness range of about 3.2 μm around the focal plane.

Figure 8(*a*) shows the fluorescent images with 13.23 μm interval (represented by the subframes from the left to the right) for the isothermal case (at 25°C). Except for several subframes around the interfaces between the liquid layer and the solid walls, the brightness was approximately the same (though becoming slightly dark along the depth direction, as will be explained later on).

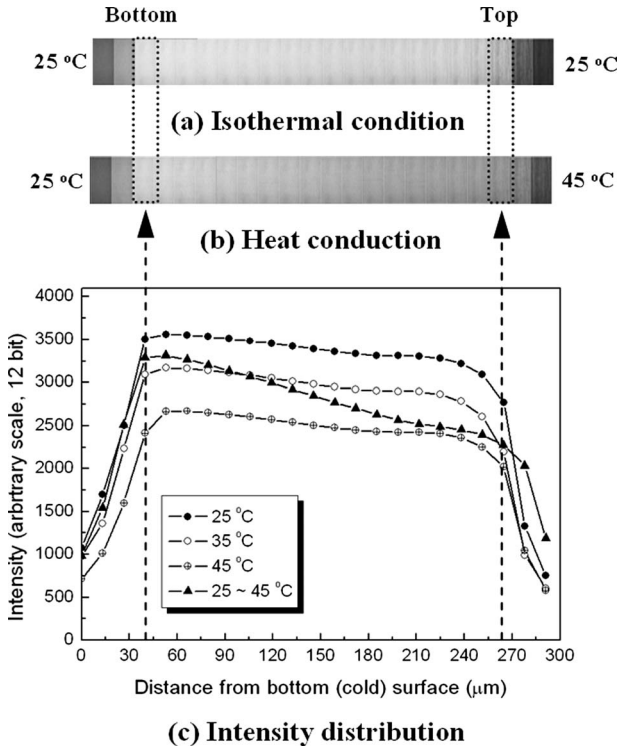

Fig. 8 Raw RB fluorescence intensity distributions along the depth direction (sample images were acquired at every 13.23 μm interval along the light-axis)

Figure 8(*b*) shows the images (again, represented by the subframes from the left to the right) obtained from the heat conduction test, with the bottom- and the top-surface temperatures at 25°C and 45°C, respectively. Here, within the liquid-layer region, the subframes look much darker as they get closer to the high temperature surface.

Figure 8(*c*) shows the variations of the fluorescence intensity (averaged for 12 times under the fixed temperature conditions at each depth) with the distance from the bottom surface. Measurements were made at every 13.23 μm interval along the optical axis. In the calibration tests (with isothermal conditions, shown in circular symbols), the fluorescence intensity decreases gradually in the same manner (with the same slope) regardless of the uniform bulk temperature, except for near the glossy walls (by reflection of the excitation light). Since there is no possibility of reabsorption in using the single-color thermometry with RB, the reduction in the excitation light intensity was considered to be due to the spherical aberration (i.e., spreading of the light-energy intensity distribution with the blurred focal volume) by refractive index (RI) mismatching in multilayer media. Figure 9 illustrates how the moving distance of the focal region changes inside the glass with advancement of the objective lens in the axial direction. With the optics aligned to make a sharp focus in the air medium (shown as ① in Fig. 9), the focal region was spread out (with the lower peak intensity) and extended to the deeper location in the glass than the actual moving distance of the optical system (shown as ② in Fig. 9). This distance stretching occurs because the RI value of the glass is higher than that of the air. The rate of the distance stretching is proportional to the ratios of RIs (Jeong and Lee [15]). The actual travel distance of the optical system was about 400 μm, which covers the transparent channel walls and some portion of the aluminum heating block, as well as the liquid layer. However, the fluorescence light signals were detected only for a portion of the travel distance of about 180 μm. Considering the rate of the distance stretching (calculated by using the RI values of air and methanol at 35°C) of the focal region, the actual

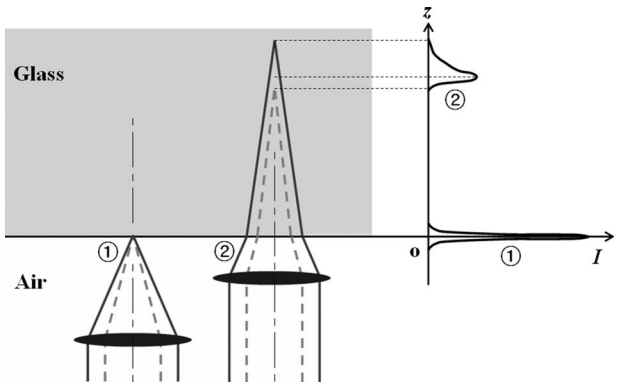

Fig. 9 RI mismatching in multilayer media

thickness of the microgap was estimated to be about 240 μm. The planar resolution of the acquired image was 256(width) $\times$256(height), and the lengths of the sides of the interrogation area were about 230 μm. The fluorescence intensity data at each depth for the conduction test were also plotted in Fig. 8 (the triangular symbols) with the top and bottom plates maintained at 45°C and 25°C, respectively.

To convert the fluorescence light intensities to actual temperature values, the results shown in Fig. 8 were normalized based on the data obtained from the 25°C calibration test and were replotted as in Fig. 10. Except at the boundaries of the liquid layer, the normalized intensities with the isothermal tests (the circular symbols) were almost constant over the entire range. For the heat conduction test (the triangular symbols), the measured intensities showed good linearity along the depth direction. Figure 11 shows the actual temperature data across the microgap based on the linear relationship between the temperature and the intensity. Again, except for the regions close to the boundaries (within 30–40 μm range from each boundary), the measured temperature distribution showed good linearity, which is a typical characteristic of the conduction heat transfer.

However, the measured results using single-color CLSM-LIF thermometry were subject to external disturbances such as the intensity fluctuation of the excitation laser and the irregular reflection of the light from the glossy walls. Therefore, to eliminate those external disturbances, a two-color ratiometric confocal-LIF thermometry (using additional fluorescent dye, R110, along with RB) is proposed in Sec. 3.2.

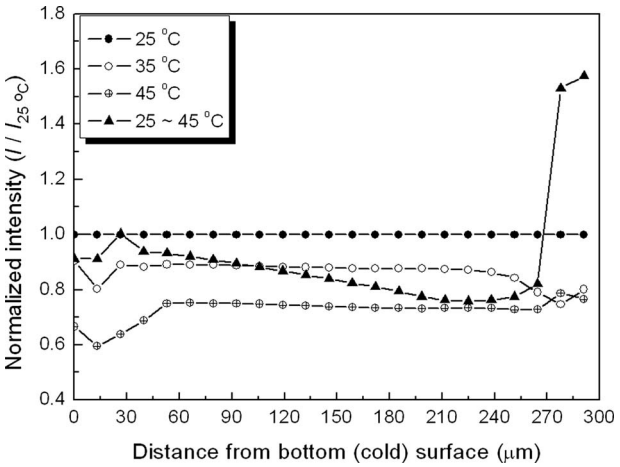

Fig. 10 Variation in normalized RB fluorescence intensity along the depth direction

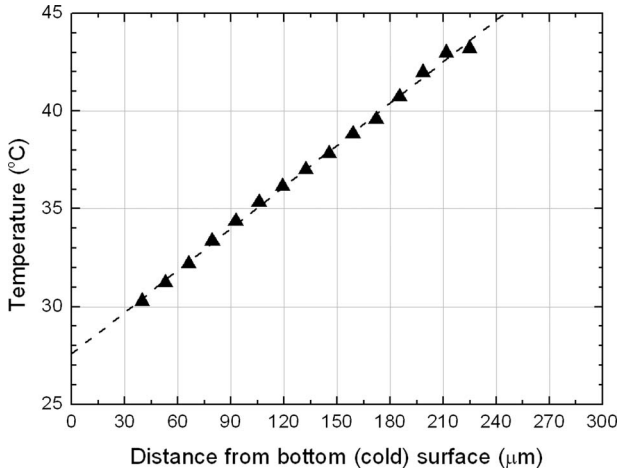

Fig. 11 Measured temperature distribution along the depth direction using a one-color thermometry

3.2 Two-Color Ratiometric Confocal-LIF Thermometry. According to the previous report (Sakakibara and Adrian [1]), the recommended concentration ratio between R110 and RB was about 1:20 to maximize the temperature resolution of the two-color method. This ratio was determined to minimize the role of R110 only in monitoring the intensity of the exciting light and in detecting most of fluorescence from RB that contains temperature information. However, a considerable reduction in the fluorescence intensity from R110 with the measuring depth restricts the measurable depth range. Moreover, with the confocal microscopy, a large portion of the fluorescence light is blocked by the pinhole, and the absolute intensity of the light from R110 is reduced considerably. Therefore, unless the temperature resolution is deteriorated, it was necessary to make the R110 concentration as high as possible to extend the measurable depth range. In this study, the concentration ratios between R110 and RB were tested for the range of 1:0–1:20. As a result, the optimum concentrations of R110 and RB were determined to be 40 mg/l and 200 mg/l, respectively (in other words, the concentration ratio was set to 1:5 in the present experiment). The temperature measurement range was within 24–44°C.

After installation of the test section on the flat stage of the confocal microscope, the fluorescent light intensity data at known temperatures and positions (along the light axis) were collected repeatedly. Then a relationship between the temperature and the intensity ratio (the ratio of the standard PMT signals from both dyes) was checked. During the calibration process for this two-color system, re-absorption of the emitted light from R110 was realized to be another phenomenon to be taken into account seriously.

Figure 12 illustrates the attenuation of the fluorescence light

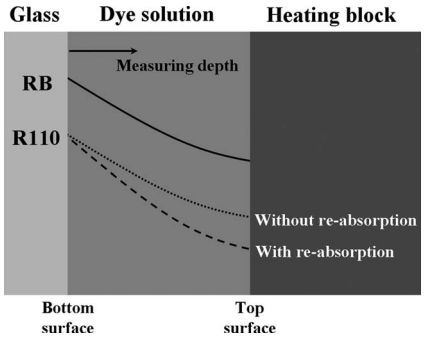

Fig. 12 Change in the intensity distribution by re-absorption

intensity from both dyes at each measuring point along the axial direction. It is usual to have an attenuation of the light intensity even through the isothermal medium. There are three main reasons for the occurrence of such a phenomenon: decrease in the excitation light intensity due to the spherical aberration (spreading of the light intensity distribution due to the blurred focal volume) by RI-mismatching in multilayer media, absorption of the excitation light to the optically thick medium (i.e., especially with the long light path or high concentration of the absorbing material), and re-absorption of the emitted light from the measuring volume. Among these, the effects of the spherical aberration and the absorption of the excitation light are common for both dyes. From the preliminary test, the intensity ratio, defined by Eq. (2), was confirmed to increase along the optical axis and it should be due to the re-absorption effect. In other words, the rate of the intensity decrease in the light signal from R110 is much larger than that from RB, as illustrated in Fig. 12. This is reasoned to be as follows.

As shown from the absorption and emission characteristics of RB and R110 in Fig. 4, the fluorescence light from RB, carrying the temperature information, is filtered by the 600 nm HPF but is not re-absorbed by the dyed solution. On the other hand, the fluorescence light from R110, filtered by the 520 nm BPF, is easily re-absorbed by both RB and R110 because the wavelength ranges of emission and absorption are partly overlapped in this band. Thus, when the light path becomes longer, the intensity of the fluorescence signal from R110 is reduced considerably due to the re-absorption effect.

Figure 13 shows the decreasing effect of the normalized intensity (based on the value at the zero depth) of the R110 fluorescence light signal ($[I_{110}]_{d=d}/[I_{110}]_{d=0}$), with increasing measuring depth in the liquid layer at 20°C for different concentration ratios between R110 and RB, i.e., 1:0, 1:5, 1:10, and 1:20. The decreasing rate of the normalized intensity with the measuring depth largely depends on the concentration of the mixture solution of R110 and RB. As shown in Fig. 13(*d*), even without RB, due to the absorption characteristics of R110 itself, the re-absorption phenomena occurred. As the concentration of RB in the mixture solution is increased, the effect of re-absorption of R110 light becomes more enhanced, and the effective measuring depth is decreased remarkably. Therefore, considering the required measuring depth in the present study, the appropriate concentration ratio between R110 and RB was determined to be 1:5. (In this case, the effective measuring depth turned out to be about 500 μm.) An illustration, shown in Fig. 14, gives an idea how to extract the actual temperature data from the measured intensity ratio distorted by the re-absorption phenomena. Here, the abscissa represents the measuring depth from the interface between the liquid layer and the window, and the ordinate the fluorescence intensity ratio between RB and R110 (I_{RB}/I_{R110}). At the interface between the window and the liquid (zero depth), there is no re-absorption at this location. Hence, the measured data show only the effect of temperature, i.e., the intensity ratio decreases with the higher temperature. For all the temperature condition, the intensity ratio increases as the measuring point moves inward due to the re-absorption effect. Thus, the intensity ratio reflects both the effects of the temperature variation and the re-absorption. Therefore, if the intensity-ratio distortion is corrected properly, the exact temperature data could be obtained.

Figure 15 shows the normalized intensity ratio with the change in the measuring depth when the liquid temperature is maintained uniformly at 24°C. Measurement was repeated for three times at each depth condition. The result clearly shows the increasing trend of the intensity ratio along the measuring depth. Thus, to compensate the depth (re-absorption) effect, a correction factor R_0, equivalent to the normalized intensity ratio, was introduced and a correlation for R_0 was obtained from the experimental results shown in Fig. 15, in terms of the measuring depth d (in microns).

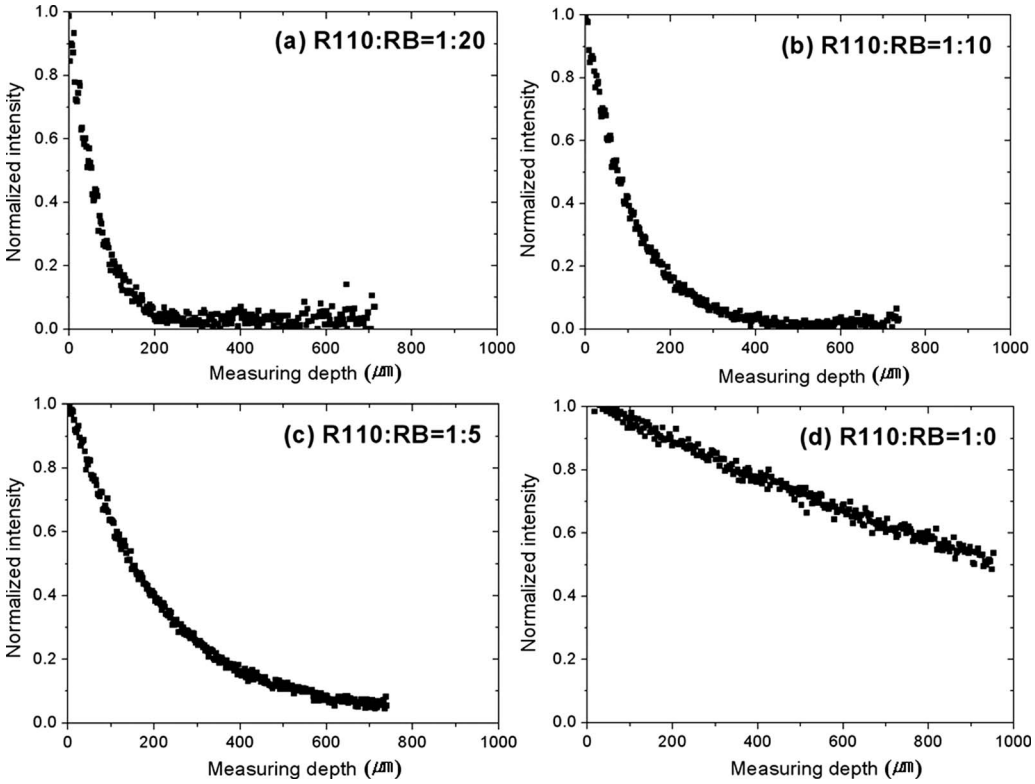

Fig. 13 Dependence of the normalized intensity on the measuring depth with different concentration ratios between R110 and RB

$$R_0 = \frac{[I_{RB}/I_{R110}]_{d=d}}{[I_{RB}/I_{R110}]_{d=0}} \tag{3}$$

$$R_0 = 1 + (3.45 \times 10^{-3}) \cdot d + (2.24 \times 10^{-5}) \cdot d^2 \tag{4}$$

According to the method proposed by Kline [16], the estimated uncertainties of $[I_{RB}/I_{R110}]_{d=0}$, $[I_{RB}/I_{R110}]_{d=d}$, and R_0 were ± 1, ± 7, and $\pm 7\%$, respectively. The proposed correlation in Eq. (4) represents the experimental data within the mean deviation of 2% at the uniform temperature condition of 24°C.

Figure 16 shows the same trends of R_0 for other temperature conditions, 36 ± 1°C and 44 ± 1.5°C, along with the correlation shown in Eq. (4). This implies that the correction factor is almost insensitive to the liquid temperature in the present experimental range. Therefore, by using Eq. (4), accurate temperature measurement became possible with the two-color ratiometric confocal-LIF thermometry regardless of the re-absorption effect.

4 Conclusion

In this work, for the liquid temperature measurement in microchannels, a noninvasive method using the two-color ratiometric LIF technique with confocal microscopy was assessed. To resolve practical limitation of volumetric illumination, the confocal microscopy that has the slicing capability along the optical axis was adopted. With this combined technique, only the fluorescent light from the tiny volume around a focusing spot could be selectively detected.

In the preliminary stage, the methanol mixed with a single temperature-sensitive dye (RB) was tested. At first, a relationship between the fluorescence intensity and the temperature was obtained by changing the temperature of the bulk liquid. Based on this relationship, the measured temperature distribution across the

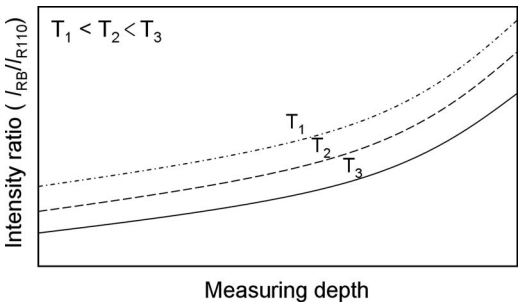

Fig. 14 Variation in the intensity ratio with the measuring depth for uniform temperature conditions

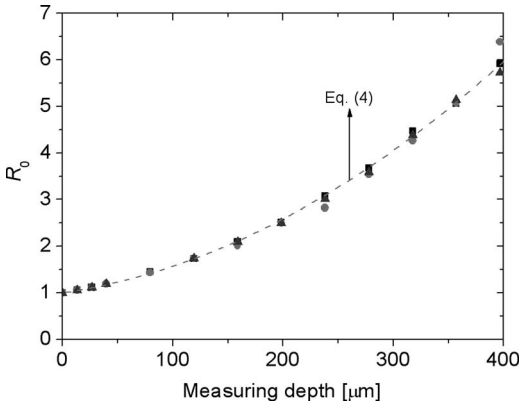

Fig. 15 Dependence of the normalized intensity ratio on the measuring depth at a constant temperature of 24°C

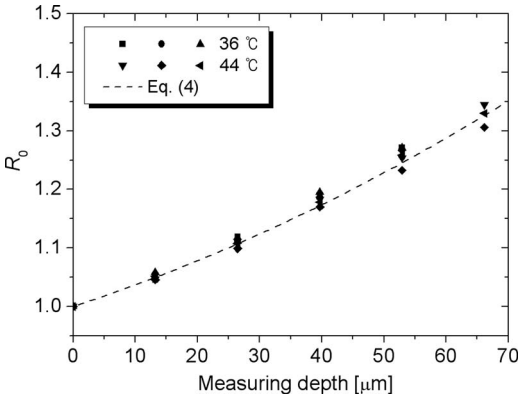

Fig. 16 Insensitiveness of the normalized intensity ratio to the liquid temperature

2D gap with its boundaries at different temperatures showed good linearity, which is a typical characteristic of the conduction heat transfer through a thin liquid layer. However, the measured results were very sensitive to external disturbances such as the excitation laser intensity fluctuation and the light reflection from the glossy walls.

In the second stage, to eliminate those external disturbances, two fluorescent dyes with different emission spectrum peaks were used simultaneously. In principle, by obtaining the intensity ratio between RB (575 nm) and R110 (temperature-insensitive dye, 520 nm), the external effects cancel out each other. However, to compensate the decrease in the fluorescence intensity from R110 (by the re-absorption phenomenon) using the two-color thermometry, an empirical correlation for the correction factor was proposed. The intensity ratio of the fluorescence lights from the two dyes, modified with the correction factor, showed good robustness and is proved to be free from the external disturbances. In summary, the proposed technique (the two-color ratiometric confocal-LIF method) was found to be a very useful tool in measuring the local temperatures of the liquid flow field in microfluidic devices.

Acknowledgment

The original content of this study was presented at the Fifth International Conference on Nanochannels, Microchannels and Minichannels sponsored by ASME in 2007 (ASME Paper No. ICNMM2007-30124). This work was financially supported by the Basic Research Program of the Korea Science and Engineering Foundation (Grant No. R01-2006-000-11298-0), Brain Korea 21 Project, and KAIST.

Nomenclature

c = dye concentration (kg/m^3)
d = measuring depth (μm)
I_0 = incident-light flux (W/m^2)
I = fluorescence intensity (W/m^3)
R_0 = (correction factor)

Greek Symbols

ε = absorption coefficient (m^2/kg)
φ = quantum efficiency

Subscripts

d = measuring depth
RB = rhodamine B
R110 = rhodamine 110

References

[1] Sakakibara, J., and Adrian, R. J., 1999, "Whole Field Measurement of Temperature in Water Using Two-Color Laser Induced Fluorescence," Exp. Fluids, **26**, pp. 7–15.
[2] Du, H., Fuh, R. A., Li, J., Corkan, A., and Lindsey, J. S., 1998, "PhotochemCAD: A Computer-Aided Design and Research Tool in Photochemistry," Photochem. Photobiol., **68**, pp. 141–142.
[3] Ross, D., Gaitan, M., and Locascio, L. E., 2001, "Temperature Measurement in Microfluidic Systems Using a Temperature-Dependent Fluorescent Dye," Lab Chip, **3**, pp. 141–149.
[4] Erickson, D., Sinton, D., and Li, D., 2003, "Joule Heating and Heat Transfer in Poly (Dimethylsiloxane) Microfluidic Systems," Anal. Chem., **73**, pp. 4117–4123.
[5] Sato, Y., Irisawa, G., Ishizuka, M., Hishida, K., and Maeda, M., 2003, "Visualization of Convective Mixing in Microchannel by Fluorescence Imaging," Meas. Sci. Technol., **14**, pp. 114–121.
[6] Jung, W. S., Kim, S. W., Kim, H. Y., and Yoo, J. Y., 2006, "Surface Temperature Measurement in Microscale With Temperature Sensitive Fluorescence," Trans. Korean Soc. Mech. Eng., Ser. B, **30**, pp. 153–160.
[7] Yoon, S. Y., Kim, J. M., Kim, S. H., and Kim, K. C., 2004, "Micro-LIF Measurement in a Micro-Channel Using a Micro Laser Light Sheet," KSME Fall Annual Conference, Daejeon, November 3–5, pp. 1540–1545.
[8] Park, J. S., Choi, C. K., and Kihm, K. D., 2004, "Optically Sliced Miro-PIV Using Confocal Laser Scanning Microscopy (CLSM)," Exp. Fluids, **37**, pp. 105–119.
[9] Wihelm, S., Gröbler, B., Gluch, M., and Heinz, H., 2005, "Confocal Laser Scanning Microscopy (Optical Image Formation and Electronic Signal Processing)," Technical Brochure, Carl Zeiss Jena GmbH, http://www.zeiss.de/lsm.
[10] Jeong, D. W., and Lee, S. Y., 2006, "Measurement of Cross-Sectional Temperature Distribution in Micro-Scale Gap Fluid Using LIF Technique in Combination With CLSM," Trans. Korean Soc. Mech. Eng., Ser. B, **30**, pp. 834–841.
[11] Migler, K. B., and Bur, A. J., 1998, "Fluorescence Based Measurement of Temperature Profiles During Polymer Processing," Polym. Eng. Sci., **38**, pp. 213–221.
[12] Bur, A. J., and Roth, S. C., 2004, "Temperature Gradients in the Channels of a Single-Screw Extruder," Polym. Eng. Sci., **44**, pp. 2148–2157.
[13] Kim, H. J., Kihm, K. D., and Allen, J. S., 2003, "Examination of Ratiometric Laser Induced Fluorescence Thermometry for Microscale Spatial Measurement Resolution," Int. J. Heat Mass Transfer, **46**, pp. 3967–3974.
[14] Kim, H. J., 2005, "Measurements of Temperature and Flow Fields With Sub-Millimeter Spatial Resolution Using Two-Color Laser Induced Fluorescence (LIF) and Micro-Particle Image Velocimetry (PIV)," J. Mech. Sci. Technol., **19**(2), pp. 716–727.
[15] Jeong, D. W., and Lee, S. Y., 2006, "Correction of Spherical Aberration by Refractive-Index Mismatch in Multi-Layer Medium in Using Confocal LIF Technique," KSME Spring Annual Conference, Jeju, June 7–9, pp. 2241–2246.
[16] Kline, S. J., 1985, "The Purposes of Uncertainty Analysis," ASME Trans. J. Fluids Eng., **107**, pp. 153–160.

Thermal Conductivity Measurements of Nylon 11-Carbon Nanofiber Nanocomposites

Arden L. Moore
Antonette T. Cummings
Justin M. Jensen
Li Shi
Joseph H. Koo

Department of Mechanical Engineering,
University of Texas at Austin,
Austin, TX 78712

Carbon nanofibers (CNFs) were incorporated into nylon 11 to form nylon 11-carbon nanofiber nanocomposites via twin screw extrusion. Injection molding has been employed to fabricate specimens that possess enhanced mechanical strength and fire retardancy. The thermal conductivity of these polymer nanocomposites was measured using a guarded hot plate method. The measurement results show that the room temperature thermal conductivity increases with the CNF loading from 0.24 ± 0.01 *W/m K for pure Nylon 11 to* 0.30 ± 0.02 *W/m K at 7.5 wt % CNF loading. The effective medium theory has been used to determine the interface thermal resistance between the CNFs and the matrix to be in the range of* $2.5–5.0 \times 10^{-6}$ m^2 *K/W from the measured thermal conductivity of the nanocomposite.* [DOI: 10.1115/1.3139110]

Keywords: thermal conductivity, nanocomposites, carbon nanofibers, nylon, measurement, thermal interface resistance

1 Introduction

Polymer nanocomposites show great promise in replacing metals in aerospace and automobile applications. The overall weight of the parts can be reduced using nanocomposites without compromising strength or fire retardancy properties. Additionally, one advantage of nanocomposites is that their physical properties can be altered with only a low weight percent loading of nanomaterials [1–5]. Nylon 11 has been a common material for several decades because of its unique mechanical and thermal properties. Currently, there is intense interest to develop nylon 11-carbon nanofiber (CNF) nanocomposites with improved mechanical strength and fire retardancy properties [4–8].

In this paper, we report the preparation and characterization of nylon 11 composites with various weight percent loadings of CNFs formed using injection molding. The measured thermal conductivity of the nanocomposites at room temperature was found to gradually increase with increased CNF loading.

2 Materials Processing

Nylon 11 is a thermoplastic with a moderate amount of molecular interaction between its polymer chains. The CNFs were incorporated into the nylon 11 pellets via twin screw extrusion. In the extrusion process, the polymer is propelled continuously along a screw through regions of high temperature and pressure, where it is melted and compacted, and finally forced through a die shaped to give the final part. An extruder can also be used to compound materials by mixing two or more components together. Twin screw extrusion provides a high shear environment to incorporate nanostructures into thermoplastics. The material delivered by an extruder is known as the extrudate. The extrudates (millimeter-sized pellets) were used to produce parts by an injection molding process. The CNFs were PR-19-PS grade purchased from a commercial vendor (Applied Sciences, Inc.). This grade of CNFs has been pyrolytically stripped by the manufacturer to remove polyaromatic hydrocarbons from the surface, but was not heat treated. The CNFs were about 150 nm in diameter and 30–100 μm long. Figure 1 shows a photograph of the nanocomposites made by injection molding. The color of the specimen changed from white for pure nylon parts to black for nanocomposites with CNF loading.

Transmission electron microscopy (TEM) micrographs were taken for the injection molded samples to characterize the dispersion and alignment of the CNFs. Figure 2 shows the TEM micrographs of nylon 11 with 5 wt % loading of CNFs. Inside the TEM imaging volume of about 5 μm lateral size, CNFs were found to be randomly aligned, and no agglomeration of the CNFs was observed. Similar results were observed at other locations of the TEM specimen. However, TEM was used to examine only limited locations of the specimen, and we cannot rule out the possibility of CNF alignment or agglomeration in other areas of the nanocomposites.

3 Thermal Conductivity Measurement Method

We followed the standard guarded hot plate method [9] shown in Fig. 3(*a*) to measure the thermal conductivity of the samples. In this method, a heater is sandwiched between two identical samples and two heat sinks, with thermocouples (TCs) placed at the interfaces between the sample and the heater and between the sample and the heat sink. The temperature drop across each sample is measured using the thermocouples, and the heat flux is determined by the electrical power dissipated in the heater. The as-made injection molded parts were $100 \times 100 \times 3.175$ mm^3. The parts were cut with a saw into $50 \times 50 \times 3.175$ mm^3 plates to measure the thermal conductivity across the plane of the composite. A polymer-coated thin planar heater purchased from Minco was sandwiched between two sample plates. The lateral dimension of the heater was the same as that of the plate (50×50 mm^2) with 0.3 mm thickness. Two aluminum heat sinks were placed at each end of the stack. K type thermocouples from Omega were placed at each interface to measure the temperature drop across the samples. To minimize heat loss through the lead wires of the thermocouples and to ensure planar contact between surfaces, we used thermocouples of the smallest diameter avail-

Contributed by the Heat Transfer Division of ASME for publication in the JOURNAL OF HEAT TRANSFER. Manuscript received July 21, 2008; final manuscript received April 7, 2009; published online June 24, 2009. Review conducted by Pamela M. Norris. Paper presented at the 2005 ASME International Mechanical Engineering Congress (IMECE 2005), Orlando, FL, November 5–11, 2005.

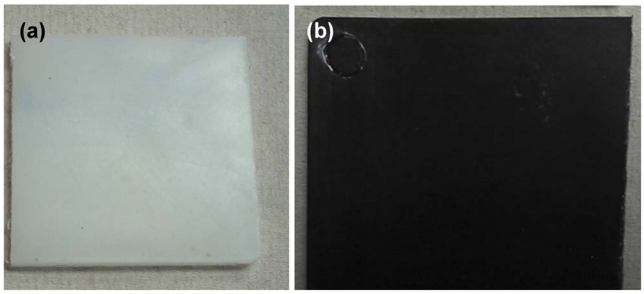

Fig. 1 Photographs of (*a*) injection molded pure nylon 11 and (*b*) nylon nanocomposites with 5% CNF loading

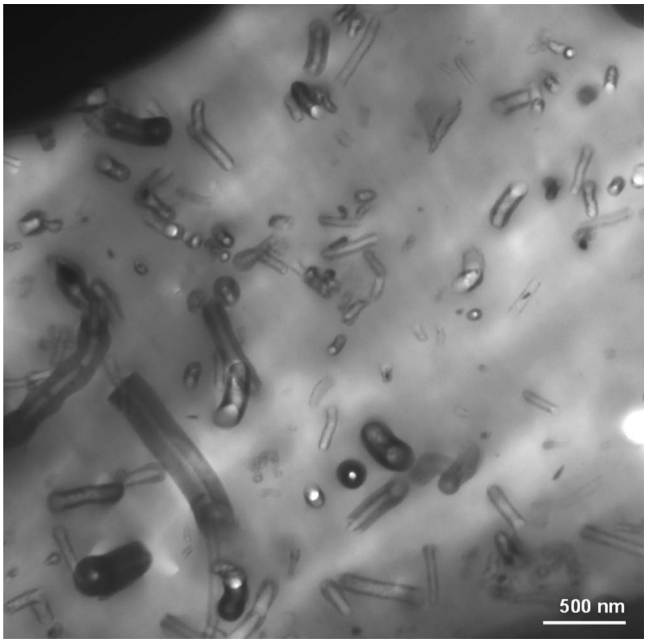

Fig. 2 Transmission electron micrograph of an injection molded 5 wt % nylon 11-CNF nanocomposite

able, specifically 0.003 in. or 76.2 μm. During several of the measurements, three thermocouples were placed at varying locations on the same interface to verify the temperature uniformity. To improve the thermal contact, a thin layer of thermal grease was used at each interface. In addition, a clamp was used to apply pressure to the stack and to hold it together. A photograph of the measurement setup with insulation and radiation shielding partly removed is shown in Fig. 3(*b*).

To determine any anisotropy in the thermal conductivity, a similar setup was used to measure the in-plane thermal conductivity of several parts with some minor modifications. The as-manufactured $100\times100\times3.175$ mm^3 plates were cut into smaller pieces of $25.4\times4.0\times3.175$ mm^3 dimension. Eight such pieces were bonded together using thermal grease to make $25.4\times25.4\times4.0$ mm^3 samples. The plates were then polished to reduce roughness along the cut faces. The measurement setup was the same as that described for the cross-plane measurement, but with a thin film heater with $25.4\times25.4\times0.3$ mm^3 dimensions to match the lateral sample size of 25.4×25.4 mm^2.

The heater was connected to a PCE Model SL100 dc power supply with an output voltage of 0–30 V and current of 0–3 A. The voltage drop (V) across and current (I) flow in the heater were measured with Omega multimeters with voltage and current accuracies of 0.1 mA and 1 mV, respectively. The heating power was obtained as $Q=IV$. The energy dissipated by the heater was conducted across the two samples on either side of the heating film to the aluminum blocks that served as heat sinks and kept at ambient temperature. The test setup was symmetric. The temperature drops across each sample were measured by the thermocouples and were used to obtain the averaged temperature drop across one plate (ΔT). The thermal conductance of the two samples was obtained as $G=Q/\Delta T$. More specifically, G was obtained as the slope of a linear fit to four sets of measured ΔT versus Q data with ΔT ranged from 1 K to 6 K, as shown in Fig. 3(*c*) for one measurement. The thermal conductivity was obtained as $k=Gt/2A$, where t and A are the thickness and area of one sample.

For the 3.175 mm and 4 mm thick samples, the total uncertainty is calculated to be less than 6%, which includes convection and radiation loss from the samples, heat loss through the thermocouple wires and heater leads, and uncertainties in dimension, temperature, and power measurements. The heat loss through the thermocouple wires and the heater leads are estimated using a fin heat transfer model to be about 2% of the total heater power for an average temperature rise of 3 K. If the setup had not been insulated on the four sides from the environment, the free convection

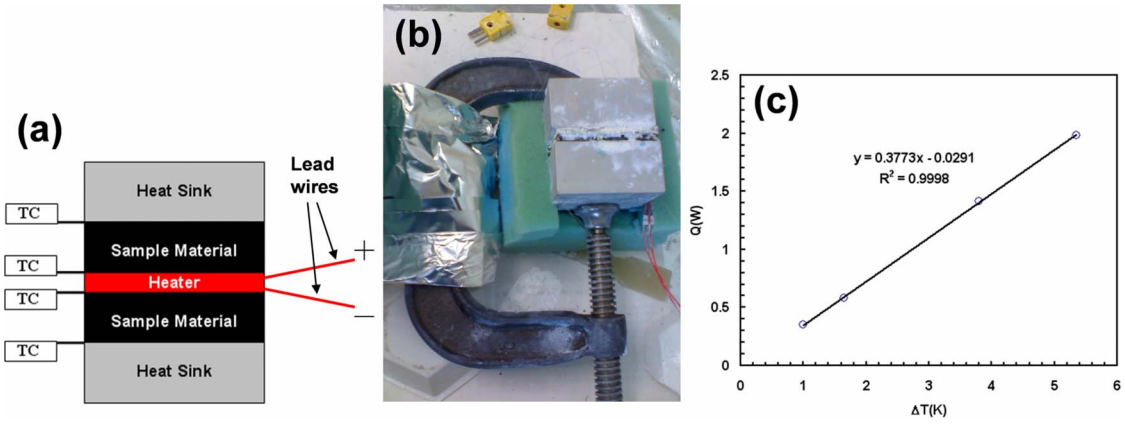

Fig. 3 (*a*) Schematic of guarded hot plate method for thermal conductivity measurement. Four thermocouples (TCs) are used to measure temperature at four locations, and an average temperature difference across the two identical samples is used for obtaining the thermal conductivity. Thermal insulation surrounding the setup is not shown. (*b*) Photograph of the measurement setup with insulation and radiation shielding partly removed. (*c*) Measured electrical power input (Q) to the heater as a function of average measured temperature drop (ΔT) across the sample.

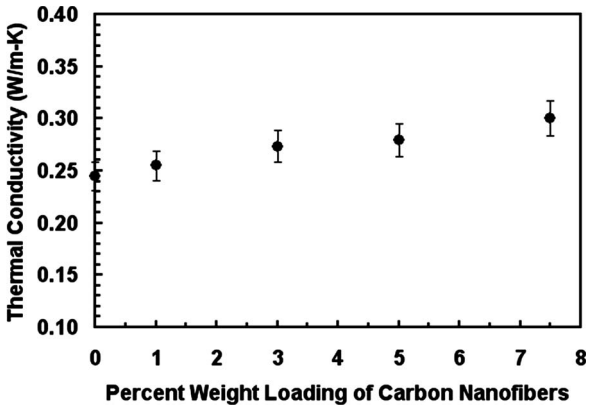

Fig. 4 Thermal conductivity of injection molded nylon 11-CNF nanocomposite as a function of the weight fraction of the CNFs for the cross-plane direction at room temperature.

heat transfer coefficient on each vertical surface of the plate during the measurement is estimated to be about 3.4 W/m^2 K at an average temperature rise of 3 K. The convection heat loss is calculated to be 7×10^{-3} W. The radiation heat loss from the sample is estimated to be 14×10^{-3} W at an average temperature rise of 3 K. The sum of radiation and convection heat losses from the sample account for about 2–3% of the total power input to the heater when the average temperature rise was about 3 K. It is important that the samples be relatively thin in order to minimize convection and radiation losses and to keep the thermal conductivity measurement accurate. If the sample thickness was 25.4 mm, for example, we calculate that the convection/radiation losses would increase to 45–50% of the total power when no insulation was applied to the four sides of the sample, making the measured thermal conductivity appear twice as high as the actual value. Several experiments were conducted with the setup surrounded by insulation for minimizing the free convection, or by a radiation shield made by an aluminum foil. No apparent changes were noted with these modifications when the sample thickness was 4.0 mm or less.

4 Thermal Conductivity Measurement Results and Analysis

Figure 4 shows the cross-plane thermal conductivity of injection molded nanocomposites at room temperature as a function of the weight fraction of CNFs. For pure nylon 11, our measured cross-plane thermal conductivity is 0.24 ± 0.01 W/m K, in good agreement with the reference literature value of 0.23 W/m K for pure nylon 11 [10]. In-plane measurements of pure nylon 11 and the 3% CNF nanocomposite gave thermal conductivity values within 3% of the cross-plane value for the respective samples, suggesting that anisotropic effects arising from either polymer chain alignment in the matrix or unobserved CNF alignment are comparable to the measurement uncertainty. For the injection molded nanocomposites, a gradual increase in thermal conductivity with CNF loading is observed at room temperature. The maximum thermal conductivity observed was 0.30 ± 0.02 W/m K for 7.5% CNF loading, a 22% increase from the thermal conductivity measured for pure nylon 11.

We have used the effective medium approach by Nan et al. [11] along with the measured thermal conductivity values to evaluate the thermal contact resistance between the CNFs and the matrix. This model assumes that the CNFs are randomly oriented, of equal size, and perfectly straight in an isotropic polymer matrix. It takes into account thermal contact resistance, volume fraction, and the aspect ratio of the nanostructures added.

In this approach, the effective thermal conductivity k_{eff} of the nanocomposites was calculated as a function of the contact resistance between the CNF and the polymeric matrix using

$$k_{\text{eff}} = k_M \frac{3 + f(\beta_x + \beta_z)}{3 - f\beta_x} \tag{1}$$

where k_M is the thermal conductivity of the matrix, and f is the volume fraction of the CNFs [11]. We used our experimentally measured thermal conductivity value for pure nylon 11 as k_M. To convert the weight percent CNF loading to volume percent used in the model, densities of 1.95 g/cm^3 and 1.04 g/cm^3 were used for CNFs [12] and nylon 11 [13], respectively. The terms β_x and β_z are given by

$$\beta_x = \frac{2(k_{11} - k_M)}{k_{11} + k_M} \tag{2}$$

$$\beta_z = \frac{k_{33}}{k_M} - 1 \tag{3}$$

with k_{11} and k_{33} representing the equivalent thermal conductivities in the transverse and longitudinal directions of a nanocomposite unit cell, as described by Nan et al. [11]. These values are calculated by

$$k_{11} = \frac{k_c}{1 + \dfrac{2ak_c}{dk_M}} \tag{4}$$

$$k_{33} = \frac{k_c}{1 + \dfrac{2ak_c}{Lk_M}} \tag{5}$$

where k_c, d, and L are the CNF thermal conductivity, diameter, and length, respectively [11]. The diameter of the CNFs used in the calculation is 150 nm with a CNF length of 50 μm. The term a is called the Kapitza radius and is defined as $a=R_ck_M$, with R_c representing the thermal contact resistance between the CNF and the matrix [11].

The thermal conductivity of the CNF product (ASI PR-19-PS) was not specified by the manufacturer. For another similar CNF product (PYROGRAF® I) with a larger diameter of 3–20 μm made by the same manufacturer, the thermal conductivity was specified to be 20 W/m K for as-grown samples and 1950 W/m K for heat-treated samples [12]. In comparison, the thermal conductivity of a 150 nm diameter CNF made by a plasma enhanced chemical vapor deposition (CVD) method was found to be about 10 W/m K [14]. In carbon fibers, the interface effect on phonon transport is dominated by scattering at interfaces between adjacent graphene layers and interlayer coupling. Because the ~150 nm diameter CNFs used in this work already consists of hundreds of graphene layers, interface effect on the axial thermal conductivity is expected to be insensitive to diameter variation from 150 nm to 20 μm if the crystal quality remains the same. The crystal quality of the pyrolytically stripped CNF samples used in this work is expected to fall between that of the as-grown CNFs and the heat-treated samples. Hence, the thermal conductivity is expected to fall between 20 W/m K for the as-grown samples and 1950 W/m K for the heat-treated samples. In the model, we have varied thermal conductivity k_c of the CNF in the range between 1 W/m K and 1950 W/m K.

Figure 5 shows the predicted effective thermal conductivity of the 1%, 3%, 5%, and 7.5% blends of injection molded parts as a function of the thermal contact resistance for several values of thermal conductivity assumed for the CNFs. By using the measured thermal conductivity of each nanocomposite, we can evaluate a range of thermal contact resistance based on the possible CNF thermal conductivities. As shown in Fig. 5, using a CNF thermal conductivity of 1 W/m K does not produce an intersec-

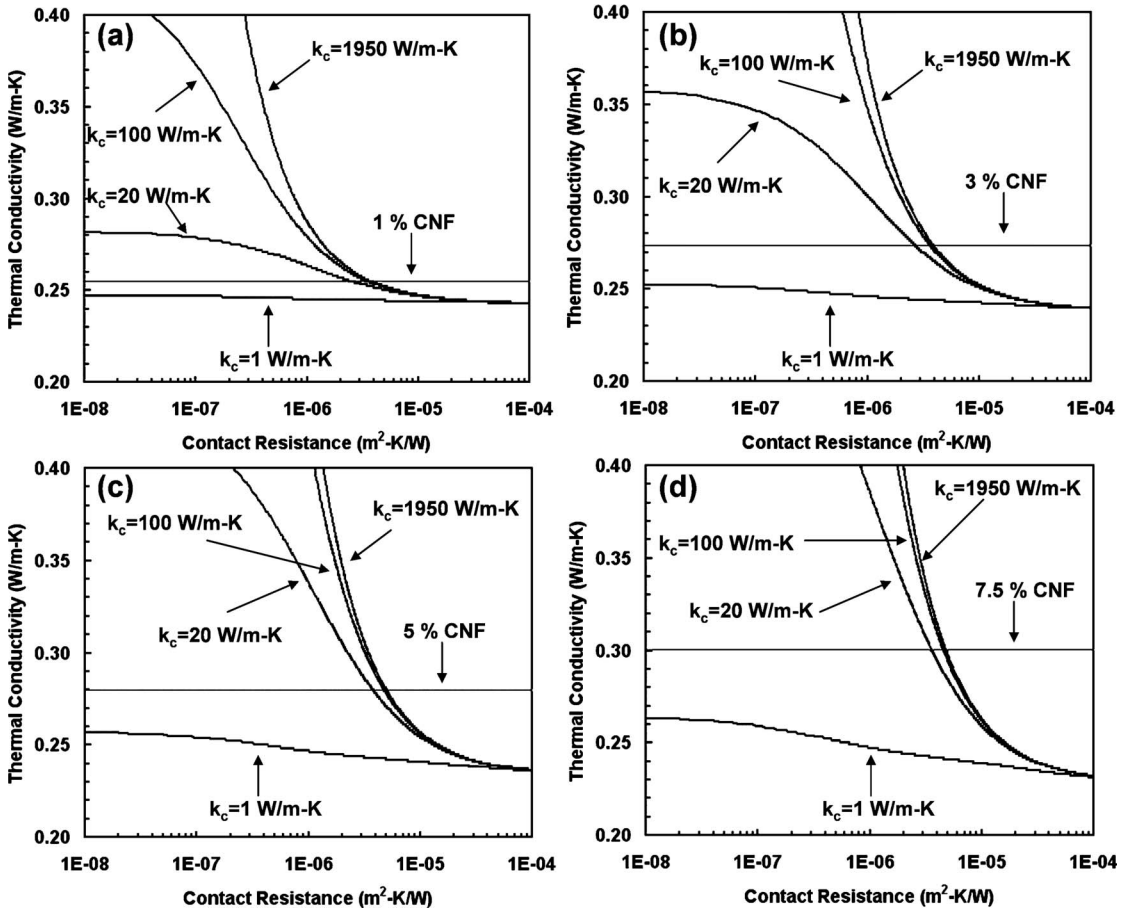

Fig. 5 Model prediction for the (*a*) 1 wt %, (*b*) 3 wt %, (*c*) 5 wt %, and (*d*) 7.5 wt % CNF blends of injection molded parts in the cross-plane direction at room temperature. Each curve corresponds to a different value for the CNF thermal conductivity k_C. The straight gray line is the experimentally measured thermal conductivity of the nanocomposite.

tion between the predicted effective thermal conductivity of the nanocomposite and the measured thermal conductivity at the corresponding CNF loading. For CNF thermal conductivity between 20 W/m K and 1950 W/m K, the thermal contact resistance ranges for the injection molded samples at room temperature are estimated to be $2.5–3.8\times10^{-6}$ m^2 K/W, $2.5–3.8\times10^{-6}$ m^2 K/W, $3.8–5.0\times10^{-6}$ m^2 K/W, and $3.6–4.8\times10^{-6}$ m^2 K/W for 1 wt %, 3 wt %, 5 wt %, and 7.5 wt % CNF loading, respectively. In heat transfer literature, values of thermal contact resistance can vary over several orders of magnitude depending on materials, surface roughness, environment, and, in the case of a solid-solid contact, applied pressure. A large degree of variation in contact resistance has also been found in carbon nanostructure-based composites, for which the thermal contact resistance between the nanostructure fillers and the matrix has been shown to depend strongly on the surrounding matrix environment [15], as well as the processing and surface treatment of the filler material [15–17]. Macedo and Ferreira [15] estimated thermal contact resistances of $4.6–5.0\times10^{-7}$ m^2 K/W and 1.3×10^{-4} m^2 K/W for vapor-grown CNFs (0.2 μm diameter) in polypropylene and polycarbonate matrices, respectively. The thermal contact resistance values in this work for CNFs in Nylon 11 thus fall in between these values. In comparison, thermal contact resistance values for carbon nanotubes (CNTs) in polymer and surfactant environments have been reported in the $2.4–83\times10^{-9}$ m^2 K/W range [17–20].

5 Conclusions

These measurements show that the thermal conductivity gradually increases with increased CNF loading from 0.24 ± 0.01 W/m K for pure Nylon 11 to 0.30 ± 0.02 W/m K for nylon 11 with 7.5% CNF loading. Using an effective medium theory model and the measured thermal conductivity values, we determine that the thermal contact resistance is in the range of $2.5–5.0\times10^{-6}$ m^2-K/W for 1 wt % to 7.5 wt % CNF loading. The uncertainty in the obtained thermal contact resistance comes from the uncertainty in the CNF thermal conductivity, which is not specified by the manufacturer for the particular grade. Despite the large range of possible CNF thermal conductivity between 20 W/m K and 1950 W/m K, the obtained thermal contact resistance range is narrow ($2.5–5.0\times10^{-6}$ m^2 K/W) at different CNF loadings. This finding reveals that thermal transport in the nanocomposite is limited by the thermal contact resistance between the CNFs and the matrix. Consequently, the thermal conductivity of the nanocomposites would increase only slightly when the thermal conductivity of the CNFs is increased from the lower limit of 20 W/m K to the upper limit of 1950 W/m K at the same contact thermal resistance.

Acknowledgment

This work is supported in part by the Thermal Transport Processes Program of National Science Foundation via Grant No.

CBET-0553649 and Air Force Office of Scientific Research.

References

[1] Biercuk, M. J., Llaguno, M. C., Radosavljevic, M., Hyun, J. K., Johnson, A. T., and Fischer, J. E., 2002, "Carbon Nanotube Composites for Thermal Management," Appl. Phys. Lett., **80**, pp. 2767–2769.

[2] Kashiwagi, T., Grulke, E., Hilding, J., Groth, K., Harris, R., Butler, K., Shields, J., Kharchenko, S., and Douglas, J., 2004, "Thermal and Flammability Properties of Polypropylene/Carbon Nanotube Nanocomposites," Polymer, **45**, pp. 4227–4239.

[3] Abramson, A. R., Kim, W. C., Huxtable, S. T., Yan, H. Q., Wu, Y. Y., Majumdar, A., Tien, C. L., and Yang, P. D., 2004, "Fabrication and Characterization of a Nanowire/Polymer-Based Nanocomposite for a Prototype Thermoelectric Device," J. Microelectromech. Syst., **13**, pp. 505–513.

[4] Koo, J. H., 2006, *Polymer Nanocomposites: Processing, Characterization, and Applications*, McGraw-Hill, New York.

[5] Koo, J. H., Pilato, L. A., Wissler, G., Cheng, J., Ho, D., Nguyen, K., Stretz, H., and Luo, Z. P., 2005, "Flammability and Mechanical Properties of Nylon 11 Nanocomposites," *Proceedings of the SAMPE 2005 ISSE, SAMPE*, Covina, CA, pp. 1–14.

[6] Wiemann, K., Kaminsky, W., Gojny, F., and Schulte, K., 2005, "Synthesis and Properties of Syndiotactic Poly(propylene)/Carbon Nanofiber and Nanotube Composites Prepared by In Situ Polymerization With Metallocene/MAO Catalysts," Macromol. Chem. Phys., **206**, pp. 1472–1478.

[7] Hammel, E., Tang, X., Trampert, M., Schmitt, T., Mauthner, K., Eder, A., and Potschke, P., 2004, "Carbon Nanofibers for Composite Applications," Carbon, **42**, pp. 1153–1158.

[8] Choi, Y. K., Sugimotot, K. I., Song, S. M., and Endo, M., 2005, "Mechanical and Thermal Properties of Vapor-Grown Carbon Nanofiber and Polycarbonate Composite Sheets," Mater. Lett., **59**, pp. 3514–3520.

[9] ASTM, 2004, "C177-04 Standard Test Method for Steady-State Heat Flux Measurements and Thermal Transmission Properties by Means of the Guarded-Hot-Plate Apparatus," ASTM, West Conshohocken, PA.

[10] Mark, J. E., 2007, *Physical Properties of Polymers Handbook*, Springer, New York.

[11] Nan, C. W., Liu, G., Lin, Y. H., and Li, M., 2004, "Interface Effect on Thermal Conductivity of Carbon Nanotube Composites," Appl. Phys. Lett., **85**, pp. 3549–3551.

[12] Available online at http://www.apsci.com/ngm-pyro1.html.

[13] Available online at http://www.goodfellow.com/E/Polyamide_-_Nylon_11.HTML.

[14] Yu, Ch., Saha, S., Zhou, J., Shi, L., Cassell, A. M., Cruden, B. A., Ngo, Q., and Li, J., 2006, "Thermal Contact Resistance and Thermal Conductivity of a Carbon Nanofiber," ASME J. Heat Transfer, **128**, pp. 234–239.

[15] Macedo, F., and Ferreira, J. A., 2003, "Thermal Contact Resistance Evaluation in Polymer-Based Carbon Fiber Composites," Rev. Sci. Instrum., **74**(1), pp. 828–830.

[16] Shenogin, S., Bodapati, A., Xue, L., Oxisik, R., and Keblinksi, P., 2004, "Effect of Chemical Functionalization on Thermal Transport of Carbon Nanotube Composites," Appl. Phys. Lett., **85**, pp. 2229–2231.

[17] Bryning, M. B., Milkie, D. E., Islam, M. F., Kikkawa, J. M., and Yodh, A. G., 2005, "Thermal Conductivity and Interfacial Resistance in Single-Wall Carbon Nanotube Epoxy Composites," Appl. Phys. Lett., **87**, p. 161909.

[18] Huxtable, S. T., Cahill, D. G., Shenogin, S., Xue, L., Ozisik, R., Barone, P., Usrey, M., Strano, M. S., Siddons, G., Shim, M., and Keblinski, P., 2003, "Interfacial Heat Flow in Carbon Nanotube Suspensions," Nature Mater., **2**, pp. 731–734.

[19] Shenogin, S., Xue, L., Ozisik, R., Keblinski, P., and Cahill, D., 2004, "Role of Thermal Boundary Resistance on the Heat Flow in Carbon-Nanotube Composites," J. Appl. Phys., **95**, pp. 8136–8144.

[20] Haggenmueller, R., Guthy, C., Lukes, J. R., Fisher, J. E., and Winey, K. I., 2007, "Single Wall Carbon Nanotube/Polyethylene Nanocomposites: Thermal and Electrical Conductivity," Macromolecules, **40**, pp. 2417–2421.

Exact Solutions Corresponding to the Viscous Incompressible and Conducting Fluid Flow Due to a Porous Rotating Disk

Mustafa Turkyilmazoglu[1]
Department of Mathematics,
Hacettepe University,
Beytepe,
Ankara 06532, Turkey
e-mail: turkyilm@hacettepe.edu.tr

A study is pursued in this paper for the evaluation of the exact solution of the steady Navier–Stokes equation, governing the incompressible viscous Newtonian, electrically conducting fluid flow motion over a porous disk, rotating at a constant angular speed. The three-dimensional equations of motion are treated analytically yielding to the derivation of exact solutions. The effects of the magnetic pressure number on the permeable flow field are better conceived from the exact velocity and induced magnetic field obtained. Making use of this solution, analytical formulas for the angular velocity and current density components, as well as for the magnetic wall shear stresses, are extracted. Interaction of the resolved flow field with the surrounding temperature is then analyzed via energy equation. The temperature field is shown to accord with the convection, viscous dissipation, and Joule heating. As a result, exact formulas are obtained for the temperature field, which takes different forms, depending on whether isothermal and adiabatic wall conditions or suction and blowing are considered.
[DOI: 10.1115/1.3139187]

Keywords: exact solutions, magnetohydrodynamic flow, porous disk, heat transfer

1 Introduction

The magnetohydrodynamic flow of fluids over porous boundaries of materials has many applications in practical science, such as levitation and pumping of liquids in mechanical engineering, boundary layer control, and transpiration processes in aerodynamics. One of the most interesting magnetofluid dynamic problems is the use of electromagnetic force to control the flight of an aircraft or a space vehicle. Owing to the fact that the electric and magnetic fields can be controlled, flight in a conducting gas can be controlled by changing the magnetic fields provided by a magnet inside the vehicle.

Kármán's swirling viscous flow over a porous rotating disk [1] is a well documented classical problem. The stability issues were attacked by many researchers such as Gregory et. al [2] and Maleque and Sattar [3]. However, all these results are either numerical or analytical numerical. Moreover Berker [4] established the existence of an infinite set of solutions to the flow of two infinite parallel rotating plates. The extension to porous plates has been given in Ref. [5]. Rao and Kasiviswanathan [6] presented an exact solution for the unsteady flow in which the eccentric disks executed nontorsional oscillations. Additionally, heat transfer problems over a rotating disk have also been studied, see for instance Ref. [7].

The exact solution examined in the current paper is connected with the hydromagnetic flow over porous boundaries. Thus, the purpose here is to present details of some new three-dimensional solutions of the Navier–Stokes equations associated with a single rotating disk. The axisymmetric solutions, in the presence of a transverse magnetic field, have been previously investigated numerically in Ref. [8]. Unlike the case of axisymmetric solutions, the current motivation focuses on searching for the velocity, pressure, induced magnetic field, and pressure fields affected by the existence of the magnetic field, together with the permeable wall conditions.

The strategy adopted here is as follows: In Sec. 2 the full equations of motion are outlined. Section 3 contains the analytical results. Wall insulation and heat conducting cases are analyzed in Sec. 4. Finally, our conclusions follow in Sec. 5.

2 Formulation of the Problem

Consider an infinite disk rotating on its axis with a constant angular velocity Ω, upon which is imposed a noncoaxially rotating 3D flow of an incompressible, electrically conducting viscous fluid about an axis originating at (r_0, α), as shown schematically in Fig. 1. The dimensionless unsteady magnetohydrodynamic equations governing the viscous fluid flow with an external uniform magnetic field $H=H_0$ are given by

$$\frac{\partial \mathbf{u}}{\partial t} + (\mathbf{u}\cdot\nabla)\mathbf{u} = -\nabla p + \frac{1}{\mathrm{Re}}\nabla^2\mathbf{u} + R_{\mathbf{H}}(\mathbf{H}\cdot\nabla)\mathbf{H} \tag{1}$$

$$\frac{\partial \mathbf{H}}{\partial t} + \nabla\times(\mathbf{u}\times\mathbf{H}) + \frac{1}{R_\sigma}\nabla^2\mathbf{H} = 0 \tag{2}$$

$$\nabla\cdot\mathbf{u} = 0, \quad \nabla\cdot\mathbf{H} = 0 \tag{3}$$

$$\frac{\partial T}{\partial t} + c_p(\mathbf{u}\cdot\nabla T) = \frac{c_p}{\mathrm{PrRe}}\nabla^2 T + \frac{1}{\mathrm{Re}}\Phi + \frac{R_{\mathbf{H}}}{R_\sigma}(\nabla\times\mathbf{H})^2 \tag{4}$$

Boundary conditions accompanying Eqs. (1)–(4) are such that the fluid adheres to the wall at $z=0$, and the quantities are bounded at far distances from the wall. Moreover, the induced magnetic field components h_1 and h_2 are subjected to zero boundary conditions on the wall and disappearing conditions away from the disk.

3 Steady-State Mean Flow

It is not hard to verify that

[1]Corresponding author.

Contributed by the Heat Transfer Division of ASME for publication in the JOURNAL OF HEAT TRANSFER. Manuscript received September 16, 2008; final manuscript received March 26, 2009; published online June 25, 2009. Review conducted by Sung Jin Kim.

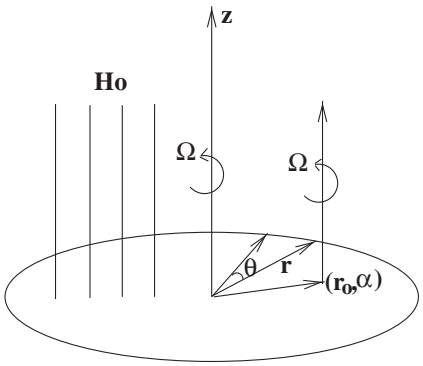

Fig. 1 Schematic description of the flow

$$u = w = 0, \quad v = r, \quad h_1 = h_2 = 0, \quad h_3 = \text{constant}, \quad p = \frac{r^2}{2} + p_0 \tag{5}$$

with p_0 constant, Eq. (5) constitutes a solution for the system equations in Eqs. (1)–(3) (rigid body motion).

Next, with the rescaling $\eta = \sqrt{\mathrm{Re}/2}z$, the flow is superimposed onto the rigid body rotation

$$u = r_0 F(\theta, \eta), \quad v = r + r_0 G(\theta, \eta), \quad w = -s\sqrt{\frac{1}{2\ \mathrm{Re}}}$$

$$h_1 = r_0 H_1(\theta, \eta), \quad h_2 = r_0 H_2(\theta, \eta), \quad h_3 = \sqrt{\frac{1}{2\ \mathrm{Re}}} \tag{6}$$

$$p = \frac{r^2}{2} - r r_0 \cos(\theta - \alpha) + p_1$$

such that the periodic solutions, with respect to θ of F, G, H_1, and H_2, are sought here. The reason for looking for solutions on Eq. (6) lies in the interest of finding exact solutions on pseudo-plane flows occurring over rigid body rotations, as in Refs. [4,9]. The constant s denotes a uniform suction if $s>0$ and injection if $s<0$. p_1 in Eq. (6) is a constant.

Substituting Eq. (6) into Eqs. (1)–(3), the continuity in the first of Eq. (3) is automatically satisfied, while the momentum and electromagnetic equations give rise to

$$F_{\eta\eta} + sF_\eta + 2G + R_H H_{1\eta} = -2\cos(\theta - \alpha)$$

$$G_{\eta\eta} + sG_\eta - 2F + R_H H_{2\eta} = 2\sin(\theta - \alpha)$$

$$H_{1\eta\eta} + sR_2 H_{1\eta} + R_2 F_\eta - 2R_2 H_2 = 0$$

$$H_{2\eta\eta} + sR_2 H_{2\eta} + R_2 G_\eta + 2R_2 H_1 = 0 \tag{7}$$

in which the parameter R_2 is defined as $R_2 = R_\sigma/\mathrm{Re}$. Further introduction of $\bar{F} = F + iG$ and $\bar{H} = H_1 + iH_2$ results in a fourth-order equation regarding $\bar{F}$ of the form

$$\bar{F}_{\eta\eta\eta\eta} + s(1 + R_2)F_{\eta\eta\eta} + [s^2 R_2 + 2(i(-1 + R_2) - R)]\bar{F}_{\eta\eta} + 4R_2\bar{F} = -4iR_2 C \tag{8}$$

whose solution satisfies the no slip, and also, the boundedness can be immediately expressed as

$$\bar{F} = C_1(e^{-\lambda_1\eta} - e^{-\lambda_2\eta}) + iC(-1 + e^{-\lambda_2\eta}) \tag{9}$$

where $R = R_H R_2/2$, $C = \cos(\theta - \alpha) - i\sin(\theta - \alpha)$, and C_1 is a constant. The roots $-\lambda_1 = -(\alpha_1 + i\beta_1)$ and $-\lambda_2 = -(\alpha_2 - i\beta_2)$ in Eq. (9) correspond to the characteristic equation of Eq. (8).

In Table 1, typical values of α_1, β_1, α_2, and β_2 are tabulated. It is seen that the effects of R_H are more dominant if it is allowed to grow large.

The value of C_1 arises from $\bar{H}(0) = 0$. Following this $\bar{H}$ can be written as

$$\bar{H} = \frac{iC}{R_H}(\lambda_2^2 - s\lambda_2 - 2i)\left\{\frac{\lambda_1}{(\lambda_2 - \lambda_1)(\lambda_1\lambda_2 + 2i)} \times \left[\left(\lambda_1 - s - \frac{2i}{\lambda_1}\right)e^{-\lambda_1\eta} + \left(-\lambda_2 + s + \frac{2i}{\lambda_2}\right)e^{-\lambda_2\eta}\right] + \frac{1}{\lambda_2}e^{-\lambda_2\eta}\right\} \tag{10}$$

Decomposing the real and imaginary parts of Eqs. (9) and (10), the solution to Eq. (7) finally follows

$$\begin{aligned} F &= f(\eta)\cos(\theta - \alpha) + g(\eta)\sin(\theta - \alpha) \\ G &= -f(\eta)\sin(\theta - \alpha) + g(\eta)\cos(\theta - \alpha) \\ H_1 &= -Y(\eta)\cos(\theta - \alpha) + X(\eta)\sin(\theta - \alpha) \\ H_2 &= X(\eta)\cos(\theta - \alpha) + Y(\eta)\sin(\theta - \alpha) \end{aligned} \tag{11}$$

where the form of the functions f, g, X, and Y in Eq. (11) are given as

$$f = -e^{-\alpha_2\eta}\sin\beta_2\eta + U(e^{-\alpha_1\eta}\sin\beta_1\eta + e^{-\alpha_2\eta}\sin\beta_2\eta) + V(e^{-\alpha_2\eta}\cos\beta_2\eta - e^{-\alpha_1\eta}\cos\beta_1\eta)$$

$$g = -1 + e^{-\alpha_2\eta}\cos\beta_2\eta + U(e^{-\alpha_1\eta}\cos\beta_1\eta - e^{-\alpha_2\eta}\cos\beta_2\eta) + V(e^{-\alpha_1\eta}\sin\beta_1\eta + e^{-\alpha_2\eta}\sin\beta_2\eta)$$

$$X = \frac{1}{R_H}\{D_1[g + 1 - e^{-\alpha_2\eta}\cos\beta_2\eta] + E_1[f + e^{-\alpha_2\eta}\sin\beta_2\eta]\}$$

Table 1 The roots calculated from the characteristic equation of Eq. (8)

s	R_H	α_1	β_1	α_2	β_2
−2	0	0.27201965	0.786151378	0.000316127774	0.000316227758
	10^2	0.27202249	0.786149620	0.000316128564	0.000316226969
	10^6	0.30048883	0.768941641	0.000323725957	0.000308048415
0	0	1.00000000	1.000000000	0.000316227766	0.000316227766
	10^2	1.00000250	0.999997500	0.000316228557	0.000316226975
	10^6	1.02530445	0.975320062	0.000323825207	0.000308038477
2	0	2.27201965	0.786151378	0.000316327774	0.000316227758
	10^2	2.27202249	0.786149620	0.000316328564	0.000316226967
	10^6	2.30048884	0.768941621	0.000323924463	0.000308028515

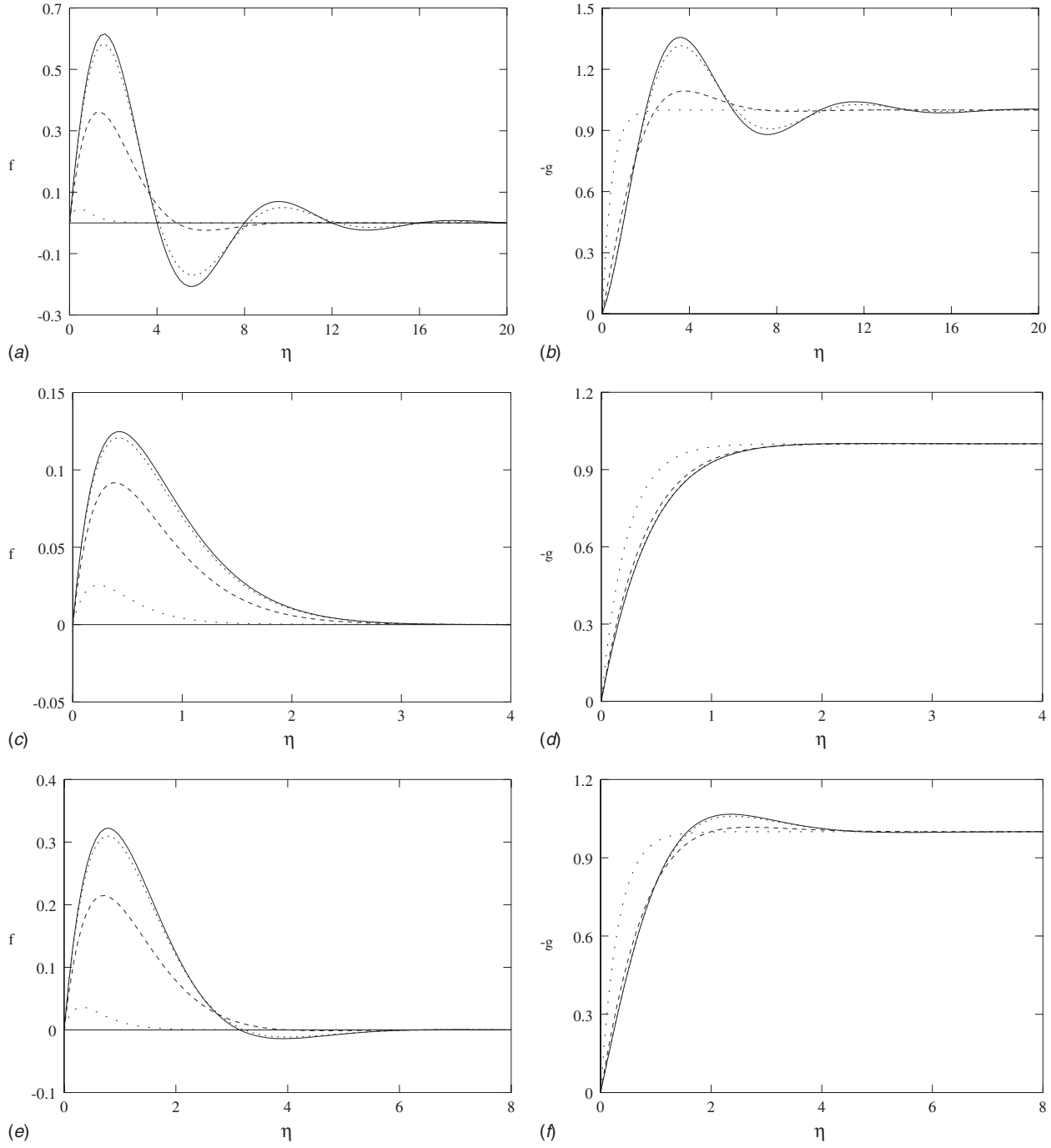

Fig. 2 The effects of magnetic field on the flow velocities f and $-g$ are demonstrated for various magnetic pressure numbers R_H at the specified injection/suction values in (*a*) $s=-2$, (*b*) $s=2$, and (*c*) $s=0$. Curves correspond to (—) $R_H=10^2$, (...) $R_H=10^6$, (– –) $R_H=10^7$, and (...) $R_H=10^8$.

$$Y = \frac{1}{R_H}\{E_1[g + 1 - e^{-\alpha_2 \eta}\cos\beta_2\eta] - D_1[f + e^{-\alpha_2\eta}\sin\beta_2\eta]\}$$

When α_2 and β_2 above are set exactly to zero, it turns out that $f=e^{-\alpha_1\eta}\sin(\beta_1\eta)$ and $g=-1+e^{-\alpha_1\eta}\cos(\beta_1\eta)$ in Eq. (11), hence we have the nonconducting fluid case with permeable wall, as studied earlier in Ref. [9]. Therefore, Eq. (11) represents a general case permitting to the interaction of electromagnetic and fluid dynamic fields. The graphs of f, g, $-Y$, and X are displayed in Figs. 2 and 3 for a variety of R_H. These graphs clearly indicate the development of a layerlike boundary structure near the surface of the disk. Also, flow reversal can be observed for $s\leq 0$. The wavy character shown in Figs. 2(*a*) and 2(*b*), particularly dominant in the case of fluid injection, is due to the form of the solution in Eq. (11).

The fluid dynamic thicknesses δ_θ and δ_r are evaluated as

$$\delta_\theta = \int_0^\infty (1+g)d\eta = \frac{\alpha_1 U + \beta_1 V}{\Lambda_1^2} - \frac{\alpha_2(U-1) - \beta_2 V}{\Lambda_2^2}$$

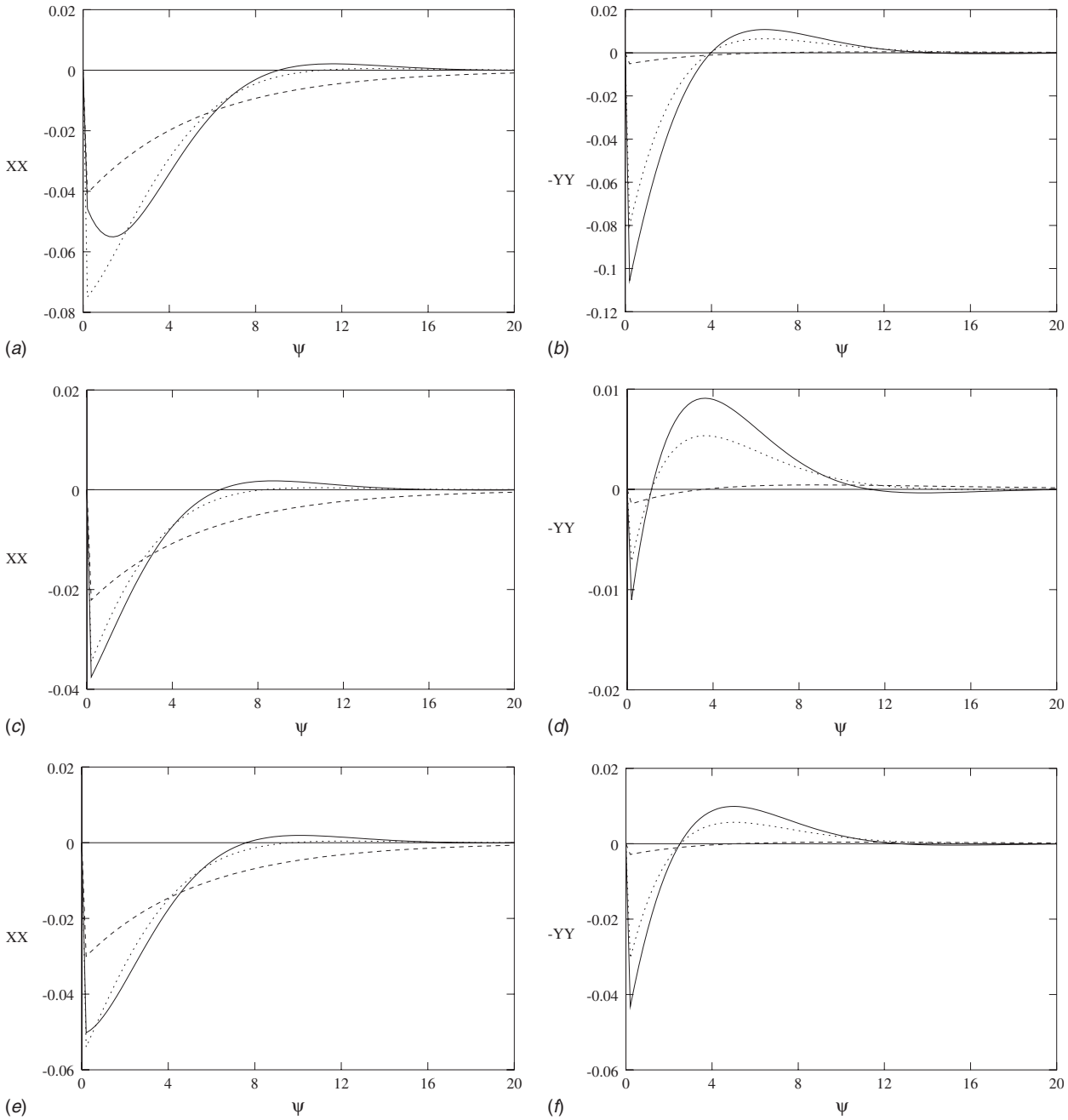

Fig. 3 The variation in the scaled induced magnetic fields $XX=10^6X$ and $-YY=-10^6Y$ are demonstrated for the magnetic pressure numbers, respectively: $R_H=10^6$ (—), $R_H=10^7$ (…), and $R_H=10^8$ (…), alongside a coordinate $\psi=10^3\eta$; (*a*) $s=-2$, (*b*) $s=2$, and (*c*) $s=0$

$$\delta_r = \int_0^\infty f d\eta = \frac{\beta_1 U - \alpha_1 V}{\Lambda_1^2} - \frac{-\beta_2(U-1) + \alpha_2 V}{\Lambda_2^2}$$

where $\Lambda_1^2=\alpha_1^2+\beta_1^2$ and $\Lambda_2^2=\alpha_2^2+\beta_2^2$. Similarly, the magnetic field thicknesses are

$$\delta_{H_1} = -\int_0^\infty Y d\eta = \frac{1}{R_H}\left[\frac{1}{\Lambda_1^2}(D_1U_{12} - E_1U_{11}) - \frac{1}{\Lambda_2^2}(D_1U_{21} - E_1U_{22})\right]$$

$$\delta_{H_2} = \int_0^\infty X d\eta = \frac{1}{R_H}\left[\frac{1}{\Lambda_1^2}(D_1U_{11} + E_1U_{12}) - \frac{1}{\Lambda_2^2}(D_1U_{22} + E_1U_{21})\right]$$

where $U_{11}=\alpha_1U+\beta_1V$, $U_{12}=\beta_1U-\alpha_1V$, $U_{21}=-\beta_2U+\alpha_2V$, and $U_{22}=\alpha_2U-\beta_2V$. The exact formulas point to a significant decay in thicknesses as the magnetic effects become large (see also Figs. 2 and 3).

Making use of the exact velocities, the shear stresses on the wall τ_r and τ_θ are

$$\tau_r = \left.\frac{\partial u}{\partial z}\right|_{z=0} = r_0\sqrt{\frac{\mathrm{Re}}{2}}[\Lambda_a\cos(\theta-\alpha) - \Lambda_b\sin(\theta-\alpha)]$$

Table 2 The variation in Nu at Prandtl number Pr=1 for injection

s	$R_H=10$	$R_H=10^2$	$R_H=10^4$	$R_H=10^6$	$R_H=10^7$	$R_H=10^8$
−5	0.0620557	0.0620592	0.06244165	0.1005498	0.4356257	3.0777197
−2	0.5440398	0.5440449	0.5446085	0.6010151	1.1078094	4.6603140
0	1.9999995	1.9999950	1.9995017	1.9575906	1.9439023	4.2513926

$$\tau_\theta = \left.\frac{\partial v}{\partial z}\right|_{z=0} = -r_0\sqrt{\frac{\mathrm{Re}}{2}}[\Lambda_b\cos(\theta-\alpha)+\Lambda_a\sin(\theta-\alpha)]$$

with Λ_a and Λ_b as constants. The stresses owing to the magnetic field effects are computed as

$$\tau_{h_1} = \left.\frac{\partial h_1}{\partial z}\right|_{z=0} = \frac{r_0}{R_H}\sqrt{\frac{\mathrm{Re}}{2}}[\Lambda_c\cos(\theta-\alpha)-\Lambda_d\sin(\theta-\alpha)]$$

$$\tau_{h_2} = \left.\frac{\partial v}{\partial z}\right|_{z=0} = -\frac{r_0}{R_H}\sqrt{\frac{\mathrm{Re}}{2}}[\Lambda_d\cos(\theta-\alpha)+\Lambda_c\sin(\theta-\alpha)]$$

with Λ_c and Λ_d as constants.

The components of vorticity $(\omega_r,\omega_\theta,\omega_z)=\nabla\times\mathbf{u}$ and the current density $(J_r,J_\theta,J_z)=\nabla\times\mathbf{H}$ can also be computed exactly, which are, respectively

$$\omega_r = -\frac{\partial v}{\partial z} = -r_0\sqrt{\frac{\mathrm{Re}}{2}}G_\eta,\quad \omega_\theta = \frac{\partial u}{\partial z} = r_0\sqrt{\frac{\mathrm{Re}}{2}}F_\eta,\quad \omega_z = 2$$
$$J_r = -\frac{\partial h_2}{\partial z} = -r_0\sqrt{\frac{\mathrm{Re}}{2}}H_{2\eta},\quad J_\theta = \frac{\partial h_1}{\partial z} = r_0\sqrt{\frac{\mathrm{Re}}{2}}H_{1\eta},\quad J_z = 0 \tag{12}$$

4 Heat Conducting Case

Analysis performed in Sec. 3 reveals that the temperature balances with the convection, the viscous dissipation $\Phi=(\partial u/\partial z)^2+(\partial v/\partial z)^2$, and with the Joule heating $(\nabla\times\mathbf{H})^2=(\partial h_1/\partial z)^2+(\partial h_2/\partial z)^2$. The dominance among these three features relies strongly upon the magnitude of the relevant parameters. Hence, the energy equation in Eq. (4) can be simplified to

$$T_{\eta\eta}+s\ \mathrm{Pr}\ T_\eta = -r_0^2\frac{\mathrm{Pr}}{c_p}[(F_\eta^2+G_\eta^2)+R_4(H_{1\eta}^2+H_{2\eta}^2)] \tag{13}$$

with $R_4=R_H/R_2$. Further defining the Eckert number $\mathrm{Ec}=r_0^2/(c_p(T_w-T_\infty))$, and making use of the replacement $\Theta=T-T_\infty/T_w-T_\infty$, Eq. (13) eventually transforms into

$$\Theta_{\eta\eta}+\mathrm{sPr}\Theta_\eta = -\mathrm{PrEc}[Ke^{-2\alpha_1\eta}+Le^{-2\alpha_2\eta}+\{M\sin\beta_s\eta+N\cos\beta_s\eta\}e^{-\alpha_s\eta}] \tag{14}$$

Here K, L, M, and N are constants.

4.1 Injection and Impermeable Wall Case. For $s\le 0$, the solution to Θ can be found by integrating Eq. (14), which yields

$$\Theta = -\mathrm{PrEc}\left[\frac{K}{-2\alpha_1(\mathrm{sPr}-2\alpha_1)}e^{-2\alpha_1\eta}+\frac{L}{-2\alpha_2(\mathrm{sPr}-2\alpha_2)}e^{-2\alpha_2\eta}+\frac{-M_2\sin\beta_s\eta+N_2\cos\beta_s\eta}{(\alpha_s^2+\beta_s^2)[(\mathrm{sPr}-\alpha)^2+\beta_s^2]}e^{-\alpha_s\eta}+C_{11}+C_{12}e^{-\mathrm{sPr}\eta}\right] \tag{15}$$

in which, C_{11} and C_{12} are integration constants, and M_2 and N_2 are appropriately defined.

Two cases now are of our concern. First, we assume that the wall is insulated with

$$\Theta'(0)=0,\quad \Theta(\infty)=0$$

The latter condition gives $C_{11}=C_{12}=0$, and the first condition produces the relation

$$\Gamma_{is} = \frac{K}{(2\alpha_1-s\mathrm{Pr})}+\frac{L}{(2\alpha_2-s\mathrm{Pr})}+\frac{\beta_sM_2+\alpha_sN_2}{(\alpha_s^2+\beta_s^2)[(s\mathrm{Pr}-\alpha_s)^2+\beta_s^2]}=0 \tag{16}$$

Second, we consider a heat transfer so that the boundary conditions imposed on Eq. (15) are

$$\Theta(0)=1,\quad \Theta(\infty)=0$$

The latter condition again gives C_{11} and C_{12}, and the first condition generates the relation

$$-\mathrm{PrEc}\Gamma_{hs}=1 \tag{17}$$

with

$$\Gamma_{hs} = \frac{K}{-2\alpha_1(\mathrm{sPr}-2\alpha_1)}+\frac{L}{-2\alpha_2(\mathrm{sPr}-2\alpha_2)}+\frac{N_2}{(\alpha_s^2+\beta_s^2)[(\mathrm{sPr}-\alpha_s)^2+\beta_s^2]}$$

Hence, the temperature on and above the disk, in this case, is governed by

$$\Theta = \left[\frac{K}{-2\alpha_1(\mathrm{sPr}-2\alpha_1)}e^{-2\alpha_1\eta}+\frac{L}{-2\alpha_2(\mathrm{sPr}-2\alpha_2)}e^{-2\alpha_2\eta}+\frac{-M_2\sin\beta_s\eta+N_2\cos\beta_s\eta}{(\alpha_s^2+\beta_s^2)[(\mathrm{sPr}-\alpha_s)^2+\beta_s^2]}e^{-\alpha_s\eta}\right]/\Gamma_{hs} \tag{18}$$

At this stage the heat transfer can be computed from the heat flux q in accordance with Fourier's heat law

$$q = -k\left(\frac{\partial T}{\partial z}\right)\bigg|_{z=0} = -k\sqrt{\frac{\mathrm{Re}}{2}}(T_w-T_\infty)\left(\frac{\partial\Theta}{\partial\eta}\right)\bigg|_{\eta=0}$$

which results in a dimensionless and normalized (by a factor of $L\sqrt{\mathrm{Re}/2}$) Nusselt number Nu

$$\mathrm{Nu} = -\left(\frac{d\Theta}{d\eta}\right)\bigg|_{\eta=0} = -\mathrm{PrEc}\Gamma_{is} = \Gamma_{is}/\Gamma_{hs}$$

The heat transfer rate Nu is presented in Table 2. It is clear that the magnetic field acts in favor of increasing the heat transfer rate, as compared with the case of the nonconducting fluid. Moreover, the effect of injection is clearly to reduce the heat transfer rate.

4.2 Suction Case. For suction at the disk, the general solution to the temperature in Eq. (14) is given by

$$\Theta = -\mathrm{PrEc}e^{-\mathrm{sPr}\eta}\left\{\int\left[\frac{K}{-2\alpha_1}e^{-2\alpha_1\eta}+\frac{L}{-2\alpha_2}e^{-2\alpha_2\eta}+\frac{M_1\sin\beta_s\eta-N_1\cos\beta_s\eta}{(\alpha_s^2+\beta_s^2)}e^{-\alpha_s\eta}\right]e^{\mathrm{sPr}\eta}d\eta+C_{11}e^{\mathrm{sPr}\eta}+C_{12}\right\} \tag{19}$$

Integration of Eq. (19) is implemented under the following restrictions:

(i) $s\mathrm{Pr}-2\alpha_1\neq 0$ and $s\mathrm{Pr}-2\alpha_2\neq 0$. Solution to Eq. (19) in this case is given in the form

Table 3 The variation in Nu at Prandtl number Pr=1 for suction

Ec	s	$R_H=10$	$R_H=10^2$	$R_H=10^4$	$R_H=10^6$	$R_H=10^7$	$R_H=10^8$
−4	2	7.0880797	7.0880899	7.0892170	7.2020169	8.2155402	15.321151
	5	15.124111	15.124118	15.124882	15.201047	15.870882	21.155291
4	2	−3.0880797	−3.0880899	−3.0892170	−3.2020169	−4.2155402	−11.321151
	5	−5.1241115	−5.1241184	−5.1248827	−5.2010476	−5.8708825	−11.155291

$$\Theta = -\mathrm{PrEc}\left[\frac{K}{-2\alpha_1(s\mathrm{Pr}-2\alpha_1)}e^{-2\alpha_1\eta} + \frac{L}{-2\alpha_2(s\mathrm{Pr}-2\alpha_2)}e^{-2\alpha_2\eta} + \frac{-M_2\sin\beta_s\eta + N_2\cos\beta_s\eta}{(\alpha_s^2+\beta_s^2)[(s\mathrm{Pr}-\alpha_s)^2+\beta_s^2]}e^{-\alpha_s\eta} + C_{11} + C_{12}e^{-s\mathrm{Pr}\eta}\right] \tag{20}$$

Due to the boundary conditions, the wall insulation yields $C_{11}=0$ and $C_{12}=-\Gamma_{is}/s\mathrm{Pr}$. If the heat transfer is allowed, then the solution results is in the form of Eq. (20), but the constants are now given by $C_{11}=0$ and $C_{12}=-\Gamma_{hs}-1/\mathrm{PrEc}$.

(ii) $s\mathrm{Pr}-2\alpha_1=0$ and $s\mathrm{Pr}-2\alpha_2\neq 0$. Solution to Eq. (19) in this case is given in the form

$$\Theta = -\mathrm{PrEc}\left[\frac{K}{-2\alpha_1}\eta e^{-2\alpha_1\eta} + \frac{L}{-2\alpha_2(s\mathrm{Pr}-2\alpha_2)}e^{-2\alpha_2\eta} + \frac{-M_2\sin\beta_s\eta + N_2\cos\beta_s\eta}{(\alpha_s^2+\beta_s^2)[(s\mathrm{Pr}-\alpha_s)^2+\beta_s^2]}e^{-\alpha_s\eta} + C_{11} + C_{12}e^{-s\mathrm{Pr}\eta}\right] \tag{21}$$

where in the case of wall insulation $C_{11}=0$ and $C_{12}=-\Gamma 1_{is}/s\mathrm{Pr}$ with $\Gamma 1_{is}=\Gamma_{is}+(s\mathrm{Pr}K)/(2\alpha_1(s\mathrm{Pr}-2\alpha_1))$. However, for the heat transfer case, the solution is still Eq. (21), but now $C_{11}=0$ and $C_{12}=-\Gamma 1_{hs}-1/\mathrm{PrEc}$ with $\Gamma 1_{hs}=\Gamma_{hs}+K/(2\alpha_1(s\mathrm{Pr}-2\alpha_1))$.

(iii) $s\mathrm{Pr}-2\alpha_1\neq 0$ and $s\mathrm{Pr}-2\alpha_2=0$. Solution to Eq. (19) in this case is given in the form

$$\Theta = -\mathrm{PrEc}\left[\frac{K}{-2\alpha_1(s\mathrm{Pr}-2\alpha_1)}e^{-2\alpha_1\eta} + \frac{L}{-2\alpha_2}\eta e^{-2\alpha_2\eta} + \frac{-M_2\sin\beta_s\eta + N_2\cos\beta_s\eta}{(\alpha_s^2+\beta_s^2)[(s\mathrm{Pr}-\alpha_s)^2+\beta_s^2]}e^{-\alpha_s\eta} + C_{11} + C_{12}e^{-s\mathrm{Pr}\eta}\right] \tag{22}$$

where in the case of wall insulation $C_{11}=0$ and $C_{12}=-\Gamma 2_{is}/s\mathrm{Pr}$ with $\Gamma 2_{is}=\Gamma_{is}+(s\mathrm{Pr}L)/(2\alpha_2(s\mathrm{Pr}-2\alpha_2))$. However, for the heat transfer case, the solution is still Eq. (21), but now $C_{11}=0$ and $C_{12}=-\Gamma 2_{hs}-\frac{1}{\mathrm{PrEc}}$ with $\Gamma 2_{hs}=\Gamma_{hs}+L/(2\alpha_2(s\mathrm{Pr}-2\alpha_2))$.

For the suction case, the heat transfer takes place in accordance with the Nusselt number

$$\mathrm{Nu} = -\left(\frac{d\Theta}{d\eta}\right)\bigg|_{\eta=0} = \mathrm{Pr}(s-\mathrm{Ec}\Gamma_s)$$

with $\Gamma_s=K/2\alpha_1+L/2\alpha_2+N_1/\alpha_s^2+\beta_s^2$. It is seen on Table 3 that the overall effect of the suction is to increase the rate of heat transfer as opposed to the effect of injection.

Finally, the thermal layer thickness defined by $\delta_t=\int_0^\infty \Theta d\eta$ can also be evaluated for the cases considered.

5 Concluding Remarks

An exact solution of the motion of incompressible viscous magnetohydrodynamic fluid flow over a disk rotating about its axis of rotation has been obtained. Solutions show that a boundary layer develops near the surface of the disk. It has been found that the effects are strongly manifested if the magnetic pressure number is increased. Closed form expressions for the vorticity and induced current density fields, the hydromagnetic shear stresses, the displacement thicknesses, as well as the thermal layer thickness have been evaluated.

The assumptions imposed on the velocity and pressure correlate the temperature with the convection, the viscous dissipation, as well as the Joule heating in the energy equation. Thus, the temperature field has been analytically derived, giving rise to different exponentially decaying temperature formulas. Additionally, heat transfer expressions have been obtained using Fourier's heat law.

Nomenclature

Ω = angular velocity
r, θ, and z = variables of cylindrical coordinates
p and T = pressure and temperature fields
u, v, and w = velocity fields
h_1, h_2, and h_3 = induced magnetic field
∇^2 and Φ = Laplacian operator and viscous dissipation
ρ, ν, and σ = density, kinematic viscosity, and electrical conductivity of the fluid
c_p and k = specific heat at a constant pressure and coefficient of thermal conductivity
ν_H and μ_e = diffusion of magnetic field and magnetic permeability
Re and Pr = Reynolds and Prandtl numbers
R_H and R_σ = magnetic pressure and magnetic Reynolds numbers
R_2 and Ec = magnetic Prandtl number and Eckert number
δ_θ and δ_r = fluid dynamic thicknesses
δ_{H1} and δ_{H2} = magnetic field thicknesses
τ_r and τ_θ = shear stresses on the wall
τ_{h1} and τ_{h2} = magnetic stresses on the wall
ω_r, ω_θ, and ω_z = vorticity components
J_r, J_θ, and J_z = current density components
q and Nu = heat flux and Nusselt number

References

[1] Kármán, T. V., 1921 "Uber Laminare und Turbulente Reibung," ZAMM, **1**, pp. 233–252.
[2] Gregory, N., Stuart, J. T., and Walker, W. S., 1955, "On the Stability of Three Dimensional Boundary Layers With Applications to the Flow Due to a Rotating-Disk," Philos. Trans. R. Soc. London, Ser. A, **248**, pp. 155–199.
[3] Maleque, Kh. A., and Sattar, Md. A., 2005, "Steady Laminar Convective Flow With Variable Properties Due to a Porous Rotating Disk," ASME J. Heat Transfer, **127**, pp. 1406–1409.
[4] Berker, R., 1982, "An Exact Solution of the Navier-Stokes Equation: The Vortex With Curvilinear Axis," Int. J. Eng. Sci., **20**, pp. 217–230.
[5] Rajagopal, K. R., 1984, "A Class of Exact Solutions to the Navier-Stokes Equations," Int. J. Eng. Sci., **22**, pp. 451–455.

[6] Kasiviswanathan, S. R., and Rao, A. R., 1987, "An Unsteady Flow Due to Eccentrically Rotating Porous Disk and a Fluid at Infinity," Int. J. Eng. Sci., **25**, pp. 1419–1425.
[7] Awad, M. M., 2008, "Heat Transfer From a Rotating Disk to Fluids for a Wide Range of Prandtl Numbers Using the Asymptotic Model," ASME J. Heat Transfer, **130**, pp. 014505.
[8] Kumar, S. K., Thacker, W. I., and Watson, L. T., 1988, "Magnetohydrodynamic Flow and Heat Transfer About a Rotating Disk With Suction and Injection at the Disk Surface," Comput. Fluids, **16**, pp. 183–193.
[9] Erdogan, M. E., 1997, "Unsteady Flow of a Viscous Fluid Due to Non-Coaxial Rotations of a Disk and a Fluid at Infinity," Int. J. Non-Linear Mech., **32**, pp. 285–290.

Determination of Heat Transfer in Ducts With Axial Conduction by Variational Calculus

A. Haji-Sheikh
Department of Mechanical and Aerospace Engineering,
University of Texas at Arlington,
Arlington, TX 76019-0023

This study uses a methodology based on the calculus of variation to determine the heat transfer in passages with two-dimensional velocity fields such as rectangular channels and in the presence of axial conduction. The mathematical procedure is presented and the subsequent numerical computations provide the Nusselt number values. To verify the accuracy of this numerical procedure, the Nusselt number values are acquired for parallel-plate channels and circular pipes and compared with similar data from the Graetz-type exact analyses. Then, rectangular passages are selected to show the capability and a square duct is used to study the domain of accuracy for this procedure. The results for small Peclet numbers lead to a simple correlation for determination of the bulk temperature and they compare well with those obtained from an asymptotic solution.
[DOI: 10.1115/1.3122776]

Keywords: axial conduction, duct flow, thermal entrance, variational calculus, heat transfer, convection

1 Introduction

As reported in the literature, it is possible to obtain the Graetz-type exact series solutions to compute the temperature field within the laminar flow passing through parallel-plate and circular ducts. However, an alternative methodology is needed for computation of the heat transfer in passages with two-dimensional velocity fields. The inclusion of axial conduction contribution makes acquisition of an analytical solution a more challenging task. Various studies are reported in the literature for determination of the heat transfer to laminar flow through passages when the axial conduction is negligible [1–5]. The available exact series solutions are limited to Graetz-type analysis for passages wherein the velocity depends on a single variable. Numerically developed solutions for different passages are also available in the literature [1–5], using different numerical schemes. The Green's function solution technique is a powerful tool and it is presented for parallel-plate ducts in Ref. [6] and for circular pipes in Ref. [7] with emphasis on porous media.

The axial conduction is expected to have a strong effect on the heat transfer to flow through various passages near the entrance region, depending on the size of the Peclet number. Using separation of variables, a mathematical procedure that includes the contribution of axial conduction is illustrated by Lahjomri and Oubarra [8]. Then, they extended their methodology in Ref. [9] to study heat transfer in thermal entrance region with a step change in wall temperature for laminar Hartmann flow. Other studies on the effect of axial conduction in circular passages, away from the thermal entrance locations, are in Refs. [10,11]. Also, different features of axial conduction effect in microchannels are reported in Refs. [12–14]. The axial conduction has a significant effect in the fluid saturated porous passages with metallic foams and the Graetz-type solutions are in Ref. [15] for parallel-plate and circular ducts.

For fluid flow in a duct with a two-dimensional velocity field, the solution is not separable and, therefore, the method of weighted residuals becomes a desirable computational procedure. The variational calculus has been used in the past to study heat transfer in fluid passages. Sparrow and Seigel [16] studied the effect of constant wall heat flux on the Nusselt number under thermally fully developed conditions. This minimization procedure is often called the Galerkin method [17]. LeCroy and Eraslan [18] studied the temperature development in the entrance region of magnetohydrodynamic (MHD) channels. A similar procedure was used in Ref. [19] to provide extensive heat transfer data in the thermal entrance regions of triangular ducts. This study extends the method of using variational calculus, as reported in Ref. [20], to include the effect of axial conduction. The minimization process using the variational calculus is often called the weighted-residual method (WRM). This methodology leads to an analytical/numerical procedure that becomes a powerful analysis tool to study the effect of axial thermal conduction in a fluid passage having a velocity field that depends on two variables. Furthermore, this methodology directly applies to flow in fluid saturated porous passages, without any modification.

2 Mathematical Analysis Using Variational Calculus

Consideration is given to flow passing through channels with constant cross section area, as shown in Fig. 1. The energy equation for hydrodynamically fully developed flow through two-dimensional passages has the form

$$\frac{\partial}{\partial \hat{y}}\left(k\frac{\partial T}{\partial \hat{y}}\right)+\frac{\partial}{\partial \hat{z}}\left(k\frac{\partial T}{\partial \hat{z}}\right)=Cu\frac{\partial T}{\partial \hat{x}}-\frac{\partial}{\partial \hat{x}}\left(k\frac{\partial T}{\partial \hat{x}}\right) \tag{1a}$$

where T is the fluid temperature, k is the fluid thermal conductivity, C stands for ρc_p, and $u=u(\hat{y},\hat{z})$ is the local velocity. In subsequent formulations, one needs to define a function θ that linearly depends on temperature T and it satisfies homogeneous boundary conditions of the first kind, the second kind, or the third kind. This transforms Eq. (1*a*) to become

$$\frac{\partial}{\partial \hat{y}}\left(k\frac{\partial \theta}{\partial \hat{y}}\right)+\frac{\partial}{\partial \hat{z}}\left(k\frac{\partial \theta}{\partial \hat{z}}\right)=Cu\frac{\partial \theta}{\partial \hat{x}}-\frac{\partial}{\partial \hat{x}}\left(k\frac{\partial \theta}{\partial \hat{x}}\right) \tag{1b}$$

It is customary to consider the following functional form for reduced temperature:

Contributed by the Heat Transfer Division of ASME for publication in the JOURNAL OF HEAT TRANSFER. Manuscript received October 29, 2008; final manuscript received December 23, 2008; published online June 26, 2009. Review conducted by Peter Vadasz.

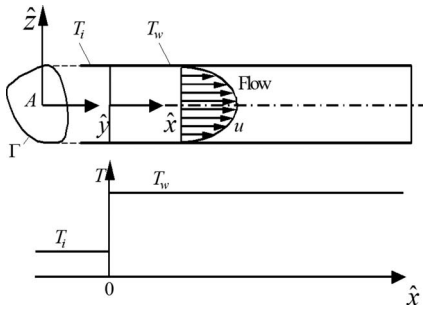

Fig. 1 Schematic of a duct with temperature change at $\hat{x}=0$

$$\theta = \Psi(y,z)e^{-\lambda x} \tag{2}$$

and after substitution for θ while assuming k to be independent of $\hat{x}$, Eq. (1) takes the form

$$\frac{\partial}{\partial \hat{y}}\left(k\frac{\partial \Psi}{\partial \hat{y}}\right) + \frac{\partial}{\partial \hat{z}}\left(k\frac{\partial \Psi}{\partial \hat{z}}\right) + \lambda C u \Psi + \lambda^2 k \Psi = 0 \tag{3}$$

Next, the variational calculus procedure as described in Ref. [20] is to be modified. The functional to be minimized now includes a new term containing λ^2 and it has the following form:

$$I = \int_A \left\{ k\left(\frac{\partial \Psi}{\partial \hat{y}}\right)^2 + k\left(\frac{\partial \Psi}{\partial \hat{z}}\right)^2 - \lambda C u \Psi^2 - \lambda^2 k \Psi^2 - \frac{1}{2}\left[\frac{\partial}{\partial \hat{y}}\left(k\frac{\partial \Psi^2}{\partial \hat{y}}\right) + \frac{\partial}{\partial \hat{z}}\left(k\frac{\partial \Psi^2}{\partial \hat{z}}\right)\right]\right\} dA \tag{4}$$

where A stands for the cross section area. It is a common practice to define a functional form for the eigenfunction Ψ that is a linear combination of a set of linearly independent basis function, that is,

$$\Psi = \sum_{j=1}^{N} d_j f_j(\hat{y},\hat{z}) \tag{5}$$

Following the substitution of this function Ψ from Eq. (5) in Eq. (4), the minimization of functional $I(d_1, d_2, \ldots, d_N)$, as described in Ref. [20], requires having

$$\frac{\partial I}{\partial d_i} = 0 \quad \text{for} \quad i = 1,2,\ldots,N \tag{6}$$

while d_i is one of the N coefficients in Eq. (5). Using Eq. (6), the differentiation of the functional I, as given in Eq. (4), with respect to a specific coefficient d_i yields

$$\frac{\partial I}{\partial d_i} = 2\int_A \left[k\left(\frac{\partial \Psi}{\partial \hat{y}}\right)\frac{\partial f_i}{\partial \hat{y}} + k\left(\frac{\partial \Psi}{\partial \hat{z}}\right)\frac{\partial f_i}{\partial \hat{z}} - (\lambda C u + \lambda^2 k)\Psi f_i \right] dA - \int_A \left[\frac{\partial}{\partial \hat{y}}\left(k\frac{\partial(\Psi f_i)}{\partial \hat{y}}\right) + \frac{\partial}{\partial \hat{z}}\left(k\frac{\partial(\Psi f_i)}{\partial \hat{z}}\right)\right] dA = 0$$

$$\text{for} \quad i = 1,2,\ldots,N \tag{7}$$

that becomes

$$2\int_A \left[\frac{\partial}{\partial \hat{y}}\left(k\frac{\partial \Psi}{\partial \hat{y}}\right) + \frac{\partial}{\partial \hat{z}}\left(k\frac{\partial \Psi}{\partial \hat{z}}\right) + (\lambda C u + \lambda^2 k)\Psi \right] f_i dA - 2\int_A \nabla\cdot[f_i(k\nabla\Psi)]dA + \int_A \nabla\cdot[k\nabla(\Psi f_i)]dA = 0$$

$$\text{for} \quad i = 1,2,\ldots,N \tag{8a}$$

The last two terms in Eq. (8*a*) can be written as

$$-2\int_A \nabla\cdot[f_i(k\nabla\Psi)]dA + \int_A \nabla\cdot[k\nabla(\Psi f_i)]dA = -\int_A \{\nabla\cdot[f_i(k\nabla\Psi)] - \nabla\cdot[\Psi(k\nabla f_i)]\}dA = -\int_\Gamma k\left\{ f_i\frac{\partial \Psi}{\partial n} - \Psi\frac{\partial f_i}{\partial n}\right\}_\Gamma d\Gamma \tag{8b}$$

using the divergence theorem over the duct's boundary Γ. Since the right-hand side of Eq. (8*b*) vanishes for homogeneous boundary conditions of the first, second, or third kind, the contribution of second and third terms in Eq. (8*a*) would also vanish. Then, after substituting Ψ from Eq. (5) in Eq. (8*a*), it reduces to

$$\sum_{j=1}^{N} d_j \left\{ \int_A \left[\frac{\partial}{\partial \hat{y}}\left(k\frac{\partial f_j(\hat{y},\hat{z})}{\partial \hat{y}}\right) + \frac{\partial}{\partial \hat{z}}\left(k\frac{\partial f_j(\hat{y},\hat{z})}{\partial \hat{z}}\right)\right] f_i dA + \lambda \int_A C u f_j f_i dA + \lambda^2 \int_A k f_j f_i dA \right\} = 0 \quad \text{for} \quad i = 1,2,\ldots,N. \tag{9}$$

In this generic formulation, the functions u, C, and k can depend on $\hat{y}$ and $\hat{z}$. This minimization procedure leading to Eq. (9) is a weighted-residual method while the weighting function is f_i.

The formulation of Eq. (9) is a modified form of the procedure in Ref. [20] that is augmented by the inclusion of axial conduction contribution. Additionally, major modifications are needed in order to lead toward the computation of temperature field and the heat flux. Accordingly, the basis functions f_j, in Eq. (5), are to be selected depending on the type of the boundary conditions, e.g., first, second, or third kind [21]. In the matrix form, Eq. (9) becomes

$$(\mathbf{A} + \lambda\mathbf{B} + \lambda^2\mathbf{C})\mathbf{d} = 0 \tag{10}$$

where the matrices **A**, **B**, and **C** have the elements

$$a_{ij} = \int\int_A f_i(\hat{y},\hat{z})\,\nabla\cdot[k\nabla f_j(\hat{y},\hat{z})]dA \tag{11a}$$

$$b_{ij} = \int\int_A C u f_i(\hat{y},\hat{z}) f_j(\hat{y},\hat{z})dA \tag{11b}$$

and

$$c_{ij} = \int\int_A k f_i(\hat{y},\hat{z}) f_j(\hat{y},\hat{z})dA \tag{11c}$$

The vector **d** in Eq. (10) stands for coefficients $d_1, d_2, \ldots, d_N$ appearing in Eq. (5). Although, in the formulation leading to Eq. (10), the thermal conductivity k and the capacitance C can depend on $\hat{y}$ and $\hat{z}$ coordinates; however, in the subsequent numerical computations, the coefficients k and C have constant values. A preferred method, as discussed in Ref. [20], is to use classical Galerkin's method for the determination of the velocity field, for flow through a duct. Furthermore, the matrix **C** in Eq. (10) stands for the contribution of axial conduction and its inclusion requires a modified mathematical procedure for computation of the fluid temperature.

3 Application to Thermal Entrance Problems

Having constant thermophysical properties, the dimensionless form of the energy equation for flow through passages with constant cross section, as shown in the Fig. 1, has the following form:

$$\frac{\partial^2\theta}{\partial y^2}+\frac{\partial^2\theta}{\partial z^2}=\frac{u}{U}\frac{\partial\theta}{\partial x}-\frac{1}{\mathrm{Pe}^2}\frac{\partial^2\theta}{\partial x^2} \tag{12}$$

where $u=u(x,y)$ is the hydrodynamically fully developed velocity distribution and U is the average velocity. The function θ is related to temperature and it should be selected to have homogeneous boundary conditions. The coordinates in Eq. (12) are dimensionless using a characteristic length L_c, which makes $y=\hat{y}/L_c$, $z=\hat{z}/L_c$, and $x=(\hat{x}/L_c)/\mathrm{Pe}$ where $\mathrm{Pe}=L_cU/\alpha$. The solution for θ with homogeneous boundary condition and nonzero entrance temperature is expressed as

$$\theta=\sum_{m=1}^{N}E_m\Psi_m(y,z)e^{-\lambda_m x} \tag{13}$$

After substitution for θ from Eq. (13) in Eq. (12), the function $\Psi_m(y,z)$ must satisfy the partial differential equation

$$\frac{\partial^2\Psi_m}{\partial y^2}+\frac{\partial^2\Psi_m}{\partial z^2}+\left(\frac{u}{U}\lambda_m+\frac{\lambda_m^2}{\mathrm{Pe}^2}\right)\Psi_m=0 \tag{14}$$

and, as in Eq. (5), the eigenfunction $\Psi_m(y,z)$ represents a linear combination of a set of basis functions defined by the relation

$$\Psi_m(y,z)=\sum_{j=1}^{N}d_{mj}f_j(y,z) \tag{15}$$

In this application, the parameter λ_m is real but it can be positive or negative. The method of selection of the basis functions $f_j(y,z)$ is in Ref. [21]. As stated earlier, the basis functions $f_j(y,z)$ are to be selected so that they satisfy the same type of homogeneous boundary conditions as those for θ, along the boundary of the duct. This task can be accomplished once the geometry and boundary conditions of a specific fluid passage are known. Next, the eigenvalues λ_m in Eq. (14) and the eigenvector coefficients d_{mj} in Eq. (15) need to be computed. The computation using variational calculus begins by finding the elements of matrices, **A**, **B**, and, **C**. The modified forms of Eqs. (11*a*)–(11*c*) are the relations

$$a_{ij}=\int\int_A f_i(y,z)\nabla^2 f_j(y,z)dA \tag{16a}$$

$$b_{ij}=\int\int_A\left(\frac{u}{U}\right)f_i(y,z)f_j(y,z)dA \tag{16b}$$

and

$$c_{ij}=\int\int_A\frac{1}{\mathrm{Pe}^2}f_i(y,z)f_j(y,z)dA \tag{16c}$$

wherein the parameter A now represents the duct's cross section area in dimensionless space. Then, the eigenvalues and eigenvectors are obtainable from Eq. (10). Next, Eq. (10) can be reduced to a classical eigenvalue problem [22] by introducing new vectors **v** and **w** so that $\mathbf{w}=\lambda\mathbf{d}=\lambda\mathbf{v}$. This leads to an eigenvalue problem that can be rewritten as

$$\begin{bmatrix}0 & \mathbf{I}\\ \mathbf{A} & \mathbf{B}\end{bmatrix}\begin{bmatrix}\mathbf{v}\\ \mathbf{w}\end{bmatrix}-\lambda\begin{bmatrix}\mathbf{I} & 0\\ 0 & -\mathbf{C}\end{bmatrix}\begin{bmatrix}\mathbf{v}\\ \mathbf{w}\end{bmatrix}=0 \tag{17}$$

Standard computational procedures are available for determination of the eigenvalues λ_m and the related coefficients d_{mj}, which are the members of eigenvectors $\mathbf{d_m}$. Each eigenvector $\mathbf{d_m}$ becomes a row of a matrix to be designated as **D**. This method has an advantage as it provides the eigenvalues without a need for an iterative procedure. However, it would double the size of the matrices in Eq. (17) in comparison to those in Eq. (10).

According to Eq. (17), there are two sets of eigenvalues, a positive set and a negative set. Therefore, there are two temperature solutions: one is for the negative eigenvalues λ_m when $x<0$,

$$\theta_1=\sum_{m=1}^{N}F_m\Psi_m(y,z)e^{|\lambda_m|x} \tag{18a}$$

and the other is for the positive eigenvalues λ_m when $x>0$,

$$\theta_2=\sum_{m=1}^{N}E_m\Psi_m(y,z)e^{-\lambda_m x} \tag{18b}$$

The next step is to develop a procedure to find E_n and F_n using the orthogonality condition.

3.1 Orthogonality Condition. It is possible to show that the $\Psi_m(y,z)$ functions are orthogonal by writing Eq. (14) as

$$\frac{\partial^2\Psi_n}{\partial y^2}+\frac{\partial^2\Psi_n}{\partial z^2}+\left(\frac{u}{U}\lambda_n+\frac{\lambda_n^2}{\mathrm{Pe}^2}\right)\Psi_n=0 \tag{19}$$

After multiplying Eq. (14) by $\Psi_n(y,z)$ and Eq. (19) by $\Psi_m(y,z)$, subtracting resulting relations, and then integrating it over the cross section area A, it produces the relation

$$\begin{aligned}(\lambda_m-\lambda_n)\int_A\frac{u}{U}\Psi_m\Psi_n dA+(\lambda_m^2-\lambda_n^2)\int_A\frac{1}{\mathrm{Pe}^2}\Psi_m\Psi_n dA\\ =\int_A\Psi_m\nabla\cdot(\nabla\Psi_n)dA-\int_A\Psi_n\nabla\cdot(\nabla\Psi_m)dA\\ =\int_\Gamma\left(\Psi_m\frac{\partial\Psi_n}{\partial n}-\Psi_n\frac{\partial\Psi_m}{\partial n}\right)_\Gamma d\Gamma\end{aligned} \tag{20}$$

where Γ stands for the boundary of the duct as depicted in Fig. 1. Since the boundary conditions are homogeneous, the right hand side of Eq. (20) vanishes at the boundary of the duct. Then, Eq. (20) reduces to take the form

$$(\lambda_m-\lambda_n)\int_A\left(\frac{u}{U}+\frac{\lambda_m+\lambda_n}{\mathrm{Pe}^2}\right)\Psi_m\Psi_n dA=0 \tag{21}$$

This equation is the orthogonality condition since the integral in this equation must vanish when $\lambda_n\neq\lambda_m$.

3.2 Solution for Boundary Condition of the First Kind. In this section, consideration is given to the case in which the wall temperature is equal to T_i when $x<0$ and it is equal to T_w when $x>0$. It is appropriate to identify $\theta_1=T-T_i$ and designate the negative eigenvalues as $\beta_m=-\lambda_m$ when $x<0$, then

$$\theta_1=\sum_{m=1}^{N}F_m\Phi_m(y,z)e^{\beta_m x}\quad\text{with}\quad\beta_m>0 \tag{22a}$$

Also, using $\theta_2=T-T_w$ when $x>0$ yields the relation

$$\theta_2=\sum_{m=1}^{N}E_m\Psi_m(y,z)e^{-\lambda_m x}\quad\text{with}\quad\lambda_m>0 \tag{22b}$$

The first compatibility condition for temperature at $x=0$ suggests

$$(\theta_1-\theta_2)_{x=0}=[T(y,z;0))-T_i-[T(y,z;0)-T_w)=-(T_i-T_w) \tag{23a}$$

and the next compatibility condition for heat flux is

$$(\partial\theta_1/\partial x)_{x_-=0}=(\partial\theta_2/\partial x)_{x_+=0} \tag{23b}$$

The substitution of functions θ_1 and θ_2 from Eqs. (22*a*) and (22*b*) into Eq. (23*a*) leads to the relation

$$\sum_{m=1}^{N} F_m \Phi_m(y,z) = -(T_i - T_w) + \sum_{m=1}^{N} E_m \Psi_m(y,z) \tag{24a}$$

and their substitution into Eq. (23*b*) leads to the relation

$$-\sum_{m=1}^{N} F_m \beta_m \Phi_m(y,z) = -\sum_{m=1}^{N} E_m \lambda_m \Psi_m(y,z) \tag{24b}$$

for determination of the coefficients E_m and F_m. After multiplying both sides of Eq. (24*a*) by $u/U+\lambda_n/\mathrm{Pe}^2$ and both sides of Eq. (22*b*) by $-1/\mathrm{Pe}^2$ and then adding the resulting relations, it produces the equation

$$\sum_{m=1}^{N} F_m \Phi_m(y,z)\left(\frac{u}{U}+\frac{\lambda_n+\beta_m}{\mathrm{Pe}^2}\right) = -(T_i - T_w)\left(\frac{u}{U}+\frac{\lambda_n}{\mathrm{Pe}^2}\right) + \sum_{m=1}^{N} E_m \Psi_m(y,z)\left(\frac{u}{U}+\frac{\lambda_m+\lambda_n}{\mathrm{Pe}^2}\right) \tag{25}$$

Then, one can multiply both sides of Eq. (25) by $\Psi_n dA$ and integrate the resulting relation over the cross section area to get

$$\sum_{m=1}^{N} F_m \int_A \left(\frac{u}{U}+\frac{\lambda_n+\beta_m}{\mathrm{Pe}^2}\right)\Phi_m(y,z)\Psi_n(y,z)dA = -\int_A (T_i - T_w)\left(\frac{u}{U}+\frac{\lambda_n}{\mathrm{Pe}^2}\right)\Psi_n(y,z)dA + \sum_{m=1}^{N} E_m \int_A \left(\frac{u}{U}+\frac{\lambda_m+\lambda_n}{\mathrm{Pe}^2}\right)\Psi_m(y,z)\Psi_n(y,z)dA \tag{26}$$

According to the orthogonality condition, the left hand side of Eq. (26) would vanish since $\lambda_n \neq \beta_m$. Also, the summation on the right hand side has a zero value when $m \neq n$. Therefore, using this orthogonality condition, Eq. (26) provides the coefficient E_n as

$$E_m = \frac{\int_A (T_i - T_w)\left(\frac{u}{U}+\frac{\lambda_m}{\mathrm{Pe}^2}\right)\Psi_m(y,z)dA}{\int_A \left(\frac{u}{U}+\frac{2\lambda_m}{\mathrm{Pe}^2}\right)\Psi_m^2(y,z)dA} \tag{27}$$

for insertion in Eq. (22*b*), when $x>0$. A similar procedure provides F_n for insertion in Eq. (22*a*). Accordingly, by multiplying Eq. (24*a*) by $u/U+\beta_n/\mathrm{Pe}^2$ and Eq. (24*b*) by $-1/\mathrm{Pe}^2$ and then adding the resulting relations will produce the following equation:

$$\sum_{m=1}^{N} F_m \Phi_m(y,z)\left(\frac{u}{U}+\frac{\beta_n+\beta_m}{\mathrm{Pe}^2}\right) = -(T_i - T_w)\left(\frac{u}{U}+\frac{\beta_n}{\mathrm{Pe}^2}\right) + \sum_{m=1}^{N} E_m \Psi_m(y,z)\left(\frac{u}{U}+\frac{\beta_n+\lambda_m}{\mathrm{Pe}^2}\right) \tag{28}$$

Multiplying both sides of Eq. (28) by $\Phi_n dA$ and then integrating it over cross section area A yields

$$\sum_{m=1}^{N} F_m \int_A \left(\frac{u}{U}+\frac{\beta_n+\beta_m}{\mathrm{Pe}^2}\right)\Phi_m(y,z)\Phi_n(y,z)dA = -\int_A (T_i - T_w)\left(\frac{u}{U}+\frac{\beta_n}{\mathrm{Pe}^2}\right)\Phi_n(y,z)dA + \sum_{m=1}^{N} E_m \int_A \left(\frac{u}{U}+\frac{\beta_n+\lambda_m}{\mathrm{Pe}^2}\right)\Psi_m(y,z)\Phi_n(y,z)dA \tag{29}$$

Using the orthogonality condition, the second term on the right hand side of Eq. (29) vanishes since $\lambda_m \neq \beta_n$ while the left hand side is equal to zero when $m \neq n$. Therefore, the final result from this orthogonality condition is the coefficient

$$F_m = -\frac{\int_A (T_i - T_w)\left(\frac{u}{U}+\frac{\beta_m}{\mathrm{Pe}^2}\right)\Phi_m(y,z)dA}{\int_A \left(\frac{u}{U}+\frac{2\beta_m}{\mathrm{Pe}^2}\right)\Phi_m^2(y,z)dA} \tag{30}$$

for insertion in Eq. (22*a*), to be used for determining θ_1 when $x<0$.

4 Verification of this Solution Method

For the purpose of verification and as a test of its accuracy, this methodology is applied to parallel-plate channels and to circular ducts. The polynomial type basis functions $f_j(y)$ with zero values at the boundary [20,21] are arbitrarily selected. These functions must contain the members of a complete set and they should be linearly independent. For laminar flow between two parallel plates with walls located at $y=\pm 1$, the selected basis functions are

$$f_j(y) = (1-y^2)y^{2(j-1)} \quad \text{with} \quad j = 1,2,\ldots,N \tag{31a}$$

Similarly, for laminar flow in a circular pipe with radius r and with wall located at $r=1$, the basis functions are

$$f_j(r) = (1-r^2)r^{2(j-1)} \quad \text{with} \quad j = 1,2,\ldots,N \tag{31b}$$

The terms $y^{2(j-1)}$ in Eq. (31*a*) and $r^{2(j-1)}$ in Eq. (31*b*) are the members of a polynomial of degree $2M$ with $M=N-1$. Then, for each of these two sets of basis functions, Eqs. (16*a*)–(16*c*) would provide the members of the matrices **A**, **B**, and **C** in which $dA=1\times dy$ for parallel-plate channels and $dA=2\pi r\times dr$ for circular pipes. Then, the eigenvalues and eigenvectors are obtainable from Eq. (17). Following the determination of the eigenvalues and eigenvectors, the temperature solution for parallel-plate channels, when $x>0$, is

$$\theta_2 = \sum_{m=1}^{N} E_m \Psi_m(y) e^{-\lambda_m x} \tag{32a}$$

with

$$\Psi_m(y) = \sum_{j=1}^{N} d_{mj}(1-y^2)y^{2(j-1)} \tag{32b}$$

and Eq. (27) for the computation of E_m coefficients reduces to

$$E_m = \frac{\int_0^1 (T_i - T_w)\left(\frac{u}{U}+\frac{\lambda_m}{\mathrm{Pe}^2}\right)\Psi_m(y)dy}{\int_0^1 \left(\frac{u}{U}+\frac{2\lambda_m}{\mathrm{Pe}^2}\right)\Psi_m^2(y)dy} \tag{32c}$$

Note that the selection of the basis functions as polynomial types greatly simplifies symbolic computation of the elements of matrices and the coefficient E_m. For heat transfer in circular ducts, similar relations are attainable by changing y to r and dy to rdr in Eqs. (32*a*)–(32*c*).

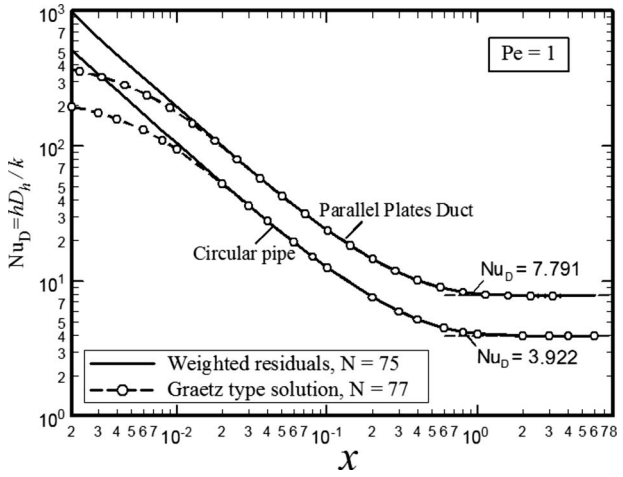

Fig. 2 A comparison of the WRM solutions with the Graetz-type solutions for parallel-plate and circular ducts

To demonstrate the behavior of WRM, it is appropriate to compute the wall heat flux. The classical definition of $\mathrm{Nu}_D = hD_h/k$ is selected from the definition $h = q_w/(T_w - T_b)$ to get

$$\mathrm{Nu}_D = \frac{q_w D_h}{k(T_w - T_b)} \tag{33a}$$

The parameter $q_w = -k(\partial T/\partial n)_{\text{wall}}$ in Eq. (33*a*) represents the wall heat flux while n stands for distance along the vector $\boldsymbol{n}$ direction normal to the wall. Furthermore, the bulk or mean temperature T_b is defined as

$$T_b = \int_A \left(\frac{u}{U}\right) T dA \tag{33b}$$

Using MATHEMATICA [23] as a computational tool, the temperatures and, subsequently, the corresponding Nusselt numbers $\mathrm{Nu}_D = hD_h/k$ are computed when Pe=1 and the results are plotted in Fig. 2 as a function of $x = (\hat{x}/L_c)/\mathrm{Pe}$. For parallel-plate channels with walls being located $2a$ apart, the characteristic length is $L_c = a$ while the hydraulic diameter is $D_h = 4a$. Also, the process is repeated for flow in circular pipes with Pe=1 and the acquired Nu_D values, plotted in Fig. 2, behave similar to those for parallel-plate ducts. For circular pipes with radius r_o, the characteristic length is $L_c = r_o$ and the hydraulic diameter is $D_h = 2r_o$. The data using WRM in Fig. 2 are computed using 75 eigenvalues. The plotted Nusselt numbers values show a near linear behavior as x becomes very small. For comparison, the exact Graetz-type series solutions, as described in Ref. [8], provided the dash lines with circular symbols, also plotted in Fig. 2. Furthermore, for comparison, numerical data from the Graetz-type series solution were acquired with 77 eigenvalues. At large values of x, the data from the weighted-residual method behave similar to those from the Graetz-type series solution. For both passages, the data in Fig. 2 indicate that the exact series solution and WRM agree when $x = (\hat{x}/L_c)/\mathrm{Pe} > 0.02$ and this agreement significantly improves as the value of x increases. However, as x decreases, the Graetz-type exact series solutions begin to depart from the expected values because of a need for a larger number of eigenvalues. These data show that the solutions based on the variational calculus have accuracies comparable to those from exact series solution at larger values of x and better accuracies at smaller values of x, using the same number of eigenvalues. This is expected since the use of variational calculus minimizes the deviations over the entire domain.

In addition to this verification, one can demonstrate the asymptotic behavior of the effect of axial conduction near the thermal entrance location. For this reason, an alternative definition of the Nusselt number is selected. When $x > 0$, this alternative definition is $\mathrm{Nu}_0 = h_0 L_c/k$ that uses the heat transfer coefficient from the relation $h_0 = q_w/(T_w - T_i)$ to get

$$\mathrm{Nu}_0 = \frac{q_w L_c}{k(T_w - T_i)} \tag{34}$$

where the quantity on the right hand side represents the dimensionless wall heat flux. Table 1 shows a sample of data for parallel-plate ducts. For WRM, the size of matrices in Eq. (10) is $N = 125$; therefore, the size of two matrices in Eq. (17) is 250×250. Then, Eq. (17) would provide combined 125 positive and 125 negative eigenvalues, to be separated and used in solutions for θ_1 and θ_2. The entries in Table 1 for the extended Graetz-type series solution are acquired using 800 eigenvalues for the computation of $h_0 a/k$ and the dimensionless bulk temperature $\theta_b = (T_b - T_w)/(T_i - T_w)$ at different values of $\hat{x}/a$. Also, this table contains samples of data for Pe=2, 5, and 10 in addition to those for Pe=1. The aforementioned process is repeated for the calculation of heat transfer in circular ducts. Samples of $h_0 r_o/k$ and θ_b values are acquired at different values of $\hat{x}/r_o$ and Table 2 contains the acquired data for Pe=1, 2, 5, and 10. As in the previous case, there is an excellent agreement between θ_b values computed by WRM and the extended Graetz-type solution. As expected, these two solution methods provide excellent agreement in $h_0 a/k$ and $h_0 r_o/k$ values at larger values of $\hat{x}/a$ and $\hat{x}/r_o$, respectively. However, as the axial coordinates $\hat{x}/a$ and $\hat{x}/r_o$ become very small, the data show small differences beginning at $\hat{x}/a = \hat{x}/r_o = 0.004$. Also, the tabulated data for each Pe value in Tables 1 and 2 show that the WRM solutions approach to similar limiting values as $\hat{x}/a$ and $\hat{x}/r_o$ reduce toward zero.

The WRM data for flow through parallel-plate ducts in Fig. 3 are for Pe=1, 2, 5, and 10. The graph shows that the lines converge to a single limiting dash line at very small $\bar{x}$. Figure 4 shows a similar behavior for heat transfer to a fluid flowing in circular ducts. In fact, in accordance to the entries in Tables 1 and 2, their limiting values are nearly the same. It is noted in Ref. [24] that conduction dominates when $\hat{x}$ becomes very small. Also, it is shown in Ref [24] (Fig. 3) that for slug flow over an infinite flat plate, $h_0\hat{x}/k$ approaches $1/\pi$ as $\bar{x}$ goes toward zero. This indicates that the $h_0\hat{x}/k$ values for slug flow over a partially heated infinite plate asymptotically approach $h_0\hat{x}/k = 1/\pi$, the solution for no flow condition. As shown in Figs. 3 and 4, this situation exists for each Peclet number and the dash lines show their limiting heat transfer behaviors. Indeed, the data clearly show a near linear behavior in log-log plot and the results from the weighted-residual method perform well. This satisfactory verification suggests that the weighted-residual method can provide acceptable results for determination of the effect of axial conduction in a fluid passing through a duct when the velocity field is two dimensional.

5 Application to Rectangular Passages

This methodology is tested for a square passage having constant wall temperature. Consideration is given to flow in a $2a \times 2b$ rectangular channel wherein $\theta = 0$ when $\hat{y} = \pm a$ and $\hat{z} = \pm b$ with symmetry conditions about $\hat{y} = 0$ and $\hat{z} = 0$ planes. The computational procedure begins after the selection of a set of basis functions that will satisfy the homogeneous boundary conditions of the first kind. As before, a set of polynomial-based basis functions is preferred mainly for convenience of symbolic integrations. Accordingly, the following set of the basis functions:

$$f_j(y,z) = (1 - y^2)(\bar{b}^2 - z^2) y^{2m_j} z^{2n_j} \quad \text{for} \quad j = 1,2,\ldots,N \tag{35a}$$

are selected, using all combinations of $m_j = 0,1,2,\ldots$ and $n_j = 0,1,2,\ldots$. As before the terms $y^{2m_j} z^{2n_j}$ are members of a poly-

Table 1 A comparison of heat transfer coefficient and bulk temperature by WRM with the Graetz-type solutions in parallel-plate ducts

		WRM		Graetz-type	
Pe	$\hat{x}/a$	h_0a/k	θ_b	h_0a/k	θ_b
	0.001	318.48	0.6692	292.95	0.6692
1	0.004	80.016	0.6669	80.012	0.6669
	0.01	32.267	0.6624	32.267	0.6624
	0.04	8.3817	0.6403	8.3816	0.6403
	0.1	3.5844	0.5987	3.5844	0.5987
	0.4	1.0967	0.4324	1.0967	0.4324
	1	0.4617	0.2293	0.4617	0.2293
	4	0.01924	0.00988	0.01924	0.00988
2	0.001	318.82	0.7841	293.28	0.7841
	0.004	80.355	0.7821	80.351	0.7821
	0.01	32.605	0.7781	32.605	0.7781
	0.04	8.7153	0.7587	8.7153	0.7587
	0.1	3.9103	0.7222	3.9103	0.7222
	0.4	1.3967	0.5711	1.3967	0.5711
	1	0.7216	0.3646	0.7216	0.3646
	4	0.07664	0.0400	0.07664	0.0400
5	0.001	319.43	0.9106	293.85	0.9106
	0.004	80.960	0.9093	80.956	0.9093
	0.01	33.207	0.9065	33.207	0.9065
	0.04	9.3037	0.8933	9.3037	0.8933
	0.1	4.4773	0.8685	4.4773	0.8685
	0.4	1.9106	0.7653	1.9106	0.7653
	1	1.2183	0.6101	1.2183	0.6101
	4	0.3936	0.2080	0.3936	0.2080
10	0.001	320.05	0.9564	294.40	0.9603
	0.004	81.576	0.9554	81.572	0.9555
	0.01	33.817	0.9535	33.817	0.9535
	0.04	9.8891	0.9442	9.8892	0.9442
	0.1	5.0235	0.9270	5.0235	0.9270
	0.4	2.3525	0.8576	2.3525	0.8576
	1	1.5982	0.7536	1.5982	0.7536
	4	0.8072	0.4274	0.8072	0.4274

nomial with a degree $2M$ in two dimensions space and each pair of (m_j, n_j) should satisfy the condition that $(m_j+n_j) \leq M$. The index j in each basis function $f_j(y,z)$ is related to (m_j, n_j) pair in this basis function; it is obtainable from an arithmetic progression relation that produces

$$j = 1 + n_j + \sum_{i=0}^{m_j+n_j} i = 1 + n_j + \frac{1}{2}(m_j + n_j)(m_j + n_j + 1) \quad (35b)$$

Also, the number of terms N is deterministic from Eq. (35*b*) by setting $m_j=0$ and $n_j=M$ to get $N=1+M(M+3)/2$. In these basis functions, the characteristic length is selected as $L_c=a$; this makes $y=\hat{y}/a$, $z=\hat{z}/a$, and $\bar{b}=b/a$.

As discussed earlier, the next task is the determination of the members of matrices **A**, **B**, and **C** using the Eqs. (16*a*)–(16*c*). Once this task is completed, Eq. (17) would provide the eigenvalues and the members of the corresponding eigenvector. This task becomes more demanding than that described earlier for passages with one-dimensional velocity fields. Also, the excellent accuracies observed for parallel-plate ducts and circular ducts cannot be realized with ease at small values of x. In the previous passages, when $N=125$, it required determination of eigenvalues and eigenvectors from Eq. (17) wherein each of the two matrices have 250×250 elements. To get a comparable accuracy for a rectangular duct, polynomials of the same degree should be used. This requires having $M=N-1=124$ and then each of the matrices **A**, **B**, and **C** will need 7875×7875 elements while the two matrices in Eq. (17) will become $15{,}750\times15{,}750$, extremely large in size. Therefore, the asymptotic solution mentioned earlier becomes a valuable tool, as it reduces the needed size of these matrices while accuracy remains reasonable. To illustrate this feature, data are acquired for a case when $\bar{b}=b/a=1$ and plotted in Fig. 5. The discrete circular symbols in Fig. 5 show the computed h_0a/k values by WRM as a function of $\hat{x}/a$ when $M=13$ while each of the matrices **A**, **B**, or **C** is having 105×105 elements. The plus symbols in Fig. 5 are for $M=14$ while each of the matrices is having 120×120 elements. This increase in the matrix size shows a small improvement in the plotted results. As before, the software MATHEMATICA [23] performed the symbolic and subsequent numerical computations. Occasionally, there was a repeated eigenvalue and it was recognized by this software.

As can be seen from discrete symbols in Fig. 5, the computed values begin to deviate from the expected solution. They depart from their expected path; increasing as $\hat{x}/a$ decreases to below 0.02 and then they decrease rapidly as $\hat{x}/a$ further decreases. Therefore, it becomes important to identify an asymptotic solution for h_0a/k values when $\hat{x}/a$ becomes very small. To accomplish this task, the solid line and the dash line in Fig. 5 are taken from Ref. [24]. The solid line is for slug flow over a infinite flat plate with an abrupt temperature change at $\hat{x}=0$ using the relation

$$\frac{h_0a}{k} = \frac{\mathrm{Pe}}{2\pi}\exp[(\hat{x}/a)\mathrm{Pe}/2]\{K_0[(\hat{x}/a)\mathrm{Pe}/2] + K_1[(\hat{x}/a)\mathrm{Pe}/2]\} \quad (36a)$$

where K_0 and K_1 are the modified Bessel functions. The dash line in Fig. 5 is for no flow over this infinite flat plate,

Table 2 A comparison of heat transfer coefficient and bulk temperature by WRM with the Graetz-type solutions in circular ducts

		WRM		Graetz-type	
Pe	$\hat{x}/r_0$	$h_0 r_o/k$	θ_b	$h_0 r_o/k$	θ_b
	0.001	318.17	0.6234	292.95	0.6234
1	0.004	79.689	0.6197	79.685	0.6197
	0.01	31.939	0.6123	31.939	0.6123
	0.04	8.0502	0.5771	8.0502	0.5771
	0.1	3.2496	0.5140	3.2496	0.5140
	0.4	0.7710	0.2959	0.7710	0.2959
	1	0.2085	0.1025	0.2085	0.1025
	4	0.00107	0.000546	0.00107	0.000546
2	0.001	318.49	0.7203	292.94	0.7203
	0.004	80.003	0.7169	79.999	0.7169
	0.01	32.251	0.7100	32.251	0.7100
	0.04	8.3544	0.6774	8.3544	0.6774
	0.1	3.5392	0.6183	3.5392	0.6183
	0.4	1.0050	0.4044	1.0050	0.4044
	1	0.3594	0.1822	0.3594	0.1822
	4	0.00701	0.00369	0.00701	0.00369
5	0.001	319.15	0.8588	293.55	0.8588
	0.004	80.664	0.8561	80.661	0.8561
	0.01	32.908	0.8508	32.908	0.8508
	0.04	8.3544	0.8257	8.9920	0.8257
	0.1	4.1450	0.7802	4.1450	0.7802
	0.4	1.5175	0.6092	1.5175	0.6092
	1	0.7749	0.3953	0.7749	0.3953
	4	0.0958	0.0519	0.0958	0.0519
10	0.001	319.87	0.9246	294.19	0.9246
	0.004	81.380	0.9226	81.377	0.9226
	0.01	33.617	0.9186	33.617	0.9186
	0.04	9.6694	0.8998	9.6694	0.8998
	0.1	4.7734	0.8662	4.7734	0.8662
	0.4	2.0211	0.7406	2.0211	0.7406
	1	1.1961	0.5749	1.1961	0.5749
	4	0.3532	0.1924	0.3532	0.1924

$$\frac{h_0 a}{k} = \frac{1}{\pi \hat{x}/a} \tag{36b}$$

The solid line approaches the dash line for pure conduction and the computed data by WRM show a similar behavior. These computed $h_0 a/k$ values by WRM exhibit good accuracies when $\hat{x}/a > 0.02$. The dash line in Fig. 5 can provide reasonably accurate asymptotic values when $\hat{x}/a < 0.02$. The remaining procedure is similar to that presented for parallel-plate ducts.

A knowledge of bulk temperature is a valuable issue in heat exchanger design application. Only a few eigenvalues are needed to obtain sufficiently accurate $\theta_b = (T_b - T_w)/(T_i - T_w)$ values. This

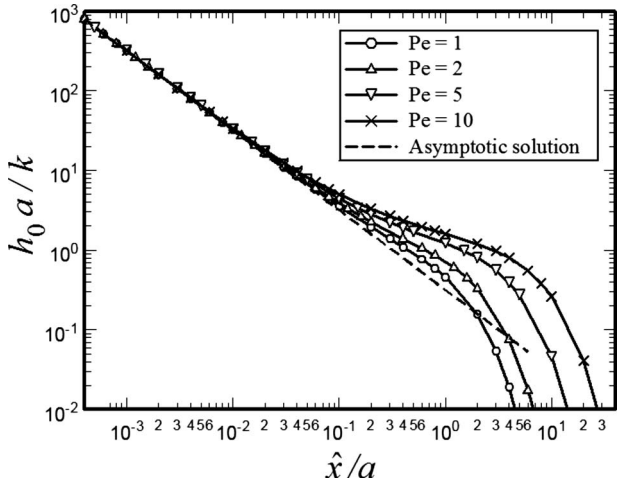

Fig. 3 Computed values of $h_0 a/k$ in parallel-plate ducts as a function of $\hat{x}/a$ by WRM for different Pe numbers

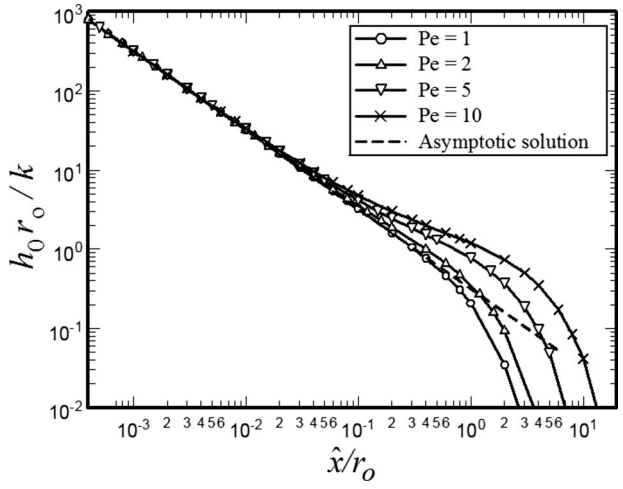

Fig. 4 Computed values of $h_0 r_o/k$ in circular ducts as a function of $\hat{x}/r_o$ by WRM for different Pe numbers

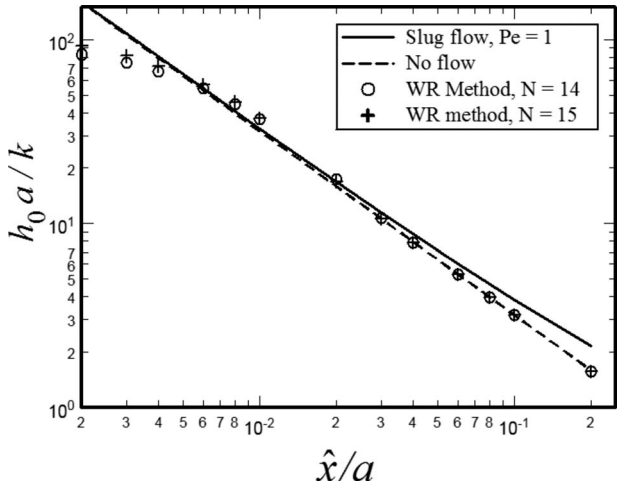

Fig. 5 Asymptotic behavior of the Nusselt number h_0a/k as a function of $\hat{x}/a$ and its comparison to slug flow over an infinite flat plate

task is accomplished and the solid lines representing the acquired $\theta_b(x)$ values are plotted as a function of $|\hat{x}|/a$ in Fig. 6(a) when $x<0$ and in Fig. 6(b) when $x>0$, for Pe=1, 2, 5, and 10. Moreover, the series solution converges well for determination of $\theta_b(0)$. When $x<0$, the asymptotic values of θ_b at small $|x|$ are obtained from the equation

$$\theta_{b,S}(|x|) = 1 - [1 - \theta_b(0)]\exp(\gamma_1 x) \tag{37a}$$

and they are plotted as dash lines with circular symbols in Fig. 6(a) as a function of $|\hat{x}|/a$. They behave well for all Pe values and extremely well for Pe=1 and 10. It is also possible to empirically define a simple correlation to predict the bulk temperature, that is,

$$\theta_b(|x|) = \left[\frac{(|\hat{x}|/L_c)D_1^- + 0.36\theta_b(0)}{D_1^- + 0.36}\right]\exp(\gamma_1 x) \tag{37b}$$

plotted with $\times$ symbols in Fig. 6(a). When $x>0$, the asymptotic values of θ_b are obtained from the equation

$$\theta_{b,S}(x) = \theta_b(0)\exp(-\lambda_1 x) \tag{38a}$$

at small x values and from the equation

$$\theta_{b,L}(x) = D_1^+(0)\exp(-\lambda_1 x) \tag{38b}$$

at large x values and they are plotted versus $\hat{x}/a$ as dash lines in Fig. 6(b). These are useful properties because combining these two limiting solutions again can lead to a simple correlation for the estimation of the often-needed bulk temperature. Then, the $\times$ symbols represent empirically predicted bulk temperature using a modified form of Eq. (37b), that is,

$$\theta_b(x) = \left[\frac{(\hat{x}/L_c)D_1^+ + 0.36\theta_b(0)}{D_1^+ + 0.36}\right]\exp(-\lambda_1 x) \tag{38c}$$

The parameters D_1^-, D_1^+, and $\theta_b(0)$ are in Table 3 for a range of Pe values. The $\times$ symbols in Fig. 6(b) are the data acquired from Eq. (38c) and they show reasonably good accuracies with an error of less than 1%, except at isolated spots within the midrange where the error moderately increases but remains below 2.5%. Therefore, the bulk temperature in heat exchanger design application becomes deterministic from a simple relation. Furthermore, it is important to note, from data in Figs. 6(a) and 6(b), that the variation of θ_b with $\hat{x}/a$ is very small in the neighborhood of $\hat{x}=0$ location.

Using the same set of Peclet numbers as those in Figs. 6(a) and 6(b), the computed values of h_0a/k for a square duct are plotted as a function of $|\hat{x}|/a$ in Fig. 7(a) when $x<0$ and in Fig. 7(b) when

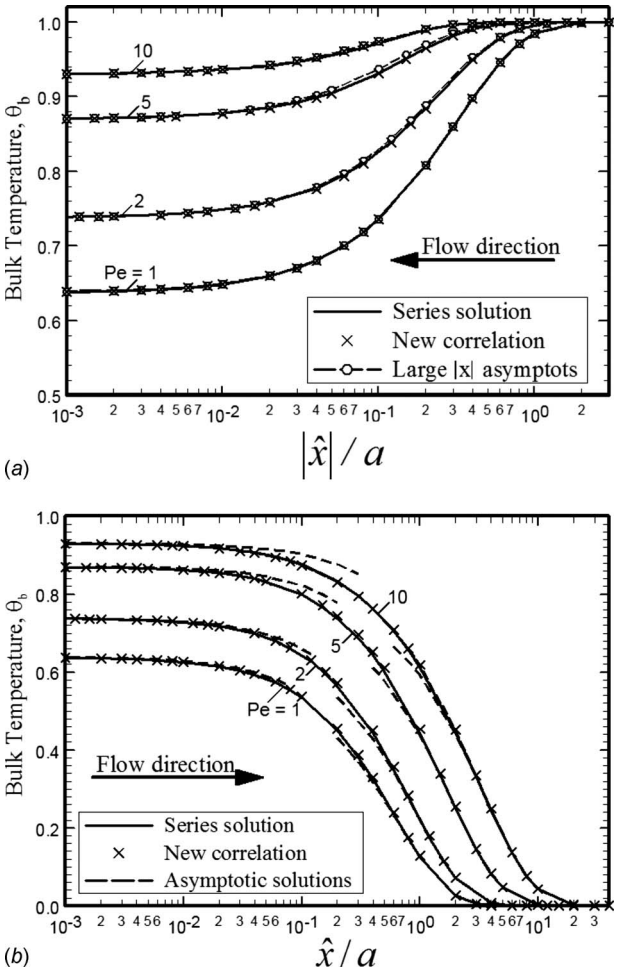

Fig. 6 Computed values of the bulk temperature θ_b in square ducts as a function of $\hat{x}/a$ by WRM for different Pe numbers: (a) when $x<0$ and (b) when $x>0$

$x>0$, using $M=14$. The convergence for determination of the Nusselt number becomes more demanding than that for determination of the bulk temperature. The computed Nusselt numbers were accurate to better than five significant figures when x is relatively large. The error begins to increase as the axial coordinate moves toward zero. The data in Figs. 7(a) and 7(b) show asymptotic behaviors for small $|x|$, similar to those plotted in Figs. 3 and 4 for parallel-plate ducts and circular ducts. However, the discrete data in Fig. 7(b) show that the error is graphically detectable as $\hat{x}/a$ decreases to below 0.02. Also, the data show that as $\hat{x}/a$ reduces to below 0.02 there is a small increase to be followed by a rapid decrease in h_0a/k for each Pe parameter. This phenomenon is not detectable in Fig. 3 or Fig. 4 where $N=125$ corresponds to $M=124$, which is much larger than $M=14$ used here. Therefore, the data behaviors in Fig. 7(b) suggest a need for the development of a methodology to improve the computed heat transfer near the entrance location.

Using the asymptotic behavior of the heat transfer results, one can get a reasonably accurate solution without having a large number of eigenvalues. As suggested by the data appearing in Fig. 7(b), the accurately computed Nusselt number values are for $\hat{x}/a>\varepsilon$ and their accuracies begin to improve as their $\hat{x}/a$ values increase to above the $\hat{x}/a=\varepsilon$ for $\varepsilon\cong 0.02$. When $\hat{x}/a<0.02$, the values of Nu_D are obtainable from an empirically augmented form of Eq. (36b), that is,

Table 3 Selected parameters for laminar flow in square ducts

$x<0$					
Pe	γ_1	E_1^-	D_1^-	$\mathrm{Nu}_D(\infty)$	$\theta_b(0)$
1	3.172	0.7213	0.3630	0.0	0.638
2	8.589	0.7478	0.2921	0.0	0.738
3	16.27	0.9124	0.2530	0.0	0.803
5	36.39	1.378	0.1872	0.0	0.870
7	60.37	1.638	0.1285	0.0	0.904
10	101.4	1.728	0.0765	0.0	0.930
$x>0$					
Pe	λ_1	E_1^+	D_1^+	$\mathrm{Nu}_D(\infty)$	$\theta_b(0)$
1	1.545	0.9373	0.5888	3.184	0.638
2	2.232	1.035	0.6714	3.083	0.738
3	2.547	1.094	0.7205	3.038	0.803
5	2.791	1.149	0.7654	3.004	0.870
7	2.877	1.171	0.7827	2.992	0.904
10	2.926	1.184	0.7932	2.985	0.930

$$\mathrm{Nu}_0 \cong \left(\frac{1}{\pi\hat{x}/a}\right)\frac{1}{1-\omega\hat{x}/a} = \frac{\mathrm{Nu}_{0,S}}{1-\omega\hat{x}/a} \tag{39}$$

Clearly the value of ω depends on the value of $\mathrm{Nu}_0(\varepsilon)$ selected at a predetermined value of $\hat{x}/a=\varepsilon$. The parameter ω can be estimated using the difference between the computed Nusselt number $\mathrm{Nu}_0(\varepsilon)$ and the asymptotic Nusselt numbers $\mathrm{Nu}_{0,S}=1/(\pi\hat{x}/a)$ from Eq. (36*b*), to be designated as $\delta=\mathrm{Nu}_0(\varepsilon)-\mathrm{Nu}_{0,S}(\varepsilon)$. Then, a simple algebra yields the estimated value of ω as $\omega=\pi\delta/(1+\varepsilon\pi\delta)$.

Next, it is interesting to show the domain wherein the effect of axial conduction should not be ignored. Therefore, a comparison of heat transfer values with and without the effect of axial conduction is of interest. To accomplish this task, data are acquired and plotted in Fig. 8 for Pe=1, 2, 5, and 10. The abscissa of this figure is $x=(\hat{x}/a)/\mathrm{Pe}$ and the ordinate is the classical Nusselt number $\mathrm{Nu}_D=hD_h/k$ wherein $h(x)=h_0(x)/\theta_b(x)$. The solid lines in Fig. 8 represent the Nusselt number using calculus of variations with $M=14$ and plotted for $\hat{x}/a\geq\varepsilon$ with $\varepsilon=0.02$ as suggested by the data appearing in Fig. 7(*b*). The dash lines plotted in Fig. 8 are for Pe=1, 2, 5, and 10 representing $\mathrm{Nu}_D=\mathrm{Nu}_0(D_h/a)/\theta_b$ using the values of Nu_0 as given by Eq. (39), with $\hat{x}/a$ being replaced by x Pe, and the estimated value of bulk temperature comes from Eq. (38*c*). This asymptotic solution is valid as x goes toward zero and it is not valid when the continuum condition begins to fail. A detailed discussion of this issue is in Ref. [24].

Neglecting the effect of axial conduction, the Nu_D values as a function of x are available in the literature. For comparison, the values of Nu_D and its asymptotic values from Refs. [25,26] are

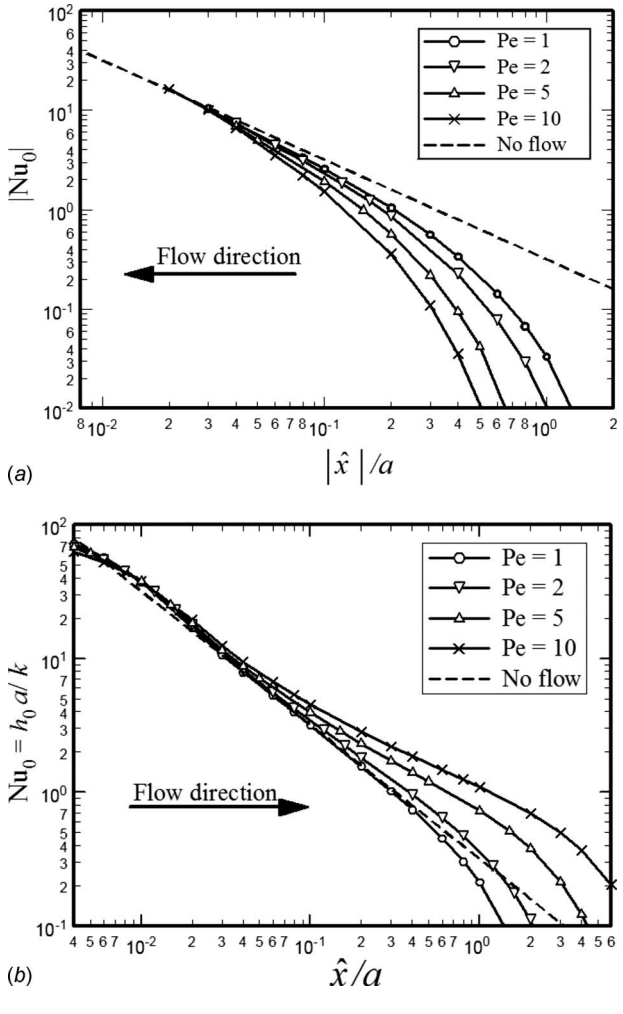

Fig. 7 Computed values of h_0a/k in rectangular ducts as a function of $\hat{x}/a$ by WRM for different Pe numbers: (*a*) when $x<0$ and (*b*) when $x>0$

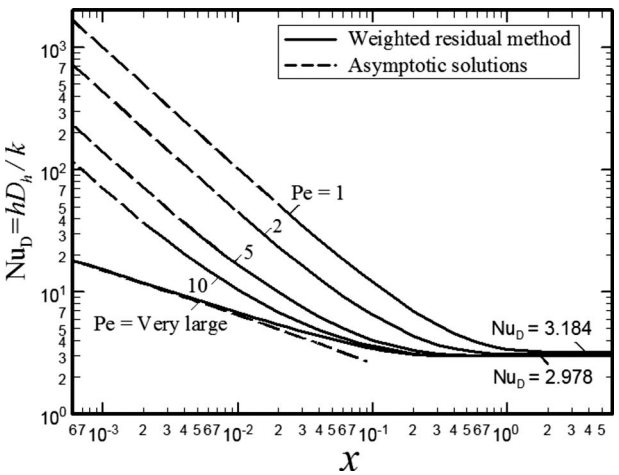

Fig. 8 Nusselt number Nu_D for a square duct as a function of axial coordinate $(\hat{x}/a)/\mathrm{Pe}$ for different Pe numbers

also plotted in Fig. 8. It is to be noted that at small x, the Nu_D values with axial conduction are significantly larger than the corresponding values in the absence of axial conduction, depending on the size of the Peclet number. The data at very large x values show that the contribution of axial conduction reduces but remains significant when Pe is small.

6 Conclusion

It is shown that the WRM based on variational calculus is a valuable tool for determination of wall heat flux in passages with two-dimensional velocity fields, e.g., rectangular ducts. This methodology is a useful tool for the study of heat transfer in other engineering applications wherein the axial conduction should not be ignored in the fluid passages. For example, it can be used for determination of heat transfer in porous ducts filled with metallic foams, in electronic cooling applications.

The acquired information in Fig. 7(*b*) shows that, at small values of $\hat{x}$, there is a relatively small dependency on the size of velocity presented as the Peclet number. Also, as can be seen from Fig. 8, the axial conduction has a significant contribution and a large error can be realized if it is ignored. In general, when the heated section is small, a relatively large error is expected if the axial thermal conduction is neglected.

Nomenclature

a, b = half of the spacing between parallel plates, m
a_{ij} = elements of matrix **A**
A = cross section area, m^2
$\mathbf{A}$ = matrix of coefficients a_{ij}
$\bar{b}$ = b/a
c_{ij} = elements of matrix **C**
c_p = specific heat, J/kg K
C = capacitance ρc_p, J/m^3 K
$\mathbf{C}$ = matrix of coefficients c_{ij}
d_{mj} = coefficient in matrix **D**
D_1 = first coefficient for $\theta_b(x)$
D_h = hydraulic diameter, $4A/\Gamma$, m
$\mathbf{D}$ = matrix with coefficients d_{mj}
E_1 = first coefficient for $Nu(x)=h_0L_c/k$
E_m, F_m = constants
h = heat transfer coefficient $q_w/(T_w-T_b)$, W/m^2 K
h_0 = heat transfer coefficient $q_w/(T_w-T_i)$, W/m^2 K
i, j = indices
f_j = basis functions in weighted-residual method
k = thermal conductivity, W/m K
L_c = characteristic length, m
M = polynomial degree
N = number of terms in series
m, n = indices
Nu_0 = h_0L_c/k, see Eq. (13)
Nu_D = hD_h/k
Pe = Peclet number, UL/α
Pr = Prandtl number $\mu c_p/k$
q_w = wall heat flux, W/m^2
r = $\hat{r}/r_o$
$\hat{r}$ = radial coordinate, m
r_o = pipe radius, m
T = temperature, K
T_b = bulk or mean temperature, K
T_i = wall temperature when $x<0$, K
T_w = wall temperature when $x>0$, K
u = velocity, m/s
U = average velocity, m/s
$\hat{x}$ = axial coordinate, m
x = $(\hat{x}/L_c)/\text{Pe}$
y, z = $\hat{y}/a$ and $\hat{z}/a$
$\hat{y}, \hat{z}$ = coordinates, m

Greek Symbols

α = thermal diffusivity, m^2/s
β_m = eigenvalues
Γ = boundary of the duct, m
δ = difference, $Nu_0(\varepsilon)-1/(\pi\hat{x}/a)$
ε = a small constant
θ = dimensionless temperature
λ_m = eigenvalues
μ = viscosity coefficient, N s/m^2
ρ = density, kg/m^3
Φ_m, Ψ_m = special functions

Subscripts

L = large
S = small
w = wall

Superscripts

$-$ = when $\hat{x}<0$
$+$ = when $\hat{x}>0$

References

[1] Kays, W. M., and Perkin, M. E., 1973, "Forced Convection: Internal Flow in Ducts," *Handbook of Heat Transfer*, W. M. Rohsenow and J. P. Hartnett, eds., McGraw-Hill, New York, Sec. 7.
[2] Shah, R. K., and London, A. L., 1978, "Laminar Flow Forced Convection in Ducts," *Advances in Heat Transfer*, Academic, New York, Supplement 1.
[3] Kays, W. M., and Crawford, H. C., 1993, *Convective Heat and Mass Transfer*, 3rd ed., McGraw-Hill, New York.
[4] Burmeister, L. C., 1993, *Convective Heat Transfer*, 2nd ed., Wiley, New York.
[5] Bejan, A., 1982, *Convection Heat Transfer*, 2nd ed., Wiley, New York.
[6] Haji-Sheikh, A., Minkowycz, W. J., and Sparrow, E. M., 2004, "Green's Function Solution of Temperature Field for Flow in Porous Passages," Int. J. Heat Mass Transfer, **47**(22), pp. 4685–4695.
[7] Haji-Sheikh, A., Minkowycz, W. J., and Sparrow, E. M., 2004, "A Numerical Study of the Heat Transfer to Fluid Flow Through Circular Porous Passages," Numer. Heat Transfer, Part A, **46**(10), pp. 929–956.
[8] Lahjomri, J., and Oubarra, A., 1999, "Analytical Solution of the Graetz Problem With Axial Conduction," ASME J. Heat Transfer, **121**(4), pp. 1078–1083.
[9] Lahjomri, J., Oubarra, A., and Alemany, A., 2002, "Heat Transfer by Laminar Hartmann Flow in Thermal Entrance Region With a Step Change in Wall Temperature: The Graetz Problem Extended," Int. J. Heat Mass Transfer, **45**(5), pp. 1127–1148.
[10] Weigand, B., and Lauffer, D., 2004, "The Extended Graetz Problem With Piecewise Constant Wall Temperature for Pipe and Channel Flows," Int. J. Heat Mass Transfer, **47**(24), pp. 5303–5312.
[11] Michelsen, M. L., and Villadsen, J., 1974, "The Graetz Problem With Axial Heat Conduction," Int. J. Heat Mass Transfer, **17**(11), pp. 1391–1402.
[12] Lelea, D., 2007, "The Conjugate Heat Transfer of the Partially Heated Microchannels," Heat Mass Transfer, **44**(1), pp. 33–41.
[13] Tiselj, I., Hetsroni, G., Mavko, B., Mosyak, A., Pogrebnyak, E., and Segal, Z., 2004, "Effect of Axial Conduction on the Heat Transfer in Micro-Channels," Int. J. Heat Mass Transfer, **47**(12–13), pp. 2551–2565.
[14] Erbay, L., Yalçin, M., and Ercan, M., 2007, "Entropy Generation in Parallel Plate Microchannels," Heat Mass Transfer, **43**(8), p. 849.
[15] Minkowycz, W. J., and Haji-Sheikh, A., 2006, "Heat Transfer in Parallel-Plate and Circular Porous Passages With Axial Conduction," Int. J. Heat Mass Transfer, **49**(13–14), pp. 2381–2390.
[16] Sparrow, E. M., and Seigel, R., 1959, "A Variational Method for Fully Developed Laminar Heat Transfer in Ducts," ASME J. Heat Transfer, **81**(2), pp. 157–167.
[17] Kantorovich, L. V., and Krylov, V. I., 1960, *Approximate Methods of Higher Analysis*, Wiley, New York.
[18] LeCory, R. C., and Eraslan, A. H., 1969, "The Solution of Temperature Development in the Entrance Region of an MHD Channel by the G. F. Galerkin Method," ASME J. Heat Transfer, **91**(2), pp. 212–220.
[19] Lakshminarayanan, R., and Haji-Sheikh, A., 1992, "Entrance Heat Transfer in Isosceles and Right Triangular Ducts," J. Thermophys. Heat Transfer, **6**(1), pp. 167–171.
[20] Haji-Sheikh, A., Sparrow, E. M., and Minkowycz, W. J., 2005, "Heat Transfer to Flow Through Porous Passages Using Extended Weighted Residuals Method—A Green's Function Solution," Int. J. Heat Mass Transfer, **48**(7), pp. 1330–1349.
[21] Beck, J. V., Cole, K. D., Haji-Sheikh, A., and Litkouhi, B., 1992, *Heat Conduction Using Green's Functions*, Hemisphere, Washington, DC.
[22] Meirovitch, L., 1967, *Analytical Methods in Vibrations*, MacMillan, New York.

[23] Wolfram, S., 2005, *The Mathematica Book*, 5th ed., Cambridge University Press, Cambridge.
[24] Haji-Sheikh, A., Amos, D. E., and Beck, J. V., 2008, "Axial Conduction of Heat in a Moving Semi-Infinite Fluid," Int. J. Heat Mass Transfer, **51**(19–20), pp. 4651–4658.
[25] Haji-Sheikh, A., 2004, "Estimation of Average and Local Heat Transfer in Parallel Plates and Circular Ducts Filled With Porous Materials," ASME J. Heat Transfer, **126**(3), pp. 400–409.
[26] Haji-Sheikh, A., and Beck, J. V., 2007, "Entrance Effect on Heat Transfer to Laminar Flow Through Passages," Int. J. Heat Mass Transfer, **50**(17–18), pp. 3340–3350.

Numerical Study of Flow and Heat Transfer Enhancement by Using Delta Winglets in a Triangular Wavy Fin-and-Tube Heat Exchanger

Liting Tian

Yaling He[1]
e-mail: yalinghe@mail.xjtu.edu.cn

Pan Chu

Wenquan Tao

State Key Laboratory of Multiphase Flow in Power Engineering,
School of Energy and Power Engineering,
Xi'an Jiaotong University,
Xi'an 710049, China

In this paper, three-dimensional numerical simulations with renormalization-group (RNG) k-ε model are performed for the air-side heat transfer and fluid flow characteristics of wavy fin-and-tube heat exchanger with delta winglet vortex generators. The Reynolds number based on the tube outside diameter varies from 500 to 5000. The effects of different geometrical parameters with varying attack angle of delta winglet ($\beta=30$ deg, $\beta=45$ deg, and $\beta=60$ deg), tube row number (2–4), and wavy angle of the fin ($\theta=0-20$ deg) are examined. The numerical results show that each delta winglet generates a downstream main vortex and a corner vortex. The longitudinal vortices are disrupted by the downstream wavy trough and only propagate a short distance along the main flow direction but the vortices greatly enhance the heat transfer in the wake region behind the tube. Nusselt number and friction factor both increase with the increase in the attack angle β, and the case of $\beta=30$ deg has the maximum value of j/f. The effects of the tube row number on Nusselt number and friction factor are very small, and the heat transfer and fluid flow become fully developed very quickly. The case of $\theta=5$ deg has the minimum value of Nusselt number, while friction factor always increases with the increase in wavy angle. The application of delta winglet enhances the heat transfer performance of the wavy fin-and-tube heat exchanger with modest pressure drop penalty.
[DOI: 10.1115/1.3139106]

Keywords: vortex generator, wavy fin-and-tube heat exchanger, enhanced heat transfer

1 Introduction

Fin-and-tube heat exchangers are widely used in many fields such as air-conditioning, refrigeration, automobile, process industry, etc. The dominant thermal resistance of fin-and-tube heat exchanger is usually on the air side, which may account for 85% or more of the total thermal resistance. The use of enhanced fin surface is the most effective way to improve the overall performance of the fin-and-tube heat exchanger to meet the demand of high efficiency and low cost. In recent years, as an air-side heat transfer enhancement strategy, longitudinal vortex generators (LVGs) widely applied in various heat exchangers to increase the heat transfer coefficient with only a small increase in pressure drop penalty were studied in many literatures. Wang et al. [1] utilized a dye-injection technique to visualize the flow structure for enlarged plain fin-and-tube heat exchanger with annular and delta winglet vortex generators. Tiwari et al. [2] made a numerical study of laminar flow and heat transfer in a channel with built-in oval tube and delta winglets. The different attack angles and the axial locations of the winglets were considered. The results indicated that vortex generators in conjunction with the oval tube definitely enhanced heat transfer of fin-tube heat exchangers. O'Brien et al. [3] presented an experimental study of forced convection heat transfer in a narrow rectangular duct fitted with an oval tube and one or two delta-winglet pairs. Mean heat transfer results indicated that the addition of the single winglet pair to the oval-tube geometry yielded significant heat transfer enhancement, averaging 38% higher than the oval-tube and no-winglet case, and the corresponding increase in friction factor was limited to less than 10%. Biswas et al. [4] presented a numerical investigation of the flow structure and heat transfer enhancement in a channel with a built-in circular tube and a pair of delta winglets. The results showed that the longitudinal vortices generated by the winglets placed in the wake region behind the tube enhanced the local heat transfer by 240%. Leu et al. [5] carried out numerical and experimental analyses to study the effects of different attack angles ($\beta=30$ deg, $\beta=45$ deg, and $\beta=60$ deg) in the three-row plain fin-and-tube heat exchanger with rectangular winglets mounted behind the tube. They reported that the case of $\beta=45$ deg provided the best heat transfer enhancement. Torii et al. [6] proposed a novel delta winglet configuration called common-flow-up. The proposed configuration was shown to be effective in delaying boundary layer separation from the tube, reducing form drag, and removing the zone of poor heat transfer from the near-wake of the tube. Jain et al. [7] numerically simulated the flow structure and heat transfer in a rectangular channel with a built-in circular tube and delta winglets in a common-flow-up configuration. The average Nusselt number for the enhanced case was improved by 35% compared with the baseline case for a Reynolds number of 1000. The friction factor was not computed. Joardar et al. [8] carried out an experimental study of the flow and heat transfer in the seven-row plain fin-and-tube heat exchanger with different delta winglet array designs in a common-flow-up configuration. The results indicated that vortex generator arrays could significantly enhance the performance of fin-and-tube heat exchangers. Wang et al. [9]

[1]Corresponding author.

Contributed by the Heat Transfer Division of ASME for publication in the JOURNAL OF HEAT TRANSFER. Manuscript received April 22, 2008; final manuscript received April 15, 2009; published online June 22, 2009. Review conducted by S. A. Sherif.

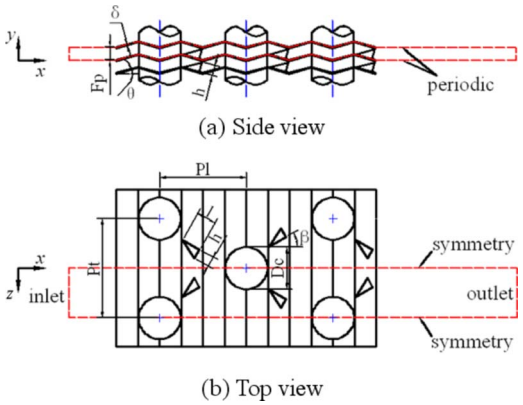

Fig. 1 Physical model and relevant geometrical parameters of the wavy fin-and-tube heat exchanger with delta winglets

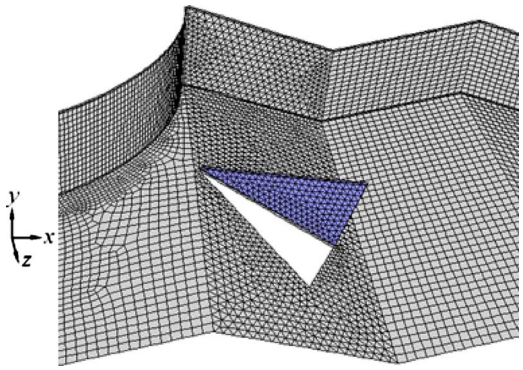

Fig. 2 Grid system around the delta winglet and tube

experimentally studied the local and average heat transfer characteristics over a complete flat tube-fin element with four vortex generators per tube. The results revealed that LVGs could efficiently enhance the heat transfer in the region near flat tube on the fin surface. Jacobi and co-workers [10,11] conducted extensive studies in LVGs: They applied wing-type longitudinal vortex generators in the offset-strip fin array and the flat tube louvered-fin compact heat exchanger. Sanders and Thole [12] combined the winglet and louvered-fin heat exchanger. The experimental studies presented heat transfer augmentation along the tube wall through the use of winglets placed on the louvers.

The foregoing literature review indicates that the LVGs were applied in various fin-and-tube heat exchangers in order to improve the air-side heat transfer, such as the plain fin-and-tube heat exchanger with round, oval, or flat tube, the offset-strip fin, the louvered-fin compact heat exchangers, etc. However, there is no report on LVG application to wavy fin-and-tube heat exchangers. The wavy fin widely used in air-conditioning and refrigeration fields can increase the heat transfer area, periodically change the main flow direction, and cause better airflow mixing. However, there are still a lot of wake regions behind the tube, which lead to the local heat transfer deterioration. The application of the delta winglet longitudinal vortex generators can effectively improve these situations.

The present study will focus on detailed study on the complex flow and heat transfer interactions resulting from deploying delta winglet vortex generators in a wavy fin-and-tube heat exchanger. Numerical simulation will also be applied to examine the effects of three geometrical parameters including attack angle of delta winglet, tube row number, and wavy angle of the fin on the heat transfer and fluid flow for this new fin pattern. Two different performance evaluation criteria (PEC) of heat exchangers are used to quantitatively assess the effects of these geometrical parameters.

2 Model Description

2.1 Physical Model. The schematic diagram of a wavy fin-and-tube heat exchanger with delta winglet longitudinal vortex generators is shown in Fig. 1. A pair of delta winglets is punched out from the triangular wavy fin symmetrically behind each round tube in a staggered arrangement. The tube outside diameter D_c is 10.55 mm, the longitudinal tube pitch P_l is 21.65 mm, the transverse tube pitch P_t is 25 mm, the fin pitch F_p is 3.2 mm, and the fin thickness δ_f is 0.2 mm. The different wavy angles of the fin θ (θ=0–20 deg) are investigated in this study. The base length l and height h of delta winglet are 5 mm and 2.5 mm, respectively. The width of the delta winglet is equal to the fin thickness. The attack angle of the delta winglet β has three different values (β=30 deg, β=45 deg, and β=60 deg). Due to symmetry, the region sketched by the dashed lines in Fig. 1 is selected as the computational domain, and the neighboring two fins' centric surfaces are selected as the upper and lower boundaries of the computational domain. The computational domain is extended upstream ten times of the fin spacing so that a uniform velocity distribution can be ensured at the domain inlet. The computational domain is also extended downstream 30 times of the fin spacing in order to avoid recirculation at the computational domain outlet, and hence the outflow boundary condition can be applied.

2.2 Governing Equations and Boundary Conditions. For this model, the air is considered as an incompressible fluid with constant physical properties. The thermal contact resistance between the tube and fin collar is ignored. Due to the relatively high heat transfer coefficient on the tube side and the high thermal conductivity of the tube wall, the tube is assumed to be at constant temperature. However, the temperature distribution in the fin surface has to be calculated, and the fluid-solid conjugate heat transfer is taken into account. The flow in the computational domain is assumed to be three-dimensional, turbulent, steady, and no viscous dissipation. The effect of turbulence on the flow field is included through the application of RNG k-ε turbulence model [13]. For the simplicity of presentation, the governing equations and boundary conditions for numerical simulation in this paper can be found in Ref. [14] and will not be restated here.

3 Numerical Methods and Grid Independence Validation

The foregoing governing equations and the boundary conditions are solved with a commercial computational fluid dynamics code (FLUENT 6.2). The multiblock hybrid approach is used to generate the meshes for the numerical simulation. The grids around the delta winglet and the tube are shown in Fig. 2. The governing equations are discretized by the finite volume method. The second-order upwind scheme is used to derive the face values for space discretization of the momentum, turbulence, and energy equations, whereas the diffusion terms are discretized by the central difference scheme. The semi-implicit method for pressure linked equations (SIMPLE) algorithm [13] is utilized to deal with the coupling of pressure and velocity.

Grid independence is investigated to ensure the accuracy and validity of the numerical results. The grid independent study is performed for the two-row case at attack angle β=45 deg, wavy angle θ=15 deg, and Re_{D_c}=2000. Three different grid numbers are studied, which have about 80,000, 130,000, and 250,000 cells, respectively. The difference in the Nusselt number between the three results is less than 1%, as shown in Table 1. The adopted grid number in the computational domain is about 130,000 for the two-row case. Similar examinations are also conducted for three-row and four-row cases. The final adopted grid numbers were about 190,000 and 255,000 for three-row and four-row cases, respectively.

Table 1 Results of different grid numbers

Grid No.	80,000	130,000	250,000
Nu	34.82	35.10	35.28
f	0.0764	0.0763	0.0762

4 Data Reduction Method

In order to present the simulation results, some parameters are defined as follows:

$$\mathrm{Re}_{D_c} = \frac{\rho u_m D_c}{\mu}, \quad \mathrm{Nu} = \frac{hD_c}{\lambda} \tag{1}$$

where D_c is the tube outside diameter and u_m is the mean velocity at the minimum flow cross-sectional area A_c.

The heat transfer coefficient h is defined in terms of the heat transfer rate Q and the log-mean temperature difference ΔT. The heat transfer rate Q is determined by the aid of FLUENT.

$$h = \frac{Q}{\eta_0 A_0 \Delta T} \tag{2}$$

The surface efficiency η_0 is calculated from the fin efficiency η_f.

$$\eta_0 = 1 - \frac{A_f}{A_0}(1 - \eta_f) \tag{3}$$

where A_f is the fin surface area, A_0 is the total surface area, and η_f is obtained by using Schmidt's method [15].

The spanwise averaged local heat transfer coefficient h_x is defined by

$$h_x = \frac{q_x}{T_{f,x} - T_{a,x}} \tag{4}$$

where q_x is the spanwise averaged local heat flux, $T_{f,x}$ is the spanwise averaged local wall temperature, and $T_{a,x}$ is the mass-weighted average air temperature of the flow cross section.

The Colbum factor j and friction factor f are defined as follows:

$$j = \frac{\mathrm{Nu}}{\mathrm{RePr}^{1/3}} = \frac{h}{\rho u_m c_p}\mathrm{Pr}^{2/3}, \quad f = \frac{\Delta p}{\frac{1}{2}\rho u_m^2} \cdot \frac{A_c}{A_0} \tag{5}$$

The PEC of heat exchangers is used to quantitatively assess the heat transfer augmentation versus the pressure drop penalty. The commonly used criteria are the "area goodness factor," j/f, and "volume goodness factor." The volume goodness factor comparison is defined as

$$Z = \eta_0 h \frac{4\sigma}{D_h}, \quad E = \Delta p\left(\frac{\dot{m}}{A_0 \rho}\right)\frac{4\sigma}{D_h} \tag{6}$$

where $\sigma = A_c/A_{\mathrm{frontal}}$ and $\dot{m}$ is the mass flow rate of the fluid. Z represents the heat transfer power per unit temperature difference and per unit core volume and E represents the fan power per unit core volume.

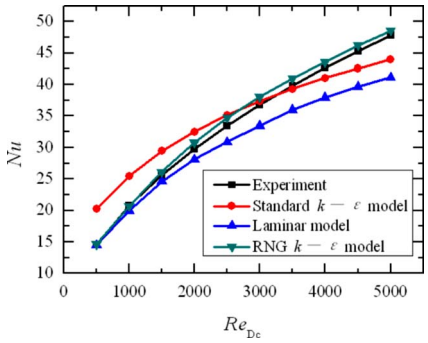

Fig. 3 Validation of numerical models with experimental results

5 Results and Discussions

5.1 Model Verification. In order to validate the reliability of the computational model and numerical method, numerical simulation is carried out at the same fin geometrical configurations and operating conditions as presented in Ref. [16]. The computation is conducted for the two-row wavy fin-and-tube heat exchanger with wavy angle $\theta = 15$ deg. The Reynolds number Re_{D_c} ranges from 500 to 5000. Three different models, namely, laminar model, standard k-ε model, and RNG k-ε model, are chosen to simulate the flow of the fin channel. The RNG model has shown substantial improvements over the standard model where the flow feature includes strong streamline curvature, vortices, and rotation. The comparisons of the numerical and experimental results are provided in Fig. 3, The RNG k-ε model seems to give the best results, and it satisfactorily predicts the relation of Nu with Re. The maximum difference in Nu of the RNG k-ε model from experimental results is 4%, which is in good agreement with the experimental results; therefore, the RNG k-ε model is selected for this study.

5.2 Longitudinal Vortex Effect. The delta winglets are punched out from the wavy fin behind the tube when the air flows over the delta winglets and the pressure difference between the front surface (facing the flow) and the back surface generates the longitudinal vortices. In order to examine the effects of the longitudinal vortices on the fluid flow and heat transfer processes in the fin channel, the three-row case with attack angle $\beta = 45$ deg and wavy angle $\theta = 15$ deg is examined. Figure 4 presents the secondary velocity vectors of the cross section ($x = 21$ mm) behind the trailing edge of the first-row delta winglet in the wavy fin for $\mathrm{Re}_{D_c} = 3000$. Beside the wake region behind the tube, there are two counter-rotating vortices generated by each delta winglet: a main vortex and a corner vortex. The main vortex, located directly downstream of the delta winglet, is formed by flow separation at

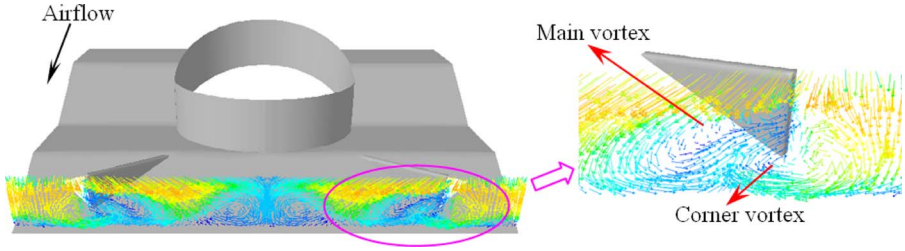

Fig. 4 Secondary velocity vectors at the cross section of $x = 21$ mm for $\mathrm{Re}_{D_c} = 3000$

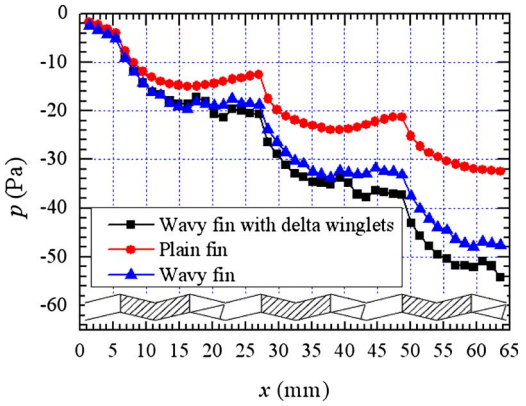

Fig. 5 Distribution of local average pressure along the streamwise direction for $Re_{D_c}=3000$

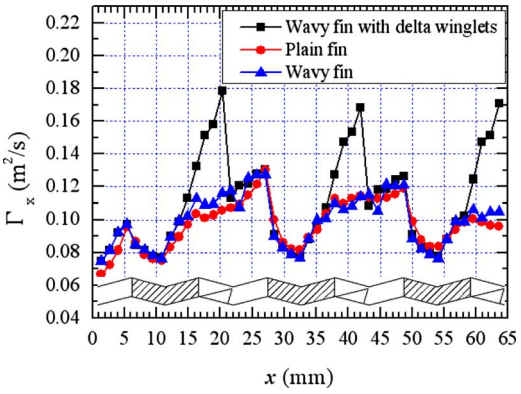

Fig. 6 Distribution of circulation of flow cross section along the streamwise direction for $Re_{D_c}=3000$

the leading edge of the delta winglet. The corner vortex featuring a horseshoe vortexlike characteristic feature, located outside of the main vortex, is generated at the junction of the upstream-facing pressure side of the winglet and the fin surface. These vortices generated by the delta winglet cause the swirling motion and enhance the fluid transport from the mainstream region to the wake region, and the size of the wake region behind the tube is reduced. At the same time, the down-wash flow appears near the fin surface, the near-wall temperature gradient is increased, and the heat transfer in this wake region is enhanced.

5.3 Heat Transfer and Fluid Flow Performance. The present study compares three different fin patterns, namely, plain fin, wavy fin with delta winglets, and wavy fin without delta winglets, to observe the heat transfer and fluid flow performance of the wavy fin-and-tube heat exchanger with delta winglets. Again the three-row heat exchanger with attack angle $\beta=45$ deg and wavy angle $\theta=15$ deg, under the condition of $Re_{D_c}=3000$, is studied. Figure 5 shows the variation in local average pressure in the main flow direction for three different fin patterns. The local average pressure at any cross section is determined by the area-weighted average static pressure at this cross section. The shadow regions in the figure represent the axial locations of the round tubes. Due to the decreased flow cross-sectional area between tubes, the flow accelerates around the tube, the local average pressure starts with a steep drop near the tube, and then increases behind the tube because of the increase in the flow cross-sectional area. For the wavy fin with delta winglets, the local average pressure has a slight drop at the axial location of the delta winglet, which is due to a small form drag induced by the slender delta winglet. In addition, the longitudinal vortices generated by the delta winglet decrease the wake region behind the tube so that the form drag of the tube decreases. According to the figure, the increase in the pressure drop penalty induced by the delta winglet is relatively small.

In order to investigate the development of the longitudinal vortices together with the main flow, Fig. 6 shows the circulation of the flow cross section along the main flow direction for three different fin patterns. The circulation of flow cross section is calculated by the area integral over magnitude of vorticity vector, $\Gamma_x=\int \xi dA=\int|\nabla\times \mathbf{U}|dA$. The circulation shows periodicity in the streamwise direction corresponding to the locations where the tubes and delta winglets are approached by the flow. The circulation increases when air encounters the tube with the horseshoe vortices being formed, and then the flow cross-sectional area gradually decreases and the flow accelerates. The vortices are compressed and the circulation decreases until it approaches the axial location corresponding to the minimum flow cross-sectional area. On the back half of the tube, the flow gradually decelerates and the circulation gradually increases. For the wavy fin with delta winglets, the circulation has an abrupt rise around the delta winglet, followed by a steep drop when the flow encounters the first wavy trough behind the delta winglet. As mentioned, when the air flows over the delta winglet, the longitudinal vortices are generated at the leading edge of the delta winglet and develop downstream together with the main flow. The vortex strength is enhanced and the circulation is increased at the position of the delta winglet. However, the main flow direction changes at the downstream wavy trough and the downstream tube blocks the flow. The vortices are disrupted by downstream wavy trough and only propagate a short distance along the streamwise direction. The vortex strength is weakened and the circulation is decreased at the position of the downstream wavy trough.

Figure 7 shows the dimensionless temperature distribution on the bottom fin surface for three different fin patterns $(T_f-T_{in})/(T_w-T_{in})$. By comparing three different fin patterns, it can be seen that the temperature gradient behind the tubes in the wavy fin with delta winglets is the largest among the three fins. The longitudinal vortices generated by the delta winglet strengthen the

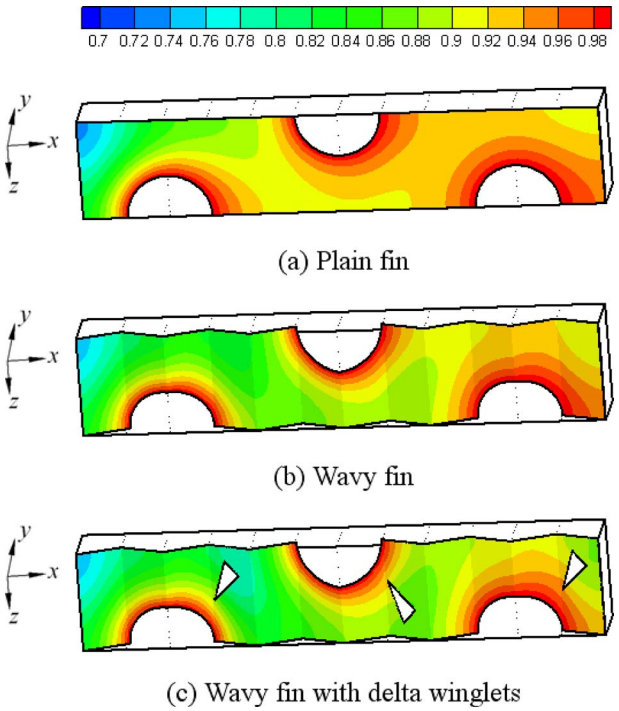

Fig. 7 Dimensionless temperature distribution on the bottom fin surface, $(T_f-T_{in})/(T_w-T_{in})$

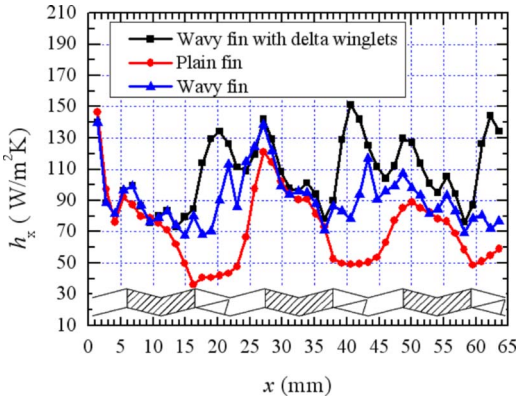

Fig. 8 Distribution of spanwise averaged local heat transfer coefficient along the streamwise direction for Re_{D_c}=3000

disturbance and mixing effects of the downstream air and spur the main flow of lower temperature to mix with the fluid of higher temperature in the tube wake. The wake region behind the tube is compressed and the heat transfer of the fin surface in the wake region is enhanced.

In order to examine heat transfer behavior along the flow direction, the spanwise averaged local heat transfer coefficient distribution on three different fins along the main flow direction is calculated and presented in Fig. 8. For the wavy fin with delta winglets, the local heat transfer coefficient is high at three locations: fin leading edge, front stagnation region of the tube, and delta winglet. The main difference in the wavy fin with and without delta winglets also occurs at the axial location of the wake region behind the tube. At the axial location of the delta winglet, the local heat transfer coefficient reaches a local maximum value due to the longitudinal vortices generated by the delta winglet. The vortices lead to better flow mixing modifying the thermal boundary layer in the wake region. The local heat transfer coefficient in the wake region behind the tube is greatly enhanced.

5.4 Attack Angle Effect. Next, the effects of three geometrical parameters on the air-side performances of the wavy fin-and-tube heat exchanger with delta winglets are investigated one by one. First, for examining the effect of the attack angle of delta winglet, the two-row case with wavy angle θ=15 deg is adopted and the attack angle has three different values of 30 deg, 45 deg, and 60 deg. Additionally, the wavy fin-and-tube heat exchanger without delta winglets at the same wavy angle and tube row number is simulated as the baseline case. Figure 9 shows the effects of the attack angle on Nusselt number and friction factor against the Reynolds number. It is clear for understanding that with the increase in the Reynolds number, the Nusselt number increases while the friction factor decreases. Comparison of the results between the wavy fin with delta winglets and the wavy fin without delta winglets shows that a wavy fin with delta winglets has larger Nusselt number and friction factor. The Nusselt number and friction factor increase with the increase in the attack angle β. Compared with the baseline case at a range of Reynolds number of the

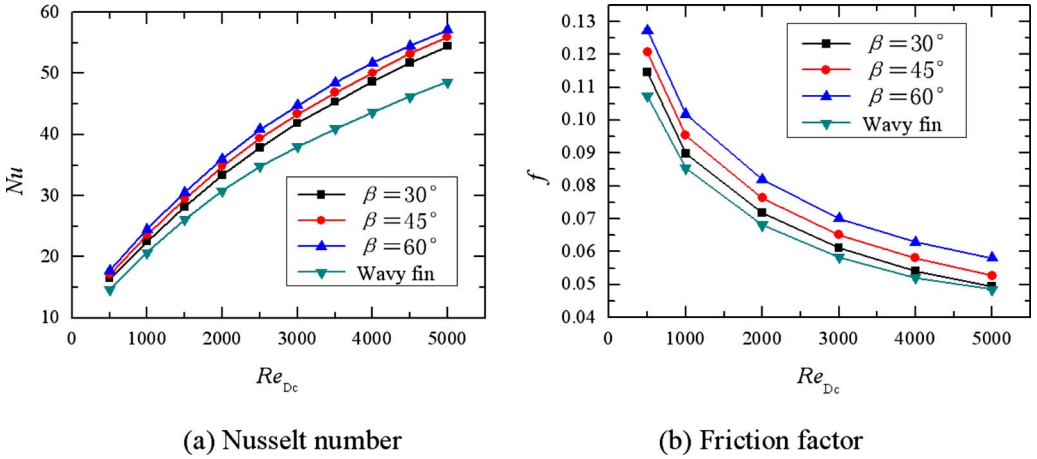

(a) Nusselt number (b) Friction factor

Fig. 9 Effects of attack angle on Nusselt number and friction factor

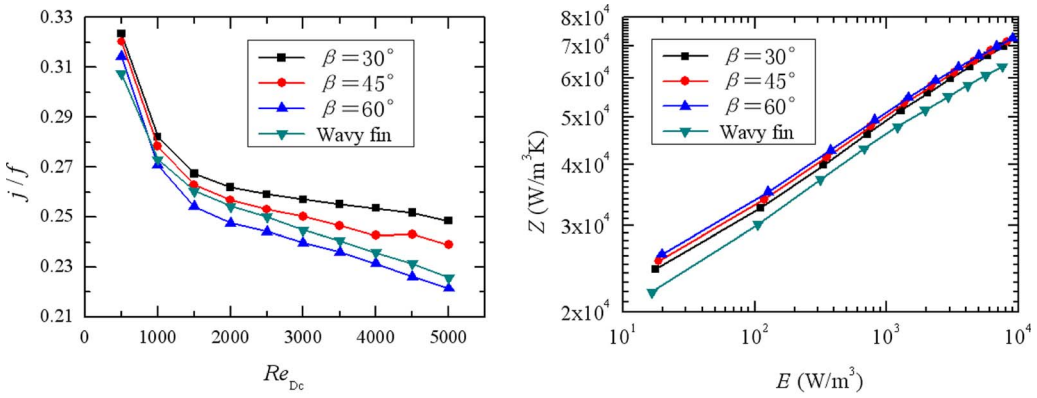

(a) Area goodness (b) Volume goodness

Fig. 10 Area goodness and volume goodness factors at different attack angles

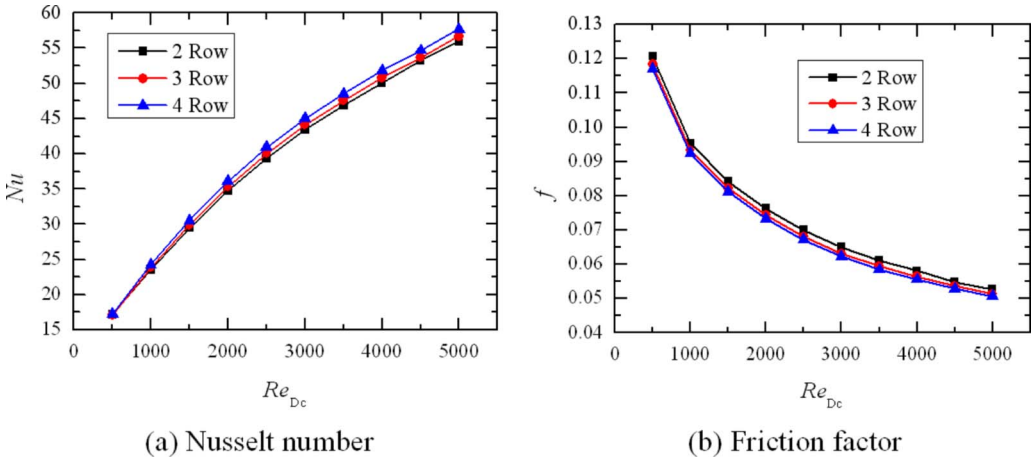

Fig. 11 Effect of tube row number on Nusselt number and friction factor

present study, the Nusselt number and friction factor increase by 8–12% and 2–7%, respectively, for the case of $\beta=30$ deg; the Nusselt number and friction factor increase by 13–17% and 9–12% for the case of $\beta=45$ deg; and the Nusselt number and friction factor increase by 17–21% and 19–21%, respectively, for the case of $\beta=60$ deg.

Figure 10 presents the area goodness and volume goodness factors for different attack angle cases compared with the baseline case. The j/f ratio of the cases of $\beta=30$ deg and $\beta=45$ deg is higher than the baseline case (shown in Fig. 10(*a*)). The case of $\beta=30$ deg shows the highest value of j/f under the same Reynolds number. It is worth noting that the j/f ratio for the case of $\beta=60$ deg is higher than the baseline case for $\mathrm{Re}_{D_c}<900$ and then the value falls below the baseline case with higher Re_{D_c} values. Another criterion is the volume goodness factor where the heat transfer power per unit temperature difference and per unit core volume (Z) is plotted against the fan power per unit core volume (E). From the viewpoint of heat exchanger volume required, a large Z versus E is better for heat exchanger design. A geometry with large value of Z will require the least core volume for a given airside performance. Figure 10(*b*) shows the volume goodness factor for different attack angle cases. It is clear that for a given E value, the wavy fin with delta winglets has higher Z value than the baseline case, and the value of Z increases with the increase in attack angle. This means that for a fixed volume of heat exchanger, the wavy fin-and-tube heat exchanger with delta winglets shows a better performance.

5.5 Tube Row Number Effect. In order to study the effect of tube row number on heat transfer and flow characteristics of the wavy fin-and-tube heat exchanger with delta winglets, the attack angle is chosen as 45 deg and the wavy angle is at 15 deg. Figure 11 shows the variations in Nusselt number and friction factor with the tube row number. Tube row numbers of 2–4 are examined. With the increase in the tube row number the Nusselt number increases slightly while the friction factor slightly decreases. The present fin channel composed of the wavy fins, the staggered tubes, and the protuberant delta winglets is very complicated. In addition, the longitudinal vortices generated by the delta winglet mix the fluid. All these result in a very complex flow in the fin channel with higher turbulent intensity, and the heat transfer and fluid flow become fully developed very quickly. So the effect of tube row number on the heat transfer and fluid flow structure is very small.

The area goodness and volume goodness factors of the wavy fin with delta winglets for different tube row numbers are presented in Fig. 12. It is very clear that the four-row case has the highest value of j/f and the three-row case comes in second while the two-row case shows the lowest. In other words, the four-row case has the best area goodness factor. Figure 12(*b*) presents the volume goodness factor for the different tube row numbers. The value of Z increases slightly with the increase in the tube row number. The effect of the tube row number on the wavy fin-and-tube heat exchanger with delta winglets is small from the viewpoint of heat exchanger volume required.

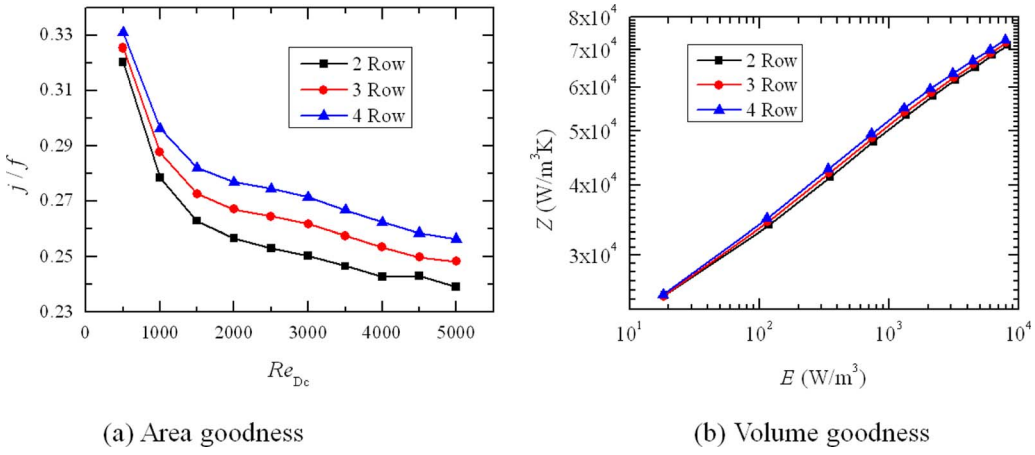

Fig. 12 Area goodness and volume goodness factors at different tube row numbers

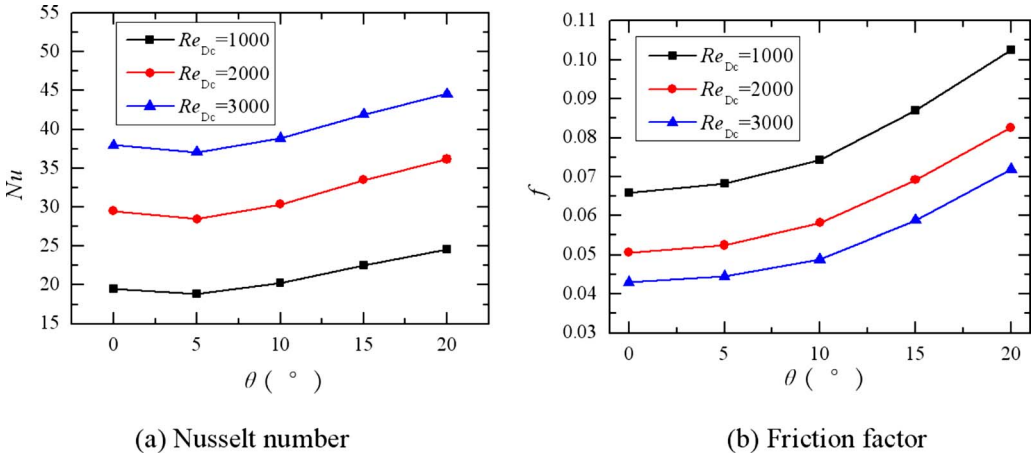

(a) Nusselt number (b) Friction factor

Fig. 13 Effect of wavy angle on Nusselt number and friction factor

5.6 Wavy Angle Effect. To investigate the effect of the wavy angle on the air-side performance of the wavy fin-and-tube heat exchanger with delta winglets, the following parameters are assumed: three-row configuration with the attack angle of $\beta = 30$ deg and the wavy angle of the fin varies from 0 deg to 20 deg for $Re_{D_c} = 1000$, $Re_{D_c} = 2000$, and $Re_{D_c} = 3000$. Figure 13 shows the relations of Nusselt number and friction factor with the wavy angle. It can be seen that the Nusselt number first decreases with the increase in the wavy angle and reaches the minimum value at the wavy angle of 5 deg then it increases with the increasing wavy angle. The friction factor always increases with the increase in wavy angle, and the trend becomes stronger at larger wavy angles.

The area goodness and volume goodness factors of the wavy fin with delta winglets for different wavy angles are presented in Fig. 14. It can be seen that the value of j/f ratio decreases with the increase in the wavy angle, and the case of $\theta = 0$ deg has the best area goodness factor. Figure 14(*b*) presents the volume goodness factor for the different wavy angles, and it is clear that for a given E, a minimum value of Z is found for the case of $\theta = 5$ deg. When the wavy angle is larger than 5 deg, the value of Z increases with the increase in the wavy angle, and the largest Z is found for the case of $\theta = 20$ deg. The value of Z for the case of $\theta = 0$ deg is larger than that of $\theta = 5$ deg from the viewpoint of heat exchanger volume required. The cases of $\theta = 0$ deg and $\theta = 10$ deg have the similar volume goodness factor.

6 Conclusions

This paper presents the results of three-dimensional numerical simulations on the air-side heat transfer and fluid flow characteristics of a wavy fin-and-tube heat exchanger with delta winglets. The following conclusions can be made.

(1) The delta winglet generates a downstream main vortex and a corner vortex. The main vortex is formed by flow separation at the leading edge of the delta winglet, and the corner vortex having the horseshoe vortexlike characteristic feature is generated at the junction of the front face of the winglet and the fin surface.

(2) Although a short distance along the main flow direction is affected by longitudinal vortices disrupted by downstream wavy trough, those vortices generated by the delta winglet greatly spur the fluid transport from the mainstream region to the wake region, compress the wake region, and enhance the heat transfer of the fin surface in the wake region where the heat transfer is the weakest in the fin-and-tube heat exchanger.

(3) The Nusselt number and friction factor both increase with the increase in the attack angle β. In the Reynolds number range of the present study ($Re_{D_c} = 500–5000$), compared with the wavy fin without delta winglets, the Nusselt number increases by 8–12%, 13–17%, and 17–21% and the friction factor increases by 2–7%, 9–12%, and 19–21% for

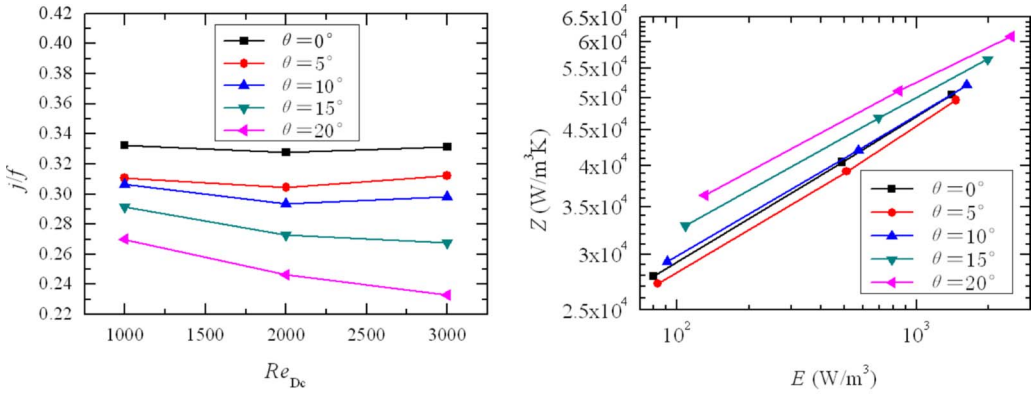

(a) Area goodness (b) Volume goodness

Fig. 14 Area goodness and volume goodness factors at different wavy angles

the case of $\beta=30$ deg, $\beta=45$ deg, and $\beta=60$ deg, respectively. The case of $\beta=30$ deg has the highest value of j/f under the same Reynolds number.

(4) The effects of the tube row number on the heat transfer and fluid flow characteristics of the wavy fin-and-tube heat exchanger with delta winglets are very small, and the heat transfer and fluid flow become fully developed very quickly.

(5) The Nusselt number first decreases and then increases with the increase in wavy angle, and the case of the wavy angle $\theta=5$ deg has the minimum value. The friction factor always increases with the increase in the wavy angle, and the trend becomes stronger at the larger wavy angles.

Acknowledgment

The present work was supported by the Key Project of National Natural Science Foundation of China (Contract No. 50736005) and National Basic Research Program of China (973 Program) (Contract No. 2007CB206902).

Nomenclature

A = cross-sectional area (m^2)
A_c = minimum flow cross-sectional area (m^2)
A_f = fin surface area (m^2)
A_0 = total surface area (m^2)
c_p = specific heat of the fluid (J/kg K)
D_c = tube outside diameter (m)
D_h = $4A_cL/A_0$, hydraulic diameter (m)
E = see Eq. (6) (W/m^3)
F_p = fin pitch (m)
f = friction factor
h = heat transfer coefficient (W/m^2 K) or height of the delta winglet (m)
j = Colburn factor
k = turbulence kinetic energy (m^2/s^2)
L = fin length along the flow direction (m)
l = length of the delta winglet (m)
Nu = Nusselt number
p = pressure (Pa)
P_l = longitudinal tube pitch (m)
P_t = transverse tube pitch (m)
Pr = Prandtl number
Q = heat transfer rate (W)
q = heat flux (W/m^2)
Re_{D_c} = Reynolds number based on tube outside diameter
T = temperature (K)
u,v,w = x,y,z velocity components (m/s)
u_m = mean velocity at the minimum flow cross-sectional area (m/s)
$\boldsymbol{U}$ = velocity vector (m/s)
x,y,z = Cartesian coordinates
X_L = $\sqrt{(P_t/2)^2+P_l^2}/2$, geometric parameter (m)
X_M = $P_t/2$, geometric parameter (m)
Z = see Eq. (6) (W/m^3 K)

Greek Symbols

β = attack angle of the delta winglet (deg)
δ_f = fin thickness (m)
μ = dynamic viscosity (kg/m s)
ρ = density (kg/m^3)
λ = thermal conductivity (W/m K)
ε = turbulent energy dissipation rate (m^2/s^3)
σ = A_c/A_{frontal}, contraction ratio of the cross-sectional area
Γ = circulation of the flow cross section (m^2/s)
θ = wavy angle of the fin (deg)
Θ = dimensionless temperature
η_f = fin efficiency
η_0 = surface efficiency

Subscripts

a = air
f = fin
in = inlet
m = mean
out = outlet
w = tube wall
x = local

References

[1] Wang, C. C., Lo, J., Lin, Y. T., and Wei, C. S., 2002, "Flow Visualization of Annular and Delta Winglet Vortex Generators in Fin-and-Tube Heat Exchanger Application," Int. J. Heat Mass Transfer, **45**, pp. 3803–3815.

[2] Tiwari, S., Maurya, D., Biswas, G., and Eswaran, V., 2003, "Heat Transfer Enhancement in Cross-Flow Heat Exchangers Using Oval Tubes and Multiple Delta Winglets," Int. J. Heat Mass Transfer, **46**, pp. 2841–2856.

[3] O'Brien, J. E., Sohal, M. S., and Wallstedt, P. C., 2004, "Local Heat Transfer and Pressure Drop for Finned-Tube Heat Exchangers Using Oval Tubes and Vortex Generators," ASME J. Heat Transfer, **126**, pp. 826–835.

[4] Biswas, G., Mitra, N. K., and Fiebig, M., 1994, "Heat Transfer Enhancement in Fin-Tube Heat Exchangers by Winglet Type Vortex Generators," Int. J. Heat Mass Transfer, **37**, pp. 283–291.

[5] Leu, J. S., Wu, Y. H., and Jang, J. Y., 2004, "Heat Transfer and Fluid Flow Analysis in Plate-Fin and Tube Heat Exchangers With a Pair of Block Shape Vortex Generators," Int. J. Heat Mass Transfer, **47**, pp. 4327–4338.

[6] Torii, K., Kwak, K. M., and Nishino, K., 2002, "Heat Transfer Enhancement Accompanying Pressure-Loss Reduction With Winglet-Type Vortex Generators for Fin-Tube Heat Exchangers," Int. J. Heat Mass Transfer, **45**, pp. 3795–3801.

[7] Jain, A., Biswas, G., and Maurya, D., 2003, "Winglet-Type Vortex Generators With Common-Flow-Up Configuration for Fin-Tube Heat Exchangers," Numer. Heat Transfer, Part A, **43**, pp. 201–219.

[8] Joardar, A., and Jacobi, A. M., 2008, "Heat Transfer Enhancement by Winglet-Type Vortex Generator Arrays in Compact Plain-Fin-and-Tube Heat Exchangers," Int. J. Refrig., **31**, pp. 87–97.

[9] Wang, L. B., Ke, F., Gao, S. D., and Mei, Y. G., 2002, "Local and Average Characteristics of Heat/Mass Transfer Over Flat Tube Bank Fin With Four Vortex Generators per Tube," ASME J. Heat Transfer, **124**, pp. 546–552.

[10] Smotrys, M. L., Ge, H., Jacobi, A. M., and Dutton, J. C., 2003, "Flow and Heat Transfer Behavior for a Vortex-Enhanced Interrupted Fin," ASME J. Heat Transfer, **125**, pp. 788–794.

[11] Joardar, A., and Jacobi, A. M., 2005, "Impact of Leading Edge Delta-Wing Vortex Generators on the Thermal Performance of a Flat Tube, Louvered-Fin Compact Heat Exchanger," Int. J. Heat Mass Transfer, **48**, pp. 1480–1493.

[12] Sanders, P. A., and Thole, K. A., 2006, "Effects of Winglets to Augment Tube Wall Heat Transfer in Louvered Fin Heat Exchangers," Int. J. Heat Mass Transfer, **49**, pp. 4058–4069.

[13] Tao, W. Q., 2001, *Numerical Heat Transfer*, 2nd ed., Xi'an Jiaotong University, Xi'an, China, in Chinese.

[14] Tian, L. T., He, Y. L., Tao, Y. B., and Tao, W. Q., 2009, "A Comparative Study on the Air-Side Performance of Wavy Fin-and-Tube Heat Exchanger With Punched Delta Winglets in Staggered and In-Line Arrangements," Int. J. Therm. Sci., in press.

[15] Schmidt, T. E., 1949, "Heat Transfer Calculations for Extended Surfaces," Refrig. Eng., **4**, pp. 351–357.

[16] Xue, W., and Min, J. C., 2004, "Numerical Predictions of Fluid Flow and Heat Transfer in Corrugated Channels," *Proceedings of the Third International Symposium on Heat Transfer and Energy Conservation*, Guangzhou, China, Jan. 12–15, Vol. 1, pp. 714–721.

Heat Transfer Enhancement Due to Frequency Doubling and Ruelle–Takens–Newhouse Transition Scenarios in Symmetric Wavy Channels

Amador M. Guzmán[1]
e-mail: amador.guzman@usach.cl

Raúl A. Hormazabal

Tania A. Aracena

Departamento de Ingeniería Mecánica,
Universidad de Santiago de Chile,
Casilla 10233
Alameda 3363,
Estación Central,
Santiago, Chile

Heat transfer enhancement characteristics, through a transition scenario of flow bifurcations in symmetric wavy wall channels, are investigated by direct numerical simulations of the mass, momentum, and energy equations using spectral element methods. Flow bifurcations, transition scenarios, and heat transfer characteristics are determined by increasing the Reynolds numbers from a laminar to a transitional flow for the geometrical aspect ratios $r=0.125$ and $r=0.375$. The numerical results demonstrate that the transition scenario to transitional flow regimes depends on the aspect ratio. For $r=0.375$, the transition scenario is characterized by one Hopf flow bifurcation in a frequency-doubling transition scenario, where further increases in the Reynolds number always lead to periodic flows; whereas, for $r=0.125$, the transition scenario is characterized by a first Hopf flow bifurcation from a laminar to a time-dependent periodic flow and a second Hopf flow bifurcation from a periodic to a quasiperiodic flow. For $r=0.125$, the flow bifurcation scenario is similar to the Ruelle–Takens–Newhouse (RTN) transition scenario to Eulerian chaos observed in asymmetric wavy and grooved channels. The periodic and quasiperiodic flows are characterized by fundamental frequencies ω_1, and ω_1 and ω_2, respectively. For the aspect ratio $r=0.375$, the Nusselt number increases slightly as the Reynolds number increases in the laminar regime until it reaches a critical Reynolds number of $Re_c \approx 126$. As the flow becomes periodic, and then quasiperiodic, the Nusselt number continuously increases with respect to the laminar regime, up to a factor of 4, which represents a significant heat transfer enhancement due to a better flow mixing. [DOI: 10.1115/1.3139108]

Keywords: heat transfer enhancement, flow transition scenarios, symmetric wavy channels

1 Introduction

An extensive amount of research has been performed in the past decades to obtain a better understanding of flow mixing and heat transfer enhancement in channels with geometrical inhomogeneities, such as symmetric and asymmetric grooved channels [1–14], wavy wall channels [15–20], and corrugated channels [21], as well as other geometrical configurations, such as channel expansions [22] and grooved tubes [23]. Asymmetric and symmetric wavy wall channels are used in industrial and biomedical applications, such as compact heat exchangers, oxygenators, and hemodialysers [24–26]. Considerable effort has been dedicated to investigating the role of flow destabilization and flow mixing in heat transfer enhancement. Investigations performed with grooved, wavy, and communicating channels have demonstrated that self-sustained oscillations, which develop in these geometries, lead to heat transfer enhancement without applying active forcing [2,9,13,15,25,26].

Symmetric and asymmetric wavy channels were considered in several earlier investigations to enhance heat and mass transfer rates in compact exchange devices such as heat exchanger and oxygenators. These channels are easy to fabricate and can provide significant heat transfer enhancement if operated in an appropriate Reynolds number range [15–20]. Early investigations found no significant heat transfer enhancement for a steady laminar flow. However, if/when the flow becomes unsteady—either through external forcing or natural transitioning to an unsteady condition—significant heat exchange enhancement can be obtained. Several investigations found that a natural transition to a time-dependent, periodic self-sustained flow regime leads to enhancement of heat transfer rates with moderate and reasonable pressure drops. Guzmán and Amon [15–17] performed numerical investigations for high transitional Reynolds numbers in converging-diverging (symmetric wavy wall) channels; they found that the flow develops a second bifurcation in addition to the first flow bifurcation at a Reynolds number $\mathrm{Re}_{c_2} > \mathrm{Re}_{c_1}$, which enhances the flow mixing and heat transfer process [27]. Experimental or numerical investigations of the effect of several geometrical aspect ratios on the flow patterns, transition scenario, and heat transfer characteristics in symmetric and asymmetric wavy channels have not been reported to date.

This work investigates the heat transfer enhancement due to flow bifurcations in symmetric wavy channels, which occurs during the transition scenarios from laminar to transitional time-dependent flow regimes by two-dimensional direct numerical simulations (DNSs) of the time-dependent, incompressible continuity, Navier–Stokes, and energy equations. Two geometric aspect ratios ($r=0.125$ and $r=0.375$) are considered in this investigation. Extended and reduced computational domains are used to (a)

[1]Corresponding author.

Manuscript received June 7, 2008; final manuscript received April 7, 2009; published online June 22, 2009. Review conducted by Sai C. Lau.

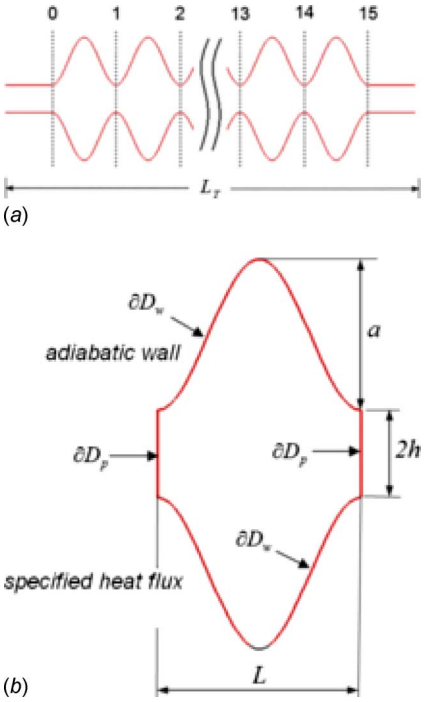

Fig. 1 Schematic of the symmetric wavy wall channel: (*a*) extended domain with 14 furrows and plane inlet and outlet regions, and (*b*) reduced domain with a spatially periodic length *L*

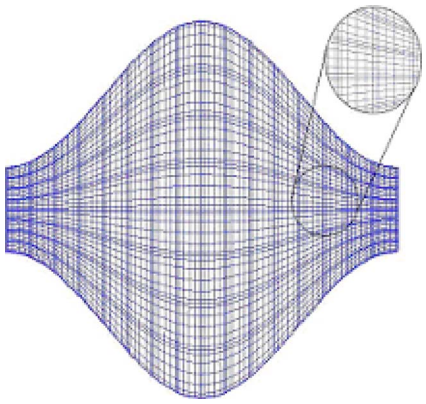

Fig. 2 Computational mesh for the reduced domain with 16 × 8 macro-elements and 8 × 8 nodal points per macro-element for the aspect ratio $r=0.125$

demonstrate and verify the existence of spatial periodicity and self-similar temperature profiles and (b) investigate in detail, with the reduced domain, the flow and heat transfer enhancement characteristics and the parameters for laminar and transitional regimes. Described first is the way in which flow evolves from a laminar to a transitional state through flow bifurcations by examining the velocity field, Fourier power spectra, and phase-portrait representations. Next, the flow and heat transfer characteristics and parameters are determined by evaluating friction factors, pumping power, and Nusselt numbers for increasing Reynolds numbers through the transitional regime.

2 Problem Formulation, Numerical Approach, and Methodology

The physical configuration of the symmetric wavy channel used in this investigation is shown in Fig. 1. The extended computational domain, with 14 symmetric furrows (cavities), and the entrance and exit plane constant cross sections are shown in Fig. 1(*a*), whereas the reduced domain created by one furrow is shown in Fig. 1(*b*). The furrow periodic length is L, $2h$ is the channel height in both ends, a is the amplitude of the sinusoidal wall, and $r=a/2L$ is the channel aspect ratio.

An incompressible and unsteady flow of a Newtonian fluid is considered for both the extended and reduced domains. The flow is governed by mass conservation and Navier–Stokes equations (1) and (2); the heat transport phenomenon is described by the energy equation (3). For the extended domain, a uniform velocity profile is imposed at the entrance of the channel (nonslip for the upper and lower walls, and outflow for the channel exit). To address the heat transfer problem, a constant temperature is imposed at the entrance, a vanishing heat flux on the upper wall, outflow for the exit, and a constant heat flux in the lower wall. For the reduced domain with one furrow, spatial periodicity in the streamwise direction is imposed. Although the velocity field is unknown in the entire domain, the resulting velocity profile at the entrance and exit of the furrow periodic domain—for a given equilibrium state—is the same regardless of the laminar or transitional nature of the flow regime. For the heat transfer problem, a self-similar temperature profile is enforced by imposing a spatial periodicity for the temperature in the streamwise direction; a vanishing heat flux on the upper wall and a constant heat flux in the lower wall are shown in Fig. 1(*b*).

$$\nabla \cdot \boldsymbol{V} = 0 \tag{1}$$

$$\rho\left(\frac{\partial \boldsymbol{V}}{\partial t} + \boldsymbol{V} \cdot \nabla \boldsymbol{V}\right) = -\nabla P + \mu \nabla^2 \boldsymbol{V} \tag{2}$$

$$\rho c_p\left(\frac{\partial T}{\partial t} + \boldsymbol{V} \cdot \nabla T\right) = k \nabla^2 T \tag{3}$$

The governing equations are solved using a computational program based on the spectral element method [28]. The computational domains are discretized with macro-elements that contain nodal points where velocity, pressure, and temperature are represented. Different computational meshes are used for the extended and reduced computational domains, with an increasing number of macro-elements and nodal points, until acceptable mesh independent results are achieved. The criterion used in this investigation is that the relative error for any given field variable, such as pressure, velocity, and temperature between two consecutive meshes, is less than 0.1%. Sufficiently long constant cross sections are considered before and after the first and last furrows, respectively, to obtain adequate representations of the field variables. Figure 2 shows a computational mesh for the reduced domain with 16×8 macro-elements and 8×8 nodal points per macro-element.

The correct determination of the transition scenario and its sequence of Hopf bifurcations depend greatly on the right calculations of the fundamental frequencies ω_i, with $i=1$, 2 or 3, and their combination pattern given by the subharmonics and superharmonics. Several meshes with an increasing number of nodes were used in this investigation. For each mesh, the exact same point was defined in the computational domain to determine the time-dependent evolution of the velocity field. For each case, the fundamental frequencies and their subharmonics and superharmonics were calculated and compared with the values obtained with the previous, less fine, mesh. The mesh chosen for all the calculations described in this article leads to fundamental frequency and subharmonic and superharmonic values that presented a difference of less than 0.1% when compared with the values obtained with the previous, less fine, mesh.

Numerical simulations were performed with the extended domain to demonstrate that periodicity indeed exists in most of the channel for laminar and transitional flow regimes. At the same

time, the numerical predictions were compared with experimental data reported by other authors. In addition, numerical simulations were performed (but not reported in this article), with a computational domain created by two furrows, using a spatial periodicity of $2L$, where L is the furrow length. It was found that, for laminar and transitional flow regimes, the flow pattern in the first and second furrows are the same. Comparisons with available experimental and numerical results, and with numerical simulations carried out with an extended domain, are performed to verify and validate the spatial periodicity assumptions for flow and temperature [20–23]. Experimental visualizations of steady, unsteady, and externally pulsatile flows [20,22,23] confirmed the spatial periodic nature of the flow up to an unsteady flow regime Reynolds number of about 300 and found that spatial periodicity hold for time-dependent flow regimes.

Numerical simulations are performed to increase Reynolds numbers in the laminar and transitional flow regimes. For this investigation, the Reynolds number is defined as $\mathrm{Re}=(3/2)\times(\hat{U}\cdot\hat{h}/\nu)$, where $\hat{U}$ is the time-average mean streamwise velocity at the inlet of the channel, calculated as Q/A, with Q and A as the volumetric flow rate and the cross sectional area, respectively; $\hat{h}$ is half-height of the channel at the inlet, and ν is the kinematic viscosity. The Prandtl number, $\mathrm{Pr}=\nu/\alpha$, is equal to 1, and α is the thermal diffusivity. Since the fluid motion is induced by an external applied pressure drop, and not for body forces, the resulting flow pattern and characteristics are independent of the imposed thermal boundary conditions and temperature distribution. Flow and heat transfer simulations are performed for Reynolds number of up to 400 for the aspect ratio $r=0.125$ and for Reynolds number of up to 850 for the aspect ratio $r=0.375$. Additionally, viscous dissipation terms are neglected, since calculations of the Eckart number, Ec, and the product of $\mathrm{Re}\cdot\mathrm{Ec}$, for the transitional Reynolds number range of this investigation, lead to small values of $\mathrm{Ec}=10^{-6}$ and $\mathrm{Re}\cdot\mathrm{Ec}=10^{-4}$; hence, viscous dissipation terms are negligible when compared with both the radial diffusion and streamwise convective terms, respectively.

The friction factor for the symmetric wavy channel is calculated as

$$f_b=\frac{-\dfrac{dp}{dx}\cdot 8\hat{h}}{2\rho\hat{U}^2} \tag{4}$$

where $dp/dx=\Delta P/L$ is the fully developed pressure gradient in the streamwise direction. The local Nusselt number is defined as

$$\mathrm{Nu}(x,t)=\frac{q(x,t)\cdot L_c}{k\cdot\langle T_w(x,t)-T_b(x,t)\rangle} \tag{5}$$

where $q(x,t)=1$ is the imposed local heat flux along the lower wall, $L_c=h$ is the characteristics length, $T_w(x)=Tw$ is the lower wall temperature, and $T_b(x,t)$ is the bulk temperature defined as

$$T_b(x_o,t)=\frac{\displaystyle\int_{-h}^{h}u(x=x_o,y,t)\cdot\theta T(x=x_o,y,t)\cdot dy}{\displaystyle\int_{-h}^{h}u(x_o,y,t)\cdot dy}$$

where x_o is the channel inlet. The time-dependent mean Nusselt number is calculated as

$$\overline{\mathrm{Nu}}(t)=\frac{\displaystyle\int_L \mathrm{Nu}(x,t)dx}{\displaystyle\int_L dx}$$

and the time-averaged mean Nusselt number as

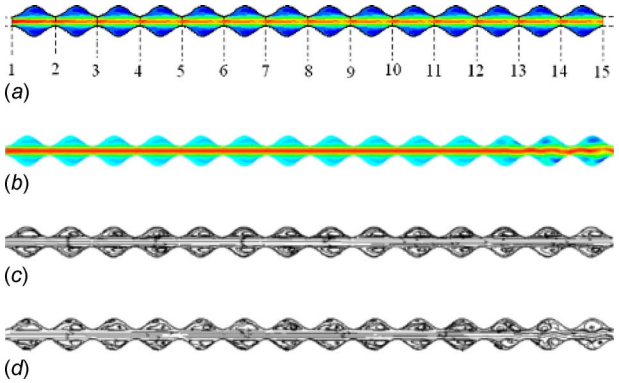

Fig. 3 Velocity characteristics for extended domain simulations for $r=0.125$: (*a*) *u*-velocity for a laminar flow, (*b*) *u*-velocity for a time-dependent flow regime, (*c*) streamlines for a laminar flow, and (*d*) streamlines for a time-periodic flow regime

$$\mathrm{Nu}=\frac{\displaystyle\int_\tau \overline{\mathrm{Nu}}(t)dt}{\displaystyle\int_\tau dt}$$

3 Numerical Results and Discussion

3.1 Flow Regimes for an Extended Domain. Numerical investigations of spatial periodicity for both laminar and transitional flow regimes are performed for both aspect ratios ($r=0.125$ and $r=0.375$) of this symmetric wavy channel. Figures 3(*a*) and 3(*b*) show the streamwise *u*-velocity for laminar and periodic flow regimes, respectively, for the aspect ratio $r=0.125$. Figures 3(*c*) and 3(*d*), show the streamlines for the same laminar and time-periodic flow regimes, respectively. For laminar flow regimes, spatial periodicity in the velocity field develops in most of the extended computational domain except in the first and last furrows due to the entrance and exit region effects. For time-periodic flow regimes, spatial periodicity is confined to most of the furrows within the wavy channel. Figure 3(*b*) shows that spatial periodicity develops between furrows 2 and 11. The entrance region effects do not allow the existence of periodicity in furrow 1, whereas the exit region effects are strong between furrows 12 and 14, where spatial periodicity does not occur. Because time-periodic flows develop a time-dependent velocity field, the velocity field described in Fig. 3(*b*) corresponds to the velocity field in any given time. At each time, the velocity field changes, but it holds spatial periodicity between furrows 2 and 11. Figure 3(*c*) shows that the vortices for laminar flow develop the same strength along the channel and remain in the same relative position with respect to the entrance to each furrow between furrows 2 and 13. Lastly, Fig. 3(*d*) shows the strong vortex dynamic that develops in each furrow for time-periodic flows and the entrance effects confined to the first furrow. These numerical results are in good agreement with the available experimental results [15–23,29]. For the aspect ratio $r=0.375$, numerical simulations with extended domain are carried out for the laminar and transitional flow regimes. The numerical results (not shown here) depicted the spatial periodicity for laminar and transitional flow regimes. These results—in terms of streamline and streamwise mean velocities—clearly demonstrated that periodicity is indeed a condition that naturally develops in wavy channels, particularly in those furrows far from the ends. Because most the experimental results reported in the literature are for the aspect ratio $r=0.125$, comparisons with experimental updated information is, thus far, not available.

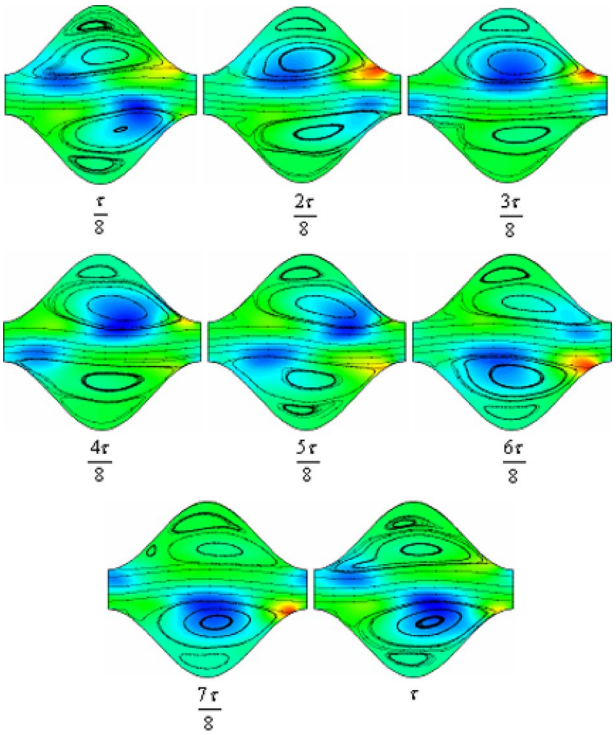

Fig. 4 Pressure field and streamlines for the aspect ratio $r=0.375$: Instantaneous representations during a time period of periodic flow regime for a Reynolds number of Re≈554.

3.2 Laminar and Transitional Flow Regimes With a Spatially Periodic Domain. The numerical simulation Reynolds number ranges for the laminar and transitional regimes, for the aspect ratios $r=0.125$ and $r=0.375$, are 10–400 and 100–850, respectively. For a laminar Reynolds number of $\mathrm{Re}=54$ and the aspect ratio $r=0.375$, the flow pattern is characterized by a symmetric flow with two large stationary vortices located at each furrow of the channel and for a parallel flow between the vortices [30]. Figure 4 shows a sequence of eight instantaneous streamlines during one τ time period in the wavy channel for a periodic transitional Reynolds number of $\mathrm{Re}=554$ and the same aspect ratio $r=0.375$. These sequences demonstrate the wavy periodic nature of the flow as it moves downstream, and it shows a flow pattern of several vortices of different sizes, which increase and decrease in size as they are ejected from the wavy channel furrows. For higher transitional Reynolds numbers, the numerical simulations show a flow pattern that remains time periodic, preserves its wavy nature, and shows a vortex dynamic that increases in intensity and presents a wider variety of vortex sizes. For the aspect ratio $r=0.125$, the flow evolves from a laminar to a time-periodic flow regime and then to a quasiperiodic flow regime as the Reynolds number increases in the range of $\mathrm{Re}=[10-400]$. A vortex dynamic of many vortices (not shown here) of different sizes and strength develops as the Reynolds numbers is further increased through the quasiperiodic transitional regime.

A flow Hopf bifurcation in fluid mechanics indicates when—in a given physical domain—a flow departs from one stable state to another stable state or condition, when a control parameter such as the Reynolds number changes. Usually, in confined flow channels, a first Hopf bifurcation occurs when a flow passes from a laminar stable state to a time-dependent stable state, which could be periodic, quasiperiodic, or intermittent. The Eulerian velocity field in a stable time-dependent state typically present an oscillatory behavior, which is characterized by either one fundamental frequency (ω_1 plus superharmonics) or by two independent fundamental frequencies (ω_1 and ω_2), plus subharmonics and superharmonics. When/if the flow passes from a periodic flow to a quasiperiodic flow, then the flow has suffered another Hopf bifurcation. When the transition contains the sequence of two Hopf bifurcations so that the flow is laminar, then periodic, and finally quasiperiodic, then this sequence is called the Ruelle–Takens–Newhouse (RTN) transition scenario. In some situations, a third Hopf bifurcation might appear after the second Hopf bifurcation, when the control parameter is further increased, which leads to another quasiperiodic flow with three independent fundamental frequencies, ω_1, ω_2, and ω_3, plus subharmonics and superharmonics. When/if a flow passes from a steady state condition to a periodic flow with one fundamental frequency and then it remains periodic (regardless of the increase in the control parameter), then this transition type is called the Feingenbaum period-doubling scenario, which is characterized by a sequence of periodic flows, where the flow time period continuously increases by a factor of 2. Both the flow mixing and heat transfer characteristics are deeply affected by the type of transition scenario because fluid particles move through different Lagrangian trajectory patterns depending on the flow regime [31,35]. Therefore, different transition scenarios lead to different heat transfer enhancement characteristics and performance.

Figure 5 presents the Eulerian flow characteristics of a periodic regime for Reynolds number of $\mathrm{Re}\approx 554$ and aspect ratio $r=0.375$, in terms of the temporal evolution of the u- and v-velocities, the Fourier power spectra of the u-velocity, and the phase portrait of the u- and v-velocity components in a characteristic point of the computational domain. For this aspect ratio, the flow evolves through successive periodic flow regimes, characterized by one fundamental frequency, ω, and its superharmonics, as the Reynolds number increases to 850 [31–35]. In this transition scenario, the flow remains periodic as the Reynolds number is further increased with the fundamental frequency ω continually increasing in a frequency-doubling transition scenario [35].

In addition to the Landau method of turbulence, there are three more possible ways to achieve turbulence—or onset of chaos—emerging from the theoretical and experimental development and ideas of Ruelle–Takens–Newhouse, Feingenbaum, and Pommeau, which lead to a sequence of bifurcations to periodic and quasiperiodic flows, periodic flows, and intermittency, respectively [15]. These scenarios seem to be universal, which means that many related, or unrelated physical phenomena, processes, and systems develop scenarios that depend on at least one control parameter. Hopf bifurcations occur because, in this channel geometry, the flow loses stability due to the existence of Tollmien–Schlichting instabilities [15]. In these confined channel flow investigations, two transitions scenarios were discovered: RTN and Feingenbaum. Thus far, it can be said that the transition scenarios depend very much on the current aspect ratio r, an additional aspect ratio $s=h/(2L)$, which measures the separation between the walls, and in some configurations, on the way the flow approaches the bifurcation points.

Figure 6 displays the normalized time period T^*/T versus the normalized Reynolds number $\mathrm{Re}/\mathrm{Re}^*$, for increasing Reynolds number flow regime. T^* is the time period for the lowest periodic flow regime, which corresponds to the Reynolds number $\mathrm{Re}^*\approx 126$. A linear relationship can be observed between the normalized time period and normalized Reynolds number $\mathrm{Re}/\mathrm{Re}^*$ in the Reynolds number of these simulations, which obey approximately the expression $T^*/T=\omega/\omega^*=\mathrm{Re}/\mathrm{Re}^*$. Furthermore, the normalized time period obeys approximately the expression $T^*/T=2^n$, with n as an integer [35]. The relationship between T^*/T and $\mathrm{Re}/\mathrm{Re}^*$ is useful for predicting either the fundamental time period or the frequency of the self-sustained flow for a given Reynolds number in this frequency-doubling scenario.

Figure 7 presents the Eulerian flow characteristics of a quasiperiodic flow regime for the aspect ratio $r=0.125$ and $\mathrm{Re}=356$. In this case, the flow has evolved to a periodic regime through a first Hopf bifurcation at $\mathrm{Re}=\mathrm{Re}_{c_1}$ and then to a quasiperiodic flow

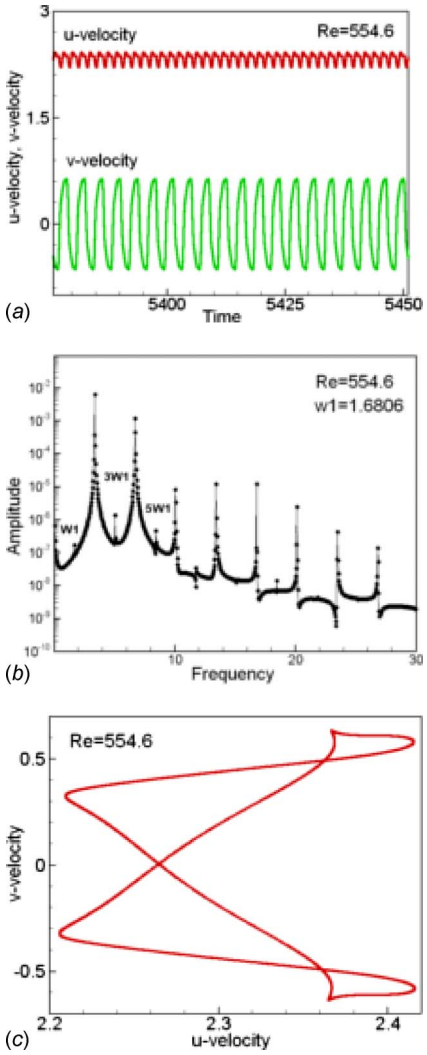

Fig. 5 Eulerian flow characteristics of a periodic flow for Reynolds number of Re≈554 and aspect ratio $r=0.375$: (*a*) temporal evolution of the *u*- and *v*-velocities, (*b*) Fourier power spectra of the *u*-velocity, and (*c*) phase-portrait of the *u*- and *v*-velocity components

regime from the periodic regime, through a second Hopf bifurcation at the critical Reynolds number, Re_{c_2}. The critical Reynolds numbers Re_{c_1} and Re_{c_2} are in the ranges of 130–136 and 148–151, respectively. Figure 8 shows a schematic representation of the

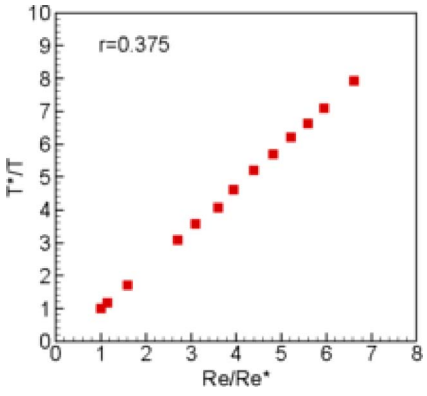

Fig. 6 Normalized time period T^*/T versus normalized Reynolds number Re/Re^* for $r=0.375$

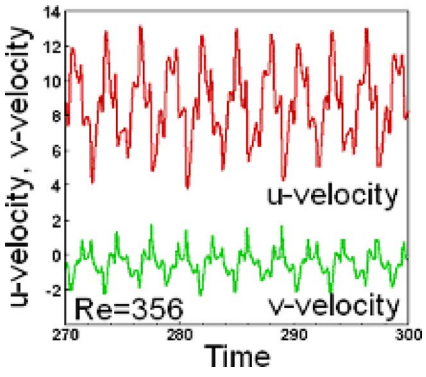

Fig. 7 Temporal evolution of the *u*- and *v*-velocities of a quasiperiodic flow for Reynolds number of Re≈356 and aspect ratio $r=0.125$

transition scenarios for the two aspect ratios of this investigation. For an aspect ratio of $r=0.125$, the transition scenario from a laminar to a quasiperiodic flow occurs because of two successive Hopf bifurcations, which occur for Reynolds numbers Re_{c_1} and Re_{c_2}, which are lower than the critical Reynolds number for a Poiseuille plane channel flow. The transition scenario developed for $r=0.125$ is very much like the RTN scenario to chaos developed in asymmetric wavy and grooved channels [15,18,31–36]. The transition scenario for the aspect ratio $r=0.375$ is characterized by the occurrence of one flow bifurcation from laminar to time-periodic flow regime occurring at the critical Reynolds number Re_c, which is somewhat higher than the first critical Reynolds number for $r=0.125$.

The flow pattern through the transition scenario is characterized by high shear stresses on the channel sinusoidal walls and, consequently, by high friction factors. Figure 9 shows the friction factor as a function of the Reynolds number for the aspect ratios $r=0.125$ and $r=0.375$ of the wavy channel and for the Poiseuille plane channel. The symmetric wavy channel friction factor f_b is calculated using the expression (4); the Poiseuille plane channel friction factor is calculated as $fp=18/Re_H$, where Re_H is the Reynolds number based on the height H of the plane channel. For both aspect ratios, $r=0.125$ and $r=0.375$, the friction factor for the symmetric wavy channel is initially higher than the Poiseuille plane channel friction factor. However, the Poiseuille channel fric-

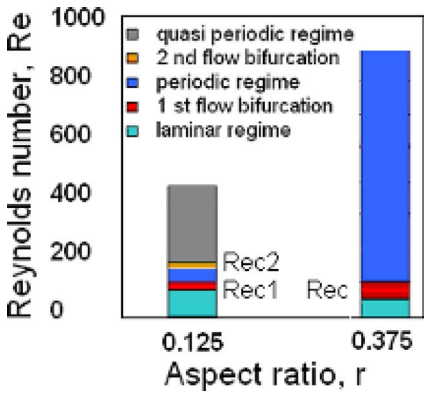

Fig. 8 Transition scenarios from laminar to transitional flows by flow bifurcations for aspect ratios $r=0.125$ and $r=0.375$. Two successive Hopf bifurcations, B_1 and B_2, for the critical Reynolds numbers Re_{c1} and Re_{c2}, respectively, developed for $r=0.125$ leading to a quasiperiodic flow through a RTN transition scenario. For the aspect ratio $r=0.375$, only one flow bifurcation from laminar to time-periodic flow regime develops at the critical Reynolds number Re_c, through a frequency-doubling transition scenario.

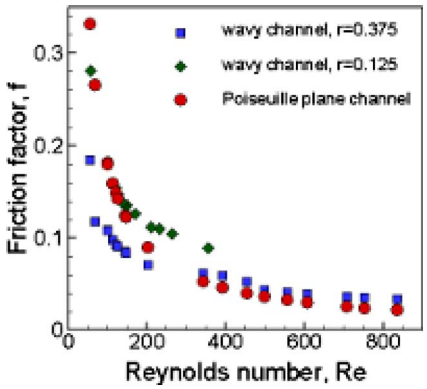

Fig. 9 Poiseuille plane channel friction factor and symmetric wavy channel friction factors for aspect ratios $r=0.125$ and $r=0.375$ for increasing Reynolds numbers

tion factor becomes larger than the symmetric wavy channel friction factor for both aspect ratios at Reynolds numbers of about 110 and 220, for $r=0.125$ and $r=0.375$, respectively.

3.3 Heat Transfer Characteristics. The temperature distribution is shown in Fig. 10 for laminar and transitional flow regimes for the aspect ratio $r=0.375$. Figure 10(a) shows a thermal stratification for the laminar Reynolds number of Re=54. Because of the existence of large stationary vortices in both furrows of the wavy channel, the high temperature region remains in the vicinity of the lower wall with a much smaller amount of heat flowing to

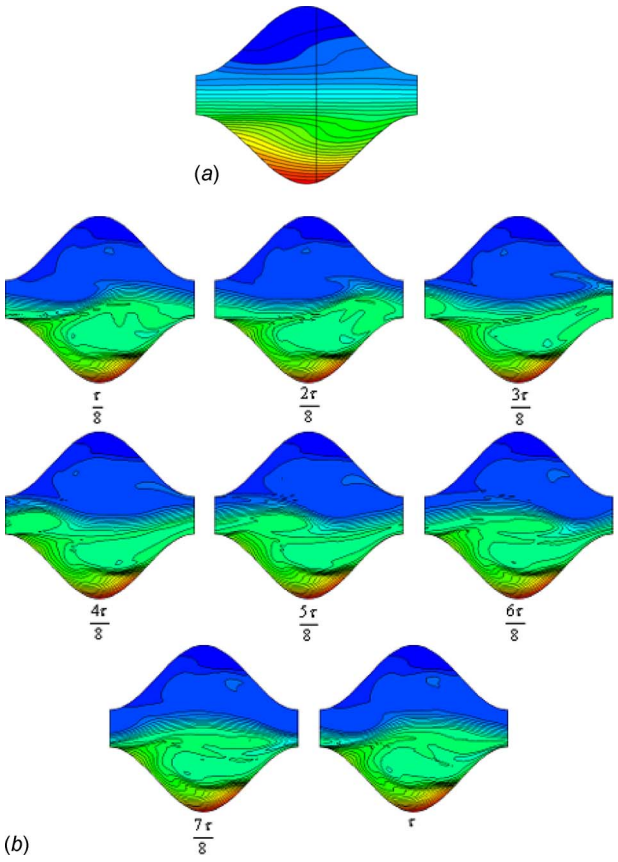

Fig. 10 Symmetric wavy channel temperature distribution for $r=0.375$: (a) laminar flow for Re≈54 and (b) eight instantaneous representations during a time period τ for a periodic flow of Re≈554

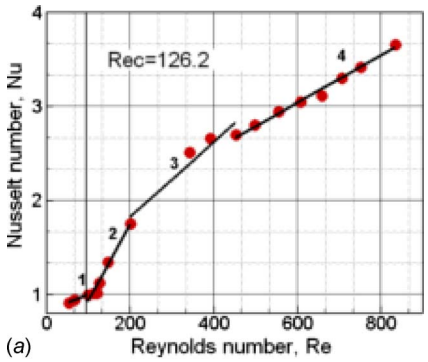

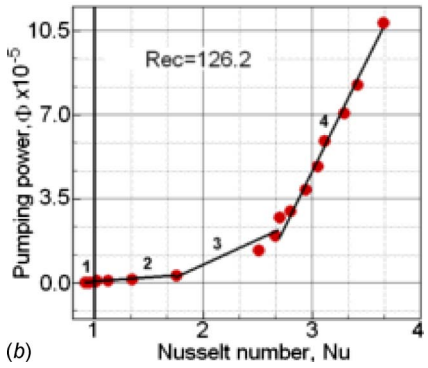

Fig. 11 Heat transfer parameters: (a) time-averaged mean Nusselt number versus Reynolds number for laminar and transitional flow regimes for the aspect ratio $r=0.375$ and (b) pumping power versus Nusselt number for laminar and transitional flow regimes

the mean flow region. Figure 10(b) shows a sequence of eight instantaneous representations of the temperature distribution in the wavy channel during one time period, τ, for a periodic flow regime of Re≈554. The temperature distribution resembles the wavy nature of the oscillatory periodic flow. The region of higher temperatures is bigger and closer to the mean flow region than in the laminar flow. Hot fluid is transported continuously from the hot lower surface to the mean flow; cold fluid is carried out to the region of high temperature due to the enhanced flow mixing associated with this periodic flow regime.

The local Nusselt and time-averaged mean Nusselt numbers are calculated to evaluate the local and global heat transfer performance of this channel as the flow evolves from laminar to transitional states. Figures 11(a) and 11(b) show the heat transfer enhancement for $r=0.375$. Figure 11(a) shows the time-averaged mean Nusselt number, or Nusselt number, as a function of the Reynolds number for laminar and transitional flow regimes. For the laminar regime, the Nusselt number increases slightly as the Reynolds number increases up to a value of $Re<Re_c\approx126$. In this regime the rate of increase in the Nusselt number is very low. As the flow becomes periodic and the Reynolds number is further increased, the Nusselt number continuously increases with respect to the laminar flow regime for a factor that fluctuates between 1 and 4, depending on the Reynolds number, which represents a significant heat transfer enhancement due to enhanced flow mixing. Figure 11(b) shows the pumping power Φ as a function of the Nusselt number for the Reynolds number range of this investigation. The rate of increase in pumping power is higher for transitional regimes than for laminar flow regimes. In laminar regimes, the requested pumping power is relatively smaller because the flow remains parallel to the channel walls, and hence the flow loses energy mostly because of the friction between the flow and channels walls. However, in transitional flow regimes, higher Nusselt numbers require higher pumping power because of a bet-

Table 1 Rates of growth of the Nusselt number and pumping power, ∂Nu/∂Re and $\partial\Phi/\partial$Nu, respectively, and the incremental Nusselt number, dNu, for laminar and periodic flow regimes of the aspect ratio $r=0.375$

Regions	$\partial\mathrm{Nu}/\partial\mathrm{Re}$	$\dfrac{\partial\Phi}{\partial\mathrm{Nu}}$	$d\mathrm{Nu}=\dfrac{\partial\mathrm{Nu}}{\partial\mathrm{Re}}\cdot d\mathrm{Re}+\dfrac{\partial\mathrm{Nu}}{\partial\Phi}\cdot d\Phi$
1	1.82×10^{-3}	5.4×10^{4}	0.0018
2	8.09×10^{-3}	3.2×10^{4}	0.0081
3	3.98×10^{-3}	2.1×10^{5}	0.0039
4	2.52×10^{-3}	9.1×10^{5}	0.0025

ter flow mixing. The flow loses energy due to friction with itself and the channels walls. Thus, in transitional flow regimes, a unitarian increase in the Nusselt number requires a higher amount of pumping power than in laminar flow. The Nusselt number versus the Reynolds number and the pumping power versus the Nusselt number curves are both divided into four regions. In each region, a square mean root fitting is performed to the numerically obtained data; the rate of growth of the Nusselt number with the Reynolds number $\partial\mathrm{Nu}/\partial\mathrm{Re}$ and the rate of growth of the pumping power with the Nusselt number $\partial\Phi/\partial\mathrm{Nu}$ are calculated. Table 1 shows these growth rates for Nu and Φ for the four regions. The best values for $\partial\mathrm{Nu}/\partial\mathrm{Re}$ are in the second and third regions; the best values for $\partial\Phi/\partial\mathrm{Nu}$ are in the first and second regions. The maximum incremental increase in the Nusselt number dNu for unitarian incremental increases of both the Reynolds number and the pumping power occurs in the second region. Thus, this region is the most convenient for better performance because the highest values for the incremental Nusselt number dNu occur in the Reynolds number range of this region.

4 Summary and Concluding Remarks

Numerical simulation results were reported for two aspect ratios $r=0.125$ and $r=0.375$, which demonstrated the effect of r in the type of transition scenario and in the flow and heat transfer characteristics.

The transition scenario in a symmetric wavy channel from laminar to time-dependent transitional flows depends on the channel aspect ratio r. A transition scenario with one Hopf flow bifurcation only develops for the aspect ratio $r=0.375$. The flow evolves from laminar to time-periodic flows through a frequency-doubling transition scenario. The Hopf bifurcation occurs at a critical Reynolds number of $\mathrm{Re}_c\approx126$. Further increases in the Reynolds number do not produce another bifurcation but lead to successive periodic flows in which the fundamental frequency continuously increases. There is a linear relationship between the normalized Reynolds number, $\mathrm{Re}/\mathrm{Re}^*$, and the normalized frequency ω/ω^*, where $\omega/\omega^*=(2)^n$, with n as an integer and ω^* as the fundamental frequency of the Hopf bifurcation. A transition scenario with two Hopf flow bifurcations develops for the aspect ratio $r=0.125$ as the Reynolds number increases from a laminar to a transitional regime. The first bifurcation at a $\mathrm{Re}=\mathrm{Re}_{c_1}$ originates a periodic flow characterized by one fundamental frequency ω_1. The second Hopf bifurcation at a $\mathrm{Re}=\mathrm{Re}_{c_2}>\mathrm{Re}_{c_1}$ originates a quasiperiodic flow with two fundamental frequencies, ω_1 and ω_2, and linear combinations of these frequencies. Re_{c_1} is in the range of 130–136 and Re_{c_2} is in the range of 148–151. In the transitional regime, the periodic and quasiperiodic flows are self-sustained, wavy in nature, and with an active flow mixing.

In the laminar regime, the temperature distribution shows a pattern of stratification with the isotherms parallel to the streamlines, whereas in the transitional regime, the temperature distribution mimics the oscillatory wavy nature of the periodic flows for both aspect ratios. For the laminar regime, the Nusselt number increases slightly as the Reynolds number increases until it reaches the critical Reynolds number $\mathrm{Re}_c\approx126$. As the flow becomes periodic, and for increasing the Reynolds numbers, the Nusselt number continuously and significantly increases with respect to the laminar flow Nusselt number, up to a factor of 4, which represents a significant heat transfer enhancement due to better flow mixing. Higher values of heat transfer rates are obtained with a need for greater of pumping power.

Acknowledgment

The authors acknowledge the support of Fondecyt, the Chilean Fund for Science and Technology, through Grant No. 1050087, and the Department of Mechanical Engineering of Universidad de Santiago de Chile.

Nomenclature

A = area
Ec = Eckart number
H = separation between walls
L = streamwise separation among furrows, periodic length
L_c = characteristic length
P = pressure
Pr = Prandtl number
Q = volumetric flow rate
Re = Reynolds number
T = temperature, time period
T^* = normalized time period
T_w = wall temperature
T_b = bulk temperature
Re_c = critical Reynolds number
Re^* = normalized Reynolds number, critical Reynolds number
Re_H = height-based Reynolds number
a = wall sinusoidal amplitude
k = thermal conductivity
n, m = integer numbers
r = aspect ratio
u, v = streamwise, crosswise velocities
Nu = global Nusselt number, time-averaged mean Nusselt number
$\overline{\mathrm{Nu}}(t)$ = time-dependent mean Nusselt number
$\mathrm{Nu}(x,t)$ = local Nusselt number
$q(x)$ = local heat flux
ΔP = pressure drop
$\hat{U}$ = time-average mean streamwise velocity
$\boldsymbol{v}$ = velocity
c_p = specific heat
$h, \hat{h}$ = half-height of the channel
f_b = wavy channel friction factor
f_p = Poiseuille plane channel friction factor

Greek Symbols

$\partial\mathrm{Nu}/\partial\mathrm{Re}$ = rate of growth of the Nusselt number with the Reynolds number
$\partial\Phi/\partial\mathrm{Nu}$ = rate of growth of pumping power with the Nusselt number
dNu = incremental Nusselt number
α = thermal diffusivity
Φ = pumping power
μ = dynamic viscosity
ν = kinematic viscosity
ρ = density
ω = fundamental (critical) frequency
ω^* = normalized fundamental frequency

References

[1] Ghaddar, N. K., Korczak, K. Z., Mikic, B. B., and Patera, A. T., 1986, "Numerical Investigation of Incompressible Flow in Grooved Channels. Part 1. Stability and Self-Sustained Oscillations," J. Fluid Mech., **163**, pp. 99–127.

[2] Amon, C. H., and Mikic, B. B., 1990, "Numerical Prediction of Convective Heat Transfer in Self-Sustained Oscillatory Flow," J. Thermophys. Heat Transfer, **4**, pp. 239–246.

[3] Greiner, M., 1991, "An Experimental Investigation of Resonant Heat Transfer Enhancement in Grooved Channels," Int. J. Heat Mass Transfer, **34**, pp. 1383–1391.

[4] Greiner, M., Chen, R. F., and Wirtz, R. A., 1995, "Augmented Heat Transfer in a Recovery Passage Downstream From a Grooved Section: An Example of Uncoupled Heat/Momentum Transport," ASME J. Heat Transfer, **117**(2), pp. 303–308.

[5] Greiner, M., Faulkner, R. J., Van, V. T., Tufo, H. M., and Fischer, P. F., 2000, "Simulations of Three-Dimensional Flow and Augmented Heat Transfer in a Symmetrically Grooved Channel," ASME J. Heat Transfer, **122**, pp. 653–660.

[6] Greiner, M., Fischer, P. F., and Tufo, H. M., 2002, "Two-Dimensional Simulations of Enhanced Heat Transfer in an Intermittently Grooved Channel," ASME J. Heat Transfer, **124**, pp. 538–545.

[7] Pereira, J. C. F., and Sousa, J. M. M., 1993, "Finite Volume Calculations of Self-Sustained Oscillations in a Grooved Channels," J. Comput. Phys., **106**, pp. 19–29.

[8] Farhanieh, B., Herman, C., and Sunden, B., 1993, "Numerical and Experimental Analysis of Laminar Fluid Flow and Forced Convection Heat Transfer in a Grooved Duct," Int. J. Heat Mass Transfer, **36**, pp. 1609–1617.

[9] Nigen, J. S., and Amon, C. H., 1994, "Time-Dependent Conjugate Heat Transfer Characteristics of Self-Sustained Oscillatory Flows in a Grooved Channel," ASME J. Fluids Eng., **116**, pp. 499–507.

[10] Wirtz, R. A., Huang, F., and Greiner, M., 1999, "Correlation of Fully Developed Heat Transfer and Pressure Drop in a Symmetrically Grooved Channel," ASME J. Heat Transfer, **121**, pp. 236–239.

[11] Nishimura, T., Kunitsugu, K., and Morega, A. M., 1998, "Fluid Mixing and Mass Transfer Enhancement in Grooved Channels for Pulsatile Flow," J. Enhanced Heat Transfer, **5**, pp. 23–27.

[12] Nishimura, T., Oka, N., Yoshinaka, Y., and Kunitsugu, K., 2000, "Influence of Imposed Oscillatory Frequency on Mass Transfer Enhancement of Grooved Channels for Pulsatile Flow," Int. J. Heat Mass Transfer, **43**, pp. 2365–2374.

[13] Adachi, T., and Uehara, H., 2001, "Correlation Between Heat Transfer and Pressure Drop in Channels With Periodically Grooved Parts," Int. J. Heat Mass Transfer, **44**, pp. 4333–4343.

[14] Herman, C., and Kang, E., 2002, "Heat Transfer Enhancement in a Grooved Channel With Curved Vanes," Int. J. Heat Mass Transfer, **45**, pp. 3741–3757.

[15] Guzmán, A. M., and Amon, C. H., 1994, "Transition to Chaos in Converging-Diverging Channel Flows: Ruelle–Takens–Newhouse Scenario," Phys. Fluids, **6**(6), pp. 1994–2002.

[16] Guzmán, A. M., and Amon, C. H., 1996, "Dynamical Flow Characterization of Transitional and Chaotic Regimes in Converging-Diverging Channels," J. Fluid Mech., **321**, pp. 25–57.

[17] Guzmán, A. M., and Amon, C. H., 1998, "Convective Heat Transfer and Flow Mixing in Converging-Diverging Channel Flows," *Proceedings of the ASME Heat Transfer Division*, Vol. 1, ASME, New York, pp. 61–68.

[18] Wang, G., and Vanka, S. P., 1995, "Convective Heat Transfer in Periodic Wavy Passages," Int. J. Heat Mass Transfer, **38**(17), pp. 3219–3230.

[19] Wang, C. C., and Chen, C. K., 2002, "Forced Convection in a Wavy-Wall Channel," Int. J. Heat Mass Transfer, **45**, pp. 2587–2595.

[20] Stephanoff, K. D., Sobey, I. J., and Belhouse, B. J., 1980, "On Flow Through Furrowed Channels. Part 2. Observed Flow Patterns," J. Fluid Mech., **96**, pp. 27–32.

[21] Nishimura, T., Murakami, S., Akarawa, S., and Kawamura, Y., 1990, "Flow Observations and Mass Transfer Characteristics in Symmetrical Wavy-Walled Channels at Moderate Reynolds Numbers for Steady Flow," Int. J. Heat Mass Transfer, **33**, pp. 835–845.

[22] Tatsuo, N., 1994, "Oscillatory Flow and Mass Transfer Within Asymmetric and Symmetric Channels With Sinusoidal Walls," Int. J. Heat Mass Transfer, **30**, pp. 269–278.

[23] Vyas, S., Zhang, J., and Manglik, R. M., 2004, "Steady Recirculation and Laminar Torced Convection in a Sinusoidal Wavy Channel," ASME J. Heat Transfer, **126**, p. 500.

[24] Manglik, R. M., Zhang, J., and Muley, A., 2005, "Low Reynolds Number Forced Convection in Three-dimensional Wavy-Plate-Fin Compact Channels: Fin Density Effects," Int. J. Heat Mass Transfer, **48**, pp. 1439–1449.

[25] Stalio, E., and Piller, M., 2007, "Direct Numerical Simulations of Heat Transfer in Converging-Diverging Wavy Channels," ASME J. Heat Transfer, **129**, pp. 769–777.

[26] Morimoto, K., Suzuki, Y., and Kasagi, N., 2008, "Higher Performance Recuperator With Oblique Wavy Walls," ASME J. Heat Transfer, **130**, p. 101801.

[27] Fabbri, G., 2000, "Heat Transfer Optimization in Corrugated Wall Channels," Int. J. Heat Mass Transfer, **43**, pp. 4299–4310.

[28] Patera, A. T., 1984, "A Spectral Element Method for Fluid Dynamics: Laminar Flow in a Channel Expansion," J. Comput. Phys., **54**(3), pp. 468–488.

[29] Ye, A., and Shimizu, M., 2001, "Augmented Longitudinal Diffusion in Grooved Tubes for Oscillatory Flow," Int. J. Heat Mass Transfer, **44**, pp. 633–644.

[30] Del Valle, M., Carrasco, A. M., and Guzmán, A. M., 2002, "Flow Transitions and Heat Transfer in Open Block Tandem Channels," ITherm 2002, International Conference on Thermal, Mechanics and Thermomechanical Phenomena in Electronic Systems, San Diego, CA, May 29–Jun. 1.

[31] Araya, P. E., 2001, "Estudio y Análisis 2D del Flujo Laminar-Transicional y la Transferencia de Calor en un Canal de Paredes Sinusoidales Paralelas," ME thesis, Universidad de Santiago de Chile, Santiago, Chile.

[32] Urzua, F., 2005, "Espectros de Fourier, Pseudo Espacio de Fase y Exponentes de Lyapounov en el Transporte de Fluido y Calor en Canales Sinusoidales Paralelos Asimétricos," ME thesis, Universidad de Santiago de Chile, Santiago, Chile.

[33] Cardenas, M. J., 2006, "Mezclado de Flujo en un Canal de Paredes Sinusoidales Asimétricas Cerca de las Bifurcaciones del Flujo," ME thesis, Universidad de Santiago de Chile, Santiago, Chile.

[34] Hormazabal, R. A., 2006, "Determinación y Evaluación Numérica de Características Lagrangianas de un Flujo Laminar-Transicional en Canales Simétricos Ondulados," ME thesis, Universidad de Santiago de Chile, Chile.

[35] Aracena, T. A., 2006, "Frequency-Doubling Escenario de Transición en Canales Sinusoidales Simétricos," ME thesis, Universidad de Santiago de Chile, Chile.

[36] Del Valle, M., 2001, "Estudio y Análisis Mediante Simulaciones Computacionales de la Mecánica de Fluidos y Transferencia de Calor en Canales con Irregularidades Geométricas," ME thesis, Universidad de Santiago de Chile, Santiago, Chile.

Three-Dimensional Numerical Study of Flow and Heat Transfer Enhancement Using Vortex Generators in Fin-and-Tube Heat Exchangers

P. Chu

Y. L. He
e-mail: yalinghe@mail.xjtu.edu.cn

W. Q. Tao

State Key Laboratory of Multiphase Flow in Power Engineering,
School of Energy and Power Engineering,
Xi'an Jiaotong University,
Xi'an,
Shaan xi 710049, China

In this paper, a three-dimensional numerical investigation was performed for heat transfer characteristics and flow structure of full scale fin-and-tube heat exchangers with rectangular winglet pair (RWP). For the Reynolds number ranging from 500 to 880, the baseline configuration (without RWP) is compared with three enhanced configurations (with RWP): inline-1RWP case, inline-3RWP case, and inline-7RWP case. It was found that the air-side heat transfer coefficient improved by 28.1–43.9%, 71.3–87.6%, and 98.9–131% for the three enhanced configurations, with an associated pressure drop penalty increase of 11.3–25.1%, 54.4–72%, and 88.8–121.4%, respectively. An overall performance comparison was conducted by using the London area goodness factor. It is revealed that among the three enhanced configurations, the inline-1RWP case obtains the best overall performance, and the inline-3RWP case is better than the inline-7RWP case. The numerical results were also analyzed on the basis of the field synergy principle to provide fundamental understanding of the relation between local flow structure and heat transfer augmentation. It was confirmed that the reduction in the average intersection angle between the velocity vector and the temperature gradient was one of the essential factors influencing heat transfer enhancement. The analysis also provides guidelines for where the enhancement technique is highly needed. [DOI: 10.1115/1.3139185]

Keywords: longitudinal vortex generator, heat transfer enhancement, fin-and-tube heat exchanger

1 Introduction

Fin-and-tube heat exchangers are widely used in various engineering fields such as heating, ventilating, air conditioning, and refrigeration (HVACR) systems, automobiles, petroleum, electronics cooling, and chemical industry. Owing to the requirement of smaller volume, less cost, quiet, and high efficiency in operation, high efficiency compact heat exchanger is very necessary to achieve these goals. The total thermal resistance for such kind of heat exchangers is comprised of three parts: the air-side convective resistance, the wall conductive resistance, and the liquid-side convective resistance. The heat transfer coefficient on the air-side is typically low due to the thermophysical property of air and relative low frontal velocity. Thus, the air-side thermal resistance is the dominant part to heat transfer and efforts to improve the performance of these heat exchangers should focus on the air-side surfaces.

Vortex generation is a new and innovative strategy, which holds promise in air-side heat transfer enhancement. Vortex generators (VGs) such as wings and winglets can introduce vortices into the flow field causing heat transfer enhancement. Vortex generators can be punched, mounted, or embossed on a heat transfer surface. When fluid flows through vortex generators, vortices are generated due to the friction and separation on the edge of the vortex generator. Extensive studies were done on heat transfer characteristics and flow structure for heat exchangers with longitudinal vortex generators (LVGs). In recent years, the implementation of vortex generators in fin-and-tube heat exchangers has received more and more attention. Fiebig [1] numerically and experimentally investigated embedded vortices in an internal flow. Deb and Biswas [2] numerically analyzed heat transfer characteristics and flow structure in laminar and turbulent flows through a rectangular channel containing built-in vortex generators by means of solutions of the full Navier–Stokes and energy equations. Jacobi and Shah [3] gave an excellent review on heat transfer surface enhancement through the use of longitudinal vortices (LVs). Biswas et al. [4] experimentally and numerically examined the flow structure and heat transfer effects of longitudinal vortices in a channel flow. Liou et al. [5] experimentally investigated heat transfer and fluid flow in a square duct with 12 different shaped vortex generators. Gentry and Jacobi [6] experimentally explored the heat transfer enhancement by delta wing-generated vortices in flat plate and developing channel flows. More recently, Joardar and Jacobi [7] experimentally evaluated the potential of winglet type vortex generator arrays for air-side heat transfer enhancement of a compact plain fin-and-tube heat exchanger by full scale wind tunnel testing. They [8] also numerically investigated the flow and heat transfer enhancement using an array of delta winglet vortex generators in a fin-and-tube heat exchanger. O'Brien et al. [9] experimentally investigated the forced convection heat transfer in a narrow rectangular duct fitted with an elliptical tube and one or two delta winglet pairs. They found that the addition of the single winglet pair to the oval tube geometry yielded significant heat transfer enhancement, averaging 38% higher than the oval tube with no winglet case.

From the traditional point of view, the reasons why the vortex generators such as wings or winglets can augment heat transfer

Contributed by the Heat Transfer Division of ASME for publication in the JOURNAL OF HEAT TRANSFER. Manuscript received September 9, 2008; final manuscript received March 2, 2009; published online June 25, 2009. Review conducted by Frank Cunha.

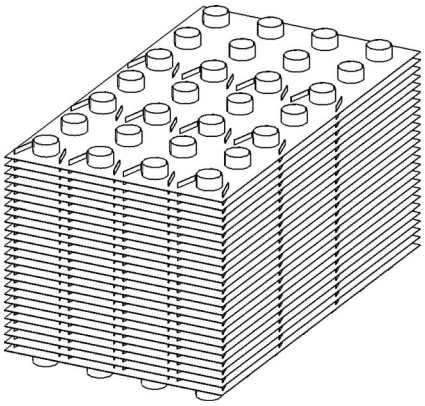

Fig. 1 Schematic of the core region of a fin-and-tube heat exchanger with RWPs

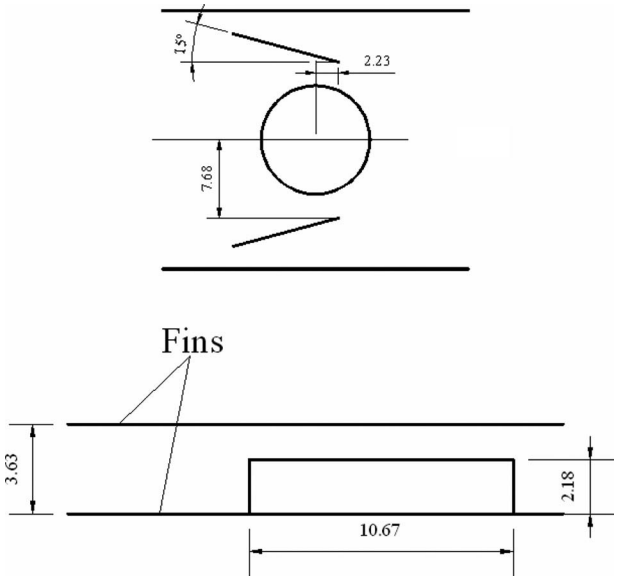

Fig. 3 Winglet type vortex generator dimensions and the placement with respect to the tube

are attributed to intensified fluid mixing, boundary layer modification, and flow destabilization. Guo et al. [10] proposed a novel concept for convective heat transfer enhancement of parabolic flow, and they indicated that the reduction in the intersection angle between the velocity and temperature gradient can effectively enhance the heat transfer. Furthermore, Tao and co-workers [11,12] proved this new concept for elliptic flow with a not too small Peclet number (greater than 100). Qu et al. [13] numerically designed several kinds of efficient slotted fin surfaces using the field synergy principle. In the present study, the effects of three parameters (the Reynolds number, the number of vortex generators, and the tube bank arrangement) on heat transfer characteristics and fluid flow structure of fin-and-tube heat exchangers with vortex generators are explored. The heat conduction in the fins and the thickness of the vortex generators are considered. The temperature distribution in the fins will be determined by solving the conjugate heat transfer problem. A full scale model is adopted in our numerical study, which involves all the tube rows in a seven-row fin-and-tube heat exchanger with vortex generators. On the basis of the field synergy principle, we will explore the fundamental mechanism for heat transfer enhancement.

2 Model Descriptions

2.1 Physical Model. The schematics of a fin-and-tube heat exchanger with longitudinal vortex generators is shown in Fig. 1. There are four basic vortex generators—delta wing, rectangular wing, delta winglet pair, and rectangular winglet pair (see Fig. 2). In this present study, we adopt the rectangular winglet pair as the vortex generator. Figure 3 shows the dimensions of rectangular winglet pairs and their placement with respect to the tube. In Fig. 4, X is the streamwise direction, Y is the spanwise direction, and Z stands for the fin pitch direction. Figure 4(a) gives a top view of the computational domain for a fin-and-tube heat exchanger with rectangular winglet pairs (RWPs), and Fig. 4(b) presents a side view of the computational domain. Two neighboring fins form a channel with $H=3.63$ mm, $B=12.7$ mm, and $L=177.8$ mm. The first tube, with diameter $D=10.67$ mm, is located at $X=12.7$ mm from the inlet of the flow channel. The fin material is aluminum and the fin thickness is $F_t=0.18$ mm. The air inlet temperature is 310.6 K and the tube temperature is 291.77 K. Because of the geometry character of the symmetry of the fin-and-tube heat exchanger, the region (in the $x-y$ plane) outlined by the dashed lines in Fig. 4(a) is selected as the computational domain. Due to the high heat transfer coefficient inside the tube and the high thermal conductivity of the tube wall, the tube temperature is set as constant. However, the temperature distribution on the fin surface is unknown and will be determined during the iteration process. In order to solve this conjugated problem, the computational domain should contain the whole fin surface during the numerical simulation. Therefore, the region (in the $x-z$ plane) outlined by the dashed lines in Fig. 4(b) is taken as the computational domain due to the geometry character of periodicity.

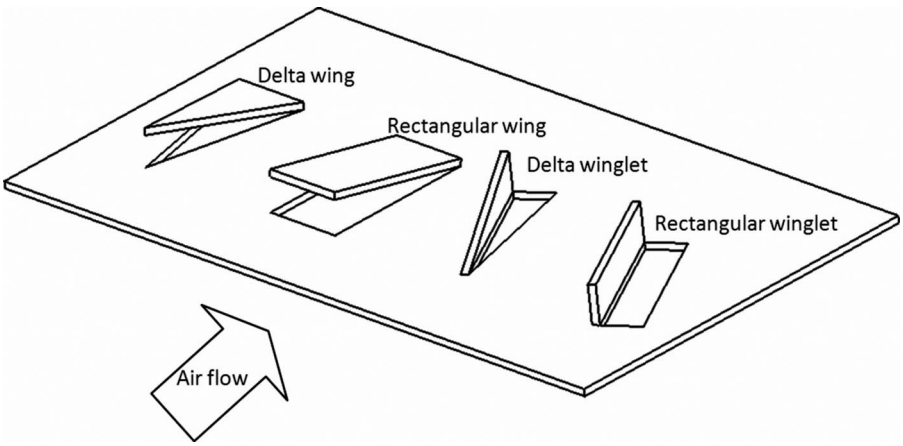

Fig. 2 Four basic vortex generator forms

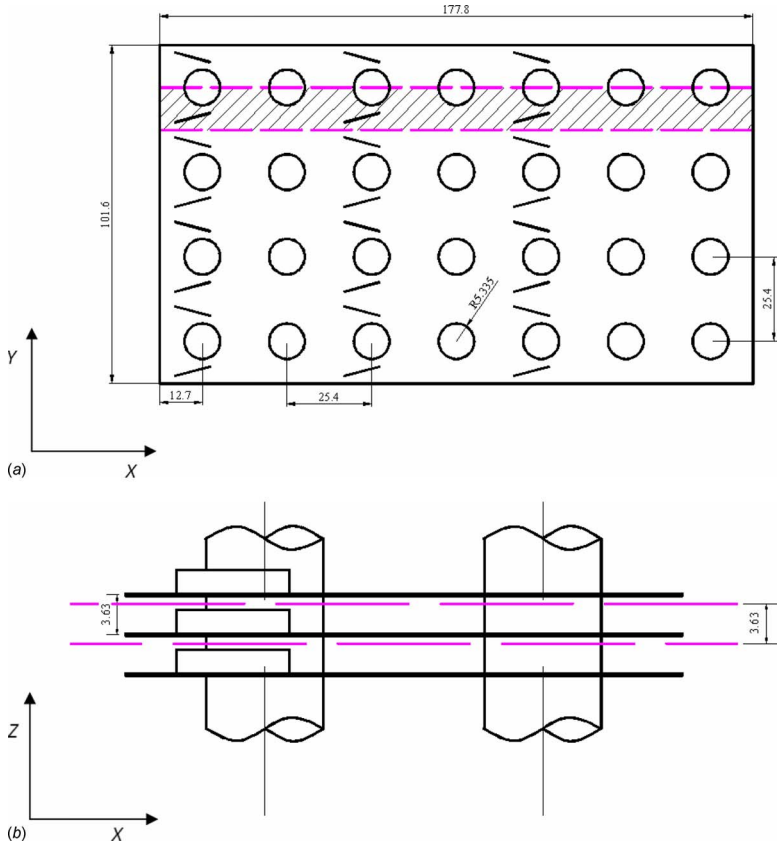

Fig. 4 Coordinate system and computational domain

The actual computation domain is extended by $5H$ at the inlet to maintain the inlet velocity uniformity, and the domain is extended by $30H$ at the exit to ensure a recirculation-free flow there. To save space, the extended domain is not pictured in Fig. 4.

2.2 Governing Equations and Boundary Conditions. The fluid is considered incompressible with constant properties. According to Ferrouillat et al. [14], the generation of longitudinal vortices is a quasi-steady phenomenon. Consequently, due to the low inlet velocity and the small fin pitch, the flow in the channel of the compact heat exchanger is assumed to be laminar and steady. Fin thickness and heat conduction in the fins and vortex generators are taken into account.

For the simplicity of presentation, the governing equations and boundary conditions for numerical simulation in this paper can be found in Ref. [13] and will not be restated here.

2.3 Numerical Methods. The Navier–Stokes and energy equations with the boundary condition equations are solved by using a computational fluid dynamics code (FLUENT). In order to improve the accuracy of the simulation results, the grids around the tubes and the vortex generators are refined. The convective terms in the governing equations for momentum and energy are discretized with the second upwind scheme. The coupling between velocity and pressure is performed with SIMPLE algorithm. The convergence criterion for the velocities is that the maximum mass residual of the cells divided by the maximum residual of the first five iterations is less than 1.0×10^{-5}, and the convergence criterion for the energy is that the maximum temperature residual of the cells divided by the maximum residual of the first five iterations is less than 1.0×10^{-8}.

2.4 Parameter Definitions. The definitions of Re number, average Nu number, friction factor f, and Colburn factor j are as follows:

$$\mathrm{Re} = \rho V_m D_h/\mu, \quad \mathrm{Nu} = hH/\lambda \tag{1}$$

$$f = \frac{\Delta P}{\frac{\rho V_m^2}{2}\frac{A_T}{A_{\min}}}, \quad j = \mathrm{St}\cdot \mathrm{Pr}^{2/3}, \quad \mathrm{St} = \frac{h}{\rho V_m c_p} \tag{2}$$

where V_m, μ, and λ are the mean velocity in the minimum flow cross section of the flow channel, dynamic viscosity, and thermal conductivity, respectively; D_h is the hydraulic diameter; ΔP is the pressure drop across computational domain; A_T is the total heat transfer surface area; $A_{\min}$ is minimum flow cross section area; and H is the height of the flow channel.

The mean temperature and pressure of a cross section are defined as

$$\bar{T} = \frac{\int\int_A uT dA}{\int\int_A u dA}, \quad \bar{p} = \frac{\int\int_A p dA}{\int\int_A dA} \tag{3}$$

The total heat transfer, pressure loss, and log mean temperature difference are defined as

$$Q = \dot{m} c_p (\bar{T}_{\mathrm{out}} - \bar{T}_{\mathrm{in}}), \quad \Delta P = \bar{p}_{\mathrm{in}} - \bar{p}_{\mathrm{out}} \tag{4}$$

$$\Delta T = \frac{(T_w - \bar{T}_{\mathrm{in}}) - (T_w - \bar{T}_{\mathrm{out}})}{\ln[(T_w - \bar{T}_{\mathrm{in}})/(T_w - \bar{T}_{\mathrm{out}})]} \tag{5}$$

The heat transfer coefficient is defined as

$$h = \frac{Q}{A\Delta T} \tag{6}$$

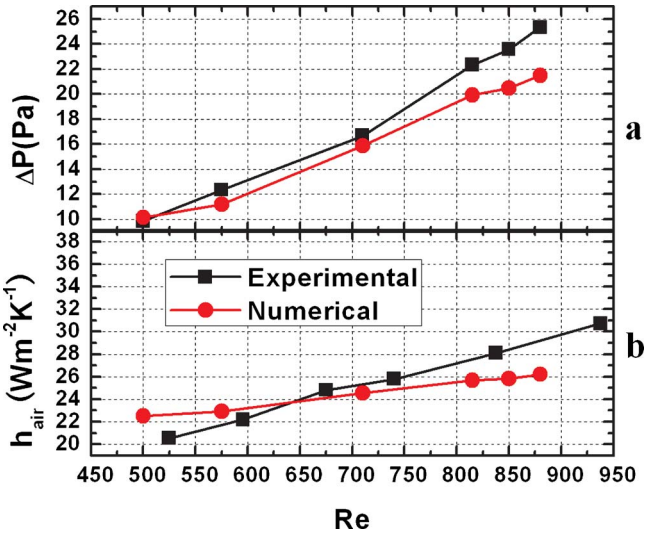

Fig. 5 Experimental numerical comparison of h_{air} and ΔP for model validation

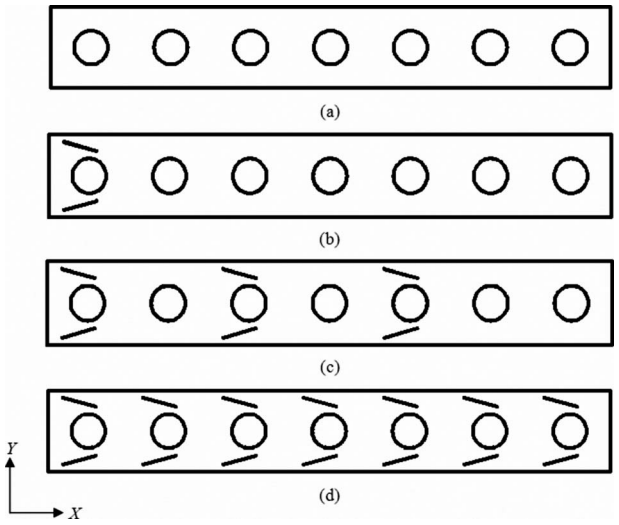

Fig. 6 Different configurations for fin-and-tube heat exchangers with and without RWPs

3 Validation of Numerical Results

In order to validate the independency of solution on the grid, three different grid systems are investigated, which include about 800,000, 1,260,000, and 1,500,000 cells, respectively, for the fin-and-tube heat exchanger with one RWP. The change in the averaged Nu number is less than 3% among the three different grid systems. For the present study, the final grid number is selected to be about 1,260,000. Similar validations are also conducted for other cases.

In order to validate the reliability of the numerical method being used, the numerical simulation is conducted for a fin-and-tube heat exchanger with the same geometrical configurations as presented in Ref. [7]. The predicted results are compared with the experimental results from Ref. [7]. The overall pressure loss penalty ΔP and the air-side heat transfer coefficient h_{air} are shown in Figs. 5(a) and 5(b), respectively. The average discrepancy between the predicted pressure loss and the experimental values is less than 11%, and the average discrepancy between the predicted air-side heat transfer coefficient and the experimental values is less than 5%. The good agreement between the predicted and experimental results indicates that the numerical model is reliable to predict heat transfer characteristics and flow structure in compact heat exchangers.

4 Results and Discussion

4.1 Flow Pattern and Heat Transfer. In order to study the influence of RWPs on the heat transfer characteristics and flow structure for fin-and-tube heat exchangers, a comparative investigation for fin-and-tube heat exchangers with and without RWPs is performed. The RWPs are symmetrically mounted adjacent to the tubes. The angle of attack α is set at 15 deg. The Re based on the hydraulic diameter ranges from 500 to 880. Figure 6 shows different configurations for fin-and-tube heat exchangers with and without RWPs.

Figure 7 presents the local velocity distribution on the middle cross section (parallel to the $x-y$ plane) for the baseline case and the inline-3RWP case at Re=850. From Fig. 7(a) it can be seen that a recirculation region behind the tube is formed. The recirculating flow is separated from the main stream, and the fluid in this region is thermally isolated. Owing to this, a poor heat transfer zone is developed. Comparing Fig. 7(a) with Fig. 7(b) we can see that the velocity distribution and the wake structure for the inline-3RWP case are totally different from those for baseline case. The RWPs for the inline-3RWP case develop longitudinal vortices, which delay the boundary layer separation from the tube, reduce the size of recirculation region, accelerate the local flow velocity, intensify the mixing between cold fluid and hot fluid, disrupt the thermal boundary layer, and thus enhance heat transfer. From Fig. 7(b) we can see that the point of separation on the tube travels downstream, and the size of the recirculation region is reduced. Figure 8 illustrates the local temperature distributions on the middle cross section (parallel to the $y-z$ plane) for the baseline case and the inline-3RWP case at Re=850. Comparing Fig. 8(a) with Fig. 8(b) we can see that the temperature distribution in the vicinity of the inlet region is almost identical for the baseline case and the inline-3RWP case. As the air approaches the RWPs, the longitudinal vortices are generated and the heat transfer is significantly enhanced. The enhancement of heat transfer is notable even far downstream of RWPs because the longitudinal vortices persist for several winglet chords. Thus, the temperature behind the RWPs for the inline-3RWP case is distinctly lower than that in the corresponding region for the baseline case. The results indicate that the RWPs can significantly enhance the heat transfer with moderate pressure loss penalty.

Figure 9 shows the longitudinal distribution of line-weighted average Nusselt number on the RWP-mounted fins for the baseline and the three enhanced configurations at Re=850. For both the baseline and enhanced configurations, the variations in the Nusselt number are almost identical up to the location of the first tube. The Nusselt number is very high in the vicinity of the inlet region and decreases gradually along the flow channel until the first fin-and-tube junction. The extremely high Nusselt number at

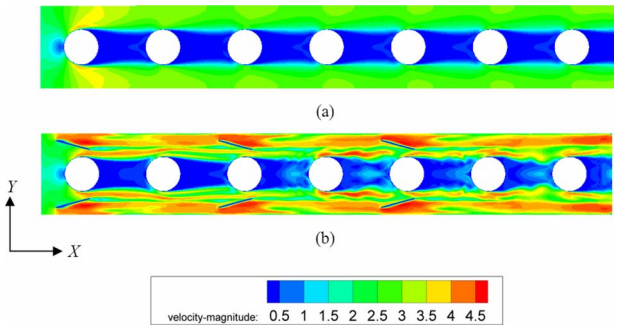

Fig. 7 Local velocity distributions on the middle cross section for the baseline case and the inline-3RWP case at Re=850

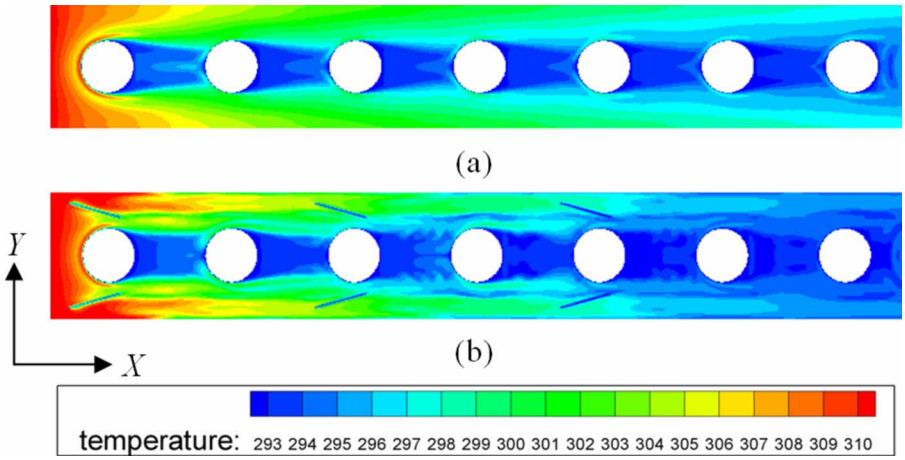

Fig. 8 Local temperature distributions on the middle cross section for the baseline case and the inline-3RWP case at Re=850

the inlet region can be primarily attributed to the large temperature gradient and the thin boundary layer at the entrance region. With the growth of velocity and thermal boundary along the channel, the Nusselt number decreases. For the baseline case, the curve shows seven peaks (the locations for the peaks are $X=25.3$ mm, 54.1 mm, 79.2 mm, 104.4 mm, 129.5 mm, 154.6 mm, and 181.6 mm) at the same intervals along the longitudinal direction, corresponding to the junctions of fin and the seven tubes. This is mainly due to the formation of horseshoe vortices at the fin-and-tube junction. After the first tube, for the baseline configuration, the curve decreases abruptly until it meets the second tube in the channel. However, for the enhanced configurations, the curves decrease a little and rise to a new peak (located at $X=30.7$ mm) before the second tube. This is mainly due to the formation of longitudinal vortices around the RWPs in the vicinity of the first tube. It can be seen clearly from the figure that the average Nusselt number in the wake region of the tube for the baseline case is apparently lower than that for the enhanced case. For the inline-7RWP case, the curve in the wake region of the tube is slightly higher than that for the inline-1RWP case and the inline-3RWP case. This can be attributed to the generation of the strong swirling flow by RWPs. The strong swirling flow can drag the fluid in the wake region to the mainstream and enhance the mixing. The wake will be suppressed by the high momentum swirling flow and the size of the wake region will be reduced and the heat transfer is augmented. Comparing the curves for the inline-1RWP case, the inline-3RWP case, and the inline-7RWP case, it can be found that there are seven pairs of peaks around tube 1 (the locations for the peak pair are $X=25.3$ mm and 30.7 mm), tube 2 ($X=46.9$ mm and 54.1 mm), tube 3 ($X=72.0$ mm and 79.2 mm), tube 4 ($X=98.9$ mm and 106.2 mm), tube 5 ($X=124.1$ mm and 131.3 mm), tube 6 ($X=149.3$ mm and 156.4 mm), and tube 7 ($X=169.0$ mm and 179.7 mm) for the inline-7RWP case, and there are three pairs of peaks around the tube 1 ($X=25.3$ mm and 30.7 mm), tube 3 ($X=73.8$ mm and 81.0 mm), and tube 5 ($X=124.1$ mm and 131.3 mm) for the inline-3RWP case. However, there is one pair of peaks for the inline-1RWP case around tube 1 ($X=25.3$ mm and 30.7 mm). But for the baseline configuration, there is only one peak in the vicinity of the tubes. It is interesting to note that the location of the pair of peaks is corresponding to the location of the tubes and RWPs. The presence of the peak pair around the tube may be due to the formation of horseshoe vortices by the fin-and-tube junction and the formation of LVs by RWPs. After the fifth tube, the heat performance of the baseline configuration gradually approaches that of the enhanced configurations.

Figure 10(*a*) presents the variation in the air-side heat transfer coefficient h_{air} versus the Re number. It can be seen from Fig. 10(*a*) that the heat transfer coefficients h_{air} for both the baseline case and the enhanced cases increase with increasing Reynolds number. With a higher value of Reynolds number, the thermal

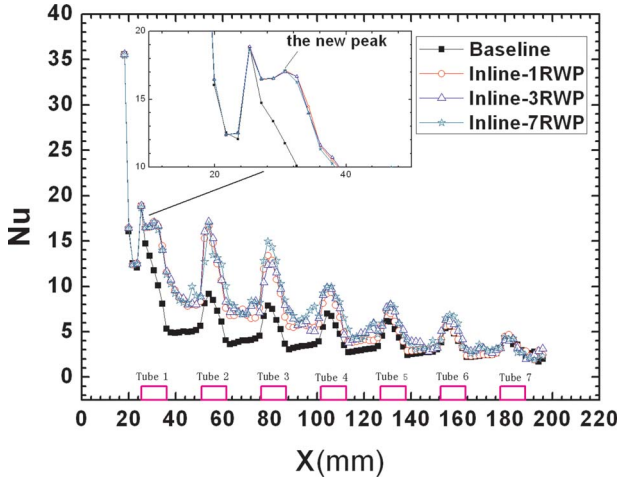

Fig. 9 Longitudinal distributions of line-weighted average Nusselt number on the RWP-mounted fins for the baseline case and three enhanced cases at Re=850

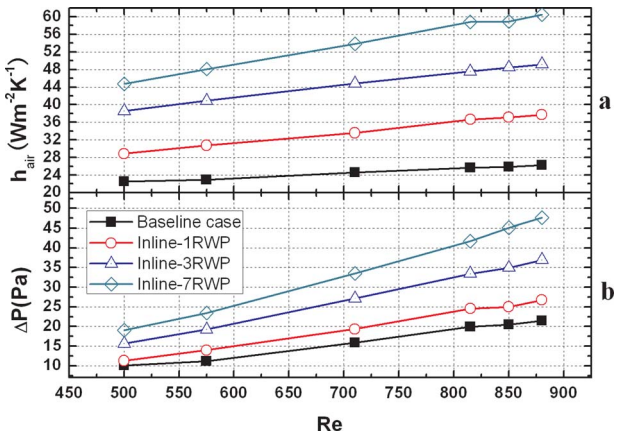

Fig. 10 Variations in the air-side heat transfer coefficient h_{air} and the pressure drop ΔP versus the Re number

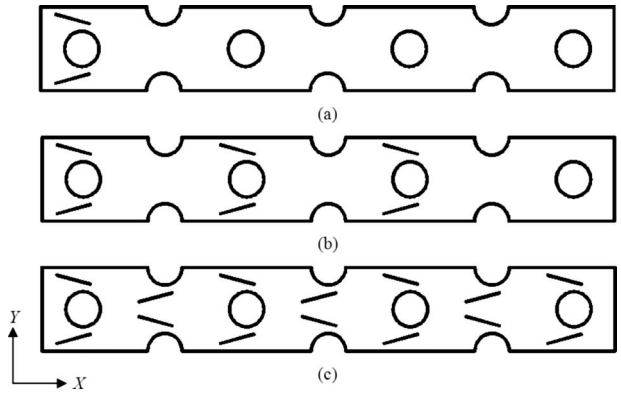

Fig. 11 Different configurations for fin-and-tube heat exchangers with staggered arrangement

boundary layer thickness decreases and the degree of fluid mixing increases. Consequently, a global augmentation in heat transfer is observed with the increase in Reynolds number. Comparing with the baseline case, the heat transfer coefficient for the inline-1RWP case is improved by 28.1–43.9% over the range of the Reynolds number considered. The heat transfer coefficient for the inline-3RWP case is increased from 71.3% at Re=500 to 87.6% at Re=880 compared with the baseline case. The inline-7RWP case improves the heat transfer coefficient h_{air} from 98.9% to 131% over the baseline case. These numerical results demonstrate that the winglet vortex generators can significantly improve the heat transfer performance of the fin-and-tube heat exchangers. Figure 10(*b*) shows the relation of the pressure drop ΔP and the Re number. The heat transfer augmentation is usually accompanied by additional pressure drop penalty. Comparing with the baseline case, the inline-1RWP case increase in ΔP by 11.3–25.1% over the range of the Reynolds number considered, the inline-3RWP case increase in ΔP by 54.4–72%, and 88.8–121.4% for the inline-7RWP case. The incremental pressure drop is mainly due to the additional formed drag induced by the winglet vortex generators.

4.2 Influence of the Tube Bank Arrangement. In order to study the influence of the tube bank arrangement on the heat transfer characteristics and the flow structure for fin-and-tube heat exchangers with RWPs, a comparative investigation for fin-and-tube heat exchangers with inline arrangement and staggered arrangement was performed. The angle of attack α is set at 15 deg. The Re based on the hydraulic diameter ranges from 500 to 880. Figure 11 shows different configurations for fin-and-tube heat exchangers with staggered arrangement.

The thermal hydraulic performances of the heat exchangers with staggered tube arrangement are compared with the heat exchangers with inline tube arrangement in Fig. 12. For the 1-RWP case, the heat transfer coefficient of the staggered-1RWP case is increased by 29.1–35.1% compared with that of the inline-1RWP case. For the 3-RWP case, the staggered-3RWP case improves the heat transfer coefficient from 19.1% to 24.2% over the inline-3RWP case. For the 7-RWP case, the staggered-7RWP case causes an increase of 17.4–20.1% in the heat transfer coefficient over the inline-7RWP case. Comparing with the inline tube arrangement, the heat transfer enhancement for staggered tube arrangement is mainly due to the horseshoe vortices generated in the fin-tube junction. For the inline tube arrangement, the second and the subsequent tubes are in the tube wake of their upstream tubes. The heat transfer in the tube wake is very poor, and therefore the tube wake greatly reduces the high heat transfer potential of the tube. However, for the staggered tube arrangement, the formation of horseshoe vortices and the large temperature gradient around the tube can play the biggest role in heat transfer augmentation.

The heat transfer enhancement is accompanied by additional pressure losses. The results presented in Fig. 12(*b*) indicate the pressure drop associated with the inline and staggered tube arrangements at different Reynolds numbers. In comparison with the inline tube arrangement, the staggered-1RWP case increases the pressure drop from 46.9% to 54.1% over the inline-1RWP

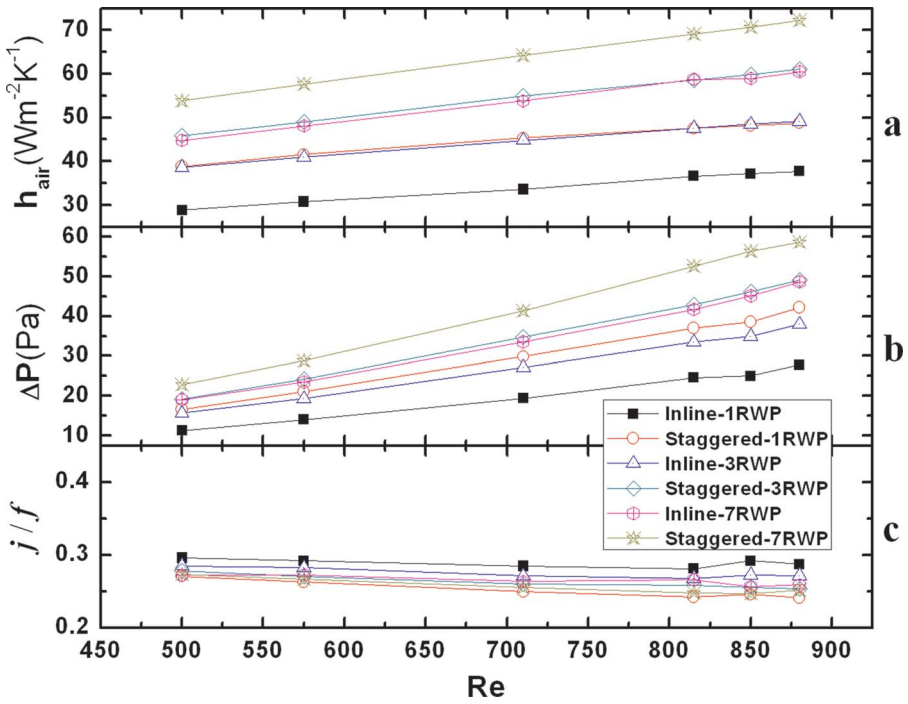

Fig. 12 Variations in the air-side heat transfer coefficient h_{air}, the pressure drop ΔP, and the overall performance j/f versus the Re number

case, the staggered-3RWP case improves the pressure drop from 22.1% to 31.9% over the inline-3RWP case, and the pressure drop of the staggered-7RWP case is increased by 19.6–25.8% compared with that of the inline-7RWP case. The additional pressure drop penalty is primarily due to the form drag of staggered tubes.

The overall performance of the fin-and-tube heat exchangers with different tube arrangements are evaluated using the criterion of the area goodness factor j/f. The staggered cases are compared with the inline cases in Fig. 12(*c*). For the Reynolds number ranging from 500 to 880, all the inline configurations have a better performance than the corresponding staggered configurations. For the case of 1-RWP, the inline-1RWP case increases the j/f ratio from 9.3% to 19.3% over the staggered-1RWP case. For the case of 3-RWP, the inline-3RWP case improves the j/f ratio from 2.6% to 7.2% compared with the staggered-3RWP case. For the case of 7-RWP, the inline-7RWP case causes an increase of 2.3–7.1% in the j/f ratio over the staggered-7RWP case. It is interesting to note that the influence of the tube arrangement on the overall performance becomes progressively small with the increasing number of the RWPs. From the viewpoint of "area goodness," the inline-1RWP case will require a smaller frontal area than the other cases.

4.3 Discussion on Fundamental Mechanism for Heat Transfer Enhancement. As mentioned above, from the traditional perspective, vortex generators can enhance convective heat transfer because they can disrupt the boundary layer, intensify the mixing, and increase the disturbance in the channel. All these functions serve ultimately to bring about heat transfer augmentation. However, this is insufficient to reveal the fundamental mechanism for heat transfer enhancement. According to the field synergy principle (FSP) proposed by Guo et al. [10], it was proved by Tao and co-workers [11,12] that the existing single phase convective heat transfer enhancement methods can be unified by FSP. For simplicity, the details about FSP can be found in relevant references [10–13] and will not be restated here.

The local intersection angle between the velocity vector and the temperature gradient at a grid node is defined as

$$\theta = \cos^{-1}\left(\frac{\boldsymbol{U}\cdot\boldsymbol{\nabla T}}{|\boldsymbol{U}||\boldsymbol{\nabla T}|}\right) = \cos^{-1}\left(\frac{u\dfrac{\partial T}{\partial x}+v\dfrac{\partial T}{\partial y}+w\dfrac{\partial T}{\partial z}}{|\boldsymbol{U}||\text{grad } T|}\right) \tag{7}$$

The average intersection angle of the computation domain can be obtained by using numerical integration

$$\theta_m = \frac{\sum_{i,j,k}\theta_{i,j,k}\Delta x_i\Delta y_j\Delta z_k}{\sum_{i,j,k}\Delta x_i\Delta y_j\Delta z_k} \tag{8}$$

where the subscripts i, j, and k refer to the control volume of the fluid.

The average intersection angles for the baseline configuration and enhanced configurations are presented in Fig. 13. From the figure we can see that the average intersection angle increases with the increasing Reynolds number for the three configurations, which indicates that the synergy between the velocity and the temperature gradient becomes worse with the increasing Reynolds number. However, at the same Reynolds number the average intersection angle θ_m for the enhanced configurations is smaller than that for the baseline configuration, which indicates that the synergy for the enhanced configurations is better than that for the baseline configuration. For the same Reynolds number, the average intersection angle of the baseline configuration is the largest, while that of the staggered-1RWP case is the smallest, which is in accordance with their corresponding heat transfer performance.

In order to have a more intuitive understanding of the field synergy principle, Fig. 14 presents the streamlines and the isothermal distributions on the middle cross section (parallel to the $x-y$ plane) for baseline configuration and enhanced configurations at Re=850. From the figures we can see that in the vicinity of the inlet regions, the isotherms are almost perpendicular to the local streamlines, which indicates that the temperature gradient are almost in the same direction as the velocity vector. This implies an excellent synergy between the velocity field and the temperature field. For the baseline case, it can be seen clearly in Fig. 14(*a*) that the recirculation regions appear in the rear of the tubes, which indicates poor heat transfer there. Furthermore, in most part of the channel for the baseline case, especially in the rear of the tubes, the isotherms are almost parallel to the local streamlines, which indicates a bad synergy between the velocity field and the temperature field. It appears that the poor heat transfer regions are the same regions of bad synergy. This is in accordance with the field synergy principle. Due to the presence of RWPs for the inline-1RWP case, the velocity field and the temperature field are modified. From Figs. 14(*c*) and 14(*d*) it can be seen clearly that the synergy between the velocity field and the temperature field for the inline-1RWP case is significantly improved, especially in the downstream region of the RWPs. However, for the inline-1RWP case, in the downstream region of the channel, the strength of longitudinal vortices decays, and the synergy between the velocity and temperature gradient is not improved a lot in comparison with the baseline configuration. For the staggered-1RWP case, we can see from Fig. 14(*e*) and 14(*f*) that the synergy between the velocity and the temperature gradient is further improved in comparison with the inline-1RWP case. The better synergy is mainly due to the staggered arrangement of the tubes. For the inline-1RWP case, the second and the subsequent tubes are in the wake region of their upstream tubes. The wake region of the tube is associated with the low heat transfer coefficient. Therefore the second and all the subsequent tubes are in poor heat transfer region, and it does nothing good to heat transfer enhancement. However, for the staggered-1RWP case, the upstream fluid will directly encounter with the front part of each tube in the channel, and horseshoe vortices will be generated to augment the heat transfer. Consequently, the heat transfer of the staggered-1RWP case is better than that of the inline-1RWP case.

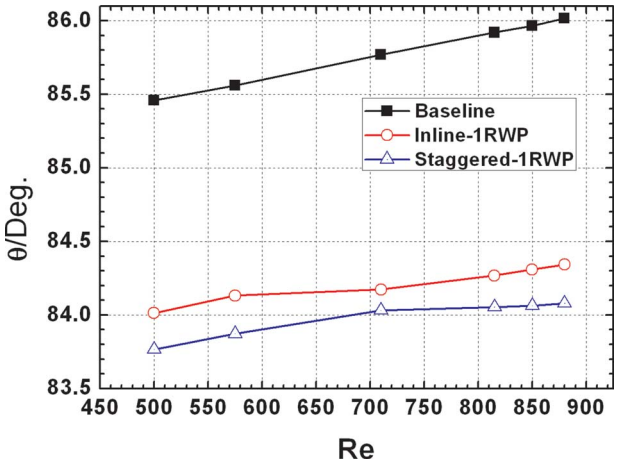

Fig. 13 The average intersection angles for baseline configuration and enhanced configurations

5 Conclusions

In this paper, three-dimensional numerical simulations are employed to investigate the heat transfer characteristics and flow structure in full scale fin-and-tube heat exchangers with RWPs. The major conclusions are drawn as follows.

(1) Comparing with the baseline case, the heat transfer coefficient of the fin-and-tube heat exchanger is improved by 28.1–43.9%, 71.3–87.6%, and 98.9–131% for the inline-

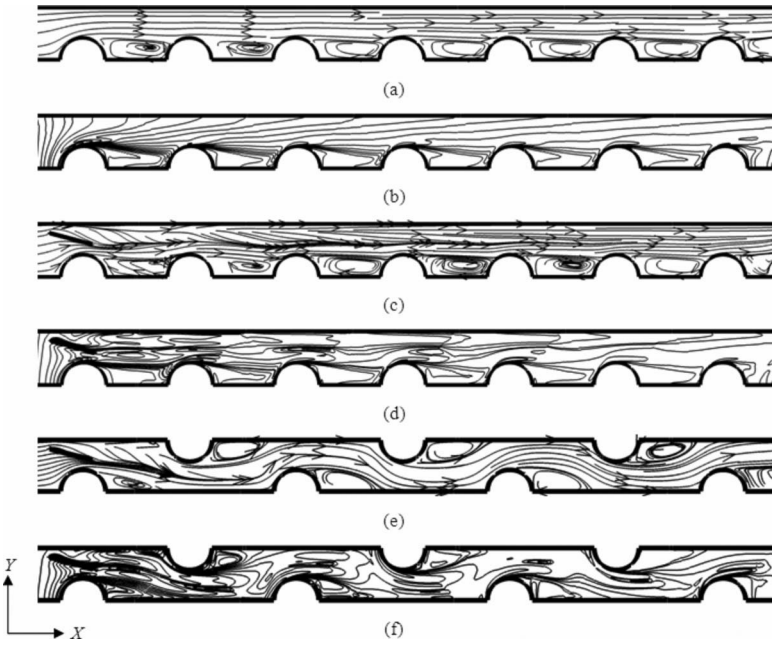

Fig. 14 Distributions of isothermals and streamlines for baseline case and enhanced cases

1RWP case, the inline-3RWP case, and the inline-7RWP case, respectively. The corresponding pressure drop penalty is also increased. The enhancement in heat transfer coefficient outweighs the additional pressure drop penalty generated by RWPs.

(2) The staggered arrangement of tube bank provides a better heat transfer coefficient for the fin-and-tube heat exchanger compared with the inline tube arrangement. The staggered tube arrangement avoided the second and all subsequent tubes being in the tube wake of their upstream tubes, which reduce the bad influence of tube wake on downstream tubes, and hence, augment the heat transfer in the flow channel. The pressure loss penalty for the staggered arrangement is also increased due to the extra form drag induced by the staggered tubes.

(3) For the range of Reynolds number considered, the average intersection angles θ_m decreases in the order of the baseline case, the inline-1RWP case, and the inline-3RWP case; however, the heat transfer performance increases in the order of the inline-3RWP case, the inline-1RWP case, and the baseline case. The smaller intersection angle θ_m means the better synergy between the velocity and the temperature gradient. The better synergy causes higher heat transfer performance for the heat exchanger.

Acknowledgment

The present work is supported by the Key Project of National Natural Science Foundation of China (Contract No. 50736005) and the National Basic Research Program of China (973 Program) (Contract No. 2007CB206902).

Nomenclature

A_T = total heat transfer surface area (m^2)
A_{min} = minimum flow area (m^2)
b = span of rectangular winglet (m)
B = channel width (m)
c = rectangular winglet chord length (m)
c_p = specific heat (J/kg K)
D = outer tube diameter (m)
D_h = hydraulic diameter, ($D_h = 4A_{min}L/A_T$)
f = friction factor
F_p = fin pitch (m)
F_t = fin thickness (m)
h = heat transfer coefficient (W/m^2 K)
H = channel height (m)
j = Colburn factor
L = flow length (m)
N = the number of control volume or point
Nu = Nusselt number
P = pressure (Pa)
ΔP = air-side pressure drop (Pa)
Pr = Prandtl number
Q = heat transfer capacity (W)
Re = Reynolds number
T = temperature (K)
T_{in} = inlet temperature (K)
T_w = wall temperature (K)
$\overline{T}$ = bulk average temperature (K)
$\overline{p}$ = bulk average pressure (Pa)
u = velocity in x-direction
u_{in} = frontal velocity (m/s)
$\boldsymbol{U}$ = velocity vector (m/s)
v = velocity in the y-direction
V_m = mean velocity at A_{min} (m/s)
w = velocity in the z-direction

Greek Symbols

α = angle of attack (deg)
μ = dynamic viscosity (Pa s)
ρ = density (kg/m^3)
λ = thermal conductivity (W/(m K))
θ = the local intersection angle (deg)
Φ = computational domain
Γ = diffusion coefficient
Λ = winglet aspect ratio

Subscripts

in = inlet parameter
m = mean value
out = outlet parameter

w = wall

References

[1] Fiebig, M., 1995, "Embedded Vortices in Internal Flow: Heat Transfer and Pressure Loss Enhancement," Int. J. Heat Fluid Flow, **16**, pp. 376–388.

[2] Deb, P., and Biswas, G., 1995, "Heat Transfer and Flow Structure in Laminar and Turbulent Flows in a Rectangular Channel With Longitudinal Vortices," Int. J. Heat Mass Transfer, **38**, pp. 2427–2444.

[3] Jacobi, A. M., and Shah, R. K., 1995, "Heat Transfer Surface Enhancement Through the Use of Longitudinal Vortices: A Review of Recent Progress," Exp. Therm. Fluid Sci., **11**, pp. 295–309.

[4] Biswas, G., Torii, K., Fujii, D., and Nishino, K., 1996, "Numerical and Experimental Determination of Flow Structure and Heat Transfer Effects of Longitudinal Vortices in a Channel Flow," Int. J. Heat Mass Transfer, **39**, pp. 3441–3451.

[5] Liou, T. M., Chen, C. C., and Tsai, T. W., 2000, "Heat Transfer and Fluid Flow in a Square Duct With 12 Different Shaped Vortex Generators," ASME J. Heat Transfer, **122**, pp. 327–335.

[6] Gentry, M. C., and Jacobi, A. M., 2002, "Heat Transfer Enhancement by Delta-Wing-Generated Tip Vortices in Flat-Plate and Developing Channel Flows," ASME J. Heat Transfer, **124**, pp. 1158–1168.

[7] Joardar, A., and Jacobi, A. M., 2008, "Heat Transfer Enhancement by Winglet-Type Vortex Generator Arrays in Compact Plain-Fin-and-Tube Heat Exchangers," Int. J. Refrig., **31**, pp. 87–97.

[8] Joardar, A., and Jacobi, A. M., 2007, "A Numerical Study of Flow and Heat Transfer Enhancement Using an Array of Delta-Winglet Vortex Generators in a Fin-and-Tube Heat Exchanger," ASME J. Heat Transfer, **129**, pp. 1156–1167.

[9] O'Brien, J. E., Sohal, M. S., and Wallstedt, P. C., 2004, "Local Heat Transfer and Pressure Drop for Finned-Tube Heat Exchangers Using Oval Tubes and Vortex Generators," ASME J. Heat Transfer, **126**, pp. 826–835.

[10] Guo, Z. Y., Li, D. Y., and Wang, B. X., 1998, "A Novel Concept for Convective Heat Transfer Enhancement," Int. J. Heat Mass Transfer, **41**, pp. 2221–2225.

[11] Tao, W. Q., Guo, Z. Y., and Wang, B. X., 2002, "Field Synergy Principle for Enhancing Convective Heat Transfer—Its Extension and Numerical Verifications," Int. J. Heat Mass Transfer, **45**, pp. 3849–3856.

[12] Tao, W. Q., He, Y. L., Wang, Q. W., Qu, Z. G., and Song, F. Q., 2002, "A Unified Analysis on Enhancing Single Phase Convective Heat Transfer With Field Synergy Principle," Int. J. Heat Mass Transfer, **45**, pp. 4871–4879.

[13] Qu, Z. G., Tao, W. Q., and He, Y. L., 2004, "Three-Dimensional Numerical Simulation on Laminar Heat Transfer and Fluid Flow Characteristics of Strip Fin Surface With X-Arrangement of Strips," ASME J. Heat Transfer, **126**, pp. 697–707.

[14] Ferrouillat, S., Tochon, P., Garnier, C., and Peerhossaini, H., 2006, "Intensification of Heat-Transfer and Mixing in Multifunctional Heat Exchangers by Artificially Generated Streamwise Vorticity," Appl. Therm. Eng., **26**, pp. 1820–1829.

Electron-Phonon Interaction Model and Its Application to Thermal Transport Simulation During Electrostatic Discharge Event in NMOS Transistor

Jae Sik Jin

Joon Sik Lee[1]
e-mail: jslee123@snu.ac.kr

School of Mechanical and Aerospace Engineering,
Seoul National University,
Seoul 151-744, Korea

First, the electron-phonon interaction model, which has recently been developed by authors for thermal predictions within the silicon devices in micro/nanoscales, is verified through the comparison with the experimental measurement of average temperature rise in the channel region of a silicon-on-insulator (SOI) transistor. The effect of the silicon layer thickness of the SOI transistor on phonon thermal characteristics is also investigated. It is found that the thickness effect on the peak temperature of the optical phonon mode in the hot spot region is negligible due to its very low group velocity. Thus the acoustic phonons in a specific frequency band, which has the highest scattering rate with the optical phonons, experience relatively less reduction in the peak temperature as the silicon layer thickness increases. Second, the electron-phonon interaction model is applied to the transient thermal transport simulation during the electrostatic discharge (ESD) event in an n-type metal-oxide-semiconductor (NMOS) transistor. The evolution of the peak temperature in the hot spot region during the ESD event is simulated and compared with that obtained by the previous full phonon dispersion model, which treats the electron-phonon scattering as a volumetric heat source. The results show that the lower group velocity acoustic phonon modes (i.e., higher frequency) and optical mode of negligible group velocity acquire high energy density from electrons during the ESD event, which might cause the devices melting problem. The heat transfer rates by individual phonon modes are also examined, and it is found that the key parameter to determine the phonon heat transfer rate during the ESD event is the product of the phonon specific heat and the scattering rates with higher energy density phonons in the hot spot region. [DOI: 10.1115/1.3133882]

Keywords: nanoscale heat transfer, electron-phonon interaction model, hot spot in SOI transistor, ESD event in NMOS transistor

1 Introduction

Transient electrostatic discharge (ESD) is a rapid discharge event that transfers a finite amount of charge between two bodies at different potentials. This event occurs because of a charge imbalance between an integrated circuit (IC) and another object in the semiconductor devices. Charge transfers from the higher potential body to the lower potential one until the voltages between them become equal. The charge movement takes place very rapidly, leading to high currents [1]. Both high-current densities and high electric fields cause thermal damage on semiconductor devices and result in melting of the devices [2,3]. Such an event accounts for more than 25% of the total failure throughout the IC life, starting from the wafer fabrication to the end user's site [4]. Thus the design of a robust ESD protection circuit is very important in the IC industry, and accurate ESD thermal simulations can help save the design time for protection circuits.

One of the challenges in the design process is a clear understanding of their thermal and electrical characteristics. The transfer of charge during the ESD event is the movement of electrons with high energy, and the energetic electrons scatter and deposit their energy in the silicon lattice through the electron-phonon interaction. The characteristic dimension of the heat generation by electron-phonon scattering is about 10 nm, which is much shorter than the phonon mean free path on the order of 100 nm at the room temperature [5]. Thus the local heating region, i.e., hot spot, is taken place because of the reduced number of phonon collisions in the heat generation region [6].

Thin oxide NMOS transistors are the most commonly used structures in ESD protection circuits in advanced complementary metal-oxide-semiconductor (CMOS) processes [3]. Since they have to be capable of dissipating all the ESD energy themselves, without incurring damage, the high-current performance of the NMOS transistors determines the minimum ESD capability of a given process [3]. The IC industry has standardized on three basic models to define how charge is transferred during the ESD event, and they can be characterized by the different origins of the charges generated. The three different models are: the human body model (HBM), the charge device model (CDM), and the machine model (MM) [1]. The HBM, which models the discharge of a human body into an IC, is the most widely used one for the ESD event prediction [1,7].

With this HBM, Sverdrup et al. [7] conducted thermal simulations of 0.35 μm NMOS devices by using a gray model approximation of the Boltzmann transport equation (BTE) and showed that the thermal failure during the ESD event can take place due to

[1]Corresponding author.

Contributed by the Heat Transfer Division of ASME for publication in the JOURNAL OF HEAT TRANSFER. Manuscript received February 4, 2008; final manuscript received April 9, 2009; published online June 22, 2009. Review conducted by Jayathi Murthy.

the temperature rise above the melting point, which cannot be reached by the classical Fourier conduction model. Recently, the ESD problem of the NMOS transistor was also numerically investigated by Narumanchi et al. [8], and the transient temperature predictions with the full phonon dispersion model were presented in comparison with those predicted by different models: the semi gray model, the gray model, and the Fourier model. In their study, they focused on the local heating region (~10 nm) considering the phonon frequency dependence of the group velocity and the relaxation time. However, they simply put the heat generation by electron-phonon scattering in the equations of the optical or acoustic, or optical and acoustic mode phonons evenly as a heat source term.

A rigorous device simulation of the energy transport at micro/nanoscales must use a concurrent electrical (electron-phonon interaction) and thermal (phonon-phonon interaction) model that takes into account the lattice heating effect. Quite recently, the electron-phonon interaction model considering the electron-phonon scattering and phonon-phonon scattering concurrently was proposed and applied for the numerical simulation of the energy transport within the SOI transistor [9]. Although there are quite a few reports on the thermal simulation for the prediction of peak temperature in the SOI transistor [5,9,10], focusing on the increase in the temperature in the local heating region and thermal transport relations between energy carriers, their results have not been validated against experimental data.

In this study, first, the thermal simulation of the SOI transistor is conducted using the electron-phonon interaction model, and the average temperature in the channel region is compared with experimental data to validate the present model. The silicon layer thickness effect on the phonon thermal characteristics is also investigated. Second, the energy transport within the NMOS transistor during the ESD event is simulated by using the electron-phonon interaction model. In order to incorporate this model in the transient thermal problem, the temporal voltage distribution equivalent to the heat generation profile is obtained from the gray model. Through this approach, we can predict the time to reach the melting temperature and transient phonon thermal characteristics. In particular, the contribution of each phonon mode to the total heat transfer rate is discussed to figure out the dominant physical parameter that governs heat transfer characteristics.

2 Electron-Phonon Interaction Model

Although the complete details of the electron-phonon interaction model have been presented by Jin and Lee [9], some important features are summarized below.

Narumanchi et al. [11] proposed the full phonon dispersion model to describe the phonon dispersion and polarization effects of phonon-phonon scattering in silicon. The acoustic mode and optical mode BTEs can be expressed, respectively, as [11]

$$\frac{\partial e_i''}{\partial t} + \nabla \cdot (v_i \hat{s} e_i'') = (e_i^0 - e_i'')\gamma_{ii} + \sum_{\substack{j=1 \\ j \neq i}}^{N_{\text{bands}}} \left\{ \left(\frac{1}{4\pi} \int_{T_{\text{ref}}}^{T_{ij}} C_i dT - e_i'' \right) \gamma_{ij} \right\} \tag{1}$$

$$\frac{\partial e_o}{\partial t} = \sum_{j=1}^{N_{\text{bands}}-1} \left(\int_{T_{\text{ref}}}^{T_{oj}} C_o dT - e_o \right) \gamma_{oj} + q_{\text{vol}} \tag{2}$$

where C_i and C_o are the specific heats of ith acoustic and optical phonon bands, respectively, e_i'' and e_o are the volumetric energy densities for a given acoustic band in a specific direction of propagation and for an optical band, respectively. e_i^0 is the equilibrium energy density, T_{ij} and T_{oj} are the interaction temperatures, γ_{ij}, γ_{ii}, and γ_{oj} are the scattering rates for each scattering process, and N_{bands} is the total number of frequency bands. Detail definitions of these quantities are given in Ref. [11]. In the present simulation, it is assumed that the phonon specific heat is independent of temperature because its value is almost constant at the high temperatures above 300 K [11]. The source term q_{vol} in Eq. (2) is the volumetric heat generation, which is the total energy transfer rate from electrons to phonons by scattering (Joule heating) in the device.

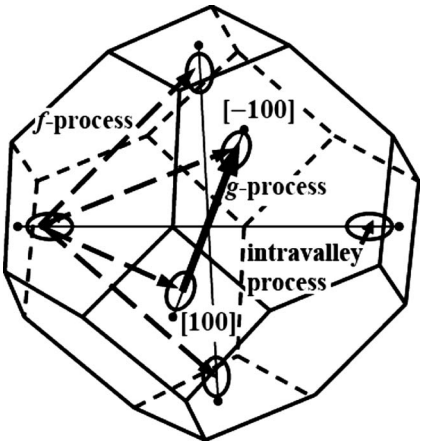

Fig. 1 Three-dimensional view of the ellipsoidal conduction band valleys of silicon within the first Brillouin zone in the momentum space with denoting intervalley (*f*- and *g*-processes) and intravalley scatterings

It is clear that in the submicron devices with high electric fields, optical phonons will be generated. Although the optical phonons interact with hot electrons, their group velocity is very low, and hence they do not conduct any heat. Hence, they eventually decay into acoustic phonons that conduct heat throughout the device, and finally to the package. It is well known that the relaxation time of the electron-phonon interaction process (≈0.1 ps) is about two orders of magnitude faster than the phonon-phonon relaxation time (≈10 ps) in silicon [12]. Each process can thus be assumed as a quasi-thermal equilibrium, and the electron-phonon interaction can be handled separately from phonon-phonon scattering. Consequently, the energy transport from electrons to phonons can be analyzed by using the present electron-phonon interaction model, and the energy change rate through phonon-phonon interaction can be determined by solving the full phonon dispersion equations.

In the electron-phonon interaction model, it is assumed that the temperature dependence of the free carrier density due to thermal excitation of electrons is negligible over the temperature range considered in this analysis under high doping conditions [9]. With the assumption that the electron relaxation times are independent of the strength and type of the perturbation, the relaxation time approximation is also valid for the electron BTE [13]. Both the impurity scattering and impact ionization of electrons are assumed negligible compared with the electron-phonon interaction in respect to the energy exchange [9].

The bottom edge of the conduction band in silicon is composed of six equivalent energy minima, or valleys, located at symmetrical positions within the first Brillouin zone, as shown in Fig. 1. The scattering by lattice vibrations can then be expected to cause two different types of electronic transitions, i.e., transitions between states within a single valley (called intravalley scattering), and transitions between states in different valleys (called intervalley scattering). The intervalley scattering can be of *g*-type, when electrons scatter between valleys on the same axis, e.g., from [100] to [−100], or *f*-type when the transition occurs between valleys on perpendicular axes, e.g., from [100] to [010] [14].

Allowed electron transitions in the momentum space due to phonon scattering are illustrated in Fig. 2. It can be shown by the simple geometrical arguments that both of these process types of

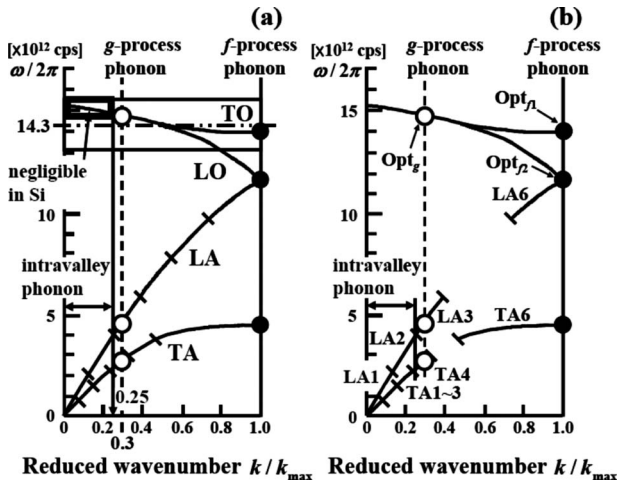

Fig. 2 (*a*) Phonon wavenumbers related to electron–phonon interaction (TO: transverse optical mode, LO: longitudinal optical mode, LA: longitudinal acoustic mode, and TA: transverse acoustic mode). (*b*) The participating phonon bands in the electron-phonon interaction.

electron-phonon scattering must occur through the Umklapp process, in which the sum of the phonon wavevector and the change of electron wavevector is equal to a principal vector of the reciprocal lattice. The wavenumbers of participated phonons in each electron transition can clearly be defined from energy and momentum conservations from the previous studies [14,15]. Those are $k_{\text{int}} \approx 0 \sim 0.25 k_{\max}$ for intravalley scattering, $k_f \approx k_{\max}$ for *f*-process, and $k_g \approx 0.3 k_{\max}$ for *g*-process. These values are shown in Fig. 2(*a*) with corresponding phonon bands of the full phonon dispersion model (six LA bands, six TA bands, and one optical band). The intravalley transitions involving optical mode phonons are negligible in silicon [16]. It is important to note from Fig. 2(*a*) that the phonon bands involved in electron transition processes are LA1 ~ LA3, LA6, TA1 ~ TA4, TA6, and the optical mode, as indicated in Fig. 2(*b*).

The electron energy is transferred by electron-phonon scattering, and the energy carriers (electron and phonon) experience the change in their energy density. These change rates can be calculated by defining the following quantities [9],

$$e_e = \int_{T_{\text{ref}}}^{T_e} C_e dT, \quad C_e = \frac{\pi^2}{2}\left(\frac{k_B T_e}{E_F}\right)\eta_e k_B,$$

$$\int_{T_{\text{ref}}}^{T_{ej}} (C_e + C_j) dT = \int_{T_{\text{ref}}}^{T_e} C_e dT + \int_{T_{\text{ref}}}^{T_j} C_j dT \tag{3}$$

where e_e is the electron energy density, T_e is the electron temperature, C_e is the electron specific heat [12], k_B is the Boltzmann constant, E_F is the Fermi energy, η_e is the doping density, and T_{ej} is the interaction temperature corresponding to the electron and acoustic phonon interaction (T_{ea}) or optical phonon interaction (T_{eo}). The index j indicates either acoustic or optical phonon. In calculating T_{ej}, we assume that the thermal interaction processes involve only one electron band so that there is no recombination process [9]. The electron-phonon interaction temperatures are calculated by the same procedure described in Ref. [11].

By the definitions given above, the BTE for the electron energy change rate can be expressed in terms of the intravalley scattering rate γ_{int}, *g*-process scattering rate γ_g, and *f*-process scattering rate γ_f as follows:

$$\frac{\partial e_e}{\partial t} + \boldsymbol{v}_d \cdot \nabla e_e + \boldsymbol{F} \cdot \frac{\partial e_e}{\partial \vec{P}} = \sum_{a=1}^{5}\left(\int_{T_{\text{ref}}}^{T_{ea}} C_e dT - e_e\right)\gamma_{\text{int}} + \sum_{a=6}^{9}\left(\int_{T_{\text{ref}}}^{T_{ea}} C_e dT - e_e\right)\gamma_{f \text{ or } g} + \left(\int_{T_{\text{ref}}}^{T_{eo}} C_e dT - e_e\right)\gamma_g + \sum_{f=1}^{2}\left(\int_{T_{\text{ref}}}^{T_{eo}} C_e dT - e_e\right)\gamma_f \tag{4}$$

The first and second terms on the right hand side account for the electron interaction with phonons in acoustic bands, and the third and forth terms represent the scattering between electrons and phonons in optical bands. $\boldsymbol{F}$ denotes the external force, which is given by $\boldsymbol{F} = \varepsilon \boldsymbol{\beta}$, where ε is the electronic charge and $\boldsymbol{\beta}$ is the electric field. The momentum ($\boldsymbol{P}$) derivative term can also be given by $\partial e_e / \partial \boldsymbol{P} = \boldsymbol{v}_d / V$, where V is the volume. The energy change rate for each acoustic and optical phonon mode can also be described by modifying the scattering terms of the right hand side in Eqs. (1) and (2), and by applying the electron-phonon interaction temperatures, T_{ea} and T_{eo}. It follows that

$$\frac{\partial e_i''}{\partial t} + \nabla \cdot (v_i \hat{s} e'') = \left(\frac{1}{4\pi}\int_{T_{\text{ref}}}^{T_{ea}} C_i dT - e''\right)\gamma_{\text{int or } (f \text{ or } g)} \tag{5}$$

$$\frac{\partial e_o}{\partial t} = \left(\int_{T_{\text{ref}}}^{T_{eo}} C_o dT - e_o\right)\gamma_g + \sum_{f=1}^{2}\left(\int_{T_{\text{ref}}}^{T_{eo}} C_o dT - e_o\right)\gamma_f \tag{6}$$

where T_e can be determined from the average electron energy $\langle E_e \rangle$, which is given by Pop et al. [17]. They calculated the heat generation profile as a function of the applied voltage, and suggested the relation of $\langle E_e \rangle \approx 0.4 \varepsilon V_a$ by using the Monte Carlo (MC) method for the ballistic diode with 20 nm channel length, where V_a is the applied voltage. Thus, T_e can be expressed as

$$T_e = \frac{2\langle E_e \rangle}{3k_B} - \frac{1}{3k_B} m^* |\boldsymbol{v}_d|^2 \tag{7}$$

by using the kinetic and potential energy of electron in the conduction band. In Eq. (7), $\boldsymbol{v}_d$ is the electron drift velocity and m^* is the electron effective mass, which can be assumed as the electron density of states effective mass $m_d = (m_t^2 m_l)^{1/3}$, where the transverse mass $m_t = 0.196 m_0$ and the longitudinal mass $m_l = 0.916 m_0$ (m_0 is the mass of a free electron) [18]. The electron drift velocity is given by $\boldsymbol{v}_d = \mu_e \boldsymbol{\beta}$, where the electron mobility, μ_e, is chosen as 80 $\text{cm}^2/\text{V s}$ at the *n*-type doping density of 10^{20} cm^{-3} [19].

3 Model Validation

Since the experimental data of the lattice temperature distribution in submicron scales is not available due to the lack of the state-of-the-art measurement technique with submicron resolution, the average temperature rise can be used to validate the simulation results. Goodson et al. [20] measured the average channel temperature rise in the SOI transistors. In their study, the gate served as an electrical-resistance thermometry for measuring the average channel temperature. As discussed in Ref. [5], the doping profiles used in the experiment of Goodson et al. [20] are unknown. In general, the doping depth of the source and drain is much shallower than the silicon layer thickness of devices. However, if the silicon layer thickness shrinks down to the fully depleted regime, the doping effect should be accounted in the device simulation [21]. In this work, the doping effect of the source and drain regions on the thermal transport is neglected. The doping in the

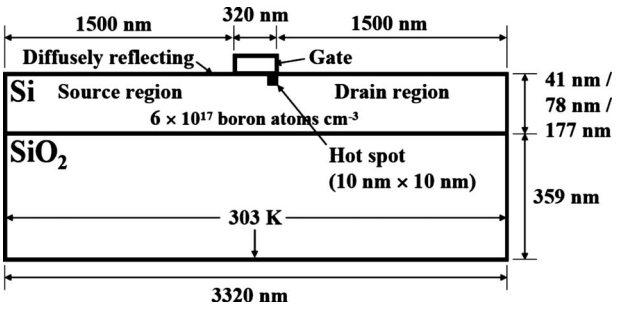

Fig. 3 Two-dimensional computational domain with experimental conditions of the silicon-on-insulator transistor

channel region is also assumed to have uniform distribution of boron atoms (6×10^{17} cm^{-3}) as given in Ref. [20].

Figure 3 depicts the schematic of the test SOI transistor of Goodson et al. [20] and simulation conditions. They measured the channel temperatures for three different cases with the silicon layer thickness of 41 nm, 78 nm, and 177 nm placed on top of a thicker insulating SiO_2 layer of 359 nm in thickness. All boundaries, except the top side, were maintained at 303 K, which served as heat sinks while the top boundary is assumed diffusely reflecting (adiabatic condition). As shown in Fig. 3, the location of the hot spot is assumed as being in the terminal of the channel by the drain side, because both theoretical [5,17,22,23] and experimental [24] works reported that the local heating has taken place near the end of the channel region by the drain side. Especially, Kwon et al. [24] measured the temperature distributions on the cross-sectional surface of an operating metal-oxide-semiconductor field-effect transistor (MOSFET) by using a scanning thermal microscopy, and showed that as the drain bias increases, the hot spot moves to the drain side. In the simulation, the hot spot size is assumed as 10×10 nm^2. In the hot spot region, the angular resolution in the octant is 8×8 and spatial grids of 10×10 are used with uniform mesh size. Although spatial grid may be related to the propagation speed, the same mesh is applied for the electron and phonon BTEs because the domain (i.e., hot spot) size is extremely small. The spatial grids are chosen as 130×64 for the silicon layer thickness of 41 nm, 130×70 for 78 nm, and 130×76 for 177 nm. The angular resolution in the octant of 4×4 is used. These grids provide converged results within 0.1% regardless of the mesh size.

The numerical procedure to calculate the energy transport from hot electrons to phonons by scattering in the hot spot region is explained in Ref. [9]. A hot strip of 10×10 nm^2 (cross section) $\times10$ μm (length), which is assumed as *n*-type single-crystal silicon doped to 10^{20} cm^{-3} of arsenic atoms (refer to Ref. [20]), is embedded in the hot spot region.

As discussed by Jin and Lee [9], we assume that the electron-phonon interaction process can be handled separately from the phonon-phonon interaction process. Thus first, the equations for the electron-phonon interaction (Eqs. (4)–(6)) are solved simultaneously until a quasi-equilibrium is reached between electrons and phonons in the hot spot region. Then, the full phonon dispersion equations (Eqs. (1) and (2)) are solved in all silicon domains including the hot spot region.

The additional dopant impurity within the silicon layer is modeled simply below, as proposed by Mazumder and Majumdar [25],

$$\gamma_{\text{imp},i}=\frac{1}{\tau_{\text{imp},i}}=\alpha\sigma_i\eta_e v_{g,i} \tag{8}$$

where α is a constant set as 50 [11], which can be empirically determined by the best fit to the experimental data, and σ_i is the scattering cross section of *i*th phonon band expressed as

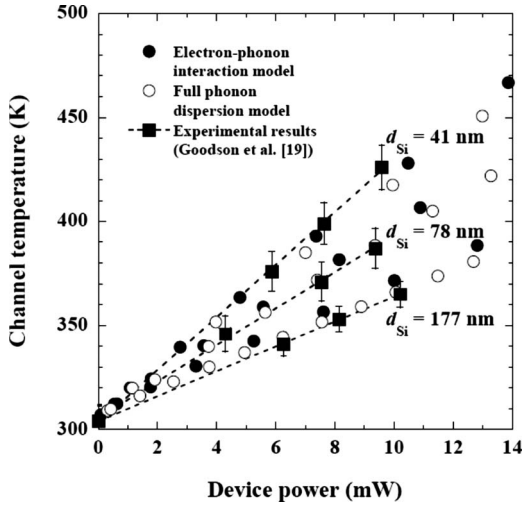

Fig. 4 Comparison of the predicted channel temperature of the SOI transistor with experimental data for various silicon layer thicknesses

$$\sigma_i=\pi r^2\left[\frac{(rk_i)^4}{(rk_i)^4+1}\right] \tag{9}$$

where r is the atomic radius of the impurity, and k_i is the *i*th band phonon wavenumber. The additional impurity scattering rate, $\gamma_{\text{imp},i}$, can be added on the right hand side of the full phonon dispersion equation (Eq. (1)) to yield

$$\frac{\partial e_i''}{\partial t}+\nabla\cdot(v_i\hat{s}e_i'')=(e_i^0-e'')(\gamma_{ii}+\gamma_{\text{imp},i})+\sum_{\substack{j=1\\ j\neq i}}^{N_{\text{bands}}}\left\{\left(\frac{1}{4\pi}\int_{T_{\text{ref}}}^{T_{ij}}C_i dT-e''\right)\gamma_{ij}\right\} \tag{10}$$

In the silicon region, the BTE is solved; while in the SiO_2 region, the heat diffusion equation is used because the phonon effective mean free path in SiO_2 is about 1 nm at room temperature [5]. The two-dimensional BTE is discretized by the finite volume method [26]. To consider the dispersion effect, each of the LA and TA branches is divided into six frequency bands, i.e., $N_{\text{LA}}=N_{\text{TA}}=6$, and the optical phonon branch is assumed in a single frequency band because the frequency variation is relatively small, as can be seen in Fig. 2. To calculate the transmission coefficient in the Si/SiO_2 interface, the diffuse mismatch model is used [10]. In the calculation, the analytic and isotropic phonon dispersion relation is used, and the phonon group velocity is extracted from the curve fits of the phonon dispersion relation. The sharp and monotonic algorithm for realistic transport (SMART) scheme is used for the spatial treatment owing to sharp changes in the thermal gradient near the hot spot region [27]. Electron-phonon scattering rates of intravalley and intervalley processes, which are functions of electron energy, are taken from Refs. [15,18], respectively. Their specific values are given in the Appendix, and the phonon-phonon scattering rates can be found in Ref. [10].

Figure 4 shows the predicted channel temperature by the electron-phonon interaction model and full phonon dispersion model in comparison with experimental data of Goodson et al. [20]. The device power is extracted by computing the phonon energy flux across the boundaries. For the three different silicon layers, the simulation results obtained by both models show good agreement with the experiment, which fall within experimental uncertainties. Considering the heat loss to the ambient air from the gate, which was used as an electrical-resistance thermometry in

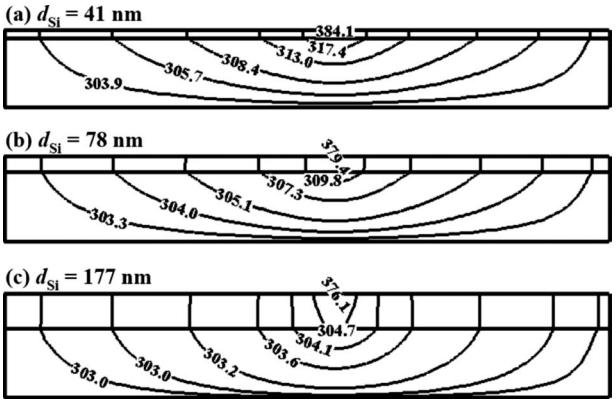

Fig. 5 Lattice temperature contours obtained by the electron-phonon interaction model for various silicon layer thicknesses at an applied voltage of V_a=3 V

the experiment, the simulated temperature should have a higher value than the experimental data. In addition to this fact, in the experiment, a very low thermal conductivity layer (5.5 nm) of SiO_2 (~1.3 W/m K) was placed between the sides of the channel and the gate, i.e., electrical-resistance thermometry. Because of these reasons, the electron-phonon interaction model predicts more accurately the thermal transport at the submicron scales.

Figure 5 shows the lattice temperature contour obtained by the electron-phonon interaction model at V_a=3 V in the hot spot region at various silicon layer thicknesses. The lattice temperature, on the whole, decreases as the silicon layer thickness increases. This is due to the increment in the heat dissipation layer (silicon) and the reduction in the effect of the phonon boundary scattering.

The peak temperatures of the individual phonon bands in the hot spot region are also depicted in Fig. 6. As expected, the peak temperature of the optical mode phonon is much higher than the acoustic one, and the peak temperature of each phonon band decreases with increasing the silicon layer thickness. Another thing to note is that the peak temperature variation of optical mode is negligible as the silicon layer thickness increases. This is due to the fact that the optical mode phonons have negligible group velocity, as shown in Fig. 2(*a*), and thus they do not recognize the

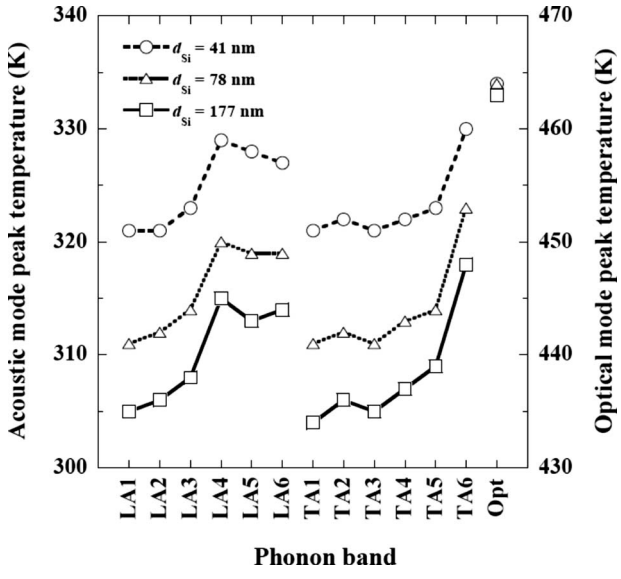

Fig. 6 Peak temperature of each phonon band in the hot spot region for various silicon layer thicknesses at an applied voltage of V_a=3 V

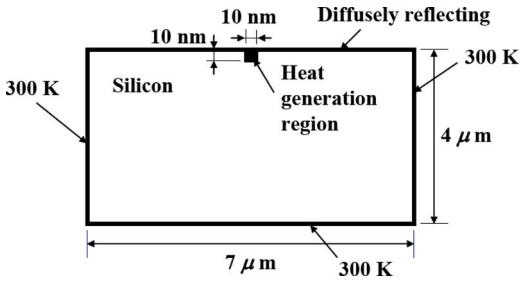

Fig. 7 Schematic of the ESD thermal simulation domain for the NMOS transistor

variation of the silicon layer thickness. This is also the reason why the peak temperature of LA6 mode, which has the highest scattering rate with the optical mode (refer to Ref. [10]), experiences relatively less decrease with increasing d_{Si} compared with other acoustic bands.

4 Temporal Distribution of Voltage Input

The detail procedure for extracting the power profile in the NMOS transistor during the ESD event by using HBM is described by Sverdrup [6]. The current from the HBM is applied to the input pad of a packaged integrated circuit. Realistic current wave forms at the NMOS protection transistor in an ESD circuit are calculated using a circuit simulator. These wave forms applied to the external I/O pins are imported into the device simulator as the current boundary condition on the NMOS. The device simulator generates the high-current I-V characteristics.

The gray model is used to extract the temporal distribution of the voltage input equivalent to the heat generation profile given by Sverdrup [6] for incorporation into the electron-phonon interaction model. In the gray model, only a single phonon mode representative of all three phonon branches is considered, and the dispersion and polarization effects are neglected. These phonons are also assumed to relax to equilibrium with the same relaxation time. This model can be written as follows [10]:

$$\frac{\partial e''}{\partial t} + \nabla \cdot (v\hat{s}e'') = \frac{e^0 - e''}{\tau_{\text{eff}}} + q_{\text{vol}} \tag{11}$$

where e'' is the energy density per unit solid angle, e^0 is the equilibrium energy density defined as $e^0 = C(T_L - T_{\text{ref}})/4\pi$, C is the phonon total specific heat, and T_L is the lattice temperature. The value of v for silicon is chosen as 6400 m/s, and C as 1.66×10^6 J/m^3 K at 300 K. The effective relaxation time τ_{eff} is 6.28 ps. All these values are taken from Ref. [10]. If the lattice temperature in the hot spot region is denoted as $T_{L,h}$, the equilibrium energy density in this region can be defined as $e_h^0 = C(T_{L,h} - T_{\text{ref}})/4\pi$. Therefore in the hot spot region, Eq. (11) can be modified as given below without the heat generation term,

$$\frac{\partial e''}{\partial t} + \nabla \cdot (v\hat{s}e'') = \frac{e_h^0 - e''}{\tau_{\text{eff},h}} \tag{12}$$

where $\tau_{\text{eff},h}$ is the effective relaxation time for hot spot region, which is defined as $\tau_{\text{eff},h} = 1/\gamma_{\text{eff}}$. If each electron-phonon scattering process in the hot spot is assumed independent of each other, the effective scattering rate γ_{eff} may be estimated by using Matthiessen's rule [28]

$$\gamma_{\text{eff}} = \sum_{i=1}^{12} \gamma_i \tag{13}$$

where the summation is conducted through all the intravalley and intervalley scattering processes.

The simplified representation of the NMOS transistor for the thermal simulation of the ESD event is depicted in Fig. 7. To

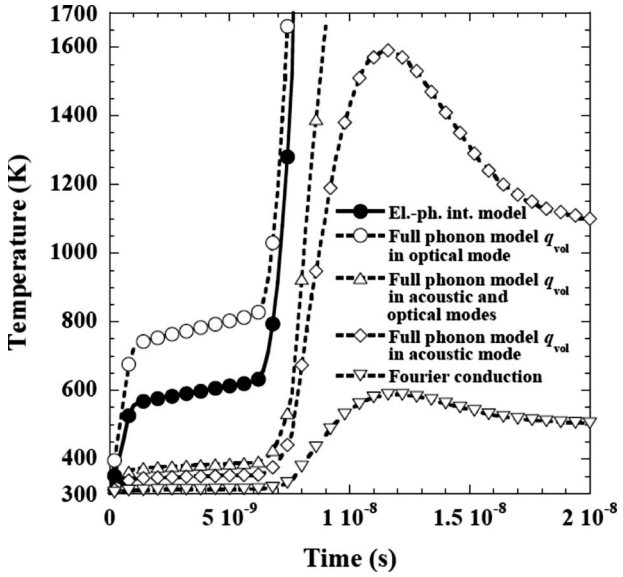

Fig. 8 Peak temperature evolution in the hot spot of the NMOS transistor

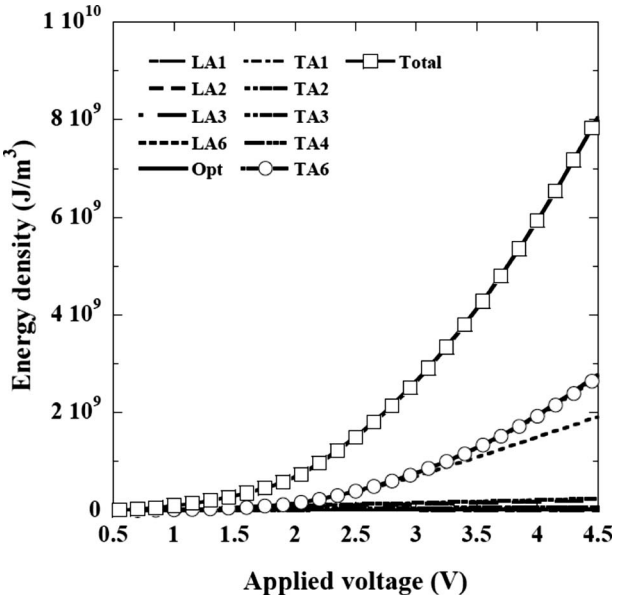

Fig. 9 Energy density of each phonon mode in the hot spot region of the NMOS transistor

describe the energy transport from charge electrons to phonons in the hot spot region, a hot strip of 10×10 nm^2 (cross section) $\times2$ μm (length), which is assumed *n*-type silicon doped to 10^{20} cm^{-3}, is embedded in the silicon substrate. The lattice temperature $T_{L,h}$ is defined similarly, as in Ref. [10], as follows.

$$e_{\text{total},h} = \int_{T_{\text{ref}}}^{T_{L,h}} C dT = \int_{T_{\text{ref}}}^{T_o} C_o dT + \sum_{i=1}^{9} \left(\int_{T_{\text{ref}}}^{T_i} C_i dT \right) \quad (14)$$

where $e_{\text{total},h}$ is the total energy density in the hot spot region. The angular resolution in the octant is 8×8 and spatial grids of 10×10 are used with uniform mesh size. From these results, it is easy to capture the relations between the voltage and the power per unit depth.

5 ESD Simulation Results and Discussion

The peak temperature in the hot spot region of the NMOS transistor is simulated by the electron-phonon interaction model, and the results are compared with those obtained by the full phonon dispersion model. The number of spatial cells is 71×40 (71 in the *x*-direction and 40 in the *y*-direction). A nonuniform grid is used with packing close to the hot spot region. The discretization in the octant is 8×8. The time step for the simulation is 0.2 ns. The lattice temperature T_L is defined as follows [10]:

$$e_{\text{total}} = \int_{T_{\text{ref}}}^{T_L} C dT = \int_{T_{\text{ref}}}^{T_o} C_o dT + \sum_{i=1}^{N_{\text{bands}}-1} \left(\int_{T_{\text{ref}}}^{T_i} C_i dT \right) \quad (15)$$

where e_{total} is the total energy density.

Figure 8 shows the evolution of the peak temperature with time in the hot spot. For the full phonon dispersion model, the heat source term q_{vol} is incorporated in the optical mode or acoustic mode. The cases in which q_{vol} is dissipated equally among the acoustic modes (12 bands) and the optical mode (1 band) are also plotted in Fig. 8. With the electron-phonon interaction model, the melting temperature of silicon ($\sim$1700 K) is reached in 7.8 ns, which is slightly slower than that obtained by the full phonon dispersion model when q_{vol} is assumed in the optical mode (7.4 ns; see Ref. [8]). Since in the full phonon dispersion model, the Joule heating was simply included in the optical BTE as a reservoir mode of negligible group velocity, it is thus dissipated indirectly through interactions with acoustic phonons of relatively high group velocity.

In the case of the electron-phonon interaction model, the acoustic phonon bands (LA6 and TA6) acquire a larger fraction (about 47%) of the total energy density from energetic electrons in the hot spot region during the ESD event, as shown in Fig. 9. Due to these facts, the full phonon dispersion model predicts faster rise in the peak temperature evolution, as shown in Fig. 8.

Figure 10 shows the summed transient heat transfer rate per unit depth (W/m) of individual phonon modes at all the boundaries of left, right, and bottom sides of the simulation domain (see Fig. 7). As shown in this figure, the main energy transport phonon modes are LA5, LA6, and TA6 (marked with solid symbols in figure) during the ESD event. Considering that in the LA and TA branches the lower numbered band denotes the higher phonon group velocity, the heat removal ability of individual phonon bands cannot directly be explained from the relative magnitude of their phonon group velocities. This may arise from the complicated physics of phonon thermal transport taking place in a very short time scale with high energy such as ESD.

Since the phonon heat flux is defined as $\boldsymbol{q}_i = \int_{4\pi} v_i \hat{s} e_i'' d\Omega$, it is obvious that the heat transfer rate of *i*th band phonon is proportional to its carried energy density (e_i''), which is also proportional to both the phonon specific heat (C_i) and the scattering rate with "hot phonons" in the hot spot region ($\gamma_{\text{hot},i}$). The hot phonons mean those with the higher energy density in the hot spot region (LA6, TA6, and Opt bands; see Fig. 9) through the electron-phonon interaction during the ESD event. From this background, a dimensionless parameter θ_i can be defined as follows:

$$|\boldsymbol{q}_i| \sim e_i'' \sim \frac{C_i}{C} \frac{\gamma_{\text{hot},i}}{\gamma_{\text{total},i}} \equiv \theta_i \quad (16)$$

where $\gamma_{\text{total},i}$ is the total scattering rate of *i*th band. Above relation of each phonon band is plotted in Fig. 11. As consistent with Fig. 10, LA5, LA6, and TA6 have the larger values of θ_i than other bands. Conclusively, in the thermal transport regime of fast high energy generation, such as in the ESD event, the heat transfer rate depends strongly on the ability for phonons to sustain the acquired energy from electrons rather than the energy carrier velocity does.

6 Concluding Remarks

A BTE based model accounting for details of the electron-phonon and phonon-phonon interactions is proposed and validated

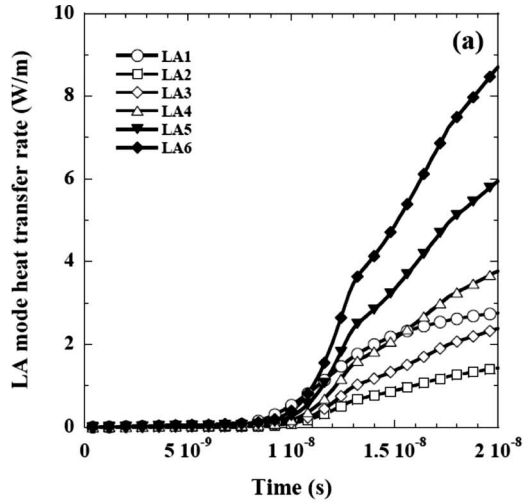

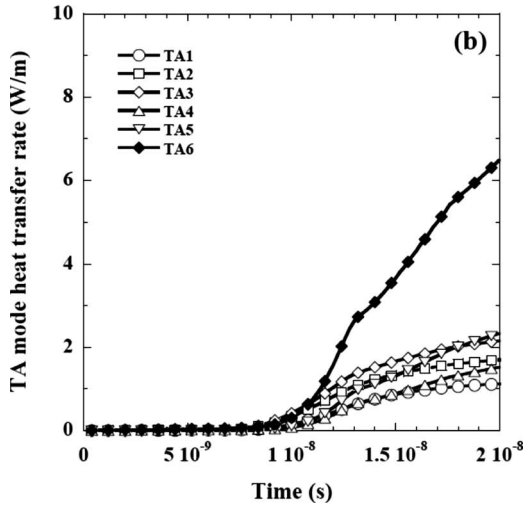

Fig. 10 Heat transfer rate through the boundaries of the NMOS transistor: (*a*) longitudinal acoustic phonon bands (LA) and (*b*) transverse acoustic phonon bands (TA)

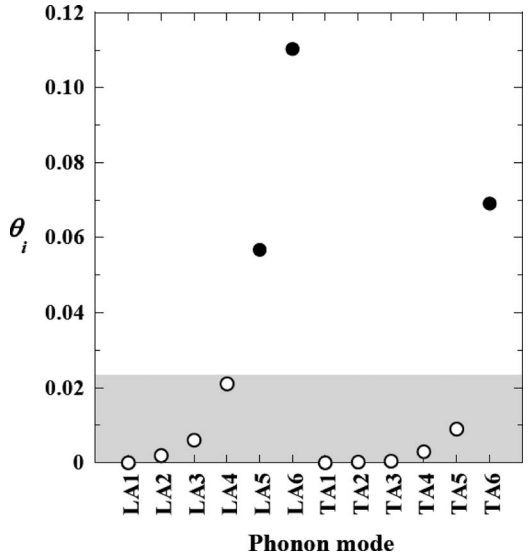

Fig. 11 The value of the dimensionless parameter θ_i for each phonon band

against experimental data. The effect of silicon layer thickness on the phonon thermal characteristics is also investigated. The optical phonons show no effect on the variation of the silicon layer thickness. For phonons in the LA6 band, which have the most probable scattering chances with the optical mode phonons, the reduction in the peak temperature in the hot spot is relatively less than the other acoustic modes as the silicon layer thickness increases. The electron-phonon interaction model is also employed to simulate the ESD event in the NMOS transistor and compared with the results obtained by the full phonon dispersion model. The results show that the melting temperature is reached at 7.8 ns primarily as a consequence of energetic electron energy deposition to acoustic phonon modes with the lower group velocity and the optical mode of negligible group velocity. The relative contribution of individual phonons to heat conduction is dependent on the product of the phonon specific heat and the scattering rates with higher energy density phonons.

Nomenclature

C = total phonon specific heat (J/m^3 K)
d_{Si} = silicon layer thickness (m)
D_A (eV) = deformation potential of acoustic phonons
e = energy density (J/m^3)
$\langle E_e \rangle$ = average electron energy (J)
E_F = Fermi energy (J)
f = phonon distribution function
$\boldsymbol{F}$ = external force (kg m/s^2)
$\hbar$ = reduced Planck's constant (1.054×10^{-34} J s)
k = phonon wavenumber (1/m)
k_B = Boltzmann constant (1.38×10^{-23} J/K)
LA = longitudinal acoustic phonon branch
LO = longitudinal optical phonon branch
m^* = electron effective mass (kg)
m_d = electron density of states effective mass (kg)
m_0 = mass of the free electron (kg)
N_{band} = total number of frequency bands ($N_{LA}+N_{TA}+1$)
Opt = optical phonon mode
$\boldsymbol{P}$ = momentum (kg m/s)
$\boldsymbol{q}$ = heat flux (W/m^2)
q_{vol} = volumetric heat generation (W/m^3)
r = atomic radius of the impurity (m)
$\hat{s}$ = unit direction vector
t = time (s)
T = temperature (K)
TA = transverse acoustic phonon branch
TO = transverse optical phonon branch
$\boldsymbol{v}, \boldsymbol{v}_g$ = phonon group velocity (m/s)
$\boldsymbol{v}_d$ = drift velocity of electron (m/s)
V = volume (m^3)
V_a = applied voltage (V)
α = constant to fit experimental data
$\boldsymbol{\beta}$ = electric field (V/m)
δ = nonparabolicity parameter (δ=0.5 eV^{-1})
γ = scattering rate (1/s)
ε = electronic charge (C)
η_e = doping density ($1/m^3$)
θ_i = dimensionless parameter defined in Eq. (16)
μ_e = electron mobility (m^2/V s)
ν = phonon frequency (1/s)
ρ = mass density (kg/m^3)
σ = scattering cross section (m^2)
τ = relaxation time (s)
ω = phonon angular frequency (rad/s)
Ω = solid angle (sr)

Table 1 Electron-phonon scattering rates ($\times 10^{12}$ s^{-1}) for intravalley and intervalley (*f*- and *g*-processes) scatterings ($\langle E_e \rangle$ unit: eV)

	Intravalley scattering (γ_{int})		*g*-scattering (γ_g)			*f*-scattering (γ_f)			
$\langle E_e \rangle$	LA1/LA2	TA1/TA2/TA3	LA3	TA4	Opt_g	LA6	TA6	Opt_{f1}	Opt_{f2}
0.4	5.26	3.34	1.66	0.22	5.20	10.79	1.08	1.30	7.08
0.8	10.32	6.56	3.31	0.43	10.77	22.03	2.15	2.69	14.66
1.2	16.52	10.50	5.34	0.70	17.60	35.79	3.46	4.40	23.96
1.6	23.91	15.21	7.76	1.01	25.78	52.25	5.02	6.44	35.08
2.0	32.52	20.68	10.58	1.37	35.32	71.47	6.84	8.83	48.08
2.4	42.34	26.92	13.80	1.79	46.25	93.44	8.92	11.56	62.96
2.8	53.38	33.95	17.43	2.26	58.57	118.19	11.26	14.64	79.72
3.2	65.65	41.75	21.46	2.78	72.27	145.72	13.86	18.07	98.37

Subscripts

- a = acoustic mode phonon
- e = electron
- eff = effective property
- f = *f*-process of intervalley scattering
- $f1$ = *f*-process of intervalley scattering with higher frequency
- $f2$ = *f*-process of intervalley scattering with lower frequency
- g = *g*-process of intervalley scattering
- h = hot spot region
- hot = hot phonon
- i = *i*th frequency band
- ij = property specific to bands *i* and *j*
- imp = impurity scattering
- int = intravalley scattering
- k = phonon wavenumber
- l = longitudinal direction
- L = lattice
- LA = longitudinal acoustic phonon
- max = maximum value
- o = optical mode phonon
- p = phonon branch
- ph = phonon
- ref = reference value
- t = transverse direction
- total = total value
- TA = transverse acoustic phonon

Superscripts

- 0 = equilibrium condition

Acknowledgment

We would like to gratefully acknowledge that this work is supported by the Micro Thermal Research Center, Seoul National University.

Appendix

The scattering rate for intravalley and intervalley scatterings, which is a function of electron energy, can be derived from the Fermi golden rule [15]. First, for the intravalley process, the scattering rate is given by [15]

$$\gamma_{int}(E_K) = \frac{\pi D_A^2 k_B T_L}{\hbar \rho_{Si} v_A^2} g_d(E_K) \tag{A1}$$

where D_A is the deformation potential of acoustic phonons, which physically means the perturbing potential of electron due to phonon scattering. The value for each phonon branch is presented by Pop et al. [18] as the isotropically averaged value, which is given as $D_{LA}=6.39$ eV and $D_{TA}=3.01$ eV [18]. ρ_{Si} is the mass density of silicon ($\rho_{Si}=2330$ kg/m^3), v_A is the acoustic velocity ($v_{LA}=9040$ m/s and $v_{TA}=5340$ m/s [15]). E_K is the electron energy of wavenumber K, which is assumed as $E_K \approx \langle E_e \rangle$. The parameter $g_d(E_K)$ in Eq. (A1) is the density of states at electron energy E_K and can be defined as [29]

$$g_d(E_K) = \frac{(2m^*)^{3/2}}{2\pi^2\hbar^3}\sqrt{E_K(1+\delta E_K)}(1+2\delta E_K) \tag{A2}$$

where δ is the nonparabolicity parameter ($\delta=0.5$ eV^{-1} [29]). Equation (A2) is an equation per energy ellipsoid in silicon. Thus this must be multiplied by a factor of six for all conduction band ellipsoids in silicon [29].

Second, for the intervalley process, the scattering rate can also be written as [18]

$$\gamma_{f \text{ or } g}(E_K) = \frac{\pi \Delta_{if}^2 Z_f}{2\rho_{Si}\omega_{k,p}}\left(N_{k,p} + \tfrac{1}{2} \mp \tfrac{1}{2}\right) g_d(E_K \pm \hbar\omega_{k,p}) \tag{A3}$$

where Δ_{if} is the scattering constant (LA3: 1.5×10^8 eV/cm, TA4: 0.3×10^8 eV/cm, Opt_g: 6.0×10^8 eV/cm, LA6: 3.5×10^8 eV/cm, TA6: 0.5×10^8 eV/cm, Opt_{f1}: 1.5×10^8 eV/cm, and Opt_{f2}: 3.5×10^8 eV/cm) [18], Z_f is the number of available final valleys (four for *f*-type and one for *g*-type scattering [18]), $N_{k,p}$ is the phonon occupation function given by $N_{k,p}=1/[\exp(\hbar\omega_{k,p}/k_BT_L)-1]$, and other symbols are the same as previously defined. The top and bottom signs in Eq. (A3) refer to phonon absorption and emission, respectively. It is important to consider the phonon dispersion relation when the electron final state is calculated. Table 1 shows the summary of electron-phonon scattering rates obtained by solving Eqs. (A1) and (A3).

References

[1] Vinson, J. E., and Liou, J. J., 1998, "Electrostatic Discharge in Semiconductor Devices: An Overview," Proc. IEEE, **86**(2), pp. 399–418.

[2] Duvvury, C., and Amerasekera, A., 1993, "ESD: A Pervasive Reliability Concern for IC Technologies," Proc. IEEE, **81**(5), pp. 690–702.

[3] Amerasekera, A., Van Roozendaal, L., Bruines, J., and Kuper, F., 1991, "Characterization and Modeling of Second Breakdown in NMOST's for the Extraction of ESD-Related Process and Design Parameters," IEEE Trans. Electron Devices, **38**(9), pp. 2161–2168.

[4] Lee, J. C., Hoque, A., Croft, G. D., Liou, J. J., Young, R., and Bernier, J. C., 2000, "An Electrostatic Discharge Failure Mechanism in Semiconductor Devices, With Applications to Electrostatic Discharge Measurements Using Transmission Line Pulsing Technique," Solid-State Electron., **44**(10), pp. 1771–1781.

[5] Sverdrup, P. G., Ju, Y. S., and Goodson, K. E., 2001, "Sub-Continuum Simulations of Heat Conduction in Silicon-on-Insulator Transistors," ASME J. Heat Transfer, **123**(1), pp. 130–137.

[6] Sverdrup, P. G., 2000, "Simulation and Thermometry of Sub-Continuum Heat Transport in Semiconductor Devices," Ph.D. thesis, Department of Mechanical Engineering, Stanford University.

[7] Sverdrup, P. G., Banerjee, K., Dai, C., Shih, W., Dutton, R. W., and Goodson, K. E., 2000, "Sub-Continuum Thermal Simulations of Deep Sub-Micron Devices Under ESD Conditions," 2000 International Conference on Simulation of Semiconductor Processes and Devices, SISPAD, Seattle, WA, pp. 54–57.

[8] Narumanchi, S. V. J., Murthy, J. Y., and Amon, C. H., 2006, "Boltzmann Transport Equation-Based Thermal Modeling Approaches for Hotspots in Microelectronics," Heat Mass Transfer, **42**(6), pp. 478–491.

[9] Jin, J. S., and Lee, J. S., 2007, "Electron-Phonon Interaction Model and Prediction of Thermal Energy Transport in SOI Transistor," J. Nanosci. Nanotech-

nol., **7**(11), pp. 4094–4100.
[10] Narumanchi, S. V. J., Murthy, J. Y., and Amon, C. H., 2005, "Comparison of Different Phonon Transport Models for Predicting Heat Conduction in Silicon-on-Insulator Transistor," ASME J. Heat Transfer, **127**(7), pp. 713–723.
[11] Narumanchi, S. V. J., Murthy, J. Y., and Amon, C. H., 2004, "Submicron Heat Transfer Model in Silicon Accounting for Phonon Dispersion and Polarization," ASME J. Heat Transfer, **126**(6), pp. 946–955.
[12] Tien, C. L., Majumdar, A., and Gerner, F. M., 1998, *Microscale Energy Transport*, Taylor & Francis, Washington, D.C.
[13] Bube, R. H., 1974, *Electronic Properties of Crystalline Solids*, Academic, New York.
[14] Long, D., 1960, "Scattering of Conduction Electrons by Lattice Vibrations in Silicon," Phys. Rev., **120**(6), pp. 2024–2032.
[15] Lundstrom, M., 2000, *Fundamentals of Carrier Transport*, 2nd ed., Cambridge University Press, Cambridge.
[16] Harrison, W. A., 1956, "Scattering of Electrons by Lattice Vibrations in Nonpolar Crystals," Phys. Rev., **104**(5), pp. 1281–1290.
[17] Pop, E., Rowlette, J. A., Dutton, R. W., and Goodson, K. E., 2005, "Joule Heating Under Quasi-Ballistic Transport Conditions in Bulk and Strained Silicon Devices," 2005 International Conference on Simulation of Semiconductor Processes and Devices, SISPAD, Tokyo, Japan, pp. 307–310.
[18] Pop, E., Dutton, R. W., and Goodson, K. E., 2004, "Analytic Band Monte Carlo Model for Electron Transport in Si Including Acoustic and Optical Phonon Dispersion," J. Appl. Phys., **96**(9), pp. 4998–5005.
[19] Mousty, F., Ostoja, P., and Passari, L., 1974, "Relationship Between Resistivity and Phosphorus Concentration," J. Appl. Phys., **45**(10), pp. 4576–4580.
[20] Goodson, K. E., Flik, M. I., Su, L. T., and Antoniadis, D. A., 1995, "Prediction and Measurement of Temperature Fields in Silicon-on-Insulator Electronic Circuits," ASME J. Heat Transfer, **117**(3), pp. 574–581.
[21] Barraud, S., Clavelier, L., and Ernst, T., 2005, "Electron Transport in Thin SOI, Strained-SOI and GeOI MOSFET by Monte-Carlo Simulation," Solid-State Electron., **49**(7), pp. 1090–1097.
[22] Sinha, S., Pop, E., Dutton, R. W., and Goodson, K. E., 2006, "Non-Equilibrium Phonon Distributions in Sub-100 nm Silicon Transistors," ASME J. Heat Transfer, **128**(7), pp. 638–647.
[23] International Technology Roadmap for Semiconductors (ITRS), http://www.public.itrs.net.
[24] Kwon, O., and Majumdar, A., 2003, "Cross-Sectional Thermal Imaging of a Metal-Oxide-Semiconductor Field-Effect Transistor," Microscale Thermophys. Eng., **7**(4), pp. 349–354.
[25] Mazumder, S., and Majumdar, A., 2001, "Monte Carlo Study of Phonon Transport in Solid Thin Films Including Dispersion and Polarization," ASME J. Heat Transfer, **123**(4), pp. 749–759.
[26] Patankar, S. V., 1980, *Numerical Heat Transfer and Fluid Flow*, Taylor & Francis, New York.
[27] Gaskell, P. H., and Lau, A. K. C., 1988, "Curvature-Compensated Convective Transport: SMART, A New Boundedness-Preserving Transport Algorithm," Int. J. Numer. Methods Fluids, **8**(6), pp. 617–641.
[28] Ziman, J. M., 1960, *Electron and Phonon*, Oxford University Press, London.
[29] Pop, E., 2004, "Self-Heating and Scaling of Thin Body Transistors," Ph.D. thesis, Department of Electrical Engineering, Stanford University.

Direct Simulation Monte Carlo Solution of Subsonic Flow Through Micro/Nanoscale Channels

Ehsan Roohi

Masoud Darbandi[1]
e-mail: darbandi@sharif.edu

Vahid Mirjalili

Department of Aerospace Engineering,
Sharif University of Technology,
P.O. Box 11365-8639,
Tehran 11365, Iran

We use a direct simulation Monte Carlo (DSMC) method to simulate gas heating/cooling and choked subsonic flows in micro/nanoscale channels subject to either constant wall temperature or constant/variable heat flux boundary conditions. We show the effects of applying various boundary conditions on the mass flow rate and the flow parameters. We also show that it is necessary to add a buffer zone at the end of the channel if we wish to simulate more realistic conditions at the channel outlet. We also discuss why applying equilibrium-based Maxwellian distribution on molecules coming from the channel outlet, where the flow is nonequilibrium, will not disturb the DSMC solution. The current velocity, pressure, and mass flow rate results are compared with different analytical solutions of the Navier–Stokes equations. Although there are good agreements between the DSMC results and the analytical solutions in low compressible flow, the analytical solutions yield incorrect velocity and mass flow rate values in short micro/nanochannel flows with high compressibility and/or choked flow conditions. [DOI: 10.1115/1.3139105]

Keywords: DSMC, nanochannel, microchannel, subsonic flow, choked flow, heat flux boundary condition

1 Introduction

Micro- and nanochannels are widely encountered in microelectromechanical systems (MEMS). To enhance the design and performance of such systems, it is necessary to achieve a deeper understanding of their flow and heat transfer behaviors. The gas rarefaction is a main parameter to evaluate these systems provided that the Knudsen number is sufficiently large. In such conditions, the solutions are to be established based on the kinetic principles such as those in treating the Boltzmann equation. The nonequilibrium gas flow problems need the numerical treatments of the Boltzmann equation. However, the complexity of the Boltzmann equation promotes the use of alternative methods such as the direct simulation Monte Carlo (DSMC). DSMC is one of the most successful particle simulation methods and is widely used in analyzing rarefied gas flows [1].

The application of DSMC for solving the rarefied micro/nanoflows was primarily focused on high speed flows [2]. The extension of DSMC to low speed micro/nanoflow applications requires specific boundary condition considerations at the inlet/outlet sections. For example, Liou and Fang [3] used the characteristics theory to specify the back pressure condition. They simulated flow in microchannels with suitable accuracy. Wang and Li [4] provided further improvement in applying inlet boundary conditions in low speed flow treatment via considering the effect of inlet pressure on the velocity field right at the channel inlet. Using this idea, Le et al. [5] studied the flow and heat transfer behavior in microchannels with parallel and series arrangements. Chong [6] also studied the choked subsonic flow in microscales. He reported that the sonic region would appear only near the midchannel. The current workers simulated channels with different flow regimes and discussed different possible choices to simulate the choked flow in micro/nanoscale channels [7].

The objective of this work is to provide a deeper understanding of subsonic flow and heat transfer behaviors in micro/nanoscale channels. The current work provides two important contributions to micro/nanoscale flow study. First, we study the effects of gas heating or cooling on the flow behavior in subsonic regimes. Second, we elaborate the choked subsonic flow more deeply and emphasize the importance of inserting a buffer zone at the channel outlet. We compare our DSMC mass flow rate magnitude, pressure distribution, and velocity profile with different analytical derivations. We consider both mono-atomic (helium) and diatomic (nitrogen) gases and discuss the differences in their behaviors. Generally, our investigation shows that the past references have neither deeply investigated the physics of flow under various heat flux boundary conditions nor practically considered the correct treatment of outlet boundary conditions in simulating the choked subsonic flow [2–6]. These topics are properly addressed in this paper.

2 The DSMC Method

DSMC is a numerical tool to solve the Boltzmann equation based on direct statistical simulation of the molecular processes described by the kinetic theory [1]. It is considered as a particle method in which particle represents a large bulk of real gas molecules. The primary principle of DSMC is to decouple the motion and collision of particles during one time step. The implementation of DSMC needs breaking down the computational domain into a collection of grid cells. The cells are divided into subcells in each direction. The subcells are then utilized to facilitate the selection of collision pairs. After fulfilling all molecular movements, the collisions between molecules are simulated in each cell separately. In the current study, variable hard sphere collision model is used and the collision pair is chosen based on the no time counter method [1].

[1]Corresponding author.

Contributed by the Heat Transfer Division of ASME for publication in the JOURNAL OF HEAT TRANSFER. Manuscript received July 4, 2008; final manuscript received April 2, 2009; published online June 24, 2009. Review conducted by Satish G. Kandlikar. Paper presented at the Sixth International Conference on Nanochannels, Microchannels and Minichannels (ICNMM2008), Darmstadt, Germany, June 23–30, 2008.

Table 1 Details of the chosen test cases $T_{in}=300$ K

Case	1	2	3	4	5	6	7	8
Gas	He	He	He	He	He	N_2	N_2	He
h (μm)	1	1	1	1	1	0.30	0.45	1.12
$AR(L/h)$	4	4	4	4	4	6.66	4.44	4.44
Kn_{in}	0.055	0.055	0.055	0.055	0.055	0.074	0.050	0.050
λ_{im} (μm)	0.055	0.055	0.055	0.055	0.055	0.022	0.022	0.056
Kn_o	0.140	0.163	0.143	0.061	0.128	0.388	0.169	0.177
M_{in}	0.192	0.182	0.218	0.425	0.257	0.156	0.24	0.214
M_o	0.586	0.585	0.609	0.648	0.640	0.875	0.943	0.923
Buffer	No	No	No	No	No	Yes	Yes	Yes
Grid[a]	A	A	A	A	A	A+B	A+B	A+B
P_b (kPa)	108	107	107	120	109	6.73	4.91	4.83
P_e (kPa) (DSMC)	108	107	107	120	109	17.5	24.5	21.1
P_{in} (kPa)	308	314	309	358	313	99.7	98.1	97.5
Applied PR	2.851	2.934	2.881	2.983	2.870	15	20	20
Real PR	2.851	2.934	2.881	2.983	2.870	5.69	4.00	4.62
Heat condition	$T_w=300$	$T_w=350$	$q_w=0$	$q_w=-5$	Variable q_w	$T_w=323$	$T_w=300$	$T_w=300$
Re_{in} (DSMC)	5.84	5.20	5.84	10.99	6.86	5.55	6.68	7.02
Re_{in} (analytical)	6.22	5.34	6.38	12.44	7.54	5.70	7.10	7.04

[a]Grid A (100×60) is for the channel and Grid B (20×60) is for the buffer zone.

Following Wang and Li [4], we use the 1D characteristics theory to apply inlet/outlet pressure boundary conditions. The channel walls are treated as diffuse reflectors using the full thermal accommodation coefficient, see Ref. [8]. The details of boundary condition implementation can be found in Ref. [7].

3 Results and Discussion

Table 1 provides a summary of the current investigated test cases. Cases 1–5 study the effects of heat transfer on the flow field behavior in subsonic regime. Cases 6–8 study the choked subsonic flow behavior for mono-atomic and diatomic gases. We consider 10% of the wall at the channel inlet as a specular reflector. Our experience has shown that this consideration would provide more realistic conditions at the real channel inlet in micro/nanoflow treatments [9–11].

3.1 Grid Study. Figure 1 shows the geometry of channel schematically. Considering a symmetric flow, we only study one-half of the domain. The computational domain consists of two rectangles: the main channel and the buffer zone. To achieve cell independent solutions, we simulate nitrogen flow in a channel with $AR=5$, $PR=2.5$, and $Kn_{in}=0.055$ using three different grid resolutions. Figure 2(*a*) shows the pressure distributions for Grid 1 (50×30), Grid 2 (100×60), and Grid 3 (150×90) in a channel with no buffer zone. A finer grid resembles that the preceding coarse cell was divided into 2×2 subcells. The solutions are compared with the first-order analytical Navier–Stokes (NS) solution [12] and DSMC [3]. Figure 2(*b*) presents the current pressure deviations from the linear pressure distribution. It is observed that Grids 2 and 3 provide similar pressure deviations. Therefore, we continue our study using Grid 2. Our study shows that Grid 2 is also accurate for choked flow simulation because the choking PR along the channel is not that high. As seen in Table 1, the highest PR is 5.69 for Case 6.

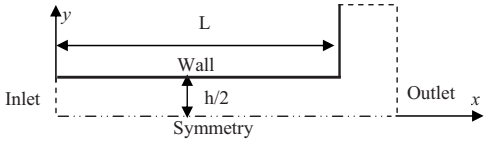

Fig. 1 Geometry of the channel and its outlet buffer

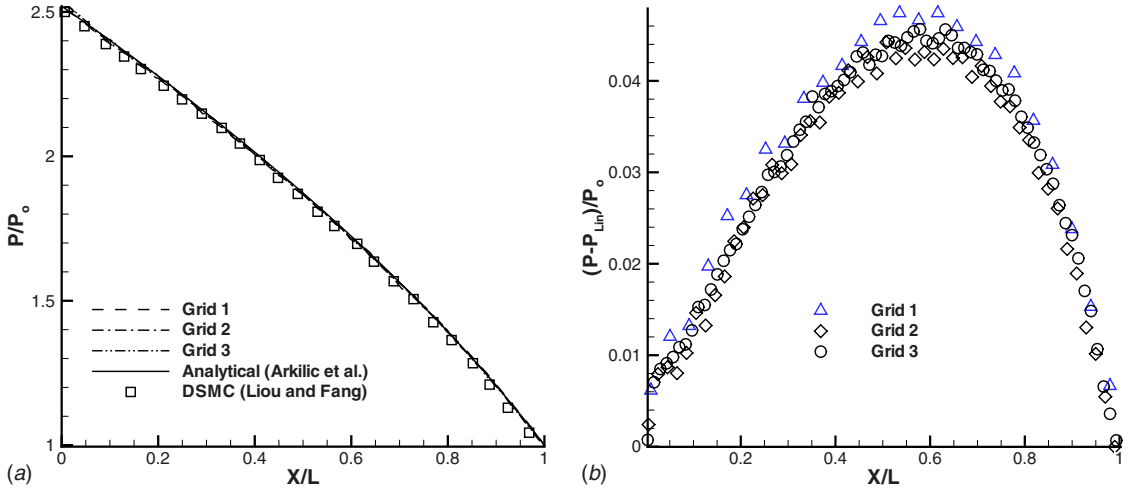

Fig. 2 Grid study and comparison with DSMC [3] and analytical NS [12] solution: (*a*) centerline pressure distribution and (*b*) centerline pressure deviation

Table 2 Comparative study of mass flow rates ($Q\times10^5$)

Current	DSMC [13]	Numerical NS [13]	Analytic NS [12]
2.18	2.17	2.16	2.17

3.2 DSMC Validation. We set 20–25 molecules in each cell at time zero. Since the gas temperature is relatively low for the chosen cases, the vibrational energy is not taken into account for the diatomic nitrogen molecules [1]. The values of mass flow rate at the inlet and outlet were monitored until achieving negligible differences between two consequent time steps. After that, we continued the computations to suppress the inherent DSMC statistical fluctuations. To validate the current mass flow rate, we observe that the past experiments in microchannels have mostly focused on long channels having low speed isothermal flows. Since our study is limited to relatively short channels, we compare our results with the DSMC and numerical NS solutions of Cai et al. [13] and the analytical NS solution of Arkilic et al. [12]. Table 2 provides the details of comparisons for a gas (oxygen) flow in a channel with $PR=2.5$ and $AR=28.30$. As seen in this table, there are good agreements among them.

3.3 Subsonic Flow With Heat Transfer, Cases 1–5. In this section, we study subsonic helium flow in a channel subject to constant wall temperature and constant/variable wall heat flux boundary conditions. Our literature survey shows that the past investigations have mostly focused on constant wall temperature study [5,14].

3.3.1 Wall Thermal Boundary Condition Study. The details of Cases 1–5 are provided in Table 1. The table also provides the DSMC and the analytical Reynolds number magnitudes defined as $\mathrm{Re}_{\mathrm{in}}=\rho uh/\mu=Q/\mu$ and $\mathrm{Re}_{\mathrm{in}}=\sqrt{\gamma\pi/2}\mathrm{M}_{\mathrm{in}}/\mathrm{Kn}_{\mathrm{in}}$, respectively. As seen, there are close agreements between the DSMC prediction and the analytical solution.

Figure 3 shows the distributions of wall heat flux per unit width (positive from the wall to the fluid) for Cases 2 and 5. For Case 2, the heat flux is calculated from

$$q_w=\frac{\sum\varepsilon^i-\sum\varepsilon^r}{A\Delta t} \tag{1}$$

where $\Sigma\varepsilon$ is the sum of the averaged molecular energies, A is the area, Δt is the interaction time, and i and r stand for the incidence and reflected molecules, respectively. Figure 3 shows that the gas is heated in Case 2 because the wall temperature is higher than

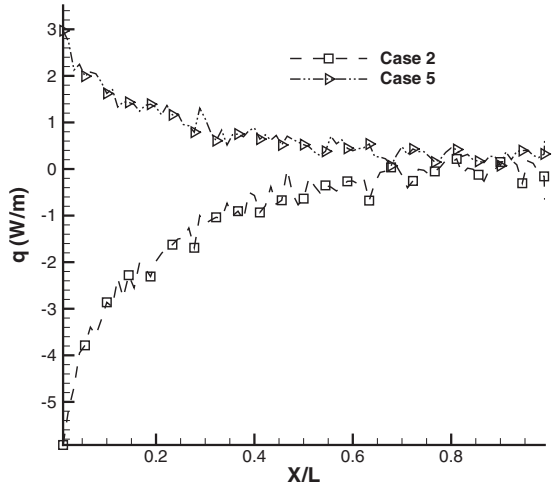

Fig. 3 Current DSMC wall heat flux distributions

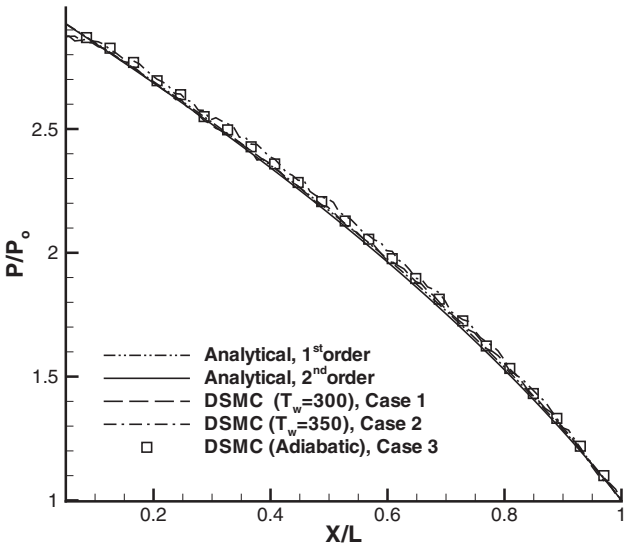

Fig. 4 Pressure distributions and comparison with the first-[12] and second-order [16] NS analytical solutions

that of the main flow. The rate of heat transfer decreases in the downstream of the channel and it almost vanishes near the exit.

In Cases 3–5, we examine the specified heat flux (SHF) boundary condition at the wall, as suggested by Wang et al. [15]. They developed an inverse temperature sampling technique, which benefits from calculating the wall temperature from the SHF at the wall. To simulate SHF in DSMC, we use

$$\bar{\varepsilon}_j^{\,r}=\bar{\varepsilon}_j^{\,i}-\Delta\bar{\varepsilon}=\bar{\varepsilon}_{\mathrm{tr}}+\bar{\varepsilon}_{\mathrm{rot}}=2kT_j+\frac{\xi_{\mathrm{rot}}kT_j}{2} \tag{2}$$

where $\Delta\bar{\varepsilon}=q_w/(\alpha AN_{\mathrm{imp}}\Delta t)$ is the average energy transferred to the wall, ξ_{rot} is the number of rotational degrees of freedom, and N_{imp} is the number of molecules impinging the surface. Hence, the wall temperature is calculated from

$$T_j=\frac{\varepsilon_j^i-\Delta\bar{\varepsilon}}{k(2+\xi_{\mathrm{rot}}/2)} \tag{3}$$

We use Eq. (3) to find the temperature at the surface. Cases 4 and 5 are modeled using variable $\Delta\bar{\varepsilon}$ distributions. In Case 3 with $\Delta\bar{\varepsilon}=0$, the total energy of incident molecules would be carried out by the reflected molecules.

3.3.2 Results and Discussion. Figure 4 shows the centerline pressure distributions for Cases 1–3 and compares them with the first-[12] and second-order [16] NS analytical solutions. Good agreement is observed between Cases 1 and 3, while Case 2 shows slight deviations from them. This can be attributed to gas heating status, which causes more serious density variation and compressibility effect. As is known, the compressibility makes the pressure distribution more nonlinear. Indeed, the analytical pressure distributions are derived assuming low Reynolds number ($\mathrm{Re}<O(1)$) isothermal flow in long microchannels, where the ratio of inertial terms (I) to diffusion terms (D), i.e., $I/D\approx\mathrm{Re}(h/L)\Delta P/P_{\mathrm{in}}$, is negligible. However, the current channel aspect ratio is small and the Reynolds number is $O(10)$. Therefore, the inertial to diffusion ratio is not negligible. This justifies the difference between the DSMC and the analytical solutions, specifically for Case 2, with gas flow heating condition.

Figure 5 shows the distributions of centerline and wall temperatures and centerline Mach number for Cases 1–5. If the wall temperature is equal to the inlet flow temperature, i.e., Case 1, gas heating becomes negligible in most of the channel length. Therefore, we expect to observe close agreement between Cases 1 and

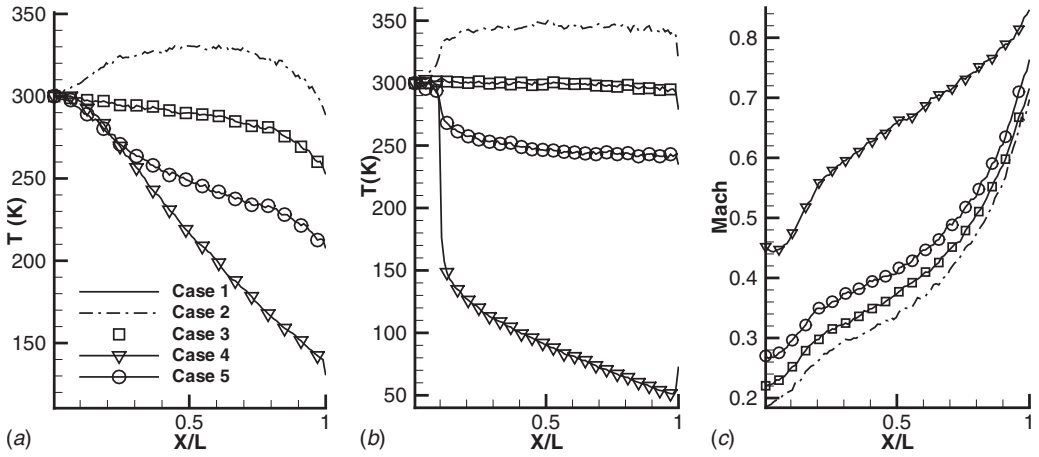

Fig. 5 Temperature and Mach number distributions, Cases 1–5: (*a*) centerline temperature, (*b*) near wall temperature, and (*c*) centerline Mach

3. For a higher wall temperature, i.e., Case 2, the centerline temperature increases initially, reaches to a maximum of 330 K around $X/L=0.6$, and starts decaying as soon as the wall heat flux vanishes (see Fig. 3). The expansion at the channel outlet reduces the temperature more rapidly. Meanwhile, the flow temperature adjacent to the wall increases to a value close to the wall temperature. The temperature distribution behaves differently for Case 1. The centerline temperature remains constant and equal to the inlet temperature up to the expansion near the outlet, where a rapid decrease occurs. The heat flux distribution applied to Case 5 causes a wall temperature drop from 300 K to 250 K along the channel. The behavior of temperature field in Case 4 shows a semilinear decrease in centerline temperature. Alternatively, its wall temperature rapidly drops from the inlet temperature to 150 K, followed by a semilinear decrease until reaching the channel exit. Vakilipour and Darbandi [10] simulated low-speed flow in microchannels using SHF boundary conditions. Their simulations showed linear increase in either wall or centerline temperatures under positive wall heat flux condition. Contrary to the simulations in Ref. [10], all the simulated cases are compressible in this study. Since the flow speed near the wall is relatively low, we observe a linear decrease in wall temperature due to a negative heat flux. The centerline temperature performs slight nonlinearity, which is due to the effects of compressibility at the midchannel.

Figure 5(*c*) shows the centerline Mach number in the channel. The maximum M_{in} belongs to Case 4 and the minimum to Case 2. Considering a fixed inlet temperature for all cases, it is concluded that gas cooling increases the velocity and mass flow rate. Figure 6 shows the Mach number and temperature maps for Case 4. The variation in the Mach number is finite in this condition. The temperature map shows a rapid decrease in temperature until the midchannel, while the reduction in the temperature is less pronounced in the second half.

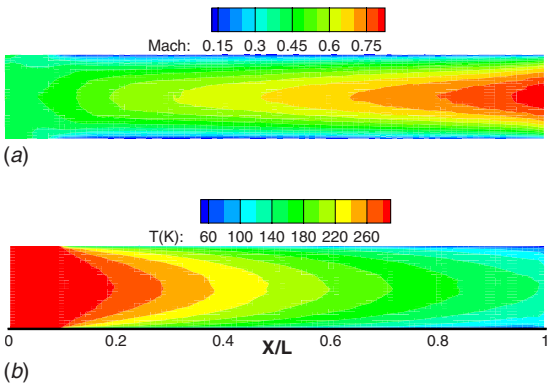

Fig. 6 Mach number and temperature maps, Case 4

3.3.3 Mass Flow Rate Study. Arkilic et al. [17], Graur et al. [18], and Karniadakis et al. [16] derived analytical solutions to predict the mass flow rate in microchannels as follows:

$$Q_{\mathrm{Ark}} = S_1[(PR^2-1)+12\ \mathrm{Kn}_o(PR-1)] \tag{4}$$

$$Q_{\mathrm{Gra}} = S_1[PR^2-1+12\ \mathrm{Kn}_o(PR-1)+S_2\ \ln(PR)] \tag{5}$$

$$Q_{\mathrm{Kar}} = S_3[(PR+1)+12\ \mathrm{Kn}_o+S_4\ \ln(S_5)] \tag{6}$$

where $S_1=h^3P_0^2/(24\mu RTL)$, $S_2=24\ \mathrm{Kn}_o^2/k_\lambda^2$, $S_3=h^3P_0(P_i-P_0)/(24\mu RTL)$, $S_4=12\ \mathrm{Kn}_o^2\ b/(PR-1)$, $S_5=(PR-b\ \mathrm{Kn}_o)/(1-b\ \mathrm{Kn}_o)$, $k_\lambda=1.02$, $b=-1$, μ is the viscosity coefficient, and R is the gas constant. The derivations of Eqs. (4)–(6) are subject to assumptions such as isothermal-low Mach number flow and long channel with locally fully developed condition. Table 3 presents the DSMC mass flow rates for Cases 1 and 2 and compares them with the analytical solutions. Evidently, the analytical solutions are not applicable to other simulated cases such as Cases 4 and 5, which are not isothermal. There are good agreements between the current DSMC results and Eqs. (4) and (6). Equation (5) predicts higher mass flow rate than the two other expressions. The analytical NS solutions given by Eqs. (4)–(6) confirm that the increase in flow temperature reduces the mass flow rate because the temperature appears in the denominator. The equation of state indicates that the increase in temperature for a given pressure ratio leads to a reduction in density. Therefore, it is expected that the mass flow rate decreases as the inlet temperature increases.

3.4 Choked Subsonic Flow. In this section, we study the choked subsonic flow and evaluate the effect of specifying back pressure at the real outlet and at the outer region of a buffer zone.

3.4.1 Role of Buffer Zone on the DSMC Solution. Back to Fig. 1, the chosen buffer zone sizes are $0.2L$ and $1.33h$. It is important to note that the use of buffer zone is to capture the choked condition at the channel exit precisely. Figure 7 shows the Mach

Table 3 DSMC and analytical mass flow rates ($Q\times10^5$)

Cases	DSMC	Eq. (4)	Eq. (5)	Eq. (6)
1	10.76	10.71	11.20	10.47
2	9.70	10.02	10.06	9.75

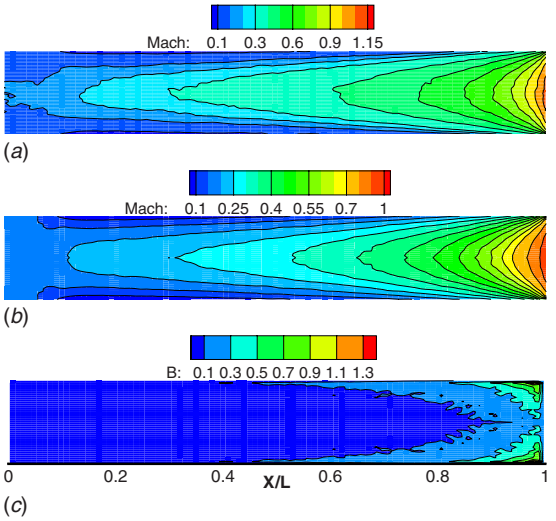

Fig. 7 Displaying results for Case 6 including: (*a*) Mach number in the channel without buffer zone, (*b*) Mach number in the channel with buffer zone, and (*c*) the parameter *B* in the channel with buffer zone

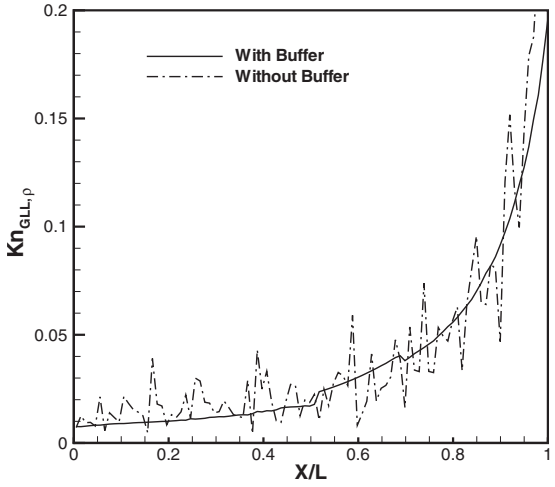

Fig. 8 Knudsen number based on GLL of density, Case 7

number maps for Case 6. Enforcing a back pressure, i.e., $P_b = 6.73$ kPa, much lower than the choking pressure, i.e., $P_e = 17.5$ kPa, at the real channel outlet, it leads to incorrect velocity or Mach number estimations at the outlet. In fact, it predicts a nonphysical supersonic flow with $M_e = 1.15$. If the pressure is specified right at the real channel outlet, two types of error appear in the solution. First, due to applying the back pressure via characteristics theory [4], the exit pressure directly influences the velocity of the molecules adjacent to the outlet boundary and the thermodynamic properties of the cells located near the outlet. Once choking occurs, the exit pressure does not drop anymore and consequently, applying a back pressure less than the choking pressure right at the channel outlet results in a nonphysical prediction of the flow field. Second, from the molecular gas dynamics point of view, we consider a Maxwellian distribution for velocity and number density of molecules that enter from the inlet and outlet boundaries to the solution domain. As the exit Mach number increases, the gradient of flow parameters increases at the channel outlet; hence, the flow parameter distributions may not exactly follow the Maxwellian distribution. There are different equilibrium breakdown parameters. One is local Knudsen number based on the gradients local length (GLL) of properties and is defined as $\mathrm{Kn}_{\mathrm{GLL},\phi} = (\lambda/\phi)|d\phi/dl|$, where ϕ is an arbitarary flow parameter and $\mathrm{Kn}_{\mathrm{GLL}} = \max(\mathrm{Kn}_{\mathrm{GLL},\rho}\ \mathrm{Kn}_{\mathrm{GLL},V}, \mathrm{Kn}_{\mathrm{GLL},T})$. The other one is the *B* parameter, which is considered as the maximum value of the shear stress and heat flux magnitudes, i.e., $B = \max(|q_i^*|, |\tau_{ij}^*|)$, where $q_i^* = -(\kappa/P)(2m/kT)^{0.5}\nabla T$ and $\tau_{ij}^* = (\mu/P)(V_{i,j} + V_{j,i} - 2/3 V_{k,k}\delta_{ij})$. Indeed, the equilibrium breakdown occurs when $\mathrm{Kn}_{\mathrm{GLL}} > 0.05$ [19]. Garcia and Aldert [20] indicated that the validity of Chapman–Enskog distribution fails if $B = 0.1$. Figure 7(*c*) shows contours of *B* in the channel. Although the variation in this parameter is small up to $X/L = 0.45$, it starts exceeding 0.1 near the wall from this point. In general, the equilibrium breakdown is due to sharp property gradients and rarefaction. We observe both of these, i.e., high flow parameter gradients and low density near the wall close to the channel outlet. It is concluded that the subsonic choked flow is highly nonequilibrium especially near the outlet region.

To study the role of the buffer zone on the solution, we compute $\mathrm{Kn}_{\mathrm{GLL},\rho}$ in the channel with and without buffer zones for Case 7. As shown in Fig. 8, $\mathrm{Kn}_{\mathrm{GLL},\rho}$ shows nonoscillatory variations for the case with a buffer zone. Meanwhile, the case without buffer zone shows a wavy behavior. $\mathrm{Kn}_{\mathrm{GLL},\rho}$ exceeds the limiting value of 0.05 as it approaches the channel outlet. Our study shows that the number of incoming molecules from the outlet is relatively low in comparison with the actual number of molecules in the domain. Therefore, using Maxwellian distribution for the incoming molecules at the channel outlet does not considerably disturb the solution. In fact, the characteristic-based implementation of back pressure right at the outlet enforces a very low back pressure there, which is nonphysical. Consequently, the magnitudes of velocity, temperature, and density of the cells adjacent to the outlet become incorrect. To implement the physics of flow properly, we apply the back pressure right at the outer region of the buffer zone. Therefore, the solution is permitted to be adjusted freely at the real outlet. This can help to obtain a reasonable Mach number ($M = 1$) at the outlet.

In order to evaluate our choked flow solution, we use an analytical solution to calculate the outlet pressure for nonisothermal flows [21] as follows:

$$\ln\left(\frac{P_o}{P_1}\right) = -\ln\left(\frac{\overline{M}_o}{M_1}\right)[1 + \chi(M_1)] \tag{7}$$

where $\chi(M_1) = \ln(J_o/J_1)/[\ln(\overline{M}_o^2/M_1^2)]$, $J_1 = (1 + (\gamma - 1)\omega M_1^2/2)$, and $\omega = (\int_A u^3 dA)/(A\overline{u}^3)$. Table 4 compares our DSMC exit pressure with the one derived from Eq. (7) for Cases 6–8. As seen, the analytical calculations predict the choked exit pressure suitably.

3.4.2 Temperature and Mach Number Distributions. Figure 9 shows the centerline temperature and Mach number distributions for Cases 6–8. For Case 6, there is an increase in the first half of the channel followed by a gas cooling in the second half. This is due to strong expansion occurring at the channel outlet. Figure 9(*a*) shows that helium (Case 8) experiences more cooling and rarefaction than nitrogen (Case 7) for the same $\mathrm{Kn}_{\mathrm{in}}$ and *PR*. Figure 9(*b*) shows that the helium Mach number is lower than that of nitrogen along the channel. Consistent with the results shown in Fig. 5(*c*), a hotter condition results in a lower Mach number along the channel.

Figure 10 shows temperature profiles at six axial sections for Case 7. It is observed that the temperature field behaves in a

Table 4 DSMC and analytical [21] choked pressures

Case	DSMC	Eq. (7)
6	17.50	16.05
7	24.50	23.10
8	21.10	20.48

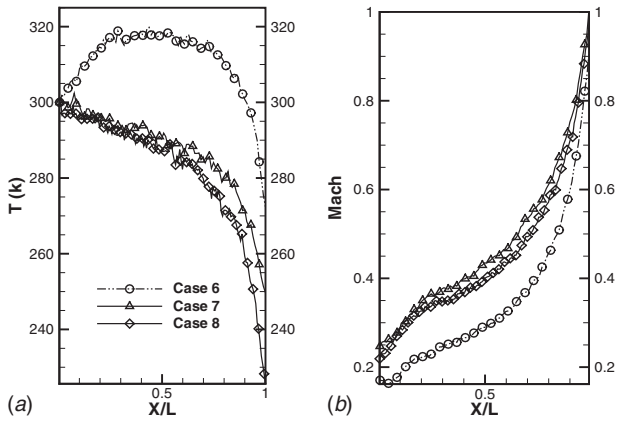

Fig. 9 Centerline temperature and Mach number distributions

complicated manner due to the mixed effects of rarefaction, wall heat transfer, thermal boundary layer development, and rapid conversion of the internal energy to a kinetic one. There is a slight heat transfer between the wall and its adjacent gas molecules close to the inlet section; therefore, we observe small temperature increase near the wall. This is followed by temperature decrease due to flow acceleration. Since the acceleration is more pronounced at the channel centerline, the temperature reduces there more rapidly. The figure shows different characteristics of mean flow and thermal boundary layer. It is observed that the thermal layer has influenced into most of the channel height at $X/L=0.6$.

3.4.3 Mass Flow Rate. Table 5 presents the DSMC mass flow rates for Cases 6–8 and compares them with the analytical solutions, i.e., Eqs. (4)–(6). We considered a choking pressure ratio along the channel instead of a real pressure ratio to calculate the analytical mass flow rates. It is observed that the analytical solutions fully underestimate the real mass flow rate in choked flow conditions. This point is expected because the underlying assumptions on which these solutions are derived are invalid here. A locally fully developed flow condition states that the pressure and density are uniform in any cross section, and the convection term is much smaller than the diffusion term in the momentum equation. As shown in Fig. 9, there are large gradients in the Mach number and temperature near the channel outlet. It was already

Table 5 DSMC and analytical mass flow rates ($Q\times10^5$)

Case	DSMC	Eq. (4)	Eq. (5)	Eq. (6)
6	9.20	0.62	0.69	0.75
7	11.00	1.62	1.69	1.84
8	13.10	1.27	1.33	1.43

shown that the rarefied flow permits more mass flow rate than the continuum one [12,17]. The current results are in contrast with the results reported by Chong [6]. His DSMC simulation showed lower mass flow rates than the NS analytical solutions [17]. Chong employed the applied pressure ratios along the channel in Eq. (4). However, we show that the applied pressure ratio may not be achieved in real physics because the channel pressure ratio does not drop anymore once the flow is choked in the channel, see Table 1.

3.4.4 Velocity Distribution. Figure 11 shows the normalized velocity profiles of the DSMC and analytical solutions of Karniadakis et al. [16] at three different axial locations for Case 8. We use the average velocity from DSMC and analytical solutions to normalize each velocity profile. Figure 11 shows that the maximum normalized velocity for the DSMC is always lower than that of the analytical solution. As shown in Table 6, this is due to a higher average velocity of the DSMC simulations and its usage to normalize the DSMC velocity profile. The mean velocities in Table 6 show that the average velocity in simulation is approximately 37–40% more than the analytical predictions at the chosen locations. This difference can be attributed to a greater pressure gradient under choked condition. As seen in Fig. 11, the slip velocities are higher than those of the analytical predictions. This was similarly observed for Cases 6 and 7.

3.5 DSMC Versus the Analytical Solutions. Up to here, we presented a few analytical solutions to show how accurate they are if they are used to calculate subsonic micro/nanochannel flows. As is known, the rarefaction and compressibility cause the microfluid behaviors to be different from those in macroscale study. The analytical solutions provided in this work are for standard hydrodynamic flows. There are many rarefaction effects which cannot be reproduced in classical hydrodynamics, including bimodal temperature profiles, nonconstant pressure profiles across the channel, and many more, see Ref. [22]. Alternatively, the higher-order

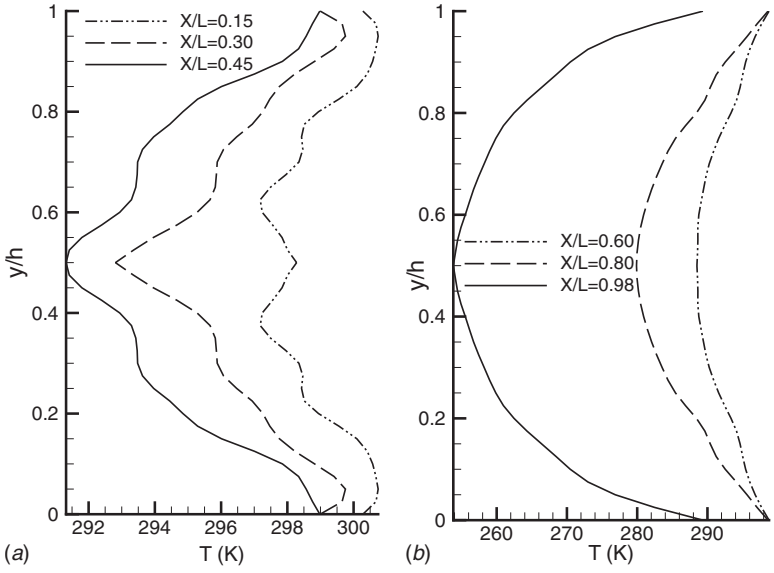

Fig. 10 Temperature profiles at different axial sections, Case 7

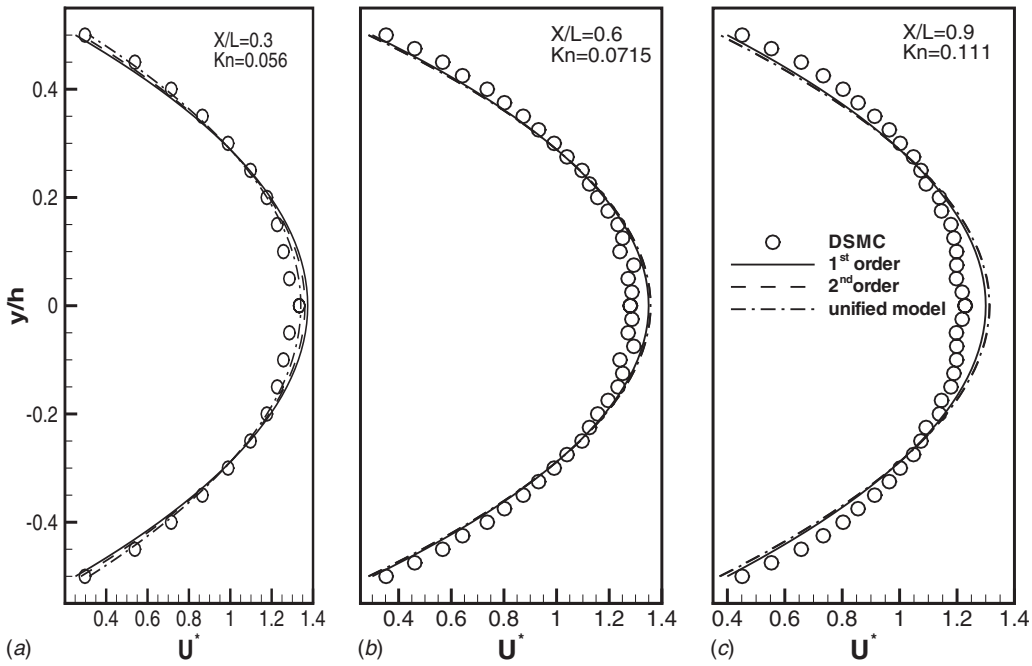

Fig. 11 Normalized velocity profiles of DSMC and analytical solutions [16], Case 8

Table 6 DSMC and the second-order analytical [16] mean velocities

X/L	0.3	0.6	0.9
$\bar{U}_{\text{analytical}}$ [16]	69.70	98.46	147.40
$\bar{U}_{\text{DSMC}}$	90.90	125.40	205.70
$\bar{U}_{\text{DSMC}}/\bar{U}_{\text{analytical}}$	1.41	1.37	1.39

continuum-based equations, such as the regularized 13 (R13) moment [23,24], were extended to reveal more unique aspects of microflows. Meanwhile, most of these latter equations are subject to some restrictions such as stability, difficulty in finding appropriate boundary conditions, and limitation to mono-atomic gases [23]. To benefit from both continuum-based equations and DSMC, the current authors are willing to extend their NS solver [25,26] to higher-order continuum equations and develop a hybrid continuum-DSMC solver.

4 Conclusion

We used DSMC to simulate subsonic flow with and without choking in micro/nanoscale channels subject to different thermal wall boundary conditions. It was observed that gas heating would increase the compressibility effects in the channel and would augment the nonlinearity in axial pressure distribution. For a specified pressure ratio along the channel, gas cooling causes an increase in mass flow rate. Alternatively, a negative heat flux wall boundary condition yields a linear decrease in centerline and wall temperatures in low compressible flows. To derive more realistic solutions in the case of the choked flow, it was suggested to implement the back pressure at the outer region of a buffer zone. Applying a nonphysical pressure just at the channel exit would result in incorrect velocity predictions for the molecules adjacent to the channel exit and incorrect thermodynamic properties of the cells located there. This consequently would lead to a wrong Mach number prediction at the exit. The DSMC mass flow rate and velocity profile were compared with the analytical Navier–Stokes solutions. It was concluded that the rarefaction and high compressibility of the choked flow would deteriorate the analytical predictions in short channels.

Nomenclature

AR = aspect ratio (L/h)
h = channel height (m)
k = Boltzmann constant (N m/K)
Kn = Knudsen number (Kn=λ/h)
L = channel length (m)
M = Mach number
P = pressure (Pa)
PR = pressure ratio
Q = mass flow rate per length (kg/ms)
T = temperature (K)
V = velocity (m/s)

Greek Symbols

α = thermal accommodation coefficient
κ = thermal conductivity (W/m K)
γ = specific heat ratio
λ = mean free path (m)
ρ = density (kg/m^3)
τ = shear stress (kg/m s^2)

Subscripts, Superscripts, and Accents

E = exit
in = inlet
i,j = cell indices in x and y directions
o = outlet
tr = translational energy
w = wall
$-$ = averaged

References

[1] Bird, G. A., 1994, *Molecular Gas Dynamics and the Direct Simulation of Gas Flows*, Clarendon, Oxford.
[2] Oh, C. K., Oran, E. S., and Sinkovits, R. S., 1997, "Computations of High-Speed, High Knudsen Number Microchannel Flows," J. Thermophys. Heat Transfer, **11**(4), pp. 497–505.
[3] Liou, W. W., and Fang, Y. C., 2000, "Implicit Boundary Conditions for Direct

Simulation Monte Carlo Method in MEMS Flow Predictions," Comput. Model. Eng. Sci., **1**, pp. 119–128.
[4] Wang, M., and Li, Z., 2004, "Simulations for Gas Flows in Microgeometries Using the Direct Simulation Monte Carlo Method," Int. J. Heat Fluid Flow, **25**, pp. 975–985.
[5] Le, M., Hassan, I., and Esmail, N., 2006, "DSMC Simulation of Subsonic Flows in Parallel and Series Microchannels," ASME J. Fluids Eng., **128**, pp. 1153–1163.
[6] Chong, X., 2006, "Subsonic Choked Flow in Microchannel," Phys. Fluids, **18**, p. 127104.
[7] Roohi, E., Darbandi, M., and Mirjalili, V., 2008, "DSMC Solution of Supersonic Scale to Choked Subsonic Flow in Micro to Nano Channels," ASME ICNMM 2008-62282, Germany, Jun. 23–25.
[8] Hong, C., and Asako, Y., 2008, "Heat Transfer Characteristics of Gaseous Flows in Microchannel With Negative Heat Flux," Heat Transfer Eng., **29**(9), pp. 805–815.
[9] Darbandi, M., and Vakilipour, S., 2007, "Developing Consistent Inlet Boundary Conditions to Study the Entrance Zone in Microchannels," J. Thermophys. Heat Transfer, **21**(3), pp. 596–607.
[10] Vakilipour, S., and Darbandi, M., 2009, "Advancement in Numerical Study of Gas Flow and Heat Transfer in Microchannels," J. Thermophys. Heat Transfer, **23**(1), pp. 205–208.
[11] Darbandi, M., and Vakilipour, S., 2009, "Solution of Thermally Developing Zone in Short Micro/Nano Scale Channels," ASME J. Heat Transfer, **131**(4), p. 044501.
[12] Arkilic, E. B., Schmidt, M. A., and Breuer, K. S., 1997, "Gaseous Slip Flow in Long Microchannel," J. Microelectromech. Syst., **6**, pp. 167–178.
[13] Cai, C., Boyd, I. D., Fan, J., and Candler, G. V., 2000, "Direct Simulation Methods for Low-Speed Microchannel Flows," J. Thermophys. Heat Transfer, **14**(3), pp. 368–378.
[14] Hadjiconstantinou, N. G., and Simek, O., 2002, "Constant-Wall-Temperature Nusselt Number in Micro and Nano-Channels," ASME J. Heat Transfer, **124**, pp. 356–364.
[15] Wang, Q. W., Yan, X., and He, Q., 2008, "Heat-Flux-Specified Boundary Treatment for Gas Flow and Heat Transfer in Microchannel Using Direct Simulation Monte Carlo Method," Int. J. Numer. Methods Eng., **74**, pp. 1109–1127.
[16] Karniadakis, G. E., Beskok, A., and Aluru, N., 2005, *Micro Flows and Nano Flows: Fundamentals and Simulation*, Springer-Verlag, New York.
[17] Arkilic, E. B., Breuer, K. S., and Schmidt, M. A., 2001, "Mass Flow and Tangential Momentum Accommodation in Silicon Micromachined Channels," J. Fluid Mech., **437**, pp. 29–43.
[18] Graur, I. A., Meolans, J. G., and Zeitoun, D. E., 2006, "Analytical and Numerical Description for Isothermal Gas Flows in Microchannels," Microfluid. Nanofluid., **2**, pp. 64–77.
[19] Lofthouse, A., Boyd, I., and Wright, M., 2007, "Effects of Continuum Breakdown on Hypersonic Aerothermodynamics," Phys. Fluids, **19**, p. 027105.
[20] Garcia, A., and Aldert, B., 1998, "Generation of the Chapman-Enskog Distribution," J. Comput. Phys., **140**, pp. 66–70.
[21] Harley, J., Huang, Y., Bau, H., and Zemel, J., 1995, "Gas Flow in Microchannels," J. Fluid Mech., **284**, pp. 257–274.
[22] Uribe, F. J., and Garcia, A. L., 1999, "Burnett Description for Plane Poiseuille Flow," Phys. Rev. E, **60**(4), pp. 4063–4078.
[23] Struchtrup, H., and Torrilhon, M., 2008, "Higher-Order Effects in Rarefied Channel Flows," Phys. Rev. E, **78**, p. 046301.
[24] Torrilhon, M., and Struchtrup, H., 2009, "Modeling Micro Mass and Heat Transfer for Gases Using Extended Continuum Equations," ASME J. Heat Transfer, **131**(3), p. 033103.
[25] Darbandi, M., and Schneider, G. E., 2000, "Performance of an Analogy-Based All-Speed Procedure Without Any Explicit Damping," Comput. Mech., **26**(5), pp. 459–469.
[26] Darbandi, M., Roohi, E., and Mokarizadeh, V., 2008, "Conceptual Linearization of Euler Governing Equations to Solve High Speed Compressible Flow Using a Pressure-Based Method," Numer. Methods Partial Differ. Equ., **24**(2), pp. 583–604.

Numerical Modeling of Chaotic Mixing in Electroosmotically Stirred Continuous Flow Mixers

Ho Jun Kim

Ali Beskok[1]
e-mail: abeskok@odu.edu

Department of Aerospace Engineering,
Old Dominion University,
Norfolk, VA 23529-0247

We present numerical studies of particle dispersion and species mixing in a ζ potential patterned straight microchannel. A continuous flow is generated by superposition of a steady pressure-driven flow and time-periodic electroosmotic flow induced by a streamwise ac electric field. ζ potential patterns are placed critically in the channel to achieve spatially asymmetric time-dependent flow fields that lead to chaotic stirring. Parametric studies are performed as a function of the Strouhal number (normalized ac frequency), while the mixer geometry, ratio of the Poiseuille flow and electroosmotic velocities, and the flow kinematics (Reynolds number) are kept constant. Lagrangian particle tracking is employed for observations of particle dispersion. Poincaré sections are constructed to identify the chaotic and regular zones in the mixer. Filament stretching and the probability density function of the stretching field are utilized to quantify the "locally optimum" stirring conditions and to demonstrate the statistical behavior of fully and partially chaotic flows. Numerical solutions of the species transport equation are performed as a function of the Peclet number (Pe) at fixed kinematic conditions. Mixing efficiency is quantified using the mixing index, based on standard deviation of the scalar species distribution. The mixing length (l_m) is characterized as a function of the Peclet number and $l_m \propto ln(Pe)$ scaling is observed for the fully chaotic flow case. Objectives of this study include the presentation and characterization of the new continuous flow mixer concept and the demonstration of the Lagrangian-based particle tracking tools for quantification of chaotic strength and stirring efficiency in continuous flow systems.
[DOI: 10.1115/1.3139109]

Keywords: chaos, chaotic stirring, chaotic mixing, Lagrangian particle tracking

1 Introduction

Flow in microfluidic devices often experience laminar or even Stokes flow conditions [1]. Predominantly laminar flows produce well-defined streamlines and flow kinematics, which are advantageous in the design and analysis of flow and species transport in various microfluidic systems [2,3]. Unfortunately these aspects, favorable for certain applications, induce great challenges in species mixing. Extremely low mass diffusivities of chemicals, macromolecules, and biological species suspended in aqueous media result in large Schmidt (Sc) numbers. Despite low Reynolds number (Re) flows, the species transport and mixing in microfluidic systems are convection dominated ($\mathrm{Pe} \equiv \mathrm{Sc} \times \mathrm{Re}$) and require extremely long mixing time- and/or length-scales (l_m). Therefore, mixing and stirring in microscale devices have attracted considerable attention in recent years. Prominent review articles on microfluidic mixing can be found in Refs. [4,5]. Overall, Microfluidic mixers can be categorized as passive and active. Passive mixers utilize co-flowing laminates of constituents in complex geometries designed to induce either secondary flows [6–8] or repetitive combination and relamination of the mixing species [9–13]. Both types of passive mixers have complex geometries, which require difficult fabrication processes, and they often have large footprint areas. Active mixers utilize an external field (other than shear) to induce stirring [14–20]. Although they may need complex fabrication processes and wiring, active mixers may ultimately enable additional control over the mixing process.

Mixing and stirring are the processes of *homogenization* of species distribution as a result of *convection* and *diffusion*. Mixing target production of a uniform concentration for continuous species while stirring aims to produce uniform particle distribution for colloidal dispersions. In either case, convection brings the constituents into close proximity, and diffusion homogenizes through blending. Based on this understanding, mixing studies must consider the effects of Reynolds and Schmidt numbers separately. Depending on the mixer geometry, variation in Reynolds number alters the flow kinematics, which may lead to favorable conditions that enhance stirring. Therefore, one first needs to determine the kinematically favorable conditions for a given mixer. However, it is also essential to address the mixing efficiency for different species (Sc) under fixed Re. This is a fundamentally important and, at the same time, a practical issue, since a good mixer should be able to mix various kinds of species within the shortest possible length or time.

From a theoretical perspective, the mixing efficiency should be characterized as a function of the Peclet number, which could be obtained by varying either Re or Sc. The mixing length for two co-flowing fluids in a straight microchannel varies as $l_m \propto \mathrm{Pe}$ [3]. This result is analogous to pure diffusion, since unidirectional flow does not stretch the interface between the two fluids. Mixing can be enhanced if the interface between the two fluids is increased by successive stretching and folding so that the species diffusion can easily homogenize the mixture over a relatively small striation thickness [21]. For certain laminar convective/diffusive transport, mixing length varies as $l_m \propto \mathrm{Pe}^{0.5}$ [22]. Exponential elongation of the species interface is known as *chaotic*

[1]Corresponding author.

Contributed by the Heat Transfer Division of ASME for publication in the JOURNAL OF HEAT TRANSFER. Manuscript received July 7, 2008; final manuscript received October 22, 2008; published online June 24, 2009. Review conducted by Satish G. Kandlikar. Paper presented at the 6th International Conference on Nanochannels, Microchannels and Minichannels (ICNMM2008), Darmstadt, Germany, June 23–30, 2008.

stirring, which drastically reduces the mixing length. Fully chaotic stirring results in $l_m \propto \ln(\mathrm{Pe})$ [21], while partially chaotic systems result in $l_m \propto \mathrm{Pe}^{\gamma}$, where $0 < \gamma < 1$ [22,23]. Actual value of γ depends on the extent of chaos within the system. For example $\gamma \leq 0.25$ was observed for certain partially chaotic flows [7,8]. The aforementioned scaling trends for chaotically stirred flows are valid, only if the Pe is varied at *fixed kinematic conditions* (i.e., fixed Re) by varying the Schmidt number.

Mixers with nonmoving boundaries often have nearly stagnant areas that experience regular (nonchaotic) flow. Often the side boundaries or geometric complexities such as grooves result in regular zones and the mixing length-scales as Pe^{γ}. This limitation is common for passive mixers, but it is also observed in active mixers. For example in a peristaltic mixer, we observed mixing time-scale as Pe^{γ} with $\gamma \approx 0.3$ despite the initially small γ values [24]. The reason for this performance reduction was a stagnant flow region within the closed mixer near a solid boundary, where the trapped species mixed with pure diffusion. Active mixers can be designed to eliminate the regular flow zones. Electroosmotic (EO) actuation induced by an externally applied electric field is one of the most appropriate methodologies for development of active mixers. Electroosmotic flow, developing within nanometers of the ζ potential patterned surfaces can be used to create active walls that eliminate stagnant flow regions near the boundaries [1]. If utilized properly, electroosmotic flows can induce chaotic stirring. Qian and Bau [2] developed an electroosmotic stirrer concept using dc electric field with time-modulated ζ potential surface patterns, and they have shown chaotic stirring under certain actuation conditions. Since the electroosmotic stirrer was a closed system, its implementation would require filling the mixing chamber, mixing, and ejecting the mix. Despite its practical limitations, their stirrer is an excellent test-bed for testing and quantification of chaotic strength due to its well-defined kinematics. In Ref. [25], we utilized the electroosmotic stirrer of Qian and Bau as a benchmark case, and reported its chaotic strength under various operating conditions using the following techniques: stirring index based on the box-counting method [26,27], Poincaré sections [2,14,19,25,28–30], finite time Lyapunov exponents [14,19,31], probability density function of the stretching field [27,32–34], and the mixing index based on the standard deviation of the scalar species distribution [20,24,25,35]. Employing the aforementioned techniques, locally optimum kinematic conditions and the actuation frequency of the stirrer that resulted in the highest mixing/stirring efficiency were identified [25].

In this paper we present continuous flow mixer concepts obtained by superposition of time-dependent electroosmotic flow and unidirectional pressure-driven flow in a straight channel to maintain the desired flow rate. Complex flow patterns that lead to chaotic stirring are obtained by ζ potential patterned surfaces, which induce electroosmotic flow under an axial ac electric field. A comprehensive review of electrokinetic mixing in microfluidics can be found in Ref. [5]. Compared with the other electroosmotically actuated continuous flow mixers in the literature [5,36–38], our conceptual design utilizes a single axial ac electric field to induce time-periodic flow, which significantly simplifies the device actuation and control. The *objectives* of this paper include demonstration of the new continuous flow mixer concept and the determination and optimization of its operating conditions. An additional objective is the demonstration of Lagrangian-based particle tracking tools for quantification of chaotic strength and stirring efficiency in continuous flow systems.

This paper is organized as follows. In Sec. 2, we describe the micromixer, its stirring mechanism, and design parameters. In Sec. 3, we provide a series of results on the direct simulation of particle dispersion to mimic the morphological behavior of interfacial layer as a function of the Strouhal number. In Sec. 4, we report qualitative dynamic analysis using Poincaré sections. In Sec. 5, we show the distribution of stretching values and provide its temporal variations at various actuation conditions. Using the scalar transport simulations, we study species mixing in Sec. 6. Section 7 includes a discussion on the dimensional parameters that satisfy the optimum operating conditions. Finally, we summarize our findings and conclude.

2 Theoretical Framework

In this section we describe the theoretical framework utilized in the design of the *chaotically stirred electroosmotic micromixer* concept. Chaotic advection is observed for cases in which the equation of motion for fluid particles can be represented as a *nonintegrable Hamiltonian system*. Hence, the particle motion is sensitive to slight variations in its position. Following the work of Aref [29], particle trajectories, located initially at $\mathbf{x}_0$ and flowing under the influence of a deterministic velocity field $\mathbf{u}(\mathbf{x},t)$, can be obtained using

$$\frac{d\mathbf{x}}{dt} = \mathbf{u}(\mathbf{x},t) \tag{1}$$

For steady two-dimensional steady flows, this dynamical system is integrable, and the particle paths coincide with the streamlines. In the Stokes flow regime, stream function plays the role of the Hamiltonian [39]. Steady 2D Stokes flow is an *integrable dynamical system*, thus it cannot be chaotic. However, for time-periodic two-dimensional flows the dynamical system becomes *nonautonomous*, and particle trajectories *may* result in chaotic advection [29]. A necessary condition for chaos is the crossing of streamline patterns at two successive times to produce either homoclinic tangles from the intersections of the stable and unstable manifolds of the same hyperbolic point, or heteroclinic tangles from the intersections of the unstable manifold of one hyperbolic point with the stable manifold of another [21,39]. These tangles induce extreme sensitivity to the initial conditions, and a consequent inability to predict the outcome of evolution in a chaotic system. Based on this premise, we designed mixers, which experience time-periodic two-dimensional flow using periodically repeating mixing blocks, as shown in Fig. 1. We present two different mixing block designs (patterns A and B), each utilizing ζ potential patterned surfaces that induce 2D EO flow under an axial electric field. Each mixing block has half channel height H and length $L = 4H$. For pattern A, we assume two different surfaces with positive and negative ζ potential values ($\pm\zeta_0$) shown by red and blue in the figure, while pattern B also includes an electrically neutral surface shown in white. The streamline patterns generated under an axial steady electric field are also shown in Fig. 1. In order to obtain a nonautonomous system, we alternate the axial electric field in the form of a cosine wave with frequency ω and superpose this flow field with a unidirectional pressure-driven flow. The EO flow under ac electric field cannot solely induce crossing of the streamlines at different times, since reversing the electric field direction simply reverses the flow direction on each streamline. Superposition of the unidirectional pressure-driven flow circumvents this problem and creates a continuous flow system with spatial and temporal periodicities.

Electroosmotic flow is generated as a result of interactions between the net electric-charge density within the electric double layer (EDL) and the externally applied electric field. In a series of papers, Dutta and Beskok [40,41] investigated the response of electroosmotic flows under ac and dc electric fields and have shown that the Helmholtz–Smoluchowski slip velocity (U_{HS}) properly models the hydrodynamics outside the thin EDL. This slip velocity is given by

$$U_{\mathrm{HS}} = -\frac{\varepsilon\varepsilon_0\zeta}{\mu}E \tag{2}$$

where ε is the dielectric constant, ε_0 is the permittivity of vacuum, and μ is the absolute viscosity. The EDL thickness for the ionic strength proposed above is on the order of 10 nm. The electroosmotic flow response time due to the temporal fluctuations of the

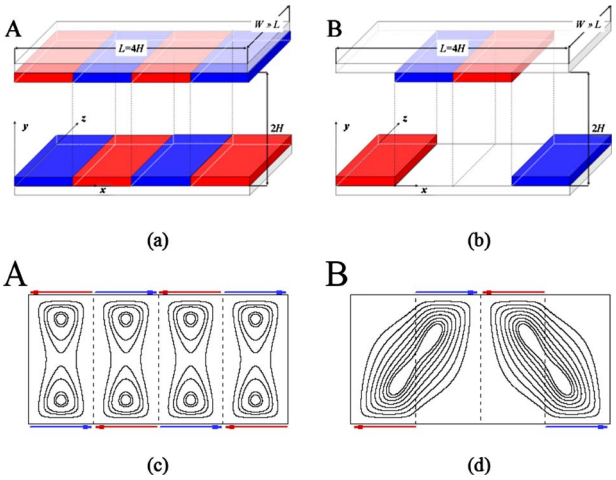

Fig. 1 The mixer consists of spatially repeating mixing blocks with ζ potential patterned surfaces as shown in (*a*) for pattern A and (*b*) for pattern B. Electroosmotic flow streamlines induced by an axial electric field are shown by solid lines in (*c*) for pattern A and in (*d*) for pattern B, while a unidirectional pressure-driven flow enables continuous flow in the system (not shown in the figure). Arrows on the top and bottom of the mixing blocks in (*c*) and (*d*) indicate the directions of the Helmholtz–Smoluchowski velocity U_{HS}. Combining the pressure-driven flow with electroosmotic flow under time-periodic external electric field (in the form of a cosine wave with frequency ω) results in two-dimensional time-periodic flow suitable to induce *chaotic stirring* in the mixer.

externally applied electric field is on the order of nanoseconds (prediction is based on the ion-diffusion time-scales through the EDL). Therefore, we expect almost immediate response from the electroosmotic flow at low frequency excitations [41]. This enables utilization of U_{HS} as an "effective slip boundary condition," by neglecting the velocity profile within the EDL, and eliminates the numerical stiffness imposed by the resolution of very thin EDL region near the surfaces. In the mixer design, Poiseuille flow channel centerline velocity (U_o) becomes an additional velocity scale. Fluid flow in the mixer is described by U_{HS}, U_o, ω, H, L, and ν (kinematic viscosity). Using *dimensional analysis*, we identify the following dimensionless parameters:

$$\mathrm{Re} = \frac{U_{HS}H}{\nu}, \quad \mathrm{St} = \frac{\omega H}{U_{HS}}, \quad A = \frac{U_0}{U_{HS}}, \quad \frac{L}{H} = 4 \tag{3}$$

where Re and St are the Reynolds and Strouhal numbers, respectively; A is the ratio of the electroosmotic and Poiseuille flow velocities; and L/H indicates the mixer geometry. For the simplicity of our design, we utilized $L/H=4$. An important requirement in our design is the maintenance of quasisteady electroosmotic flow in the system. At very high actuation frequencies, it is possible to obtain dynamic flow response, similar to that of Stokes' second problem [41]. Frequency ranges that exhibit quasisteady electroosmotic flow is determined by the Stokes number (β), which is the ratio of the diffusion and oscillation characteristic time-scales ($\beta^2 \equiv \mathrm{St} \times \mathrm{Re}$). Quasisteady flow exhibits almost immediate development of steady viscous flow pattern in response to temporal variations in U_{HS}. Such conditions are satisfied for $\beta \leq 0.2$ [41].

Due to the physical limitations of electroosmotic flow imposed by the external electric field and the ζ potential, simulations were restricted to Stokes flow at Re=0.01. The Strouhal number was varied as $1/4\pi \leq \mathrm{St} \leq 3/2\pi$ to maintain low β conditions. In order to test the sensitivity of flow kinematics to Reynolds number, we simulated the Re=0.1 case by reducing the Strouhal number to keep β unchanged. Comparisons between the Re=0.1 and Re=0.01 cases verified that the streamline patterns were *insensitive* to the Reynolds number in the Stokes flow regime (results not shown for brevity). Hence the Reynolds number is not a critical design parameter for our mixer, for as long as $\mathrm{Re} < 1$ and $\beta \leq 0.2$ are satisfied simultaneously. We also chose $A=0.8$ in order to reduce the parametric space to the investigation of the effects of Strouhal frequency variations in patterns A and B. For practical purposes $A \approx 1$ so that continuous flow can be maintained in the channel, where EO and Poiseuille flows have similar order of magnitudes, and the streamlines cross each other at different instances. In Secs. 3–5, we will utilize the Lagrangian particle tracking techniques to obtain the Poincaré sections [14,19], and stretching calculations for fluid filaments [21,27,32,33,42] to identify the *locally optimized* operating conditions. For brevity only a limited subset of results are presented.

3 Particle Dispersion

Dispersion of passive tracers in the mixing domain can provide both qualitative and quantitative information on mixing efficiency. In Ref. [25], we presented Lagrangian particle tracking techniques that utilize numerical integration of Eq. (1) using a fourth-order Runge–Kutta algorithm. An essential feature of our approach is the utilization of a spectral element discretization for the velocity field, which results in exponential convergence upon *p*-type refinements. Specifically, each mixing block was discretized using 128 spectral elements (16 and 8 elements in the x and y directions, respectively). The velocity field from the solution of the Navier–Stokes equations using sixth-order spectral expansions matched the analytical results obtained by superposition of the pressure-driven channel flow and two-dimensional electroosmotic flow with double precision accuracy. For particle tracking, we utilized the numerical results from the eighth-order spectral element discretizations with a time step of $\Delta t = 10^{-3}$, which maintains the maximum error in the tracked particle velocity and particle location below 10^{-11} for each time step. This allows us to perform long time integration of particle paths with great computational efficiency and accuracy, as previously shown in Ref. [25]. In Fig. 2 we present a series of particle dispersion results as a function of the Strouhal number. Particularly, the development of an interfacial layer is conducted by continuously feeding red and blue fluid particles to the flow near the channel entrance. Color labeling of the particles indicate their species entering the mixer from the top and bottom of the channel, respectively. For poor mixing cases, the results in Fig. 2 provide qualitative information on the behavior of the interface between the two liquids. However, for better mixing cases two different colored passive tracer particles disperse uniformly to the whole mixing domain, which can be considered as a chaotically stirred state. Chaotic motion is characterized by the divergence of nearby trajectories in the phase space. Exponential divergence of initially nearby particles means that the neighboring particle will soon behave quite differently from the original particle [43]. Sensitivity to the initial conditions is the main characteristic of chaotic systems. Chaotic motion enhances particle dispersion and increases the stirring efficiency. Therefore global chaotic stirring is highly desirable for design of efficient micromixers.

Particle dispersion results in Fig. 2 for case A at $\mathrm{St} = 1/2\pi$ and $3/2\pi$, and case B at $\mathrm{St} = 1/4\pi$ and $3/2\pi$ show oscillatory vertical motions of the red/blue particle interface in the vicinity of the channel centerline, which does not enhance particle stirring. However, case A at $\mathrm{St} = 1/\pi$ and case B at $\mathrm{St} = 1/2\pi$ in Fig. 2 exhibit extensive particle dispersion. In Figs. 2(*b*) and 2(*e*), the material lines undergo severe stretching and form extremely convoluted periodic patterns of scattered clusters flowing along the straight channel. These dramatic morphological changes in material lines represent the evolution of an initially straight interfacial layer. Generation of lobelike structures by the periodic perturbation increases the surface contact area between the two-streaming fluids. A time-periodic stretching and folding process can be clearly observed in these cases toward the downstream of the mixer. One

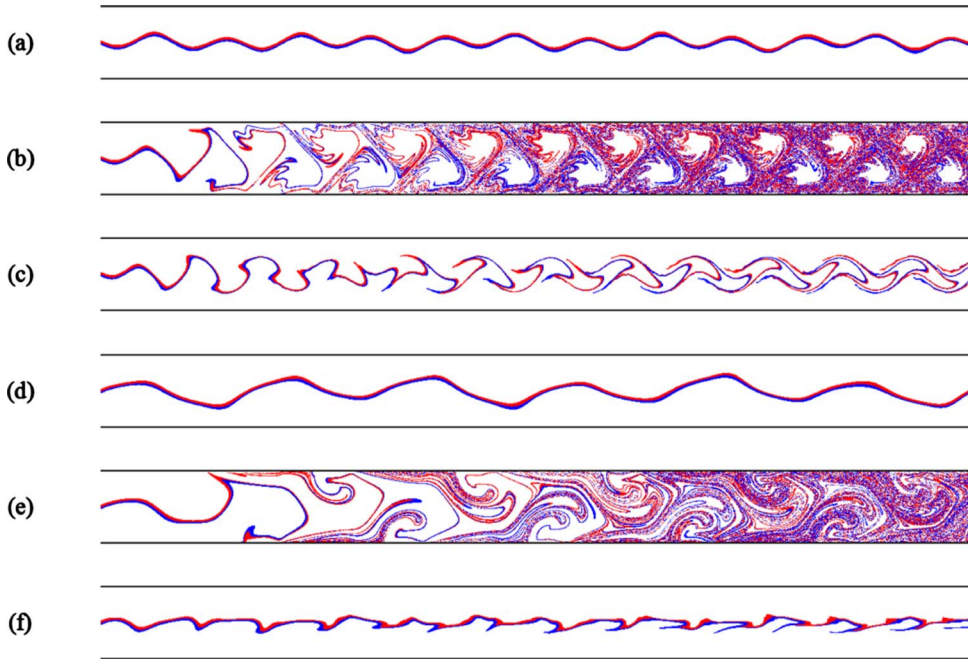

Fig. 2 Snapshots of passive particle dispersion at time $t=20\pi$: (*a*) case A at St=$1/2\pi$, (*b*) case A at St=$1/\pi$, (*c*) case A at St=$3/2\pi$, (*d*) case B at St=$1/4\pi$, (*e*) case B at St=$1/2\pi$, and (*f*) case B at St=$3/2\pi$

should note the void regions surrounded by well-dispersed particles in Fig. 2(*b*). As we will show later in Sec. 4, these regions are due to the Kolmogorov–Arnold–Moser (KAM) boundaries that separate the chaotic and regular regions of the flow, preventing transport of particles between both regions. Mixing requires uniform dispersion of passive tracer particles in the entire mixing domain [25]. Therefore, efficient chaotic mixers should avoid KAM boundaries.

Particle dispersion results need to be quantified to obtain objective measures of the stirring efficiency. For closed mixers, we can precisely measure the dispersion state in the mixer using conservation of total number of passive tracers [25]. For continuous flow mixers, parabolic velocity profile induces particle dispersion along the channel length, and as a consequence, one cannot employ the conservation of total number of passive tracers within each mixing block. Therefore, parametric studies of the Strouhal number effects on mixing will be discussed using dynamic system tools appropriate for continuous flow systems in Secs. 4 and 5.

4 Poincaré Section

In order to investigate the effects of the excitation frequency in detail, we gradually increase the Strouhal number (St) for cases A and B and utilize the Poincaré sections to investigate the best stirring state. The Poincaré section is a stroboscopic image of passive tracer particles, obtained as a collection of points where the trajectory pierces the phase plane. In a closed flow system, the time interval between two successive visits of the trajectory in the Poincaré section is the period of motion [44]. Thus, spatial trajectories of passive tracer particles are projected onto the Poincaré sections by mapping every time period. However, for an open flow system such as the channel flow, it is impossible to obtain images to display the dynamic states in a physical channel domain (x-y) through time-periodic projections, because motions of passive tracer particles are not bounded within a limited physical domain. Niu and Lee [14] proposed a useful mapping method to develop Poincaré sections for open flow systems. The continuous flow mixer utilizes time-periodic flow in periodically repeating mixing blocks. Utilizing this fact, we choose the Poincaré section to be $x_n=n\times L$ for the trajectory of any initial point, where L is the length of the mixing block and $n=1,2,\ldots,N$. Particle trajectories will intersect boundaries of the mixing blocks successively at points $P_1,P_2,\ldots,P_N$. This mapping can be defined as

$$P_{n+1}=\mathbf{\Phi}_p(P_n) \tag{4}$$

where $\mathbf{\Phi}_p$ is the Poincaré mapping. At point P_n, the vertical positions of the passive tracer particles are recorded in the y axis of the Poincaré section, while time (t) increases to infinity with the repetition of mapping. In order to convert t into a periodic variable, we adopt a new variable α. Since the flow is periodic with a specified St, and 2π is a common factor in our definition of St, we defined $\alpha=\text{modular}(t,2\pi)$. The values of α are recorded in the horizontal axis of the Poincaré section. Thus, mathematical expression of projection points on the Poincaré section is $P_n(\alpha_n,y_n)$ [14,19]. This repetitive process of projection can significantly reduce the complexity of analysis by decreasing one degree of freedom of the dynamical system.

Figures 3(*a*) and 3(*b*) depict the Poincaré sections for cases A and B at different excitation frequencies, respectively. A single passive tracer particle that was initially placed at (0.02, 0.0) is tracked for 10^5 convective time-scales (i.e., H/U_{HS}). Initial location of the particle was near the mixer entrance and on the interface between the two flow streams. In Fig. 3(*a*), the Poincaré sections for case A at St=$1/2\pi$ and $3/2\pi$ show regular patterns in the form of sinusoidal curves. Our use of 2π in the definition of α manifests itself as a sinusoidal curve with one and three periods for St=$1/2\pi$ and $3/2\pi$ cases, respectively. These ordered formations indicate quasiperiodic motions of passive tracer particles. In case A at St=$1/\pi$, the Poincaré section loses its structural coherence in most of the α-y plane with the exception of four void zones. Despite the temporal integration performed for 10^5 convective time-scales, the particle cannot penetrate these void zones, which are regular islands surrounded by the chaotic sea.

The scattering of the passive tracer particle in the Poincaré section qualitatively implies a chaotic state, while the quasiperiodic flow generates an asymptotic barrier called the KAM boundary. If the particle trajectory exhibits exponential divergence, then the trajectory on its second visit to a particular neighborhood will have subsequently different behavior than its previous visit, de-

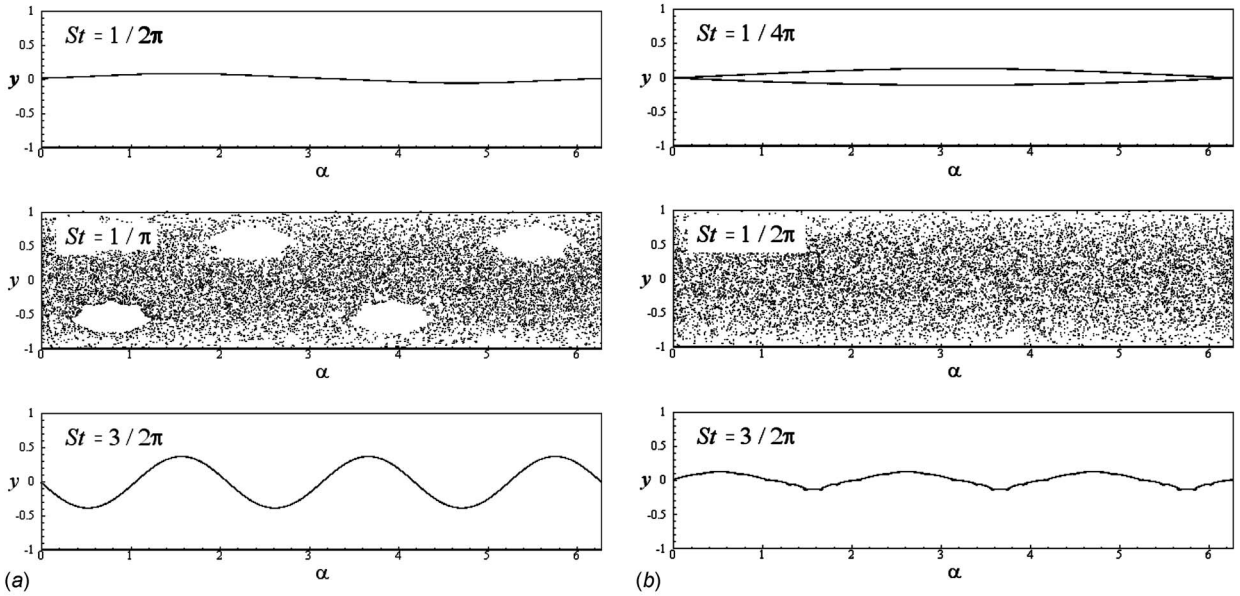

Fig. 3 Poincaré sections for (*a*) case A at St=1/2π, 1/π, 3/2π, and (*b*) case B at St=1/4π, 1/2π, 3/2π, on the α-*y* plane. Passive tracer particles were initially placed at (0.02, 0.0), which is near the entrance of the channel and on the interface between the two fluids.

stroying the KAM boundaries [43]. The route from quasiperiodic to chaos is built up by the destruction of KAM curves and shrinkage of the quasiperiodic areas (i.e., regular islands), showing morphological irregularity in the phase plane. Thus, a successive record of such behavior is the signature of chaos in the entire flow domain. Based on these premises, regularly shaped void zones should not survive in the Poincaré section. In Fig. 3(*b*), case B at St=$1/4\pi$ and $3/2\pi$ still show presence of the sinusoidal curves. However, the Poincaré section for case B at St=$1/2\pi$ is filled with scattered dots—*chaotic sea*. Qualitatively, case B at St $=1/2\pi$ is dominated under a globally chaotic state and it can be considered as a *locally optimum* case among all selected cases.

It is already known that the Poincaré section provides an intuitive and visually convincing result to qualitatively estimate the stirring performance. However, once the Poincaré sections become featureless, it is hard to determine the cases with higher chaotic strength [25]. In addition, Poincaré sections require integration of passive tracer's motion for an extremely long time. Consequently, integration times may exceed the physical diffusion time-scale ($t_{\text{diff}}=H^2/D$), and the final position of the passive tracer can overshoot the channel length. These are the drawbacks for the utilization of the Poincaré section as a *general mixing metric*. In Sec. 5, we provide the distribution of stretching values of infinitesimally small fluid filaments for explicit quantification of mixing performance.

5 Stretching of Fluid Filaments

Analysis of the stretching field of infinitesimally small fluid filaments provides physical insights in mixing studies. Important aspects of the spatial structure of stirring can be revealed by direct examination of the stretching field [32]. Attenuation of the striation thickness by stretching is the key for the enhancement of mixing efficiency [21]. Higher stretching results in increased contact area, and thus shorter diffusion distances between the mixing fluids [33]. For practical design of microscale mixers, several researchers utilized stretching fields to quantify the mixing performance [27,32,33,45]. The total amount of stretching at time t is determined by tracking the position $\mathbf{x}$ and length l of an infinitesimally small vector $l(0)$, where the net stretching h is defined as

$$h = \frac{|l|}{|l(0)|} \tag{5}$$

The fluid filaments can lose their structural coherence by dispersion, if their initial length $l(0)$ is set too coarsely (i.e., $l(0) > 1.0 \times 10^{-2}$), resulting in physically meaningless h values after a certain time [46].

In Fig. 4, we present the stretching contours for case A at St $=1/2\pi$, $1/\pi$, and $3/2\pi$ and case B at St=$1/4\pi$, $1/2\pi$, and $3/2\pi$ with h values obtained at time $t=100$. In the figure, x and y are the horizontal and vertical coordinates of the *initial positions* of fluid filaments, while the depth and the contour colors indicate $\ln(h)$. For each case, we utilized a particle pair separated by a distance of 1.0×10^{-6} H to represent a fluid filament, and we utilized 250,000 fluid filaments that were uniformly distributed through *the entire mixing domain of the first mixing block*. For case A at St=$1/2\pi$, $3/2\pi$ and case B at St=$1/4\pi$, $3/2\pi$, $\ln(h)<1$ are detected in the vicinity of the centerline of the channel, which corresponds to contracting filaments. Obviously, the results in Figs. 4(*a*), 4(*c*), 4(*d*), and 4(*f*) correspond to poor mixing cases, consistent with the corresponding results shown in Figs. 2 and 3. Particle stretching contours for case A at St=$1/\pi$, show low $\ln(h)$ values within the regular zones that are sharply segregated from the chaotic regions by KAM boundaries. Uniform distribution of high stretching values can be found only in case B at St=$1/2\pi$. Overall, the results from the stretching contours are consistent with the particle tracking results shown in Figs. 2 and 3.

Fluctuations of h are described by the calculation of the probability density function (H_n) of $\ln h$ (hereafter, PDF), defined as

$$H_n(\ln h) = dN(\ln h)/d(\ln h) \tag{6}$$

where $dN(\ln h)$ is the number of particles experiencing the stretching values in the range of $[\ln h, \ln h + d(\ln h)]$ [32]. By this definition, stretching values smaller than unity correspond to contraction, while values larger than unity show stretching in the computed direction. Initial positions of particles are located in a uniform array, distributed in the whole mixing domain of the first mixing block. These positions include both chaotic and nonchaotic zones inside the KAM boundaries. It is intuitively expected

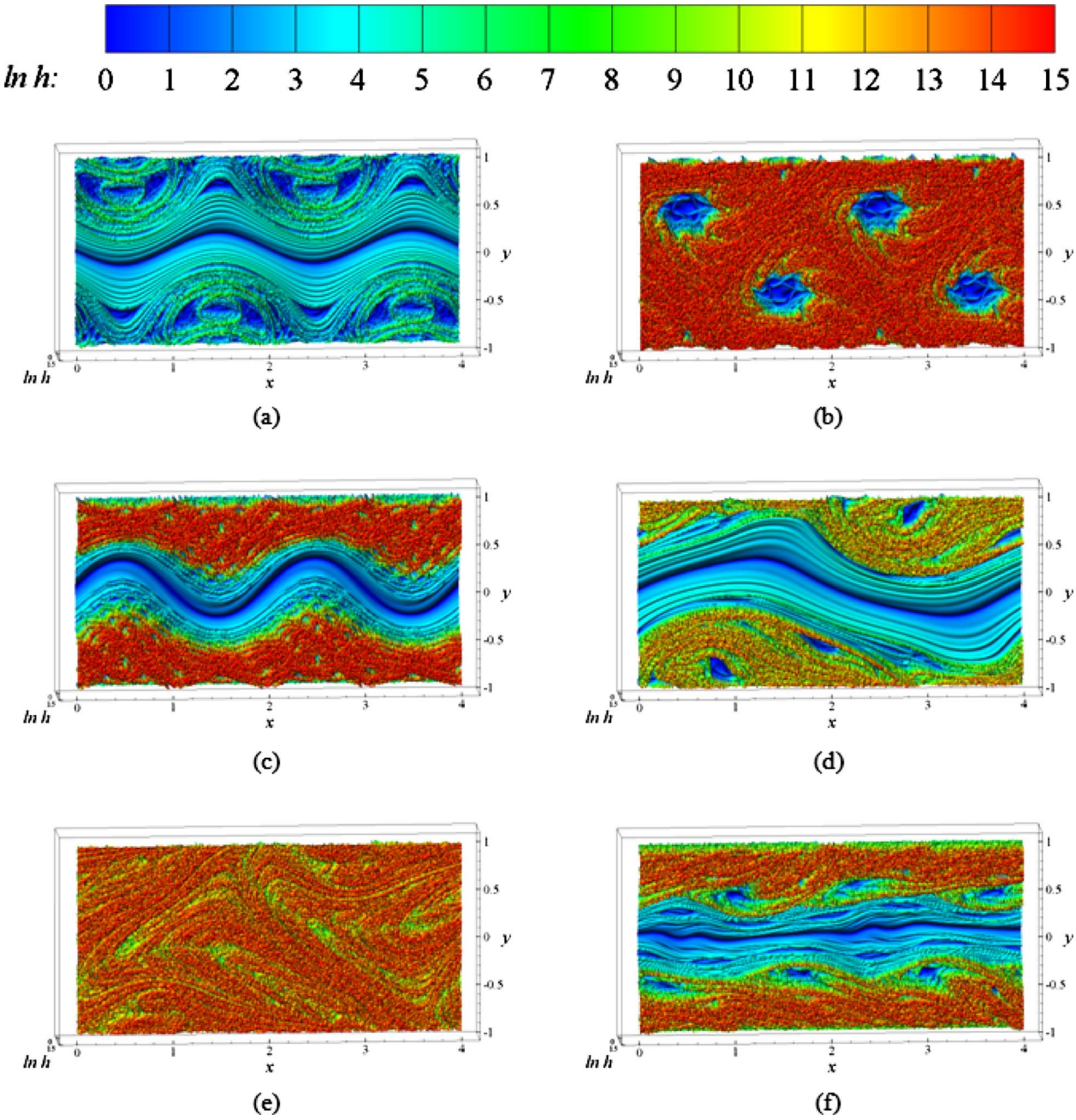

Fig. 4 Stretching contours, h, at $t=100$ for case A at (*a*) St=1/2π, (*b*) 1/π, (*c*) 3/2π, and case B at (*d*) St=1/4π, (*e*) 1/2π, (*f*) 3/2π. Red and blue parts are regions of high and low stretching values, respectively.

that points of low stretching values are placed on nonchaotic zones, while high stretching values are found in strongly chaotic regimes.

Figure 5 shows H_n computed for case A at (a) St=1/2π, (b) 1/π, and (c) 3/2π and case B at (d) St=1/4π, (e) 1/2π, (f) 3/2π using 250,000 filaments. The figure shows distributions of stretching values computed until $t=100$ with time interval of 20. As t increases, all H_n curves shift to the right. In Fig. 5(*a*), after a few convection times, the central part of each curve develops a bell shape. However, the peak of the curve is located only around the low stretching part. Regions populated by particles experiencing the highest and lowest stretching values correspond to the regions of best and worst stirrings, respectively. Figures 5(*b*)–5(*d*) and 5(*f*) show PDF with two peaks. While the peak to the right is bell-shaped and corresponds to the chaotic region, the peak to the left is produced by the regular islands, and it is characterized by the presence of multiple subpeaks. As t increases, the peak associated with the chaotic region moves to the right, indicating exponential stretching of fluid filaments, while the peak corresponding to the regular region hardly moves at all. The low stretching part of each case shows a significant amount of malformation when compared with the globally chaotic case that exhibits Gaussian distribution. These malformations are expected since fluid filaments are prevented from stretching due to KAM boundaries. In other words, an elliptic periodic point at the center of the regular island prevents stretching of fluid filaments due to its strong periodicity, as we already observed from the particle dispersion results in Fig. 2 and the Poincaré sections in Fig. 3. Compared with the other cases, H_n curves for case B at St=1/2π, shown in Fig. 5(*e*), display only the peaks populated by the chaotic regions. This indicates that case B at St=1/2π is *free of regular zones*.

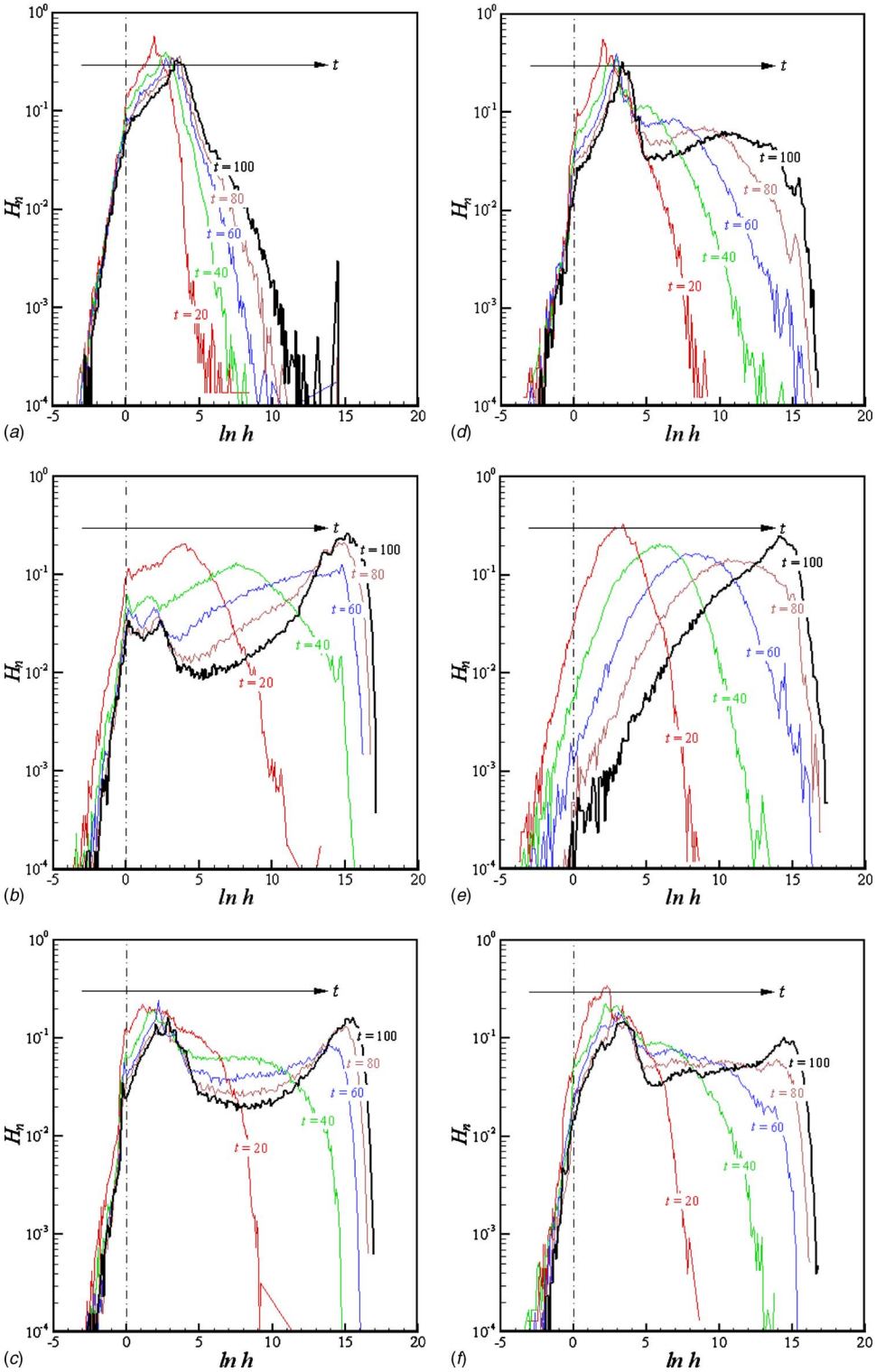

Fig. 5 Time evolution of the PDF of stretching for case A at (*a*) St=1/2π, (*b*) 1/π, (*c*) 3/2π, and case B at (*d*) St=1/4π, (*e*) 1/2π, (*f*) 3/2π

6 Numerical Simulation of Scalar Transport

In Secs. 4–6, we have shown the kinematic dependence of stirring and stretching effects using Lagrangian passive particle tracking results. In this section, we present the species mixing results as a function of channel length and Pe. Numerical simulation of mixing requires solution of the flow field from the incompressible Navier–Stokes and the species transport equations given by

$$\frac{\partial \mathbf{u}}{\partial t} + \mathbf{u} \cdot \nabla \mathbf{u} = -\nabla p + \frac{1}{\mathrm{Re}} \nabla^2 \mathbf{u} \tag{7a}$$

$$\nabla \cdot \mathbf{u} = 0 \tag{7b}$$

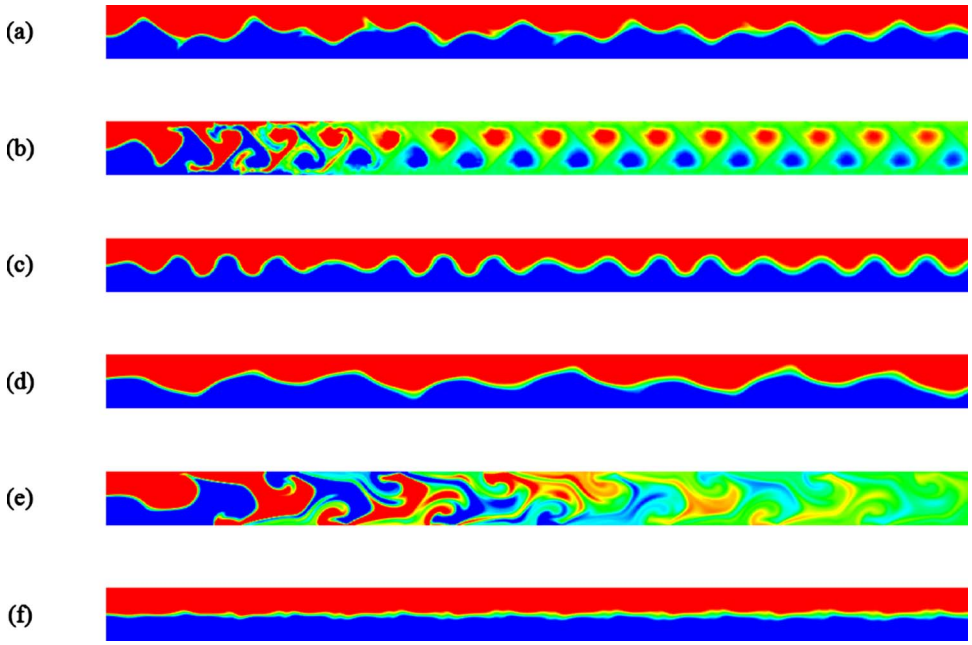

Fig. 6 Species concentration contours at Re=0.01 and Pe=1000 for case A at (*a*) St=1/2π, (*b*) 1/π, (*c*) 3/2π, and case B at (*d*) St=1/4π, (*e*) 1/2π, (*f*) 3/2π. The mixing domain is within the range of $0 \le x \le 24$ (six blocks). Each computation has reached a time-periodic state, while results are shown at time $t=20\pi$.

$$\frac{\partial C}{\partial t} + (\mathbf{u} \cdot \nabla)C = \frac{1}{\mathrm{Pe}} \nabla^2 C \tag{7c}$$

where **u** is a divergence free velocity vector, p is the pressure, and C is the species concentration.

Our numerical algorithm is based on the spectral element method, which utilizes modal expansions within an element using a subset of Jacobi polynomials. Overall, the algorithm results in exponential convergence upon increasing the number of modes within an element, known as p-type refinements. Especially for the cases that do not exhibit any geometric or boundary condition induced numerical singularities, such as the flow considered in this study, the coefficient of each mode decays exponentially with increased number of modes, similar to the Fourier series approximation. As a result, it is possible to obtain numerical solutions with an accuracy equivalent to the "computer evaluation" of analytical solutions. Further details of the numerical formulation and code verification can be found in Refs. [25,47,48].

Overall, the mixing of two miscible fluids is analogous to the open heat exchanger problem, where hot and cold fluids mix. Although the governing equations and boundary conditions for these two problems are identical, the Peclet number (Pe=Re $\times$ Pr) in heat transfer is based on the Prandtl number (Pr), while the mixing problems utilize Pe=Re$\times$Sc. Despite these similarities, we present here the chaotic mixing of low mass diffusivity species (Sc=1.0×10^5) utilizing electroosmotic flows, which require aqueous media with Pr$\approx$7. Therefore, the following mixing results are not directly applicable to the open heat exchanger problem.

In Fig. 6, we show a series of numerical simulation results of the mixing of a scalar marker at Pe=1000 in an eight-block mixer. Each mixing block was discretized using 128 spectral elements employing eighth-order expansions. Higher Pe cases required utilization of tenth-order elements. At the entry of the mixer (left) the marker has concentration values of $C=1$ (red) and $C=0$ (blue) in the upper and lower halves of the domain. Therefore, a perfect mix would reach $C_\infty=0.5$ (green). It is observed that case A at St=1/π and case B at St=1/2π achieve fast homogenization of concentration field, while the others show poor mixing. The difference in mixing efficiencies can be explained by the exponential stretching of fluid filaments under *high chaotic strength*. Exponentially stretched fluid filaments enhance mixing by increasing the area available for diffusion and by increasing the concentration gradients normal to the striations. Thus, changing the striation thickness can control the local diffusion time-scale. Similarities between the contour plots and the particle tracing results in Fig. 2 are noteworthy.

In general, it is crucial to utilize a metric to describe the mixing efficiency directly based on the concentration values. In order to estimate the mixing efficiency, we used the mixing index (M), which is based on the homogenized distribution of concentration values in the domain (i.e., concentration variance). The mixing index is defined as [24,25,35,49]

$$M = \frac{\sigma}{C_\infty} = \frac{1}{C_\infty}\sqrt{\langle C^2\rangle - \langle C\rangle^2} \approx \sqrt{\frac{1}{N-1}\sum_{i=1}^{N}\left(\frac{C_i}{C_\infty}-1\right)^2} \tag{8}$$

where C_i is the average concentration inside the ith section of a total of N interrogation areas, and i is the numerically calculated concentration value at a grid point. The $\langle \ldots \rangle$ symbol denotes averaging over the *volume of a single mixing block*. Based on the initial distribution of the species, a perfect mix would reach $C_\infty=0.5$. According to the definition in Eq. (8), a perfect mix results in $M=0$. Hence, a smaller value of M shows better mixing. For the continuous mixer considered here, the mixing index varies as a function of the channel length, and it can be used as a metric to assess the mixing efficiency. Better comparisons between the various cases are possible using the *mixing index inverse* (M^{-1}). Since $M^{-1}\to\infty$, while $M\to0$. One can associate the M^{-1} values with the concentration range ($C_\infty \pm \sigma$) using Eq. (9). For example, $M^{-1}=20$ corresponds to $\sigma=0.025$, which gives 95% mixing efficiency, defined as $(1-\sigma/C_\infty)\times100\%$. Similarly, $M^{-1}=10$ corresponds to 90% mixing.

In Fig. 7, we present variation of M^{-1} as a function of the number of mixing blocks for case A at St=1/π and case B at St

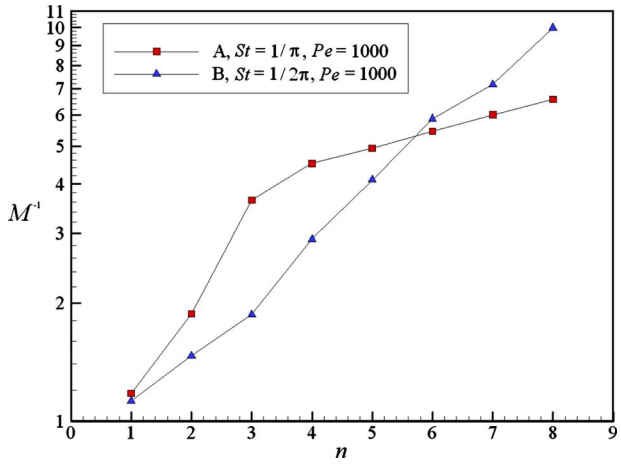

Fig. 7 M^{-1} variation for case A at St=1/π and case B at St =1/2π as a function of the number of mixing blocks at Pe =1000 and Re=0.01

$=1/2\pi$ in a logarithmic-linear graph. Within the first five mixing blocks ($n \leq 5$), M^{-1} grows faster for case A at St$=1/\pi$ than case B at St$=1/2\pi$. However, this growth slows down after the fifth mixing block, and case B results in a better mixing efficiency for $n > 5$. The slowing down of mixing for case A at St$=1/\pi$ is due to the regular flow regions observed in Figs. 2(*b*), 4(*b*), and 6(*b*). Adverse effects of these regular flow zones on mixing will become more visible for higher Pe cases, where the species trapped within these zones will mix by diffusion. However, the fully chaotic case B at St$=1/2\pi$ will continue homogenizing the mix exponentially even for high Pe flows. The rate of homogenization of the concentration field for high Pe values can be predicted from the statistics of stretching of multiple fluid filaments [22]. In Fig. 8(*a*), we plot the concentration contours obtained at four different instances within a period of excitation. In Fig. 8(*b*), we show the temporal evolution of M^{-1} for case B at St$=1/2\pi$ in the eighth mixing block. The M^{-1} value varies in time due to time-periodic flow, and its fluctuations are limited within an acceptable range to guarantee a stable mixing quality at all times. The root mean square (RMS) value of M^{-1} is consistently above the requirement for 90% mixing (i.e., $M^{-1}=10$). Therefore, all M^{-1} values in Fig. 7 achieved their corresponding statistically steady values for Pe $=1000$ flow. In Fig. 7 we observe the *exponential growth* of M^{-1} in the streamwise direction for case B at St$=1/2\pi$. A good mixer should be able to sustain this behavior with increased Pe, where the increase in Pe should be achieved by increasing Sc, while keeping the flow kinematics and, hence, *Re* unaltered. We performed mixing simulations within the range of $500 \leq \mathrm{Pe} \leq 2000$, and obtained M^{-1} variation as a function of the mixing block. In Fig. 9, we present the number of mixing blocks required to achieve 90% mixing (n_{90}) as a function of the Peclet number for case B at St$=1/2\pi$. The results show $l_{m,90} \propto \ln(\mathrm{Pe})$ behavior. This logarithmic dependence is expected for the *fully chaotic* state. Implications of this for mixing different Sc fluids are substantial. Based on the trends in Fig. 9, our mixer design can yield 90% mixing at $l_{m,90}=58\ H$ (i.e., within 15 mixing blocks) and $l_{m,90}=83\ H$ (i.e., within 21 mixing blocks) for Pe$=10{,}000$ and Pe $=20{,}000$, respectively.

7 Practical Considerations

In this section, we present the possible dimensions and corresponding actuation conditions for the mixer (case B at St$=1/2\pi$). Our design requires utilization of three different surfaces with ζ potentials of $\pm\zeta_o$ and zero, which could be maintained by carefully selecting the buffer solution and the surface materials. A possible solution is the utilization of polymethyl-methacrylate (PMMA), which exhibits $\zeta=-34$ mV in 1 mM KCl solution at pH$=7$ [50]. In order to induce positive and almost equal ζ poten-

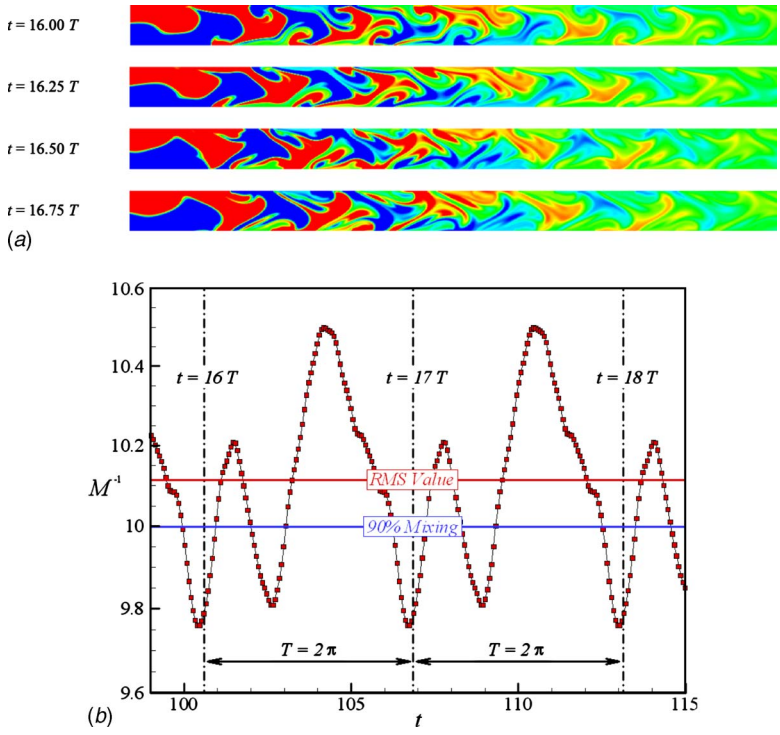

Fig. 8 Temporal evolution of M^{-1} for case B at St$=1/2\pi$ within eight mixing blocks. (*a*) A series of snapshots obtained during a period with a time interval of 0.25*T*. (*b*) Time history of M^{-1} in the eighth mixing block exhibits consistent and stable mixing quality.

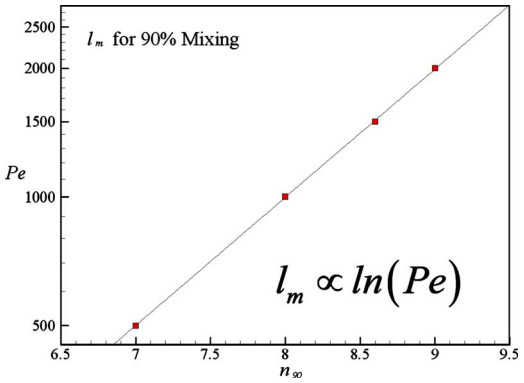

Fig. 9 Number of mixing blocks as a function of the Peclet number required to obtain 90% mixing. The results for case B at St=1/2π are shown at Re=0.01 and various Pe.

tial, one can choose aluminum-oxide surface coating that experiences $\zeta=37$ mV [51]. Electrically neutral surface (i.e., $\zeta=0$ mV) can be obtained by depositing a chromium-oxide layer on the PMMA, which will be at its iso-electric point for 1 mM KCl solution at pH=7 [52]. These materials and buffer conditions satisfy the ζ potential requirements in the featured mixer concept. Other material and buffer combinations also exist.

Next we choose a characteristic dimension that would lead to Re=0.01 flow. Fortunately one can have several choices that satisfy the physical operating conditions. First, we choose $H=100$ μm, for which a single mixing block would be 400 μm. Consequently, $U_{HS}=100$ μm/s can be obtained using an axial electric field of 4 V/mm, while the pressure-driven flow centerline velocity would be $U_o=80$ μm/s. The desired Strouhal frequency would be achieved using ac electric field frequency of 1/7 Hz or a time period of 6.25 s (which corresponds to $\beta\approx0.04$). Given these dimensions, 90% mixing will be achieved for Pe=1000 flow (i.e., $Sc=1\times10^5$) within eight mixing blocks, which corresponds to a mixing length of $l_m=3.2$ mm. An alternative choice of length scale of $H=50$ μm results in 200 μm for a mixing block. Consequently, $U_{HS}=200$ μm/s can be obtained using an axial electric field of 8 V/mm and the desired dimensional frequency of actuation becomes 4/7 Hz. As a result, 90% mixing for Pe=1000 flow will be achieved in a mixing length of $l_m=1.6$ mm. It is clear that miniaturization of a mixing block by a factor of two results in doubling of the applied electric field amplitude and quadrupling of the electric field frequency. Other possibilities, such as the decrease in the Reynolds number will decrease the applied electric field and at the same time lower the Peclet number for a given species (Sc), resulting in much shorter mixing lengths. Therefore it is imperative to make comparisons of the mixing efficiencies of various micromixer designs using proper nondimensional parameters.

Locally optimum mixing is observed at a specific value of the Poiseuille to Helmholtz–Smoluchowski velocity ratio ($A=0.8$). Numerical simulations of particle dispersion in various aspect ratio (W/H) rectangular ducts have shown off-design conditions near the no-slip side boundaries, where the desired kinematic conditions cannot be maintained due to the retardation of flow velocity. Fortunately, such off-design effects are limited within δ distance from each side-boundary. In our simulations, we observed δ vary from 1.45H to 1.49H for $W/H=10$ and $W/H=30$, respectively. As a result, the optimum mixing conditions can be maintained within 71% and 90% of the channel width for $W/H=10$ and $W/H=30$ cases, respectively. Therefore, having a large aspect ratio channel is essential for good mixing performance.

8 Conclusions

We presented detailed analysis of a chaotically stirred continuous micromixer, conceptually designed and optimized using the diagnosis tools based on chaos theory. The mixer utilizes ζ potential patterned surfaces and an axially applied ac electric field, which creates time-dependent electroosmotic flow. This is superposed with a steady pressure-driven flow that maintains the desired flow rate. In the current study, the kinematic condition is kept constant at Re=0.01, and the mixing length is characterized as a function of the Peclet number by varying Sc.

Three different diagnostic tools based on the Lagrangian particle tracking of passive tracers were utilized to observe and quantify the stirring induced by the design. Particle dispersion simulations, obtained by tracking hundreds of thousands of particles along the channel, enabled the identification of locally optimum actuation conditions for two different designs. Case A at St=$1/\pi$ and case B at St=$1/2\pi$ exhibited enhanced dispersion of colored particles with dramatic morphological changes in material lines that represent the evolution of an interfacial mixing layer. Poincaré sections were utilized to identify the regular and chaotic regions at different ac frequencies. Chaotic regions appeared as a random array of dots while the regular regions were identified by the presence of KAM boundaries. Poincaré sections for cases A and B were consistent with the particle dispersion results. Case B at St=$1/2\pi$ has shown a globally chaotic state, while case A at St=$1/\pi$ exhibited KAM boundaries. Although the Poincaré sections provide qualitative comparisons between the various cases, they often require extremely long time integration of passive tracers' motion. In addition, it is impossible to distinguish higher chaotic strength once the Poincaré sections become featureless. To avoid these drawbacks, distributions of the stretching values were investigated to provide further physical interpretations. Due to the KAM boundaries, the probability density function of stretching values H_n for case A at St=$1/\pi$ has shown subpeaks in the low stretching region, while H_n for case B at St=$1/2\pi$ exhibited only one peak in the high stretching region, corresponding to a Gaussian distribution. These were consistent with the partially and globally chaotic behaviors exhibited by case B at St=$1/2\pi$ and case A at St=$1/\pi$, respectively.

The Lagrangian particle tracking studies enabled identification of "locally optimized" operation conditions for the continuous electroosmotic mixer, at which a globally chaotic state was observed. Numerical solutions of the species transport equations were utilized to calculate the mixing index based on the standard deviation of scalar species distribution. Using numerical solutions at fixed kinematic conditions (Re) and various Schmidt numbers, variation of mixing length as a function of the Peclet number at fixed mixing efficiency ($M^{-1}=10$) was obtained. The mixing length l_m was shown to scale as ln(Pe) for the globally chaotic flow, which would minimize l_m for mixing species with various Schmidt numbers. On the other hand, nonoptimum stirring is known to result in regular flow zones with $l_m \propto Pe^{\gamma}$ scaling [25]. Therefore, the presence of nonchaotic zones can significantly reduce the mixing performance, while proper utilization of electroosmotic flows can minimize or eliminate the regular flow zones.

Acknowledgment

This work was supported by the National Science Foundation under Grant No. 0306622.

Nomenclature

A = velocity ratio, $=U_0/U_{HS}$
C = dimensionless concentration
D = mass diffusivity
h = net stretching, $=l/l_0$
H = half channel height

H_n = probability density function of stretching
l = overall stretching
l_0 = initial stretching or initial length of fluid filament
l_m = mixing length
$l_{m,90}$ = required mixing length for 90% mixing
L = length of mixing block
n = number of mixing blocks
n_{90} = number of mixing blocks for 90% mixing
Pe = Peclet number, $=U_{\mathrm{HS}}H/D$
Re = Reynolds number, $=U_{\mathrm{HS}}H/\nu$
Sc = Schmidt number, $=\nu/D$
St = Strouhal number, $=\omega H/U_{\mathrm{HS}}$
t = dimensionless time
T = period of the ac electric field
U_{HS} = Helmholtz–Smoluchowski velocity
U_0 = Poiseuille flow channel centerline velocity
x = dimensionless horizontal coordinate
y = dimensionless vertical coordinate

Greek

α = modular $(t, 2\pi)$
β = Stokes number $(\beta^2 \equiv \mathrm{St} \times \mathrm{Re})$
γ = exponent of Pe for scaling of the mixing length
δ = distance from the side boundaries where a specific A value can be maintained
σ = standard deviation of concentration values
ν = kinematic viscosity
ω = frequency of the ac electric field

References

[1] Karniadakis, G., Beskok, A., and Aluru, N., 2005, *Microflows and Nanoflows: Fundamentals and Simulation*, Springer, New York.
[2] Qian, S., and Bau, H. H., 2002, "A Chaotic Electroosmotic Stirrer," Anal. Chem., **74**, pp. 3616–3625.
[3] Holden, M. A., Kumar, S., Castellana, E. T., Beskok, A., and Cremer, P. S., 2003, "Generating Fixed Concentration Arrays in a Microfluidic Device," Sens. Actuators B, **92**(1–2), pp. 199–207.
[4] Hessel, V., Löwe, H., and Schönfeld, F., 2005, "Micromixers—A Review on Passive and Active Mixing Principles," Chem. Eng. Sci., **60**, pp. 2479–2501.
[5] Chang, C. C., and Yang, R. J., 2007, "Electrokinetic Mixing in Microfluidic Systems," Microfluid. Nanofluid., **3**, pp. 501–525.
[6] Stroock, A. D., Dertinger, S. K. W., Ajdari, A., Mezic, I., Stone, H. A., and Whitesides, G. M., 2002, "Chaotic Mixer for Microchannels," Science, **295**(5555), pp. 647–651.
[7] Kang, T. G., and Kwon, T. H., 2004, "Colored Particle Tracking Method for Mixing Analysis of Chaotic Micromixers," J. Micromech. Microeng., **14**, pp. 891–899.
[8] Camesasca, M., Manas-Zloczower, I., and Kaufman, M., 2005, "Entropic Characterization of Mixing in Microchannels," J. Micromech. Microeng., **15**, pp. 2038–2044.
[9] Kim, D. S., Lee, I. H., Kwon, T. H., and Cho, D. W., 2004, "A Barrier Embedded Kenics Micromixer," J. Micromech. Microeng., **14**, pp. 1294–1301.
[10] Jeon, M. K., Kim, J. H., Noh, J., Kim, S. H., Park, H. G., and Woo, S. I., 2005, "Design and Characterization of a Passive Recycle Micromixer," J. Micromech. Microeng., **15**, pp. 346–350.
[11] Xia, H. M., Shu, C., Wan, S. Y. M., and Chew, Y. T., 2006, "Influence of the Reynolds Number on Chaotic Mixing in a Spatially Periodic Micromixer and its Characterization Using Dynamical System Techniques," J. Micromech. Microeng., **16**, pp. 53–61.
[12] Lee, S. W., Kim, D. S., Lee, S. S., and Kwon, T. H., 2006, "A Split and Recombination Micromixer Fabricated in a PDMS Three-Dimensional Structure," J. Micromech. Microeng., **16**, pp. 1067–1072.
[13] Cha, J. H., Kim, J. S., Ryu, S. K., Park, J. Y., Jeong, Y. W., Park, S. W., Park, S. H., Kim, H. C., and Chun, K. J., 2006, "A Highly Efficient 3D Micromixer Using Soft PDMS Bonding," J. Micromech. Microeng., **16**, pp. 1778–1782.
[14] Niu, X., and Lee, Y., 2003, "Efficient Spatial-Temporal Chaotic Mixing in Microchannels," J. Micromech. Microeng., **13**, pp. 454–462.
[15] Glasgow, I., Batton, J., and Aubry, N., 2004, "Electroosmotic Mixing in Microchannels," Lab Chip, **4**, pp. 558–562.
[16] Lee, C. Y., Lee, G. B., Fu, L. M., Lee, K. H., and Yang, R. J., 2004, "Electrokinetically Driven Active Micro-Mixers Utilizing Zeta Potential Variation Induced by Field Effect," J. Micromech. Microeng., **14**, pp. 1390–1398.
[17] Goullet, A., Glasgow, I., and Aubry, N., 2006, "Effects of Microchannel Geometry on Pulsed Flow Mixing," Mech. Res. Commun., **33**, pp. 739–746.
[18] Coleman, J. T., McKechnie, J., and Sinton, D., 2006, "High-Efficiency Electrokinetic Micromixing Through Symmetric Sequential Injection and Expansion," Lab Chip, **6**, pp. 1033–1039.
[19] Niu, X., Liu, L., Wen, W., and Sheng, P., 2006, "Hybrid Approach to High-Frequency Microfluidic Mixing," Phys. Rev. Lett., **97**, p. 044501.
[20] Sundaram, N., and Tafti, D. K., 2004, "Evaluation of Microchamber Geometries and Surface Conditions for Electrokinetic Driven Mixing," Anal. Chem., **76**, pp. 3785–3793.
[21] Ottino, J. M., 1989, *The Kinematics of Mixing: Stretching, Chaos, and Transport*, Cambridge University Press, Cambridge, UK.
[22] Fereday, D. R., Haynes, P. H., and Wonhas, A., 2002, "Scalar Variance Decay in Chaotic Advection and Batchelor-Regime Turbulence," Phys. Rev. E, **65**, pp. 035301.
[23] Balkovsky, E., and Fouxon, A., 1999, "Universal Long-Time Properties of Lagrangian Statistics in the Batchelor Regime and Their Application to the Passive Scalar Problem," Phys. Rev. E, **60**, pp. 4164–4174.
[24] Kumar, S., Kim, H. J., and Beskok, A., 2007, "Numerical Simulations of Peristaltic Mixing," ASME J. Fluids Eng., **129**, pp. 1361–1371.
[25] Kim, H. J., and Beskok, A., 2007, "Quantification of Chaotic Strength and Mixing in a Micro Fluidic System," J. Micromech. Microeng., **17**, pp. 2197–2210.
[26] Jones, S. W., 1991, "The Enhancement of Mixing by Chaotic Advection," Phys. Fluids A, **3**(5), pp. 1081–1086.
[27] Liu, M., Muzzio, F. J., and Peskin, R. L., 1994, "Quantification of Mixing in a Aperiodic Chaotic Flows," Chaos, Solitons Fractals, **4**, pp. 869–893.
[28] Anderson, P. D., Galaktionov, O. S., Peters, G. W. M., Vosse, F. N., and Meijer, H. E. H., 2000, "Chaotic Fluid Mixing in Non-Quasi-Static Time-Periodic Cavity Flows," Int. J. Heat Fluid Flow, **21**, pp. 176–185.
[29] Aref, H., 1984, "Stirring by Chaotic Advection," J. Fluid Mech., **143**, pp. 1–21.
[30] Hwu, T., Young, D. L., and Chen, Y. Y., 1997, "Chaotic Advections for Stokes Flows in Circular Cavity," J. Eng. Mech., **123**, pp. 774–782.
[31] Suzuki, H., Ho, C., and Kasagi, N., 2004, "A Chaotic Mixer for Magnetic Bead-Based Micro Cell Sorter," J. Microelectromech. Syst., **13**, pp. 779–790.
[32] Liu, M., Peskin, R. L., Muzzio, F. J., and Leong, C. W., 1994, "Structure of the Stretching Field in Chaotic Cavity Flows," AIChE J., **40**, pp. 1273–1286.
[33] Muzzio, F. J., Swanson, P. D., and Ottino, J. M., 1991, "The Statistics of Stretching and Stirring in Chaotic Flows," Phys. Fluids A, **3**(5), pp. 822–834.
[34] Kim, H. J., and Beskok, A., 2005, "Characterization of Mixing in an Electroosmotically Stirred Continuous Micro Mixer," Bull. Am. Phys. Soc., **50**, pp. 160.
[35] Gleeson, J. P., 2005, "Transient Micromixing: Examples of Laminar and Chaotic Stirring," Phys. Fluids, **17**, p. 100614.
[36] Biddiss, E., Erickson, D., and Li, D., 2004, "Heterogeneous Surface Charge Enhanced Micromixing for Electrokinetic Flows," Anal. Chem., **76**, pp. 3208–3213.
[37] Sasaki, N., Kitamori, T., and Kim, H. B., 2006, "AC Electroosmotic Micromixer for Chemical Processing in a Microchannel," Lab Chip, **6**, pp. 550–554.
[38] Wu, H.-Y., and Liu, C.-H., 2005, "A Novel Electrokinetic Mixer," Sens. Actuators, A, **118**, pp. 107–115.
[39] Ott, E., 1993, *Chaos in Dynamical Systems*, Cambridge University Press, Cambridge, UK.
[40] Dutta, P., and Beskok, A., 2001, "Analytical Solution of Combined Electroosmotic/Pressure Driven Flows in Two-Dimensional Straight Channels: Finite Debye Layer Effects," Anal. Chem., **73**, pp. 1979–1986.
[41] Dutta, P., and Beskok, A., 2001, "Analytical Solution of Time Periodic Electroosmotic Flows: Analogies to Stokes' Second Problem," Anal. Chem., **73**, pp. 5097–5102.
[42] Voth, G. A., Haller, G., and Gollub, J. P., 2002, "Experimental Measurements of Stretching Fields in Fluid Mixing," Phys. Rev. Lett., **88**, p. 254501.
[43] Hilborn, R. C., 1994, *Chaos and Nonlinear Dynamics*, Oxford University Press, New York.
[44] Sprott, J. C., 2003, *Chaos and Time-Series Analysis*, Oxford University Press, New York.
[45] Lee, T. H., and Kwon, T. H., 1999, "A New Representative Measure of Chaotic Mixing in a Chaos Single-Screw Extruder," Adv. Polym. Technol., **18**, pp. 53–68.
[46] Kim, H. J., 2004, "Quantification of Chaotic Mixing in Microfluidic System," MS thesis, Department of Mechanical Engineering, Texas A&M University, College Station, TX.
[47] Beskok, A., and Warburton, T. C., 2001, "An Unstructured *hp* Finite-Element Scheme for Fluid Flow and Heat Transfer in Moving Domains," J. Comput. Phys., **174**, pp. 492–509.
[48] Sert, C., and Beskok, A., 2006, "Spectral Element Formulations on Nonconforming Grids: A Comparative Study of Pointwise Matching and Integral Projection Methods," J. Comput. Phys., **211**, pp. 300–325.
[49] Antonsen, T. M., Fan, Z., Ott, E., and Garcia-Lopez, E., 1996, "The Role of Chaotic Orbits in the Determination of Power Spectra of Passive Scalars," Phys. Fluids, **8**(11), pp. 3094–3104.
[50] Soper, S. A., Henry, A. C., Vaidya, B., Galloway, M., Wabuyele, M., and McCarley, R. L., 2002, "Surface Modification of Polymer-Based Microfluidic Devices," Anal. Chim. Acta, **470**, pp. 87–99.
[51] Lopez-Navarrete, E., and Ocana, M., 2001, "Fine Spherical Particles of Narrow Size Distribution in the Cr2O3–Al2O3 System," J. Mater. Sci., **36**, pp. 2383–2389.
[52] Kallay, N., Torbit, Z., Golie, M., and Matijevit, E., 1991, "Determination of the Isoelectric Points of Several Metals by an Adhesion Method," J. Phys. Chem., **95**, pp. 7028–7032.

Analytical and Experimental Analysis of a High Temperature Mercury Thermosyphon

André Felippe Vieira da Cunha
Assistant Researcher

Marcia B. H. Mantelli
Professor

Department of Mechanical Engineering,
Heat Pipe Laboratory (LABTUCAL),
Federal University of Santa Catarina,
Florianópolis, SC 88040-970, Brazil

High temperature thermosyphons are devices designed to operate at temperatures above 400°C. They can be applied in many industrial applications, including heat recovery from high temperature air fluxes. After a short literature review, which shows a deficiency of models for liquid metal thermosyphons, an analytical model, developed to predict the temperature distribution and the overall thermal resistance, is shown. In this model, the thermosyphon is divided into seven regions: three regions for the condensed liquid, including the condenser, adiabatic region, and evaporator; one region for vapor; one for the liquid pool; one for the noncondensable gases; and another for the tube wall. The condensation phenomenon is modeled according to the Nusselt theory for condensation in vertical walls. Numerical methods are used to solve the resulting equations and to determine the temperature distribution in the tube wall. Ideal gas law is applied for the noncondensable gases inside the thermosyphon, while the evaporator and condenser heat transfer coefficients are obtained from literature correlations. Experimental tests are conducted for thermosyphon with mercury as working fluid, designed and constructed in the laboratory. The results for two thermosyphons with different geometry configurations are tested: one made of a finned tube in the condenser region and another of a smooth tube. The finned tube presents lower wall temperature levels when compared with the smooth tube. The experimental data are compared with the proposed model for two different liquid pool heat transfer coefficients. It is observed that the comparison between the experimental data and theoretical temperature profiles is good for the condenser region. For the evaporator, where two distinct regions are observed (liquid film and pool), the comparison is not so good, independent of the heat transfer coefficient used. In a general sense, the model has proved to be a useful tool for the design of liquid metal thermosyphons. [DOI: 10.1115/1.3089551]

Keywords: thermosyphon, high temperature, liquid metal, mercury, heat pipe

1 Introduction

Thermosyphons are high thermal conductance devices able to transfer high amount of heat. In its most simple form, a thermosyphon is an evacuated metal pipe, charged with a predetermined volume of an appropriate working fluid. It can be divided into three main sections: evaporator, where heat is delivered to the device, an adiabatic section (which can or cannot exist), and a condenser, where the transferred heat is released. In the evaporator section, heat evaporates the working fluid. Usually two subregions are found in the thermosyphon evaporator: a liquid film, attached to the tube wall and a pool on the bottom of the device. The vapor generated in the evaporator moves toward the condenser region, where it condenses, and the condensed liquid returns to the evaporator by gravity.

High temperature thermosyphons work at temperatures above 400°C. They can be applied for industrial equipment. One good example is regenerative heat exchangers in petroleum plants assisted by thermosyphons. This equipment is used to recover heat from high temperature streams, such as those released from furnaces, and uses the energy to preheat air.

The usual working fluids for high temperature thermosyphons are liquid metals, including potassium, sodium, mercury, or lithium. Table 1 shows the melting and boiling points of these materials and the range of operation temperatures of the thermosyphons [1]. They present good heat transfer characteristics: high thermal conductivities, high heats of vaporization, and high surface tension coefficients. However, sodium, potassium, and lithium are elements that require careful handling. They are highly reactive with water and humidity, liberating flammable gases. On the other hand, mercury is a highly toxic substance and has been avoided in thermosyphons for industrial applications.

The tube material must be chemically compatible with the working fluid to avoid chemical reactions, which could produce undesirable noncondensable gases. The material of the tubes must also resist corrosion, keeping its mechanical properties at the high working temperatures. In this work, stainless steel was used to manufacture the mercury thermosyphons that attend well the temperature range of this working fluid. Alternative materials for thermosyphons are ceramics, such as silicon carbide and alumina. These materials have excellent corrosion and erosion resistances and high strength in high temperature. Some working fluids, such as lithium, are not compatible with ceramic materials [2]. Therefore, ceramic pipes should be provided with a protective inner liner, which matches with the ceramic expansion characteristics.

Ranken and Lundberg [2] described some high temperature ceramic heat pipes. The authors discussed the deposition of a metal layer in the inner wall to prevent corrosion of the pipe by the liquid metal. The following combinations between tube material and protective layers were studied: alumina/niobium and silicon carbide/tungsten. Note that the alumina and silicon carbide have different chemical and physical properties. Sodium and lithium were used as the working fluid in both cases.

Merrigan [3] initially conducted experiments of alumina heat pipes with sodium as the working fluid. The alumina case was

Contributed by the Heat Transfer Division of ASME for publication in the JOURNAL OF HEAT TRANSFER. Manuscript received April 24, 2008; final manuscript received January 29, 2009; published online June 22, 2009. Review conducted by Yutaka Asako.

Table 1 Melting and boiling points of liquid metals at atmospheric pressure (1 atm)

Working fluids	Melting point (°C)	Boiling point (°C)	Usual range (°C)
Sodium	98	892	600–1200
Lithium	179	1340	1000–1800
Potassium	62	774	500–1000
Mercury	−39	357	300–600

used due to the low cost and safe operation without protective metal. None of the heat pipes tested survived the thermal shock imposed during the operation startup. The first successful operation of Merrigan [3] with high temperature heat pipes was observed for silicon carbide heat pipes using a protective layer of tungsten. The working fluid was sodium, operating in air and flue gas at temperatures of around 927°C. After 100 h of operation and 30 start-up cycles, the tube was sectioned and examined to verify the presence of some deterioration and corrosion. The corrosion of tungsten by sodium was considered acceptable.

The main objective of the present study is to develop technologies for high temperature thermosyphons aiming at industrial equipment applications, such as heat exchangers for chemical and petroleum industries. Therefore, a complete easy to handle analytical model to predict the temperature distribution and the heat transfer capacity of liquid metal thermosyphons is developed. Also, experimental studies are conducted to produce data that are compared with model results.

In this work, thermosyphons and heat pipes are considered as different devices. Thermosyphons use gravity to return the condensate to the evaporator, while heat pipes employ capillary forces provided by its internal porous media.

2 Literature Review

Yamamoto et al. [4] conducted one of the first studies in high temperature heat pipes with screen mesh porous media. They investigated the lifetime and performance of stainless steel case heat pipes with sodium as the working fluid. These heat pipes were subjected to temperatures levels of 600°C, 650°C, and 700°C for 1200 h of operation, with the condenser exposed to the environment. After each test, each heat pipe was cut, and its inner surface and screen mesh were analyzed. A small corrosion was observed. Other literature experimental works concerning high temperature thermosyphons and heat pipes include Refs. [5–7].

Yamamoto et al. [5] conducted an experimental study about mercury thermosyphons and heat pipes. The tested tubes were exposed to temperatures between 350°C and 600°C. The temperature profile along the tube was measured. The tubes reached the steady state conditions in about 30 h. After the completion of the tests, the materials of the internal sections were analyzed, and the authors concluded that the metal corrosion was small.

Reid et al. [6] manufactured heat pipes using lithium as the working fluid and molybdenum as the tube material. They tested the tube in horizontal orientation. The heat pipe was able to achieve 1400 K above the room temperature in 20 min.

Park and Boo [7] developed an experimental apparatus to analyze the performance of heat pipes using sodium as the working fluid. The evaporator region was heated by means of an electric furnace. The tube was manufactured with 316L stainless steel. They observed that the temperature distribution depended on the heat transfer rate of the device.

Few studies in the literature involve analytical or numerical models for predicting the performance of thermosyphons. This is particularly true for liquid metal thermosyphons. Reed [8] and Reed and Tien [9] presented an analytical model for the thermal performance of thermosyphons, but the working fluid was not liquid metal. Their model is based on mass, momentum, and energy balances for the vapor and for the liquid film, in several sections of the thermosyphon. The objective of the model was to determine the operation characteristics of this device, including the liquid film thickness, the mass flow rate, and temperature of vapor, as well as to provide the drying and flooding limits. Both transient and steady regimes were analyzed.

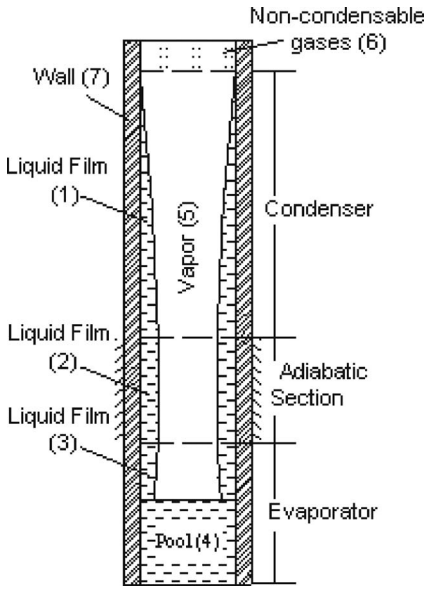

Fig. 1 Schematic high temperature thermosyphon model

Storey [10] modeled numerically the operation of a water thermosyphon in the transient regime. The numerical model includes conduction of the wall, the shear stress between the vapor and liquid film, the influence of the liquid mass in the pool, and the effective length due to the expansion and contraction of noncondensable gases in the vapor nucleus. The model assumes one-dimensional flow of the vapor and of the condensed liquid film, and two-dimensional conduction of wall. The transient behavior in the liquid pool was also modeled.

Ling and Cao [11] analyzed miniature high temperature rotating heat pipes by employing appropriate flow and heat transfer models. To obtain data to compare with the model, they performed an experimental investigation of these devices. The effects of noncondensable gases on temperature distribution along heat pipe length were also investigated. They concluded that these noncondensable gases have adverse effect on the heat pipe performance, resulting in a large temperature gradient near the condenser end, reducing the heat pipe heat transfer capacity. Their models consider zero heat transfer coefficients between the noncondensable gas region and case wall. Therefore, only conduction heat transfer is considered in this region.

Harley and Faghri [12] presented a transient two-dimensional thermosyphon model that accounts for conjugate heat transfer through the wall and the falling condensate film. The vapor flow and pipe wall regions were solved by complete transient two-dimensional conservation equations, and the liquid film was modeled using a quasisteady Nusselt-type solution. This model does not consider the effects of noncondensable gases, but investigates the effects of vapor compressibility in a high temperature thermosyphon that can be significant in some cases.

3 Proposed Model

A model for high temperature thermosyphons operating in steady state conditions is proposed with the objective of predicting the thermal performance of this device. For modeling purposes, the thermosyphon is divided into seven regions, as shown in Fig. 1. Region 1 encompasses the condensed liquid film in the

inner surface of the condenser wall. Region 3 includes the liquid film that is in contact with the evaporator internal wall. Region 2, located within the adiabatic region, is considered thermally insulated from the environment. It includes the condensed liquid, which leaves the condenser. Region 4 encompasses the liquid pool under the effect of the incoming heat. The vapor inside the thermosyphon is considered to be within Region 5. All the noncondensable gases eventually present in the system are considered to be within Region 6. Finally, Region 7 includes the metallic pipe wall.

3.1 Liquid Film. Not many studies for heat transfer related to flow of condensed metal inside vertical tube walls can be found in the literature. In the present paper, a model based on the classical Nusselt theory is considered. It is assumed that the ratio between the film thickness and tube diameter is very small ($\delta/d \ll 1$). Consequently, the inside vertical tube wall is considered a flat vertical surface. The condensed film is returned to the condenser by means of gravity. The vapor is assumed to be at the saturated temperature, and no shear forces are considered.

The Nusselt theory assumes laminar flow, constant properties in the film liquid, pure vapor with uniform temperature (T_{sat}), and no shear stresses in the liquid-vapor interface. The mean heat transfer coefficient of the film, $\bar{h}_L$, is determined by the integration of local heat transfer coefficient, $h_x = k/\delta$, over the condenser length, L_c, resulting in:

$$\bar{h}_L = \frac{1}{L_c}\int_0^{L_c} h dx \rightarrow \bar{h}_L = 0.943\left[\frac{\rho_l g(\rho_l - \rho_v)h'_{lv}k_l^3}{\mu_l(T_{\text{sat}} - T_w)L_c}\right]^{1/4} \quad (1)$$

where $h'_{lv} = h_{lv} + 0.68C_{pl}(T_{\text{sat}} - T_w)$, and C_{pl} is the liquid heat capacity. The properties of the liquid are evaluated at the average temperature between the wall and the vapor.

In the adiabatic section, the equations derived from the Nusselt analysis are not applied to the adiabatic section because there is no radial heat transfer in this region. The axial heat conduction is relatively small due to the small wall tube thickness and to the low thermal conductivity of its material. Then, the thickness of the liquid film is uniform and is the same as that which leaves the condenser region.

In the evaporator section, the vapor temperature level is considered lower than the wall temperature. The film thickness in the evaporator ($\delta_{La+Lc+\Delta x}$) and the film mean heat transfer coefficient ($\bar{h}_{\text{ef}}$) are modeled based on the same Nusselt theory of condensation for a flat vertical surface and are given by the following equations, respectively:

$$\delta_{L_a+L_c+\Delta x} = \left[\delta^4_{L_a+L_c} + \frac{4k_l\mu_l(T_{\text{sat}} - T_w)(x - L_a - L_c)}{g\rho_l(\rho_l - \rho_v)h_{lv}}\right]^{1/4} \quad (2)$$

where δ_{La+Lc} is the film thickness at the end of the adiabatic section.

3.2 Liquid Pool. In the liquid pool region, nucleate boiling is considered. For mercury, some correlations for the heat transfer coefficients of the pool were obtained from the literature, such as those of Subbotin [13] and Ratiani [14], given, respectively, by

$$h_{ep} = C_s(q^{2/3})\left(\frac{k_l h_{lv}\rho_l}{\sigma T^2}\right)^{1/3}\left(\frac{P_l}{P_c}\right)^s \quad (3)$$

$$h_{ep} = \frac{0.007k_l}{r_n}\left(\frac{qr_n^2 h_{lv}\rho_g}{\sigma T_{\text{sat}}k_l}\right)^{7/10}\left(\frac{\rho_l\sigma T_{\text{sat}}c_{pl}}{h_{lv}^2\rho_g^2 r_n}\right)^{1/4} \times\left(\frac{r_n p^{1/2}(\rho_g^{-1} - \rho_l^{-1})^{1/2}}{\mu_l/\rho_l}\right)^{1/4} \quad (4)$$

where $C_s = 8.0$ and $s = 0.45$ for $P_l/P_c < 0.001$, $C_s = 1.0$ and $s = 0.15$ for $P_l/P_c \geq 0.001$, P_c is the critical pressure of fluid, P_l is the liquid pressure in contact with heated surface, r_n is the radius of the nucleation site (equals 20×10^{-6} m^2, characteristic of industrial surfaces), and T is the average between saturation (T_{sat}) and wall (T_w) temperatures, in Kelvin.

3.3 Vapor Region. This region encompasses the nucleus of evaporator, condenser, and adiabatic sections, where the vapor is located. The vapor is assumed to be at the saturated temperature level and at the same temperature along the pipe. Vieira da Cunha [15] presented a model for the vapor pressure distribution inside the tube, which can be applied to the vapor region of thermosyphon. He concluded that the vapor pressure difference between condenser and evaporator is negligible for the mercury thermosyphon under investigation. Then, in the present model, no vapor pressure or temperature distributions are considered. Vapor entrainment in any of the thermosyphon regions, due to liquid drag forces, is not considered. This means that no shear stresses are considered, in accordance with Nusselt's model hypothesis. All vapor produced in the evaporator is considered condensed in the condenser.

3.4 Noncondensable Gas Region. The present model also considers the noncondensable gases, which can be eventually found inside the thermosyphon. The major problem is to determine the amount of noncondensable gases. During the fabrication process, the tube is cleaned and evacuated before the addition of the working fluid. The noncondensable gases are generally formed from the chemical reaction between the fluid and the tube material. The volume of these gases is hard to predict. In the present model, only the noncondensable gases (air, for instance), remaining after vacuum is created inside the tube, is considered. In other words, the fluid is considered completely compatible with the tube material not producing noncondensable gases.

Noncondensable gases are clustered in the upper condensation region during operation, decreasing the effective length of the thermosyphon. Actually, in the regions where the noncondensable gases are present, the heat transfer coefficient inside the tube decreases significantly because condensation no longer happens inside the tube. Furthermore, it is well known that the capacity of exchanging heat in gases is very limited. As a result, in present model the noncondensable gas region is considered adiabatic.

For modeling this region, the pressure, the mass, and the temperature of these gases in the start-up conditions are considered known. In steady state conditions, the final volume of the noncondensable gases are obtained from the ideal gas law, considering that the temperature of the gas is known, as well as the pressure, which is considered the same as the vapor pressure in the upper part of the condenser region. Actually, the model is a design tool, and this region was included to help in the adjustment of the theoretical model to experimental data that will be eventually available.

3.5 Distribution of Wall Temperature. The temperature distribution of the thermosyphon wall is determined through the method of finite volumes [16]. In this method, the wall is divided into several small volumes, where a balance of energy, for steady state conditions, is performed. Each volume consists of a ring of thickness Δx, as illustrated in Fig. 2. The differential volume of temperature T_p is submitted to the following heat flux (q) through the boundary areas: conduction from north (n) and south (s) and convection for east (e') and west (w') side areas. The volume is in contact with outside and inside fluids at temperature levels of T_o and T_i, respectively, where T_o is the environmental temperature, considered uniform for each section, while T_i is assumed at the vapor or pool temperatures, depending on the region of the thermosyphon. The following finite volume equation resulted from this balance for each volume:

$$A_p T_p = A_n T_N + A_s T_S + B \quad (5)$$

where the coefficients are given by: $A_p = h_{w'}A_{w'} + A_s + A_n + h_{e'}A_{e'}$,

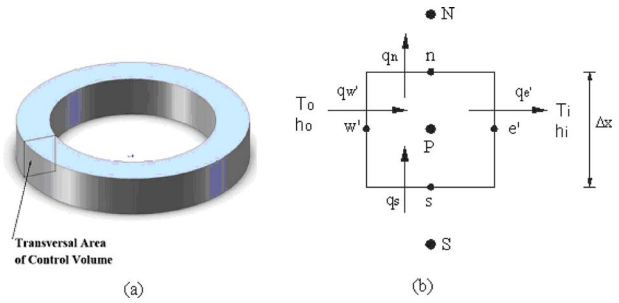

Fig. 2 (*a*) Control volume and (*b*) energy balance in the cross-sectional area of the control volume

$A_s=(k_wA_{xs})/\Delta x$, $A_n=(kA_{xn})/\Delta x$, and $B=h_{w'}A_{w'}T_o+h_{e'}A_{e'}T_i$.

Equation (5) is applied to each control volume of the thermosyphon wall. All the equations together form a system of linear equations, which is solved by means of iterative methods. An initial temperature guess is applied to all the volumes, and the temperature, for the $k+1$ iteration, is related to the temperature of the k iteration by the following self-adjustable equation, according to the Gauss–Seidel [16] method:

$$A_pT_p^{k+1}=A_sT_S^{k+1}+A_nT_N^k+B \tag{6}$$

The heat transfer coefficient inside the tube depends on the thermosyphon region under consideration. As already mentioned, two subregions are found in the evaporator region: the pool and the falling liquid film. Equation (2) is used for the falling liquid subregion, and Eq. (3) or Eq. (4) for the pool subregion, depending on whether the volume is in contact with the falling film or with the pool. In the condenser, the internal heat transfer coefficient is given by Eq. (1) for each control volume.

The outside face of the wall receives a uniform heat flux rate ($Q_{w'}$) in the evaporator. Then, the coefficients A_p and B of Eq. (5) for this region turns out to be $A_p=A_s+A_n+h_iA_{e'}$ and $B=Q_{w'}+h_iA_{e'}T_i$. For the condenser, the outer heat transfer coefficient is calculated by experimental data or through appropriate correlations of literature.

3.6 Numerical Solution. As already mentioned, the model is solved numerically by means of an iterative process using FORTRAN. The input data for the model are: lengths of the condenser (L_c), adiabatic section (L_a), and evaporator (L_e); mass of fluid; external heat transfer coefficients; condenser external wall temperature; tube inner diameter (d_i); and heat transfer rate ($\dot{Q}$). The model determines the wall temperature distribution and the film thickness of the thermosyphon for steady state conditions. A check of the minimum amount of fluid to guarantee that the entire internal wall is in contact with the condensate film is performed by comparing the calculated mass of condensate film with total working fluid mass of thermosyphon.

First, the model calculates the effective length of thermosyphon, defined as the region where there is significant exchange of heat (in other words, the region not in contact with the noncondensable gases). Then, the effective length of thermosyphon is divided into several control volumes. The energy equilibrium equations for each control volume, including the heat transfer coefficients and liquid film thickness, were obtained according to the seven regions (see Fig. 1), using the formulation presented in the last section. These control volume equations are solved numerically based on the method of finite volumes [16].

The whole tube is initially considered at uniform temperature in the design working temperature level. This temperature basically depends on the amount of heat that the device is supposed to transfer. A good initial guess reduces the computational time so that the convergence is obtained after a few hours of computation. The convergence is considered achieved when the comparison between the heat transfer rate numerically calculated and the input data is within an established tolerance. When these values are unbalanced, the vapor temperature, which is considered uniform along the whole tube, is adjusted; decreased, if the heat output is larger than the heat input or increased if the heat output is lower than the heat input.

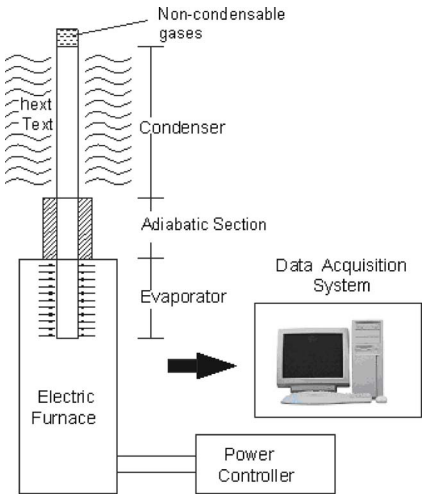

Fig. 3 Schematic of the experimental apparatus

4 Experimental Work

4.1 Experimental Setup. The experimental apparatus is composed by an electric furnace, a power controller, and a data acquisition system, as illustrated in the schematic in Fig. 3. The furnace contains three blocks of electric resistances, each one 200 mm in length and 50 mm in diameter. Each resistance has a digital temperature controller that keeps its temperature above the maximum value of 1200°C. The resistances transfer heat to the evaporator section through radiation. This furnace is isolated by ceramic fiber. In addition, a box of wood with vermiculite (natural mineral) is built around it to minimize the heat loss through the walls. A device located at the top of the furnace, consisting of four adjustable connecting rods, is built to support the pipe, so that the thermosyphon remains upright.

The heat flux rate, which is dissipated by the resistances, is regulated by a power controller that varies the voltage to up to 220 V. The voltages and temperatures are measured by a data acquisition system (HP 34970 Bench-Link Data Logger), and the resulting data are stored in a computer..

The test laboratory is open to the environment, as a safety procedure concerning the use of mercury. Therefore, the condenser region room temperatures and external heat transfer coefficients are not controlled, and depend on the environmental conditions. The external heat transfer condenser coefficients employed in this work are obtained from experimental data.

4.2 Description of Thermosyphons. Two devices, Thermosyphon A and Thermosyphon B, were designed, constructed, and tested. Both are made of stainless steel 316L tubes, with a length of 1.0 m, and outer and inner diameters of 25.4 mm and 21 mm, respectively. The condenser region of Thermosyphon A of approximately 500 mm has 31 fins with a diameter of 50 mm, which are 14.6 mm distant from each other. Thermosyphon B is smooth in all regions. The amount of mercury used was approximately 30.5 ml for Thermosyphon A and 40 ml for Thermosyphon B.

Inside both thermosyphons, a small diameter tube (capillary tube) is located in the central axis and welded to the cap of the thermosyphons. The region between these inner and outer tubes is sealed. A thermocouple, which slides through the capillary tube,

Table 2 Specification of tests for the thermosyphons

Description	Thermosyphon A (finned condenser)		Thermosyphon B (all smooth)	
Heat transfer rate	485 W	1609 W	486 W	1922 W
Condenser length	700 mm	690 mm	640 mm	640 mm
Evaporator length	200 mm	210 mm	200 mm	200 mm
Adiabatic section length	100 mm	100 mm	140 mm	140 mm
Filling ratio	48.5%	48.5%	63.5%	63.5%

measures the vapor temperature. The material of the small tube is stainless steel 316L, with an outer diameter of 6.35 mm and a thickness of 1.0 mm.

An analysis of heat losses by conduction through the capillary tube was performed, showing that they are negligible and that the temperature readings inside the tube are good measurements of the vapor or liquid pool temperatures (depending on the position of the thermocouple inside the capillary tube).

4.3 Experimental Methodology. The thermosyphons were instrumented with K-type thermocouples manufactured by OMEGA. These thermocouples were spot welded on the external wall of the tube to guarantee good contact with the wall and, consequently, good measurements of temperature. The thermocouples are protected against the radiation and convection through aluminum strips.

Another thermocouple was inserted inside the capillary tube to monitor the vapor temperature along the entire length of thermosyphon. This K-type thermocouple 1.5 m in nominal length is manufactured by ECIL. The thermocouple has an external protection consisting of a sheath of stainless steel, with mineral as insulation between the wire and the aluminum. The tests were conducted in steady state conditions that were considered reached after several operation hours, when the temperature variation was less than 9°C in all thermocouples. Then, the data acquisition system was used to acquire data in regular time intervals of 10 s. The descriptions of the thermosyphons tested (condenser, evaporator, and adiabatic section lengths), as well the power inputs applied in each test, are found in Table 2.

4.4 Experimental Results. The data collected from the tests allow for the plot of Thermosyphons A and B external and internal temperature profiles. The heat transfer rate for each thermosyphon ($\dot{Q}$) is determined by the difference between power dissipated by the electric furnace resistances and the heat losses from the furnace to the environment. In the present case, the heat losses through the furnace walls are considered negligible, which is a good hypothesis, considering the vermiculite insulation around the furnace. Then, the heat transfer rate is calculated by the well known equation, where V is the electrical potential applied to the electric resistance R.

An analysis of the uncertainty of the temperature measurements and of the heat transfer rate was carried out. An accuracy of ± 2 W was obtained for the 485 W and 486 W power inputs and of about ± 8 W for the 1609 W and 1922 W power inputs. Accuracies of around ± 8.2°C are estimated for temperatures from 200°C to 600°C and of ± 8.9°C for temperatures from 600°C to 1000°C. This relatively high uncertainty was also observed by White [17], who reports nonuniform temperature measurements related to high temperature levels and installation problems.

Figure 4 shows the wall and vapor temperature profiles for Thermosyphon A (finned in the condenser region), with heat transfer rates of 485 W and 1609 W, respectively. Temperature measurement uncertainties are also presented in these figures for each point, through vertical bars. In Fig. 4, it can be noted that in almost the whole tube, the vapor temperature levels are higher than the wall temperature, but an intersection of these curves is observed for the 0.8 m position (condenser). Actually, the sudden

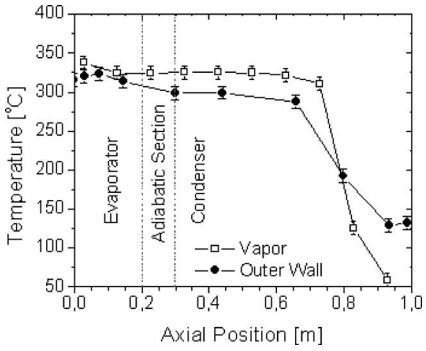

Fig. 4 Temperature profile of Thermosyphon A subjected to 485 W of heat power

temperature drop shows the region where the noncondensable gases concentrate at the tip of the condenser. In this region, the heat exchange between gases and tube is very poor, and the heat conduction through the solid materials takes the major role. One should note that the axial heat conduction through the thermosyphon wall is much higher than the axial conduction of the inner capillary tube wall, whose thickness is much thinner than the thermosyphon wall.

The outer wall temperatures should be lower than vapor temperatures (capillary tube) in the condenser region because the heat leaves the thermosyphon in the radial direction. On the other hand, in the evaporator, which is a region where the tube receives heat, the outer wall temperatures should be higher than the vapor temperatures. The plots show this trend but also show that there are some points in the evaporator where the inverse is observed (see Fig. 4). This is an unexpected behavior, which is attributed to the problem related to high temperature measurements, as already observed. Despite this inconsistency, it is important to emphasize that these differences between vapor internal (capillary tube) and external (outer wall) temperatures, also considering the difference of temperature in thickness wall, are within the uncertainty of temperature measurements. Due to its problem, many measurement repetitions and parallel experimental studies, not shown in this paper, were conducted (Fig. 5).

For Thermosyphon B, which has no fins, two testes were also performed, as show in Table 2. Figure 6 shows the tube wall and vapor temperature profiles for these tests, for heat transfer rates of 486 W and 1922 W, respectively. The experimental points of these plots also present vertical bars, representing the experimental uncertainties. It can be noted, in both cases (Fig. 6), that the outer wall temperatures are higher than the vapor temperatures along the tube. It was expected that, in the condenser region, the vapor temperature should be higher than the wall temperatures, but this is not verified by the data. On the other hand, one should note that,

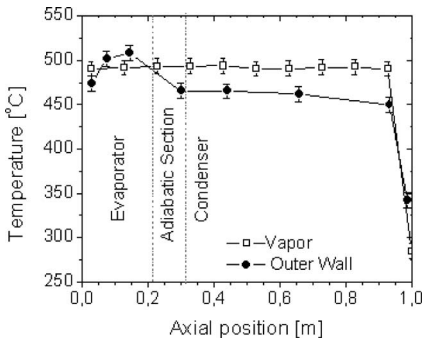

Fig. 5 Temperature profile of Thermosyphon A subjected to 1609 W of heat power

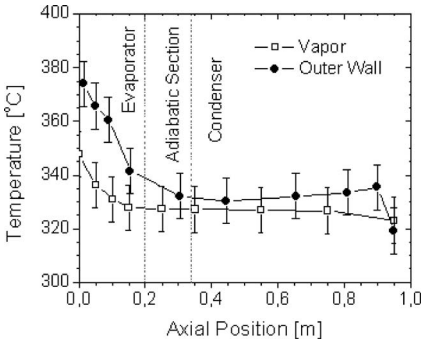

Fig. 6 Temperature profile of Thermosyphon B subjected to 486 W

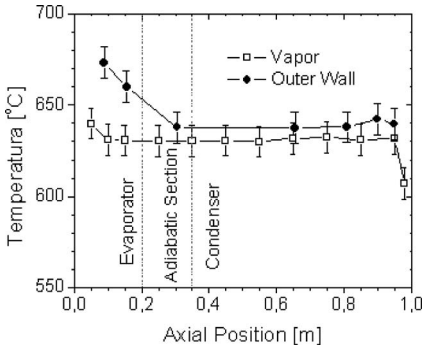

Fig. 7 Temperature profile of Thermosyphon B subjected to 1922 W

again, the temperature differences between wall and vapor in this region are within the temperature measurement uncertainties, also considering the conduction radial temperature difference.

The wall temperature for Thermosyphon A, which is finned, is compared with the wall temperature profile of Thermosyphon B, which is smooth, for a similar level of heat transfer rates. It is observed that the outer wall temperature profile for Thermosyphon A (finned) is lower than for Thermosyphon B (smooth), as expected, since the finned region promotes a better heat exchange with the environment, decreasing the temperature levels. In addition, the temperature differences between the two thermosyphons increase when the power increases due to the same reasons. It can also be observed that the region occupied by noncondensable gases is larger for Thermosyphon B because the lower levels of temperature lead to lower vapor pressures, causing a minor compression of these gases.

The radial differences of temperature can be significant, due to the low thermal conductivity of the wall tube. This radial thermal resistance represents the largest individual resistance of the overall thermal resistance circuit of thermosyphon (R_t). The thermal resistance, which represents the capacity of the device to transfer heat, is given by

$$R_t = \Delta\bar{T}/\dot{Q} \tag{7}$$

where $\Delta\bar{T}$ is the mean temperature difference between the condenser and evaporator. It can be noted that the thermal resistance decreases with the heat transfer rate increase. The thermal resistance of Thermosyphon A, for 485 W, is smaller than that for Thermosyphon B, for 486 W (note that the power is practically the same). Two facts may have contributed to a lower thermal resistance of Thermosyphon A: the smaller filling ratio of Thermosyphon A and the presence of fins, which provides better heat exchange in the condenser external area.

5 Comparison Between Theoretical and Experimental Results

The model presented in Sec. 4 was implemented in the computer using thermophysical and geometric properties of Thermosyphons A and B, shown in Table 2, and compared with the experimental temperature distribution of the outer wall.

Only the gases that remain after the tube evacuation were considered as the noncondensable gases in the present simulation. A remaining pressure of 100 Pa was assumed after the evacuation. The perfect gas model showed that the tube length occupied by the noncondensable gases is negligible. However, in actual cases, other noncondensable gases are formed, mainly due to the chemical reaction between the fluid and tube. As already discussed, they can occupy a considerable volume, especially when the temperature level is low for low heat power transport, as observed in Fig. 4, for Thermosyphon A. Therefore, all model simulations were performed considering only the effective length of the thermosyphons tested (Fig. 7).

The results for Thermosyphon A for 485 W are compared with the proposed model, for the two pool correlations, in Fig. 8. A good comparison of the temperature profiles resulting from the simulation and experimental data is observed in the condenser and the liquid film region of evaporator. In the liquid pool, levels of temperatures are different for the two simulations. Observing Fig. 8, one can note that the model with Ratiani correlations shows a step in the temperature profile of the evaporator region, while the model with the Subbotin correlation shows a much smoother behavior. Obviously, this happens because the values of the pool heat transfer coefficients obtained from Ratiani are lower than those of Subbotin's correlation. The temperature data in this region present a higher level than the model, therefore, the model with the Ratiani correlation has better comparison with data.

In Fig. 8, it can be observed that, in the adiabatic section, there is a linear variation in temperature for both models because in this region only the axial heat conduction by the wall of thermosyphon is considered. The models used to determine the temperature distribution of the evaporator liquid film, adiabatic, and condenser regions are the same for both theoretical plots.

The outer wall temperature profiles for dissipations of 486 W and 1922 W, for Thermosyphon B, were also simulated using both theoretical correlations for the pool heat transfer coefficients. Figure 9 presents the comparison between models and data for these profiles. The observations made for the thermal behavior of Thermosyphon A are valid here; again the theoretical model employing the Ratiani correlation presents reasonable comparison with data for the evaporator region, while the comparison between the model and data is very good for the rest of the thermosyphon.

In general, the theoretical temperature profiles show a uniform (constant value) distribution in the condenser, in the pool region, and in the evaporator liquid film region, and a linear profile in the adiabatic section. The linear profile of adiabatic section is justified only by the presence of the axial conduction of the wall. The

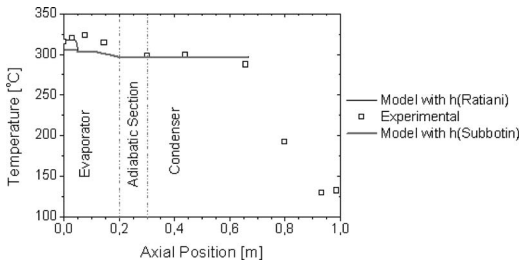

Fig. 8 Comparison: experimental data and model for Thermosyphon A to 485 W

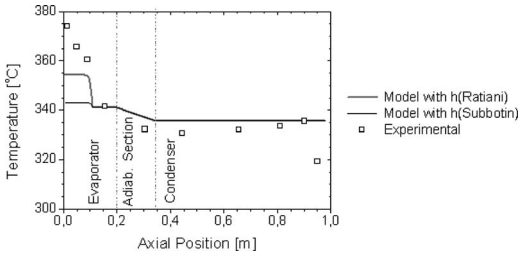

Fig. 9 Comparison: experimental data and model for Thermosyphon B to 486 W

uniform profile in other regions shows uniform heat transfer coefficients, both in the pool and in the liquid film regions. Actually, these profiles are combinations of the internal and external heat transfer coefficients, connected to the low axial thermal resistance of the tube wall. These facts show that the accuracy of model is essentially related to the precision with which heat transfer coefficients are determined.

6 Conclusion

This paper presents a theoretical and experimental study of mercury thermosyphons. The outer wall and vapor temperature profiles, as well as the thermal resistance, were shown for two distinct thermosyphons: Thermosyphon A, which is finned in the condenser, and Thermosyphon B, which is all smooth. The outer temperatures, measured on the external surface of tube, are lower for the Thermosyphon A, and the difference in these temperatures between the two thermosyphons increases when the level of power also increases.

In both thermosyphons, the difference in mean temperature between the condenser and evaporator is significant due to the high thermal resistances of the wall in the radial direction, as the material of this wall (stainless steel 316L) presents low thermal conductivity and relatively thick walls.

Data obtained from experimental tests of mercury thermosyphons were confronted with theoretical results from the proposed model, through the comparison of the outer wall temperature profiles. The simulations were conducted using two different correlations for the pool heat transfer coefficients: Subbotin [13] and Ratiani [14] correlations. The uniform temperature profiles for the condenser and evaporator liquid film regions are due to the uniform characteristics of the heat transfer coefficients. The two steps found in the evaporator theoretical temperature distribution curves are because the pool and the liquid film regions present two uniform and different levels of heat transfer coefficients.

Within the regions, the uniformity is possible because the heat transfer coefficients inside the thermosyphon are much higher than that due to the tube wall material. A good choice of the heat transfer coefficient correlations is very important for a good theoretical model.

For the present studied cases, the comparison between the experimental data and theoretical temperature profiles is good, especially in the condenser and adiabatic sections. In the evaporator, this comparison is poorer, independent of the theoretical correlation used for the determination of the heat transfer coefficient. Even when considering this poorer comparison, the model was shown to be very reasonable and can be used as major tool for the design of liquid metal thermosyphons for industrial applications.

References

[1] Vieira da Cunha, A. F., and Mantelli, M. B. H., 2006, "Modeling of High Temperature Thermosyphons," Ninth AIAA/ASME Joint Thermophysics and Heat Transfer Conference, San Francisco, CA.
[2] Ranken, W. A., and Lundberg, L. B., 1978, "High Temperature Heat Pipes for Terrestrial Applications," Third International Heat Pipe Conference, CA, May 22–24.
[3] Merrigan, M. A., 1981, "Heat Pipes for High Temperature Industrial Waste Heat Recovery," Eighth Energy Technology Conference, Washington, DC.
[4] Yamamoto, T., Tanaka, Y., Sasaki, M., and Hatori, H., 1982, "Study on Life of Sodium Heat Pipe," J. Heat Recovery Syst., **2**(4), pp. 369–376.
[5] Yamamoto, T., Nagata, K., Katsuta, M., and Ikeda, Y., 1994, "Experimental Study of Mercury Heat Pipe," Exp. Therm. Fluid Sci., **9**, pp. 39–46.
[6] Reid, R. S., Sena, J. T., and Merrigan, M. A., 1999, "Transient Tests of a Molybdenum-Lithium Heat Pipe," 11th International Heat Pipe Conference, Tokyo, Japan.
[7] Park, S. Y., and Boo, J. H., 2004, "An Experimental Study on the Heat Transfer Characteristics of High-Temperature Cylindrical Heat Pipes," Korean Journal of Air-Conditioning and Refrigeration Engineering, **16**(1), pp. 70–76.
[8] Reed, J. G., 1985, "Analytical Modeling of the Two-Phase Thermosyphon," Ph.D. thesis, Department of Mechanical Engineering, University of California, Berkeley, CA.
[9] Reed, J. G. and Tien, C. L., 1987, "Modeling of the Two-Phase Closed Thermosyphon," ASME J. Heat Transfer, **109**(3), pp. 722-730.
[10] Storey, J. K., 2003, "Modeling the Transient Response of a Thermosyphon," Ph.D. thesis, Department of Mechanical Engineering, Brigham Young University, Provo, UT.
[11] Ling, J., and Cao, Y., 2000, "Closed-Form Analytical Solutions for Radially Rotating Miniature High-Temperature Heat Pipes Including Non-Condensable Gas Effects," Int. J. Heat Mass Transfer, **43**(19), pp. 3661–3671.
[12] Harley, C., and Faghri, A., 1994, "Complete Transient Two-Dimensional Analysis of Two-Phase Closed Thermosyphons Including the Falling Condensable Film," ASME J. Heat Transfer, **116**, pp. 418–426.
[13] Carey, V. P., 1992, *Liquid-Vapor Phase-Change Phenomena: An Introduction to the Thermophysics of Vaporization and Condensation Processes in Heat Transfer Equipment*, Taylor & Francis, London.
[14] Bullerschen, K.-G., and Wilhelmi, H., 1991, "Cooling of Arc Furnace Electrodes With Heat Pipes," Chem. Eng. Technol., **14**, pp. 45–53.
[15] Vieira da Cunha, A. F., 2008, "Análise de Termossifões que operam em Altas Temperaturas," MS thesis, Mechanical Engineering Department, Federal University of Santa Catarina.
[16] Maliska, C. R., 1995, *Transferência de Calor e Mecânica dos Fluidos Computacional*, LTC.
[17] White, D. R., 2005, "Calibration and Standards in Temperature Measurement," *Handbook of Measuring System Design*, P. H. Sydenham and R. Thorn, eds., Wiley, New York.

Gibbs–Thomson Effect on Spherical Solidification in a Subcooled Melt

Yeong-Cheng Lai
Graduate Student

Chun-Liang Lai[1]
e-mail: cllai@ntu.edu.tw

Hsieh-Chen Tsai
Graduate Student

Department of Mechanical Engineering,
National Taiwan University,
Taipei 106,
Taiwan, R.O.C.

This study aims to investigate theoretically the growth of a spherical nucleus due to solidification in an infinite domain of a subcooled melt. The effects on the spherical growth due, respectively, to the subcooling, the Gibbs–Thomson condition, and the density-difference induced convection are analyzed and discussed systematically. With the Gibbs–Thomson effect considered, no exact solutions can be found easily. Thus, a binomial temperature distribution in the liquid phase is reasonably assumed to approximate the actual one with the satisfaction of the energy balance at the solidification front and other boundary conditions.
[DOI: 10.1115/1.3133883]

Keywords: subcooling, Gibbs–Thomson effect, solidification, critical radius

1 Introduction

The theoretical analysis of solidification is difficult due to the moving boundary front and the energy release condition on it so that analytical solutions in the closed form can only be found for very simple configurations and conditions [1]. Among the earliest works, Carslaw and Jaeger (refer to Ref. [1]) solved independently, the one-dimensional solidification problem in a semi-infinite domain analytically with similarity solutions, and predicted that the solidification front propagates with the square root of time. Different topics related to the solidification phenomenon were also identified and studied [2]. Among them, solidification of pure substance in a subcooled condition is one of the topics with both academic and technical interests.

In general, the solidification process in a subcooled liquid possesses three main stages. In the earliest stage, nuclei of different sizes are formed [3]. For those nuclei whose radii are greater than the so-called critical radius R_0^* as predicted by the Gibbs–Thomson condition, subsequent growth will proceed as the subcooled liquid solidifies on the interface that is called the spherical-growth stage [4,5]. In the final stage, dendritic growth issues are present due to instability [6–8].

The Gibbs–Thomson condition takes into account the thermal effect of surface tension γ at the interface, which will change the freezing/melting temperature T_f^* when the interface is flat to the equilibrium temperature $\tilde{T}_f^*$ at the curved interface. For the growth with a radius R^* of the spherical interface, the Gibbs–Thomson condition can be written as

$$R^* = \frac{2\gamma T_f^*}{L(T_f^* - \tilde{T}_f^*)}$$

where L is the latent heat per unit volume of the solid phase. Therefore, if $\tilde{T}_f^*$ is replaced by T_∞^*, which is the surrounding temperature, it gives the critical radius for the onset of solidification, that is

$$R_0^* = \frac{2\gamma T_f^*}{L(T_f^* - T_\infty^*)}$$

In other words, for the nuclei whose radii are smaller than R_0^*, solidification will not occur because the modified freezing temperature due to the surface tension effect becomes lower than the surrounding temperature of the subcooled liquid.

In addition to the Gibbs–Thomson effect, the solidification will induce a convective flow due to the density difference between the solid and liquid phases, which will also affect the spherical growth of the nuclei.

2 Mathematical Formulation

The main interest of this study is the effect on the growth of a spherical nucleus and the temperature distribution due, respectively, to the subcooling, the Gibbs–Thomson condition and the convection induced by the density difference between the solid and liquid phases during solidification.

The following assumptions are made first to simplify the problem.

(1) The subcooled liquid is a pure substance.
(2) The growth of the nucleus remains spherical during the solidification process.
(3) The thermodynamic properties of both the liquid and solid phases are assumed constant.
(4) Except the density-difference induced convection, no other convective effects are considered, and the induced flow is incompressible.
(5) Initially, there exists a spherical nucleus with radius $a > R_0^*$, the critical radius.
(6) Since the growing spherical solid during solidification considered herein is very small, the temperature distribution in the solid sphere is assumed uniform.
(7) A binomial temperature distribution in the liquid phase is assumed to approximate the actual distribution. With the satisfaction of the energy balance at the solidification front and other boundary conditions, such distribution is expected to provide reasonably accurate predictions of the solidification front and growth rate, although the detailed information regarding the temperature distribution is sacrificed.

The nondimensionalization schemes, $T_i = T_i^* - T_f^*/T_\infty^* - T_f^*$, $r = r^*/a$, $R = R^*/a$, and $t = t^*/a^2/\alpha_l$ are chosen for the convenience of analysis and discussion. In the above expressions, the variables with superscript (*) denote the dimensional ones, $i = s$ or l denote the solid or liquid phase, T_∞^* and T_f^* as the temperature at infinity and the freezing temperature, and α_l as the thermal diffusivity of the liquid phase. With the above nondimensionalization scheme and the sixth approximation, the dimensionless governing equations and initial and boundary conditions can be written as follows:

$$T_s = \frac{\beta}{\Delta}\frac{1}{R}, \quad 0 \le r \le R \tag{1}$$

[1]Corresponding author.

Contributed by the Heat Transfer Division of ASME for publication in the JOURNAL OF HEAT TRANSFER. Manuscript received November 2, 2007; final manuscript received March 20, 2009; published online June 19, 2009. Review conducted by Yogendra Joshi.

$$\frac{\partial T_l}{\partial t} - \varepsilon \frac{R^2}{r^2}\frac{dR}{dt}\frac{\partial T_l}{\partial r} = \frac{2}{r}\frac{\partial T_l}{\partial r} + \frac{\partial^2 T_l}{\partial r^2}, \quad R \le r \le \infty \tag{2}$$

$$\frac{dR}{dt} = \Delta \left.\frac{\partial T_l}{\partial r}\right|_R \quad \text{with} \quad R(0) = 1 \tag{3}$$

$$T_l|_R = \frac{\beta}{\Delta}\frac{1}{R} \tag{4}$$

$$T_l = 1 \quad \text{as} \quad r \to \infty \tag{5}$$

In the above equations, $\varepsilon = \rho_s - \rho_l/\rho_l$ and $(-\varepsilon R^2/r^2 dR/dt)$ is the density-difference induced velocity, which is derived from the continuity equation and the mass conservation at the solidification front $R^*(t)$. c_s and c_l represent, respectively, the specific heat of the solid phase and liquid phase. Two important dimensionless parameters are involved. They are the Stefan number $\Delta = c_l(T_f^* - T_\infty^*)/L$, an index of subcooling, and $\beta = 2\gamma c_l T_f^*/aL^2$, which is a dimensionless parameter indicating the Gibbs–Thomson effect.

When the Gibbs–Thomson effect is neglected, i.e., $\beta = 0$, the similarity solutions could be found by assuming $R = h(t+c)^{1/2}$ and the similarity variable $\eta = r/(t+c)^{1/2}$, with constants h and c being determined. With Eq. (2) being rewritten in terms of η and then being integrated, it yields

$$T_l = 1 + AF(\eta) \quad \text{with} \quad F(\eta) = \int_\eta^\infty z^{-2} \exp\left(-\frac{z^2}{4} + \frac{\varepsilon h^3}{2z}\right) dz \quad \text{and} \quad A = \text{constant} \tag{6}$$

Substituting expressions for $R(t)$ and $T_l(\eta)$ into Eq. (3), constant A can be determined as

$$A = -\frac{h^3}{2\Delta}\exp\left(\frac{h^2}{4} - \frac{\varepsilon h^2}{2}\right) \tag{7}$$

From Eq. (4), i.e., $T_l|_{r=R} = T_l|_{\eta=h} = 0$, it yields

$$\Delta = \frac{h^3}{2}\exp\left(\frac{h^2}{4} - \frac{\varepsilon h^3}{2}\right)F(h) \tag{8}$$

Equation (8) gives constant h in terms of Stefan number Δ implicitly. We then have

$$T_l(\eta) = 1 - \frac{F(\eta)}{F(h)} \tag{9}$$

which satisfies the boundary condition at infinity, i.e., Eq. (5).

Also with the aid of $R(0) = 1$, the expression for the similarity solution of $R(t)$ reduces to

$$R(t) = h(t + h^{-2})^{1/2} \tag{10}$$

The similarity solution of growth rates at any instant can finally be calculated by

$$V(t) = \frac{dR(t)}{dt} = \frac{h}{2}(t + h^{-2})^{1/2} \tag{11}$$

However, when the binomial temperature distribution is assumed as suggested by Hill [2], let

$$T_l = a_1(t)\left(\frac{1}{r} - \frac{1}{R}\right) + a_2(t)\left(\frac{1}{r} - \frac{1}{R}\right)^2 + \frac{\beta}{\Delta}\frac{1}{R} \tag{12}$$

The coefficients $a_1(t)$ and $a_2(t)$ are solved as follows:

$$a_1(t) = \frac{\frac{\beta}{2} - R(t) \pm \sqrt{(1 - 2\Delta - 2\Delta\varepsilon)R^2(t) + \beta(1 + 2\varepsilon)R(t) + \frac{\beta^2}{4}}}{\Delta(1+\varepsilon)} \tag{13}$$

$$a_2 = \tfrac{1}{2}[\beta a_1 - \Delta(1+\varepsilon)a_1^2] \tag{14}$$

In order for the sum within the square root to remain positive, the coefficient in front of $R^2(t)$ must be positive, i.e., $\Delta < 1/2(1+\varepsilon)$ must be satisfied. In addition, from the numerical calculations presented in Sec. 3, only the positive sign in front of the square root has to be chosen so that $0 \le T_l \le 1$ condition always holds.

To determine the solidification front $R(t)$, Eq. (3) is employed, which gives

$$V = \frac{dR}{dt} = -\frac{a_1\Delta}{R^2} \tag{15}$$

After integration, it yields

$$\int_1^R \frac{R^2}{a_1} dR = -\int_0^t \Delta dt = -\Delta t \tag{16}$$

Thus, with β, Δ, and ε given, the solidification front, growth rate, and temperature distribution at any instant can be calculated iteratively.

When $\beta = 0$, i.e., the neglected Gibbs–Thomson effect, Eq. (16) can be integrated explicitly to attain the following relation between R and t:

$$R = \left[\frac{2(1 - \sqrt{1 - 2\Delta - 2\Delta\varepsilon})}{1+\varepsilon}\right]^{1/2}\left[t + \frac{1+\varepsilon}{2(1 - \sqrt{1 - 2\Delta - 2\Delta\varepsilon})}\right]^{1/2} \tag{17}$$

which possesses the same functional form $R = h(t+c)^{1/2}$, with h and c being constant, as predicted by the similarity solution. Therefore, approximations by such a binomial temperature distribution are consistent with the predictions by the exact solution for situations when the Gibbs–Thomson effect is neglected.

3 Results and Discussion

The $R-t$, $V-R$, and $T-r$ relations are to be presented and discussed in this section. The parametric ranges investigated are $\Delta: 10^{-3} \sim 10^{-1}$, $\beta: 10^{-6} \sim 10^{-3}$, and $\varepsilon \sim \pm 0.1$, which are typical for the solidification of water and $\alpha-$Fe melt, with $\Delta T^* = T_f^* - T_\infty^*$, $=1\ ^\circ\text{C} \sim 5\ ^\circ\text{C}$, and $a = 10^{-4} \sim 10^{-3} m$.

Comparing $R-t$ and $V-R$ relations for situations with $\beta = 0$, $\varepsilon = 0$, and different Δ, the errors between the binomial solutions and the similarity solutions are all below 10% within the calculation ranges, which therefore provide satisfactory accuracies, especially for situations with small values of Δ. Since Mullins and Sekerka [6] predicted that the spherical nuclei will become unstable when the radii of the nuclei grow to beyond $7R_0^*$, this study will thus present only the results for $R^* \le 5R_0^*$ or $R \le 5$. In addition, both the binomial and similarity solutions predict that for a larger value of Δ, the spherical nuclei will grow faster, and the growth rate decreases as time proceeds.

The $R-t$ diagram with different values of β is shown in Fig. 1. The $V-R$ diagram is displayed in Fig. 2. Illustrated in Fig. 3 are the $T-r$ relations at two different stages, i.e., at $R=2$ and $R=5$. From Fig. 3, it can be seen that with a larger β the difference between the subcooled temperature of the surrounding melt and the freezing temperature of the small nucleus becomes smaller. Consequently, the growth of the nucleus is slower with a larger value of β, as indicated in Figs. 1 and 2. Moreover, as time proceeds and the nucleus grows, the Gibbs–Thomson effect is reduced due to a larger radius of curvature, and in the mean time,

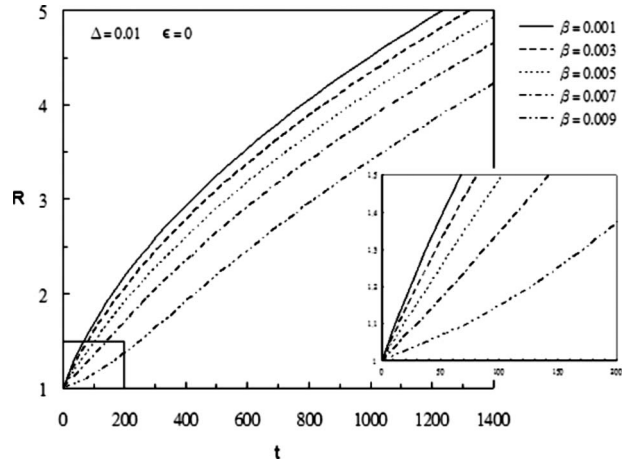

Fig. 1 The Gibbs–Thomson effect on the spherical growth of a small nucleus

the temperature distribution in the melt becomes milder due to the release of energy, resulting in a smaller growth rate of the nucleus in general.

Interestingly, the $V-R$ diagram (Fig. 2), shows a peak value of V for larger β when Δ is fixed, and correspondingly, the $R-t$ diagram (Fig. 1), shows an inflection point at the early stage of growth. This phenomenon is due to the existence of two opposing factors during the spherical growth when the Gibbs–Thomson effect is considered, i.e., as the melt solidifies, the latent heat released on one hand, generally heats up the surrounding melt to make the temperature gradient near the nucleus milder and thus reduces the growth rate. On the other hand, when the nucleus grows, the Gibbs–Thomson effect is reduced due to the increase in the radius, which then makes the cooling effect of the subcooled melt relatively stronger. As a result, the growth rate increases. For our calculations with $\Delta=0.01$ and $\varepsilon=0$, this effect prevails only in the early stage of growth and with a stronger Gibbs–Thomson effect, i.e., when $\beta \geq 0.005$. Moreover, such an effect sustains longer when the Gibbs–Thomson effect is stronger. Therefore, the peak value in the $V-R$ diagram appears at larger R when β increases from 0.005 to 0.009. Instead of $V-R$ diagram, the variation of V versus $R(\Delta/\beta)$, a modified radius of the nucleus by the combined effect of subcooling and the Gibbs–Thomson condition, shows the peak values of V for different β appearing at $R(\Delta/\beta) \approx 2$.

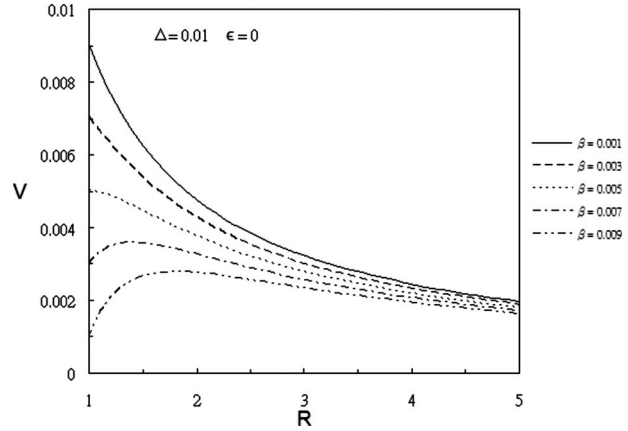

Fig. 2 The Gibbs–Thomson effect on the growth rate of a spherical nucleus

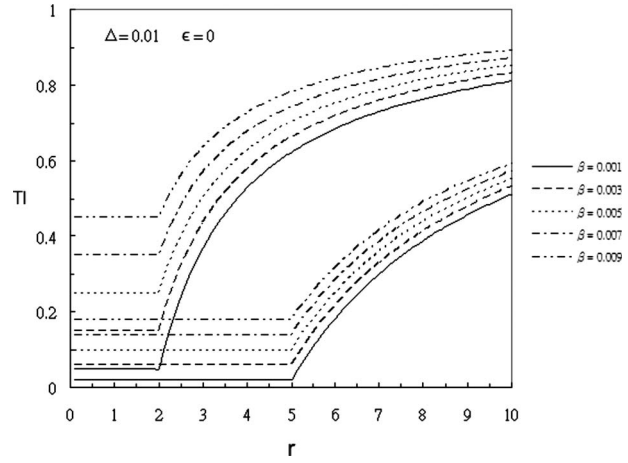

Fig. 3 The Gibbs–Thomson effect on the temperature distribution of the melt at two different stages during growth

The effect on the spherical growth of a small nucleus due to the density-difference induced convection is negligibly small in general with $\Delta \leq 0.01$; however, such an effect is clearly demonstrated by the growth condition with $\Delta=0.1$. When the density of the solid phase is greater than the liquid phase, i.e., $\varepsilon>0$, the solidification will induce a convective flow toward the interface. As a result, the spherical growth rate becomes larger. On the other hand, when $\varepsilon<0$, the solidification process will be induced by a convective flow away from the interface, and thus reduces the growth rate.

4 Conclusions

The spherical growth of a small nucleus under a subcooled condition is theoretically studied herein. The effects on the growth rate and the temperature distribution of the melt due, respectively, to the subcooling, the Gibbs–Thomson relation, and the density-difference induced convection are systematically investigated and discussed. Since no exact solutions can be found easily with the Gibbs–Thomson effect considered, an approximate binomial solution for the temperature distribution of the melt is therefore pursued with the satisfaction of energy balance at the solidification front and other boundary conditions. Such a binomial solution provides reasonably accurate predictions of the solidification front and growth rate. It is concluded that with a stronger subcooled condition or a weaker Gibbs–Thomson effect, the spherical nucleus will grow faster. With a fixed subcooled condition, the growth rate may increase in the early stage and then decreases monotonically as time proceeds, resulting in a peak value of V, if the Gibbs–Thomson effect is strong enough. When the density of the solid phase is greater than the liquid phase, the solidification will induce a convective flow toward the interface, resulting in a larger growth rate. When the density of the solid phase is smaller than the liquid phase, the solidification process will be induced by a convective flow away from the interface, and thus reduces the growth rate.

Nomenclature

a = initial radius
c_l = specific heat of the liquid phase
c_s = specific heat of the solid phase
L = latent heat per unit volume of the solid phase
R^* = radius of the spherical interface
R_0^* = critical radius
r^* = coordinate in radial direction
T_l^* = temperature of the liquid phase
T_s^* = temperature of the solid phase
T_f^* = freezing/melting temperature

$\tilde{T}_f^*$ = equilibrium temperature at the interface
T_∞^* = surrounding temperature
t^* = time
V = growth rate of the solidification front

Greek Symbols

α_l = thermal diffusivity of the liquid phase
β = dimensionless parameter indicating the Gibbs–Thomson effect
Δ = Stefan number
ε = $(\rho_s - \rho_l)/\rho_l$
γ = surface tension between the solid and liquid phases
ρ_l = density of the liquid phase
ρ_s = density of the solid phase

Superscripts

$\tilde{}$ = equilibrium condition
$*$ = dimensional variable

Subscripts

l = liquid phase
f = freezing/melting condition
s = solid phase

References

[1] Carslaw, H. S., and Jaeger, J. C., 1959, *Conduction of Heat in Solids*, 2nd ed., Clarendon, Oxford.
[2] Hill, J. M., 1987, *One-Dimensional Stefan Problem: An Introduction*, Longmans, Green, New York.
[3] Mutaftschiev, B., 1993, "Nucleation Theory," *Handbook of Crystal Growth*, Vol. 1, D. T. J., Hurle, ed., North-Holland, Amsterdam, pp. 187–247.
[4] Stewartson, K., and Waechter, R. T., 1976, "On Stefan's Problem for Spheres," Proc. R. Soc. London, Ser. A, **348**, pp. 415–426.
[5] Davis, G. B., and Hill, J. M., 1982, "A Moving-Boundary Problem for the Sphere," IMA J. Appl. Math., **29**, pp. 99–111.
[6] Mullins, W. W., and Sekerka, R. F., 1963, "Morphological Stability of a Particle Growing by Diffusion or Heat Flow," J. Appl. Phys., **34**, pp. 323–329.
[7] Langer, J. S., and Muller-Krumbhaar, H., 1978, "Theory of Dendritic Growth—I. Elements of a Stability Analysis," Acta Metall., **26**, pp. 1681–1687.
[8] Glicksman, M. E., and Marsh, S. P., 1993, "The Dentrite," *Handbook of Crystal Growth*, Vol. 1, D. T. J., Hurle, ed., North-Holland, Amsterdam, pp. 1075–1122.

Thermal Homogenization in Spherical Reservoir by Electrohydrodynamic Conduction Phenomenon

Miad Yazdani
e-mail: myazdan1@iit.edu

Jamal Seyed-Yagoobi
e-mail: yagoobi@iit.edu

Department of Mechanical, Materials and Aerospace Engineering,
Two-Phase Flow and Heat Transfer Enhancement Laboratory,
Illinois Institute of Technology,
Chicago, IL 60616

Effect of electric conduction phenomenon on the mixing mechanism is studied numerically to thermally homogenize a dielectric liquid with an initial nonuniform temperature distribution. The fluid is stored in a spherical reservoir, and the electrodes are embedded on the reservoir surface such that the resultant local electric body forces mix the fluid. The electric field and electric body force distributions along with the resultant velocity field at the final steady-state condition are presented. The mixing mechanism is illustrated by the time evolution of temperature distribution inside the reservoir. The effects of primary dimensionless numbers on the mixing time are studied.
[DOI: 10.1115/1.3139111]

Keywords: EHD conduction mixing, heterocharge layer, charge dissociation

1 Introduction

Nonmechanical fluid circulation/mixing inside an enclosure is of significant importance in various applications. Wang et al. (Ref. [1] and references therein) used ac electro-osmosis and nonlinear electrokinetics to induce mixing in microscale reservoirs. Electrohydrodynamic (EHD) ion injection has been used to thermally mix buoyancy driven flows [2]. EHD conduction phenomenon can also be utilized to mix one or multiple fluids. The EHD conduction pumping deals with nonequilibrium behavior of dissociation-recombination of charges at the vicinity of electrodes [3]. The main advantage of EHD conduction to the traditional ion drag pumping is its operation without direct injection of ions, which, in turn, does not degrade the fluid properties. Yazdani and Seyed-Yagoobi [4] extended investigated an isothermal liquid circulation within a spherical reservoir induced by EHD conduction phenomenon and studied two types of electrode designs under a wide range of operating conditions.

As an extension of Yazdani and Seyed-Yagoobi's [4] work, this paper investigates the thermal homogenization of a dielectric liquid within a spherical reservoir due to the EHD conduction mechanism. The electric field, electric body force, flow structures, and time evolution of temperature field within the enclosure along with the effects of primary dimensionless numbers on the mixing time are presented and analyzed.

Contributed by the Heat Transfer Division of ASME for publication in the JOURNAL OF HEAT TRANSFER. Manuscript received August 22, 2008; final manuscript received April 14, 2009; published online June 24, 2009. Review conducted by Ofodike A. Ezekoye. Paper presented at the ASME 2008 Summer Heat Transfer Conference (HT2008), Jacksonville, FL, August 10–14, 2008.

2 Theoretical Model

The solution domain for the problem in hand is presented in Fig. 1. The reservoir dimensions along with the details of the electrode design are provided in Table 1. It is assumed that the problem is unsteady-state and laminar. In addition, the upper and lower parts of the reservoir are filled with fluid with identical liquid, with constant and identical mobility and diffusion constants for positive and negative ions, but separated due to a temperature jump across the middle plane. The density of the liquid varies with temperature according to the Boussinesq approximation. The reservoir wall is assumed to be an isolator solid with no volumetric electric charge.

2.1 Governing Equations. The liquid inside the spherical reservoir obeys the continuity equation, which in dimensionless form is

$$\nabla^* \cdot \mathbf{u}^* = 0 \tag{1}$$

The momentum and energy equations account for the presence of electric body force and Joule heating, respectively. The time-dependent dimensionless form of the momentum and energy equations is as follows:

$$\frac{\partial}{\partial t^*}\begin{pmatrix}\mathbf{u}^*\\ T^*\end{pmatrix} + (\mathbf{u}^* \cdot \nabla^*)\begin{pmatrix}\mathbf{u}^*\\ T^*\end{pmatrix} = -\left(\frac{1}{\mathrm{Re}_{\mathrm{EHD}}{}^2}\right)\begin{pmatrix}\nabla^* P^*\\ 0\end{pmatrix} + \frac{1}{\mathrm{Re}_{\mathrm{EHD}}}\nabla^{*2}\begin{pmatrix}\mathbf{u}^*\\ \frac{1}{\mathrm{Pr}}T^*\end{pmatrix} + M_o{}^2 C_0(p^* - n^*) \times\begin{pmatrix}\mathbf{E}^*\\ 0\end{pmatrix} + \begin{pmatrix}\hat{\mathbf{g}}Gr(T^* - T^*_{\mathrm{sat}})\\ J^*_e\end{pmatrix} \tag{2}$$

The Boussinesq approximation is applied to bring the effects of natural convection into consideration. The last term on the right hand side is the Joule heating and defined as $J^*_e = \sigma|\mathbf{E}|^2(d/c_p u_e T_{\mathrm{sat}})$

The electric body force and the Joule heating are the results of applied electric field. These terms require the solution of the following Maxwell's relations:

$$\nabla^* \cdot \mathbf{E}^* = C_0(p^* - n^*), \quad \mathbf{E}^* = -\nabla^* \phi^* \tag{3}$$

and charge conservation equations based on dissociation and recombination of neutral impurities (i.e., electrolytes) inside the reservoir

$$\frac{\partial}{\partial t^*}\begin{pmatrix}p^*\\ n^*\end{pmatrix} + \nabla^* \cdot \left[\begin{pmatrix}p^*\\ -n^*\end{pmatrix}\mathbf{E}^* + \begin{pmatrix}p^*\\ n^*\end{pmatrix}\mathbf{u}^* - \alpha\nabla^* + \begin{pmatrix}p^*\\ n^*\end{pmatrix}\right] = 2C_0(F(\omega) - p^* n^*) \tag{4}$$

with d, $u_e = bV/d$, $\mu^2/\rho d^2$, T_{sat}, V/d, and n_{eq}, respectively, selected as scaling parameters for length, velocity, pressure, temperature, electric field, and free charges. Here, $\mathrm{Re}_{\mathrm{EHD}} = bV/\nu$, $\mathrm{Pe}_{\mathrm{EHD}} = \mathrm{Re}_{\mathrm{EHD}}\ \mathrm{Pr}$, $M_o = \sqrt{\epsilon/\rho b^2}$, $\mathrm{Gr} = |g|\beta d T_{\mathrm{sat}}/u_e{}^2$, $C_0 = \sigma d^2/2b\epsilon V$, and $\alpha = D/bV$. Note that the charge concentration at equilibrium, n_{eq}, is defined as $n_{\mathrm{eq}} = \sigma/2b$. The liquid inside the reservoir is in contact with the reservoir wall, which is assumed to be a solid insulator. Therefore, with no volumetric electric charges within the solid zone, the Laplace equation governs the potential field

$$\nabla^{*2}\phi^*_s = 0 \tag{5}$$

The boundary conditions for the liquid and solid regions are presented in Table 2. Note that the continuity of potential field is applied across the solid/liquid interface, where the liquid is in contact with the wall, while the reservoir outer surface is grounded. No boundary condition is required for velocity, temperature, and electric charges inside the solid wall, since the corresponding equations are not solved there. The initial conditions,

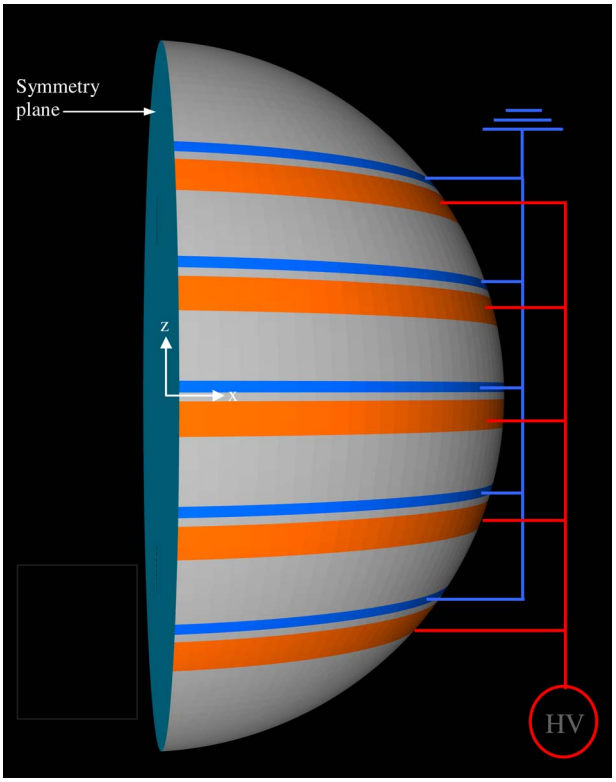

Fig. 1 Schematic of three-dimensional spherical reservoir (not to scale)

at $t^*=0$ is to set $p^*-n^*=0$, $\phi^*=0$, and $\mathbf{u}^*=0$.

The temperature jump across the virtual separator central plane is specified by identifying the temperature of the liquid for the top and bottom hemispheres as T_1^* and T_2^*, respectively. Note that when $T_1^*>T_2^*$, the mixing is initially accomplished solely by EHD conduction mechanism regardless of whether the gravity body force is present. On the other hand, in the case of $T_1^*<T_2^*$, the EHD conduction and gravity body forces jointly mix the colder liquid at the top with the warmer liquid at the bottom.

3 Results and Discussions

The code solves the transport equations using finite volume discretization scheme. The governing equations are discretized in Cartesian coordinates. The discretization equations are solved iteratively by the line-by-line application of the tridiagonal matrix algorithm. Central difference scheme is applied to Gauss' law, and the upwind scheme based on the electric field direction is applied to the charge conservation equations. First order implicit formulation is incorporated to track the time evolution of all parameters. The governing equations are discretized over 3.4×10^6 hexagonal elements. The convergence criteria, $|\psi_{i+1}-\psi_i/\psi_i|<10^{-5}$, is applied for all involved parameters. The solution results are grid independent. In addition, an adaptive function is defined to dynamically refine the grid as the solution proceeds.

Table 2 Summary of electrostatic and flow boundary conditions

HV electrode	Ground electrode	Liquid/solid interface	Reservoir outer wall
$u_x^*=u_y^*=u_z^*=0$	$u_x^*=u_y^*=u_z^*=0$	$u_x^*=u_y^*=u_z^*=0$	-
$\phi^*=1$	$\phi^*=0$	$\phi^*=\phi_s^*$	$\phi^*=0$
$p^*=0$, $\mathbf{n}\cdot\nabla n^*=0$	$n^*=0$, $\mathbf{n}\cdot\nabla p^*=0$	$\mathbf{n}\cdot\nabla n^*=\mathbf{n}\cdot\nabla p^*=0$	-
$\mathbf{n}\cdot\nabla T^*=0$	$\mathbf{n}\cdot\nabla T^*=0$	$\mathbf{n}\cdot\nabla T^*=0$	-

The results presented in this section illustrate the mixing mechanism due to the effect of EHD conduction phenomenon. The effects of primary dimensionless numbers on the mixing time are presented as well. The reference values selected to calculate the dimensionless parameters correspond to the properties of refrigerant R-123 as the working fluid. The values of the dimensionless numbers for the basic case are presented in Table 3. These values correspond to the case where the reservoir is in the absence of gravity and applied voltage of 10 kV.

The interelectrode region is characterized by a high intensity electric field, which is because of the closeness of the two electrodes surfaces. On the other hand, the majority of the interior of the spherical reservoir is characterized by zero values of electric field in both directions, indicating that the electric conduction is confined solely to the region near the reservoir wall. In addition, the heterocharge layers are thicker, close to the wider (HV) electrodes than close to the narrower (ground) electrodes due to the high intensity electric field.

The resultant steady-state electric body force contours are illustrated in Fig. 2. The major part of the body force is within the interelectrode region facing toward the electrodes, which is because of the high intensity electric field and net charge density in this region. The asymmetry of the electrodes, however, results in the dominance of electric body force directed toward the wider (HV) electrode yielding in downward flow in this region. The opposing electric body force, however, results in fluid circulation, which is restricted to the wall region due to the acting body force toward the electrodes surfaces. The contours of velocity magnitude embedded by the velocity streamtraces are displayed in Fig. 3. As stated previously, the downward flow near the reservoir wall is clearly illustrated in this figure. Of course, this flow is associated with the upward motion within the interior of the reservoir, as required by fluid continuity.

Time evolution of temperature distribution for the base case at two intermediate time steps is presented in Fig. 4. The contour lines represent the modified dimensionless temperature at the x^*z^*-plane on $y^*=0$. The modified dimensionless temperature is defined as

$$\theta^* = \frac{T^* - T_1^*}{T_2^* - T_1^*} \tag{6}$$

Note that at $t^*=0$, θ^* at the upper and lower hemispheres are 0 and 1, respectively. At the steady-state, θ^* reaches 0.5 everywhere in the reservoir. As observed in Fig. 4, mixing is utilized as the cold fluid moves toward the warm fluid close to the wall and vice versa in the interior region with a small contribution of thermal diffusion.

Table 1 Dimensions of reservoir and electrodes

Reservoir radius (mm)	Wall thickness	Ground electrode width (mm)	HV electrode width (mm)	Electrode gap (mm)	Electrode pair spacing (mm)
$R_0=150$	$Y_w=7.5$ ($Y_w^*=0.05$)	$\xi_g=4$ ($\xi_g^*=0.027$)	$\xi_{HV}=12$ ($\xi_{HV}^*=0.08$)	$\eta=3$ ($\eta^*=0.02$)	$\zeta=24$ ($\zeta^*=0.16$)

Table 3 Numerical values of dimensionless numbers for the base case

Dimensional number	Numerical value
Re_{EHD}	1385
Pe_{EHD}	8305
C_0	128
M_o	4.39
Gr	0

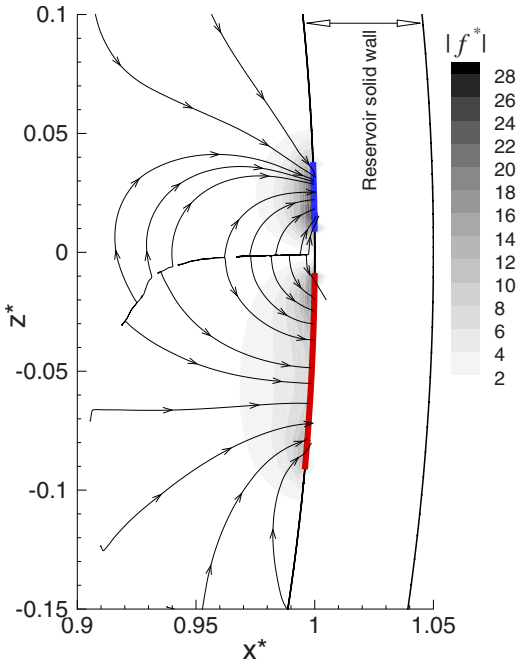

Fig. 2 Steady-state dimensionless contours of electric body force magnitude and streamtraces of electric body force at the x^*z^*-plane at $y^*=0$

To understand how the mixing mechanism is affected by the controlling parameters, one needs to explore the effects of primary dimensionless parameters on the time required to completely mix the two liquids. The complete mixing state is assumed to be

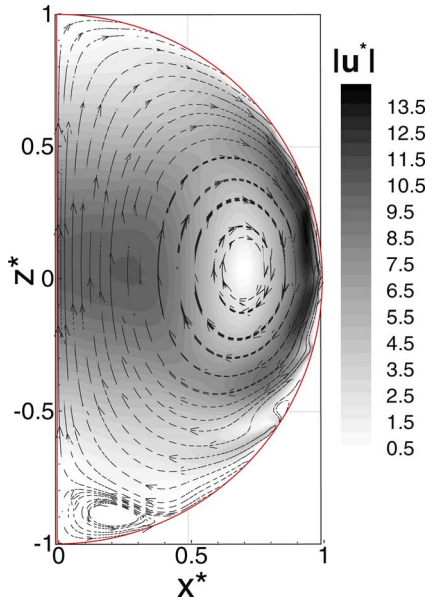

Fig. 3 Steady-state contours of velocity magnitude and velocity streamtraces at $y^*=0$ and $z^*=0$

achieved when the temperature reaches 99% of the initial average temperature throughout the reservoir. While the conduction-convection ratio, C_0, and electric Reynolds number, Re_{EHD}, are related by the value of applied voltage, any change in geometric length scale, d, is solely associated with the changes of C_0 and the modified Grashof number, Gr. The variation in dimensionless mixing time with the primary dimensionless numbers for two initial temperature jumps is presented in Figs. 5 and 6. As observed in Fig. 5, the mixing occurs more rapidly as the Pe_{EHD} increases (or C_0 decreases) due to the increase in applied potential. Furthermore, higher applied voltage is also associated with the suppression of viscous and thermal diffusions, as governed by Eq. (2). Figure 6 primarily represents the effect of modified Grashof number on the dimensionless mixing time by simply varying the reservoir diameter. For a nonzero Grashof number, the reservoir is under terrestrial gravity. For the case $\Delta T_0^*<0$, the mixing induced by the EHD mechanism is initially assisted by the natural circulation, since the two forces are opposed to each other; EHD con-

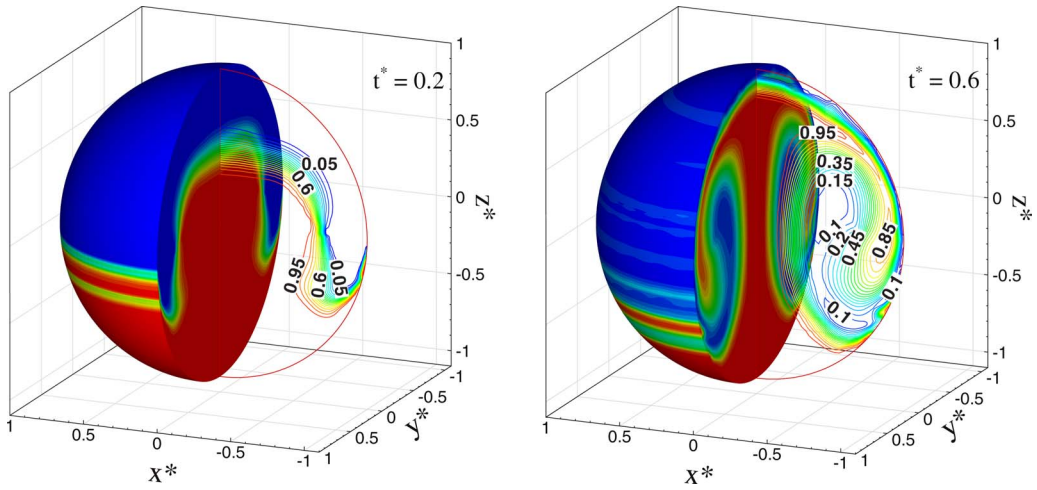

Fig. 4 Dimensionless time evolution of dimensionless temperature distribution and contours of isotherms at two intermediate time steps in the absence of gravity body force, Gr=0. Contour labels represent the value of modified dimensionless temperature, θ^*, defined in Eq. (6).

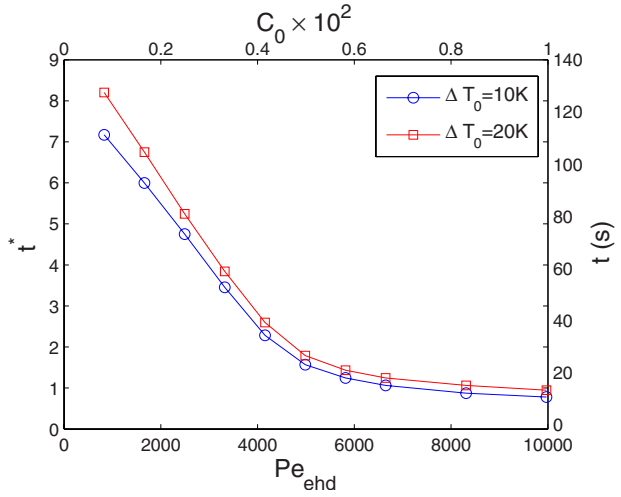

Fig. 5 Variation in mixing time with C_0 and Peclet number with other dimensionless numbers fixed: $M_o=4.39$, Gr=0

duction drives the liquid downward, with the natural circulation moving the liquid upward yielding in an enhanced mixing. This is why the mixing occurs at a faster pace with $\Delta T_0^*<0$ compared with $\Delta T_0^*>0$ beyond a certain threshold. However, up to this point, the mixing time for $\Delta T_0^*<0$ is slightly larger due to the adverse impact of upward naturally convected flow on the downward EHD flow near the wall, which is more pronounced at smaller Gr values. For $\Delta T_0^*>0$, on the other hand, the EHD mixing neither assisted nor resisted by the natural circulation at initial stages of mixing. Therefore, as the EHD induced flow, which is the dominant mechanism at smaller Gr (i.e., reservoir diameter), is suppressed with the reservoir diameter, the mixing time ultimately increases for greater values of Grashof number.

4 Conclusions

The effect of EHD conduction mechanism to thermally homogenize a fluid with temperature jump within a spherical reservoir was numerically studied. The results confirmed that EHD conduction mechanism can be utilized to effectively circulate and mix a thermally nonhomogenous liquid inside a reservoir. The proposed electrode design was especially effective for reservoirs with small diameters given the fact that the resultant electric body forces are confined to the reservoir wall region. For larger diameter reservoirs, electrodes penetrated into the liquid will be more effective

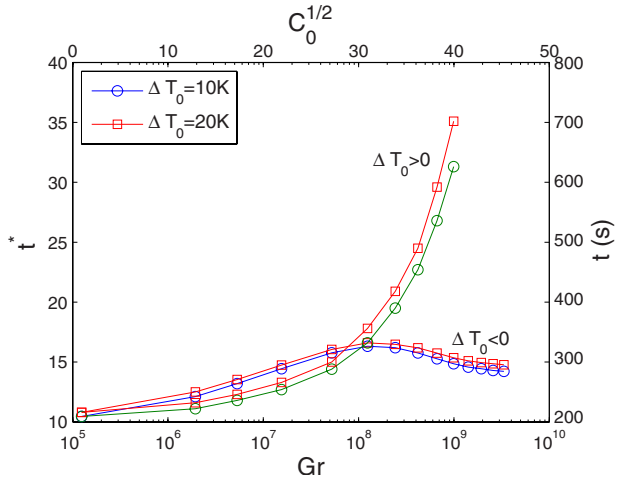

Fig. 6 Variation in mixing time with Gr and C_0 with other dimensionless numbers kept constant

[5]. Although not presented in the paper, the liquid temperature increase due to the Joule heating was practically negligible. The nonmechanical mixing of a liquid inside a reservoir should be very attractive to outer space, microgravity, and certain terrestrial applications.

Acknowledgment

This work was financially supported by the NASA Microgravity Fluid Physics Program.

Nomenclature

b = charge mobility coefficient
D = charge diffusion constant
c_p = constant pressure specific heat
d = spherical reservoir diameter
e = electron charge
$\mathbf{E}$ = electric field vector
$F(\omega)$ = $I_1(2\omega)/\omega$
$\hat{\mathbf{g}}$ = gravity unit vector, $\hat{\mathbf{g}}=\mathbf{g}/|g|$
k = thermal conductivity
k_B = Boltzmann universal constant
n = negative charge density
p = positive charge density
P = pressure
T = absolute temperature
t = time
$\mathbf{u}$ = velocity vector
u_e = EHD reference velocity, $u_e=bV/d$
V = applied electric potential
$\mathbf{x}$ = Cartesian coordinate unit vector
Y_w = reservoir wall thickness
β = thermal expansion
ϵ = absolute electric permittivity
ζ = electrode pairs distance
η = electrode gap
γ = thermal diffusivity
μ = dynamic viscosity of fluid
ν = kinematic viscosity of fluid
ξ = electrode width
ω = dissociation rate coefficient, $\omega=[e^3|E|/4\pi\epsilon k_B{}^2T_{\text{sat}}]^{1/2}$
ρ = mass density
σ = electric conductivity of fluid
θ = normalized temperature
ϕ = electric potential

Subscripts

eq = equilibrium
g = ground electrode
HV = high voltage electrode

Superscript

$*$ = nondimensionalized variable

References

[1] Wang, S.-C., Chen, H.-P., Lee, C.-Y., Yu, C.-C., and Chang, H.-C., 2006, "AC Electro-Osmotic Mixing Induced by Non-Contact External Electrodes," Biosens. Bioelectron., **22**(4), pp. 563–567.
[2] Yan, Y., Zhang, H., and Hull, J., 2004, "Numerical Modeling of Electrohydrodynamic (EHD) Effect on Natural Convection in an Enclosure," Numer. Heat Transfer, Part A, **46**, pp. 453–471.
[3] Atten, P., and Seyed-Yagoobi, J., 2003, "Electrohydrodynamically Induced Dielectric Liquid Flow Through Pure Conduction in Point/Plane Geometry," IEEE Trans. Dielectr. Electr. Insul., **10**, pp. 27–36.
[4] Yazdani, M., and Seyed-Yagoobi, J., "Fluid Circulation Within a Spherical Reservoir With EHD Conduction Pumping," IEEE Trans. Ind. Appl. 45 (in press).
[5] Yazdani, M., 2009, "Electrically Driven Liquid and Liquid Film Flows in Macro- and Micro-Scales in the Presence and Absence of Phase Change," Ph.D. thesis, Mechanical, Materials and Aerospace Engineering Department, Illinois Institute of Technology, Chicago, IL.

Probabilistic Approach to Particle-Wall Contact Time in Fluidized Beds

Reza Zarghami

Navid Mostoufi
e-mail: mostoufi@ut.ac.ir

Rahmat Sotudeh-Gharebagh

Process Design and Simulation Research Centre,
Oil and Gas Centre of Excellence,
School of Chemical Engineering,
University of Tehran,
P.O. Box 11155/4563,
Tehran, Iran

The heat transfer between submerged surface and particles in fluidized bed is affected by particle migration to and from the exchanger surface. A new probabilistic model was developed for particle migration and particle-wall contact time distribution based on a classical gamma function. The existing models suggest a decrease in contact time by increasing the gas velocity. However, it has been experimentally shown that the contact time increases in turbulent regime by increasing the gas velocity. A theoretical probabilistic model was developed to represent such a trend. The model is in good agreement with the experimental data. [DOI: 10.1115/1.3139112]

Keywords: contact time, fluidization, heat transfer, particle contact time distribution, convective heat transfer

1 Introduction

The convective heat transfer between a gas fluidized bed and a heat exchanging surface can be described by two major components: particle convection and gas convection. The particle convective heat transfer coefficient, h_{PC}, corresponds to the heat transfer due to the motion of solids carrying heat to and from the surface, and the gas convective heat transfer coefficient, h_{GC}, describes the transfer of heat by the motion of gas between the particles. The significance of particle and gas convection depends mostly on the type of particles.

The process of particle to wall heat transfer is concerned with the heat transfer from a surface when it is in contact with the particulate emulsion phase, instead of the void/bubble phase. Mickley and Fairbanks [1] mentioned that in the bubbling regime of fluidization, particle convective heat transfer can become significant due to the large heat capacity of the solids. They established that the convective motion of packets of particles is responsible for heat transfer from the wall to the bed in the bubbling fluidized bed. They introduced the packet renewal theory, which needs determination of residence time of the packet at the heat exchanging surface. Based on this theory, they developed an expression for the particle convective local transient heat transfer coefficient at the wall as follows:

$$h_{pc} = \sqrt{\frac{(k\rho c)_{\text{packet}}}{\pi\tau}} \tag{1}$$

Although the gas convection component is easy to predict, the contribution of particle convection remains inadequately described and strongly depends on the hydrodynamics of the bed. Therefore, comprehensive understanding of the bed hydrodynamics becomes crucial in determining the heat transfer rates within the fluidized beds.

While many studies have been conducted on heat transfer in bubbling fluidized bed, only a few studies have been conducted for turbulent fluidization due to the complexity of the phenomena within this regime. Any mathematical analysis to study the physical phenomena can be done separately in two general approaches, deterministic analysis [2] and probabilistic assessment. In this work, a probabilistic study of the particle-wall contact time distribution was carried out, and a new model is developed for departure rate of particle (as defined by Molerus et al. [3]) from the surface element to the bulk of fluidized bed. This model is applicable to both bubbling and turbulent fluidized beds.

2 Theory

The heat transfer between submerged surface or wall of fluidized bed and particles is influenced by particle migration to and from the surface. In order to develop a probabilistic methodology for the particle migration, a small part of the wall is considered as the surface element whose conditions are assumed to be the same as the rest of the wall surface. It is also assumed that the particles have a random behavior at any state of the fluidized bed.

If the random variable x represents the residence time of a particle on the surface element or time to detach from the surface element of a particle, the availability of the particle near the surface at any time t would be defined as

$$P[x > t] = 1 - F(t) \tag{2}$$

in which $P[x>t]$ is the probability assigned to each random variable x, which has the residence time greater than t, and $F(t)$ is the cumulative distribution function (CDF) of the random variable x.

In order to develop a probabilistic model for particle-wall contact time distribution, consider a surface element, as shown in Fig. 1. It is obvious that particles choose different routes through the bed, and thus spend different lengths of time to move near the wall. At first, imagine a surface element with marked particles adjacent to it (white particles in Fig. 1, $t<0$). At time $t=0$, particles approach from the bulk of the bed to the surface element (black particles), and the number of white particles among the departing particles from the surface element starts to increase. At any time $t>0$, black particles, and only black particles, among the departing particles from the surface element are younger than t, and the white particles still on the surface are older than t. Therefore, the probability of the existence of particles younger than t (black particles) among departing particles is $P[x \leq t]$ or $F(t)$, and the probability of the particles, which remain at the surface and are older than t (white particles), is $P[x>t]$. Therefore, a fraction of black particles in the particles departing from the surface element is equal to the fraction of particles departing from the surface element and is younger than t. The first term is simply F, while the second is $1-F$.

The rate of departure of particles from the surface element to the bulk of the fluidized bed can be defined by a departure-rate function (DRF), $\lambda(t)$. Molerus et al. [3] first deduced statistical particle migration rate toward the bulk of fluidized bed perpendicular to a solid surface. They showed that $\lambda(t)$ is reciprocal of the mean residence time of particles close to the wall, based on their image analysis experimental work. In the present work, a new expression is developed for $\lambda(t)$ and its performance is investigated using the experimental data from the literature for sand particles in the dense region of the bed.

Contributed by the Heat Transfer Division of ASME for publication in the JOURNAL OF HEAT TRANSFER. Manuscript received August 31, 2008; final manuscript received March 21, 2009; published online June 24, 2009. Review conducted by Louis C. Chow.

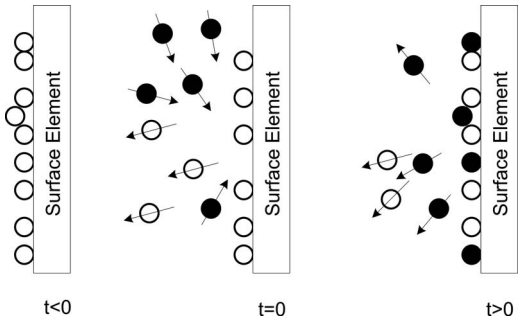

Fig. 1 Status of marked (black, white) particles near surface element

The DRF, $\lambda(t)$, may be interpreted as the instantaneous detach rate (migration rate) or the conditional density of departure from the wall at time t, given that the particle has been near the surface until time t

$$f(t|x \geq t) = \frac{d}{dt}F(t|x \geq t) \tag{3}$$

where $f(t)$ is the probability density function (pdf) of the random variable x. In addition, frequency of occurrences over short intervals of length Δt, say $[t, t+\Delta t]$, is at least approximately proportional to the length of the interval, Δt, where the proportionality factor could depend on t and is equal to $f(t)$, the pdf of x

$$P[t \leq x \leq t + \Delta t] = F(t + \Delta t) - F(t) = f(t)\Delta t \tag{4}$$

where the error in the approximation is negligible relative to the length of the interval, Δt, the exact probability in equation is represented by the area of the shaded region under the graph of $f(t)$ versus t, while the approximation is the area of the corresponding rectangle with height $f(t)$ and width Δt. The smaller the value of Δt, the closer this approximation becomes.

According to the rules of conditional probability calculus and considering Eqs. (2) and (4), Eq. (3) can be rewritten as

$$f(t|x \geq t) = \lim_{\Delta t \to 0} \frac{P[t \leq x \leq t + \Delta t | x \geq t]}{\Delta t} \tag{5}$$

since the two events, $t \leq x \leq t+\Delta t$ and $x \geq t$, are dependent, the probability of both occurring (right hand side) is

$$f(t|x \geq t) = \lim_{\Delta t \to 0} \frac{P[t \leq x \leq t + \Delta t]}{\Delta t(1 - F(t))} \tag{6}$$

or

$$f(t|x \geq t) = \lim_{\Delta t \to 0} \frac{f(t)\Delta t}{\Delta t(1 - F(t))} = \frac{f(t)}{1 - F(t)} = \lambda(t) \tag{7}$$

Under steady state conditions, increasing DRF would indicate that the particles are more likely to detach in the next increment of time $(t, t+\Delta t)$ than it would be in an earlier interval of the same length. That is, the particle residence time on the surface element is decreased with time. Similarly, a decrease in DRF suggests an increase in the residence time of particles with time. It will be shown in Sec. 3 that a constant DRF occurs for an exponential probability distribution of contact time.

Molerus et al. [3] found that the behavior of wall contact time of particle, $f(t)$, could be described by an exponential decay distribution as

$$f(t; \alpha) = \frac{1}{\alpha}\exp\left(-\frac{t}{\alpha}\right) \tag{8}$$

then, according to Eq. (7).

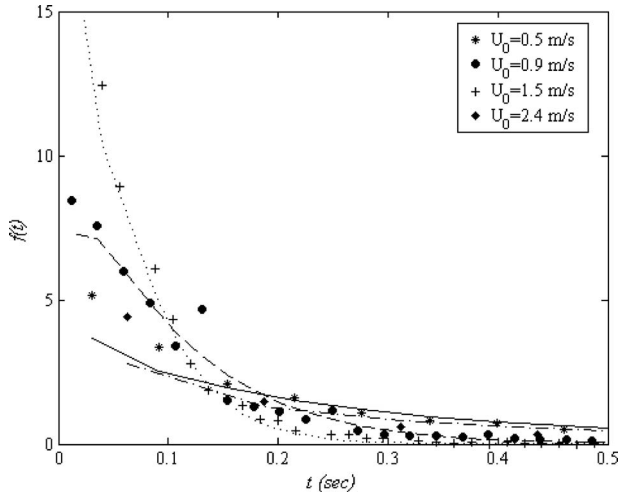

Fig. 2 Residence time distribution function of particle-wall contact time for sand particles at various gas velocities

$$\lambda(t) = \frac{f(t)}{1 - F(t)} = \frac{\frac{1}{\alpha}\exp\left(-\frac{t}{\alpha}\right)}{\exp\left(-\frac{t}{\alpha}\right)} = \frac{1}{\alpha} \tag{9}$$

In such a case, the expected value of x (i.e., mean residence time of the particles at the wall) is α. In other words, the departure rate is reciprocal to the mean residence time and does not depend on the age of the particle. This is in agreement with experimental work of Molerus et al. [3].

Wang and Rhodes [4] studied particle-wall contact by the discrete element method (DEM) simulation and suggested that the particle-wall contact time distribution may be expressed by a Ziegler gamma distribution [5], with a shape parameter equal to one and for some cases may also be approximated by a gamma distribution of a shape parameter equal to zero. Hamidipour et al. [6], however, investigated particle-wall contact distribution experimentally and found that the exponential decay with a value of α best fits the distribution function of contact time. In fact, this function is also a simplified form of the gamma function. Therefore, in order to ease modeling of DRF, the associated pdf was also compared with a proposed gamma distribution, which is different from the Ziegler gamma distribution. This gamma distribution function is expressed as

$$f(t; \theta, \beta) = \frac{1}{\Gamma(\beta)\theta^{\beta}} t^{\beta-1} \exp\left(-\frac{t}{\theta}\right) \tag{10}$$

Parameter β is called the shape parameter because it determines the basic shape of the graph of the pdf, $f(t)$. The value of θ, on the other hand, determines the location of the peak and is called the scale factor. In this case, mean residence time of particles on the surface, τ, is $\beta\theta$. The values of θ and β can be determined by fitting the model to the experimental data.

3 Results and Discussion

In this work, parameters θ and β of $f(t)$ were determined by fitting the proposed gamma distribution to the experimental data of Hamidipour et al. [7] at various superficial velocity in bubbling and turbulent regimes of fluidization for sand particles with an average particle size of 0.385 mm and a particle density of 2650 kg/m^3 (Group B particles). These experimental wall-particle contact time distributions, as well as the corresponding gamma distribution for four examples of gas superficial velocities, are shown in Fig. 2. The onset of turbulent fluidization (U_c) in the

Table 1 Values of θ, β, and τ at various gas velocities

U_0 (m/s)	θ	β	τ (s)
0.5	0.322	0.8402	0.2705
0.9	0.082	1.2407	0.1017
1.5	0.039	1.7073	0.0666
2.4	0.509	0.5316	0.2706

bed of above mentioned particles occurs at a superficial velocity of 1.5 m/s. This figure shows the good agreement between the experimental distributions and the experimental data, which indicates that the contact time distribution could be satisfactorily described by the gamma function (Eq. (10)). It is worth noting that such a trend was observed for all the data reported by Hamidipour et al. [6]. The values of θ and β for different superficial velocity in bubbling and turbulent regimes of fluidization are given in Table 1. It can be seen that mean residence time of particles on the surface, τ, decreases in the bubbling regime of fluidization while it increases in the turbulent regime of fluidization, when the gas velocity is increased. In other words, the mean particle-wall contact time reaches minimum at the onset of turbulent fluidization.

If $f(t)$ is expressed by the above gamma distribution, it is not easy to express its DRF. Nevertheless, the DRF increases for $\beta > 1$ and decreases for $\beta < 1$. For $\beta > 1$, the DRF approaches $1/\theta$ asymptotically from below, while for $\beta < 1$ the DRF approaches $1/\theta$ asymptotically from above. This means that the DRF needs a delay time to reach $1/\theta$, which should be noted during experimental tests. In other words, recording experimental value of the DRF should be started after assurance of the stability of $\lambda(t)$. As it is shown in Fig. 3, this delay time is about 6–10 s at $U_0 = 0.9$ m/s.

Although the pdfs in these cases appear quite similar, they clearly have somewhat different characteristics considering residence time distribution; the DRF is a very meaningful property for distinguishing between these densities. Indeed, specifying a DRF completely determines the $F(t)$ and vice versa.

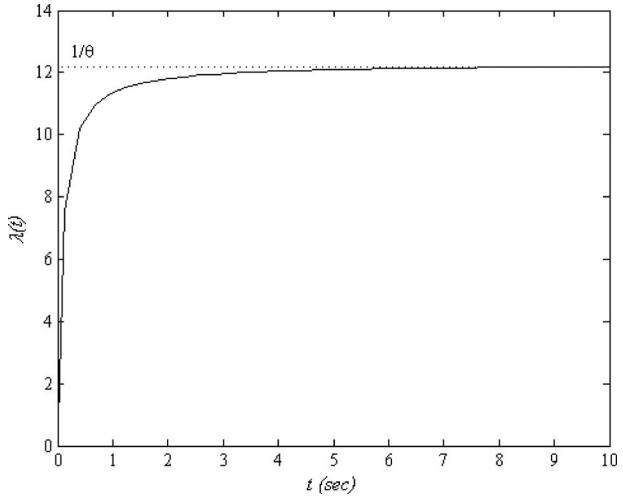

Fig. 3 The departure-rate function, sand particles, $U_0 = 0.9$ m/s, $\theta = 0.082$, and $\beta = 1.2407$

4 Conclusions

Particle-wall contact time distribution is studied and indicated that this distribution is according to a classical gamma function. The parameters of gamma distribution were determined by curve fitting, using the experimental points of Hamidipour et al. [6]. A new model for particle migration rate toward a heat exchanging surface, which is called particle detach-rate function was also developed. According to the results presented in this work, the delay time for recording experimental points is required in each superficial velocity due to stability condition of DRF. In addition, it has been shown in this work that in a bed of sand particles, the contact time decreases by increasing the gas velocity only in the bubbling regime of fluidization and increases in the turbulent regime of fluidization when the gas velocity in the bed is increased.

Nomenclature

- c = heat capacity of the packets of particles, J/kg K
- f = probability density function
- F = cumulative distribution function
- h_{GC} = gas convective heat transfer coefficient, W/m^2 K
- h_{PC} = particle convective heat transfer coefficient, W/m^2 K
- k = thermal conductivity of the packets of particles, J/kg K
- P = probability
- t = time, s
- U_0 = superficial gas velocity, m/s
- U_c = onset of turbulent fluidization, m/s
- x = random variable, represents the lifetime of particle on the surface element, s

Greek Letters

- α = parameter of exponential distribution
- β = shape parameter of gamma distribution
- Γ = gamma function
- θ = scale factor of gamma distribution
- λ = departure rate function, 1/s
- ρ = density of the packets of particles, kg/m^3
- τ = particle contact time at surface, s

References

[1] Mickley, H. S., and Fairbanks, D. F., 1955, "Mechanism of Heat Transfer to Fluidized Beds," AIChE J., **1**, pp. 374–384.

[2] Zarghami, R., Mostoufi, N., Sotudeh-Gharebagh, R., and Chaouki, J., 2007, "Analysis and Modeling of Particle-Wall Contact Time in Gas Fluidized Beds," Chem. Eng. Sci., **62**, pp. 4573–4578.

[3] Molerus, O., Burschka, A., and Dietz, S., 1995, "Particle Migration at Solid Surfaces and Heat Transfer in Bubbling Fluidized Bed—I. Particle Migration Measurement Systems," Chem. Eng. Sci., **50**, pp. 871–877.

[4] Wang, X. S., and Rhodes, M. J., 2003, "Determination of Particle Residence Time at the Walls of Gas Fluidized Beds by Discrete Element Method Simulation," Chem. Eng. Sci., **58**, pp. 387–397.

[5] Ziegler, E. N., Koppel, L. B., and Brazelton, W. T., 1964, "Effect of Solid Thermal Properties on Heat Transfer to Gas Fluidized Beds," Ind. Eng. Chem. Fundam., **3**, pp. 324–328.

[6] Hamidipour, M., Mostoufi, N., Sotudeh-Gharebagh, R., and Chaouki, J., 2005, "Experimental Investigation of Particle Contact Time at the Wall of Gas Fluidized Beds," Chem. Eng. Sci., **60**, pp. 4349–4357.

[7] Hamidipour, M., Mostoufi, N., Sotudeh-Gharebagh, R., and Chaouki, J., 2005, "Monitoring the Particle-Wall Contact in a Gas Fluidized Bed by RPT," Powder Technol., **153**, pp. 119–126.

Numerical Study on Stagnation Point Heat Transfer by Jet Impingement in a Confined Narrow Gap

Y. Q. Zu

Y. Y. Yan[1]
e-mail: yuying.yan@nottingham.ac.uk

School of the Built Environment,
University of Nottingham,
Nottingham NG7 2RD, UK

J. Maltson
Siemens Industrial Turbomachinery Limited,
Lincoln LN5 7FD, UK

In this paper, the heat transfer characteristics of a circular air jet vertically impinging on a flat plate near to the nozzle ($H/d=1-6$, where H is the nozzle-to-target spacing and d is the diameter of the jet) are numerically analyzed. The relative performance of seven turbulent models for predicting this type of flow and heat transfer is investigated by comparing the numerical results with available benchmark experimental data. It is found that the shear-stress transport (SST) $k-\omega$ model and the large Eddy simulation (LES) time-variant model can give better predictions for the performance of fluid flow and heat transfer; especially, the SST $k-\omega$ model should be the best compromise between computational cost and accuracy. In addition, using the SST $k-\omega$ model, the effects of jet Reynolds number (Re), jet plate length-to-jet diameter ratio (L/d), target spacing-to-jet diameter ratio (H/d), and jet plate width-to-jet diameter ratio (W/d) on the local Nusselt number (Nu) of the target plate are examined; a correlation for the stagnation Nu is presented.
[DOI: 10.1115/1.3139183]

Keywords: jet impingement, heat transfer, stagnation point, turbulence models

1 Introduction

Jet impingement is one of the most efficient solutions of cooling hot objects in industrial processes as it produces a very high heat transfer rate of forced-convection. The effects of nozzle geometry, jet-to-surface spacing, jet-to-jet spacing, cross flow, operating conditions, etc., on flow and heat transfer have been studied and reviewed [1–5].

Most applications of impingement flows in narrow gap cavities involve turbulent flow, and modeling turbulent flow presents a great challenge for rapidly and accurately predicting impingement heat transfer even under a single round jet. Although no single model has been universally accepted to be superior to all classes of problems, various turbulent models have been developed to roughly predict impingement flow and heat transfer. However, only a limited number of studies are concerned with the comparisons of the reliability, availability, and capability of different turbulent models for impingement flows. The low Reynolds number $k-\varepsilon$, standard $k-\varepsilon$, and RSM modules have been evaluated, respectively, by researchers in Refs. [3,5,6].

In the current work, a confined circular air jet vertically impinging on a flat plate near to nozzle is performed; through the numerical study, the most suitable model(s) for predicting this type of flow and heat transfer is recommended.

2 Problem Description

2.1 Geometry and Boundary Conditions. Figure 1 shows the physical domain and boundary conditions of the modeling. Air flow at high velocity passes through a round jet with both length and diameter d, vertically impinging on the confined target plate with two side walls positioned at spanwise distances of $y=\pm W/2$. The jet after impingement was restricted to discharge in two opposite directions parallel to the x-axis, and two channel outlets are placed at $x=\pm L/2$. The target plate was kept at constant heat flux of 1000 $\mathrm{W/m^2}$; all other walls are adiabatic.

2.2 Turbulent Models. The standard $k-\varepsilon$ model, the renormalization group (RNG) $k-\varepsilon$ model, the realizable $k-\varepsilon$ model, the standard $k-\omega$ model, the SST $k-\omega$ model, the RSM, and the LES time-variant model are applied.

The $k-\varepsilon$, $k-\omega$, and RSM turbulence models belong to the Reynolds-averaged approach. The Reynolds-averaged Navier–Stokes (RANS) equations are written as

$$\frac{\partial \rho}{\partial t} + \nabla \cdot (\rho \mathbf{u}) = 0 \tag{1}$$

$$\frac{\partial}{\partial t}(\rho \mathbf{u}) + \nabla \cdot (\rho \mathbf{u}\mathbf{u}) = -\nabla p + \nabla \cdot [\mu(\nabla \mathbf{u} + (\nabla \mathbf{u})^T)] + \rho \mathbf{g} + \nabla \cdot (-\rho \overline{\mathbf{u}'\mathbf{u}'}) \tag{2}$$

The $k-\varepsilon$ models and $k-\omega$ models employ the Boussinesq hypothesis to relate the Reynolds stresses to the mean flow velocity gradients as follows:

$$-\rho \overline{\mathbf{u}'\mathbf{u}'} = \mu_t [\nabla \mathbf{u} + (\nabla \mathbf{u})^T] - \tfrac{2}{3}(\rho k + \mu_t \nabla \cdot \mathbf{u})\mathbf{I} \tag{3}$$

The standard, RNG, and realizable $k-\varepsilon$ models have similar forms with transport equations for k and ε. The main difference is how to compute the turbulent viscosity μ_t. In the standard $k-\varepsilon$ model [7], μ_t is computed as follows:

$$\mu_t = \rho C_\mu \frac{k^2}{\varepsilon} \tag{4}$$

where C_μ is a constant. In the RNG $k-\varepsilon$ model [8], the scale elimination results in a differential equation for turbulent viscosity in high Re limit and also enables original differential relation for low Re effects. While in the realizable $k-\varepsilon$ model [9], C_μ is a function of mean strain and rotation rates, angular velocity of system rotation, and turbulence fields. In the standard $k-\omega$ model [10], the transport equations for k and ω are solved, and μ_t is computed as follows:

$$\mu_t = \alpha^* \frac{\rho k}{\omega} \tag{5}$$

where α^* is a function of high Re. In the SST $k-\omega$ model [11], μ_t is given as follows:

$$\mu_t = \frac{\rho k}{\omega} \frac{1}{\max[1/\alpha^*, \Omega F_2/\alpha_1 \omega]} \tag{6}$$

where Ω is a function of mean rate-of-rotation tensor, F_2 is the blending function, and α_1 is a constant. This feature gives the SST $k-\omega$ model an advantage in terms of performance over both the standard $k-\omega$ model and the standard $k-\varepsilon$ model. The RSM

[1]Corresponding author.

Contributed by the Heat Transfer Division of ASME for publication in the JOURNAL OF HEAT TRANSFER. Manuscript received September 4, 2008; final manuscript received February 19, 2009; published online June 25, 2009. Review conducted by Satish G. Kandlikar. Paper presented at the Sixth International Conference on Nanochannels, Microchannels and Minichannels (ICNMM2008), Darmstadt, Germany, June 23–30, 2008.

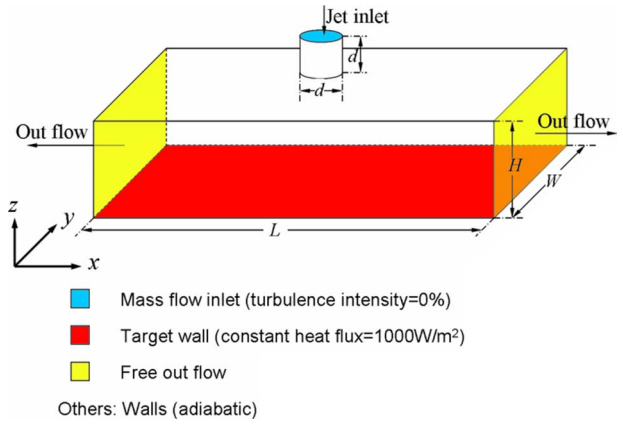

Fig. 1 The physical domain and boundary conditions

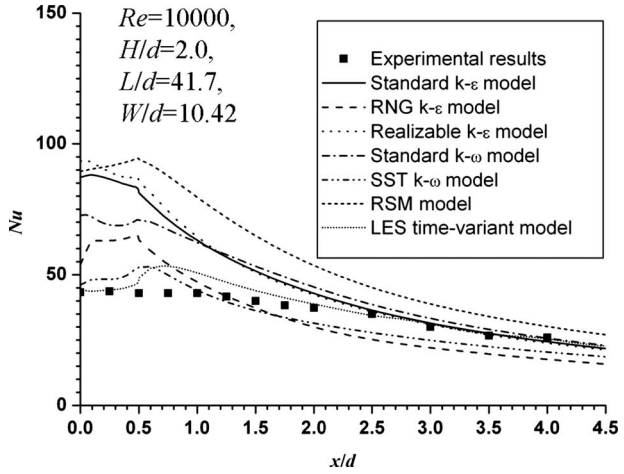

Fig. 2 Local Nusselt number distribution on the positive *x*-axis

model [12] solves exact transport equations for the transport of Reynolds stresses and also includes an additional scale determining equation for ε.

Unlike the $k-\varepsilon$, $k-\omega$, and the RSM models, which are based on the RANS equations, the LES model provides an alternative approach in which large eddies are computed in a time dependent simulation using a set of filtered N–S equations [13].

2.3 Numerical Procedure. The numerical simulations are carried out using computational fluid dynamics (CFD) code FLUENT 6.1.18. GAMBIT 2.0.4 is used to generate mesh for the computational domain, which is a quarter of the real physical geometry due to the symmetry of the problem. Nonuniform hexahedral elements are used for meshing the geometry. Both the radius and the length of impingent hole occupy 30 grid points for all the cases. For the case of $H/d=2.0$, $L/d=41.7$, $W/d=10.42$, the numbers of grid points occupied by the channels in the x, y, and z directions are 160+30 (points occupied by radius of the impingement hole), 80+30 and 90, respectively. The mesh near the walls of the impingement hole and channel is fined to obtain accurate velocity and thermal boundary layers. A study of grid sensitivity is performed. The changes in local temperature on the wall are less than 0.09% when the gird is fined doubly. The numbers of grid points occupied by the rectangular channel in the x, y, and z directions are increased or reduced linearly on the basis of the mesh used.

For the jet discharge, a mass flow inlet boundary is applied, and an outflow boundary is applied to the outlet of the computational domain. At two symmetric sections ($x=0$ and $y=0$), the symmetry type of boundary is specified. The no-slip wall condition is used for all the other boundaries. Hereinto, a constant heat flux of 1000 $\mathrm{W/m^2}$ at the bottom wall, and a zero heat flux on the other walls. In the computation, the mean velocity and temperature were normalized with the velocity and temperature of the jet, respectively. The inlet air property is given as $\rho=1.225$ $\mathrm{kg/m^3}$, $n=0.0242$ W/m K, and $\mu=1.7894\times10^{-5}$ kg/ms. The implicit and segregated solver is used for the solution of the system of governing equations. In the simulations, the wall-adjacent cells within the region where $y^+>1$ are refined; thus, the y^+ values can be limited to less than 28 anywhere for all the cases. The solution is assumed to be converged when the normalized residual of the energy equation is lower than 10^{-6} and the normalized residuals of continuity and other variables are less than 10^{-3}.

3 Results and Discussion

For Re=10,000, $H/d=2.0$, $L/d=41.7$, $W/d=10.42$, the local Nusselt number distribution is simulated. The relative performance of seven different turbulent models is investigated numerically and compared with experimental data [4], which has the maximum 5% deviation on jet Reynolds number and up to 5.81% uncertainty on measured heat transfer parameters. Figure 2 shows that the SST $k-\omega$ and the LES time-variant models give better predictions of flow and heat transfer than the others. The comparison shows that the $k-\varepsilon$, standard $k-\omega$, and RSM have 28–116% errors and give bad predictions. The computational cost and accuracy are summarized as shown in Table 1. Although the LES time-variant model gives excellent results, the computational cost and resources requirement is very high. Therefore, the SST $k-\omega$ model is recommended as the best compromise between the computational cost and accuracy and is used for all of the following simulations.

The effect of W/d on the stagnant point Nusselt number $\mathrm{Nu_{sg}}$ for $H/d=3.0$ and $L/d=50$ is shown in Fig. 3. The Nusselt number increases with Re but decreases with W/d.

Figure 4 shows the effect of L/d on $\mathrm{Nu_{sg}}$ for $H/d=3.0$ and $W/d=10$ at different Reynolds number; the effect is relatively weaker than that of W/d. With increasing W/d, the decrease in $\mathrm{Nu_{sg}}$ is caused by the mixing of recirculated hot air from down-

Table 1 Comparison of different turbulence models for impingement heat transfer

Turbulence models	Computational cost	Accuracy	Error of $\mathrm{Nu_{sg}}$ (versus experiments) (%)
Standard $k-\varepsilon$	Low	Poor	101
RNG $k-\varepsilon$	Low	Poor	28
Realizable $k-\varepsilon$	Low	Poor	116
Standard $k-\omega$	Moderate	Poor	67
SST $k-\omega$	Moderate	Good	7
RSM	Moderate	Poor	107
LES	High	Excellent	4

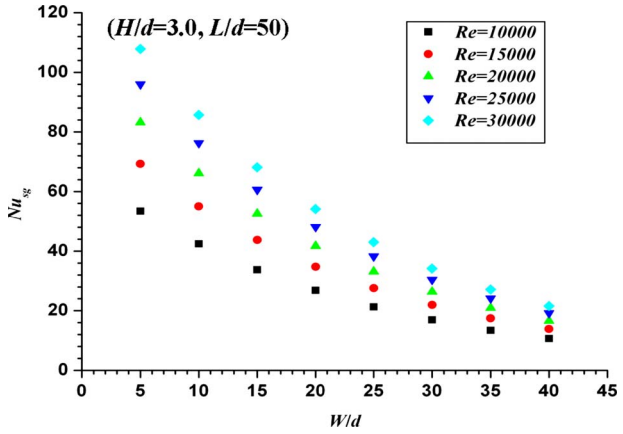

Fig. 3 Effects of W/d on Nu_{sg}

stream with the air near the jet orifice; while with increasing L/d, the decrease in Nu_{sg} is mainly caused by flow-mixing near the stagnation point, which has less effect than the enhancement of flow-mixing near the jet orifice on the impingement heat transfer.

Figure 5 shows that Nu_{sg} decreases with the increase in H/d because a larger jet-to-target spacing allows a longer time of mixing and heat transfer between the cooler jet and the surrounding hot air and therefore decrease the heat transfer near the stagnation point.

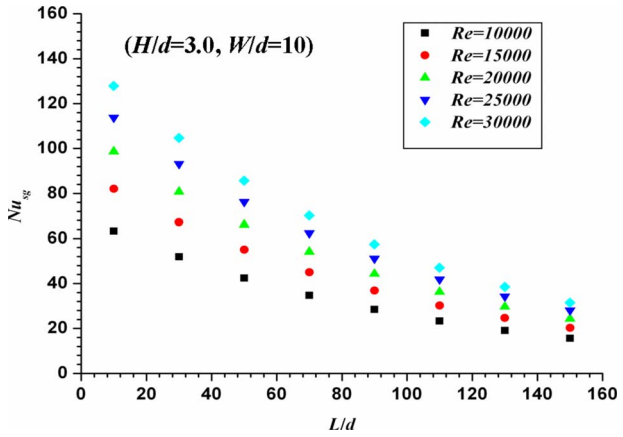

Fig. 4 Effects of L/d on Nu_{sg}

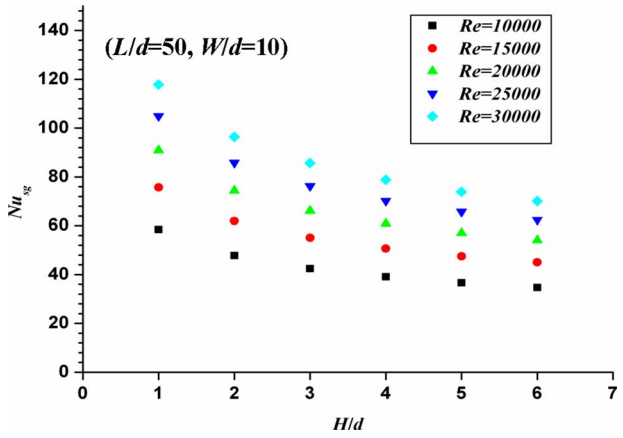

Fig. 5 Effects of H/d on Nu_{sg}

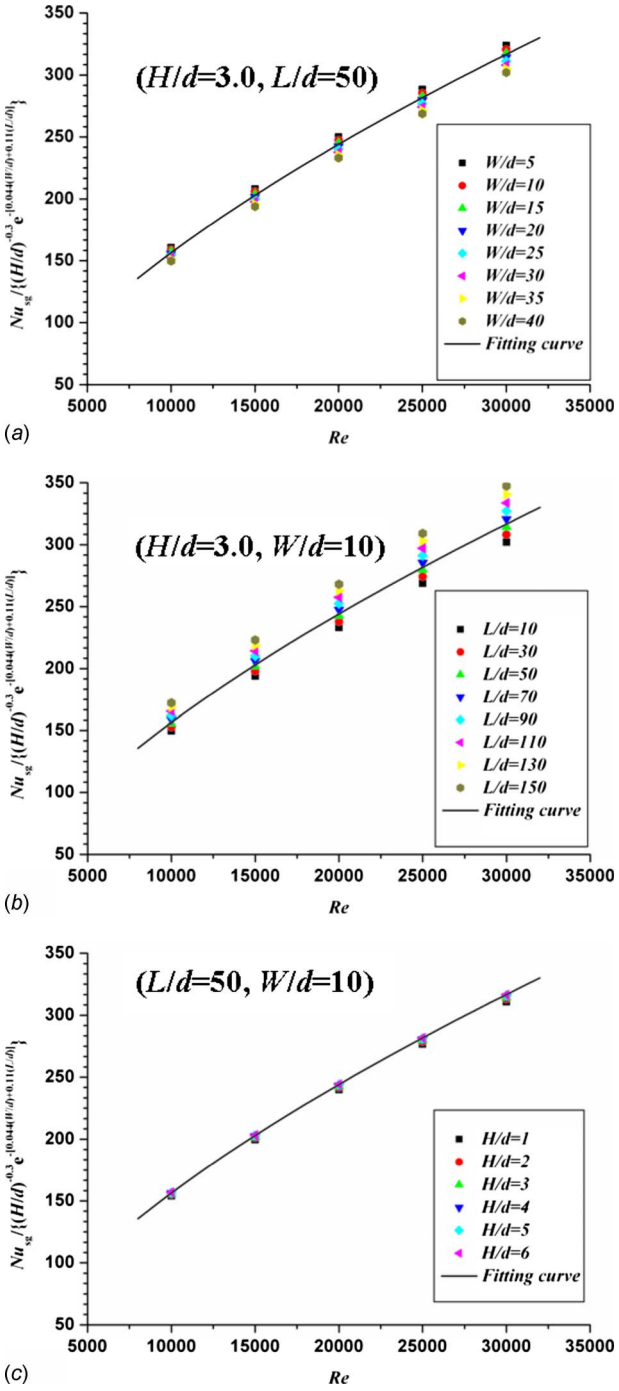

Fig. 6 Comparison of numerical results with correlation: (*a*) $H/d=3.0$, $L/d=50$; (*b*) $H/d=3.0$, $W/d=20$; and (*c*) $L/d=50$, $W/d=20$

The correlation for Nu_{sg} was suggested by experiment [4] as a function of $(H/d)^{-0.3}e^{-[0.044(W/d)+0.011(L/d)]}$, which is validated by the present numerical study, and a new correlation for stagnation point Nusselt number is obtained as

$$Nu_{sg} = 0.423\ Re^{0.642}(H/d)^{-0.3}e^{-[0.044(W/d)+0.011(L/d)]}$$

$$\text{for } 5 \le W/d \le 40, \quad 10 \le L/d \le 150$$

$$1 \le H/d \le 6, \quad 10{,}000 \le Re \le 30{,}000 \tag{7}$$

Figure 6 shows the comparison between numerical results and

the correlation. It is noted that the values of $Nu_{sg}/\{(H/d)^{-0.3}e^{-[0.044(W/d)+0.011(L/d)]}\}$ are approximated well by fitting curve $0.423\ Re^{0.642}$; the maximum errors on Nu_{sg} is of 4.87%, 8.83%, and 1.87% for variable values of W/d, L/d, and H/d, respectively.

4 Conclusions

The relative performance of seven turbulent models for predicting jet impingement flow and heat transfer have been evaluated by comparing the numerical results with benchmark experimental data. The SST $k-\omega$ model is therefore recommended as the best compromise between the computational cost and accuracy. Using the SST $k-\omega$ model, the effects of jet Reynolds number, jet plate length-to-jet diameter ratio, target spacing-to-jet diameter ratio, and jet plate width-to-jet diameter ratio on the local Nusselt number of the target plate are examined. The results show that Nu_{sg} increases with jet Reynolds number, while the increase in parameters such as W/d, H/d, and H/d can all result in the decrease in Nu_{sg}. Moreover, a correlation has been obtained.

Acknowledgment

The work is supported by Siemens Industrial Turbomachinery Ltd. (UK).

Nomenclature

d = jet diameter (m)
h = convective heat transfer coefficient (W/m^2 K)
H = jet plate-to-impingement plate spacing (m)
$\mathbf{I}$ = identity tensor
k = turbulence kinetic energy
L = jet plate length (m)
n = thermal conductivity of air (W/m K)
q = surface heat flux (W/m^2)
Q = volumetric flow rate (m^3/s)
T_{aw} = adiabatic wall temperature (K)
T_j = jet total temperature (K)
T_w = local wall temperature (K)
$\mathbf{u}$ = velocity vector
U = jet mean velocity (m/s)
W = jet plate width or heated surface width (m)
x, y, z = coordinate (m)
y^+ = dimensionless distance, $y^+ = u_\tau y\rho/\mu$

Greek Symbols

α = thermal diffusivity (m^2/s)
μ = dynamic viscosity (kg/ms)
μ_t = turbulent viscosity
ρ = density (kg/m^3)
ε = dissipation rate of turbulence kinetic energy k
ω = specific dissipation rate of turbulence kinetic energy k

Subscripts and Superscripts

aw = adiabatic wall
sg = stagnation point
T = transpose of tensor
w = wall

References

[1] San, J. Y., Huang, C. H., and Shu, M. H., 1997, "Impingement Cooling of a Confined Circular Air Jet," Int. J. Heat Mass Transfer, **40**(6), pp. 1355–1364.
[2] Dano, B. P. E., Liburdy, J. A., and Kanokjaruvijit, K., 2005, "Flow Characteristics and Heat Transfer Performances of a Semiconfined Impinging Array of Jets: Effect of Nozzle Geometry," Int. J. Heat Mass Transfer, **48**(3–4), pp. 691–701.
[3] Wang, S. J., and Mujumdar, A. S., 2005, "A Comparative Study of Five Low Reynolds Number k-ε Models for Impingement Heat Transfer," Appl. Therm. Eng., **25**(1), pp. 31–44.
[4] San, J. Y., and Shiao, W. Z., 2006, "Effects of Jet Plate Size and Plate Spacing on the Stagnation Nusselt Number for a Confined Circular Air Jet Impinging on a Flat Surface," Int. J. Heat Mass Transfer, **49**(19–20), pp. 3477–3486.
[5] Zuckerman, N., and Lior, N., 2005, "Impingement Heat Transfer: Correlations and Numerical Modeling," ASME J. Heat Transfer, **127**(5), pp. 544–552.
[6] Thakre, S. S., and Joshi, J. B., 2000, "CFD Modeling of Heat Transfer in Turbulent Pipe Flows," AIChE J., **46**(9), pp. 1798–1812.
[7] Launder, B. E., and Spalding, D. B., 1972, *Lectures in Mathematical Models of Turbulence*, Academic, London.
[8] Yakhot, V., and Orszag, S. A., 1986, "Renormalization Group Analysis of Turbulence. I. Basic Theory," J. Sci. Comput., **1**(1), pp. 3–51.
[9] Shih, T. H., Liou, W. W., Shabbir, A., Yang, Z. G., and Zhu, J., 1995, "A New k-ε Eddy Viscosity Model for High Reynolds-Number Turbulent Flows," Comput. Fluids, **24**(3), pp. 227–238.
[10] Wilcox, D.C., 1998, *Turbulence Modeling for CFD*, DCW Industries, Inc., La Cacada.
[11] Menter, F. R., 1994, "2-Equation Eddy-Viscosity Turbulence Models for Engineering Applications," AIAA J., **32**(8), pp. 1598–1605.
[12] Launder, B. E., Reece, G. J., and Rodi, W., 1975, "Progress in Development of a Reynolds-Stress Turbulence Closure," J. Fluid Mech., **68**, pp. 537–566.
[13] Galperin, B. A., and Orszag, S. A., 1993, *Large Eddy Simulation of Complex Engineering and Geophysical Flows*, Cambridge University Press, Cambridge, England.

Numerical Analysis of a Two-Dimensional Jet Impinging on an Oscillated Heat Transfer Surface

Koichi Ichimiya
Mechanical Systems Engineering Division,
Interdisciplinary Graduate School of Medicine and Engineering,
University of Yamanashi,
Takeda-4,
Kofu, Yamanashi 400-8511, Japan
e-mail: ichimiya@yamanashi.ac.jp

Shuichi Watanabe
Plant Engineering Division,
Tokyo Gas Engineering Co., Ltd.,
Nishishinjuku 3-7-1,
Shinjuku, Tokyo 163-1018, Japan

Numerical analyses were performed to determine the oscillation effect of an impingement surface on the impingement heat transfer and flow with a confined wall. As a moving boundary problem, two-dimensional governing equations were solved for the Reynolds numbers Re=200 and 500, the Prandtl number Pr=0.71, the dimensionless space between the nozzle and impingement surface H=1.0, and the Strouhal number Sf=0–1.0. Oscillation induced both the enhancement and depression of the local heat transfer. The local heat transfer was improved at a comparatively low frequency due to the flow fluctuation. On the other hand, at a high frequency, it was depressed due to the flow in an upper direction near the impingement surface. The oscillation effect spatially appeared downstream after the impingement.
[DOI: 10.1115/1.3139188]

Keywords: thermal engineering, heat transfer, flow, impingement jets, oscillated surface, numerical analysis

1 Introduction

Impinging jets are often used as a simple method to improve the local heat transfer and mass transfer [1,2]. Most of the impingement surfaces in previous studies have been stationary and smooth. However, there are various kinds of impingement surfaces including inclined or rotating surface and so on. Ichimiya [3] conducted experiments to determine the heat transfer of an oblique impinging circular jet within closely confined walls. Two-dimensional profiles of the local Nusselt number and temperature changed with the jet angle. This produced a peak shift in the local Nusselt number to the minor flow region with a decrease in the angle together with a plateau of the local heat transfer in the major flow region. One major application of jet impingement is the heat removal from a heat engine (for example, gas turbine). The surface oscillates during the working period. Due to the industrial uses for impinging jets on an oscillated surface, extensive research has been conducted to better understand heat transfer characteristics. Heat transfer control by oscillation alone has been performed in several ways. Davidson [4] obtained the heat transfer and flow from a circular cylinder oscillating in an unbounded viscous fluid. The fluid was ejected along the axis of oscillation in the form of a jet, and the heat carried over the surface of the cylinder was swept away along the axis. Momose et al. [5] numerically investigated the influence of horizontal vibrations on the heat transfer from a horizontal cylinder, and showed that the local heat transfer rate depends on the inner vortex for low frequency vibration and the outer vortex for high frequency vibration. The combined heat transfer of an impinging jet and oscillation may lead to useful practical applications. Ichimiya et al. [6] measured the impingement heat transfer characteristics on the oscillated surface in a turbulent region. Their experimental results showed that a heat transfer enhancement was carried out at a low Reynolds number and low frequency, and that the local heat transfer was depressed at a high Reynolds number. However, we found no reports that included a numerical analysis of the combined heat transfer.

In the present research, for a comparison with those results without oscillation, we numerically predicted the basic heat transfer and flow characteristics on a smooth impingement surface with oscillation in a laminar flow region.

2 Description of the Problem

The surface of a heat engine corresponding to an impingement surface is oscillated when impinging jets are applied for heat removal. Impinging jets usually behave in a three-dimensional manner. However, we tried to simplify them to two-dimensional phenomena using a slit-type nozzle and to numerically evaluate the effect of oscillation of an impingement surface on the local heat transfer and flow.

The central axes of the nozzle and the horizontal direction are the Y $(=y/d)$ and X $(=x/d)$ axes, respectively, in the coordinate system (Fig. 1). A confined insulated wall is set on the same level as the exit from the nozzle. The dimensionless exit distance of nozzle is placed at $Le(=\ell e/d)=2$ from the confined wall level to mollify the effect of the wave propagation of the oscillation to the nozzle exit. The velocity distribution and fluid temperature at the nozzle exit have a fully developed laminar distribution and $T=T_o$, respectively. The size of the flow passage is as follows: nozzle width d, length of the flow passage $\ell=15d$, and space between the thermally insulated upper wall and impingement surface h. The impingement surface oscillates as $y=-a\cos(2\pi ft)$, where a, f, and t are amplitude, frequency, and time, respectively, and is heated at $T=T_H$. The confined upper wall is stationary. The actual oscillation of a heat engine ranges from low to high frequencies.

3 Numerical Analysis

Figure 1 shows the coordinate system. The heated smooth impingement surface oscillates vertically, while the confined upper insulated wall is stationary. Therefore, the computational domain expands and contracts, and its shape moves vertically. In the present analysis we applied computational grids, which change with the moving boundary [7]. The dimensionless moving veloc-

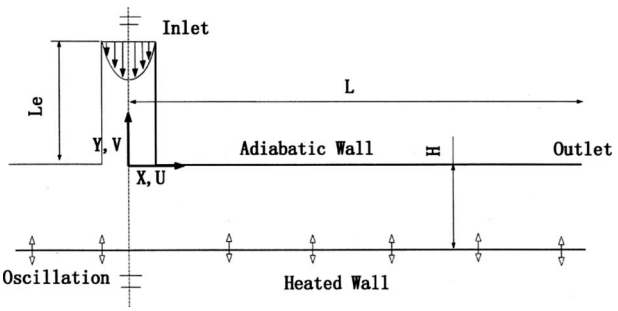

Fig. 1 Coordinate system

Contributed by the Heat Transfer Division of ASME for publication in the JOURNAL OF HEAT TRANSFER. Manuscript received October 29, 2008; final manuscript received April 2, 2009; published online June 25, 2009. Review conducted by Sung Jin Kim. Paper presented at the Japan National Heat Transfer Symposium.

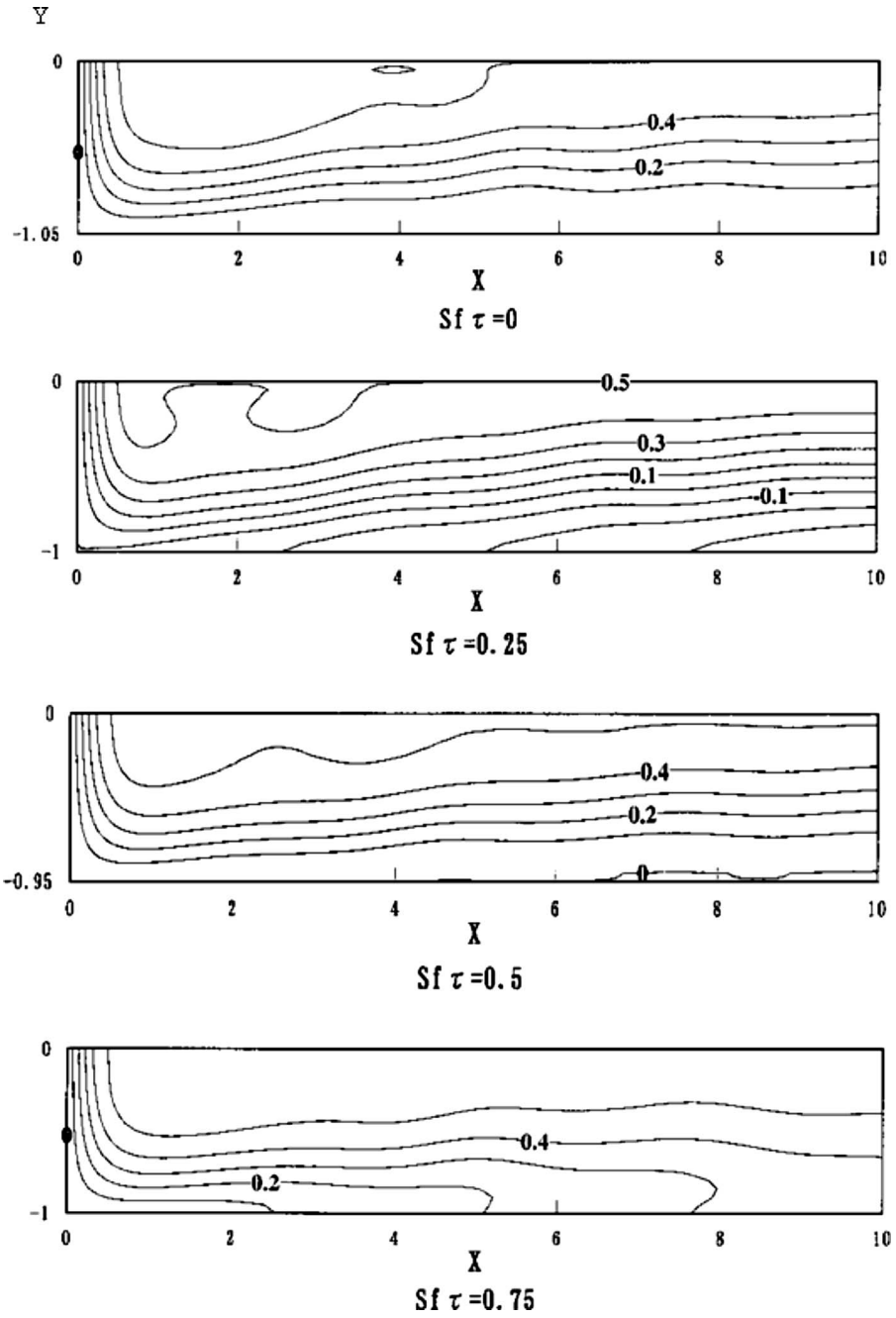

Fig. 2 Dimensionless stream function with oscillation (Re=500, Sf=0.125, *A*=0.05)

ity of each grid is V_G ($=v_g/v_o$), where v_g and v_o are lattice moving speed and average velocity at nozzle exit, respectively. Dimensionless governing equations are as follows:

- conservation equation of mass

$$\frac{dD}{d\tau} + \int_S U \cdot n_x dS + \int_S (V - V_G) n_Y dS = 0$$

- conservation of momentum

$$\frac{d}{d\tau}\int_D U dD + \int_S UU \cdot n_X dS + \int_S U(V - V_G) n_Y dS$$

$$= -\int_S P \cdot n_X dS + \frac{1}{\mathrm{Re}}\int_S \frac{\partial U}{\partial X} n_X dS$$

$$\frac{d}{d\tau}\int_D V dD + \int_S VU \cdot n_X dS + \int_S V(V - V_G) n_Y dS$$

$$= -\int_S P \cdot n_Y dS + \frac{1}{\mathrm{Re}}\int_S \frac{\partial V}{\partial X} n_X dS$$

- conservation of energy

$$\frac{d}{d\tau}\int_D \Theta dD + \int_S \Theta U \cdot n_X dS + \int_S \Theta(V - V_G) n_Y dS$$

$$= \frac{1}{\mathrm{RePr}}\int_S \frac{\partial \Theta}{\partial X} n_X dS + \frac{1}{\mathrm{RePr}}\int_S \frac{\partial \Theta}{\partial Y} n_Y dS$$

where D is the dimensionless control volume, n_X and n_Y are the

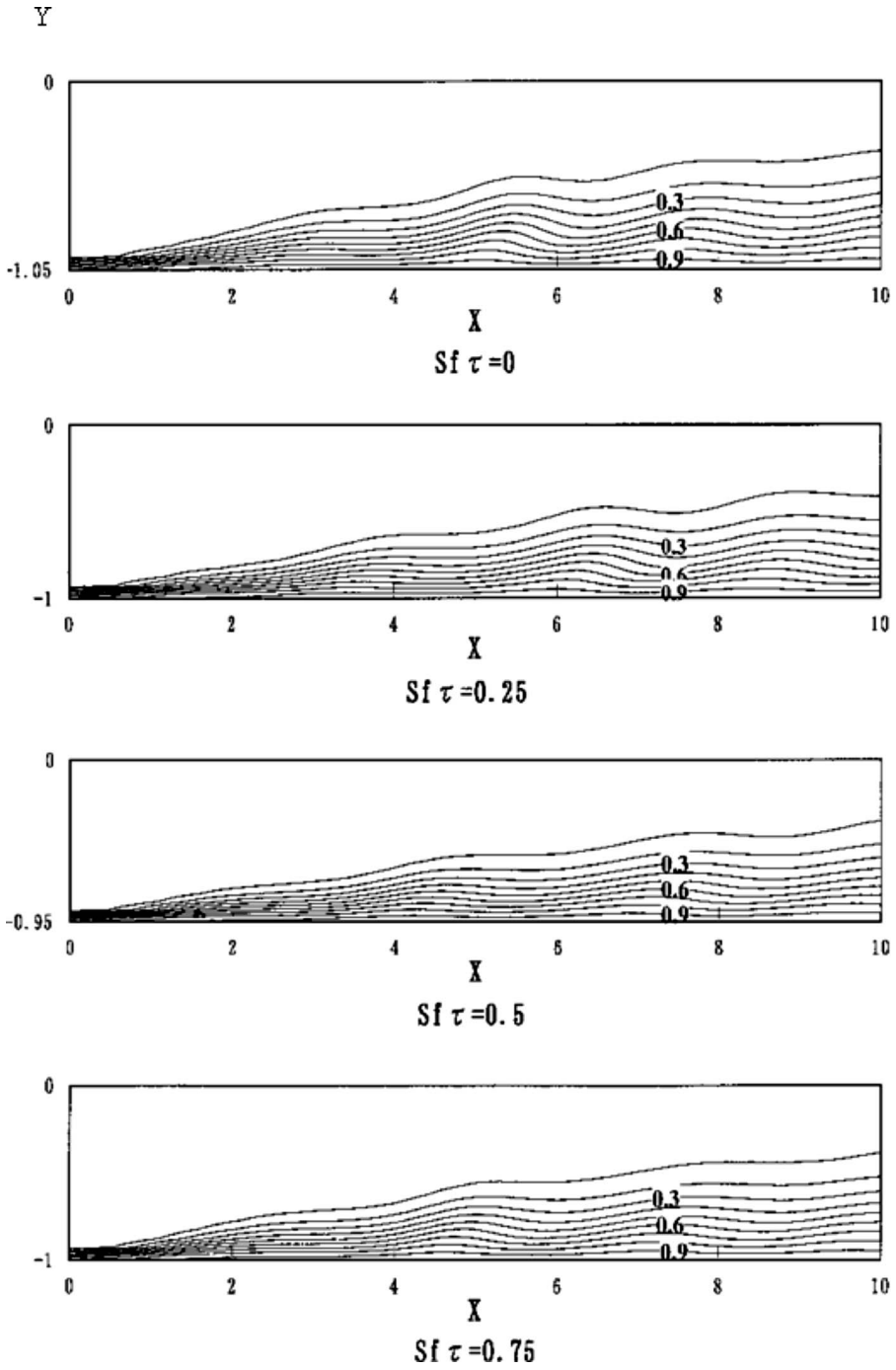

Fig. 3 Temperature field (Re=500, Sf=0.125, A=0.05)

directional cosines, S is the dimensionless surface area of a control volume, U and V are the dimensionless velocities ($=u/v_o$, v/v_o), τ is the dimensionless time ($=tv_o/d$), and Θ is the dimensionless temperature ($=(T-T_o)/(T_H-T_o)$).

In the present analysis, the grids and moving velocities along the Y direction are used because the impingement surface oscillates vertically. The dimensionless moving velocity of a grid, V_G, and dimensionless control volume, D, must satisfy the geometrical conservation written as

$$\frac{dD}{d\tau} - \int_S V_G dS = 0$$

As a dimensionless parameter of frequency, the Strouhal number Sf is defined by fd/v_o. Dimensionless boundary conditions are imposed as follows:

(1) at the nozzle exit ($0 \le X \le 1/2$, $Y=2$); $V=(-3/2)(2X-1)^2$, $U=0$, $\Theta=0$

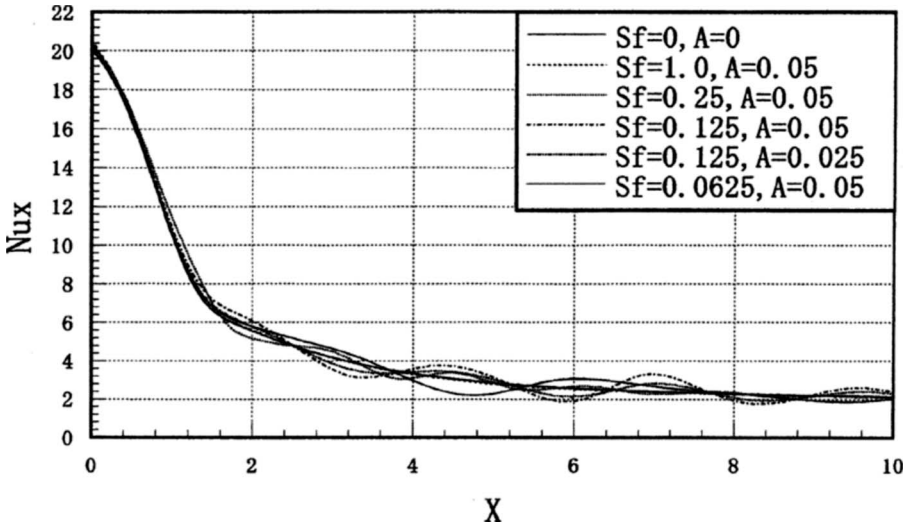

Fig. 4 Local Nusselt number (Re=500, Sfτ=0.25)

(2) on the confined upper wall ($0 \le X \le 15$, $Y=0$); $U=V=0$, $\partial\Theta/\partial Y=0$
(3) on the impingement surface ($0 \le X \le 15$), which oscillates as $Y=-A\cos(2\pi \mathrm{Sf}\tau)$; $U=0$, $V=2\pi A\mathrm{Sf}\sin(2\pi \mathrm{Sf}\tau)$, $\Theta=1$
(4) symmetrical condition (central axis of nozzle) ($X=0$); $U=0$, $\partial V/\partial X=\partial\Theta/\partial X=\partial P/\partial X=0$
(5) at the flow passage exit ($X=15$); $\partial U/\partial X=\partial V/\partial X=\partial\Theta/\partial X=0$, $P=0$

where P is dimensionless pressure $=(p-p_e)/\rho v_o^2$

Governing equations are discretized by using the control volume method in staggered grids. The flow and pressure fields are analyzed using the semi-implicit method for pressure-linked equations (SIMPLE) algorithm [8], and algebra equations are solved using the successive over-relaxation (SOR) method.

The solution domain in the X and Y directions has a dimensionless length of $L=15$ and a dimensionless space from 0.95 to 1.05. Initial grid distance is $\Delta X=\Delta Y=0.05$. The total number of grids is 6400. The grid width, ΔY, changes from 0.0475 to 0.0525 along the Y direction, but the number remains constant. The grid moving velocity of the jth grid from the impingement surface along the Y direction, $(V_G)_j$, is expressed using the grid width adopted at the previous step, ΔY_0

$$(V_G)_j = (V_G)_1 + (j-1)(\Delta Y - \Delta Y_0)/\Delta\tau$$

where

$$(V_G)_1 = \{A\cos[2\pi \mathrm{Sf}(\tau+\Delta\tau)] - A\cos(2\pi \mathrm{Sf}\tau)\}/\Delta\tau$$

where A is dimensionless amplitude $=a/d$.

The time step $\Delta\tau$ depends on the Strouhal number Sf and was determined as $\Delta\tau=0.0008$ due to the numerical stability. A steady solution without oscillation is applied to initial conditions, and the oscillation starts at the lowest position. The computation is iterated until the difference between the arbitrary Nusselt number ($=\alpha d/\lambda$: α is heat transfer coefficient) and that from the previous period is less than 5×10^{-4}, and this state is defined to be metastable. The numerical calculation is carried out at low Reynolds numbers of Re($=v_o d/\upsilon$)=200 and 500, Strouhal numbers of Sf =0, 0.065, 0.125, 0.25, 0.5, and 1.0, a dimensionless space H($=h/d$)=1.0, and the Prandtl number Pr=0.71.

4 Results and Discussions

4.1 Flow Characteristics. Figure 2 shows the dimensionless stream function at a comparatively low frequency of Sf=0.125 at Re=500 and $A=0.05$. The dimensionless stream function is determined by

$$\Psi = -\int VdX$$

The left vertical axis in Fig. 2 indicates the distance from the center of the nozzle in the impinging direction, and the horizontal axis represents the distance along the impingement surface. The horizontal length scale is compressed to half size compared with the vertical distance. One period is divided by four in the product of Sf and τ. Sfτ=0 indicates the lowest position of the heat transfer surface (the impingement surface). At Sfτ=0.25 (one quarter period), the heat transfer surface elevates, and the flow is forced out to the exit. From Sfτ=0.5–0.75, the heat transfer surface drops, and the flow is drawn from the exit of the flow passage. In Fig. 2, near $X=4$, $X=6$, and $X=8$ during the oscillation development, the jet flow overtakes the previous flow due to a deceleration along the flow direction by the drawing flow in previous period and tends to become stagnant. The entire flow fluctuates and affects at the end of stream function on the impingement surface.

4.2 Heat Transfer Characteristics. Figure 3 shows a temperature field corresponding to the flow field in Fig. 2. The horizontal scale is compressed to half size compared with the vertical one. At Sf=0.125 in Fig. 3, the isothermal lines fluctuate periodically after $X=4$, and the space between them changes. The temperature gradient on the heat transfer surface (impingement surface) indicates the local heat flux, showing that it changes periodically along flow direction.

The heat transfer on the impingement surface is represented by the local Nusselt number defined by the following equation:

$$Nu = \alpha d/\lambda = qd/(T_H - T_o)\lambda = -(\partial\Theta/\partial Y)$$

Figure 4 denotes the local Nusselt number for various Strouhal numbers at Sfτ=0.25. The solid line expresses the local Nusselt number without oscillation. Within a half nozzle width of $X=1$, where the jet flow impinges on the heat transfer surface, oscillation does not affect the heat transfer. After the local Nusselt num-

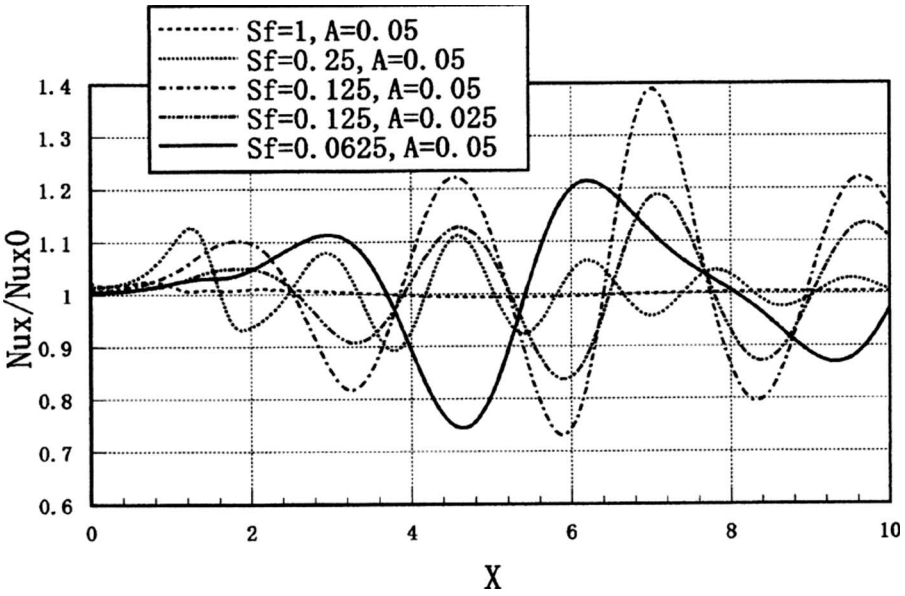

Fig. 5 Local Nusselt number ratio (Re=500, Sf$_\tau$=0.25)

ber takes a peak at $X=0$ and the flow direction changes perpendicularly, the local heat transfer is enhanced or depressed periodically in the downward flow region by the elevation and drop of the heat transfer surface due to oscillation. Particularly, the local Nusselt number fluctuates at Sf=0.125 for $A=0.05$ within the present conditions. Therefore, Fig. 5 shows the degree of heat transfer enhancement and depression by the Nusselt number ratio with and without oscillation, Nu x/Nu xo. In $A=0.05$ and Sf=1, the ratio Nu x/Nu xo is nearly 1.0, and the oscillation effect does not appear at a high frequency. That ratio changes periodically with a decrease in Sf and locally amounts to 1.4 at Sf =0.125. However, it decreases again at Sf=0.0625. This demonstrates that the optimum frequency exists to promote heat transfer among the Reynolds number, the space between the nozzle and impingement surface, and the amplitude. Numerical results show that the oscillation effect appears at a comparatively low frequency. This agrees qualitatively with the experimental results at a high Reynolds number [6]. At a constant Strouhal number, the comparison between a one point-chain line $A=0.05$, and a two-point line $A=0.025$ in Fig. 5 confirms the effectiveness of high amplitude in the heat transfer.

5 Conclusions

The heat transfer and flow characteristics of impinging jets from a slit-type nozzle on a vertically oscillated smooth heat transfer surface were evaluated numerically. Conclusions are as follows.

(1) Oscillation of the impingement surface contributes to both local heat transfer enhancement and depression.
(2) The local heat transfer is enhanced at a comparatively low frequency. The optimum frequency for heat transfer enhancement exists and depends on the Reynolds number, the space between the nozzle and impingement surface, and the amplitude.
(3) Oscillation at high frequency generates a rising flow in the flow passage and depresses the local heat transfer. On the other hand, oscillation at low frequency generates the flow fluctuation in the flow passage and promotes it.
(4) Oscillation effect appears in the downward flow region rather than beneath the nozzle.

References

[1] Jambunathan, K., Lai, E., Moss, M.A., and Button, B.L., 1992, "A Review of Heat Transfer Data for Single Circular Jet Impingement," Int. J. Heat Fluid Flow, **13**(2), pp. 106–115.
[2] Martin, H., 1977, "Heat and Mass Transfer Between Impinging Gas Jets and Solid Surfaces," *Advanced Heat Transfer*, Vol. 13, J. P. Hartnett and T. F. Irvine, eds., Hemisphere, Washington, DC, pp. 1–27.
[3] Ichimiya, K., 1995, "Heat Transfer and Flow Characteristics of an Oblique Turbulent Impinging Jet Within Confined Walls," ASME J. Heat Transfer, **117**, pp. 316–322.
[4] Davidson, B. J., 1973, "Heat Transfer From a Vibrating Circular Cylinder," Int. J. Heat Mass Transfer, **16**, pp. 1703–1727.
[5] Momose, K., Setokawa, T., Asami, Y., and Hosokawa, Y., 1992, "Local Characteristics of Heat Transfer From a Vibrating Cylinder," JSME Int. J., Ser. B, **58**, pp. 3437–3444 (in Japanese).
[6] Ichimiya, K., and Yoshida, Y., 2009, "Oscillation Effect of Impingement Surface on Two-Dimensional Impingement Heat Transfer," ASME J. Heat Transfer, **131**, p. 011701.
[7] Rosenfeld, M., and Kwak, D., 1991, "Time–Dependent Solutions of Viscous Incompressible Flows in Moving Coordinates," Int. J. Numer. Methods Fluids, **13**, pp. 1311–1328.
[8] Patankar, S. V., 1980, *Numerical Heat Transfer and Fluid Flow*, Hemisphere, Washington, DC, pp. 113–134.

Homotopy Analysis for Stagnation Slip Flow and Heat Transfer on a Moving Plate

T. Javed

Z. Abbas[1]

Faculty of Applied Sciences,
Department of Mathematics,
IIU,
Islamabad 44000, Pakistan
e-mail: za_qau@yahoo.com

T. Hayat
Department of Mathematics,
Quaid-I-Azam University,
Islamabad 45320, Pakistan

S. Asghar
Department of Mathematical Sciences,
COMSATS Institute of Information Technology,
H-8, Islamabad 44000, Pakistan

*The development of two-dimensional or axisymmetric stagnation flow of an incompressible viscous fluid over a moving plate with partial slip has been investigated. The effects of partial slip on the flow and heat transfer characteristics are considered. The equations of conservation of mass, momentum, and energy, which govern the flow and heat transfer, are solved analytically using homotopy analysis method. The convergence of the series solution is analyzed explicitly. Comparison of the present homotopy results is made with the existing numerical and asymptotic solution (Wang, 2006, "Stagnation Slip Flow and Heat Transfer on a Moving Plate," Chem. Eng. Sci., **23**, pp. 7668–7672) and an excellent agreement is achieved.* [DOI: 10.1115/1.2952759]

Keywords: stagnation flow, partial slip, heat transfer, homotopy analysis method, moving plate

1 Introduction

The study of viscous flow near a stagnation point dates back to 1911. Hiemenz [1] and Homann [2], respectively, gave the solutions for the two-dimensional and the axisymmetric flows for a Newtonian fluid. Howarth [3] and Pavey [4] obtained the solution for a general three-dimensional flow. Stuart [5] investigated the two-dimensional oblique stagnation flow. Tamada [6] obtained an exact solution of the Navier–Stokes equations for steady two-dimensional oblique stagnation flow. Here numerical discussion of the flow field is highlighted and comparison with an existing theory is presented. Dorrepaal [7] analyzed the two-dimensional but nonorthogonal stagnation-point flow and obtained the similarity solution. For Newtonian fluids the governing problems in two dimensions for stagnation flow have a particularly simple solution, which has been given by Rott [8] but for the axisymmetric flow; Wang [9] solved the governing boundary value problem numerically. Libby [10] studied the three-dimensional stagnation flows on a moving plate. Weidman and Mahalingam [11] considered the axisymmetric stagnation-point flow impinging on an oscillating flat plate with a uniform suction. The solution to the arising problem is developed by two dimensionless groups, namely, the suction parameter and the frequency parameter. Numerical integrations by Runge–Kutta routine yield an exact solution to the Navier–Stokes equation. Recently Baris and Dokuz [12] presented an interesting study for three-dimensional stagnation-point flow of a second grade fluid toward a moving plate. They solved the governing problems numerically by employing the MATLAB solver singular boundary value problem (SBVP).

In all the above mentioned studies, no-slip conditions have been taken into account. However, there are situations wherein this condition does not hold. Mention may be made to the rarefied gases [13], coated surfaces such as Teflon, and resist adhesion. Navier [14] proposed a partial slip condition. In rarefied gases, there is a regime where Navier–Stokes equation holds in the presence of slip condition [13]. On the other hand the solid surface may be rough or porous such that equivalent slip is present [15]. In Ref. [15] the author studied the impinging stagnation flows toward a plate with Navier's slip condition by shooting method. In another paper Wang [16] analyzed the Stokes shear flow over a surface with evenly spaced, finite depth rectangular grooves by employing eigenfunction expansion method and matching. In continuation, Wang [17] discussed the influence of stagnation slip flow on the heat transfer from a moving plate. Numerical and asymptotic solutions of the governing equations are given in Ref. [17].

The present paper investigates the homotopy analysis method (HAM) solution for the problem considered by Wang [17]. Different from perturbative and nonperturbative techniques, the HAM itself provides us with a convenient way to control and adjust the convergence region and the rate of approximation series when necessary. Liao [18] observed that Adomian decomposition method, δ-expansion method, and artificial small parameter method are all limited cases of HAM. HAM is a newly developed, powerful analytic technique, which has already been used by several investigators [19–37] for various interesting problems. Expressions for velocity and temperature fields are developed. The influence of partial slip on the flow and heat transfer characteristics is analyzed through graphs.

2 Statement of the Problem

Let us consider an incompressible, laminar two-dimensional stagnation flow in the $x-z$ plane. The plate is placed at $z=0$ moving with velocities U and V in the x- and y-directions, respectively. In Ref. [17] the dimensionless problem statements for velocity and temperature fields are as follows.

2.1 Two-Dimensional Stagnation Flow

$$f''' + ff'' - f'^2 + 1 = 0 \tag{1}$$

$$g'' + fg' - f'g = 0 \tag{2}$$

$$K'' + fK' = 0 \tag{3}$$

$$\theta'' + \Pr f\theta' = 0 \tag{4}$$

with boundary conditions

$$f'(0) = 1 + \lambda f''(0), \quad g(0) = 1 + \lambda g'(0), \quad K(0) = 1 + \lambda K'(0) \tag{5}$$

$$f'(\infty) = 1, \quad g(\infty) = 0, \quad K(\infty) = 0 \tag{6}$$

$$\theta(0) = 1 + \beta\theta'(0), \quad \theta(\infty) = 0 \tag{7}$$

[1]Corresponding author.

Contributed by the Heat Transfer Division of ASME for publication in the JOURNAL OF HEAT TRANSFER. Manuscript received April 27, 2007; final manuscript received March 9, 2008; published online June 26, 2009. Review conducted by Minking Chyu.

2.2 Axisymmetric Stagnation Flow

$$f''' + 2ff'' - f'^2 + 1 = 0 \tag{8}$$

$$g'' + 2fg' - f'g = 0 \tag{9}$$

$$\theta'' + 2\ \mathrm{Pr}\ f\theta' = 0 \tag{10}$$

with the following boundary conditions:

$$f(0) = 0, \quad f'(0) = 1 + \lambda f''(0), \quad g(0) = 1 + \lambda g'(0) \tag{11}$$

$$f'(\infty) = 1, \quad g(\infty) = 0 \tag{12}$$

$$\theta(0) = 1 + \beta\theta'(0), \quad \theta(\infty) = 0 \tag{13}$$

Here $\lambda = N\rho\sqrt{\nu a}$ is the nondimensional slip factor, $\beta = S\sqrt{a/\nu}$ is the nondimensional thermal slip parameter, ν is the kinematic viscosity, a is the strength of the stagnation flow, ρ is the density, N is the slip constant, S is the constant of proportionality for thermal slip, and Pr is the Prandtl number. In a two-dimensional flow, for an impermeable plate we take $f(0) = 0$.

3 Basic Idea of Homotopy Analysis Method

To describe the basic idea, let us consider the following differential equation:

$$\mathcal{N}[\Phi(x)] = 0 \tag{14}$$

where $\mathcal{N}$ is the nonlinear operator, Φ is an unknown dependent function, and x denotes the independent function. For simplicity, we ignore all the boundary or initial conditions, which can be treated similarly. To generalize the traditional homotopy method, Liao [18] constructed the zero-order deformation equation

$$(1-p)\mathcal{L}[\hat{\Phi}(x;p) - \Phi_0(x)] = p\hbar\mathcal{N}[\hat{\Phi}(x;p)] \tag{15}$$

where $p \in [0,1]$ is an embedding parameter, $\hbar$ is a nonzero-auxiliary parameter, $\mathcal{L}$ is an auxiliary linear parameter, and $\Phi_0(x)$ is an initial approximation, which must satisfy all the boundary conditions. It is important that one has great freedom to choose the initial approximation and auxiliary linear operator. When $p = 0$ and $p = 1$, it satisfies

$$\hat{\Phi}(x;0) - \Phi_0(x) \quad \text{and} \quad \hat{\Phi}(x;1) - \Phi(x) \tag{16}$$

respectively. Thus as p increases from 0 to 1, the solution $\hat{\Phi}(x;p)$ varies from initial approximation $\Phi_0(x)$ to the solution $\Phi(x)$. Expanding $\hat{\Phi}(x;p)$ in Taylor series with respect to p, we have

$$\hat{\Phi}(x;p) = \Phi_0(x) + \sum_{m=1}^{\infty} \Phi_m(x)p^m, \quad \Phi_m(x) = \left.\frac{1}{m!}\frac{\partial^m\hat{\Phi}(x,p)}{\partial p^m}\right|_{p=0} \tag{17}$$

Differentiating Eq. (2) m times with respect to the embedding parameter p and dividing by $m!$ and then finally setting $p = 0$, we have the mth order deformation equation as

$$\mathcal{L}[\Phi_m(\eta) - \chi_m\Phi_{m-1}(\eta)] = \hbar\mathcal{R}_m(\Phi_{m-1}) \tag{18}$$

where

$$\mathcal{R}_m(\Phi_{m-1}) = \left.\frac{1}{(m-1)!}\frac{\partial^{m-1}\hat{\Phi}(x,p)}{\partial p^{m-1}}\right|_{p=0} \tag{19}$$

$$\chi_m = \begin{cases} 0, & m \le 1 \\ 1, & m > 1 \end{cases} \tag{20}$$

which can easily be solved by using symbolic computation software such as MAPLE and MATHEMATICA. If the auxiliary linear operator, the initial approximation, and the auxiliary parameter $\hbar$ are properly chosen, the series (17) converges at $p = 1$, one has

$$\Phi(x) = \Phi_0(x) + \sum_{m=1}^{\infty} \Phi_m(x) \tag{21}$$

which must be one of the solutions of the original nonlinear equation (Eq. (14)).

4 HAM Solution

Employing the basic idea of HAM given in Sec. 3, the series solutions can be written as follows.

4.1 Two-Dimensional Stagnation Flow. For details the reader may be referred to Ref. [18]. The velocity and temperature distributions $f(\eta)$, $g(\eta)$, $K(\eta)$, and $\theta(\eta)$ can be expressed by the set of base functions

$$\{\eta^k \exp(-n\eta) | k \ge 0, n \ge 0\}$$

in the form

$$f(\eta) = a_{0,0}^0 + \sum_{n=0}^{\infty}\sum_{k=0}^{\infty} a_{m,n}^k \eta^k \exp(-n\eta)$$

$$g(\eta) = \sum_{n=0}^{\infty}\sum_{k=0}^{\infty} b_{m,n}^k \eta^k \exp(-n\eta) \tag{22}$$

$$K(\eta) = \sum_{n=0}^{\infty}\sum_{k=0}^{\infty} c_{m,n}^k \eta^k \exp(-n\eta)$$

$$\theta(\eta) = \sum_{n=0}^{\infty}\sum_{k=0}^{\infty} d_{m,n}^k \eta^k \exp(-n\eta) \tag{23}$$

in which $a_{m,n}^k$, $b_{m,n}^k$, $c_{m,n}^k$, and $d_{m,n}^k$ are constants. Here we choose the initial approximations $f_0(\eta)$, $g_0(\eta)$, $K_0(\eta)$, and $\theta_0(\eta)$ of $f(\eta)$, $g(\eta)$, $K(\eta)$, and $\theta(\eta)$ as

$$f_0(\eta) = \eta - \frac{1}{1+\lambda}(1 - \exp(-\eta)), \quad g_0(\eta) = \frac{\exp(-\eta)}{1+\lambda} \tag{24}$$

$$K_0(\eta) = \frac{\exp(-\eta)}{1+\lambda}, \quad \theta_0(\eta) = \frac{\exp(-\eta)}{1+\beta} \tag{25}$$

and the auxiliary linear operators $\mathcal{L}_1$ and $\mathcal{L}_2$ are

$$\mathcal{L}_1[\hat{f}(\eta;p)] = \frac{\partial^3\hat{f}(\eta;p)}{\partial\eta^3} - \frac{\hat{f}(\eta;p)}{\partial\eta}$$

$$\mathcal{L}_2[\hat{f}(\eta;p)] = \frac{\partial^2\hat{f}(\eta;p)}{\partial\eta^2} - \hat{f}(\eta;p) \tag{26}$$

with the properties

$$\mathcal{L}_1[C_1 + C_2\exp(\eta) + C_3\exp(-\eta)] = 0$$

$$\mathcal{L}_2[C_4\exp(\eta) + C_5\exp(-\eta)] = 0 \tag{27}$$

in which C_i $(i = 1,2,\ldots,5)$ are arbitrary constants. Then the series solutions are

$$f(\eta) = f_0(\eta) + \sum_{m=1}^{\infty} f_m(\eta), \quad g(\eta) = g_0(\eta) + \sum_{m=1}^{\infty} g_m(\eta) \tag{28}$$

$$K(\eta) = K_0(\eta) + \sum_{m=1}^{\infty} K_m(\eta), \quad \theta(\eta) = \theta_0(\eta) + \sum_{m=1}^{\infty} \theta_m(\eta) \tag{29}$$

4.2 Axisymmetric Stagnation Flow. The series solutions for axisymmetric stagnation flow are as follows:

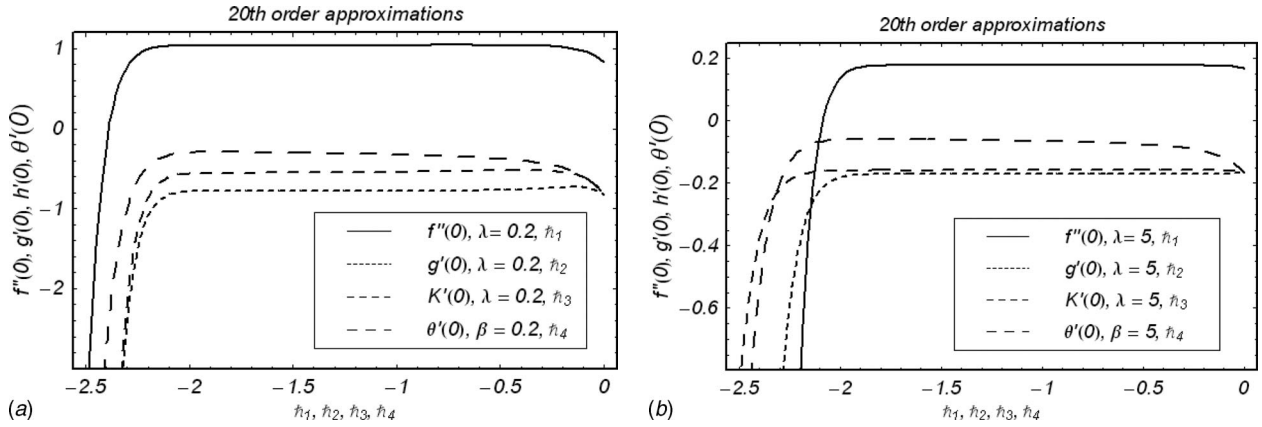

Fig. 1 $\hbar$-curves: (*a*) For two-dimensional stagnation flow and (*b*) for axisymmetric stagnation flow

$$f(\eta) = e^0_{0,0} + \sum_{n=0}^{\infty}\sum_{k=0}^{\infty} e^k_{m,n}\eta^k \exp(-n\eta) \tag{30}$$

$$g(\eta) = \sum_{n=0}^{\infty}\sum_{k=0}^{\infty} f^k_{m,n}\eta^k \exp(-n\eta), \quad \theta(\eta) = \sum_{n=0}^{\infty}\sum_{k=0}^{\infty} g^k_{m,n}\eta^k \exp(-n\eta) \tag{31}$$

where $e^k_{m,n}$, $f^k_{m,n}$, and $g^k_{m,n}$ are coefficients and the series solutions for axisymmetric stagnation flow are as follows:

$$f(\eta) = f_0(\eta) + \sum_{m=1}^{\infty} f_m(\eta), \quad g(\eta) = g_0(\eta) + \sum_{m=1}^{\infty} g_m(\eta)$$

$$g(\eta) = g_0(\eta) + \sum_{m=1}^{\infty} g_m(\eta), \quad \theta(\eta) = \theta_0(\eta) + \sum_{m=1}^{\infty} \theta_m(\eta) \tag{32}$$

5 Convergence of the HAM Solution

The series in Eqs. (28), (29), and (32) are the solutions of the considered problems for two-dimensional and axisymmetric stagnation flow, respectively, if one guarantees the convergence of these series solutions. As pointed out by Liao [18] the convergence and rate of approximation for the HAM solution strongly depend on $\hbar$. The admissible range of $\hbar$ is the region for which $\hbar$-curve is horizontal. By drawing the different order of approximation of the solution for $\hbar$-curve (Fig. 1) we can easily observe that a particular range of $\hbar$-curve is retained. That is, different order of approximation does not change the admissible range for $\hbar$-curve. Each value of $\hbar$ from the admissible range of $\hbar$-curve produces a convergent solution but with a different rate of convergence [18]. The most appropriate value of $\hbar$ is the value from admissible range for which the solution converges most rapidly. Similarly we can find different $\hbar$-curves for different values of the parameter involved in the equations and we can choose the most appropriate value of $\hbar$ for each different value of the parameter. In order to obtain the admissible value of $\hbar$ for the present problems, the $\hbar$-curves are plotted for 20th order of approximations by taking $\lambda = \beta = 0.2$. It can be easily seen from Figs. 1(*a*) and 1(*b*) that the range for the admissible value of $\hbar$ is $-2 \le \hbar_{1,2,3,4,5,6,7} < -0.1$. The presented calculations clearly indicate that the series (28), (29), and (32) converge rapidly for the whole region of η when $\hbar_{1,2,3,5,6} = -1$ and $\hbar_{4,7} = -0.5$.

6 Results and Discussion

In this section our interest lies in the physical interpretation of slip (λ) and thermal slip (β) parameters For this purpose we plotted Figs. 2 and 3. Both cases (two dimensional and axisymmetric) are considered and the influence of λ and β on the temperature distribution is seen for 10th order of approximations. Here, the influence of thermal slip parameter β on $-\theta'(0)$ versus the slip λ is analyzed through Fig. 2 when Pr=7. This figure depicts that $-\theta'(0)$ decreases when β is increased. It is also noted from this figure that for small values of Pr the magnitude of $-\theta'(0)$ decreases. Figure 3 depicts that for axisymmetric flow the effects of β on $-\theta'(0)$ are similar to the case of a two-dimensional flow.

Tables 1 and 2 are made to see the effects of λ on the wall stresses $f''(0)$, $g'(0)$, and $K'(0)$ in two-dimensional and axisymmetric flows. These tables also provide the comparison between numerical, asymptotic, and HAM solutions, respectively. Tables 1 and 2 show that the magnitude of $f''(0)$, $g'(0)$, and $K'(0)$ is de-

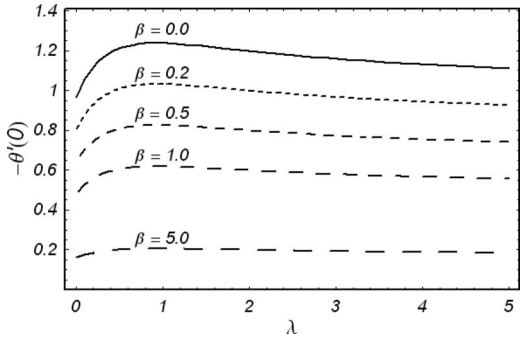

Fig. 2 Effects of thermal slip parameter β on $-\theta'(0)$ ($\hbar = -0.5$, Pr=7) for two-dimensional flow

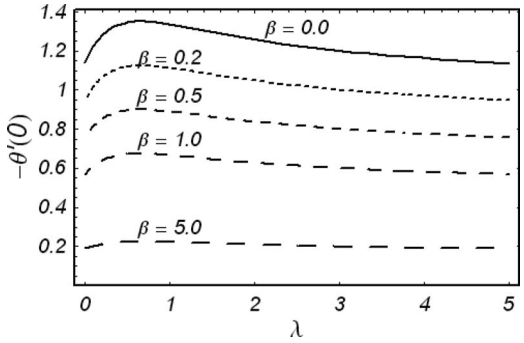

Fig. 3 Effects of thermal slip parameter β on $-\theta'(0)$ ($\hbar = -0.5$) for axisymmetric flow at Pr=7

Table 1 Comparison of initial values for various slip factors λ for numerical solution, asymptotic values [17], and HAM solution in the case of a two-dimensional stagnation flow

	Numerical solution (asymptotic values)			HAM solution		
λ	$f''(0)$	$g'(0)$	$K'(0)$	$f''(0)$	$g'(0)$	$K'(0)$
0	1.23259	−0.81130	−0.57047	1.23259	−0.81130	−0.57047
0.2	1.04259	−0.77521	−0.55440	1.04259	−0.77521	−0.55440
0.5	0.82148	−0.67196	−0.50283	0.82148	−0.67196	−0.50283
1	0.59346	−0.52189	−0.41618	0.59346	−0.52189	−0.41618
2	0.37589	−0.34911	−0.29951	0.37589	−0.34911	−0.29951
5	0.17726 (0.1749)	−0.17163 (−0.1681)	−0.15897 (−0.1499)	0.17726	−0.17163	−0.15897
10	0.094036 (0.09202)	−0.092485 (−0.09202)	−0.088712 (−0.08747)	0.094036	−0.092485	−0.088712
20	0.048472 (0.048433)	−0.048065 (−0.048005)	−0.047030 (−0.046867)	0.048472	−0.048065	−0.047030
50	0.019752 (0.019749)	−0.019685 (−0.019681)	−0.019509 (−0.019499)	0.019752	−0.019685	−0.019509
∞	0 (0)	0 (0)	0 (0)	0	0	0

Table 2 Comparison of initial values for various slip factors λ for numerical solution, asymptotic values [17], and HAM solution in the case of axisymmetric stagnation flow

	Numerical solution (asymptotic values)		HAM solution	
λ	$f''(0)$	$g'(0)$	$f''(0)$	$g'(0)$
0	1.311938	−0.93873	1.311951	−0.93874
0.2	1.11097	−0.88766	1.11098	−0.88770
0.5	0.86688	−0.74987	0.86619	−0.74988
1	0.61730	−0.56453	0.61730	−0.56453
2	0.38526	−0.36643	0.38526	−0.36643
5	0.17928 (0.1774)	−0.17549 (−0.1734)	0.17928	−0.17549
10	0.094597 (0.09436)	−0.093568 (−0.09324)	0.094597	−0.093568
20	0.048620 (0.04859)	−0.048352 (−0.04831)	0.048620	−0.048352
50	0.019776 (0.019774)	−0.019732 (−0.019730)	0.019776	−0.019732
∞	0 (0)	0 (0)	0	0

creased as λ increases and finally goes to zero when $\lambda \to \infty$. These tables further provide an excellent agreement between the numerical, asymptotic, and HAM solutions.

7 Concluding Remarks

In the present analysis, we study the stagnation flow of viscous fluid and heat transfer in two-dimensional and axisymmetric flows. The governing equations are solved analytically using HAM. It is found that the temperature field $-\theta'(0)$ is decreased when β increases and Pr decreases. However, $-\theta'(0)$ is larger for axisymmetric flow when compared with the two-dimensional flow. It is also worth mentioning that the HAM solution is in excellent agreement with the numerical and asymptotic solutions [17].

Acknowledgment

The authors are grateful to a reviewer for his/her valuable comments. The authors are also grateful to Pakistan Academy of Sciences for the financial support.

Nomenclature

u, v, w = velocities in x-, y-, z-direction
x, y, z = spatial coordinates
a = the strength of stagnation flow
U, V = constant velocities
p^*, p_0 = pressure and stagnation pressure
p = embedding parameter
$\mathcal{L}_1, \mathcal{L}_2$ = auxiliary linear operators
$\mathcal{N}_{1\ldots7}$ = nonlinear operators
$\hbar_{1\ldots7}$ = nonzero-auxiliary parameters
f, f', g, K = real functions
η = similarity variable
μ = dynamic viscosity
ν = kinematic viscosity
ρ = density
λ = nondimensional slip factor
N = slip constant
β = thermal slip parameter
S = constant of proportionality

References

[1] Hiemenz, K., 1911, "Die Grenzschicht Neinem in den Gleichförmigen Flüssigkeitsstrom Eingetauchten Geraden Kreiszylinder," Dinglers Polytechniches Journal, **326**, pp. 321–410.
[2] Homann, F., 1936, "Der Einfluss Grosser Zähigkeit bei der Strömung um den Zylinder und um die Kugel," Z. Angew. Math. Mech., **16**, pp. 153–164.
[3] Howarth, L., 1951, "The Boundary Layer in Three-Dimensional Flow, Part II: The Flow Near a Stagnation Point," Philos. Mag., **42**, pp. 1433–1440.
[4] Davey, A., 1961, "Boundary Layer Flow at a Saddle Point of Attachment," J. Fluid Mech., **10**, pp. 593–610.
[5] J. T. Stuart, 1959, "The Viscous Flow Near a Stagnation Point When the External Flow has Uniform Vorticity," J. Aerosp. Sci., **26**, pp. 124–125.
[6] Tamada, K., 1979, "Two-Dimensional Stagnation Point Flow Impinging Obliquely on a Plane Wall," J. Phys. Soc. Jpn., **46**, pp. 310–311.
[7] Dorrepaal, J. M., 1986, "An Exact Solution of the Navier-Stokes Equation Which Describes Non-Orthogonal Stagnation-Point Flow in Two Dimensions," J. Fluid Mech., **163**, pp. 141–147.
[8] Rott, N., 1956, "Unsteady Viscous Flow in the Vicinity of a Stagnation Point," Q. Appl. Math., **13**, pp. 444–451.
[9] Wang, C. Y., 1973, "Axisymmetric Stagnation Flow Towards a Moving Plate," AIChE J., **19**, pp. 1080–1081.
[10] Libby, P. A., 1974, "Wall Shear at a Three-Dimensional Stagnation Point With a Moving Wall," AIAA J., **12**, pp. 408–409.
[11] Weidman, P. D., and Mahalingam, S., 1997, "Axisymmetric Stagnation Point Flow Impinging on a Transversely Oscillating Plate With Suction," J. Eng. Math., **31**, pp. 305–318.
[12] Baris, S., and Dokuz, M. S., 2006, "Three-Dimensional Stagnation Point Flow of a Second Grade Fluid Towards a Moving Plate," Int. J. Eng. Sci., **44**, pp. 49–58.
[13] Shairpov, F., and Selezev, V., 1998, "Data on Internal Rarefied Gas Flows," J. Phys. Chem. Ref. Data, **27**, pp. 657–706.

[14] Navier, C. L. M. H., 1827, "Sur les lois du Mouvement des Fluides," Mem. Acad. Sci. Inst. Fr., **6**, pp. 389–440.
[15] Wang, C. Y., 2003, "Stagnation Flow With Slip: Exact Solution of the Navier-Stokes Equations," Z. Angew. Math. Phys., **54**, pp. 184–189.
[16] Wang, C. Y., 2003, "Flow Over a Surface With Parallel Grooves," Phys. Fluids, **15**, pp. 1114–1121.
[17] Wang, C. Y., 2006, "Stagnation Slip Flow and Heat Transfer on a Moving Plate," Chem. Eng. Sci., **61**, pp. 7668–7672.
[18] Liao, S. J., 2003, *Beyond Perturbation: Introduction to Homotopy Analysis Method*, Chapman and Hall, London/CRC, Boca Raton, FL.
[19] Liao, S. J., 2004, "On the Homotopy Analysis Method for Nonlinear Problems," Appl. Math. Comput., **147**, pp. 499–513.
[20] Liao, S. J., and Cheung, K. F., 2003, "Homotopy Analysis of Nonlinear Progressive Waves in Deep Water," J. Eng. Math., **45**, pp. 105–116.
[21] Wu, W., and Liao, S. J., 2005, "Solving Solitary Waves With Discontinuity by Means of Homotopy Analysis Method," Chaos, Solitons Fractals, **26**, pp. 177–185.
[22] Liao, S. J., 1999, "A Uniformly Valid Analytic Solution of 2D Viscous Flow Past a Semi-Infinite Flat Plate," J. Fluid Mech., **385**, pp. 101–128.
[23] Tan, Y., Xu, H., and Liao, S. J., 2007, "Explicit Series Solution of Travelling Waves With a Front of Fisher Equation," Chaos, Solitons Fractals, **31**, pp. 462–472.
[24] Liao, S. J., 2006, "An Analytic Solution of Unsteady Boundary-Layer Flows Caused by an Impulsively Stretching Plate," Commun. Nonlinear Sci. Numer. Simul., **11**, pp. 326–339.
[25] Liao, S. J., 2005, "Comparison Between the Homotopy Analysis Method and Homotopy Perturbation Method," Appl. Math. Comput., **169**, pp. 1186–1194.
[26] Abbasbandy, S., 2008, "The Application of Homotopy Analysis Method to Nonlinear Equations Arising in Heat Transfer," Phys. Lett. A, **360**, pp. 109–113.
[27] Hayat, T., and Khan, M., 2005, "Homotopy Solution for a Generalized Second Grade Fluid Past a Porous Plate," Nonlinear Dyn., **42**, pp. 395–405.
[28] Hayat, T., and Abbas, Z., 2008, "Heat Transfer Analysis on the MHD Flow of a Second Grade Fluid in a Channel With Porous Medium," Chaos, Solitons Fractals, **38**, pp. 556–567.
[29] Hayat, T., Abbas, Z., and Javed, T., 2008, "Mixed Convection Flow of a Micropolar Fluid Over a Non-Linearly Stretching Sheet," Phys. Lett. A, **372**, pp. 637–647.
[30] Hayat, T., and Sajid, M., 2007, "On Analytic Solution for Thin Film Flow of a Fourth Grade Fluid Down a Vertical Cylinder," Phys. Lett. A, **361**, pp. 316–322.
[31] Hayat, T., Abbas, Z., and Sajid, M., 2007, "On the Analytic Solution of MHD Flow of a Second Grade Fluid Over a Shrinking Sheet," ASME J. Appl. Mech., **74**, pp. 1165–1171.
[32] Hayat, T., Khan, M., and Ayub, M., 2004, "Couette and Poiseuille Flows of an Oldroyd 6-Constant Fluid With Magnetic Field," J. Math. Anal. Appl., **298**, pp. 225–244.
[33] Hayat, T., Abbas, Z., and Sajid, M., 2006, "Series Solution for the Upper-Convected Maxwell Fluid Over a Porous Stretching Plate," Phys. Lett. A, **358**, pp. 396–403.
[34] Sajid, M., Hayat, T., and Asghar, S., 2006, "On the Analytic Solution of the Steady Flow of a Fourth Grade Fluid," Phys. Lett. A, **355**, pp. 18–26.
[35] Abbas, Z., Sajid, M., and Hayat, T., 2006, "MHD Boundary-Layer Flow of an Upper-Convected Maxwell Fluid in a Porous Channel," Theor. Comput. Fluid Dyn., **20**, pp. 229–238.
[36] Hayat, T., Abbas, Z., Sajid, M., and Asghar, S., 2007, "The Influence of Thermal Radiation on MHD Flow of a Second Grade Fluid," Int. J. Heat Mass Transfer, **50**, pp. 931–941.
[37] Sajid, M., Hayat, T., and Asghar, S., 2007, "Comparison of the HAM and HPM Solutions of Thin Film Flow of Non-Newtonian Fluids on a Moving Belt," Nonlinear Dyn., **50**, pp. 27–35.